UNIVERSITY OF BIRMINGHAM

Radiation Damage in Xenotime: An Atomistic Modelling and X-ray Total Scattering Study

by

Geoffrey Cutts

A thesis submitted to
the University of Birmingham
for the degree of
Doctor of Philosophy

The School of Chemistry
College of Engineering and Physical Sciences
The University of Birmingham
December 2016

Abstract

Understanding radiation damage processes within nuclear waste forms is crucial to gain an insight into their long term stability. Zircon and xenotime represent two candidate ceramic waste forms for the disposal of high level waste. Though these phases are isostructural, they exhibit very different responses to radiation damage with natural samples of zircon regularly found to be metamict. Xenotime on the other hand is rarely found to be metamict, demonstrating superior resistance to the accumulation of radiation damage.

As such this thesis focuses on understanding radiation damage processes due to α-decay events in the xenotime structure. This was achieved through the development of novel atomistic potentials which were empirically derived using a reverse Monte Carlo fitting routine. This routine was developed throughout the course of this work and has proved valuable in fitting a variety of transferable potential across multiple phases. These potentials were validated using morphological predictions which showed very strong agreement with the crystal morphologies observed in naturally occurring samples of xenotime and zircon. The low index non-polar surfaces have been modelled, taking into account micro-faceting which was shown to have a profound impact on the relative surface energies.

Intrinsic defects were modelled within the xenotime lattice using a grid search methodology which identified a variety of different defect configurations. It is valuable to consider not only the lowest energy defects, but a wide range of defects which may be present to a lesser or greater extent within radiation damage simulations. The binding energies were calculated for many of these defects to gain insight into the clustering behaviour. Extrinsic defects were also investigated for the substitution of a selection of

lanthanide elements onto the isovalent yttrium site. The solution energies were calculated and found to be relatively unfavourable, especially for the lanthanides with larger atomic radii which generally adopt the monazite orthophosphate structure.

Molecular dynamics simulations were utilised to model damage cascades within xenotime and zircon to compare and contrast the type of damage accumulated during an α-decay event. Though the potentials used for these phases were not from a consistent set, clear differences were observed in the distributions of defects and indeed the polymerisation of the tetrahedral units which may contribute to the observed differences in the radiation resistance of these materials. A method for determining the threshold displacement energy for each element within xenotime was developed utilising the Fibonacci lattice. The resulting values showed good agreement with literature sources and may be of use in future experimental studies.

Finally samples of xenotime which had been irradiated with swift heavy ions were investigated by analysing the X-ray pair distribution function (PDF). Unfortunately these samples contained only a small fraction of damaged material which was not identifiable using this method. A fission track simulation was performed to help inform the experiment as to the type of damage which may be present. The ordering of strontium atoms within mixed Ca/Sr fluorapatite samples was also investigate using X-ray PDF analysis. A range of concentrations and synthesis methods were used, however it was not possible to quantify the degree of ordering and alternative modelling techniques may be required to analyse the data in more detail.

Acknowledgements

Firstly I would very much like to thank my supervisors Dr. Joseph Hriljac and Dr. Mark Read. They have encouraged my ideas and creativity throughout this work whilst keeping me focussed. They have supported me through the challenging times and I thank them for the opportunity they gave me. I would like to thank both the former and present members of the Hriljac and Read groups for the interesting conversation about work, amongst other things. Similarly I would like to thank the members of the solid state chemistry group on the fifth floor for making my time studying one I will fondly remember.

I would especially like to thank Evin for giving up her time to help with data collection at Diamond, I know it was a hard slog. One of the turning points in my work came about after the MRS conference in Boston. This was an enlightening conference and I would like to thank Joe, Sav and George for all the laughs along the way. It will be the last time I try to do something nice for Sav and I hope he forever more remembers his T-pass. My time would not have been the same without George Day and Matt Howard. I don't think there are words to describe the impact they have had on my work, we had some great times and some very abstract conversations.

I would like thank my family for their continued support and words of encouragement like "Oh, you're still doing that" and "just write it". I would like to thank Dr. Julie Rutter who has been a constant help throughout the four years, providing moral support and lots of encouragement. Thanks for listening to my many hair-brained ideas. I would like to thank Dave and Spartacus the cats for 'helping' and in no way distracting me from my work, especially during Skype meetings.

Lastly I would like to thank the EPSRC and the University of Birmingham for funding, BlueBEAR for access to the university supercomputer and Diamond Light Source for accepting my beam time proposals.

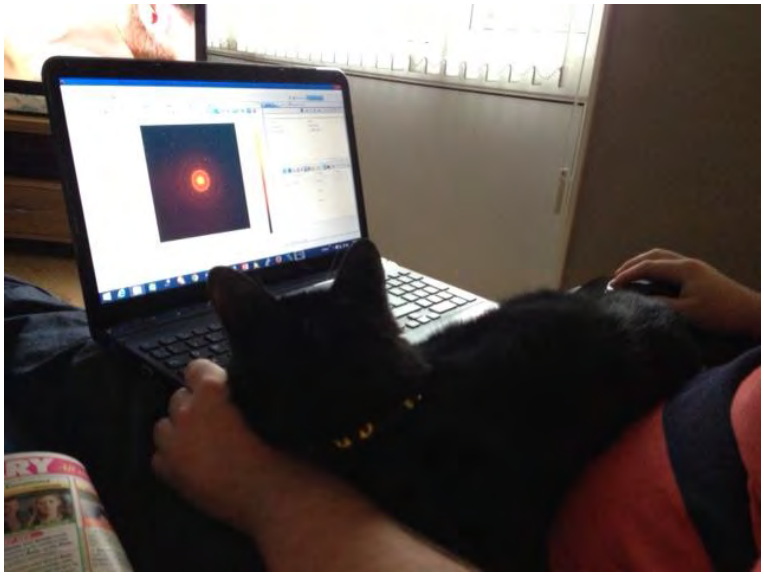

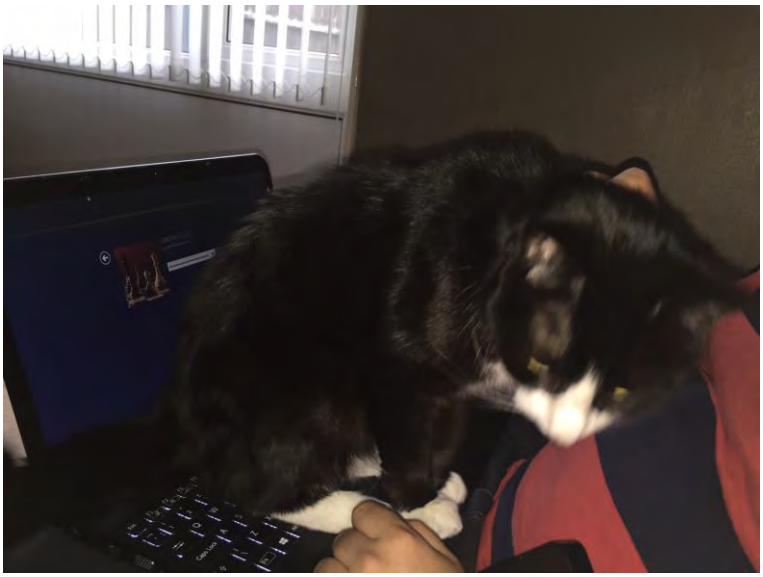

Abbreviations

BCA	Binary Collision Approximation
GSAS	General Structural Analysis System
GULP	General Utilities Lattice Program
HIP	Hot Isostatically Pressed
HLLW	High Level Liquid Waste
HLW	High Level Waste
MD	Molecular Dynamics
METADISE	Minimum Energy Techniques Applied to Dislocation, Interface and Surface Energies
PBC	Periodic Boundary Conditions
PDF	Pair Distribution Function
PKA	Primary Knock-On Atom
PXRD	Powder X-ray Diffraction
RDF	Radial Distribution Function
SHI	Swift Heavy Ions
SRIM	Stopping and Range of Ions in Matter
WD-XRF	Wavelength Dispersive X-ray Fluorescence Spectroscopy
XRD	X-ray Diffraction

Table of Contents

Chapter 1: Introduction

Chapter 2: Methodology

Chapter 3: Derivation of Pair Potentials

Chapter 4: Defects in the Xenotime Lattice

Chapter 5: Atomistic Simulation of Xenotime Surfaces

Chapter 6: Simulation of Radiation Damage Cascades

Chapter 7: Structural Analysis of Xenotime and Fluorapatite Samples Using X-Ray PDF

Appendices

CHAPTER 1

Introduction

Table of Contents

Table of Figures

1.1 Nuclear Waste

In 2010 an estimated 14% of our global electricity production was supplied by nuclear power[1]. The low CO_2 production (two orders of magnitude lower for nuclear than for fossil fuels[2]) and good green credentials help hit government targets to reduce emissions of greenhouse gasses. This combined with the high energy density of nuclear fuel relative to fossil fuels makes the expansion of nuclear energy an attractive prospect to meet the worlds growing energy needs. While environmental concerns regarding the release of radioactive waste has been a topic of discussion for many years[3], the recent Fukushima Daiichi disaster has once again highlighted public concerns regarding the safety of the plants themselves, reinforcing the perception that radioactive wastes are highly dangerous. There are many challenges to overcome when considering the expansion of the nuclear industry including; site selection, availability of natural resources and the safety and the disposal of increased quantities of radioactive waste. Opposition to this idea could argue that it would be irresponsible to consider the expansion of nuclear power production without addressing the issue of the large quantities of waste that would be produced throughout the plants lifetime and then also upon their decommissioning[4]

The radioactive waste can be classified into several different types as dictated by their relative activities as shown in Table 1.1. Although only ~0.1% of the waste falls into the HLW category, this fraction contains ~95% of the radioactivity[5]. One contributor to the amount of HLW is the waste from reprocessing spent nuclear fuel (SNF). Within a nuclear reactor the actinide elements such as ^{235}U and ^{239}Pu within the fuel pellet undergo fission reactions which release energy. In doing so the concentration of fission products build up in the fuel and decreases the efficiency of the fission process.

Eventually it is no longer economically viable to continue irradiating the fuel pellet and it must be removed and replaced. The SNF still contains valuable elements that can be reprocessed and extracted. One of the traditional methods of reprocessing is the PUREX (Plutonium URanium EXchange) process where the fuel pellet is firstly dissolved in nitric acid and any insoluble fission products are removed. The actinide elements can then be separated using a solvent extraction method. The resulting waste slurry contains a variety of radioactive components including fission products (e.g. Cs, Sr, Nb, Y, Zr *etc.*)[6-8], alloying elements (e.g. Fe and Si), elements from the fuel cladding (e.g. Al and Mg) and transuranic elements (e.g. Am, Cm)[9, 10]. Alternatively HLW can also be produced from the dismantling of nuclear weapons. This may be partially incorporated into MOX (Mixed OXide) fuel or disposed of in a geological disposal site.

Table 1.1: Classifications of nuclear waste

Category of waste	Definition[3]	Volume in UK as of April 2010[5] / m^3
Very low level waste (VLLW)	< 0.4 x 10^9 Bqm^{-3} β/γ	-
Low level waste (LLW)	< 4 x 10^9 Bqt^{-1} α < 12 x 10^9 Bqm^{-3} β/γ	4,400,000
Intermediate level waste (ILW)	Heat generating < 2 kW m^{-3} > 4 x 10^9 Bqt^{-1} α < 12 x 10^9 Bqm^{-3} β/γ	290,000
High level waste (HLW)	Highly heat generating > 2 kW m^{-3}	1,000

1.2 Geological Disposal

One of the greatest challenges after the HLW has been extracted is deal with the waste over a long timescales, with the waste remaining radioactive for hundreds to hundreds of thousands of years[11]. The waste can be stored at the processing facility on a

temporary basis, however a more long term strategy is required. A wide range of disposal options are available, from disposal in sealed drums at sea to disposal in space[3]. Of the possible methods the most promising is geological disposal in an underground repository using a multi-barrier approach, of which the immobilised waste form would be one constituent part[3,12]. There are several ways in which stored radionuclides could reach the biosphere including;

- Denudation
- Destruction of the repository due to tectonic processes
- Dissolution in magmas
- Opening by mine workers, and
- Dissolution in ground waters

Of these the first four can be minimised by the correct site selection in a geologically stable environment with minimal tectonic or volcanic activity[13]. With this in mind the only mechanism by which the waste could reach the biosphere would be by dissolution of the waste form in ground water followed by migration to the surface[12]. The principal behind immobilizing radioactive waste in a glass or ceramic material is to make a waste form which is more easily stored or disposed of than the liquid waste[12].

1.3 Waste Forms

There are a variety of ways in which this can be achieved including dissolution of waste elements within the host matrix on an atomic scale or encapsulation of the waste in an inert matrix as depicted in Figure 1.1[12]. Generally monolithic forms of waste materials are favoured to reduce the relative surface area to help prevent leaching[2]

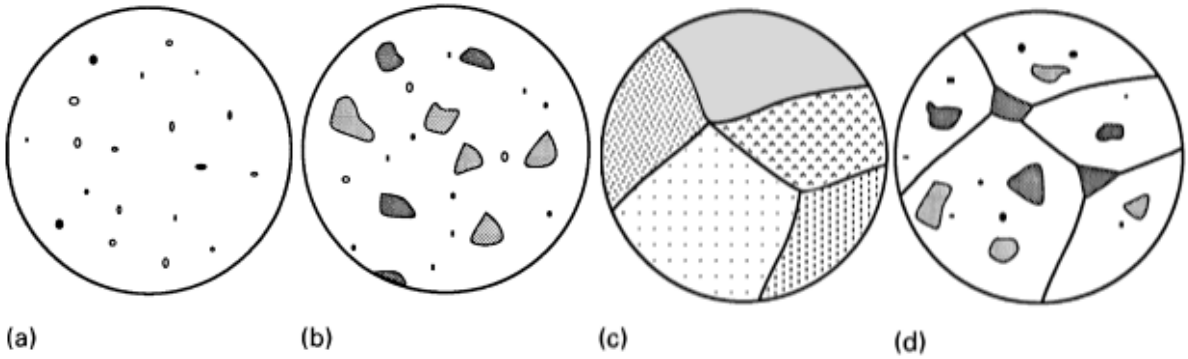

Figure 1.1: Schematic representing different immobilisation strategies, (a) homogenous glass with some bubbles and inclusions, (b) waste phases within a glass matrix, (c) ceramic with waste elements in solution and (d) ceramic with encapsulated waste phases

1.3.1 Glass Vs Ceramic

Vitreous waste forms have been extensively studied and the process of immobilizing the waste is well established. A glass host is used to dissolve the HLW to form a vitreous homogenous product which can then be cast into various forms including large glass blocks[12]. In principal vitreous waste forms would seem the ideal matrix for HLW immobilization as they can tolerate quite high levels of waste loading (~25-30 wt%), accommodate a wide range of waste elements, and show relatively good radiation stability. However the thermodynamic stability of the glass matrix is a fundamental issue. Glasses are inherently metastable and if the glass is not sufficiently stable then crystallisation can occur over geological timescales in an uncontrolled manner[12]. The radioactive decay of the constituent waste elements can cause substantial heating of the waste matrix which may be high enough to cause devitrification. This undesirable crystallisation can cause stresses to build up within the matrix, which may cause the glass to crack[12]. The leach rate of the radionuclides out of the glass matrix may be substantially increased with the accumulation of cracks as a result of the increased surface area[12]. The chemical stability of some glasses, including borosilicate glass, have been brought into question as the chemical durability is significantly reduced when

under repository condition (*ie.* at higher temperatures, over longer timescales and under acid conditions). This raises serious questions as to whether glass matrices are a viable waste form. Borosilicate glasses form the basis of the commercial glass industry and are commonly used for the immobilization of HLW[12]. This material was selected for the following key reasons[14];

- an anticipated ease of processing (glass frit and the waste are mixed, melted at relatively low temperatures, and poured into canisters)
- the technology is well demonstrated for actual radioactive waste
- the ability to incorporate a wide variety of different constituents of HLW while also being readily modified to optimize its properties for a particular waste composition[3, 12]
- The glass would show only a minor response to the effects of radiation, especially from α-decay events.

While vitreous silica would have the greatest durability it is unacceptable as a waste material as the processing temperature is too high and so boric oxide is used to modify the glass to lower the vitrification temperature whilst still maintaining good durability[12]. The prevalence of this material in the literature over many years means that borosilicate glasses are well characterized and their properties are well documented, this makes them an ideal "bench mark" to compare other waste forms against. As a result many countries have adopted borosilicate glass as the preferred waste form for the immobilization of high level liquid waste (HLLW).

Ceramic waste forms, in contrast to glasses generally exhibit excellent chemical durability and thermal stability[12] however the effects of radiation damage on ceramic materials are of some concern. Unlike glasses the crystalline material may become metamict over time which can be accompanied by quite large volume changes. As for

glasses these volume changes can in turn cause cracking which can result in increased leach rates. A composite material that has seen some success and is employed in some countries is SYNROC. The three main ceramic phases present are zirconalite, hollandite and perovskite. After the HLW is immobilised within the matrices the resulting powder is often hot isostatically pressed (HIPed) to achieve a monolith of up to 99 % of theoretical density. Some advantages and disadvantages for these different waste forms have been summarised in Table 1.2.

Table 1.2: Summary of the advantages and disadvantages of glass and ceramic waste forms

Waste form	Advantages	Disadvantages	Comments
Glass	Extensive technology base in existence (glass industry). A wide range of glass compositions are known. Very composition tolerant. Very good radiation stability (only small density changes as a result of radiation damage).	Limited solubility of some elements (eg. Actinides, sulphates and halides). Issues with the volatility of some elements (eg. Cs, Ru, Tc and Mo).	Moderate melting temperatures (<1200 °C). Passable chemical durability and thermal stability (poor durability >110 °C). Some natural analogues but unclear how analogous these are to borosilicate glass (eg. Volcanic tektites, rhyolites, obsidian and basaltic glasses).
Ceramic	Superior chemical durability and thermal stability. (Stable in a wet environment at 300 °C, could be placed directly into a repository with no need for interim storage). Highly composition tolerant (high actinide solubility). Higher density so the same quantity of waste can be immobilized in up to as little as 50% of the volume of glass that would be required. Many natural analogues (monazite, zircon, appatite).	Less mature technology base compared to glass industry.	Questionable radiation stability. Ceramic can become metamict with time resulting in large density/volume changes (in many cases chemical durability remains significantly superior to most glasses even after incurring considerable radiation damage).

1.4 Sources of Radiation Damage

The principal sources of radiation in HLW are a result of either α-decay from actinide elements or β-decay from fission products, summarised in Table 1.3. A recoil nucleus will also be produced as a consequence of an α or β decay event however the energy of the β-recoil nucleus is generally relatively low compared to the α-recoil nucleus. The interactions of these particles with matter broadly fall into 2 categories; Displacive (elastic collisions) and electronic (ionization/excitation). The method by which these particles disperse their energy can be indicated by considering the relative velocity of the bombarding particle and that of the orbital electrons of the target ion[15]. If the particle energy is below that of the orbital electrons then it is unlikely to result in electronic excitation and therefore elastic interactions are more likely[15].

Table 1.3 Interactions of particles with matter

Type of particle	Primary interactions with matter	Comments
α-particle	Electronic	Long range
α-recoil nucleus	Electronic & Elastic collisions	Initially electronic then some elastic collisions as velocity decreases
β-particle	Electronic	
β-recoil nucleus	Electronic	
γ-particle	Electronic	

While the α-particle carries roughly 98% of the energy from the decay event and has a much larger range than the recoil nucleus (μm scale), it primarily interacts with the waste matrix through electronic interactions and is only involved in ~ 100 elastic collisions towards the end of its trajectory[15]. The majority of the atomic displacements that will result in the bulk amorphization of the waste form are as a result of the α-recoil nucleus. The recoil nucleus is involved in a sequence of elastic interactions, resulting in a

branching cascade of atomic displacements, with individual cascades having a short range (nm scale), causing highly localized damage along the trajectory of the recoil nucleus. These elastic collisions occur with increasing probability over the range of the recoil nucleus, as its energy decreases. The first lattice atoms involved in each of the proceeding displacement cascades is known as a primary knock-on atom (PKA). The thermal spike model describes better the inelastic interactions of the recoil nucleus, with the probability of these types of interactions decreasing with increasing track length and decreasing energy. Though the energy imparted to each atom within the track volume is small, the combined lattice vibrations can cause localised melting. Cascades are sometimes referred to as 'hot zones' as the dissipation of energy may be enough to cause melting of the cascade volume within a very short time frame (eg. 10^{-12} s)[15]. Often elastic collisions are approximated to consider only binary collision, known as the binary collision approximation (BCA), though this breaks down for heavy ions where energy dissipation is high (>1 eV $atom^{-1}$). In some materials the particles may be channelled through the structure which would increase the range of the particle and decrease the number of collisions[15]. The classical image of a cascade depicts the displaced atoms occupying interstitial sites around the periphery of the cascade volume and the vacancies concentrated in the interior. The displacement cascade can reach its maximum size within picoseconds followed by rapid epitaxial recrystallisation of the cascade volume[16]. These isolated cascades eventually begin to overlap, culminating in the bulk amorphization of the waste form. These models are summarised in Figure 1.2.

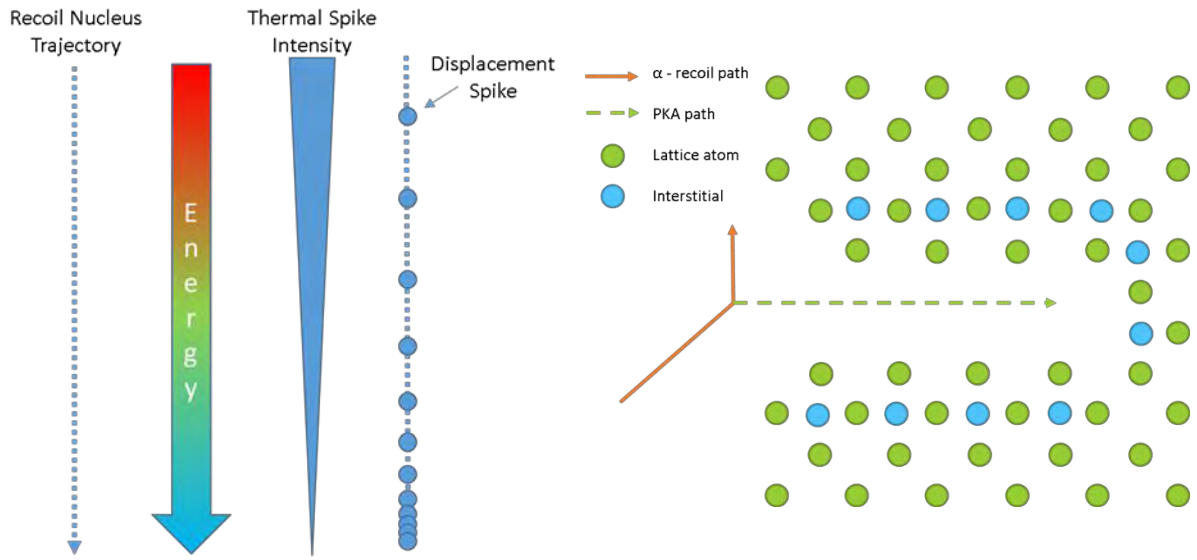

Figure 1.2: Schematic representation of the thermal spike and displacement spike models (left) and a radiation damage cascade (right)

There are other ways in which both glasses and ceramics can be damaged by radiation. Transmutations of fission products (primarily β-decay of ^{137}Cs and ^{90}Sr) can result in damage to the waste form as when they decay changes occur to both atomic radii and valence[17]. Cs^{+} decays to Ba^{2+} while Sr^{2+} decays to Y^{3+} which in turn decays to Zr^{4+}, these decay pathways result in a final atomic radius decrease of 20% and 29% respectively[17]. The decay products from both β and α-decay must be incorporated into the waste form which can impact on the properties of the waste form and the solubility of these products. Large volume changes can be observed as a result of radiation damage which can cause cracks to form in the material and therefore could influence leach rates. Similarly the melting and subsequent recrystallization of host matrix due to 'thermal spikes' can also result in stresses within the structure causing the material to crack[17]. Helium atoms can be formed if the α-particle picks up 2 electrons, these atoms can sit in interstitial sites, be trapped in defects, aggregate to form bubbles or be released from the surface[17]. This accumulation of He may cause swelling and subsequent micro-

fractures within the waste form. The final damaged state does not occur as a result of just radiation damage processes; there is a balance between the rate of radiation damage and various recovery processes such as pair recombination, defect migration, defect aggregation and the degree of epitaxial recrystallisation[17]. The events following an α-decay event as summarised in Figure 1.3.

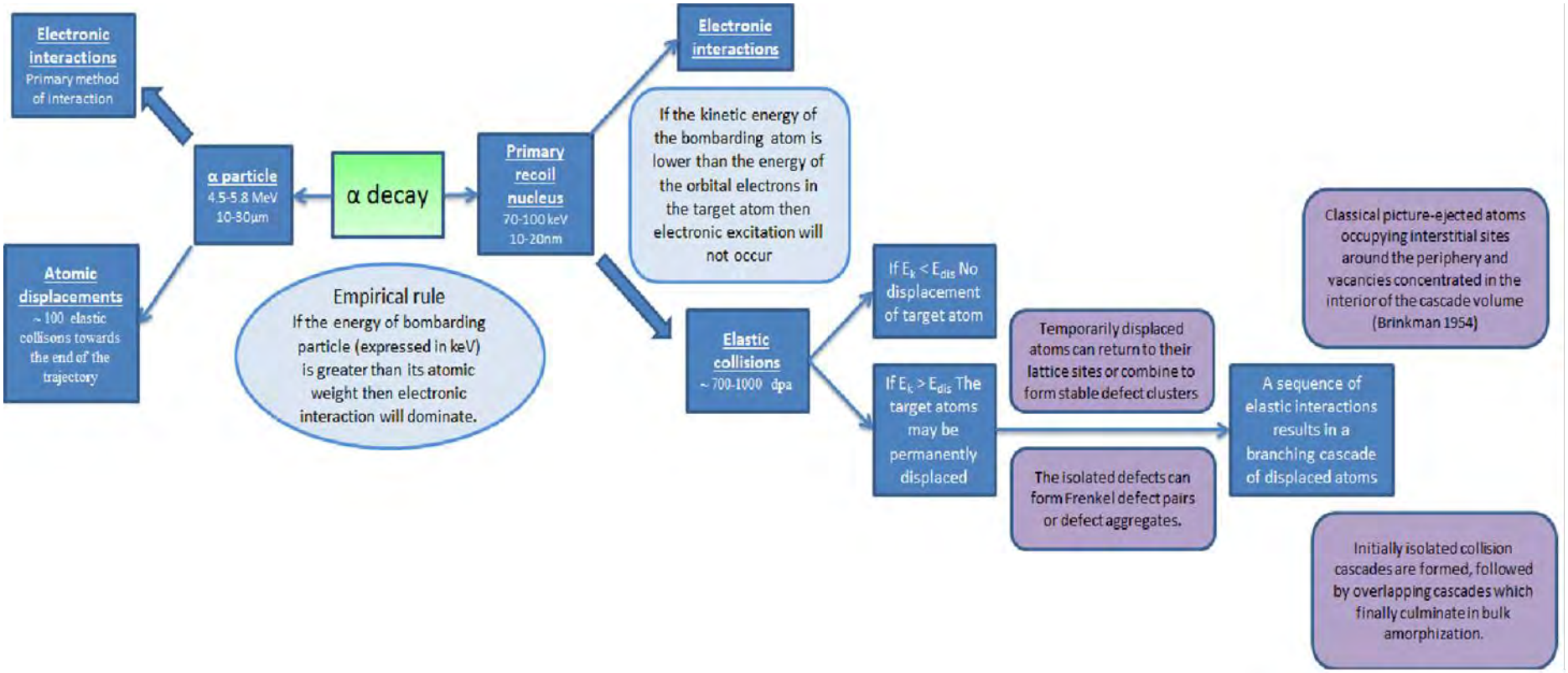

Figure 1.3: Summary of the α-decay damage processes

1.5 Investigating Radiation Damage

The aforementioned radiation damage can accumulate in waste forms over thousands to millions of years from relatively low dose rates however it is desirable to experimentally investigate these effects over a much shorter time scale. This can be achieved through a variety of methods summarised in Table 1.4.

Table 1.4: Summary of the experimental methods for investigating radiation damage

Technique		Damage Process				Comments
		α-particle	α-recoil nucleus	β-particle	γ-rays	
Actinide incorporation		✓	✓	×	×	Internationally accepted technique
Natural analogues		✓	✓	✓	✓	Not always available
Charge Particle Irradiation	**electron**	×	×	✓	✓	
	α-particle	✓	×	×	×	
	Heavy ions	×	✓	×	×	
γ-rays		×	×	✓	✓	Generally used to look at radiolytic processes
Neutron beam		~	~	×	×	

The incorporation of short lived actinides such as ^{238}Pu and ^{244}Cm into the proposed waste form can effectively simulate the long term effect of α-decay. These actinides must be incorporated into the waste form in adequate concentrations to achieve ~ 10^8-10^9 α-decay events over the period of the experiment (up to several years)[14]. This is a much higher dose rate than would be experienced in the repository and so the damage accumulation occurs at a much faster rate. This technique relies on the α-decay of the actinides to damage the material and as such gives a good simulation of the simultaneous damage from the α-particles and the α-recoil nuclei[14]. It is often possible to achieve an inhomogeneous distribution of the actinides within the waste form allowing phenomena such as phase separation or partial devitrification to be modelled. The similarities of this technique to the way in which the waste form will be used in its final application are a huge advantage and as such it has become a standard method in order to test the stability of waste forms to α-decay damage, as approved by the International Organization for Standardization (ISO 6962)[14].

Natural analogues are a very useful tool in the evaluation of a new waste form. In the case of ceramics there are often natural minerals that contain comparable concentrations of actinides and their fission products. Once these minerals have been dated it is possible to see the long-term damage in a material from the α-decay of these actinides on a geological time scale[14]. If the thermal history of these minerals is known then reasonable conclusions can be drawn regarding the thermal annealing process over such time scales. One consideration when using natural analogues is the purity of the natural sample, as other impurity elements may affect the long term behaviour of the mineral. This technique is of limited use for glasses as, whilst natural glasses do contain actinides such as ^{238}U, ^{235}U and ^{232}Th, the concentrations of the actinides are too low and so the dose experienced by the glass is not sufficient to be used as a natural analogue for

a proposed waste form[14]. However fission tracks, caused by fission fragment of high energy (~ 10^2 MeV), have been observed in some natural glasses, offering the opportunity to study the track annealing[14].

Electrons, α-particles and heavy ions can be used to simulate radiation damage from HLW. Irradiation of the sample with the different charged particles can be used to simulate different processes within the waste form. These techniques often use extremely high dose rates from particle accelerators and as a result often very quick to run (e.g. Minutes)[14]. However these techniques only result in a thin layer of damage on the surface of the material in a very specific area[14]. Implantation of the bombarding ions (e.g. Pb) can result in a change in the composition of the irradiated region which may give questionable results[14]. Finally the technique produces a homogenous distribution of damage in the target area and therefore it doesn't simulate radiation effects caused by an inhomogeneous distribution of actinides and fission products within the waste form[14].

Gamma ray irradiation can be used primarily to simulate the effects of β-particles and γ-rays on the waste form. Generally ^{60}Co or ^{137}Cs sources are used and high dose rates can be achieved. The highly penetrating nature of γ-rays means that the material can be irradiated in bulk[14].

Neutron irradiation can be used to simulate ballistic processes in the waste form, however the number of displacements are much smaller than that of an α-decay event[14]. No information about He build up is given and they cannot be used to simulate an inhomogeneous distribution of actinides within the waste form[14].

1.5.1 Critical Temperature Measurements

As previously mentioned it is important to understand the interplay between the radiation damage mechanisms and various recovery processes that occur in a potential waste form to better understand how it will perform in repository conditions. A good indication of the radiation resistance of a prospective waste form is to look at the rate of thermal annealing with respect to the rate of radiation damage. As such the critical temperature (T_c, the temperature at which the rate of thermal annealing is the same as the rate of damage, preventing amorphization) is evaluated and compared to other waste forms. It is important to note when comparing this information that the rate of the recovery processes can also be influenced by the mass and energy of the irradiating ion and the melting temperature of the irradiated material[17]. It should also be noted that in some cases irradiation of a sample may also increase the extent of recovery from radiation-assisted recovery processes. Table 1.5 shows a comparison of some common minerals which have been evaluated using this technique. Some example critical temperature plots are illustrated in figure, taken from (a) Meldrum *et al*[18] and (b) Weber *et al*[19].

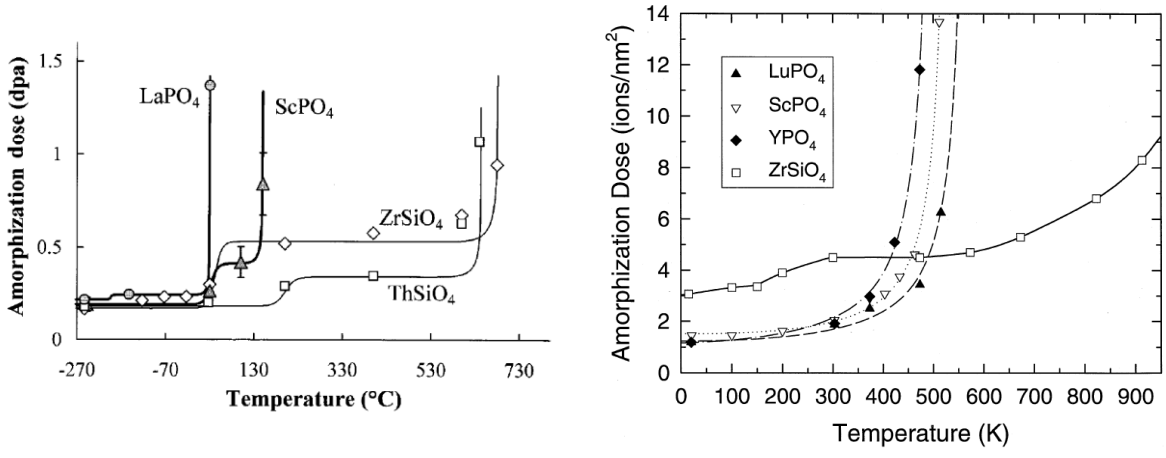

(a) (b)

Figure 1.4: Critical temperature plots for the amorphisation of various orthophosphate and orthosilicate materials

Table 1.5: Summary of the critical temperature studies for a selection of materials

Mineral	Critical Temperature Studies
Zircon Tetragonal $I4_1/amd$ Z = 4	**General Formula: $ZrSiO_4$** Relatively low concentrations of U and Th are commonly reported (10^2-10^3 ppm, >1 wt % UO_2 is rare) however natural zircon is often found to be metamict. When irradiated with a 1.5 MeV Kr^+ source a two stage process was observed with respect to the radiation dose for complete amorphization over the temperature range of 0 – 1000 K. Stage 1 (<300 K) has been provisionally attributed to the intra-cascade recombination of closely spaced defects[15]. Stage 2 (>473 K) is assumed to be associated with the thermal mobility of cascade defects or irradiation enhanced epitaxial recrystallization process. The high T_c that has been calculated (~ 1100 K) is in concordance with the observation that zircon is often found to be metamict[15].
Monazite Monoclinic $P2_1/n$ Z = 4	**General Formula: APO_4** (where A = lanthanides; commonly La, Ce, Pr, Nd, Sm and Eu)[20] Commonly found to contain significant quantities of U and Th (10-20 wt %) and the large, irregular AO_9 polyhedra allow for a large number of cations to be incorporated into the structure. Natural monazite is almost never found to be metamict despite relatively high concentrations of radionuclides. This is in concordance with the low critical temperature of 428 K when irradiated with a 1.5 MeV Kr^+ source[15].
Xenotime Tetragonal $I4_1/amd$ Z = 4	**General Formula: YPO_4** Isostructural with zircon, xenotime is a relatively common accessory mineral in plutonic and metamorphic rocks[21]. It is commonly found containing reasonable concentrations of U and Th. Unlike zircon it is rarely found to be metamict and has a much lower critical temperature (512 K when irradiated with an 800 keV Kr^{2+} source[15].
Apatite Hexagonal $P6_3/m$	**General Formula: $Ca_{10}(PO_4)_6(OH,F)_2$** Natural samples contain minor quantities of U and Th substituting on the Ca site. The Oklo natural reactors provide evidence for the durability and radiation resistance of natural apatite whereby the material has retained its crystalline structure after two billion years despite being enriched with ^{235}U and fission-products in significant concentrations[15]. Rarely found to be metamict however fission tracks are common. This observation is supported by Wang et al[15] demonstrating a critical temperature ~ 473 K when a sample of fluorapatite was irradiated with a 1.5 MeV Kr^+ source. Low critical temperature was attributed to low activation energy for recovery processes as a result of fluorine mobility.

1.6 Simulation of Materials

Computer modelling of materials allows for systems to be examined under extreme conditions which may be difficult to study experimentally. Similarly, features that would prove difficult to observe experimentally may be modelled explicitly. However, it is important to note that generally computer models use a range of assumptions to simplify the problem at hand in order to make it computationally tractable. In relation to atomistic simulations, the results obtained from such simulations are only as robust as the set of atomistic potentials used to generate them. Many of these assumptions have been validated over many years and within many different systems and are shown to produce robust and meaningful results. Computational modelling has proved valuable in modelling a wide range of properties within materials ranging from bulk properties[22-24], defect properties[22, 25-33], surfaces[34-37], grain boundaries[38-40], morphological predictions[41-43] and radiation damage simulations[44-49]. As such atomistic simulations are ideal for investigating the effects of radiation damage within candidate waste forms across a range of regimes, from static calculations to dynamic simulations. Despite being a common accessory mineral in plutonic rocks there have been relatively few studies of radiation effects within the xenotime structure using these modelling techniques[50-52].

1.7 Xenotime Structure

Xenotime is isostructural with zircon and belongs to the tetragonal space group $I4_1/amd$ (No. 141) with the origin at (0, 0.25, 0.375)[53]. The structure consists of alternating chains of edge sharing PO_4 and YO_8 polyhedra running parallel to the *c* axis, Figure 1.5. The phosphate tetrahedra are isolated, with each oxygen atom coordinating to one phosphorus atom and two yttrium atoms. The yttrium and the phosphorus atoms lie on

special positions on a four-fold screw axis and are related by a translation of $\left(0,0,\frac{1}{2}\right)$. The four P-O bonds are equivalent with an interatomic separation of ca. 1.54 Å.

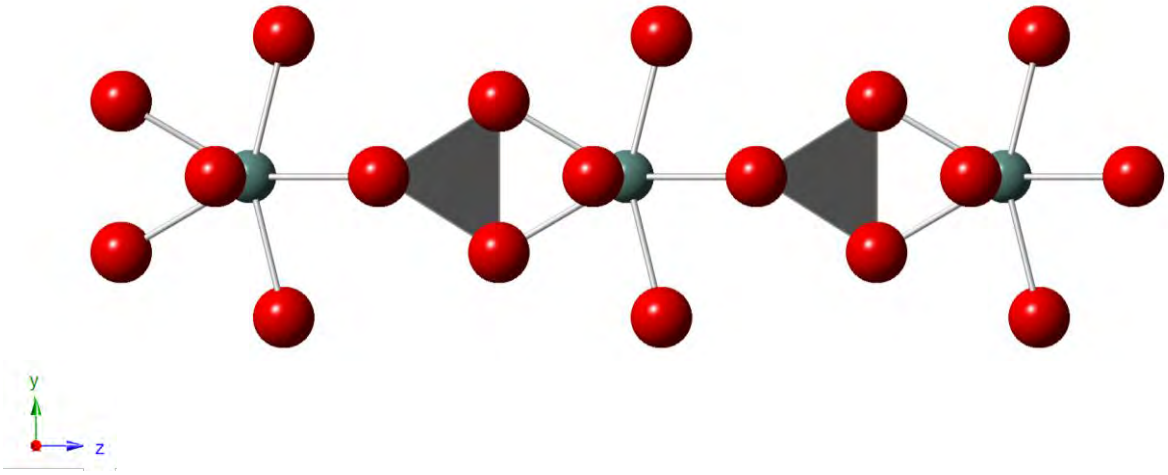

(a)

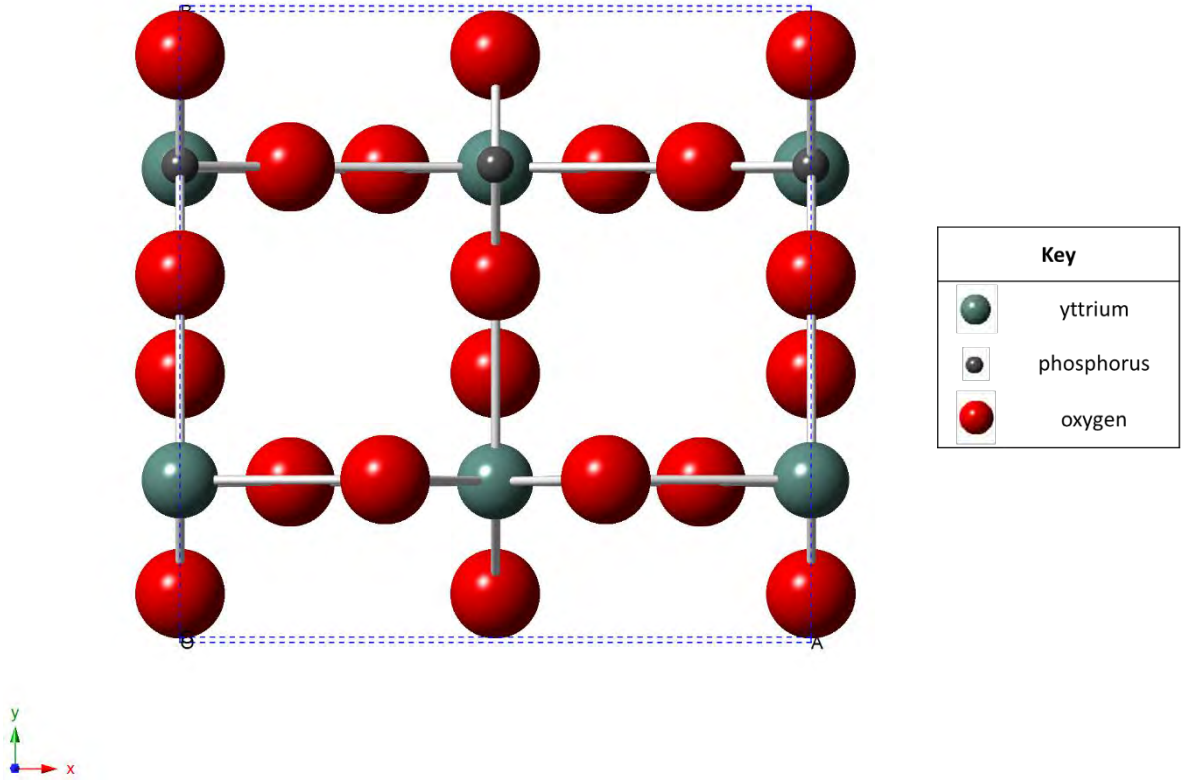

(b)

Figure 1.5: Structure of xenotime (a) chains of edge sharing polyhedra parallel to the *c* axis and (b) unit cell

1.8 Aims

This study aims to develop new robust potentials for the xenotime system to ultimately model the effects of α-decay events within this candidate waste form. This work will explore the intrinsic and extrinsic defects within this system, followed by surface simulations and morphological predictions to validate the potentials. These will be performed within the static regime. Furthermore this work seeks to calculate threshold displacement energies for the constituent elements within xenotime using molecular dynamics which may be of use in future experimental studies. Collision cascades will be simulated in both the xenotime and zircon systems to compare and contrast the type of damage accumulated, to elucidate the observed differences in the relative resistance to radiation damage between these materials. Additionally X-ray pair distribution function experiments will be used to attempt to observe the damage accumulated within a sample of xenotime after irradiation with swift heavy ions to compare to the results of the simulations. Finally the local structure of strontium dopant atoms within the fluorapatite system will be investigated to attempt to identify cation ordering.

1.9 References

1. M. Englert, L. Krall and R. C. Ewing, *Mrs Bulletin*, 2012, **37**.
2. M. M. Abu-Khader, *Progress in Nuclear Energy*, 2009, **51**.
3. I. W. Donald, *Waste immobilization in glass and ceramic based hosts : Radioactive, toxic and hazardous wastes*, John Wiley & Sons, 2010.
4. D. Abbott, *Bulletin of the Atomic Scientists*, 2012, **68**, 23-32.
5. Radioactive wastes in the uk: A summary of the 2010 inventory, http://www.nda.gov.uk/ukinventory/documents/Reports/upload/2010-UK-

Radioactive-Waste-Inventory-Summary-of-the-2010-Inventory.pdf, (accessed 18/01/2013, 2013).

6. H. Kleykamp, J. O. Paschoal, R. Pejsa and F. Thummler, *Journal of Nuclear Materials*, 1985, **130**, 426-433.
7. C. Sari, G. Schumacher and C. T. Walker, *Journal of Nuclear Materials*, 1979, **79**, 255-259.
8. K. A. Romberger, C. F. Baes and H. H. Stone, *Journal of Inorganic & Nuclear Chemistry*, 1967, **29**, 1619.
9. T. L. Markin and E. C. Crouch, *Journal of Inorganic & Nuclear Chemistry*, 1970, **32**, 77.
10. F. A. Heyn, A. H. W. Aten and C. J. Bakker, *Nature*, 1939, **143**, 516-517.
11. M. I. Ojovan and W. E. Lee, in *An introduction to nuclear waste immobilisation (second edition)*, Elsevier, Oxford, 2014, DOI: http://dx.doi.org/10.1016/B978-0-08-099392-8.00001-2, pp. 1-6.
12. I. W. Donald, B. L. Metcalfe and R. N. J. Taylor, *Journal of Materials Science*, 1997, **32**, 5851-5887.
13. N. P. Laverov, B. I. Omel'yanenko and S. V. Yudintsev, *Russian Journal of General Chemistry*, 2011, **81**, 1980-1993.
14. W. J. Weber, R. C. Ewing, C. A. Angell, G. W. Arnold, A. N. Cormack, J. M. Delaye, D. L. Griscom, L. W. Hobbs, A. Navrotsky, D. L. Price, A. M. Stoneham and W. C. Weinberg, *Journal of Materials Research*, 1997, **12**, 1946-1978.
15. R. C. Ewing, A. Meldrum, L. M. Wang and S. X. Wang, *Transformation Processes in Minerals*, 2000, **39**, 319-361.
16. A. Meldrum, L. A. Boatner, W. J. Weber and R. C. Ewing, *Geochimica Et Cosmochimica Acta*, 1998, **62**.

17. W. J. Weber, R. C. Ewing, C. R. A. Catlow, T. D. de la Rubia, L. W. Hobbs, C. Kinoshita, H. Matzke, A. T. Motta, M. Nastasi, E. K. H. Salje, E. R. Vance and S. J. Zinkle, *Journal of Materials Research*, 1998, **13**.

18. A. Meldrum, L. A. Boatner and R. C. Ewing, *Mineralogical Magazine*, 2000, **64**.

19. W. J. Weber, R. C. Ewing and A. Meldrum, *Journal of Nuclear Materials*, 1997, **250**.

20. L. A. Boatner, *Phosphates: Geochemical, Geobiological, and Materials Importance*, 2002, **48**, 87-121.

21. A. Meldrum, L. A. Boatner and R. C. Ewing, *Physical Review B*, 1997, **56**.

22. I. M. Boswarva and A. B. Lidiard, *Philosophical Magazine*, 1967, **16**, 805.

23. G. V. Lewis and C. R. A. Catlow, *Journal of Physics C-Solid State Physics*, 1985, **18**, 1149-1161.

24. J. R. Walker and C. R. A. Catlow, *Journal of Physics C-Solid State Physics*, 1981, **14**, L979-L983.

25. G. Busker, A. Chroneos, R. W. Grimes and I. W. Chen, *Journal of the American Ceramic Society*, 1999, **82**, 1553-1559.

26. R. A. Jackson, A. D. Murray, J. H. Harding and C. R. A. Catlow, *Philosophical Magazine a-Physics of Condensed Matter Structure Defects and Mechanical Properties*, 1986, **53**, 27-50.

27. S. J. Zinkle and C. Kinoshita, *Journal of Nuclear Materials*, 1997, **251**, 200-217.

28. I. M. Boswarva, *Philosophical Magazine*, 1967, **16**, 827.

29. R. A. Jackson, A. D. Murray and C. R. A. Catlow, *Physica B Condensed Matter*, 1985, **131**, 136-138.

30. R. A. Jackson, M. E. G. Valerio and J. F. deLima, *Journal of Physics-Condensed Matter*, 1996, **8**, 10931-10937.

31. J. B. Amaral, D. F. Plant, M. E. G. Valerio and R. A. Jackson, *Journal of Physics-Condensed Matter*, 2003, **15**, 2523-2533.

32. R. A. Buckingham, *Proceedings of the Royal Society of London Series a-Mathematical and Physical Sciences*, 1938, **168**, 264-283.

33. R. W. Grimes and C. R. A. Catlow, *Philosophical Transactions of the Royal Society a-Mathematical Physical and Engineering Sciences*, 1991, **335**, 609-634.

34. P. W. Tasker, *Journal of Physics C-Solid State Physics*, 1979, **12**, 4977-4984.

35. E. A. Colbourn, W. C. Mackrodt and P. W. Tasker, *Journal of Materials Science*, 1983, **18**, 1917-1924.

36. P. M. Oliver, G. W. Watson and S. C. Parker, *Physical Review B*, 1995, **52**, 5323-5329.

37. N. H. de Leeuw and S. C. Parker, *Molecular Simulation*, 2000, **24**, 71.

38. G. W. Watson, E. T. Kelsey, N. H. deLeeuw, D. J. Harris and S. C. Parker, *Journal of the Chemical Society-Faraday Transactions*, 1996, **92**, 433-438.

39. D. M. Duffy and P. W. Tasker, *Philosophical Magazine a-Physics of Condensed Matter Structure Defects and Mechanical Properties*, 1983, **48**, 155-162.

40. D. M. Duffy and P. W. Tasker, *Philosophical Magazine a-Physics of Condensed Matter Structure Defects and Mechanical Properties*, 1983, **47**, 817-825.

41. N. H. de Leeuw and S. C. Parker, *Journal of Physical Chemistry B*, 1998, **102**, 2914-2922.

42. T. E. Littleford, R. A. Jackson and M. S. D. Read, *Physica Status Solidi C: Current Topics in Solid State Physics, Vol 10, No 2*, 2013, **10**, 156-159.

43. T. E. Littleford, R. A. Jackson and M. S. D. Read, *Surface Science*, 2012, **606**, 1550-1555.

44. F. W. Clinard, G. F. Hurley and L. W. Hobbs, *Journal of Nuclear Materials*, 1982, **108**, 655-670.

45. R. Smith, D. Bacorisen, B. P. Uberuaga, K. E. Sickafus, J. A. Ball and R. W. Grimes, *Journal of Physics-Condensed Matter*, 2005, **17**, 875-891.

46. D. Bacorisen, R. Smith, B. P. Uberuaga, K. E. Sickafus, J. A. Ball and R. W. Grimes, *Physical Review B*, 2006, **74**.

47. J. A. Ball, S. T. Murphy, R. W. Grimes, D. Bacorisen, R. Smith, B. P. Uberuaga and K. E. Sickafus, *Solid State Sciences*, 2008, **10**, 717-724.

48. P. Moreira, R. Devanathan, J. G. Yu and W. J. Weber, *Nuclear Instruments & Methods in Physics Research Section B-Beam Interactions with Materials and Atoms*, 2009, **267**, 3431-3436.

49. P. Moreira, R. Devanathan and W. J. Weber, *Journal of Physics-Condensed Matter*, 2010, **22**, 9.

50. F. Gao, H. Y. Xiao, Y. G. Zhou, R. Devanathan, S. Y. Hu, Y. L. Li, X. Sun and M. A. Khaleel, *Computational Materials Science*, 2012, **54**, 170-175.

51. J. A. L. Rabone and N. H. De Leeuw, *Journal of Computational Chemistry*, 2006, **27**, 253-266.

52. V. S. Urusov, A. E. Grechanovsky and N. N. Eremin, *Glass Physics and Chemistry*, 2012, **38**, 55-62.

53. Y. X. Ni, J. M. Hughes and A. N. Mariano, *American Mineralogist*, 1995, **80**, 21-26.

Chapter 2

Methodology

Table of Contents

Table of Figures

2.1 Simulation Techniques

2.1.1 Atomic Interactions

The simulations described in this thesis all rely on atomistic modelling techniques which are based around the Born model of ionic solids. Here the crystalline lattice is described as an infinite array of point charges. The interatomic forces acting between these ions can be described as a function of the relative distance between them. As such the total energy of the system (U) can be defined as an expansion in terms of the sum of the contributions to the potential energy from all atoms and electrons at all length scales. This presents an intractable problem which as such, must be simplified by making key assumptions. Firstly the electrons are not modelled explicitly and are incorporated implicitly into the potentials. Furthermore the expansion for the total energy of the system is truncated to give a good approximation as to the total energy of the system, following equation (2.1), as the contribution from these terms becomes progressively less. Finally the potentials are truncated to provide a cut-off to the range over which the interaction is applied. It is crucial that these interactions are parameterised to accurately describe the behaviour of the system in order to validate the predictions which ensue.

$$U = \sum_{i=1}^{N} U_i + \frac{1}{2}\sum_{i=1}^{N}\sum_{j=1}^{N} U_{ij} + \frac{1}{6}\sum_{i=1}^{N}\sum_{j=1}^{N}\sum_{k=1}^{N} U_{ijk} \qquad \textbf{(2.1)}$$

2.1.1.1 Pair Potentials

Pair potentials describe the potential energy of a pair of interacting ions as a function of the interatomic separation between them. This interaction can be resolved into long and short range contributions following equation (2.2).

$$U_{ij}(r_{ij}) = \phi_{long}(r_{ij}) + \phi_{short}(r_{ij}) \quad \textbf{(2.2)}$$

2.1.1.1.1 Long-Range Interactions

The long range contribution to the pair potential arises from the electrostatic interactions between them which are given by Coulomb's law, equation (2.3).

$$\phi_{long}(r_{ij}) = \frac{q_i q_j}{4\pi\mathcal{E}_0 r_{ij}} \quad \textbf{(2.3)}$$

Where q_i and q_j are the effective charge on species i and j respectively, r_{ij} is the interatomic separation between the two ions and $\mathcal{E}_0$ is the permittivity of free space. Though this interaction is simple to define, it is computationally difficult to evaluate. As such the Ewald Summation[1] method is employed to make the calculation tractable for three dimensional periodic systems.

2.1.1.1.2 Short-Range Interactions

The coulombic interaction described previously does not describe the behaviour of the interacting ions at very close separation and as such the short-range interactions must also be specified. One popular example used in many simulations of ionic solids is the Buckingham potential[2], equation (2.4). Here the potential is parameterised into an attractive and a repulsive component. The attractive component describes interactions due to van der Waals forces and has an r^{-6} dependence, whereas the repulsive part

describes effects such as electron cloud repulsion and takes an exponential form. Here A_{ij}, ρ_{ij} and C_{ij} are adjustable parameters. Another potential form relevant to this work is the Morse potential, equation (2.5). This potential is often used to describe interactions with more covalent character as it is harmonic at its minimum and leads to dissociation at larger interatomic separation. The parameters can be fitted to experimental data although they do hold some physical significance, where D_{ij} is the dissociation energy, r_0 is the equilibrium bond length and α_{ij} is related to the vibrational frequency of the stretching modes.

$$\phi_{short}(r_{ij}) = A_{ij} exp\left(\frac{-r_{ij}}{\rho_{ij}}\right) - \frac{C_{ij}}{r_{ij}^6} \quad \textbf{(2.4)}$$

$$\phi_{short}(r_{ij}) = D_{ij}\left[\left(1 - exp\left(-\alpha_{ij}(r_{ij} - r_0)\right)\right)^2 - 1\right] \quad \textbf{(2.5)}$$

2.1.1.2 Three-Body Potentials

Three body potentials may be included to help constrain and improve the rigidity of a particular coordination geometry. The potential can be contextualised as the repulsion between bonding pairs of electrons. As such a harmonic form is often used which invokes an energy penalty for deviations from the ideal angle, θ_0, equation (2.6).

$$U_{jik}(\theta) = \frac{k}{2}(\theta_{jik} - \theta_0)^2 \quad \textbf{(2.6)}$$

2.1.1.3 Polarisability

The shell model can be used to describe the effect of an electric field on an ion's electric charge density. A simple model has been derived by Dick and Overhauser[3] in which a massive core is coupled to a massless shell *via* a harmonic spring with force constant k_{cs}.

The dipolar polarisability, α, is expressed in terms of the charge on the shell, Y, and the spring constant following equation (2.7), where $\mathcal{E}_0$ is the permittivity of free space. The charge is partitioned over the core and the sell in such a way that the sum of these two components is equal to the relative charge of the ion.

$$\alpha = \frac{1}{4\pi\mathcal{E}_0}\left(\frac{Y^2}{k_{cs}}\right) \quad \textbf{(2.7)}$$

2.1.2 Energy Minimisation

The potential model is only an approximation to the real material, and as such will have some deviations from experimental results, including the positions of the atoms within the lattice. Therefore the structure must be allowed to relax to adopt the lowest energy configuration with respect to the potentials used. The aim of this process is to minimise the total force on the system, equation (2.8). The force exerted upon an ion, *i*, by a neighbouring ion, *j*, is given by the first derivative of the potential function .The geometry optimisations performed in this work were all performed under constant pressure conditions and therefore the unit cell dimensions were allowed to change so as to reduce the strain on the cell. The positions of the ions within the cell is also varied in order to minimise the forces acting upon them.

$$F = \frac{dU}{dr} = 0 \quad \textbf{(2.8)}$$

The internal energy may be expressed at any given point in configuration space as a Taylor series, equation (2.9). Here the expansion can be truncated at either the first or second derivatives. In the case where it is truncated to the first derivatives the direction of a subsequent move is determined from the first derivatives, which will hereafter be

referred to as the gradient vector, $\boldsymbol{g}$. Once the direction is determined the magnitude of the step is determined using a line search.

$$U(x+\delta x) = U(x) + \frac{\partial U}{\partial x}\delta x + \frac{1}{2!}\frac{\partial^2 U}{\partial x^2}(\delta x)^2 + \ldots \quad \textbf{(2.9)}$$

The line search uses the 'golden section' approach to determine the optimum magnitude to move in a given direction from a point P_1 on the energy landscape. This is achieved by selecting two more points on the line (P_2 and P_3) such that the energy at P_2 is less than the energy at P_1 and P_3, and that P_2 lies closer to P_3 than P_1, equations (2.10) and (2.11). A fourth point, P_4, is then selected at a fractional distance of 0.38197 into the region between P_1 and P_2. If $E_4 < E_1$ then P_1 is discarded and replaced with P_4. One can then iterate over this process until the optimum solution is identified. The conjugate gradient method is an efficient was of approaching the local minima when the starting point is far from the local minimum. Here successive line searches are made orthogonal to the previous search vector.

$$E_2 < \min(E_1, E_3) \quad \textbf{(2.10)}$$

$$\left|\overline{P_2P_3}\right| < \left|\overline{P_1P_2}\right| \quad \textbf{(2.11)}$$

Although the conjugate gradient is relatively inexpensive, it becomes less efficient near the minimum. As such it is advantageous at this point to use other methods which evaluate the second derivatives such as a Newton-Raphson[4] procedure. Hereafter the second derivatives matrix will be referred to as the Hessian matrix, H. Here the displacement vector, Δx, is defined following equation (2.12). The scaling factor, α, is required as in

reality the energy surface is unlikely to be harmonic and therefore the minimum cannot be achieved in one step. The scaling factor is determined by performing a line search along the search vector. It is then possible to iterate over this process until the minimum is found. This method is far more computationally expensive than the simple conjugate gradient method but is very efficient when near the minimum.

$$\Delta x = -\alpha H^{-1} \quad \textbf{(2.12)}$$

A final point to consider is that these optimisation procedures are designed to find the local minimum relative to the starting configuration and not necessarily the global minimum. As such the starting configuration is very important but relatively easily determined for the systems investigated in this work from experimental data.

2.1.3 Defect Calculations

Once the configuration has been geometry optimised and the relaxations inherent in the potential model have been accounted for it is possible to include lattice defects. The lattice will then respond to the defect and the ions closest to the defect will undergo relaxations to accommodate it. The degree of relaxation of the lattice ions reduces with increasing separation from the defect centre. As such the Mott-Littleton[5] approximation was constructed to improve the computation efficiency of such calculations. Here the ions within a spherical region closest to the defect centre, which exhibits the majority of the lattice relaxations, are allowed to relax to zero strain explicitly. This region is referred to as region I. Region II includes all ions outside of the region I cut-off and extends to infinity. Within this region the displacements for the lattice ions are assumed to occur as a result of the polarisation due to the effective charge of the defect, summarised in equation (2.13); where P is the polarisation, q is the charge of the defect and ε is the static dielectric

constant of the material. This region is subdivided into spherical shells, region IIa and IIb. Region IIa acts as a buffer between region I and region IIb, where the energy contribution from the displaced lattice ions are calculated explicitly as for region I. The total energy of the system can be calculated following equation (2.14)where $U_{11}(x)$ is the energy of region I with respect to the Cartesian coordinates, $U_{22}(\xi)$ is the energy of region II as a function of the Cartesian displacements and $U_{12}(x,\xi)$is the energy of interaction between the two regions. The energy of region IIb can be calculated as a function of the Cartesian displacements and the hessian matrix, *H22*, for region IIb, summarised in equation (2.15) where the response of the atoms within this region are treated as purely harmonic as the forces acting on region II are small. By assuming the displacements within this region will be at equilibrium the condition in equation (2.16) can be defined. By rearranging and substituting equations (2.15) and (2.16) into equation (2.14) the total energy of the system can be calculated without evaluating the energy of region II and the infinite hessian matrix, following equation (2.17). The defect energy can then be calculated following equation (2.18).

$$P = \frac{q}{4\pi r^2}\left(1 - \frac{1}{\varepsilon}\right) \tag{2.13}$$

$$U_{Total}(x,\xi) = U_{11}(x) + U_{12}(x,\xi) + U_{22}(\xi) \tag{2.14}$$

$$U_{22}(\xi) = \frac{1}{2}\xi^T H_{22}\xi \tag{2.15}$$

$$\left(\frac{\partial U_{tot}(x,\xi)}{\partial \xi}\right)_x = \left(\frac{\partial U_{12}(x,\xi)}{\partial \xi}\right)_x + H_{22}\xi = 0 \tag{2.16}$$

$$U_{Total}(x,\xi) = U_{11}(x) + U_{12}(x,\xi) - \frac{1}{2}\left(\frac{\partial U_{12}(x,\xi)}{\partial \xi}\right)_x \xi \tag{2.17}$$

$$U_{defect}(x,\xi) = U^{d}_{Total}(x,\xi) - U^{p}_{Total}(x,\xi) \quad \textbf{(2.18)}$$

Convergence testing has been performed for all defect simulations to identify the appropriate region sizes to select. One such plot for a Frenkel Pair cluster defect is illustrated in Figure 2.1. Here it can be seen that the defect energy converges with increasing region I radius, however the calculation time increases. As such there is a balance between computational accuracy and efficiency. The region I cut-off is specified within the relevant chapters for the defect simulations, but in all cases the region IIa radius is twice that of region I.

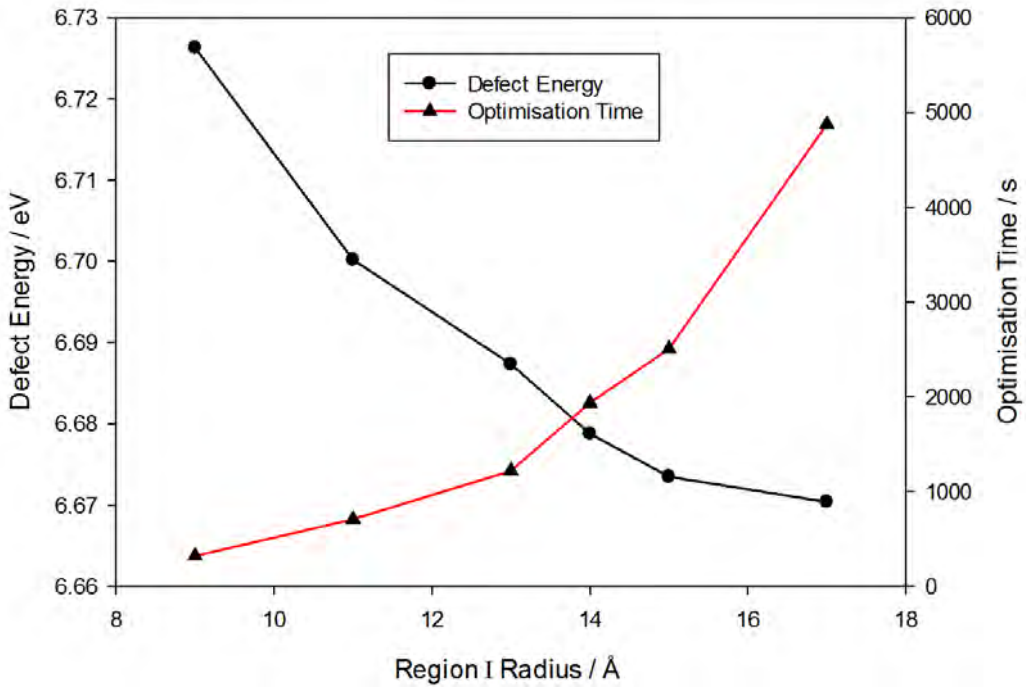

Figure 2.1: Defect energy convergence and simulation time as a function of region I radius

2.1.4 Surface Simulations

The surface simulations presented in this work were carried out using the METADISE[6] code, using the same atomistic potential model described previously. The surface simulations involved cutting the bulk material at the Miller index of interest and defining units which are repeated as a function of distance from the surface. Progressive slices can then be taken through layers of atoms within the repeating unit to find valid surface cuts. The criteria for defining a valid cut is that it is non-polar, with these surfaces defined as either type 1 or 2 by Tasker[7]. Simple examples of these surfaces are illustrated in Figure 2.2, along with a type 3 surface which does not meet this criteria and is therefore invalid. One valid surface cuts have been identified the surface energy can be calculated and optimised through the methods discussed previously. The only modification required is to use a method comparable to the Ewald summation for three dimensional systems,

developed by Parry[8], to evaluate the coulombic interactions in two dimensional periodic systems.

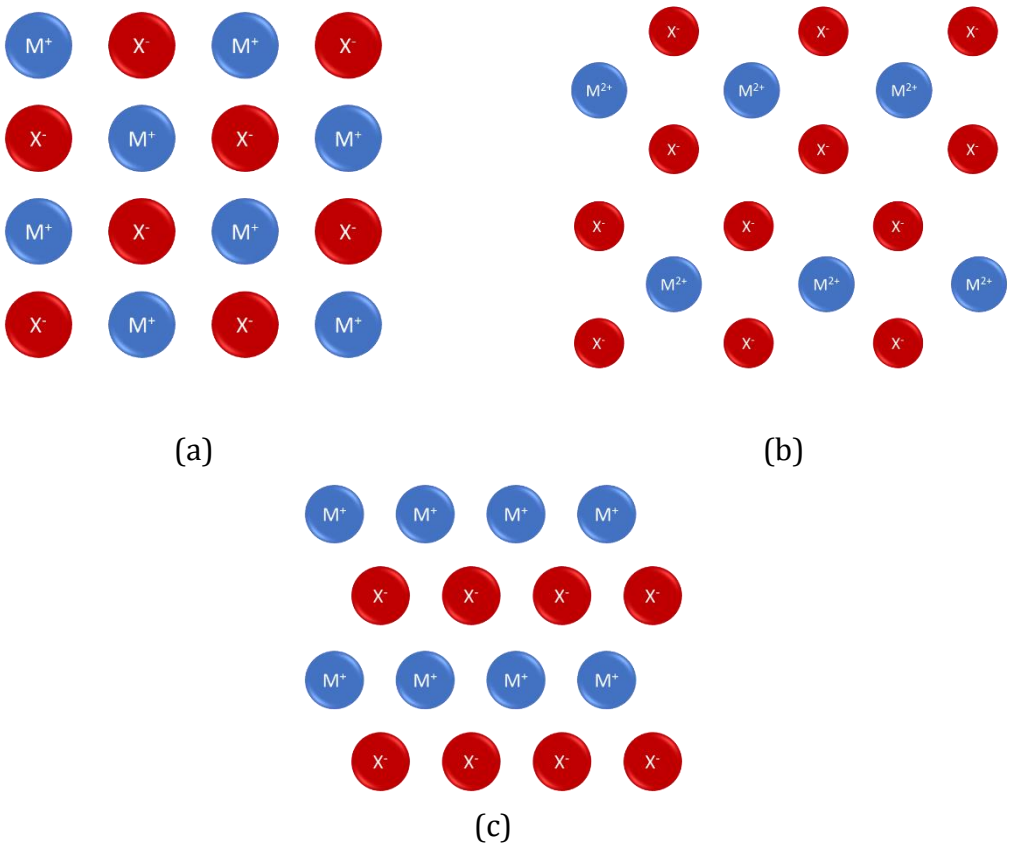

Figure 2.2: Schematic representation of the different surface types as defined by Tasker. (a) Type 1, (b) Type 2 and (c) Type 3

A two region approach (schematic illustrated in Figure 2.3 (a)) is taken within the METADISE code in which the atoms within region I are those nearest to the surface which undergo the largest relaxations and as such are allowed to relax freely to achieve zero force. All ions outside of this region belong to region II. Here the ions are constrained to their lattice sites and as such an appropriate depth for region I must be identified so as there are no distortions to the bottom layers of ions. A plot of the atomic displacements as a function of depth for a cut of the (110) surface after optimisation is illustrated in

Figure 2.3 (b). It can be seen that the magnitude of the displacement for the ions converges to zero for the ions at the bottom of region I and therefore an acceptable region I size has been used. This analysis was performed for all cuts of the surfaces of interest. A region II size of twice that of region I was found to be sufficient for convergence for all surface simulations.

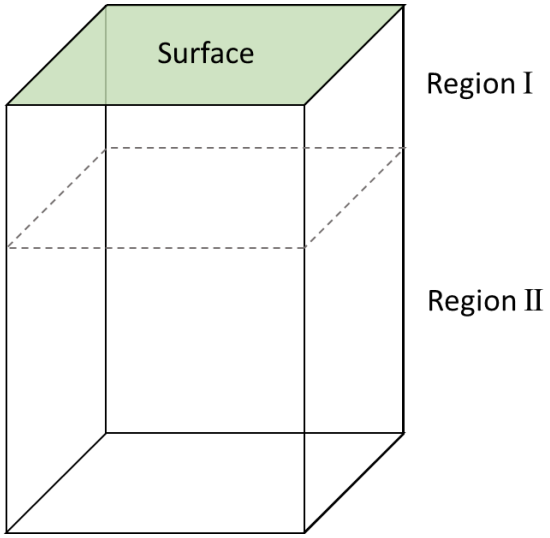

(a)

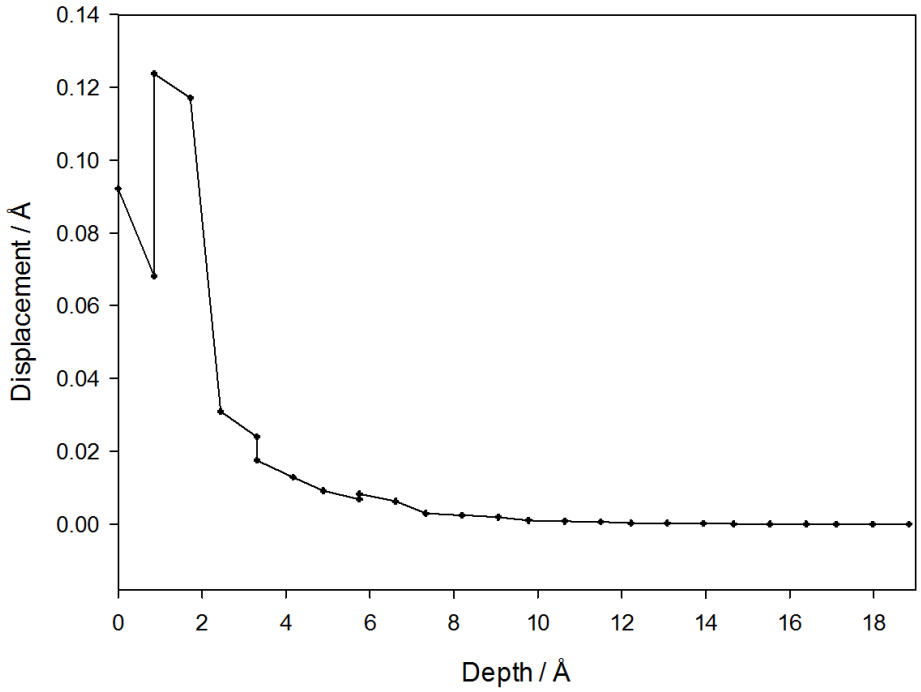

(b)

Figure 2.3: (a) Schematic of the two region approach taken in METADISE and (b) Magnitude of the displacement of the atoms upon relaxation as a function of perpendicular distance from the surface

2.1.4.1 Surface and Attachment Energies

The surface energy, γ, can be conceptualised as the energy required to cleave the bulk crystal to expose the surface and is defined in equation (2.19). Here U_{surf} and U_{bulk} are the energy of the simulation cell containing the surface and that of a bulk simulation respectively. The bulk energy is scaled so as the energy is expressed in terms of the equivalent number of ions as are in surface region (*ie.* the ratio between the number of ions in region I and II). The energy is expressed per unit area and, as surfaces tend to be higher in energy than the bulk, a small positive value would be indicative of a stable surface.

$$\gamma = \frac{\left(U_{surf} - \frac{1}{2}U_{bulk}\right)}{A} \qquad \textbf{(2.19)}$$

An alternative description of the stability of a surface is the attachment energy. This can be conceptualised as the energy released when a new layer with thickness d_{hkl} is added to the surface. This can be used to predict the 'kinetic morphology' as it describes the ease with which a new layer can be added to the surface, and therefore is related to the rate of growth perpendicular to the surface. One of the limitations of this method is that it assumes bulk termination of the surface and therefore does not take into account surface relaxations.

2.1.4.2 Morphology Prediction

It has been suggested that the equilibrium morphology of a crystal is dictated by the relative energies of the surfaces so as the total surface free energy is minimised[9]. The surface free energies can be approximated at 0 K from the surface energies calculated in static calculations. The Wulff construction can then be used to determine the relative

height, normal to the surface from the centre of the crystal, for each surface as the length of this vector is proportional to the surface energy. This morphology is known as the 'equilibrium morphology' as it assumes that all surfaces are grown at equilibrium. This does not however take into account kinetic factors and as such the kinetic morphology can also be determined using a similar construction. In this case the modulus of the attachment energies are used so as surfaces with the lowest attachment energy, with the highest rate of growth normal to the surface, are expressed least in the morphology of the crystal. It is often difficult to compare surface energies explicitly to experimental data, however it is much easier to compare the predicted morphology with those of real crystals. There are still however challenges with this approach which will be discussed further within the appropriate chapter.

2.1.5 Molecular Dynamics (MD)

MD simulations allow the properties of a system to be evaluated as a function of time. This is achieved by through numerical integration of Newton's equations of motion to determine the trajectories of the ions within the system for a given set of interatomic potentials. Principally the force can be described following equation (2.20), where a_i, v_i and r_i are the acceleration, velocity and the position of ion, i, at a given time, t, respectively. The mass of the ions, m_i remains constant throughout the simulation. The force acting upon an ion is related to the first derivative of the interatomic potential with respect to the position relative to all other ions in the system. The velocity and position of a particle moving under the action of a force over a given time step, τ, can therefore be defined following equations (2.21) and (2.22) respectively. The initial atomic positions are taken from the crystal structure to generate the simulation supercell, whilst the initial velocities are drawn randomly from a Maxwell-Boltzmann distribution. As the ions move

the forces acting upon them change and as such a small time step is required. The kinetic and potential energy of the system can then be evaluated following equations (2.23) and (2.24)

$$F_i = m_i a_i = m_i \frac{\partial v_i}{\partial t} = m_i \frac{\partial^2 r_i}{\partial t^2} = -\nabla_i U \tag{2.20}$$

$$v_i(\tau) = v_i(0) + \int_0^\tau \frac{dv_i}{dt} dt \tag{2.21}$$

$$r_i(\tau) = r_i(0) + \int_0^\tau v_i(t)\, dt \tag{2.22}$$

$$E_{kin}(t) = \frac{1}{2} \sum_1^N m_i v_i^2(t) \tag{2.23}$$

$$E_{pot}(t) = \sum_i \sum_{j>i} U_{ij}\left(r_{ij}(t)\right) \tag{2.24}$$

2.1.5.1 Integration Algorithm

The work presented here uses the velocity Verlet algorithm, based on the original Verlet algorithm, to efficiently integrate these equations. The initial stage in this algorithm is to evaluate the velocities of the ions after half a time step followed by the positions after a full time step, following equations (2.25) and (2.26). The force is then recalculated as the positions have changed which then allows for the half step velocities to be advanced to those after a full step using the new force, equation (2.27).

$$v_i\left(t + \frac{1}{2}\tau\right) = v_i(t) + \frac{1}{2} a_i(t)\tau \tag{2.25}$$

$$r_i(t+\tau) = r_i(t) + v_i(t)\tau + \frac{1}{2} a_i(t)\tau^2 = r_i(t) + \tau v_i(t)\left(t + \frac{1}{2}\tau\right) \tag{2.26}$$

$$v_i(t+\tau) = v_i\left(t+\frac{1}{2}\tau\right) + \frac{1}{2}a_i(t+\tau)\tau \quad \textbf{(2.27)}$$

These equations can then be repeatedly solved whilst incrementing the time by a time step, τ, until the desired simulation time is reached. The need to keep τ small limits the timescales accessible to MD simulations to the order of picoseconds.

2.1.5.2 Periodic Boundary Conditions (PBC)

Even the largest simulations conducted in this work only contain 1.2 x 10^6 ions which is extremely small in comparison to Avogadro's constant. In order to attempt to model an infinite lattice periodic boundary conditions are employed. In this construct the simulation supercell is surrounded by periodic images of itself, which are updated throughout the simulation. An ion leaving through one of the periodic boundaries will re-join the simulation cell on the opposite side, Figure 2.4. Within this construct the minimum image convention is employed so as ions will only interact with closest images of the remaining ions.

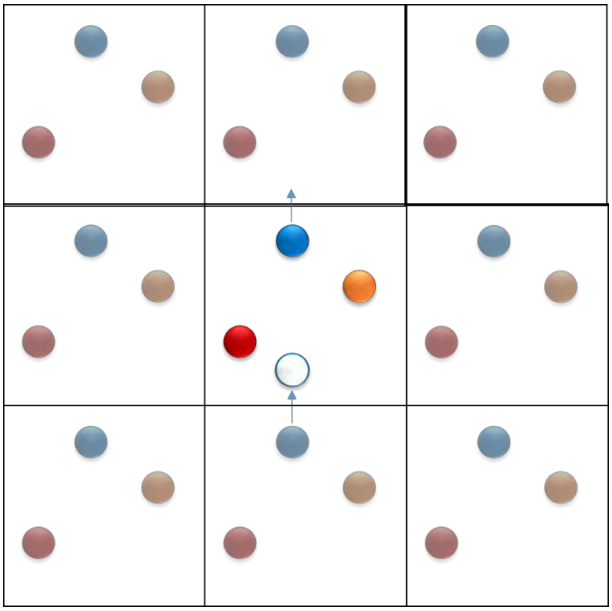

Figure 2.4: Two dimensional representation of periodic boundary conditions. The simulation cell is at the centre of the array with periodic images surrounding.

2.1.5.3 Ensembles

In statistical mechanics an ensemble is a probability distribution over a collection of possible microstates of a system. The properties of the system can be described by a small number of observables known as state variables, from which all other thermodynamic properties can be inferred. In a basic MD simulation number of atoms, N, the volume, V, and the total energy of the system, E, remain constant and therefore all MD frames share these state variables in common and therefore belong to the NVE ensemble, also known as the micro canonical ensemble. It follows that that time average taken over all MD frames is equivalent to the ensemble average. This is known as the ergodic hypothesis. Other ensembles are available including the isobaric-isothermal (NPT) ensemble. In this ensemble a thermostat and barostat must be used to make sure the time average temperature and pressure remains constant. The thermostat couples the system to a heat bath, allowing heat to transfer in and out of the system. The Berendsen thermostat has

been used in all of the MD simulations that follow. This scales the velocities of the ions in the system based on a target thermostat energy, σ, which is derived from the total degrees of freedom, f, and the target temperature of the system, T_{ext}, as described in equation (2.28). The scale factor for the velocities, χ, is calculated following equation (2.29), where $\mathcal{T}_T$ represents a time constant for temperature fluctuations which has been set to 1 ps in this work. The velocities are then scaled following equation (2.30).

$$\sigma = \frac{f}{2} k_B T_{ext} \tag{2.28}$$

$$\chi(t+\tau) = \left[1 + \frac{\tau}{\mathcal{T}_T}\left(\frac{\sigma}{E_{kin}(t+\tau)}\right) - 1\right]^{\frac{1}{2}} \tag{2.29}$$

$$v(t+\tau) = v(t+\tau)\chi \tag{2.30}$$

Similarly the system is coupled to the Berendsen barostat. In the simplified case for an isotropic system the MD cell volume is scaled by a factor, η, and the coordinates and cell vectors are scaled by $\eta^{1/3}$, following equations (2.31) to (2.34). Here the scale factor is calculated from the target pressure of the system, $\mathcal{P}_{ext}$, and the instantaneous pressure of the system, $\mathcal{P}(t)$, where $\beta\tau$, $\mathcal{T}_P$, $\mathcal{W}_{atomic}$ and $\underline{H}$ are the isothermal compressibility of liquid water, the time constant for pressure fluctuations, the forcefield virial and the cell matrix respectively. All of the simulations in this work were allowed to equilibrate within the NPT ensemble before being taken and equilibrated in the NVE ensemble.

$$\mathcal{P}(t) = \frac{2E_{kin}(t) - \mathcal{W}_{atomic}(t)}{3V(t)} \tag{2.31}$$

$$\eta(t) = 1 - \frac{\beta\tau}{\mathcal{T}_P}\left(\mathcal{P}_{ext} - \mathcal{P}(t)\right) \tag{2.32}$$

$$V(t+\tau) = \eta(t)V(t) \tag{2.33}$$

$$\underline{H}(t+\tau) = \eta(t)^{\frac{1}{3}}\underline{H}(t) \tag{2.34}$$

2.1.5.4 Defect Identification

Two defect detection method have been employed in this work, the radius and the Voronoi method. A schematic of the radius method is illustrated in Figure 2.5. Here the lattice sites for an undamaged reference cell are represented by crosses, referred to as nodes hereafter, and atoms are represented by red spheres. A cut-off radius, R_{def}, is selected so as to define regions associated with each node. If atoms lie within the region belonging to a node then they become claimees of that node. Any atoms that do not belong to a node are classed as general interstitials and any node with no claimees is classed as a vacancy site. When two or more atoms claim a nodes the atom closes to the node becomes the 'true claimee' and therefore the other atoms become interstitials associated with the node.

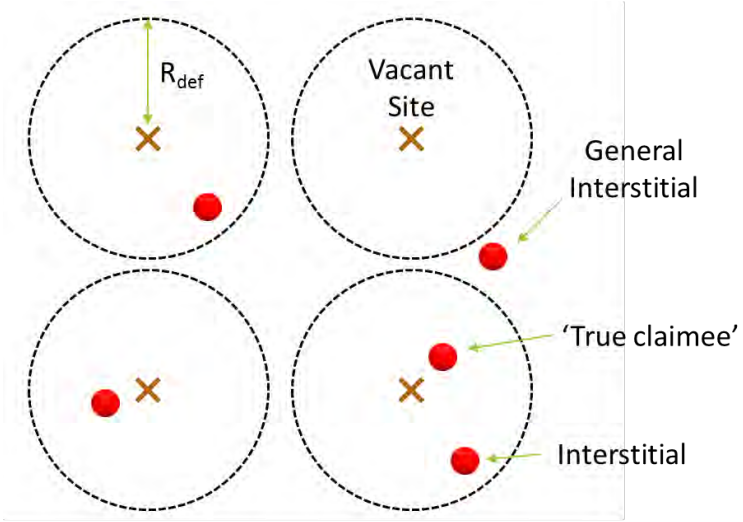

Figure 2.5: Two dimensional representation of the radius method for defect identification

The Voronoi method for defect detection follows a similar concept using the sites in a reference configuration as nodes, however a cut-off radius is not used and a Voronoi diagram is constructed. A schematic showing the process by which this is constructed in two dimensions is shown in Figure 2.6. Firstly the Delaunay triangulation for the reference nodes is constructed such that no reference nodes lie within the circumcircles defined by the triangles. The Voronoi diagram can then be constructed by connecting the centres of the circumcircles.

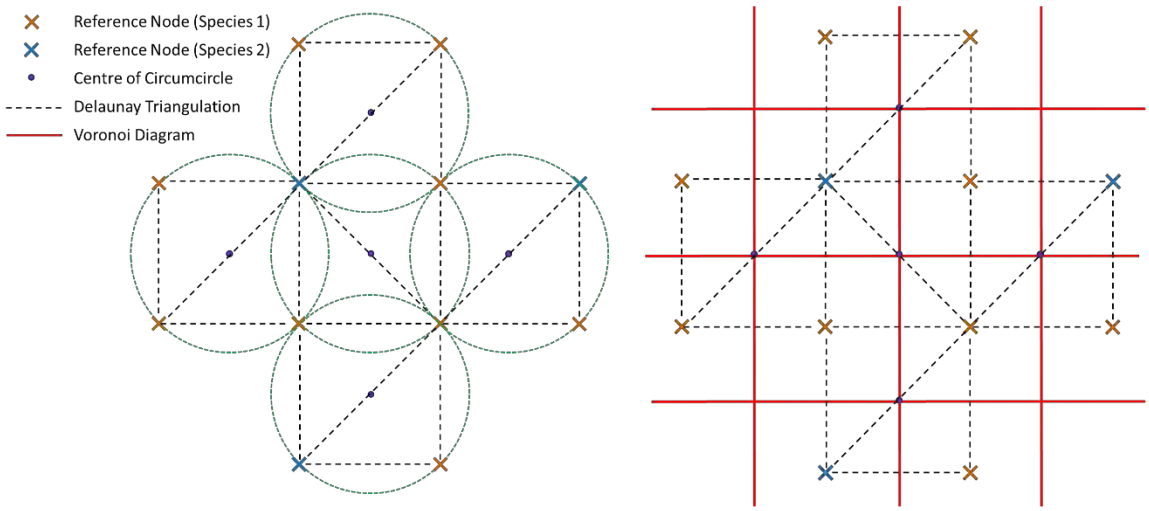

Figure 2.6: Construction of the Voronoi diagram in two dimensions

Once the Voronoi diagram has been constructed the claimees for the nodes can defined in a similar was as for the radius method. A schematic is illustrated in Figure 2.7. A major difference between the Voronoi method and the radius method is that there are no general interstitial as there are no gaps between the voronoi cells. Additionally the nodes can be related to a particular species in the reference configuration and as such anti-site

defects are identified if the true claimee of the node is of a different species to that of the node (*ie.* a yttrium atom claiming a phosphorus node).

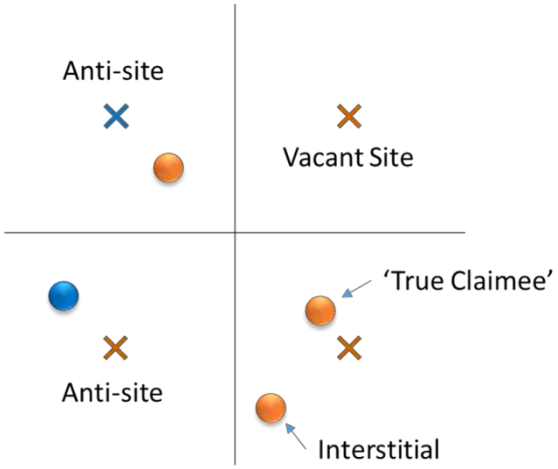

Figure 2.7: Two dimensional representation of the Voronoi method for defect identification

2.2 Experimental Techniques

2.2.1 Synthesis of Mixed Ca/Sr Fluorapatite

Samples of fluorapatite containing various concentrations of Ca and Sr have been synthesised using a solution based method and microwave synthesis.

2.2.1.1 Solution Synthesis

The desired fluorapatite materials were synthesised *via* a precipitation reaction where 9 cm^3 of a solution containing $(NH_4)HPO_4$ and NH_4F was taken from a 10 cm^3 stock solution (0.6599 and 0.0619 g of $(NH_4)HPO_4$ and NH_4F respectively). This was then heated and stirred in a round bottom flask until a temperature of 70 °C was achieved and all of the solids had dissolved. A 15 cm^3 solution of the mixed metal nitrates was then added dropwise at a rate of ca. 1 drop per second to the vigorously stirring phosphate solution. Once added the

flask was allowed to stand for ca. 12 hours at room temperature. The resulting precipitate was collected by vacuum filtration, dried in an oven and pressed into an 8 mm pellet. The samples were then sintered at 1200 °C for 6 hours before being allowed to cool to room temperature. The relative masses of the nitrate salts used for each sample are summarised in Table 2.1.

Table 2.1: Masses of the metal nitrate salts used to produce the mixed Ca/Sr fluorapatite samples *via* the solution method

Sample	$Ca(NO_3)_2.4H_2O$ / g	$Sr(NO_3)_2$ / g	Target Sr Concentration / mol %
Solution 1	1.6291	0.1270	8
Solution 2	1.4166	0.3175	20
Solution 3	1.2395	0.4762	30
Solution 4	0.8854	0.7937	50
Solution 5	0.3542	1.2698	80

2.2.1.2 Microwave Synthesis

The samples were produced using the same salts as described for the solution method. A 60 cm^3 stock of the metal nitrate solutions was produced using the masses summarised in Table 2.2. Similarly a 40 cm^3 stock solution of the $(NH_4)HPO_4$ and NH_4F salts was produced (2.4012 and 0.2224 g of $(NH_4)HPO_4$ and NH_4F respectively). 30 cm^3 of the metal nitrate solution was added directly to 20 cm^3 of the phosphate solution within a Teflon lined microwave vessel. The lid was tightened and the solution was heated to 200 °C for 3 hours. The resulting precipitate was filtered by vacuum filtration.

Table 2.2 Masses of the metal nitrate salts used to produce the mixed Ca/Sr fluorapatite samples *via* the microwave method

Sample	$Ca(NO_3)_2.4H_2O$ / g	$Sr(NO_3)_2$ / g	Target Sr Concentration / mol %
Microwave 1	6.5484	0.5104	8
Microwave 2	4.9825	1.9141	30
Microwave 3	2.8471	3.8282	60
Microwave 4	1.4236	5.1043	80

2.2.2 X-Ray Fluorescence Spectroscopy (XRF)

Wavelength Dispersive X-ray fluorescence spectroscopy (WD-XRF) was used to measure the concentration of calcium and strontium within the aforementioned samples. In this method the samples are exposed to high energy X-rays produced using rhodium anode which causes electronic excitations. Upon relaxation to the ground state, X-rays of a lower energy are fluoresced and detected by a scintillation counter. The wavelengths of the emitted photons are indicative of the elements that are present in the sample. There can however be some overlap of the fluorescence from different orbitals for different elements and as such care should be taken when considering which peaks in the spectrum to analyse. In WD-XRF a monochromator is positioned between the sample and the detector to select for photons with the wavelength of interest, helping to resolve peaks in the spectrum. The concentration of the element is proportional to the intensity of the peaks in the spectrum, allowing for the relative concentrations of each to be evaluated. These measurements were performed on a Bruker AXS S8 Tiger wavelength dispersive x-ray fluorescence spectrometer.

2.2.2.1 Sample Preparation

Both the calibration standards and the mixed Ca/Sr fluorapatite samples were prepared for WD-XRF analysis by producing fused beads. The samples were mixed in a 10:1 ratio of flux (3.5 g) to sample (0.35 g). The flux material was a mixture of lithium meta and tetraborate. These were ground together in a mortar and pestle and then heated in a crucible (95 % platinum 5 % gold) at 1250 °C for 6 minutes. After this time a small amount (ca. 15 mg) of ammonium iodide was added as a releasing agent and the crucible was returned to the furnace for a further 6 minutes. The crucible was subsequently removed from the furnace and the molten bead was swirled around to remove any air bubbles.

Finally the crucible was returned to the furnace for a further 30 seconds before being removed and allowed to cool, producing a bead with a diameter of 28 mm and a thickness of ca. 3.5 mm.

2.2.2.2 Calibrations

A calibration can be used to help account for any matrix effects which have not been removed by using appropriate sample preparation methods. The calibration curves for calcium, strontium and phosphorus are illustrated in Figure 2.8 (a), (b) and (c) respectively. The concentration range over which the calibration was constructed extends above and below the expected concentrations of these elements within the samples. A strong linear relationship was observed for all elements, indicating valid calibration curves were produced.

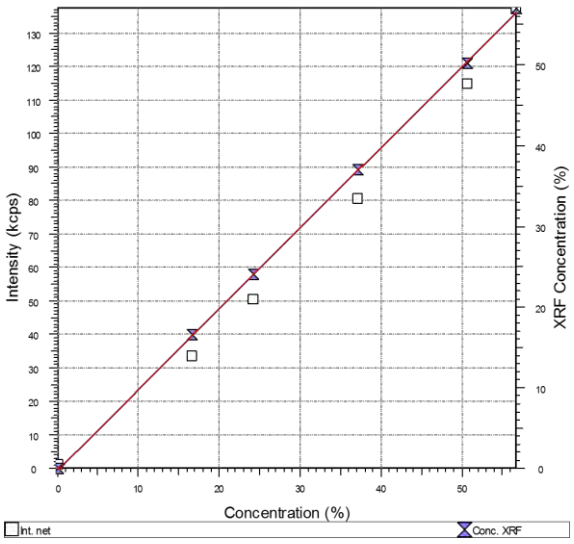

(a)

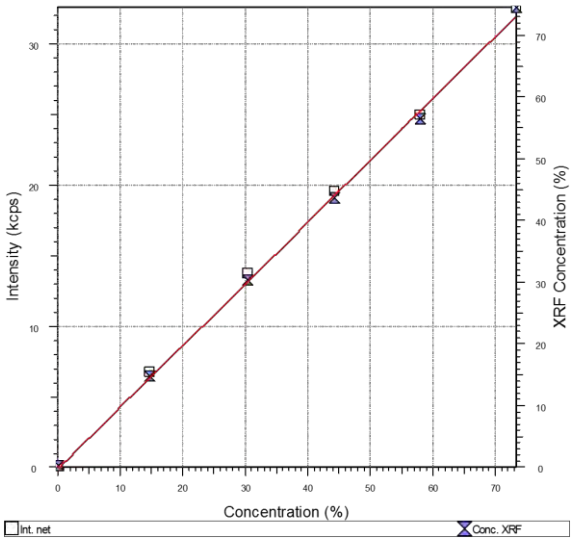

(b)

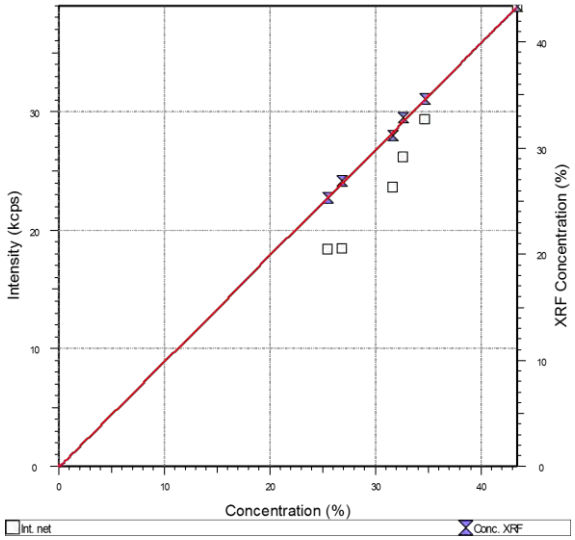

(c)

Figure 2.8: XRF calibration curves for (a) strontium, (b) calcium and (c) phosphorus

The calibration beads were prepared *via* the fused bead method using appropriate masses of the salts summarised in Table 2.3.

Table 2.3: Reagents used to make the calibration beads and the corresponding oxidation products

Reagents Used	Oxidation Products
$Ca_3(PO_4)_2$	CaO SrO P_2O_5
$Sr_3(PO_4)_2$	
CaF_2	
SrF_2	

2.2.3 X-Ray Diffraction (XRD)

Powder X-ray diffraction (PXRD) can be used to investigate the long range order within crystalline materials. Different crystalline materials will have different PXRD patterns which can be used to identify the phases present within a sample. In this work PXRD has been used to determine sample purity.

The technique relies upon the assumption that the infinite crystal lattice can be represented by a small repeating unit known as the unit cell. This is the smallest irreducible unit which expresses all of the symmetry elements of the crystal structure, which can be tessellated to generate the entire crystal structure. The lattice parameters describe the dimensions of the unit cell, with the a, b and c parameters describing the length of the axes, whilst α, β and γ describe the angles between them. There are seven possible primitive (P) lattice systems which describe the shape of the unit cell, which may be combined with the three different lattice centrings. These include body centred (I), face centred (F) and base centred (C). This produces the 14 different lattice types known as Bravais lattices, Figure 2.9, which contain symmetry information inherently expressed within the crystal structure.

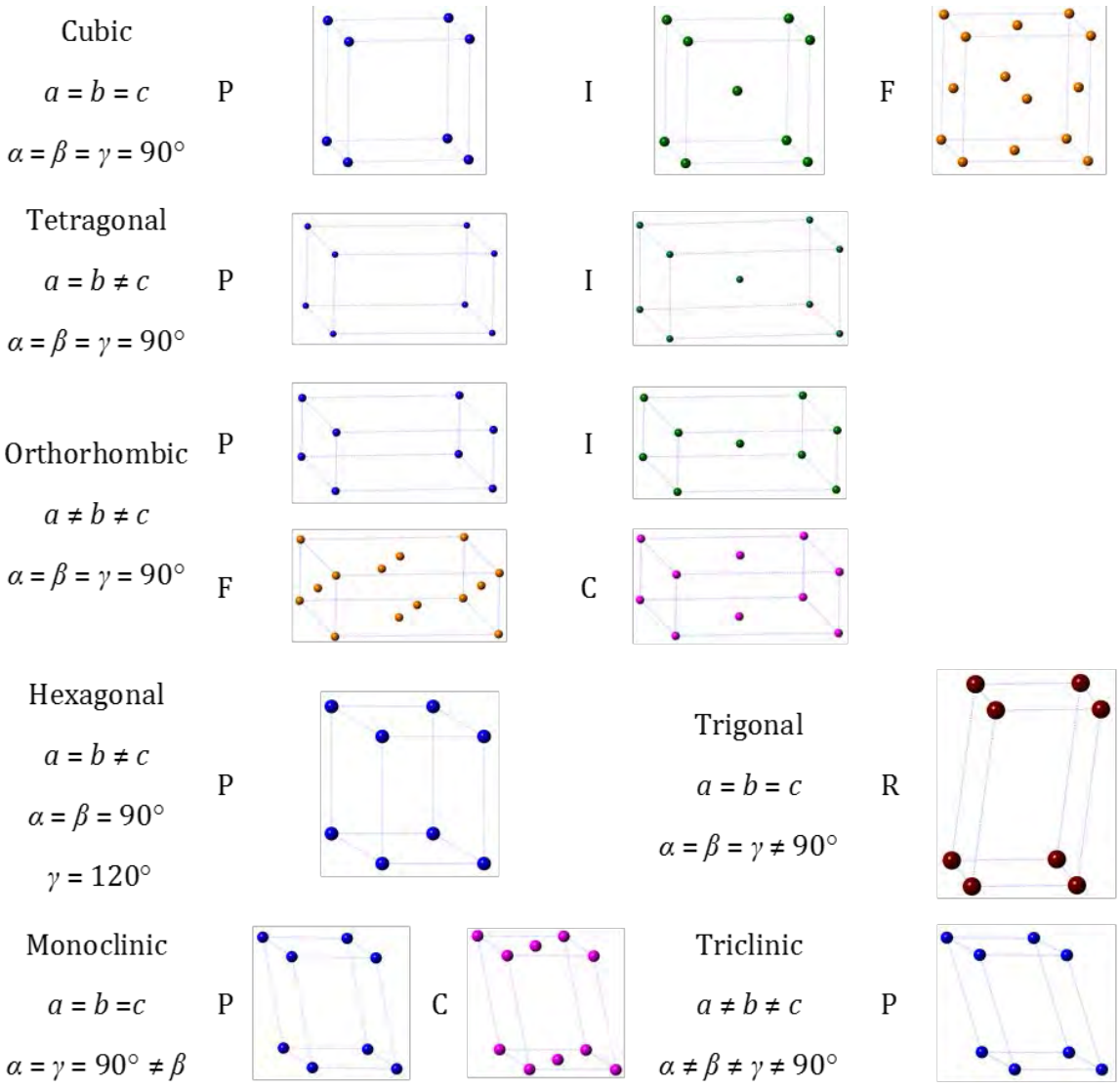

Figure 2.9: The 14 Bravais lattices

The positions of the atoms within the unit cell are described in terms of fractional coordinate along the three unit cell axes. The addition of atoms to the unit cell introduces further symmetry elements including screw axes and glide planes. The combination of these symmetry operations for a 3 dimensional object with the Bravais lattices generates a total of 230 space groups[10].

2.2.3.1 Lattice Planes

The link between diffraction experiments and crystallography comes with the concept of lattice planes. These are sets of equally spaced parallel planes constructed from repeating arrays of lattice points. A lattice plane can be described by the vector normal to the plane passing through the origin or by a set of three indices, known as Miller indices. These indices for a generic plane are labelled *h*, *k* and *l*, and are the reciprocal of the fractional intercept along the crystallographic axes *a*, *b* and *c* respectively, Figure 2.10. The formal representation of the miller indices for a set of planes is {*hkl*}. In some crystallographic systems sets of planes with different miller indices are equivalent due to symmetry (*ie.* {100}, {010} and {001} for a cubic lattice) and therefore a multiplicity is assigned to each set of planes to reflect this. These infinite arrays of lattice planes are separated by a perpendicular distance, d_{hkl}, referred to as the d-spacing.

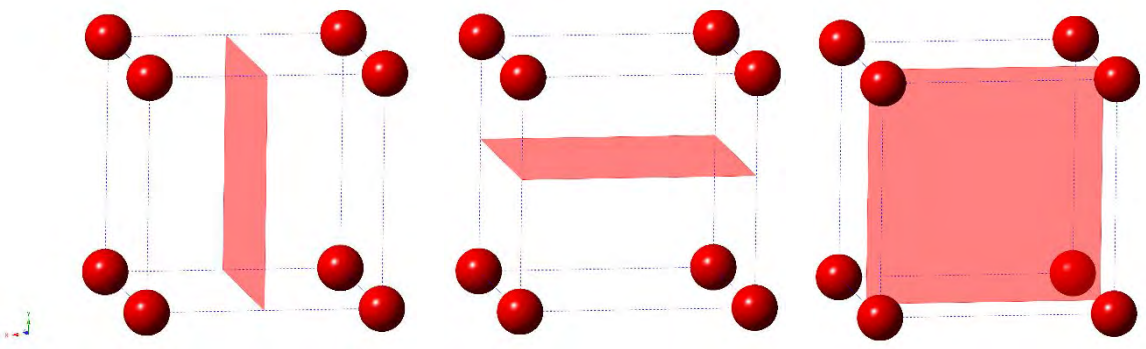

Figure 2.10: Examples of the (200), (020) and (002) lattice planes

2.2.3.2 Bragg's Law

X-ray diffraction experiments are founded on the concept that an incident X-ray beam is diffracted by the lattice planes. This is possible as the wavelength of the X-rays is similar to that of the d-spacing between the planes. A schematic illustrating the diffraction of an

incident beam by two parallel lattice planes, separated by a distance, d_{hkl}, is illustrated in Figure 2.11.

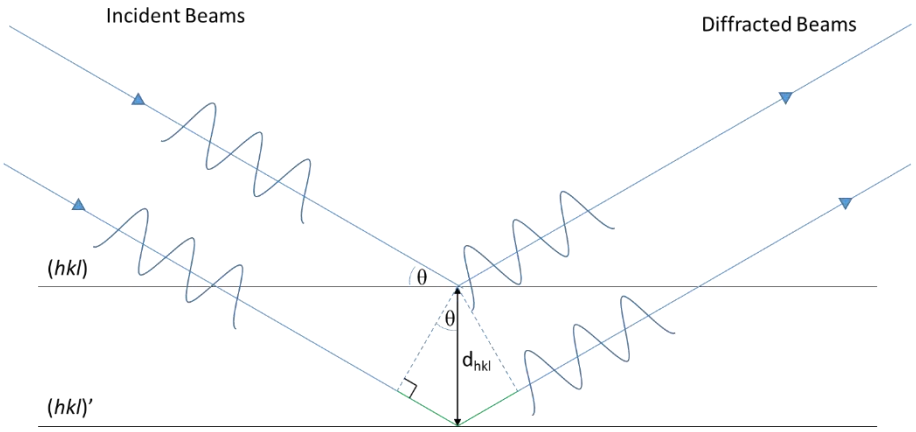

Figure 2.11: Geometric representation of Bragg's Law in real space

The second beam in the schematic has a longer path length than that of the first incident beam. In order for the diffracted X-ray beams to add constructively the difference in path length between the two beams bust be an integer multiple of the wavelength. This is inherently linked to the incident angle through equation (2.35), known as Bragg's law.

$$n\lambda = 2d_{hkl}\sin(\theta) \tag{2.35}$$

It is also useful to consider this formalisation in reciprocal space using the Ewald sphere construction. A schematic representation in two dimensions is illustrated in Figure 2.12, where d^* is the reciprocal lattice vector $\left(\frac{1}{d_{hkl}}\right)$. The lattice for a single crystal is described as an array of reciprocal lattice points. An imaginary sphere of radius $\frac{1}{\lambda}$ is centred on the single crystal such that the origin lies on the surface of the sphere. The reciprocal lattice may then be rotated about the origin, bringing reciprocal lattice points through the

surface of the sphere. As discussed previously Bragg scattering is an elastic process (*ie.* the wavelength of the incident and diffracted beams are equivalent) and as such this condition is only satisfied for those reciprocal lattice points that lie on the surface of the sphere.

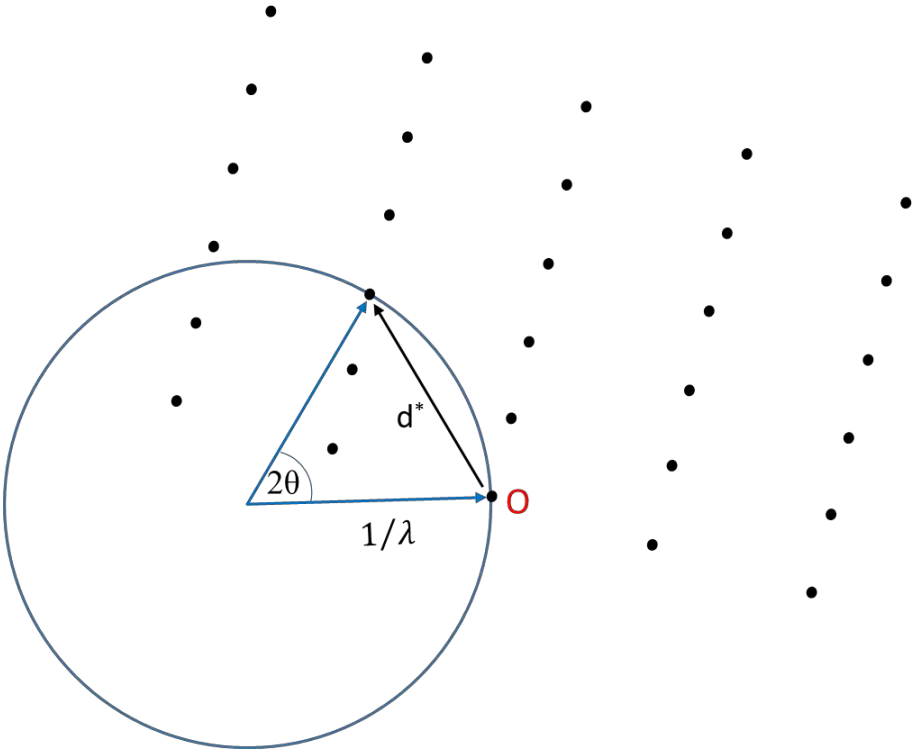

Figure 2.12: Geometric representation of Bragg's Law in reciprocal space using the Ewald's sphere construction

An ideal powder contains an infinite number of crystallites which are randomly orientated in all directions with uniform probability. As such the 2D diffraction pattern of an ideal powder consists of rings of uniform scattered intensity. Generally 1D PXRD patterns are recorded as a function of 2θ.

2.2.3.3 Diffraction Patterns

A large amount of information is contained within the PXRD pattern. The peak position is dictated by the d-spacing as described previously. However, there are also experimental factors which may contribute including the zero point error of the instrument and the wavelength of the incident X-ray beam. As well as Bragg peaks a PXRD pattern will also contain a continuous background which is present under and between these peaks. Sample effects such as X-ray absorbance, fluorescence, amorphous material and incoherent scattering will contribute. This background component is disregarded for analysis using the Rietveld method (discussed later) and is accounted for using relatively arbitrary functions to correct peak intensities. The peak intensity, I_{hkl}, is the corrected peak intensity after background subtraction, equation (2.36).

$$I_{hkl} = \sum_{i=1}^{n} \left(Y_i^{obs} - Y_{bi} \right) \quad \textbf{(2.36)}$$

The integrated intensity relies on a variety of factors from the sample and the instrumentation and can be calculated following equation (2.37), the terms in this equation are outline in Table 2.4.

$$I_{hkl} = K \times \rho_{hkl} \times L_\theta \times P_\theta \times A_\theta \times T_{hkl} \times |F_{hkl}|^2 \quad \textbf{(2.37)}$$

Table 2.4: Summary of parameters contributing to the intensity of a Bragg peak

Variable	Term	Definition
$\boldsymbol{K}$	Scale Factor	Normalises the calculated intensities to the observed intensities.
$\boldsymbol{\rho_{hkl}}$	Multiplicity Factor	Multiplicity of {hkl}.
$\boldsymbol{L_\theta}$	Lorentz Multiplier	Accounts for the geometry of the diffractometer.
$\boldsymbol{P_\theta}$	Polarisation Factor	Polarisation of the X-ray beam.
$\boldsymbol{A_\theta}$	Absorption Multiplier	Accounts for self-absorption of the incident and diffracted beams by the sample.
$\boldsymbol{T_{hkl}}$	Preferred Orientation	Accounts for a non-random distribution of crystallite orientations
$\boldsymbol{F_{hkl}}$	Structure Factor	Interaction of the incident radiation with the atoms in the lattice.

The major component dictating the intensity of the peak is the structure factor, which describes the interaction of the diffracted waves with the atoms within the unit cell. It can be calculated following equation (2.38), where x_j, y_j and z_j are the atomic coordinates and f_j is the atomic scattering factor of the jth atom. The atomic scattering factor describes how efficiently the electron cloud associated with the atom scatter the X-rays as a function of incident angle and is proportional to the atomic number, Z_j. Thermal motion of the atoms can serve to reduce the peak intensity and broaden the peaks.

$$F_{hkl} = \sum_{j}^{n} f_j \exp\left(2\pi\left(hx_j + ky_j + lz_j\right)\right) \quad \textbf{(2.38)}$$

The shape of the Bragg peaks depends on many factors, many of which are instrumental factors. Besides these the greatest contribution to peak shape is likely the size of the crystallites which for small crystallites serves to broaden the peaks and can be evaluated using the Scherrer equation.

2.2.3.4 Laboratory Equipment

Powder X-ray diffraction data were collected on a Bruker D8 diffractometer in transmission geometry. A curved germanium monochromator was used to provide monochromatic radiation, from a copper X-ray source, with a wavelength 1.5406 Å. The diffracted X-rays were detected using a position sensitive detector (PSD) with a 3° window. Diffraction patterns were collected in the range $10 \leq 2\theta \leq 90°$ for a duration of 3 hours. Samples were prepared by placing a small amount of sample between two layers of Scotch® Magic™ tape and were rotated in the plane perpendicular to the beam.

2.2.3.5 Rietveld Refinement

The Rietveld method is an analytical procedure by which structural information can be extracted from diffraction data by producing a model of the system[11, 12]. A reasonable starting model/models for the phase/phases present in the sample are required, describing the shape and size of the unit cell, atomic coordinates and site occupancies for the elements present. This information is then combined with a range of experimental parameters to calculate a diffraction pattern for the model. This model is fit to the experimental pattern through a least-squares refinement which minimises the residual, S_y, over all data points, equation (2.39). Here the least-squares difference between the

experimental data, y_i, and the calculated pattern, y_{ci}, is scaled by a weighting factor, w_i, equation (2.40). This is achieved by iteratively altering the selected refinement parameters.

$$S_y = \sum_{i=1}^{n} w_i \, (y_i - y_{ci})^2 \tag{2.39}$$

$$w_i = \frac{1}{y_i} \tag{2.40}$$

The progress of the refinement can be monitored in several ways including, visually, *via* statistical values and by the chemical sense of the resulting model. An example Rietveld plot is illustrated in Figure 2.13.

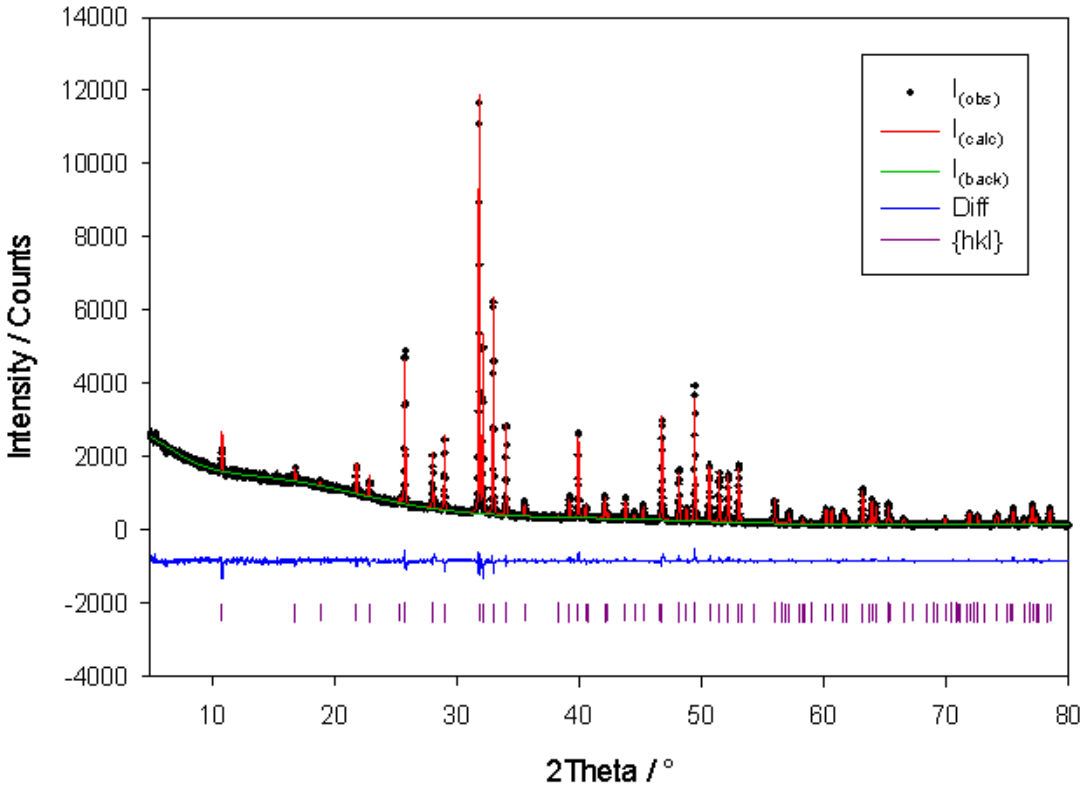

Figure 2.13: Example of a GSAS plot for a Rietveld refinement for a fluorapatite sample

The changes in the difference line give a visual indication as to the quality of the model, with a flat difference line indicating a perfect fit between the data and the model. Several statistical values are also useful for monitoring the quality of the fit, known collectively as R-Factors. Two of the R-Factors are biased toward the starting model information, the Structure Factor, R_{F^2}, and the Bragg Factor, R_B, defined in equations (2.41) and (2.42) respectively.

$$R_{F^2} = \frac{\sum \left| \left(I_{hkl}(obs)\right)^{\frac{1}{2}} - \left(I_{hkl}(calc)\right)^{\frac{1}{2}} \right|}{\sum \left(I_{hkl}(obs)\right)^{\frac{1}{2}}} \quad \textbf{(2.41)}$$

$$R_B = \frac{\sum |I_{hkl}(obs) - I_{hkl}(calc)|}{\sum I_{hkl}(obs)} \quad \textbf{(2.42)}$$

Three other R-Factors which are determined by the fit of the whole pattern including R profile, R_p, R weighted-pattern, R_{wp} and R expected, R_{exp}. These are defined in equations (2.43) to (2.45), where n is the number of observables, p is the number of refined parameters and c is the number of constraints.

$$R_p = \frac{\sum |y_i - y_{ci}|}{\sum y_i} \quad \textbf{(2.43)}$$

$$R_{wp} = \left[\frac{\sum w_i (y_i - y_{ci})^2}{\sum w_i (y_i)^2} \right]^{\frac{1}{2}} \quad \textbf{(2.44)}$$

$$R_{exp} = \left[\frac{n-p-c}{\sum w_i(y_i)^2}\right]^{\frac{1}{2}} \quad \textbf{(2.45)}$$

The value of R_{wp} is often the most meaningful of these as it contains the function being minimised. The value of R_{exp} indicates the best possible R-value for a dataset and therefore the ratio between R_{wp} and R_{exp} can be monitored to give one final statistical value describing the quality of fit χ^2, equation (2.46).

$$\chi^2 = \left(\frac{R_{wp}}{R_{exp}}\right)^2 \quad \textbf{(2.46)}$$

These statistical values and the visual fit may sometimes be misleading as the resulting chemical information, including bond lengths and angles, may not make chemical sense and as such these should be treated with caution. The Rietveld refinements of the PXRD data in this work were performed using the General Structural Analysis System (GSAS)[13] and EXPGUI[12].

2.2.4 X-Ray Pair Distribution Function (PDF)

The pair distribution function (PDF) can be conceptualised as the relative probability of finding two atoms separated by a distance, r. Firstly it is useful to describe the relationship between the PDF and the radial distribution function (RDF), which is readily calculated from computational models. A schematic illustrating how the RDF is calculated in two dimensions is shown in Figure 2.14.

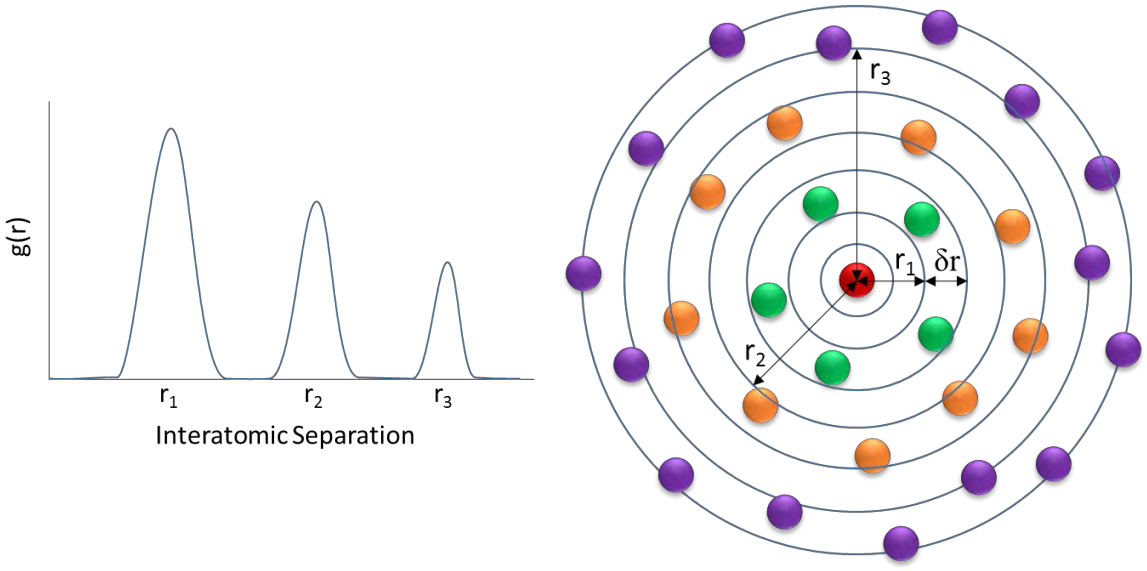

Figure 2.14: Schematic representation of an RDF in two dimensions

The distances between an atom, i, and all other atoms in the configuration are measured and binned into a histogram with uniform bin width, δr. The density of these spherical shells are then calculated and the RDF (or g(r)) is expressed as the quotient of the number density of the spherical shell, $\rho(r)$, and the average number density of the configuration, ρ_0. The RDF for a three dimensional configuration can therefore be calculated following equation (2.47), where $n(r)$ is the number of atoms within the spherical shell. The limiting values for the RDF are outline in equation (2.48). Where r^0 is the shortest distance of approach between any two atoms. This can then be converted to the PDF following equation (2.49).

$$g(r) = \frac{n(r)}{4\pi r^2\, \delta r\, \rho_0} = \frac{\rho(r)}{\rho_0} \tag{2.47}$$

$$\begin{matrix} g(r < r^0) = 0 \\ g(r \to \infty) = 1 \end{matrix} \tag{2.48}$$

$$G^{PDF}(r) = 4\pi r \rho_0 [g(r) - 1] = 4\pi r [\rho(r) - \rho_0] \tag{2.49}$$

The X-Ray pair distribution function (X-PDF) can be used to extract structural information from total scattering data. This uses the Bragg scattering discussed previously as well as the diffuse scatter. The diffuse scatter arises from effects such as thermal motion of atoms and defects within the crystal, indeed any effect which causes a departure of the atoms from the ideal lattice sites will increase the amount of diffuse scatter. As such structural information about the long and short range structure of a material may be extracted. This technique has historically been applied to the study of amorphous systems and has increasingly been used to study local ordering in crystalline materials. Unfortunately there are many different formulations of the PDF[14] and as such some useful definitions have been outlined in equation (2.50), where c_i and $f_i(Q)$ are the concentration (expressed as atomic fraction) and the scattering factor for element i respectively. The formalisation of the PDF referred to in this work is the $G^{PDF}(r)$.

$$G^{PDF}(r) = 4\pi r \rho_0 [g(r) - 1] = 4\pi r \rho_0 G_{norm}(r) = 4\pi r \rho_0\, G(r) \Big/ \left(\sum_{i=1}^{n} c_i f_i(Q) \right)^2 \tag{2.50}$$

The diffraction data are collected in momentum space, I(Q), where the scattering vector, Q, is the momentum transfer between the incident and scattered radiation. The relationship between Q and θ is expressed in equation (2.51) .

$$Q = \frac{4\pi \sin(\theta)}{\lambda} \tag{2.51}$$

Firstly, the total scattering structure factor, S(Q) is calculated from the intensity data following equation (2.52). This differs from the simple case for neutron scattering data as the X-ray scattering factors for each element are Q-dependent[15]. As such the X-ray scattering factors are often approximated following equation (2.53). The effect of this approximation is illustrated in Figure 2.15.

$$S(Q) = \frac{I(Q) - \sum_{i=1}^{n} c_i |f_i(Q)|^2}{\left|\sum_{i=1}^{n} c_i f_i(Q)\right|} + 1 \tag{2.52}$$

$$f_i(Q) \cong Z_i \sum_{i=1}^{n} c_i f_i(Q) \Big/ \sum_{i=1}^{n} c_i Z_i \tag{2.53}$$

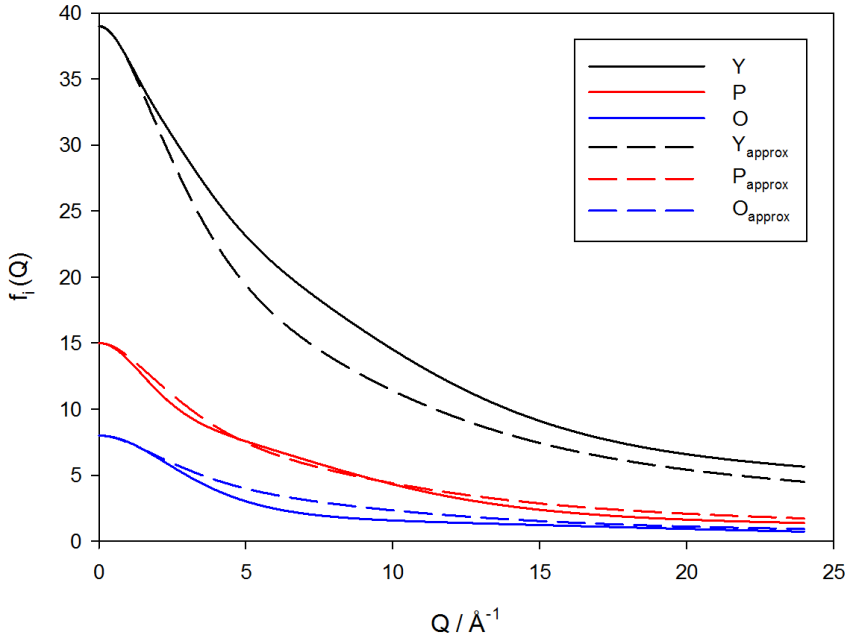

Figure 2.15: X-ray scattering factors for Y, P and O as a function of Q and the related approximated curve used in producing the PDFs

The PDF can then be calculated as the sine Fourier transform of the reduced total scattering structure factor, F(Q), equation (2.54).

$$G^{PDF}(r) = \frac{2}{\pi}\int_0^{\infty} Q[S(Q) - 1]\ \sin(Qr)\ dQ = \frac{2}{\pi}\int_0^{\infty} F(Q)\ \sin(Qr)\ dQ \qquad \textbf{(2.54)}$$

2.2.4.1 Synchrotron X-Ray Sources

The PDF data presented in this work were collected on beamline I15 at the Diamond Light Source in Oxfordshire. This is a national synchrotron facility producing high intensity X-rays allowing for very fast data collection. The X-rays are produced by bending high speed electrons around the synchrotron using bending magnets.

When collecting data for PDF analysis, it is important to collect over as large a range in Q as is possible to minimise termination errors within the final PDF[15]. For the Fourier transform in equation (2.54) to be exact, intensity data would be required within the range $0 \leq Q \leq \infty$ Å^{-1}which is clearly not possible. The termination ripples that arise as a result of truncating the I(Q) at a value of Q_{max} tend to have a higher amplitude at low r and increase in severity with decreasing Q_{max}. The high energy X-rays produced at a synchrotron source are therefore ideal for accessing the high Q range required. Additionally the distance between the sample and the detector is minimised in order to maximise the Q range over which data is collected. Though this is detrimental to the Q-space resolution of the data, the real space resolution is improved. Experimental factors also prevent data being collected at very low Q as a beam stop is used to prevent damage to the detector plate from direct irradiation with the X-ray beam. As such the I(Q) will be truncated at a value of Q_{min}. This also introduces errors into the final PDF in the form of intensity variations especially at low r.

2.3 References

1. P. P. Ewald, *Annalen Der Physik*, 1921, **64**, 253-287.
2. R. A. Buckingham, *Proceedings of the Royal Society of London Series a-Mathematical and Physical Sciences*, 1938, **168**, 264-283.
3. B. G. Dick and A. W. Overhauser, *Physical Review*, 1958, **112**, 90-103.
4. W. H. Press, S. A. Teukolsky, W. T. Verterling and B. P. Flannery, *Numerical recipes in fortran*, Cambridge University Press, Cambridge, 1992.
5. M. F. Mott and M. J. Littleton, *Transactions of the Faraday Society*, 1938, **34**, 0485-0499.

6. G. W. Watson, E. T. Kelsey, N. H. deLeeuw, D. J. Harris and S. C. Parker, *Journal of the Chemical Society-Faraday Transactions*, 1996, **92**, 433-438.
7. P. W. Tasker, *Journal of Physics C-Solid State Physics*, 1979, **12**, 4977-4984.
8. D. E. Parry, *Surface Science*, 1975, **49**, 433-440.
9. G. Wulff, *Zeitschrift Fur Krystallographie Und Mineralogie*, 1901, **34**, 449-530.
10. V. K. Pecharsky and P. Y. Zavalij, *Fundamentals of powder diffraction and structural characterisation of materials*, Springer, Second edn., 2009.
11. H. M. Rietveld, *Journal of Applied Crystallography*, 1969, **2**, 65.
12. B. H. Toby, *Journal of Applied Crystallography*, 2001, **34**, 210-213.
13. A. C. Larson and R. B. V. Dreele, *Journal*, 1994.
14. D. A. Keen, *Journal of Applied Crystallography*, 2001, **34**, 172-177.
15. T. Egami and S. J. L. Billinge, *Materials Today*, 2003, **6**, 57.

CHAPTER 3

Derivation of Pair Potentials

Table of Contents

Table of Figures

3.1 Introduction

Pair potentials form the foundation upon which atomistic simulations are based. It is crucial that these produce a model that describes the experimentally observed behaviour of the material in order to make valid predictions. To date there are 4 sets of potentials that have been published for the xenotime system summarised in Table 3.1. Most of these are rigid body potentials apart from those published by De Leeuw *et al*.[1] which have used the shell model to take into account the polarisability of the oxygen atoms within the structure. A three-body harmonic potential has been used to constrain the tetrahedral angle within the phosphate molecular ion for the sets of potentials published by Gao *et al*.[2] and De Leeuw *et al*., improving the rigidity of the tetrahedral unit. A Morse potential has been used to describe the more covalent P-O interaction in the potentials of Urusov *et al*.[3] and De Leeuw *et al*.

Table 3.1: Summary of the previously published sets of potentials for the xenotime system

	Buckingham					
Urusov Xen1[3]	Atom 1	Atom 2	A / eV	ρ / Å	C / eV Å^{-6}	r_{max} / Å
	$Y^{2.30}$	$O^{-1.25}$	6532.426240	0.240173	0.000	10
	$O^{-1.25}$	$O^{-1.25}$	1033.456662	0.344104	0.000	10
Urusov Xen2 [3]	$Y^{1.40}$	$O^{-1.20}$	11716.218760	0.253502	260.217	10
	$P^{3.40}$	$O^{-1.20}$	9034.208000	0.192640	19.880	10
	$O^{-1.20}$	$O^{-1.20}$	1388.770000	0.362320	175.000	10
Gao [2]	$Y^{1.80}$	$O^{-1.20}$	29526.980000	0.211377	50.477	10
	$P^{3.00}$	$O^{-1.20}$	27722.00000	0.181900	86.8600	10
	$O^{-1.20}$	$O^{-1.20}$	1844.745800	0.343645	192.580	10
De Leeuw [1]	$Y^{3.00}$	$O^{-1.632}$	3484.460000	0.273722	0.000	10
	$O^{-1.632}$	$O^{-1.632}$	16372.000000	0.213000	3.470	10
	Morse					
	Atom 1	Atom 2	D / eV	α / Å^{-2}	r_0 / Å	r_{max} / Å
Urusov Xen1	$P^{2.70}$	$O^{-1.25}$	3.47	2. 41153	1.60	10
De Leeuw	$P^{1.18}$	$O^{-1.632}$	3.47	2.03000	1.60	10
	Three-body					
	Atom 1	Atom 2	Atom 3	k / eV rad^{-2}	θ / deg	r_{max} (1,2) / Å
Gao	$P^{3.00}$	$O^{-1.20}$	$O^{-1.20}$	3.5000	109.47	1.8
De Leeuw	$P^{1.85}$	$O^{-1.632}$	$O^{-1.632}$	1.322626	109.47	1.8
	Spring					
	Atom 1	Atom 2	k / eV Å^{-2}			
De Leeuw	$O^{0.587}$	$O^{-1.632}$	507.40			

The suitability of these potentials has been analysed for the investigation of radiation damage in xenotime. Immediately it is apparent that three of the set of potentials are inappropriate for use in radiation damage simulations due to the relative charges of the ions. The set of potentials used in the work of Gao *et al.* is the only set to have all of the ions charges scaled equally and therefore the only set that can describe phase separation suitably within the model. The other three sets use unequal partial charges and therefore would not maintain charge neutrality when modelling Y_2O_3 or P_2O_5. The quality of the fit to experimental data is summarised in Table 3.2. It can be seen that the fit is not unreasonable although there are definitely areas for further improvement. Consequently new interatomic potentials will be derived for the xenotime system

Table 3.2 Summary of the quality of fit between the model and experimental data for the potentials of Gao et al.

	Experiment	Calculated	Δ_{calc}%	Reference
Lattice Parameters (Å)				
a	6.8947	6.7658	-1.87	Ni *et al.*[4]
c	6.0276	6.2349	3.44	
Elastic Constants (Gpa)				
C_{11}	220.0	319.5	45.23	Mogilevski *et al.*[5]
C_{12}	55.0	56.2	2.19	
C_{13}	86.0	97.7	13.65	
C_{33}	332.0	284.6	-14.29	
C_{44}	64.6	76.6	18.56	
C_{66}	17.3	24.4	40.87	
Interatomic Separation (Å)				
Y-O	2.31	2.29	-0.86	Ni *et al.*[4]
Y-O	2.38	2.51	5.63	
P-O	1.54	1.49	-3.13	
Bulk Modulus (Gpa)				
Reuss	144	164	13.97	Lacomba-Perales[6]
Voigt		164	14.04	
Hill		164	14.00	

3.2 Basic Fitting Methodology

All static calculations discussed in this chapter were performed using the GULP[7] code described in Chapter 2. Initial attempts were made to fit pair potentials for xenotime following a similar methodology as outlined by Read *et al*.[8]. A grid search methodology was employed to fit pair potentials of the Born-Mayer functional form for the Y-O and O-O potentials, whilst a Morse potential form was chosen for the P-O potential to reflect to strong covalent nature of this interaction. The charges were fixed as formal charges. This methodology yielded very limited success for xenotime. To improve upon this method, a Reverse Monte Carlo (RMC) method was employed for sampling the potential surface. The quality of the fit to experimental data was determined by the least-squares method outlined in equation (3.1), where the experimental data are split into different categories such as lattice parameters, bond lengths and mechanical properties. Each category is given a weighting factor, β_i, which allows for the fit to be weighted towards the chosen parameters. The least squares difference is normalised to the experimental value so the contribution from each value within a category is unbiased. The probability of accepting a move is given by equation (3.2), where σ is a variable which could be altered to change the proportion of bad moves which would be accepted. Each RMC search samples the hypersurface δ times and was repeated *k* times. For each move a potential parameter was selected at random and modified by a random amount within a set range.

$$LSq_w = \sum_i \beta_i \sum_j \left(\frac{y_{j\,calc} - y_{j\,exp}}{y_{j\,exp}} \right)^2 \quad \textbf{(3.1)}$$

$$P(x') = \min\left(1, \exp\left(\frac{-\Delta LSq_w}{\sigma}\right)\right) \quad \textbf{(3.2)}$$

This approach was initially tested on the cubic Gd_2O_3 phase as a simple test case. Here the O-O potential was fixed to a well-known and utilised potential derived by Catlow *et al*.[9] and the charges were once again fixed to formal. The acceptance parameter, σ, was set to 2 and the surface was sampled 200 times and repeated 100 times. The distribution of the Gd-O potentials which were sampled using this method is shown in Figure 3.1. Here it can be seen that whilst a wide range of potentials have been sampled, the majority of the sampling is localised to a smaller area. This indicates that the methodology is allowing for the hypersurface to be explored sufficiently whilst the majority of the sampling is serving to optimise the potentials.

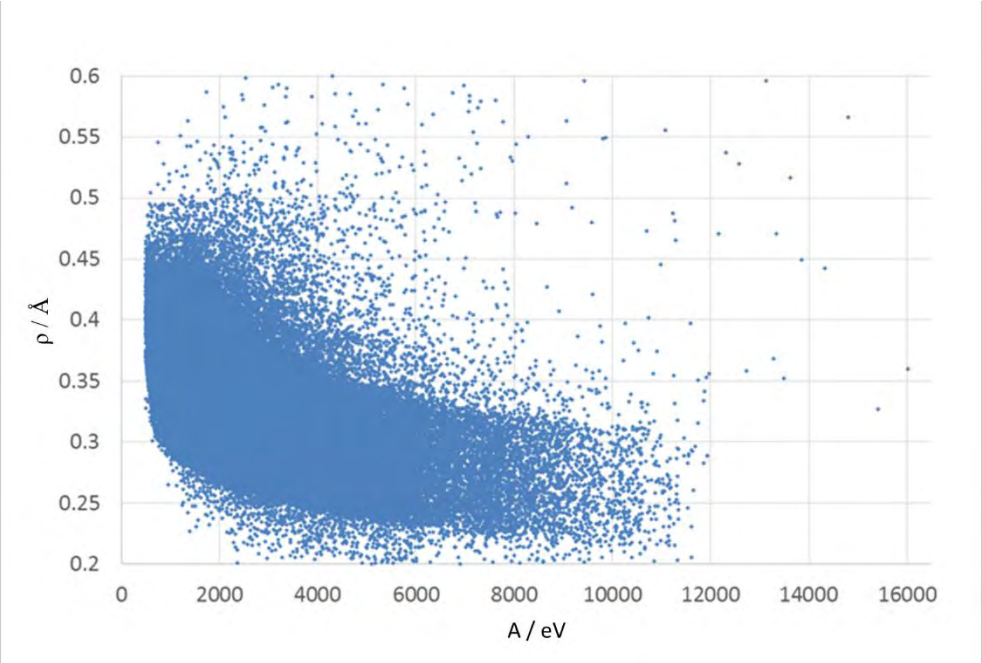

Figure 3.1: Sampling of the potential hypersurface for Gd_2O_3 using the RMC method

The best result from each of the RMC runs are shown in Figure 3.2. Here a surface mesh has been constructed from the sampled potentials. It can be seen that the RMC searches all lie along a similar contour at a weighted least-squares value close to zero. These

potentials were taken forward for further processing as a solution set. All potentials within the solution set lie within the region that was sampled most heavily.

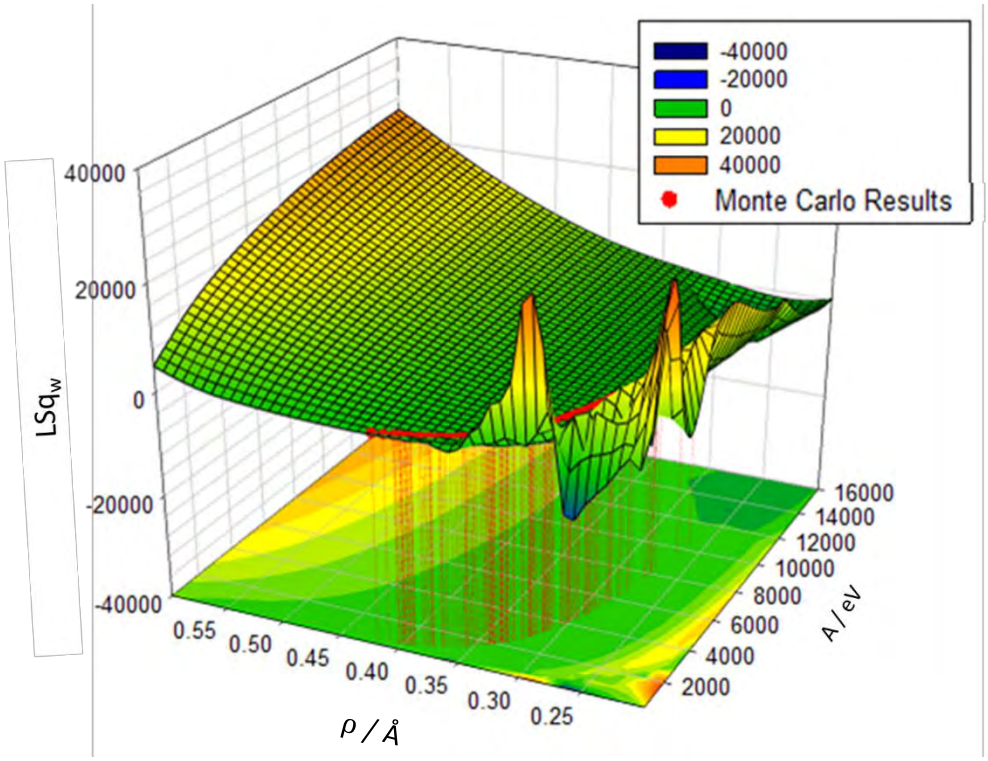

Figure 3.2: Potential hypersurface constructed from the potential parameters sampled using the RMC method. The best fits from each run (the solution set) are highlighted in red

These 100 potentials were taken forward for further analysis where the fits to the lattice parameters and the bulk modulus were investigated in more detail. It was found that the lattice parameters were within a percentage difference range of 0 ± 0.3 %. The fit to the bulk modulus as a function of the A potential parameter can be seen in Figure 3.3. Here it can clearly be seen that there is a strong correlation between the bulk modulus and the potential and so the set of potentials with the best fit to the bulk modulus was selected.

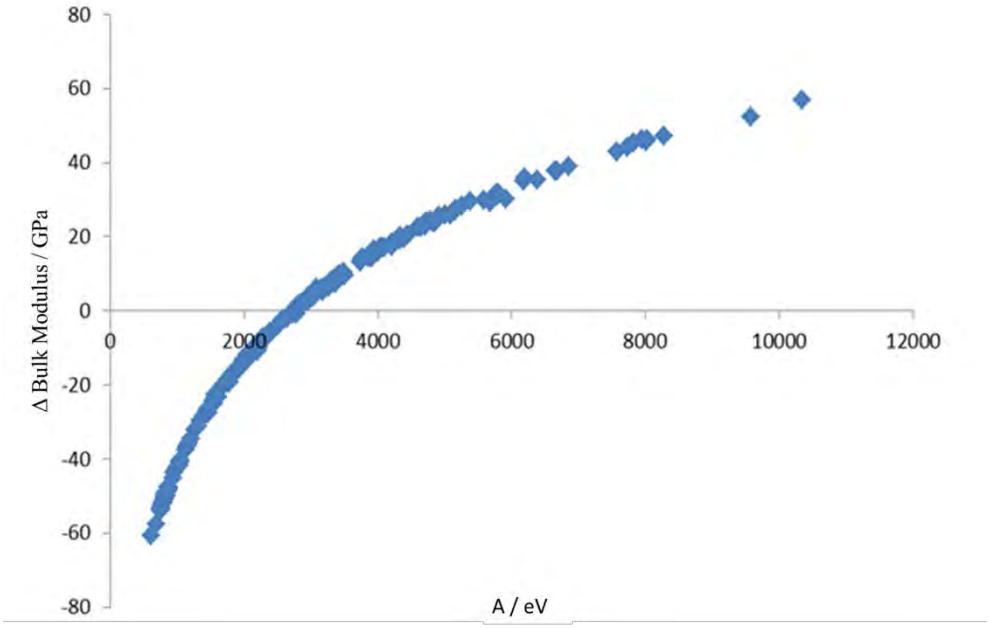

Figure 3.3: Difference between the experimental and simulated value of the bulk modulus as a function of the *A* potential parameter for the solution set of potentials

The quality of fit to experimental data for the cubic Gd_2O_3 system is summarised in table 3.3. Here it can be seen that there is very good agreement between the model and the experimental data, with the fit to the crystallographic and mechanical properties well within acceptable limits. This provided strong evidence that the fitting methodology was appropriate and could be transferred to the xenotime system.

Table 3.3: Summary of the quality of fit between the model and experimental data for Gd_2O_3

	Experimental	Calculated	Δ_{calc} %	**Reference**
a / Å	10.722	10.723	0.01	Ni *et al.*[4]
Bulk Modulus / GPa	125	125	-0.03	Zhang *et al.*[10]
Gd – O / Å	2.28	2.31	1.28	Ni *et al.*[4]
Gd – O / Å	2.26	2.27	0.08	
Gd – O / Å	2.31	2.31	0.10	
Gd – O / Å	2.39	2.34	-1.96	

The same approach was taken within the xenotime system to fit new formal charge potentials. The potentials were fitted to lattice parameters, interatomic separations, elastic constants and the bulk modulus. The best fit achieved by this method is summarised in Table 3.4. It can be seen that there is a relatively good agreement with the experimental data though it proved impossible to achieve a good fit to both the *a* and *c* lattice parameters. Similarly, the elastic constants were not fitted within an acceptable percentage different to the experimental values, consequently this was also manifest in the fit to the bulk modulus.

Table 3.4: Summary of the quality of fit between the model constructed using formal charges and experimental data for xenotime

	Experiment	Calculated	Δ_{calc}%
Lattice Parameters (Å)			
a	6.8947	6.8409	-0.78
c	6.0276	6.1873	2.65
Elastic Constants (Gpa)			
C_{11}	220.0	160.8	-26.93
C_{12}	55.0	50.8	-7.63
C_{13}	86.0	101.1	17.54
C_{33}	332.0	397.8	19.83
C_{44}	64.6	53.9	-16.64
C_{66}	17.3	1.7	-90.32
Interatomic Separation (Å)			
Y-O	2.31	2.31	-0.11
Y-O	2.38	2.42	1.67
P-O	1.54	1.54	-0.07
Bulk Modulus (Gpa)			
Reuss	144	101	-29.53
Voigt		130	-9.40
Hill		116	-19.46

The fitting methodology was adapted further to allow for the potentials to be fit to multiple phases simultaneously. This is important when considering the intended use for

these potentials to model radiation damage. In this regime the atoms in the damaged region may be far from the equilibrium structure of xenotime. A set of potentials fitted to only one phase may reproduce the properties of that phase very well at equilibrium, but may fail to describe the behaviour of the system at different length scales. Fitting the potentials to multiple phases ensures the transferability of the potentials between the systems as well as other phases formed from the same elements, accounting for phase separation, and can help to increase the validity of the potentials as they fit over a range of distances. As such it is important that the potentials not only fit well to the xenotime system, but also to both the Y_2O_3 and P_2O_5 systems. As well as fitting multiple phases simultaneously, the fitting code was expanded to fit multiple potentials simultaneously, along with three-body potentials and the scaling parameter for the ion charges. Within each move a random potential was chosen for fitting, followed by a randomly selected parameter which was then randomly altered by a small amount within a defined range. Each phase could be weighted independently, as defined in equation (3.3), to bias the fit towards the phase of choice whilst still achieving a good fit within the other phases. Some of the tested potentials are inevitably inappropriate and may not successfully optimise, have unphysical elastic constants or in some cases cause GULP to hang during a calculation. As such criteria were incorporated to allow a maximum time limit on calculations, check for negative elastic constants and check for optimisation. If any of these criteria were not met then the step would be repeated with new random choices.

$$LSq_w = \sum_n \alpha_n \sum_i \beta_i \sum_j \left(\frac{y_{j\,calc} - y_{j\,exp}}{y_{j\,exp}} \right)^2 \qquad \textbf{(3.3)}$$

3.2.1 Xenotime Potentials

Due to the difficulty experienced in fitting to xenotime using formal charges, the model was scaled to a partial charge model at 60 % of formal charge as in the work by Devanathan *et al*.[11] on zircon. The Morse potential form was chosen for the P-O interaction to reflect the covalent nature of the bond. The initial parameters were taken from Rabone *et al*.[1], with the r_0 parameter modified and fixed to the ideal bond length of 1.54 Å. The initial O-O and Y-O potentials were taken from the 'Xenotime 2' set of potential parameters by Urusov *et al*.[3] taking the Buckingham form. These potentials were initially fitted within the P_2O_5 system, where the Y-O potential was omitted from the fitting process. Unsurprisingly this initial concoction of potentials did not optimise and so the potentials were randomly tweaked until an optimising starting point was achieved. The potentials were fitted to the lattice parameters and atomic coordinates. The best fit from this was then taken forward to fit to the xenotime system. Again the potentials did not optimise in the xenotime system and so the Y-O potentials was tweaked until an optimising starting point was achieved. Only the Y-O potential was fitted in the xenotime phase. The potentials were fitted to the xenotime lattice parameters, atomic coordinates and the C_{11}, C_{12}, C_{13} and C_{33} elastic constants. The fit was repeated 9 times with 900 cycles per fit. The fit quality of the best set of potential parameters as a function of the cycle number for the 9 fits is summarised in Figure 3.4 a. Here it can be seen that the fit quality gets better with increasing cycle number but there is a reasonable amount of variation between the different fits. This highlights the importance of performing multiple fits to find the most appropriate potentials. The best set of potentials was found on fit number five. The fit quality for the potentials that were sampled on each cycle are summarised in Figure 3.4 b. Here it can be seen that this methodology is allowing the surface to be

sampled, not only in the minima but also at worse fits, allowing for more free movement about the hypersurface.

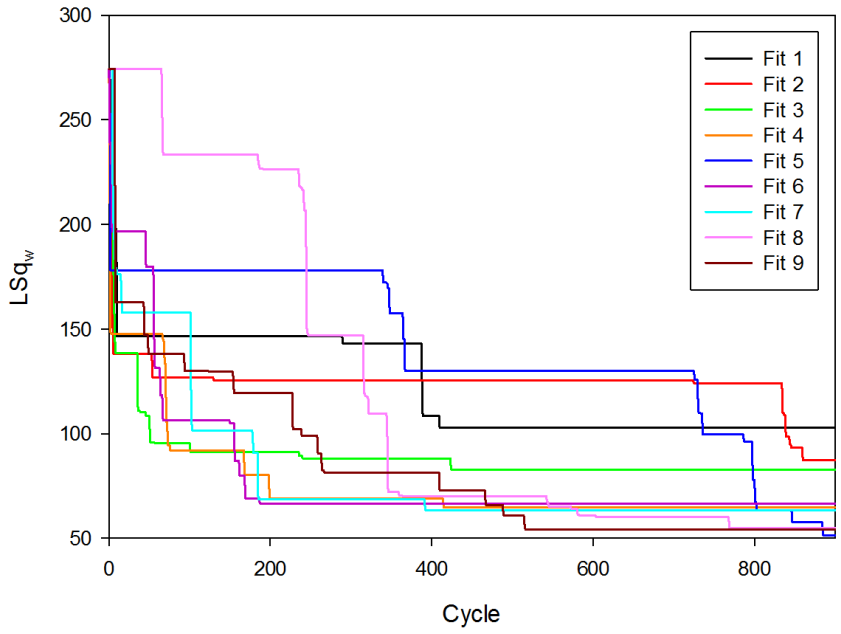

(a)

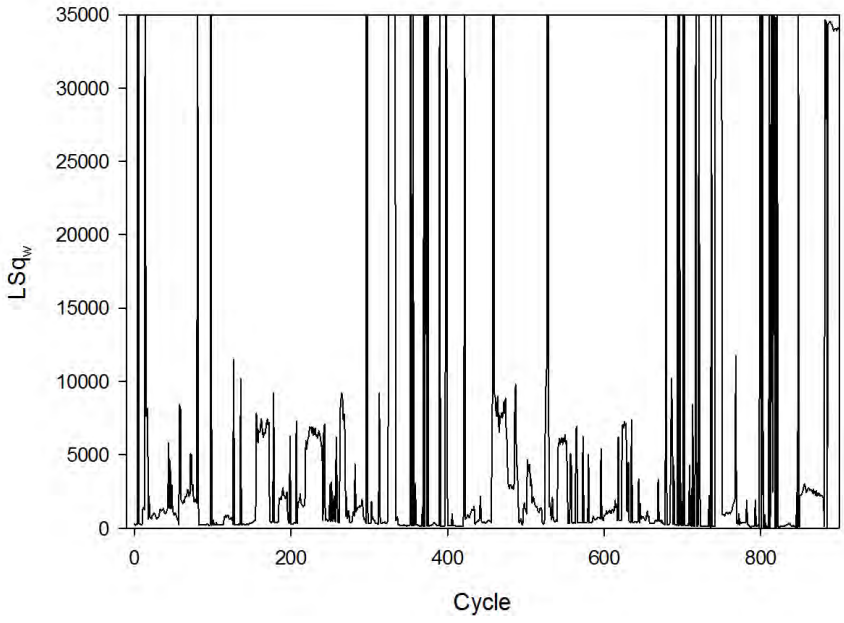

(b)

Figure 3.4: Weighted least-squares fit for successive cycles during the RMC fitting process for (a) the potentials with the best fit for each run and (b) the tested potential at each cycle for fit number 5

The final potentials were then transferred into the Y_2O_3 system where the fit was deemed suitable for the potentials to be taken forward. The quality of the fits to YPO_4, P_2O_5 and Y_2O_3 can be seen in Table 3.5 – Table 3.7 respectively. The potentials give fairly good agreement to the experimental data, especially for the xenotime phase. One of the limitations of these potentials is that they are rigid body potentials and therefore do not take into account the polarizability of the ions. However, the incorporation of the shell model to overcome this can prove troublesome during MD simulations, giving rise to high frequency vibrations which would require very short simulation time steps to compensate. As these potentials are intended for modelling radiation damage in the MD regime, the compromise made here was deemed acceptable.

Table 3.5: Summary of the quality of fit between the model constructed using scaled partial charges and experimental data for YPO_4

YPO_4	Experiment	Calculated	Δ_{calc}%
Lattice Parameters (Å)			
a	6.8947	6.8747	-0.29
c	6.0276	6.0511	0.39
Elastic Constants (Gpa)			
C_{11}	220.0	282.1	28.23
C_{12}	55.0	44.0	-19.99
C_{13}	86.0	84.7	-1.51
C_{33}	332.0	278.6	-16.09
C_{44}	64.6	66.4	2.74
C_{66}	17.3	14.9	-13.94
Interatomic Separation (Å)			
Y-O	2.31	2.32	0.26
Y-O	2.38	2.42	1.80
P-O	1.54	1.52	-1.27
Bulk Modulus (Gpa)			
Reuss	144	144	-0.24
Voigt		144	0.00
Hill		144	-0.12

Table 3.6: Summary of the quality of fit between the model constructed using scaled partial charges and experimental data for P_2O_5

P_2O_5 (orthorhombic)	Experiment	Calculated	Δ_{calc}%
Lattice Parameters (Å)			
a	16.314	16.435	0.74
b	8.115	8.164	0.60
c	5.265	5.260	-0.10
Interatomic Separation (Å)			
P-O	1.44	1.51	4.69
P-O	1.56	1.53	-2.16
P-O	1.58	1.53	-3.29
P-O	1.58	1.53	-3.45

Table 3.7: : Summary of the quality of fit between the model constructed using scaled partial charges and experimental data forY_2O_3

Y_2O_3 (cubic)	Experiment	Calculated	Δ_{calc}%
Lattice Parameters (Å)			
a	10.604	10.513	-0.86
Interatomic Separation (Å)			
Y-O	2.29	2.27	-1.05
Y-O	2.27	2.26	-0.27
Y-O	2.34	2.29	-2.10
Y-O	2.36	2.25	-4.80
Bulk Modulus (Gpa)			
Voigt	146	117	-19.64

The final potentials are summarised in Table 3.8. The charge on the ions has been scaled to 37 % of formal charge and all pair potentials were applicable to a cut-off radius of 10 Å. It can be seen that the Buckingham potentials both have quite large C parameters which, combined with the need to scale the charges may explain the difficulty experienced in fitting potentials using the basic methodology discussed earlier in this section.

Table 3.8: Potential parameters derived for the scaled partial charge model of xenotime using the RMC method

Buckingham					
Atom 1	Atom 2	A / eV	ρ / Å	C / eV Å^{-6}	r_{max} / Å
$Y^{1.11}$	$O^{-0.74}$	27025.72941	0.22225	188.27260	10
$O^{\mathbf{-0.74}}$	$O^{-0.74}$	1458.23941	0.33460	99.41669	10
Morse					
Atom 1	Atom 2	D / eV	α / Å^{-2}	r_0 / Å	r_{max} / Å
$P^{1.85}$	$O^{-0.74}$	3.51305	3.76122	1.54000	10
Three-body					
Atom 1	Atom 2	Atom 3	k / eV rad^{-2}	θ / deg	r_{max} (1,2) / Å
$P^{1.85}$	$O^{-0.74}$	$O^{-0.74}$	3.5000	109.47	1.8
$O^{\mathbf{-0.74}}$	$P^{\mathbf{1.85}}$	$P^{\mathbf{1.85}}$	20.9326	135.58	1.8

r_{max} (1,3) / Å	r_{max} (2,3) / Å						
1.8	3.2						
1.8	3.2						

3.2.2 Lanthanide Potentials

New pair potentials have been fitted for a range of lanthanides including La, Nd, Sm, Gd, Er and Lu in both the sesquioxide and orthophosphate phases. Further modifications were required for the methodology outlined previously in this chapter to construct stability criteria for the elastic constants and to include a simulated annealing feature. The elastic stability criteria were taken from the work of Mouhat *et al*.[12] where necessary and sufficient criteria for the elastic constants have been outlined for the different crystal systems. These help to constrain the search of the hypersurface to avoid accepting moves about the hypersurface to sets of potentials with unphysical elastic constants. For the simulated annealing fits the average target percentage difference was set to a maximum value and systematically lowered as the MC cycles progress to a set minimum value. This could be performed using either a linear or logarithmic quenching regime. In the linear

regime the acceptance percentage, Pc_{lin}, for cycle, N_i, can be defined simply form the total number of cycles, the maximum percentage and the minimum percentage (N, Pc_{max} and Pc_{min} respectively) as defined in equations (3.4 and equation (3.5. Similarly the acceptance percentage for a given cycle in the logarithmic simulated annealing regime, Pc_{log}, can be defined following equations (3.6 and equation (3.7. Here the average target percentage difference to be achieved by half way through the run, Pc_{mid}, must be defined. This allows for the function to be scaled in such a way that half of the simulation is focussing on searching the hypersurface, whilst the latter half is more biased toward optimisation of the potentials.

$$\delta Pc = \frac{(Pc_{max} - Pc_{min})}{(N-1)} \tag{3.4}$$

$$Pc_{lin} = Pc_{max} - (N_i - 1)\delta Pc \tag{3.5}$$

$$k_{log} = \frac{2\,(\ln(Pc_{mid}) - \ln(Pc_{max}))}{\delta Pc(-N+2)} \tag{3.6}$$

$$Pc_{log} = Pc_{max}\, exp\left(k_{log}(Pc_{lin} - Pc_{max})\right) \tag{3.7}$$

A plot showing the difference between these two regimes is illustrated in Figure 3.5. Here it can be seen that the advantage of defining the target percentage half way through the run is that the bias toward optimisation can be controlled. In this example the average acceptance value at the midpoint was set to 1 %. This value is only achieved in the linear regime after ca. 90 cycles, leaving only 10 cycles at this lower acceptance rate.

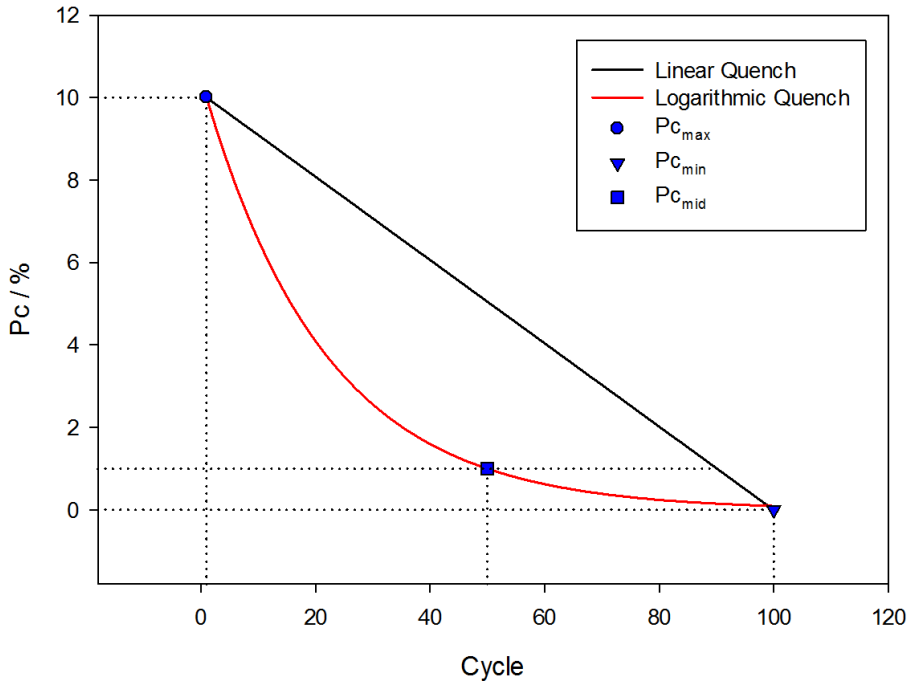

Figure 3.5: Quenching regime for the linear (black) and logarithmic (red) simulated annealing options

The probability of accepting a move is defined in equation (3.8). Here the weighted least-squares value is calculated for a hypothetical fit with a percentage difference of P_c % across all of the parameters being fitted, taking into account the weighting factors used for each phase and category. As such the acceptance rate for 'bad' moves is reduced with decreasing average target percentage difference.

$$P(x') = \min\left(1, \exp\left(\frac{-\Delta LSq_w}{LSq_{w\,Pc}}\right)\right) \tag{3.8}$$

An example plot showing the probability of accepting a bad move as a function of the MC step is shown in Figure 3.6. A plot of the difference in the weighted least-squares value between the previous and current MC step is also superimposed. This fit was run over 400

MC cycles using a logarithmic quench, with Pc_{min}, Pc_{mid} and Pc_{max} values of 0, 3 and 25 respectively. For ease of interpretation all moves with a negative ΔLSq_w value are plotted with an acceptance probability of 1 and a ΔLSq_w value of 0. It can be seen that at the start of the fit, moves with a small positive ΔLSq_w are accepted with a relatively higher probability than an equivalent move in the latter part of the fit, again showing the balance between exploration of the hypersurface and optimisation of the potentials.

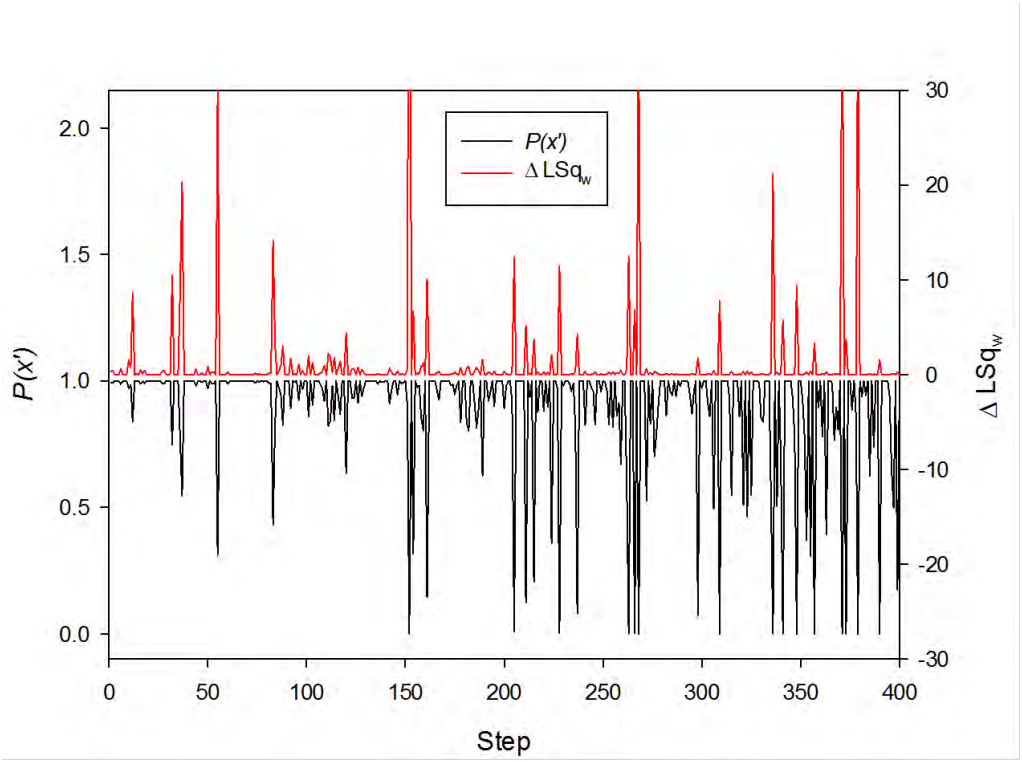

Figure 3.6: Probability of accepting tested move (black) and the difference in weighted least-squares (red) for successive RMC cycles. For ease of interpretation moves that improved the fit have been set to a ΔLSq_w value of 0

The fits to the sesquioxide and orthophosphate phases are summarised in appendix 1. These potentials were fitted to both crystallographic[4, 13-18] and mechanical properties[6, 19-31]. The fits were determined to be of a suitable quality across all of the phases. The interatomic potentials derived using this methodology are summarised in Table 3.9.

Table 3.9: Potential parameters derived for La, Nd, Sm, Gd, Er and Lu. Parameters were fit using the RMC method to the sesquioxide and orthophosphate phases

Buckingham					
Atom 1	Atom 2	A / eV	ρ / Å	C / eV Å^{-6}	r_{max} / Å
$La^{1.11}$	$O^{-0.74}$	9678.23908	0.26763	290.96621	10
$Nd^{1.11}$	$O^{-0.74}$	11211.09278	0.26216	322.53612	10
$Sm^{1.11}$	$O^{-0.74}$	12320.91001	0.25628	295.88669	10
$Gd^{1.11}$	$O^{-0.74}$	11209.51659	0.26121	335.04929	10
$Er^{1.11}$	$O^{-0.74}$	30905.08845	0.22286	229.38141	10
$Lu^{1.11}$	$O^{-0.74}$	37989.69923	0.21388	204.8133	10
$La^{1.11}$	$La^{1.11}$	50729.14588	0.29997	305.65373	10
$Nd^{1.11}$	$Nd^{1.11}$	34544.23811	0.31251	372.94383	10
$Sm^{1.11}$	$Sm^{1.11}$	33201.71835	0.31048	397.66323	10
$Gd^{1.11}$	$Gd^{1.11}$	41417.83918	0.30007	329.52195	10
$O^{\mathbf{-0.74}}$	$O^{-0.74}$	1458.23941	0.33460	99.41669	10
Morse					
Atom 1	Atom 2	D / eV	α / Å^{-2}	r_0 / Å	r_{max} / Å
$P^{1.85}$	$O^{-0.74}$	3.51305	3.76122	1.54000	10

Three-body							
Atom 1	Atom 2	Atom 3	k / eV rad^{-2}	θ / deg	r_{max} (1,2) / Å	r_{max} (1,3) / Å	r_{max} (2,3) / Å
$P^{1.85}$	$O^{-0.74}$	$O^{-0.74}$	3.5000	109.47	1.8	1.8	3.2
$O^{\mathbf{-0.74}}$	$\mathbf{P^{1.85}}$	$\mathbf{P^{1.85}}$	20.9326	135.58	1.8	1.8	3.2

3.2.3 Other Phases

This methodology has also been extended to other members of the research group who have used it to successfully derive transferable potentials to 19 phases in order to

investigate the charge compensation mechanisms relating to the incorporation of barium into the $Cs_2TiNb_6O_{18}$ phase. The fit quality to a selection of these phases are summarised in Table 3.10. This work has contributed considerably to the student's body of work and was presented at the Materials Research Society conference in 2016[32].

Table 3.10: Summary of the quality of fit between the models and experimental data for various phases fit using the RMC method

Phase	Experiment	Δ_{calc}%
BaO		
Lattice Parameters (Å)		
a	5.517	-0.52
Bulk Modulus (Gpa)	66	-0.30
$BaTiO_3$		
Lattice Parameters (Å)		
a	4.006	-0.34
Bulk Modulus (Gpa)	195	-5.41
Ti_2O_3		
Lattice Parameters (Å)		
a	5.158	-0.09
c	13.611	0.15
Bulk Modulus (Gpa)	260	8.86
$Cs_2TiNb_6O_{18}$		
Lattice Parameters (Å)		
a	7.533	-2.04
c	8.189	2.94
$BaTi_3Nb_4O_{13}$		
Lattice Parameters (Å)		
a	6.639	-1.34
b	8.957	0.16
c	21.145	1.04

3.3 Modifications

The potentials derived in the previous section for xenotime system fit well to the equilibrium properties. However, some modifications were necessary in order to translate these potentials for use in a molecular dynamics regime. Firstly the potentials were subject to a linear shift in order to force the potential energy to be 0 at the cut-off. This is necessary to avoid a step in the potential energy between atoms at this separation. Similarly the three-body potentials were adapted to take the form of a truncated harmonic potential, equation (3.9), so as the energy contribution from these terms fell smoothly to zero when the P-O distance was greater than 1.75 Å. This allows for oxygen atoms at larger interatomic separation from the phosphorus atom to feel the three-body force much more weakly than those that are closer to the phosphorus atom. The value of 1.75 Å was chosen fairly arbitrarily and as such may be a parameter which requires further investigation. The potential energy surface for the O-P-O truncated harmonic three body potential, pertaining to the angles within the phosphate tetrahedra, is shown in Figure 3.7.

$$U(\theta_{jik}) = \frac{k}{2}(\theta_{jik} - \theta_0)^2 exp\left(\frac{-r_{ij}^8 - r_{ik}^8}{\rho^8}\right) \quad \textbf{(3.9)}$$

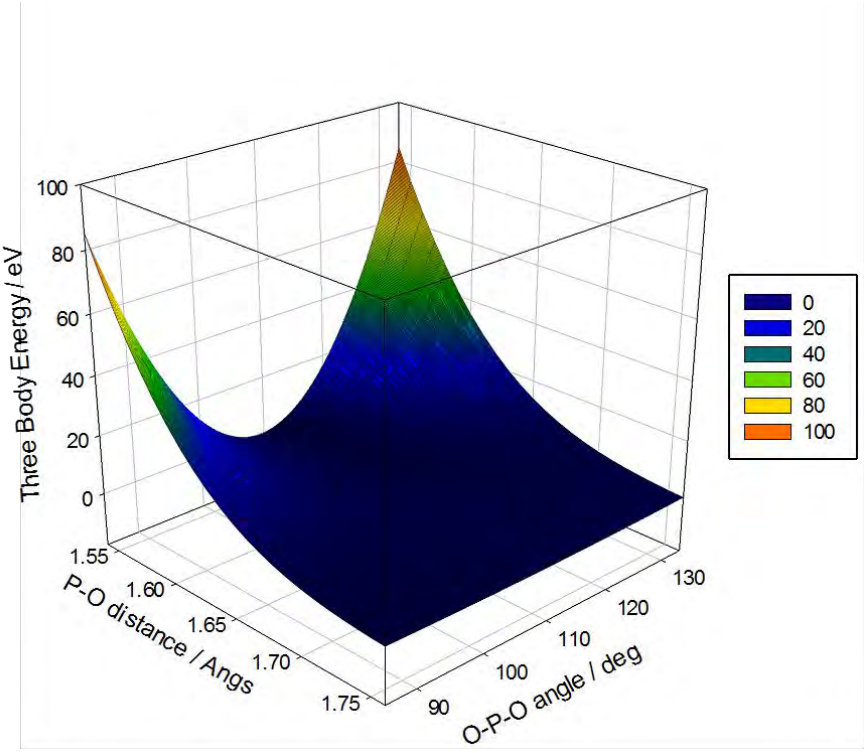

Figure 3.7: Energy contribution from a truncated harmonic potential for the O-P-O angles within the phosphate tetrahedra as a function of angle and P-O distance

Figure 3.8 shows the impact these modifications have on the equilibration of the simulation cell in the NPT ensemble. It is clear that there are relatively large spikes in the total energy of the system which are not present after the modifications have been made, resulting in a well equilibrated simulation cell.

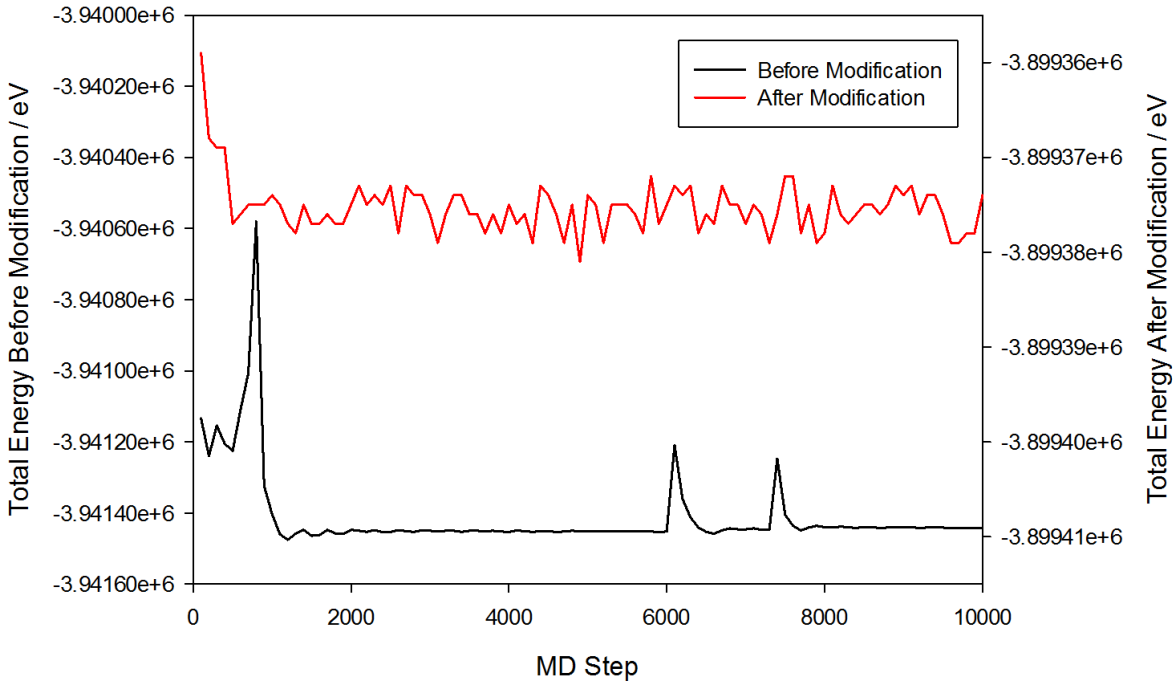

Figure 3.8: Equilibration phase for the MD simulation cell before (black) and after (red) modifications were made to the potentials

The final modification to the potentials is to spline them with a repulsive potential developed by Ziegler *et al.*[33] known as the ZBL potential at short interatomic separation. The necessity for this modification is made clear in Figure 3.9. Here it can be seen that the pair potential is strongly attractive at short interatomic separation, mainly as a result of the positive value for the *C* parameter in the Buckingham short-range potential. This means that whilst the potentials describe the equilibrium structure well, if these ions were to come too close to each other throughout the course of a simulation ten they would become subject to a strong unphysical attraction. This scenario is very likely to occur during radiation damage cascade simulations where the ions are undergoing collisions. Cation-cation interactions which only interact *via* coulombic interactions were also splined to the ZBL potential for consistency.

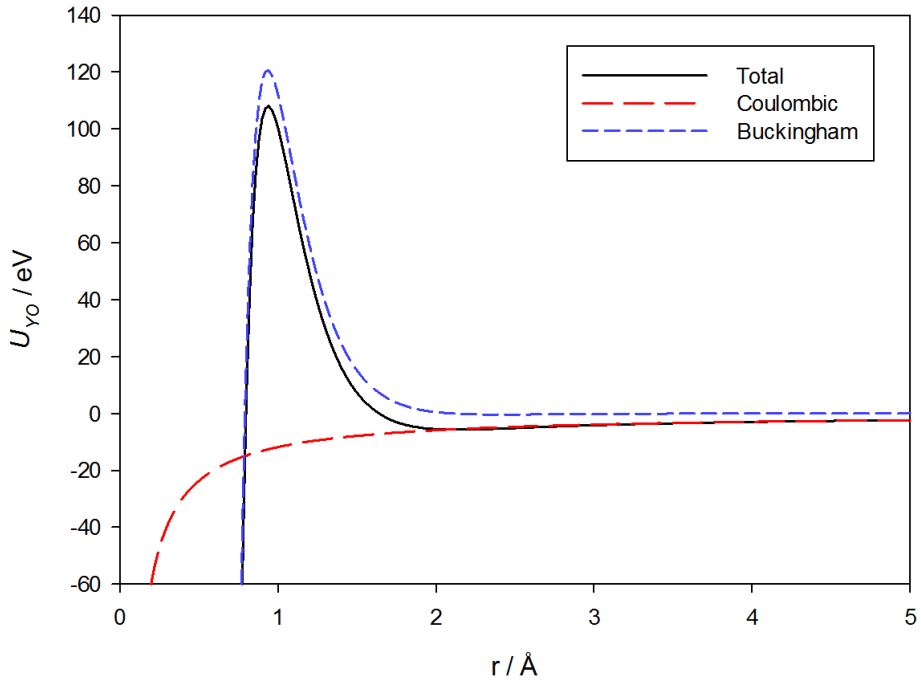

Figure 3.9: Pair potential for the Y-O interaction

The ZBL potential is described for a given pair of interacting ions following equations (3.10) – (3.22). Here Z_1 and Z_2 are the atomic number of species 1 and 2 respectively.

$$q = 1.602 \times 10^{-19}\ C \tag{3.10}$$

$$\varepsilon_0 = 8.854 \times 10^{-22}\ F\text{Å}^{-1} \tag{3.11}$$

$$a_0 = 0.529\ \text{Å} \tag{3.12}$$

$$E = \frac{q}{4\pi\varepsilon_0} \tag{3.13}$$

$$V(r) = \frac{c_1 e^{d_1 r} + c_2 e^{d_2 r} + c_3 e^{d_3 r} + c_4 e^{d_4 r}}{r} \tag{3.14}$$

$$c_1 = Z_1 Z_2 E \times 0.181750 \quad \textbf{(3.15)}$$

$$c_2 = Z_1 Z_2 E \times 0.509860 \quad \textbf{(3.16)}$$

$$c_3 = Z_1 Z_2 E \times 0.280220 \quad \textbf{(3.17)}$$

$$c_4 = Z_1 Z_2 E \times 0.028171 \quad \textbf{(3.18)}$$

$$d_1 = \frac{-3.19980 \times {Z_1}^{0.23} {Z_2}^{0.23}}{0.88534 \times a_0} \quad \textbf{(3.19)}$$

$$d_2 = \frac{-0.94229 \times {Z_1}^{0.23} {Z_2}^{0.23}}{0.88534 \times a_0} \quad \textbf{(3.20)}$$

$$d_3 = \frac{-0.40290 \times {Z_1}^{0.23} {Z_2}^{0.23}}{0.88534 \times a_0} \quad \textbf{(3.21)}$$

$$d_4 = \frac{-0.20162 \times {Z_1}^{0.23} {Z_2}^{0.23}}{0.88534 \times a_0} \quad \textbf{(3.22)}$$

The potentials were splined using a fifth order exponential polynomial, ensuring continuity of the first and second derivatives at the cut-offs. The final potential for the Y-O interaction is illustrated in Figure 3.10. Here it can be seen that the unphysical attraction at low interatomic separation has been replaced with a highly repulsive potential which is splined smoothly to the Buckingham potential. The range over which the spline function was applied for each of the pair potentials are summarised in Table 3.11.

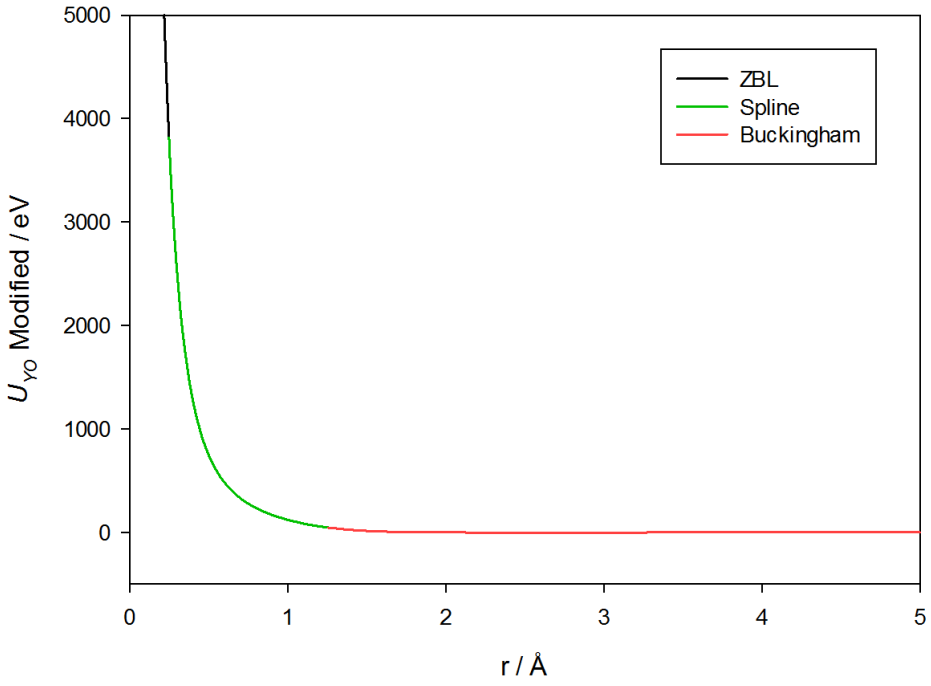

Figure 3.10: Pair potential for the Y-O interaction after being splined to the ZBL potential. The ZBL potential, fifth order exponential polynomial spline function and Buckingham potential are shown in black, green and red respectively

Table 3.11: Range over which the potentials were splined for xenotime

Atom 1	Atom 2	r_{min} / Å	r_{max} / Å
Y	O	0.24	1.25
O	O	0.40	1.37
Y	Y	1.30	2.5
Y	P	1.00	1.90
P	P	0.80	1.25

The zircon potentials taken from Devanathan *et al.*[34] were also modified and splined to a ZBL potential at low interatomic separation. They achieved a similar result by splining to a Lennard-Jones potential. Though the form of the repulsive potential is different, the goal

is the same and so any discrepancies seen in the zircon simulations between this work and that previously published may be as a result of this modification. The range over which the potentials were splined are summarised in Table 3.12. A TABLE file was produced for these potentials to be used in MD simulations.

Table 3.12: Range over which the potentials were splined for zircon

Atom 1	Atom 2	r_{min} / Å	r_{max} / Å
Zr	O	0.40	1.22
Si	O	0.24	1.20
O	O	0.24	1.70
Zr	Zr	0.40	1.22
Zr	Si	0.80	1.30
Si	Si	0.65	1.10

In order to input these modified potentials into GULP it was necessary to decompose the short-range component of the splined potential into an exponential polynomial and a Morse potential, following equation (3.23). The potential parameters were fit using a least-squares method and the resulting potential for the Y-O potential can be seen in Figure 3.11. Here it can be seen that the modified potential fits very well at length scales > 1 Å, which accounts for the region of the potential applicable to the equilibrium bond lengths. There is more of a discrepancy between the modified potential and the ZBL splined potential from the DL_POLY TABLE file at shorter interatomic separations. This is less of a concern as the potential is still strongly repulsive at these distances. These modified potential parameters for the xenotime system are summarised in Table 3.13.

$$U_{ij} = A\,exp\left(B_0 + B_1\,r_{ij} + B_2\,r_{ij}^2 + B_3\,r_{ij}^3\right) + D\left[\left(1 - exp\left(-\alpha\left(r_{ij} - r_0\right)\right)\right)^2 - 1\right] \quad \textbf{(3.23)}$$

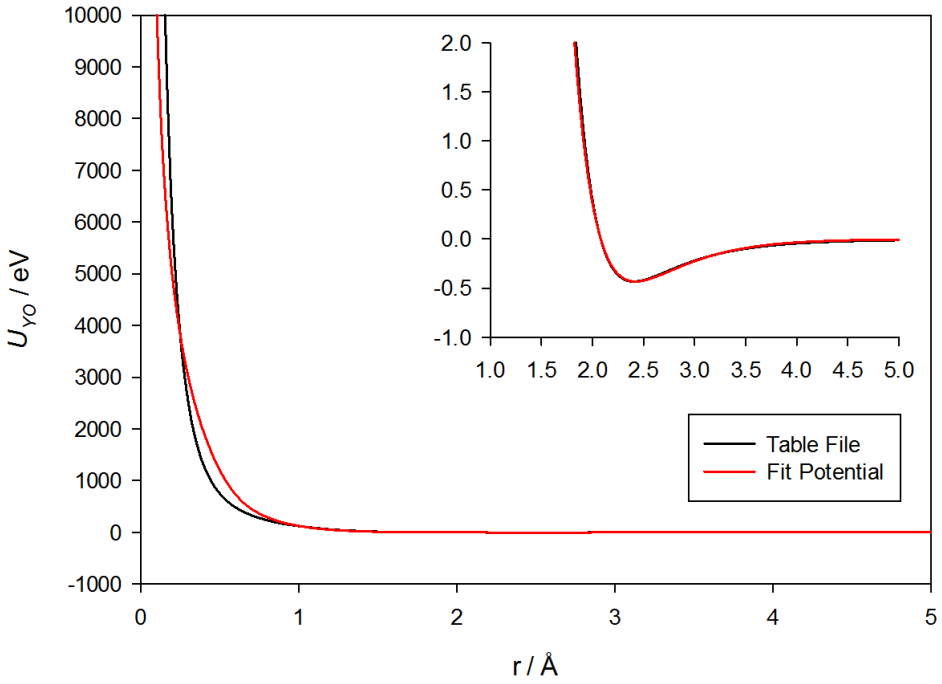

Figure 3.11: Comparison between the ZBL splined potential from the TABLE file and the fit potential consisting of a summed exponential polynomial and Morse potential

Table 3.13: Potential parameters after modification for use in static calculations

Exponential Polynomial							
Atom 1	Atom 2	A / eV	B_0	B_1 / Å^{-1}	B_2 / Å^{-2}	B_3 / Å^{-3}	r_{max} / Å
$Y^{1.11}$	$O^{-0.74}$	-3.937e^{-6}	16.316	7.995	-8.617	0.497	10
$O^{\mathbf{-0.74}}$	$O^{-0.74}$	3.232	9.358	-25.539	55.926	-52.763	10

Morse					
Atom 1	Atom 2	D / eV	α / Å^{-2}	r_0 / Å	r_{max} / Å
$Y^{1.11}$	$O^{-0.74}$	0.444	2.143	2.405	10
$O^{\mathbf{-0.74}}$	$O^{-0.74}$	0.017	1.404	3.782	10
$P^{1.85}$	$O^{-0.74}$	3.51305	3.76122	1.54000	10

Three-body							
Atom 1	Atom 2	Atom 3	k / eV rad^{-2}	θ / deg	r_{max} (1,2) / Å	r_{max} (1,3) / Å	r_{max} (2,3) / Å
$P^{1.85}$	$O^{-0.74}$	$O^{-0.74}$	3.5000	109.47	1.8	1.8	3.2
$O^{\mathbf{-0.74}}$	$P^{1.85}$	$P^{1.85}$	20.9326	135.58	1.8	1.8	3.2

It is necessary for these modifications to be made to maintain a level of consistency across the potentials used in the different regimes. The method used in the subsequent chapter to investigate defect within the xenotime lattice relies on a grid search method and as such the interstitial atoms may be placed at very short interatomic separation from the other lattice atoms. Without these modifications the interstitial atoms may experience the unphysical attraction inherent in the original potentials. The fit quality is summarised in Table 3.14. Here it can be seen that the quality of the fit to the xenotime phase is reduced slightly after the modifications have been made. These discrepancies most likely arise from the linear shift or the fitting of the exponential polynomial and Morse potential. The fit is still of a sufficient quality to be used in defect calculations.

Table 3.14: Summary of the quality of fit between the model and experimental data for the modified potentials for xenotime

YPO_4	Experiment	Δ_{calc}% Original	Δ_{calc}% Modified
Lattice Parameters (Å)			
a	6.8947	-0.29	0.90
c	6.0276	0.39	-0.12
Elastic Constants (Gpa)			
C_{11}	220.0	28.23	21.61
C_{12}	55.0	-19.99	-35.37
C_{13}	86.0	-1.51	-8.08
C_{33}	332.0	-16.09	-17.67
C_{44}	64.6	2.74	0.60
C_{66}	17.3	-13.94	-13.77
Interatomic Separation (Å)			
Y-O	2.31	0.26	1.12
Y-O	2.38	1.80	2.07
P-O	1.54	-1.27	-1.23
Bulk Modulus (Gpa)			
Reuss	144	-0.24	-6.75
Voigt		0.00	-6.13
Hill		-0.12	-6.44

3.4 Conclusion

Here a methodology has been derived for fitting interatomic potentials based on a Reverse Monte Carlo methodology. The potentials can be fitted to various properties, including both crystallographic and mechanical properties, which can be weighted independently. Multiple phases can be fit simultaneously to help improve the transferability of the potentials. This methodology has been utilised in this work to fitted new potentials for the sesquioxide and orthophosphate phases of yttrium and a selection of lanthanides. Similarly the methodology has proved valuable for other members of the group within their work. Various modifications were made to the potentials so as they are appropriate for simulating radiation damage events in a molecular dynamics regime. This included a linear shift to ensure the potential is zero at the cut-off, the use of a truncated harmonic potential to allow the contribution from the three-body potentials to reduce as the interatomic separation between the species increases. The most significant modification was the splining of the pair potentials to the ZBL potential at short interatomic distances to remove the inherent unphysical attraction within the potentials and allow ions to undergo collisions in the MD regime. These modifications were translated to the static regime by fitting a combination of an exponential polynomial and Morse potentials to the modified potential function. This was achieved with minimal impact to the calculated properties for the equilibrium structure.

3.5 Future Work

- The fitting methodology described here is still in relatively early stages of development and as such many modifications could be made. One of the easiest modifications would be to include fits to more experimental data such as infrared or Raman spectroscopy which may be more appropriate for fitting three-body potentials.
- Similarly the fitting method could be expanded to include small molecular dynamics simulations to fit to properties such as the heat capacity and the thermal expansion coefficients for the system. This would help to overcome one of the more subtle issues with deriving potentials *via* empirical methods in the static regime, in that the experimental data will inevitably have been collected at temperatures above 0 K and as such the potentials will include some temperature effects.
- If the potentials need to be modified for use in the MD regime then the fit should be determined after these modification are made rather than sacrificing the quality of the fit.
- Other searching and optimisation algorithms such as genetic algorithms could prove to be more efficient and produce better quality potentials. As such these methods could be investigated.

3.6 References

1. J. A. L. Rabone and N. H. De Leeuw, *Journal of Computational Chemistry*, 2006, **27**, 253-266.
2. F. Gao, H. Y. Xiao, Y. G. Zhou, R. Devanathan, S. Y. Hu, Y. L. Li, X. Sun and M. A. Khaleel, *Computational Materials Science*, 2012, **54**, 170-175.
3. V. S. Urusov, A. E. Grechanovsky and N. N. Eremin, *Glass Physics and Chemistry*, 2012, **38**, 55-62.
4. Y. X. Ni, J. M. Hughes and A. N. Mariano, *American Mineralogist*, 1995, **80**, 21-26.
5. P. Mogilevsky, E. B. Zaretsky, T. A. Parthasarathy and F. Meisenkothen, *Physics and Chemistry of Minerals*, 2006, **33**, 691-698.
6. R. Lacomba-Perales, D. Errandonea, Y. Meng and M. Bettinelli, *Physical Review B*, 2010, **81**, 9.
7. J. D. Gale and A. L. Rohl, *Molecular Simulation*, 2003, **29**, 291-341.
8. M. S. D. Read and R. A. Jackson, *Journal of Nuclear Materials*, 2010, **406**, 293-303.
9. G. V. Lewis and C. R. A. Catlow, *Journal of Physics C-Solid State Physics*, 1985, **18**, 1149-1161.
10. F. X. Zhang, M. Lang, J. W. Wang, U. Becker and R. C. Ewing, *Physical Review B*, 2008, **78**.
11. J. G. Yu, R. Devanathan and W. J. Weber, *Journal of Materials Chemistry*, 2009, **19**, 3923-3930.
12. F. Mouhat and F. X. Coudert, *Physical Review B*, 2014, **90**.
13. M. Guzik, J. Pejchal, A. Yoshikawa, A. Ito, T. Goto, M. Siczek, T. Lis and G. Boulon, *Crystal Growth & Design*, 2014, **14**, 3327-3334.
14. Y. A. Malinowskii and O. S. Bondareva, *Kristallografiya*, 1991, **36**, 1558-1560.

15. A. M. Pires, M. R. Davolos, C. O. Paiva-Santos, E. B. Stucchi and J. Flor, *Journal of Solid State Chemistry*, 2003, **171**, 420-423.

16. M. Mitric, J. Blanusa, T. Barudzija, Z. Jaglicic, V. Kusigerski and V. Spasojevic, *Journal of Alloys and Compounds*, 2009, **485**, 473-477.

17. D. T. Cromer, *Journal of Physical Chemistry*, 1957, **61**, 753-755.

18. P. Aldebert and J. P. Traverse, *Materials Research Bulletin*, 1979, **14**, 303-323.

19. L. G. Bai, J. Liu, X. D. Li, S. Jiang, W. S. Xiao, Y. C. Li, L. Y. Tang, Y. F. Zhang and D. C. Zhang, *Journal of Applied Physics*, 2009, **106**.

20. S. Jiang, J. Liu, C. L. Lin, L. G. Bai, W. S. Xiao, Y. F. Zhang, D. C. Zhang, X. D. Li, Y. C. Li and L. Y. Tang, *Journal of Applied Physics*, 2010, **108**.

21. K. K. Pandey, N. Garg, A. K. Mishra and S. M. Sharma, Bhabha Atom Res Ctr (BARC), Mumbai, INDIA, 2011.

22. S. Jiang, J. Liu, C. L. Lin, X. D. Li and Y. C. Li, *Journal of Applied Physics*, 2013, **113**.

23. C. M. Lin, K. T. Wu, T. L. Hung, H. S. Sheu, M. H. Tsai, J. F. Lee and J. J. Lee, *Solid State Communications*, 2010, **150**, 1564-1569.

24. S. Sharma, N. L. Heda, K. K. Suthar, S. Bhatt, K. Sharma and B. L. Ahuja, *Computational Materials Science*, 2015, **104**, 205-211.

25. D. Richard, L. A. Errico and M. Renteria, *Computational Materials Science*, 2015, **102**, 119-125.

26. X. T. Ren, X. Z. Yan, P. Wang, Y. Li, S. M. Wang, F. Peng, L. Xiong, J. Liu and D. W. He, *High Pressure Research*, 2014, **34**, 70-77.

27. Q. X. Guo, Y. S. Zhao, C. Jiang, W. L. Mao, Z. W. Wang, J. Z. Zhang and Y. J. Wang, *Inorganic Chemistry*, 2007, **46**, 6164-6169.

28. S. D. Pandey, K. Samanta, J. Singh, N. D. Sharma and A. K. Bandyopadhyay, *Aip Advances*, 2013, **3**.

29. J. Feng, B. Xiao, R. Zhou and W. Pan, *Acta Materialia*, 2013, **61**, 7364-7383.

30. J. Y. Wang, Y. C. Zhou and Z. J. Lin, *Applied Physics Letters*, 2005, **87**.

31. J. P. McClure, PhD Thesis, University of Nevada 2009.

32. G. Day, personal communication.

33. J. F. Ziegler, M. D. Ziegler and J. P. Biersack, *Nuclear Instruments & Methods in Physics Research Section B-Beam Interactions with Materials and Atoms*, 2010, **268**, 1818-1823.

34. P. Moreira, R. Devanathan and W. J. Weber, *Journal of Physics-Condensed Matter*, 2010, **22**, 9.

CHAPTER 4

Defects in the Xenotime Lattice

Table of Contents

4.1 Table of Figures

4.1 Introduction

In the previous chapter we have considered only the perfect crystalline lattice for Xenotime, however in reality all solids at temperatures above absolute zero will contain intrinsic defects. There is indeed a thermodynamic basis for this observation which can be rationalised by calculating the Gibbs energy of the solid, equation (4.1). Although the enthalpy of formation (ΔH_f) for the point defects is normally endothermic, the introduction of disorder into the crystalline lattice at T > 0 K results in an increase in its entropy (S). The cumulative effect of these factors results in a minimum in the Gibbs energy of the solid at a defect concentration > 0 and therefore the formation of point defects is spontaneous.

$$G = H - TS \tag{4.1}$$

The Kröger-Vink notation for the intrinsic defect processes within Xenotime are summarised in equations (4.2) – (4.8). The Schottky defect process involves the formation of vacancies on the relevant lattice sites in stoichiometric quantities to maintain charge neutrality within the crystal. A Frenkel defect is essentially a point defect resulting from the displacement of an atom from its lattice site into an interstitial position, resulting in the formation of a vacancy and an interstitial pair, whilst conserving the stoichiometry and charge neutrality of the crystal. Finally, an anti-site defect is produced when two

atoms of different species exchange lattice sites. The lattice energies calculated for YPO_4, Y_2O_3 and P_2O_5 using the force field derived in Chapter 3 were -57.99, -27.02 and -182.08 eV, respectively.

$$Y_Y^{\times} + P_P^{\times} + 4O_O^{\times} \rightleftharpoons V_Y^{'''} + V_P^{'''''} + 4V_O^{\cdot\cdot} + YPO_4 \quad \textbf{(4.2)}$$

$$2Y_Y^{\times} + 3O_O^{\times} \rightleftharpoons 2V_Y^{'''} + 3V_O^{\cdot\cdot} + Y_2O_3 \quad \textbf{(4.3)}$$

$$2P_P^{\times} + 5O_O^{\times} \rightleftharpoons 2V_P^{'''''} + 5V_O^{\cdot\cdot} + P_2O_5 \quad \textbf{(4.4)}$$

$$Y_Y^{\times} \rightleftharpoons V_Y^{'''} + Y_i^{\cdot\cdot\cdot} \quad \textbf{(4.5)}$$

$$P_P^{\times} \rightleftharpoons V_P^{'''''} + P_i^{\cdot\cdot\cdot\cdot\cdot} \quad \textbf{(4.6)}$$

$$O_O^{\times} \rightleftharpoons V_O^{\cdot\cdot} + O_i^{''} \quad \textbf{(4.7)}$$

$$Y_Y^{\times} + P_P^{\times} \rightleftharpoons Y_P^{''} + P_Y^{\cdot\cdot} \quad \textbf{(4.8)}$$

The network rings in xenotime are hereafter described using the following notation, $R_j^i(N)$, where a network ring, R, contains a total of N atoms of which there are i yttrium nodes and j phosphorus nodes. Gao *et al*[1]. identified 3 favourable interstitial positions shown in Figure 4.1. The first defect position is an interstitial in the centre of the channel running parallel to the *c* axis forming a distorted tetrahedron, corner sharing with four phosphate tetrahedra. Site 2 is an interstitial located at the centre of the $R_2^2(8)$ large window in the *bc* plane. There are six oxygen neighbour atoms available for coordination from two faces of separate phosphate tetrahedra. The third site is located in the centre of the $R_0^2(4)$ small window in the *bc* plane surrounded by two oxygen atoms and two yttrium atoms. Frenkel defect formation energies were calculated using both *ab initio* methods and empirically derived potentials, the results of which are summarised in Table 4.1.

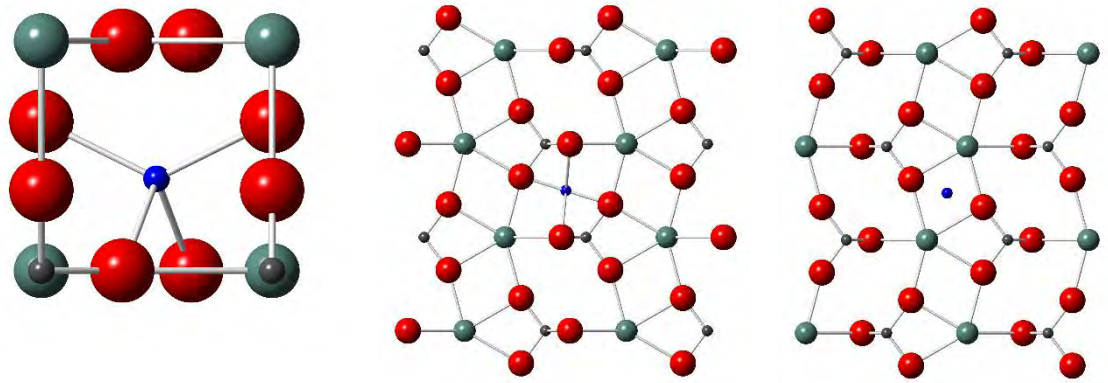

Figure 4.1: Three fundamental interstitial positions identified by Gao et al. (a) Site 1, centre of the channel running parallel to the c axis, (b) Site 2, six fold coordinate site in the centre of the large window in the bc plane, and (c) Site 3,interstitial site in the middle of the small window in the bc plane.

Table 4.1: Frenkel defect formation energies calculated by Gao *et al.*

Interstitial Site	Formation energy / eV (*ab initio*)			Formation energy / eV (atomistic *potentials*)		
	Y	P	O	Y	P	O
1	7.3	16.9	4.4	13.7	18.9	11.2
2	11.0	17.7	6.7	18.7	15.8	11.9
3	14.9	18.7	6.5	20.5	16.3	12.7

In order to investigate the lowest energy positions for interstitial atoms, a grid search method was used whereby the unit cell was divided into 15625 regions (25 x 25 x 25). An interstitial atom was placed at the centre of each region sequentially and allowed to relax freely. The final coordinates and defect energies were recorded. Similarly to the vacancy calculations, a Mott-Littleton methodology was employed using a region 1 and 2a size of 7.00 and 14.00 Å respectively. Once the initial defect sites had been isolated, convergence testing was performed to generate the final defect energy. Convergence was achieved using a region 1 and region 2a radius of 17.00 and 34.00 Å, respectively. In the case of defect cluster calculations the unit cell was divided into 1000 regions (10 x 10 x 10). An

interstitial atom was placed at the centre of each region sequentially and allowed to relax freely. The vacancy site was kept constant throughout. The final coordinates and defect energies were recorded. Similarly to the previous interstitial calculations a Mott-Littleton methodology was employed using a region 1 and 2a size of 7.00 and 14.00 Å, respectively, centred at the geometric centre between the initial vacancy and interstitial sites. Once the initial defect sites had been isolated, convergence testing was performed to generate the final defect energy. Convergence was achieved using a region 1 and region 2a radius of 17.00 and 34.00 Å, respectively.

4.2 Intrinsic Defects

4.2.1 Schottky Defects

4.2.1.1 Infinite Dilution

There are three possible vacancy sites in Xenotime relating to the different crystallographic sites for each species. The yttrium vacancy defect configuration can be found in Figure 4.2. Here the removal of the yttium atom results in the disruption of two $R_2^2(8)$ rings, two $R_0^2(4)$ rings and an $R_1^1(4)$ ring in the *bc* plane The equivalent rings are also disrupted in the *ac* plane. Similarly new $R_4^4(16)$ rings are also introduced. There is little distortion to the surrounding lattice and the defect energy is calculated to be 14.71 eV.

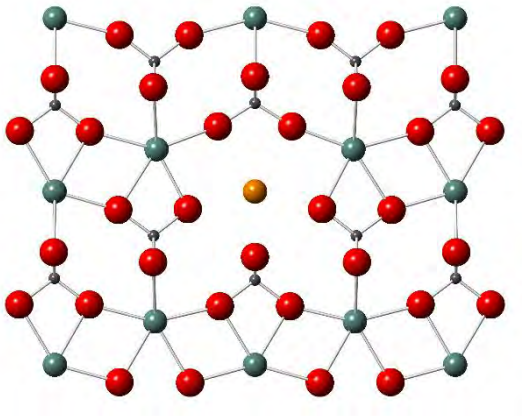

Figure 4.2: Yttrium vacancy point defect. Vacancy site is highlighted in orange

The phosphorus vacancy defect configuration is shown in Figure 4.3. Here the removal of the phosphorus atom has disrupted the $R_1^1(4)$ ring of which it was a member and the two adjacent $R_2^2(8)$ rings. There is also some distortion of the surrounding lattice as the adjacent yttrium atoms in the *c* direction are shifted towards the vacancy site, removing them from the coordination sphere of the subsequent phosphate units. This in turn reduces the coordination from eight to six and disrupts two $R_2^2(8)$ rings, two $R_0^2(4)$ rings and one $R_1^1(4)$ ring. New $R_1^3(8)$, $R_2^4(12)$ and $R_3^3(12)$ rings are also introduced in the *bc* plane, with the equivalent rings also generated and disrupted in the *ac* plane. The defect energy for the phosphorus vacancy point defect is calculated to be 48.25 eV.

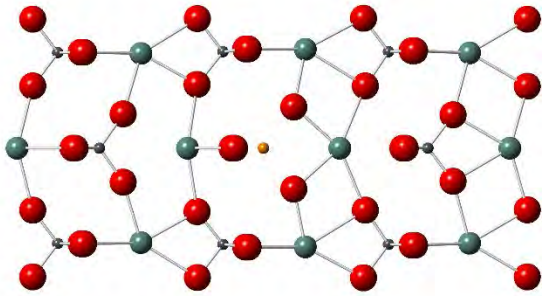

Figure 4.3: Phosphorus vacancy point defect. Vacancy site is highlighted in orange

The oxygen vacancy defect configuration is shown in Figure 4.4. Here the removal of the oxygen atom disrupts the adjacent $R_2^2(8)$, $R_0^2(4)$ and $R_1^1(4)$ rings. The phosphorus atom that was coordinated to the oxygen atom at the vacancy site has shifted into the adjacent $R_2^2(8)$ ring and has polymerised with a neighbouring phosphate group to form a pyrophosphate group (P_2O_7). The formation of the pyrophosphate group causes a slight rotation of the original phosphate unit which removes an oxygen atom from the coordination sphere of two neighbouring yttrium atoms, reducing their coordination number to seven. This also disrupts an $R_0^2(4)$ and an $R_1^1(4)$ ring, combining them to make a new $R_2^2(8)$ with similar cations occupying adjacent cation nodes as opposed to alternating in the inherent lattice $R_2^2(8)$ ring. A new $R_2^1(6)$ ring is also generated. The defect energy for the oxygen vacancy point defect is calculated to be 5.98 eV.

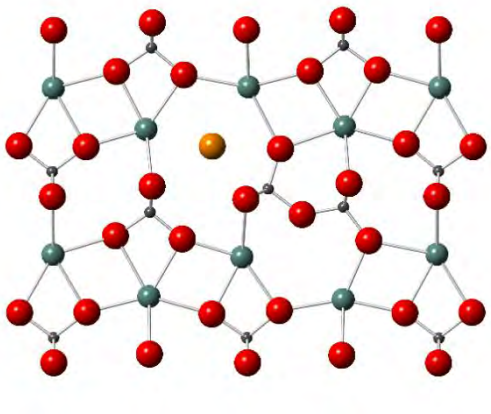

Figure 4.4: Oxygen vacancy point defect. Vacancy site is highlighted in orange

4.2.1.2 Clusters

The high defect energy calculated for the phosphorus vacancy point defect indicates that it is very unfavourable to remove the phosphorus from the centre of a phosphate unit. As such a vacancy cluster has been analysed whereby an entire phosphate unit has been removed from the lattice to determine if the clustering of these vacancies stabilises the defect in comparison to the case at infinite dilution (Figure 4.5). Here it can be seen that two $R_2^2(8)$ rings, two $R_0^2(4)$ rings and an $R_1^1(4)$ ring have been disrupted in the *bc* plane, with the generation of a new $R_2^4(12)$ ring. There is only a small amount of distortion to the surrounding lattice as the two phosphate groups involved in the $R_2^4(12)$ ring are slightly shifted towards the vacancies. This reduces the coordination of two local yttrium lattice atoms from eight to seven and the disruption of two $R_0^2(4)$ and two $R_1^1(4)$ rings to generate two new $R_1^2(6)$ rings. The equivalent rings will also be generated and disrupted in the *ac* plane. The defect energy for the phosphate vacancy cluster is calculated to be 53.25 eV.

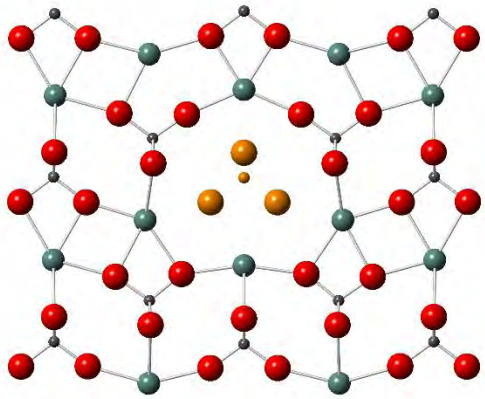

Figure 4.5: Phosphate vacancy cluster. (Vacancy sites are highlighted in orange)

Similarly two YPO_4 vacancy clusters with different orientations have been investigated as shown in Figure 4.6. These differ based on the orientation of the yttrium vacancy site in relation to the phosphate group, with the yttrium vacancy site in the same chain in the *c* axis for configuration (a), and on the adjacent yttrium site in the *b* direction for configuration (b). The defect energies for the YPO_4 vacancy clusters (a) and (b) are calculated to be 64.04 and 64.57 eV respectively.

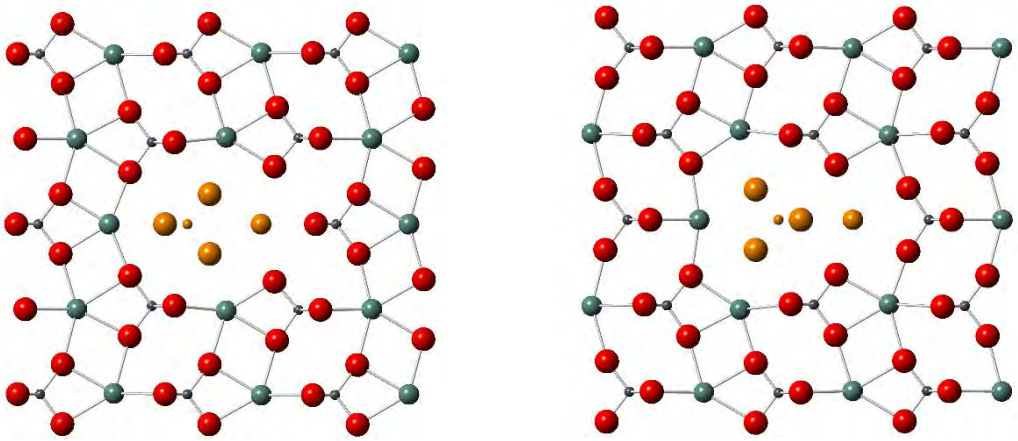

(a)

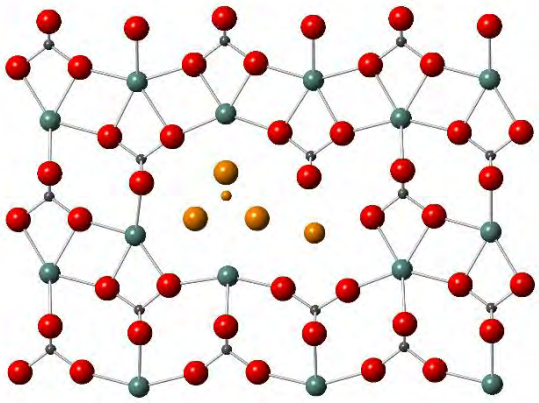

(b)

Figure 4.6: YPO_4 vacancy clusters with the yttrium vacancy site in, (a) the same chain, and (b) the adjacent chain as the phosphate vacancy in the c axis. (Vacancy sites are highlighted in orange)

The defect energies for the vacancy configurations are summarised in Table 4.2. Here the braces indicate defects which are clustered together.

Table 4.2: Summary of vacancy defect energies

Vacancy configuration	Defect Energy / eV
$V_Y^{'''}$	14.71
$V_P^{''''}$	48.25
$V_O^{\cdot\cdot}$	5.98
$\{V_P^{''''} + 4V_O^{\cdot\cdot}\}$	53.25
$\{V_Y^{'''} + V_P^{''''} + 4V_O^{\cdot\cdot}\}_a$	64.04
$\{V_Y^{'''} + V_P^{''''} + 4V_O^{\cdot\cdot}\}_b$	64.57

The Schottky defect formation energies and associated binding energies have been calculated following equation (4.2) and are summarised in Table 4.3. These give the relative energies required to form the defects and the stabilisation of the defects due to clustering, respectively. In the case where there are multiple equivalent configurations, the lowest energy configuration was used.

Table 4.3: Summary of Schottky defect formation and binding energies.

Schottky Defect	Formation Energy / eV	Binding Energy / eV
$V_Y^{'''} + V_P^{''''} + 4V_O^{\cdot\cdot}$	28.89	-
$V_Y^{'''} + \{V_P^{''''} + 4V_O^{\cdot\cdot}\}$	9.96	-18.94
$\{V_Y^{'''} + V_P^{''''} + 4V_O^{\cdot\cdot}\}_a$	6.05	-22.84

The lowest energy defect configuration for a Schottky defect was found to be the cluster in which the yttrium vacancy was situated on the adjacent yttrium lattice site to the phosphate vacancy in the *c* axis. As expected there was found to be a large binding energy associated with the removal of an entire phosphate unit compared to removing the constituent atoms at infinite dilution.

4.2.2 Schottky-like defects

It is also possible to consider Schottky-like defects where the neutral vacancy cluster is associated with the formation of Y_2O_3 and P_2O_5, following equations (4.3) and (4.4).

4.2.2.1 Y_2O_3 Clusters

Two Y_2O_3 Schottky-like clusters have been highlighted in Figure 4.7. The lowest energy of these is illustrated in Figure 4.7 (a). Here the two yttrium vacancies lie in the same chain down the *c* axis along with two of the oxygen vacancies. The third oxygen vacancy is located in the subsequent plane, where it causes the coordinating phosphorus atom to displace and polymerise with a neighbouring phosphate unit. This also becomes polymerised with a third phosphate unit forming a P_3O_{10} unit. Similarly a P_2O_7 unit is formed in the same plane as the yttrium vacancies as a result of one of the other oxygen vacancies. The second configuration is illustrated in Figure 4.7 (b). Here the yttrium vacancies are in the same chain down the *c* axis with one of the oxygen vacancies. The other two oxygen vacancies are located in adjacent planes symmetrically about one of the yttrium vacancies. The phosphorus lattice atom located between the yttrium vacancies is displaced, forming a P_2O_7 unit. The defect energies for these configurations are calculated to be 38.52 and 44.18 eV respectively.

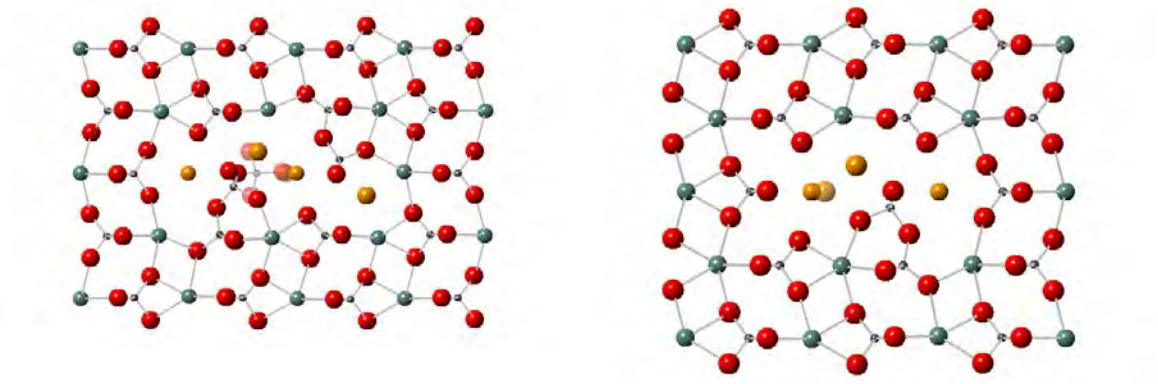

(a) (b)

Figure 4.7: Y_2O_3 vacancy cluster. (Vacancy sites are highlighted in orange)

The Schottky-like defect formation energies and associated binding energies have been calculated following equation (4.3) and are summarised in Table 4.4. In the case where there are multiple equivalent configurations, the lowest energy configuration was used.

Table 4.4: Summary of Y_2O_3 Schottky-like defect formation and binding energies.

Schottky Defect	Formation Energy / eV	Binding Energy / eV
$\boldsymbol{2V_Y^{'''} + 3V_O^{\cdot\cdot}}$	20.34	-
$\boldsymbol{\{2V_Y^{'''} + 3V_O^{\cdot\cdot}\}}$	11.48	-8.86

The lowest energy Y_2O_3 Schottky-like defect was found to be the cluster illustrated in Figure 4.7 (a), with a formation energy of 11.48 eV. This defect cluster has a very large binding energy of -8.855 eV, indicating that is extremely favourable for the vacancies to cluster together in this way compared to the vacancies at infinite dilution. This defect cluster is not as energetically favourable as the clustered YPO_4 Schottky defect (6.05 eV).

4.2.2.2 P_2O_5 Clusters

Two P_2O_5 vacancy clusters have been highlighted in Figure 4.8. The lowest energy of these is illustrated in Figure 4.8 (a). Here the phosphorus vacancy sites are constituents of the same $R_2^2(8)$ ring, as are the oxygen vacancies. The oxygen vacancies are partitioned over the two phosphorus sites, with one phosphorus site having three nearest neighbour vacancies and the other having two. This also reduces the coordination of the neighbouring yttrium atoms to between five and seven. The second cluster is illustrated in Figure 4.8 b. Here the phosphorus atoms lie within the same chain down the *c* axis and do not belong to the same ring system. One again the oxygen vacancies are distributed over the two phosphorus vacancies, with one phosphorus site having three nearest neighbour vacancies and the other having two. The local ring structure is again disrupted,

forming a large $R_4^6(20)$ ring. There is a large displacement of a yttrium lattice atom towards one of the phosphorus vacancy sites, this yttrium atom has its coordination reduced to four. The surrounding yttrium atoms are also reduced in coordination to six and seven. The defect energies for these clusters are calculated to be 95.74 and 95.76 eV respectively.

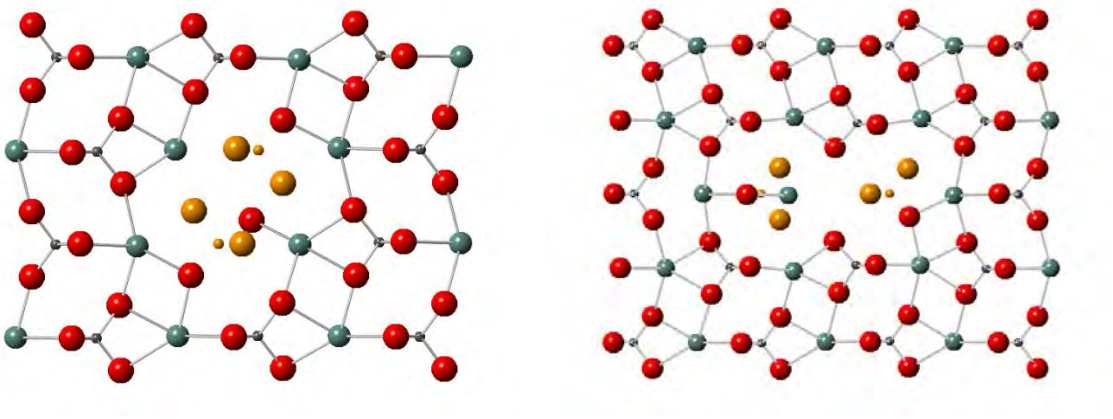

(a) (b)

Figure 4.8: P_2O_5 vacancy cluster. (Vacancy sites are highlighted in orange)

The Schottky-like defect formation energies and associated binding energies have been calculated following equation (4.4) and are summarised in Table 4.5. In the case where there are multiple equivalent configurations, the lowest energy configuration was used.

Table 4.5: Summary of P_2O_5 Schottky-like defect formation and binding energies.

Schottky Defect	Formation Energy / eV	Binding Energy / eV
$2V_P^{''''} + 5V_O^{\cdot\cdot}$	40.82	-
$V_P^{''''} + V_O^{\cdot\cdot} + \{V_P^{''''} + 4V_O^{\cdot\cdot}\}$	21.89	-18.94
$\{V_P^{''''} + V_O^{\cdot\cdot}\} + \{V_P^{''''} + 4V_O^{\cdot\cdot}\}$	14.33	-26.49
$\{2V_P^{''''} + 5V_O^{\cdot\cdot}\}_a$	10.14	-30.68

The lowest energy P_2O_5 Schottky-like defect was found to be the cluster with the vacancy sites located in the same $R_2^2(8)$ ring, with a formation energy of 10.14 eV. This defect cluster has a very large binding energy of -30.68 eV, indicating that is extremely favourable for the vacancies to cluster together in this way compared to the vacancies at infinite dilution. This defect cluster is not as energetically favourable as the clustered YPO_4 Schottky defect (6.03 eV).

4.2.3 Frenkel Defects

A wide range of defects are discussed hereafter which are intended as reference material for future studies. These are proceeded by a summary of a selection of defects of interest in section 4.4.

4.2.3.1 Yttrium Frenkel Defects

A summary of the yttrium interstitial defect configurations can be found in Table 4.6. The lowest energy yttrium interstitial position was found to be the seven coordinate site associated with the ideal site 1 position in the centre of the channel running parallel to the *c* axis. A summary of the defect energies for the yttrium Frenkel pair clusters can be found in Table 4.7. The lowest energy cluster was found to be a yttrium split interstitial near the site 1 position.

Table 4.6: Summary of defect energies for yttrium interstitial positions at infinite dilution

Description	Defect Energy / eV	Associated ideal site	Polymerised phosphate?	Split interstitial?	Figure
Six coordinate	-5.90	1	×	×	Figure 4.9 (a)
Seven coordinate	-5.90	1	×	×	Figure 4.9 (b)
Six coordinate	-2.69	2	×	×	Figure 4.10 (a)
Six coordinate	-2.53	3	×	×	Figure 4.10 (b)
Residual oxygen coordinating pseudo-equatorial position	-4.73	1	✓	×	Figure 4.12 (a)
Residual oxygen coordinating pseudo-axial position	-3.94	1	✓	×	Figure 4.12 (b)
Six coordinate phosphorus shift in plane.	-3.21	2	✓	×	Figure 4.13 (a)
Six coordinate phosphorus shift perpendicular to plane.	-2.50	2	✓	×	Figure 4.13 (b)
Both six coordinate split in {110} direction.	-5.58	1	×	✓	Figure 4.14 (a)
Both six coordinate split in {101} direction.	-3.79	1	×	✓	Figure 4.14 (b)
Four coordinate split with phosphorus in {110} direction.	-3.49	1	✓	✓	Figure 4.15

Table 4.7: Summary of defect energies for yttrium Frenkel pair clusters.

Description	Defect Energy / eV	Associated ideal site	Polymerised phosphate?	Split interstitial?	Figure
Six coordinate, vacancy distance 5.46 Å	6.53	1	×	×	Figure 4.16 (a)
Six coordinate, vacancy distance 7.13 Å	7.00	1	×	×	Figure 4.16 (b)
Six coordinate, vacancy distance 7.62 Å	7.26	1	×	×	Figure 4.16 (c)
Seven coordinate, vacancy distance 5.46 Å	6.67	1	×	×	Figure 4.17 (a)
Seven coordinate, vacancy distance 5.95 Å	6.87	1	×	×	Figure 4.17 (b)
Seven coordinate, vacancy distance 7.42 Å	7.19	1	×	×	Figure 4.17 (c)
Six coordinate, vacancy distance 3.99 Å	8.96	2	×	×	Figure 4.18 (a)
Six coordinate, vacancy distance 6.31 Å	10.16	2	×	×	Figure 4.18 (b)
Six coordinate, vacancy distance 5.63 Å	10.00	2	×	×	Figure 4.18 (c)
Five coordinate, vacancy distance 5.32 Å	10.10	3	×	×	Figure 4.19

Six coordinate, vacancy distance 2.85 Å. Residual oxygen in pseudo-equatorial position	4.93	1	✓	×	Figure 4.20 (a)
Six coordinate, vacancy distance 2.11 Å. Residual oxygen in pseudo-equatorial position	5.419	1	✓	×	Figure 4.20 (b)
Six coordinate, vacancy distance 5.18 Å. Residual oxygen in pseudo-axial position	7.383	1	✓	×	Figure 4.21 (a)
Six coordinate, vacancy distance 5.39 Å. Residual oxygen in pseudo-axial position	7.510	1	✓	×	Figure 4.21 (b)
Six coordinate, vacancy distance 5.22 Å. Residual oxygen in pseudo-equatorial position	7.648	1	✓	×	Figure 4.21 (c)
Six coordinate, vacancy distance 2.69 Å. Residual oxygen in coordination sphere.	5.850	2	✓	×	Figure 4.22
Two six coordinate split in in {110} direction.	7.317	1	×	✓	Figure 4.23 (a)
One six and one four coordinate split in in {110} direction.	6.645	1	×	✓	Figure 4.23 (b)
Two six coordinate split in in {101} direction.	4.501	1	×	✓	Figure 4.24 (a)

Two six coordinate split in in {101} direction.	5.354	1	×	✓	Figure 4.24 (b)
Two six coordinate split in in {101} direction.	7.975	1	×	✓	Figure 4.24 (c)
Six coordinate split centred on Phosphorus lattice site.	6.626	1	✓	✓	Figure 4.25

4.2.3.1.1 Infinite Dilution

The most energetically favourable self-interstitials were found to be closely associated with the proposed site 1 interstitial position. The yttrium interstitial is shifted down the channel in the *c* direction from the ideal site 1 position for both defect configurations. A six fold coordinate interstitial was found closest to the ideal site one position (Figure 4.9 (a)), sharing one edge and four corners with five phosphate tetrahedra. The edge sharing oxygen ions are located at distance of 2.21 Å from the yttrium interstitial, with the two nearest neighbour oxygen atoms at a distance of 2.16 Å and the remaining oxygen atoms at a distance of 2.41 and 2.42 Å. A seven fold coordinate interstitial was also found at a slightly larger distance from the ideal position (Figure 4.9 b). This interstitial is edge sharing with two and corner sharing with three phosphate tetrahedra. The edge sharing oxygen atoms are located at distances of 2.15, 2.55, 2.20 and 2.22 Å from the yttrium interstitial, with the other corner sharing oxygen atoms at a distances of 2.17, 2.34 and 2.53 Å. The six and seven coordinate defect configurations have defect energies of -5.90 and -5.90 eV respectively.

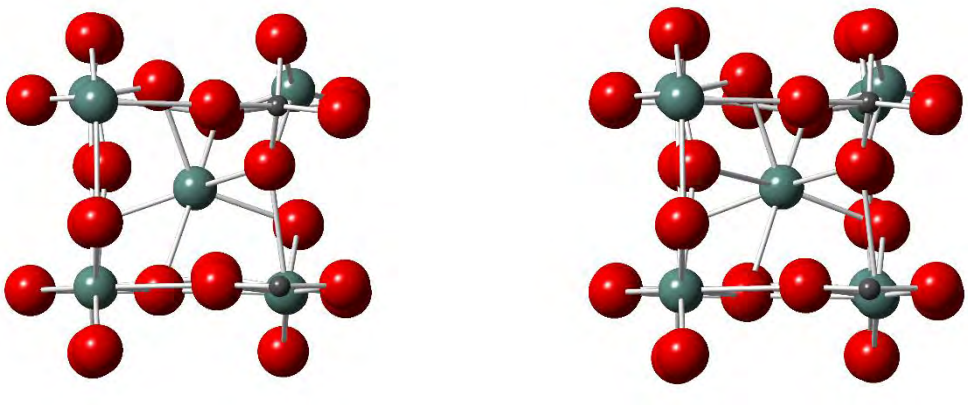

(a) (b)

Figure 4.9: Lowest energy Y self-interstitials in the site 1 defect position (a) six fold coordinate and (b) 7 fold coordinate

The yttrium self-interstitial is also stable in both the site 2 and 3 positions (Figure 4.10 (a) and (b) respectively). The site 2 position can accommodate the yttrium interstitial with minimal distortion to the lattice. The yttrium interstitial sits in a six coordinate position, face sharing with two phosphate tetrahedra. There is a small expansion of the large window with the Y-Y and P-P distances between lattice atoms elongating from 5.70 and 3.79 Å to 6.08 and 4.58 Å, respectively. By considering the O-P-O angles between the non-coordinating oxygen atom and the three coordinating oxygen atoms it can be seen that there is a small distortion to the phosphate tetrahedra. The angle between the non-coordinating oxygen atom and the coordinating oxygen that is also a member of the $R_1^1(4)$ ring remains relatively unchanged (ca. 106.55° to ca. 106.93°). However the angles made with the other two coordinating oxygen atom are enlarged from ca. 110.90° to 117.00° in the defect configuration. None of the original network rings are disrupted by the interstitial and new $R_1^1(4)$ and $R_0^2(4)$ rings are introduced. The defect energy for the yttrium self-interstitial at site 2 is calculated to be -2.69 eV.

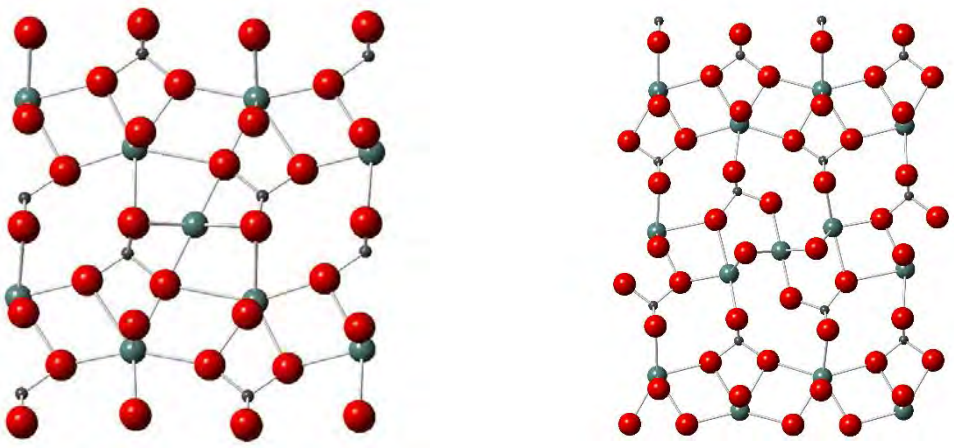

(a) (b)

Figure 4.10: Yttrium self-interstitial in the (a) site 2 and (b) site 3 defect positions identified by Gao *et al.*

The site 3 position on the other hand undergoes quite considerable deformation. The yttrium interstitial adopts a six coordinate distorted octahedral position, corner sharing with six phosphate tetrahedra. The four equatorial oxygen atoms are edge sharing with two six coordinate yttrium lattice atoms. The $R_1^1(4)$ rings adjacent to the interstitial atom are disrupted forming $R_1^2(6)$ rings. The two oxygen atoms that were originally part of the $R_1^1(4)$ ring now occupy the axial sites in the distorted octahedron, while the two yttrium lattice atom which were part of this ring are now only seven coordinate. The equatorial oxygen atoms are shifted toward the yttrium interstitial bringing the oxygen atoms out of the orthogonal plane, reducing the O_{ax}-Y_{latt}-O_{eq} angle from 93.74 to 81.90°. Similarly the rotation of the phosphate units also deforms the adjacent $R_0^2(4)$ rings. The six coordinate interstitial atom is very similar to the distorted octahedral yttrium lattice site in Y_2O_3, with the O_{ax}-Y-O_{eq} angles of ca. 95.00 and 85.00° in the defect configuration compared with 98.21 and 81.79° in Y_2O_3. Similarly the Y-O interatomic distances also differ with Y-O_{ax} and Y-O_{eq} distances in the defect configuration of ca. 2.08 and 2.53 Å. respectively compared with 2.28 Å in Y_2O_3. The defect energy for the yttrium self-interstitial at site 3 is calculated to be -2.53 eV.

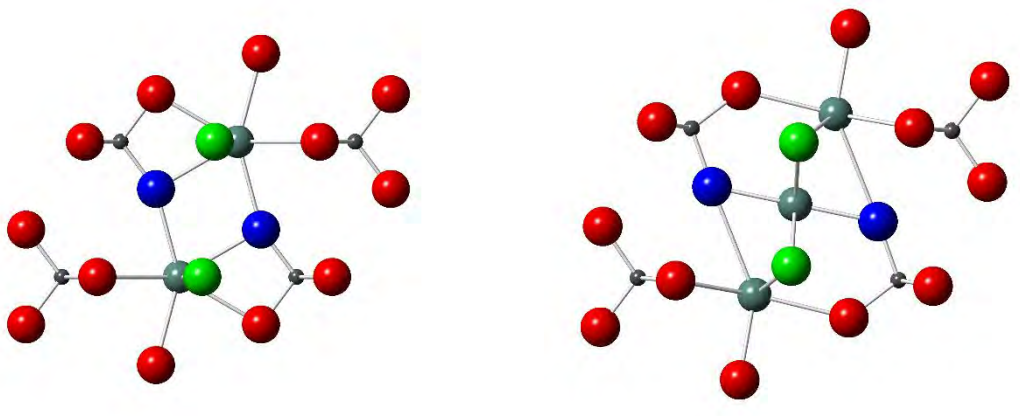

(a) (b)

Figure 4.11: Site 3 interstitial position (a) pristine and (b) defect configuration. Axial and equitorial oxygen atoms have been highlighted in blue and green. respectively.

Two closely related defects have also been identified which not only include the yttrium self-interstitial, but also a shift of a phosphorus atom into a position where it is polymerised with an adjacent phosphate unit. Figure 4.12 (a) and (b) shows two such defect configurations with the yttrium interstitial in a six coordinate position close to the ideal position for site 1. In both configurations the phosphorus atom has shifted away from the interstitial parallel to the *a* axis. This leaves an oxygen atom coordinated to the yttrium interstitial which is no longer coordinated to any phosphorus atoms (highlighted in blue). The shifted phosphorus atom is located at a similar distance from the yttrium interstitial in both cases, 3.21 and 3.12 Å for configuration (a) and (b) respectively, but the key difference is the position of the oxygen atom which is no longer coordinating to the phosphorus atom within the coordination sphere of the yttrium interstitial. In Figure 4.12 (a) it can be seen that the aforementioned oxygen atom is located in a pseudo-equatorial position in contrast to Figure 4.12 (b), where it is located in a pseudo-axial position. This configurational dissimilarity is manifested in the calculated defect energies of -4.73 and -3.94 eV (Δ = 0.80 eV) for configuration (a) and (b) respectively.

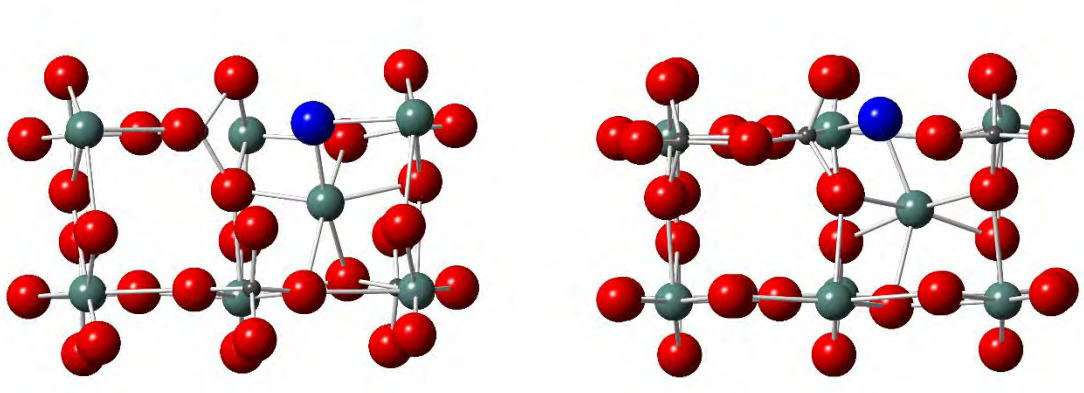

(a) (b)

Figure 4.12: Four yttrium interstitial defect configurations associated with the ideal site 1 position which include a polymerised phosphate unit. The residual oxygen atom is highlighted in blue.

Two similar defect configurations have been identified for the site 2 interstitial position, shown in Figure 4.13. The yttrium interstitial in defect configuration (a) is in a six coordinate position and the phosphorus atom has been shifted in the *bc* plane. The residual oxygen atom from the polymerisation of the phosphate units remains in the coordination sphere of the yttrium interstitial, which is also edge sharing with the polymerised phosphate unit and face sharing with a lattice phosphate tetrahedron. The rotation of this lattice phosphate tetrahedron removes an oxygen atom from the coordination sphere of two adjacent yttrium atoms reducing their coordination to seven.

The yttrium interstitial in defect configuration (b) is also in a six coordinate position however in this case the phosphorus atom is shifted out of the *ac* plane in the b direction and polymerises with another phosphate tetrahedron in the plane behind (shown translucent in Figure 4.13 (b). In contrast to the previous case for the defects associated with the ideal site 1 position, here the yttrium interstitial with the accompanying shift of a phosphorus atom stabilises the defect site when that shift is in the same plane as the yttrium interstitial but destabilises the defect when the shift is in the perpendicular plane. This is evident from the calculated defect energies where configurations a and b have defect energies of -3.21 and -2.50 eV respectively in comparison with the defect energy of the site 2 interstitial with no polymerisation of -2.69 eV.

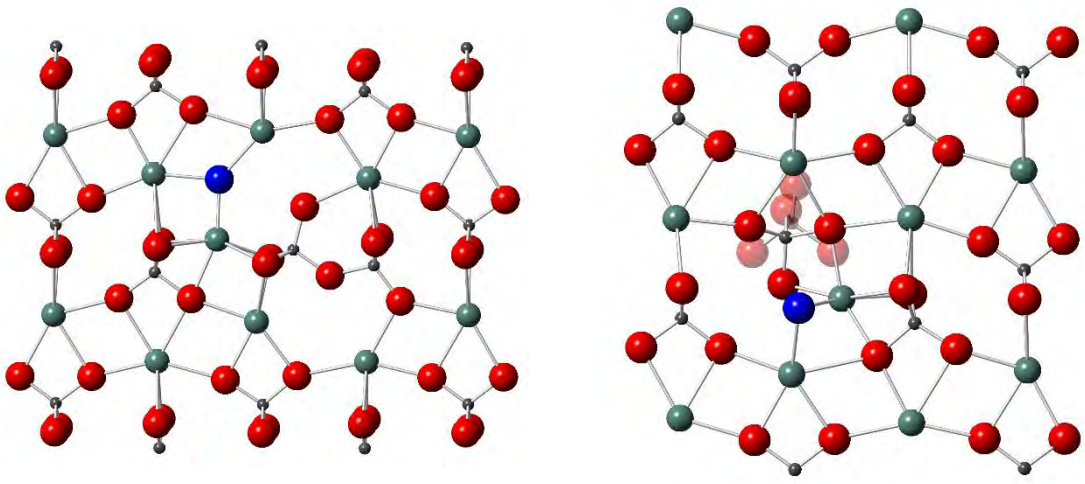

(a) (b)

Figure 4.13: Two yttrium interstitial defect configurations associated with the ideal site 2 position which include a polymerised phosphate unit. The residual oxygen atom is highlighted in blue.

Several yttrium split interstitials were also identified by this procedure which can be associated with the ideal site 1 position, as shown in Figure 4.14. The first defect configuration is shown in Figure 4.14 (a) and consists of two six coordinate yttrium interstitials surrounding a central yttrium vacancy. The interstitials are split in the {110} direction with an interatomic separation of 3.79 Å. There is a degree of distortion to the surrounding phosphate tetrahedra involving a small rotation. Similarly the defect configuration shown in Figure 4.14 (b) consists of two six coordinate yttrium interstitials surrounding a yttrium vacancy. The interstitials are split in the {101} direction and shifted out of the ac plane into the channels, with an interatomic separation of 3.67 Å. Once again there is a degree of distortion to the local phosphate tetrahedra resulting in a small rotation. The defect energies for the defect configurations (a) and (b) are -5.58 and -3.79 eV, respectively.

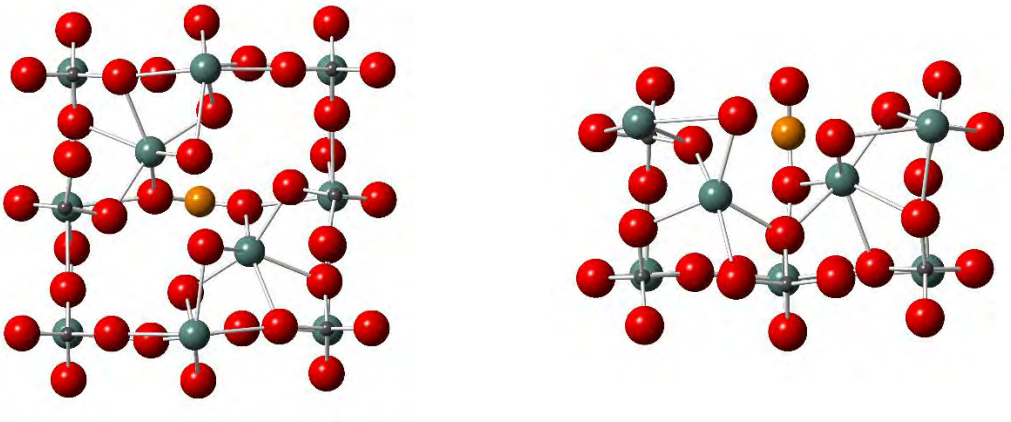

(a) (b)

Figure 4.14: Yttrium split interstitials associated with the ideal site 1 position (a) centred on yttrium vacancy, and (b) offset from yttrium vacancy. Vacancy position is highlighted in orange.

A four coordinate yttrium split interstitial has also been identified which centres around a phosphorus vacancy, shown in Figure 4.15. Here the yttrium interstitial is split diagonally in the (110) direction with a four coordinate phosphorus interstitial at an interatomic separation of 4.02 Å. The phosphate tetrahedron formed by the phosphorus interstitial is polymerised with two other phosphate units through corner sharing, producing a P_3O_{10} chain. The defect energy is calculated to be -3.49 eV.

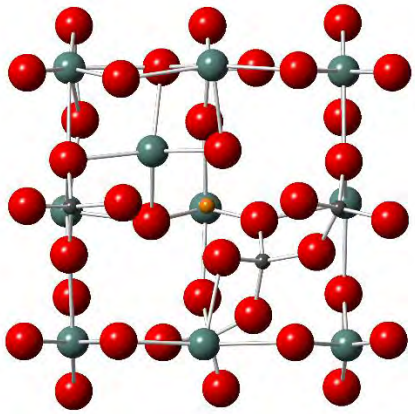

Figure 4.15: Yttrium split interstitial centred on a phosphorus lattice site. Vacancy position is highlighted in orange.

A summary of the yttrium defect configurations can be found in Table 4.6. The lowest energy yttrium interstitial position was found to be the seven coordinate site associated with the ideal site 1 position in the centre of the channel running parallel to the *c* axis.

4.2.3.1.2 Cluster Calculations

Three Frenkel pair clusters have been identified consisting of a six coordinate yttrium interstitial associated with the ideal site 1 position and a yttrium vacancy (Figure 4.16). The primary difference between these configurations is the distance between the interstitial and the vacancy position (highlighted in orange). In configurations a and b the vacancy is located in the *bc* plane adjacent to the yttrium interstitial and is part of the neighbouring channel in the *b* direction at a distance of 5.46 and 7.13 Å respectively. In contrast in defect configuration c the vacancy is located in the *bc* plane of the neighbouring channel in the *ab* direction that is furthest from the interstitial, at a distance of 7.62 Å. The defect energies calculated for these clusters are 6.53, 7.00 and 7.26 eV respectively which suggests that the local vacancy stabilises the yttrium interstitial.

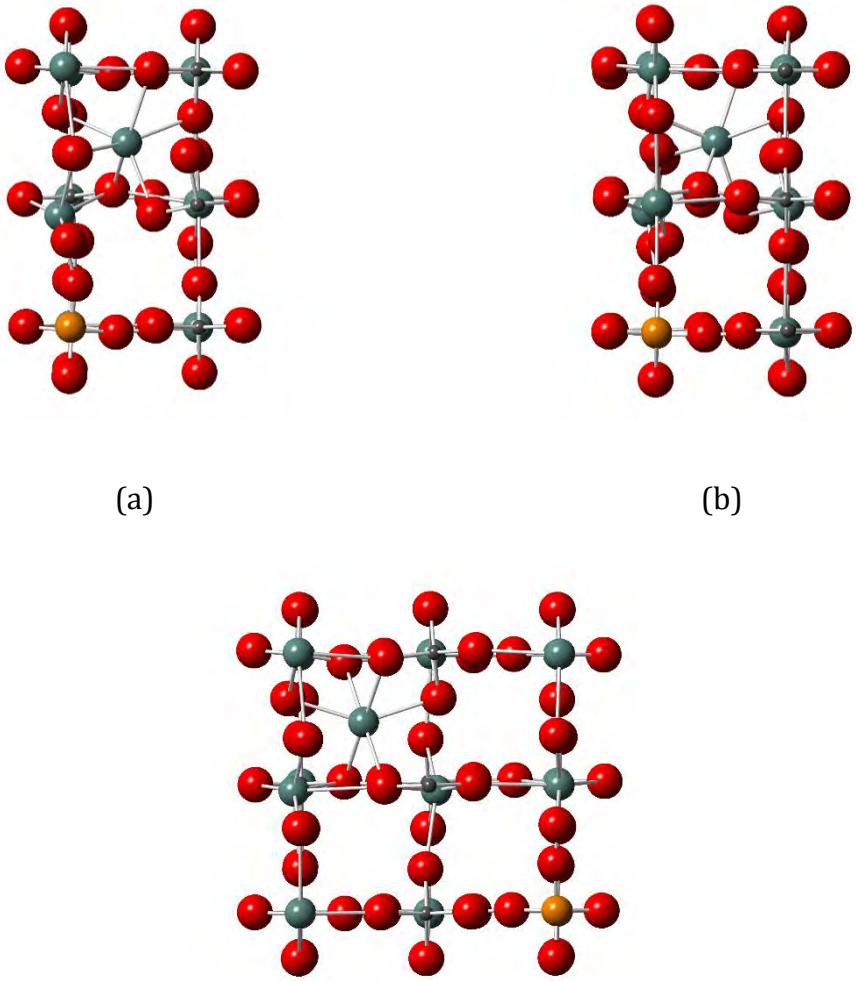

(a) (b)

(c)

Figure 4.16: Six coordinate yttrium Frenkel pair clusters associated with the ideal site 1 position. The vacancy site is highlighted in orange.

Similarly three Frenkel pair clusters have been identified consisting of a seven coordinate yttrium interstitial associated with the ideal site 1 position and a yttrium vacancy (Figure 4.17). As before the key difference is the distance between the yttrium interstitial and vacancy site which were measured as 5.46, 5.95 and 7.42 Å for the configurations in figure (a), (b) and (c) respectively. A positive correlation is identified between this distance and the defect energy, with Frenkel pair cluster defect energies of 6.67, 6.87 and 7.19 eV, respectively.

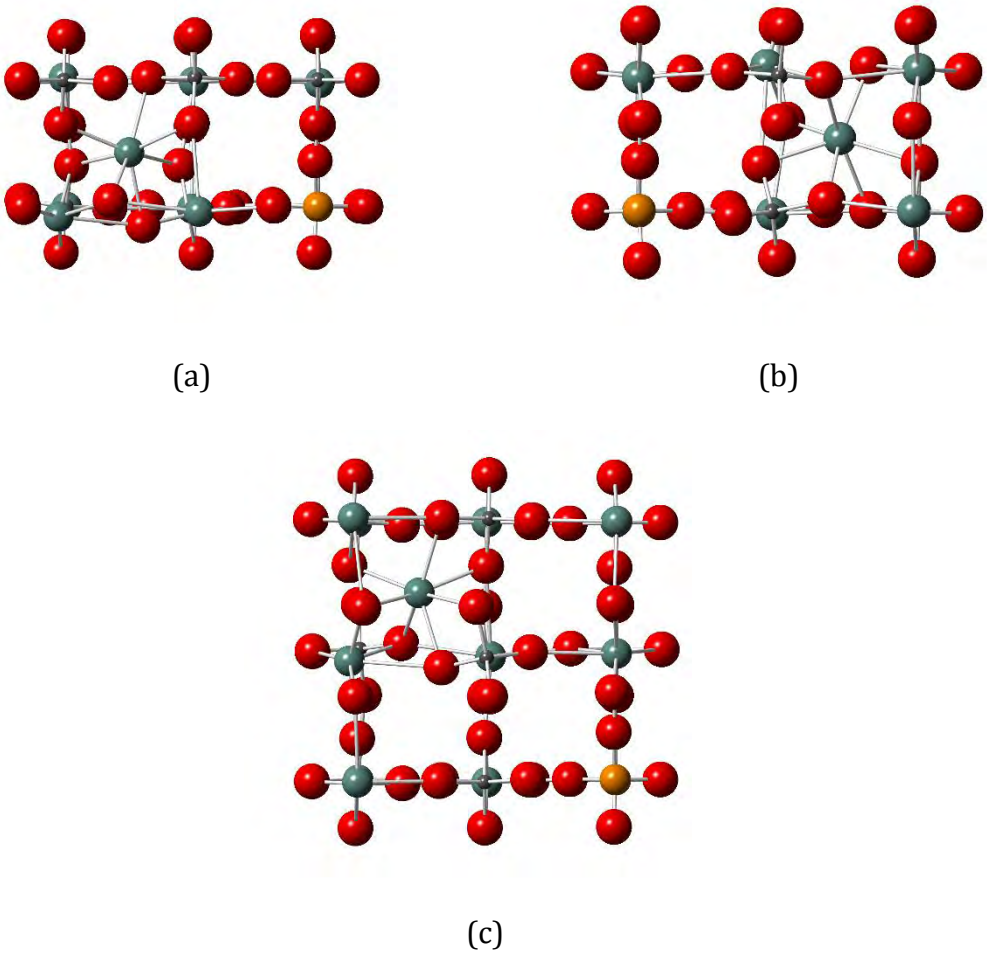

(a) (b)

(c)

Figure 4.17: Seven coordinate yttrium Frenkel pair clusters associated with the ideal site 1 position. The vacancy site is highlighted in orange.

Two Frenkel pair clusters were identified using the grid methodology which are associated with the site 2 ideal interstitial position (Figure 4.18). In both cases the yttrium vacancy is located in the plane behind the interstitial atom, located at distances of 3.99 and 6.31 Å for the configurations (a) and (b), respectively. This difference is again manifested in the calculated Frenkel pair defect energies of 8.96 and 10.16 eV respectively. It was not possible to isolate any Frenkel pair defect configurations with the vacancy in the same plane as the yttrium interstitial in the site 2 position using the grid methodology as these optimised to a lower energy site 1 configuration. To avoid this the interstitial was fixed at the site 2 position and the lattice allowed to relax around it (Figure

4.18 c). In this configuration the vacancy is located at a distance of 5.63 Å from the interstitial position with a Frenkel pair defect energy of 10.03 eV.

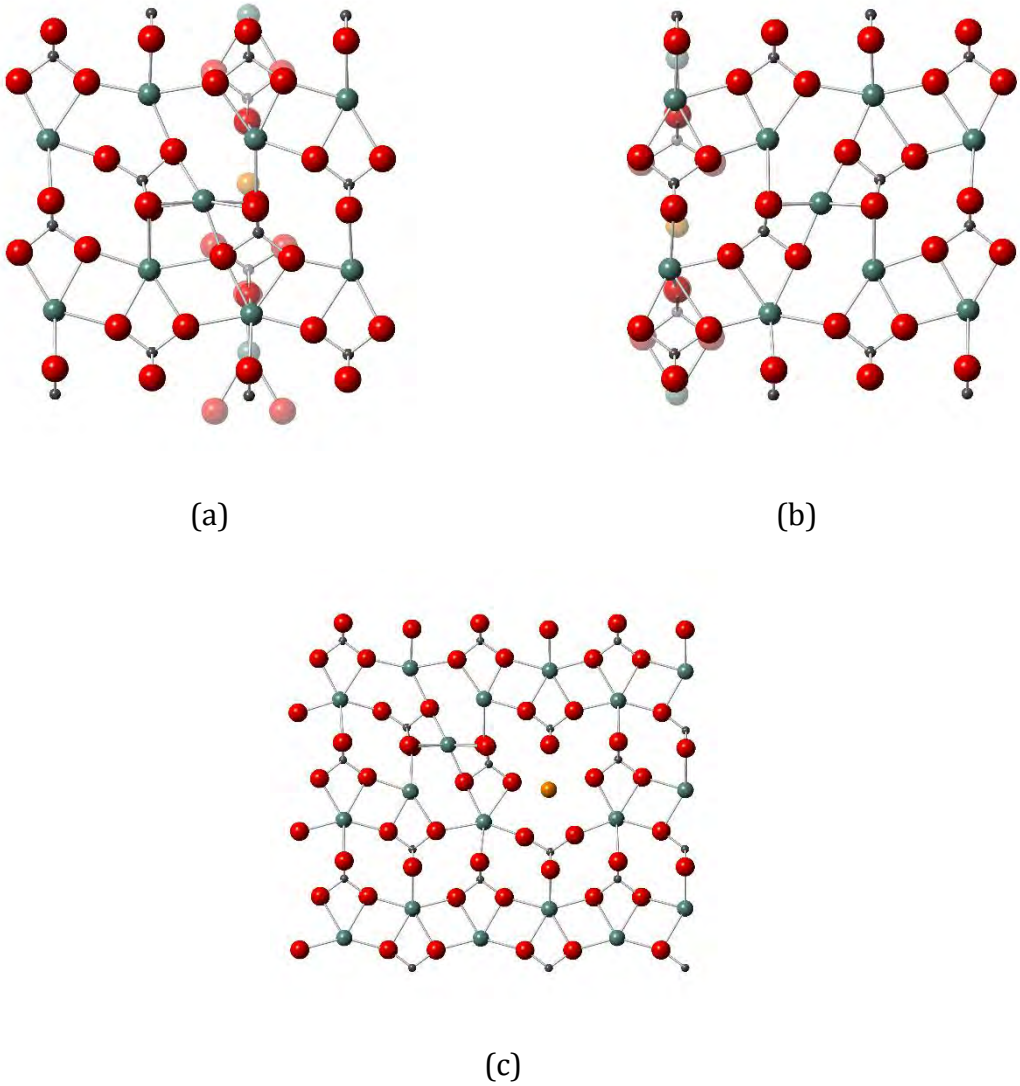

Figure 4.18: Six coordinate yttrium Frenkel pair clusters associated with the ideal site 2 position. The vacancy site is highlighted in orange.

Only one Frenkel pair defect cluster has been identified with the interstitial in the site 3 position. Here the yttrium interstitial is in a five coordinate site which is corner sharing with three phosphate groups and edge sharing with one, with the vacancy in the subsequent *bc* plane at a distance of 5.32 Å (Figure 4.19). This is in contrast to the six coordinate site at infinite dilution which is corner sharing with six phosphate groups.

Unlike the case at infinite dilution, the yttrium interstitial is not equidistant from the two yttrium lattice atoms that were part of the $R_0^2(4)$ ring. As such the interstitial is only edge sharing with one of the six coordinate yttrium atoms. A new $R_2^3(10)$ ring is introduced similar to the case at infinite dilution, however the second $R_2^3(10)$ ring is expanded to an $R_3^3(12)$ ring. The edge sharing phosphate group is rotated which results in an oxygen atom moving out of the coordination sphere of the third nearest neighbour yttrium lattice atom, decreasing its coordination number from eight to seven and disrupting an $R_0^2(4)$ and an $R_2^2(8)$ ring to generate a new $R_2^3(10)$ ring. The defect energy for this configuration is calculated to be 10.10 eV.

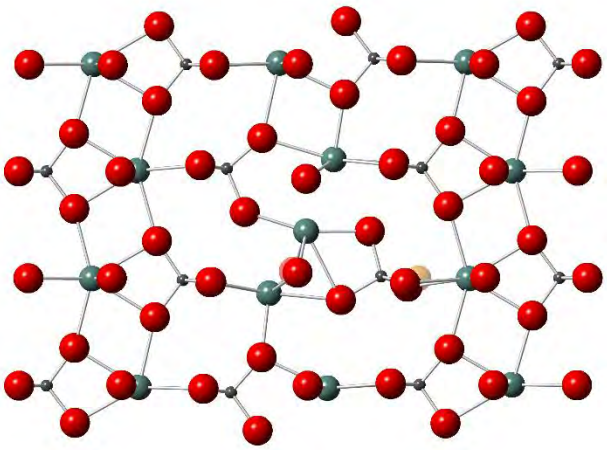

Figure 4.19: Five coordinate yttrium Frenkel pair cluster associated with the ideal site 3 position. The vacancy site is highlighted in orange.

Five Frenkel pair configurations related to the six coordinate ideal site 1 interstitial position have been identified which also include a polymerised phosphate group. Two of these were found to stabilise the cluster and allow for the vacancy site to be closer to the yttrium interstitial (Figure 4.20). In both cases the residual oxygen atom remains in the coordination sphere of the interstitial atom, however the location of the vacancy differs. The vacancy is in the same plane as the displacement vector of the phosphorus atom in

configuration a, whereas in configuration b it is the subsequent plane parallel to the phosphorus displacement vector. The distances between the interstitial atom and the vacancy site for configurations a and b were 2.85 and 2.11 Å respectively, which are much smaller than the smallest distance for the equivalent configuration without the polymerised phosphate unit of 5.46 Å. This helps to stabilise these defect configurations, with calculated Frenkel pair defect energies of 4.93 and 5.42 eV, respectively, in comparison to the equivalent configuration without the polymerised phosphate unit (6.53 eV).

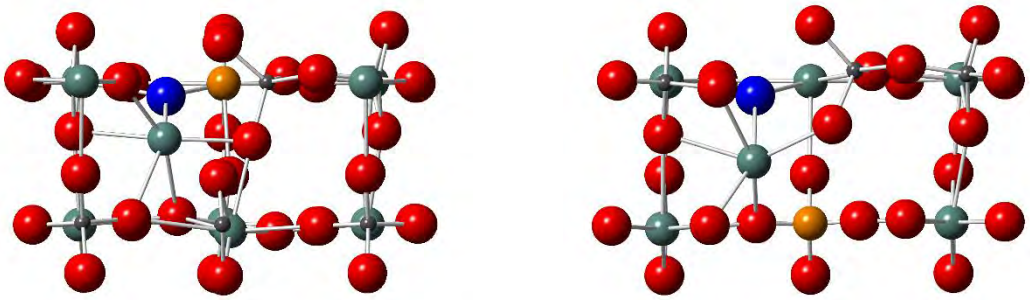

(a) (b)

Figure 4.20: Six coordinate yttrium Frenkel pair clusters associated with the site 1 position which include a polymerised phosphate unit. The residual oxygen atom is highlighted in blue and the vacancy site is highlighted in orange.

In the other three defect configurations it was found that the presence of the polymerised phosphate unit destabilises the Frenkel pair (Figure 4.21). In all three cases the residual oxygen atom remains in the coordination sphere of the yttrium interstitial with the key difference being the orientation of the vacancy site relative to the polymerised phosphate unit. In configurations (a) and (b) the vacancy is located in the same unit cell as the interstitial atom however; in configuration (a) it is in the same plane as the displacement vector of the phosphorus atom, in contrast to configuration (b) where it is in the

subsequent parallel plane. In configuration c the vacancy is located adjacent unit cell in the plane perpendicular to the displacement vector of the phosphorus atom. In all three configurations the distance between the vacancy site and interstitial atom (5.18, 5.39 and 5.22 Å respectively) is shorter than in the equivalent configuration without the polymerised phosphate unit of 5.46 Å, however the Frenkel pair defect energies are higher (7.38, 7.51 and 7.65 eV respectively) in comparison to 6.53 eV.

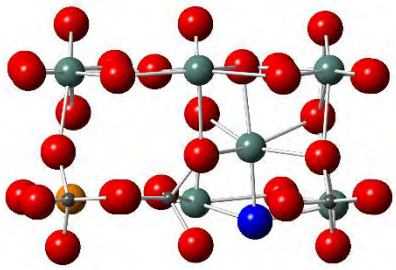

(a)

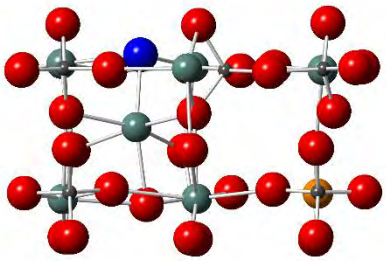

(b)

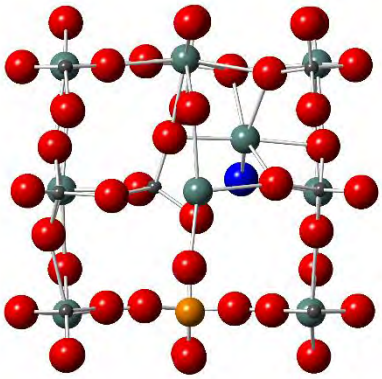

(c)

Figure 4.21: Six coordinate yttrium Frenkel pair clusters associated with the site 1 position which include a polymerised phosphate unit. The residual oxygen atom is highlighted in blue and the vacancy site is highlighted in orange.

Figure 4.22 shows the defect configuration for a site 2 yttrium interstitial with local vacancy and polymerised phosphate groups. The polymerised phosphate units cause the associated disruption of the $R(4)$ rings and introduction of the $R_2^1(6)$ ring as seen previously at infinite dilution in Figure 4.13 (a). However the inclusion of the vacancy disrupts the $R_2^2(8)$ ring seen at infinite dilution and instead generates a new $R_3^3(12)$ ring. The yttrium interstitial is shifted from the centre of the large window towards the vacancy site and polymerised phosphate units. This in turn distorts the face sharing phosphate tetrahedron which generates an $R_1^2(6)$ ring from two $R(4)$ rings. The polymerised phosphate groups stabilise the Frenkel pair defect which allows for a more localised vacancy site to the interstitial atom, 2.69 Å compared with 3.99 Å for the equivalent defect without polymerisation. This results in a lower Frenkel pair defect energy of 5.85 eV compared to 8.96 eV for the equivalent defect without polymerisation.

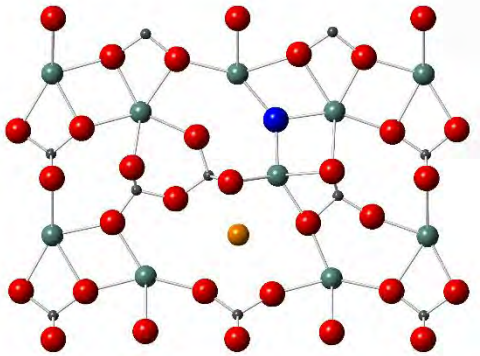

Figure 4.22: Six coordinate yttrium Frenkel pair cluster associated with the site 2 position which includes a polymerised phosphate unit. The residual oxygen atom is highlighted in blue and the vacancy site is highlighted in orange.

Two yttrium split interstitial Frenkel pair clusters have been identified which are equivalent to the defect configuration at infinite dilution in Figure 4.14 (a). The Frenkel pair defect configuration Figure 4.23 (a) is very similar with both yttrium interstitials in

a six coordinate position, separated by a distance of 3.79 Å. The second vacancy site is located in an adjacent channel to both interstitial atoms at distances of 6.02 and 6.08 Å. In contrast the configuration in Figure 4.23 (b) consists of a six coordinate yttrium interstitial at the ideal site 1 position and a four coordinate yttrium interstitial close to the corner of the channel. The interstitials are separated by a distance of 3.80 Å, however they are not centred on the vacancy site with the four coordinate interstitial closer at a distance of 1.44 Å compared to the six coordinate interstitial at 2.39 Å. The second vacancy is located in the same channel as the six coordinate yttrium interstitial atom at a closer distance of 3.47 Å compared to the four coordinate interstitial atom at 7.04 Å. The Frenkel pair defect energies for configurations (a) and (b) were calculated to be 7.32 and 6.65 eV, respectively.

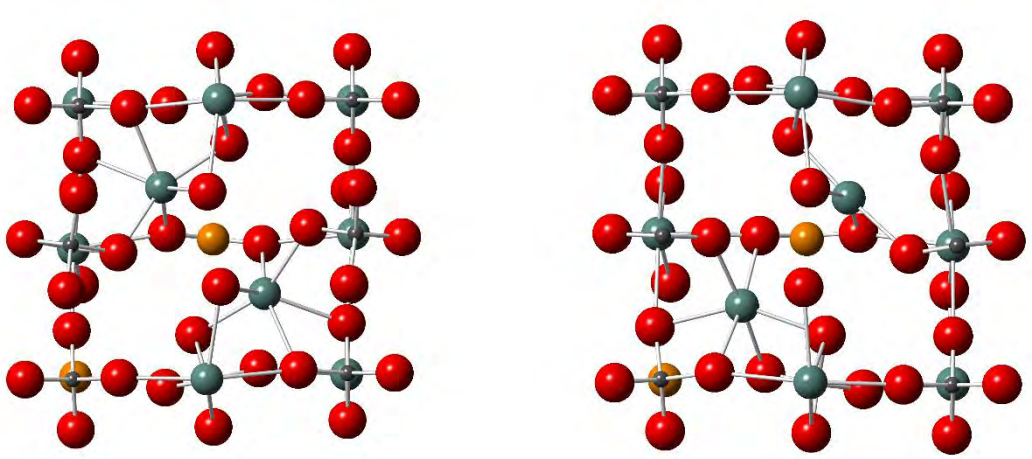

(a) (b)

Figure 4.23: Yttrium split interstitial Frenkel defects associated with the ideal site 1 position, split diagonally in the ab plane. The vacancy sites are highlighted in orange.

Three yttrium split interstitial Frenkel pair clusters have been identified which are equivalent to the defect configuration at infinite dilution in Figure 4.14 (b). These split interstitials are offset from both of the yttrium vacancy sites. The defect configurations

shown in Figure 4.24 (a) and (b) can essentially be described by a rotation of the $R_0^2(4)$ ring. In configuration a the rotation is by less than 90° and the ring becomes slightly skewed with the oxygen atoms shifting out of the *bc* plane, resulting in a decrease in the Y-Y distance from 3.79 to 3.34 Å and an elongation of the O-O distance from 2.85 to 3.03 Å. Both yttrium interstitials occupy six coordinate sites near the corner of the channel at distances of 1.93 and 3.01 Å from the vacancy sites. In configuration b the rotation is by 90° about the O-O vector. Similarly the $R_0^2(4)$ ring is distorted, resulting in a decrease in the Y-Y distance from 3.79 to 3.10 Å and an elongation of the O-O distance from 2.85 to 3.15 Å. The yttrium interstitials are located at a distance of ca. 2.45 Å from the vacancy sites. In configuration (c) the vacancies are not in the same plane and the yttrium interstitials occupy six coordinate sites near the corner of the channels at a distance of ca. 2.04 Å from the nearest vacancy site. The interstitial atoms are separated by a distance of 3.11 Å and at distances of 4.21 and 6.40 Å from the second vacancy site. The Frenkel pair defect energies for configurations (a), (b) and (c) are calculated to be 4.50, 5.35 and 7.98 eV, respectively.

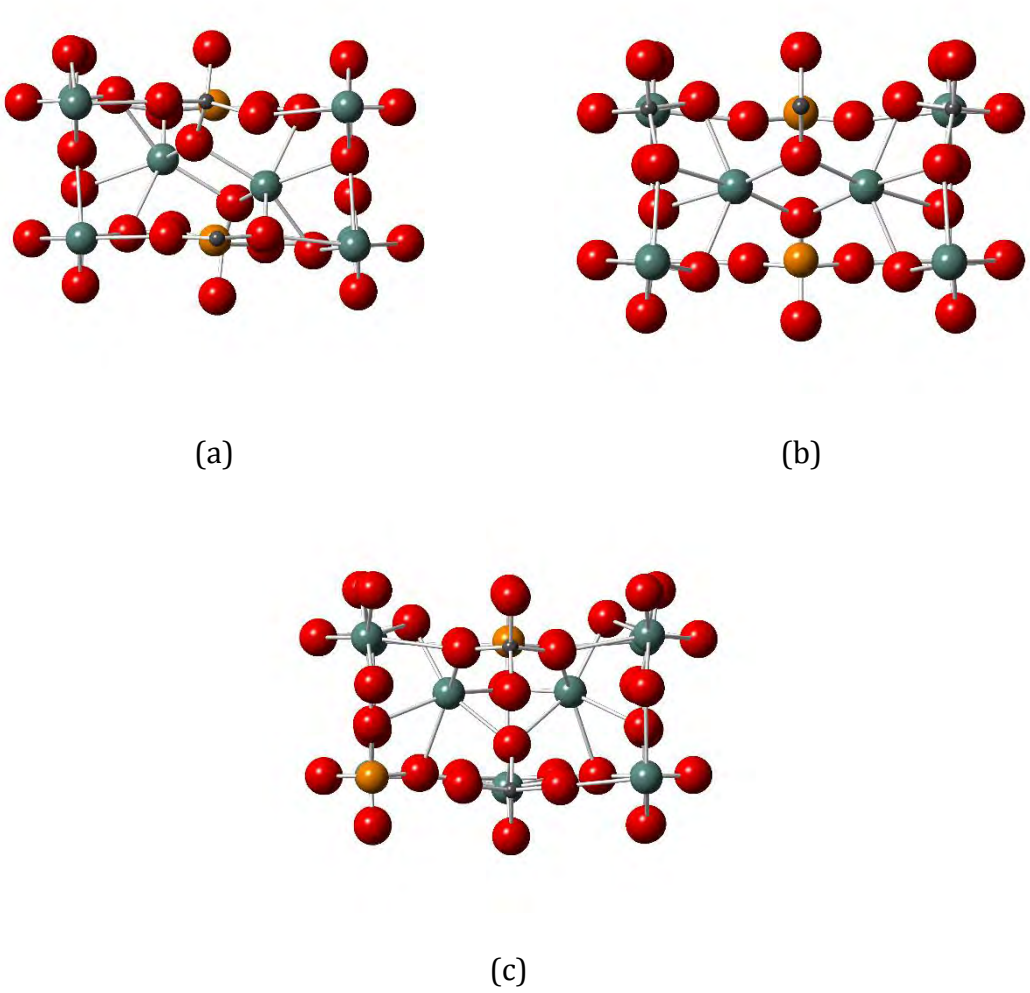

(a) (b)

(c)

Figure 4.24: Yttrium split interstitial Frenkel defects associated with the ideal site 1 position, offset from yttrium lattice site vacancy. The vacancy sites are highlighted in orange.

One Frenkel pair defect cluster has been identified consisting of a split interstitial centred on a phosphorus lattice site in which the yttrium vacancy site is located in the same channel down the *c* axis as the phosphorus interstitial, at a distance of 6.94 Å from the yttrium interstitial (Figure 4.25). The configuration is very similar to the case at infinite dilution with a notable difference in the coordination of the yttrium interstitial of six, as opposed to four. The defect energy calculated for this configuration is 6.63 eV.

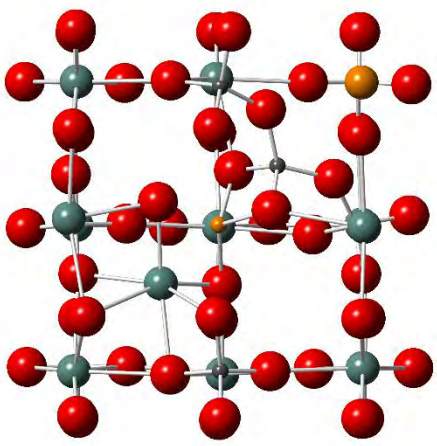

Figure 4.25: Yttrium split interstitial Frenkel defect centred on a phosphorus lattice site. Vacancy positions are highlighted in orange.

4.2.3.1.3 Formation Energies

The Frenkel defect formation energies and associated binding energies have been calculated following equation (4.5) and are summarised in Table 4.8. In the case where there are multiple equivalent configurations, the lowest energy configuration was used. There is a negative binding energy calculated for all Frenkel pair configurations which indicates that the localised vacancy and interstitial stabilises the defect. The lowest energy configuration was found to be the split interstitial offset from the vacancy sites resulting from a rotation of the $R_0^2(4)$ by less than 90°.

Table 4.8: Summary of yttrium Frenkel defect formation and binding energies.

Frenkel Defect	Formation Energy at Infinite dilution / eV	Formation Energy of cluster / eV	Binding Energy / eV
Site 1	8.82	6.53	-2.28
Site 2	12.03	8.96	-3.06
Site 3	12.18	10.10	-2.09
Site 1 with polymerised phosphate.	9.98	4.93	-5.05
Site 2 with polymerised phosphate.	11.50	5.85	-5.65
Split interstitial centred on yttrium lattice site	9.13	6.65	-2.49
Split interstitial offset from yttrium lattice site	10.92	4.50	-6.42
Split interstitial centred on phosphorus lattice site	11.23	6.63	-4.60

The defect energies calculated in this study vary greatly from the energies calculated by Gao *et al.* Here the interstitial in the site 2 position is lower in energy than the site 3 position which is in contrast to the findings of Gao *et al.* The Frenkel pair defect energy at infinite dilution was calculated by Urusov *et al.,* to be 9.53 eV which is similar to that calculated in this study for the site 1 position (Δ% = -7.7 %). The Frenkel pair formation energy at infinite dilution calculated in this study lies well within the range of values in the literature.

Table 4.9: Comparison of yttrium Frenkel defect formation energies.

Frenkel Defect	Formation Energy (Gao et al.) / eV	Formation Energy ∞ (this study) / eV	Δ / eV	Δ %	Formation Energy Cluster (this study) / eV	Δ / eV	Δ %
Site 1	7.37	8.82	1.45	17.9	6.53	-0.84	-12.1
Site 2	14.86	12.03	-2.83	-21.0	8.96	-5.9	-49.5
Site 3	10.95	12.18	1.23	10.6	10.10	-0.85	-8.1

4.2.3.2 Phosphorus Frenkel Defects

A summary of the phosphorus interstitial configurations can be found in Table 4.10 . The lowest energy phosphorus interstitial position was found to be the four coordinate site associated with the ideal site 1 position in the centre of the channel with a localised polymerised phosphate unit. A summary of the defect energies for the phosphorus Frenkel pair clusters can be found in Table 4.11. The lowest energy Frenkel pair was found to be in the site 2 position forming a P_2O_7 unit.

Table 4.10: Summary of defect energies for phosphorus interstitial positions at infinite dilution

Description	Defect Energy / eV	Associated ideal site	Polymerised phosphate?	Split interstitial?	Figure
Four coordinate, corner sharing only	-26.81	1	✓	×	Figure 4.26 (a)
Four coordinate, edge and corner sharing	-19.20	1	✓	×	Figure 4.26 (b)
Three coordinate	-22.34	1	✓	×	Figure 4.27 (a)
Five coordinate	-18.47	1	✓	×	Figure 4.27 (b)
Four coordinate, face sharing and corner sharing	3.94	2	✓	×	Figure 4.28
Four coordinate $R_1^1(4)$ ring	-24.05	n/a	✓	×	Figure 4.29
Five coordinate $R_1^1(4)$ ring	-11.41	n/a	✓	×	Figure 4.30
Four coordinate, separate P_2O_7 unit	-27.41	1	✓	×	Figure 4.31 (a)
Four coordinate, P_5O_{16} unit	-27.41	1	✓	×	Figure 4.31 (b)
Four coordinate, edge sharing P_5O_{16} unit	-18.64	1	✓	×	Figure 4.31 (c)
Five coordinate, edge sharing P_5O_{16} unit	-15.63	1	✓	×	Figure 4.32
Split interstitial in the *bc* plane	-16.63	2	✓	✓	Figure 4.33
Orthogonal split, $R_2^0(4)$ ring in middle of chain	-17.423	2	✓	✓	Figure 4.34 (a)
Orthogonal split, $R_2^0(4)$ ring at end of chain	-15.42	2	✓	✓	Figure 4.34 (b)
Orthogonal split, no $R_2^0(4)$ ring, three coordinate	-20.88	2	✓	✓	Figure 4.35
Diagonal split about yttrium vacancy	-27.11	1	✓	✓	Figure 4.36 (a)
Split in adjacent channels near yttrium vacancy	-26.00	1	✓	✓	Figure 4.36 (b)
Split in adjacent channels near yttrium vacancy	-25.05	1	✓	✓	Figure 4.36 (c)

Table 4.11: Summary of defect energies for phosphorus Frenkel pair clusters.

Description	Defect Energy / eV	Associated ideal site	Polymerised phosphate?	Split interstitial?	Figure
Four coordinate, 2 corner sharing.	6.02	1	✓	×	Figure 4.37 (a)
Four coordinate, 3 corner sharing	9.87	1	✓	×	Figure 4.37 (b)
Four coordinate, 4 corner sharing	15.77	1	✓	×	Figure 4.37 (c)
Four coordinate, 1 edge and 1 corner sharing	17.47	1	✓	×	Figure 4.37Figure 4.38 (d)
Four coordinate, 4 corner sharing, vacancy distance 7.27 Å	16.11	1	✓	×	Figure 4.38 (a)
Four coordinate, P_3O_9 chain with O interstitial	13.44	1	✓	×	Figure 4.39
Four coordinate, P_3O_{10} chain with O interstitial	8.00	1	✓	×	Figure 4.40 (a)
Four coordinate, P_3O_{10} chain with O interstitial	9.07	1	✓	×	Figure 4.40 (b)
Five coordinate, P_4O_{14} chain with O interstitial	9.90	1	✓	×	Figure 4.41
Four coordinate, P_2O_7 chain with new $R_2^2(8)$ ring	3.02	2	✓	×	Figure 4.42 (a)
Four coordinate, P_2O_7 chain with new $R_3^2(10)$ ring	4.60	2	✓	×	Figure 4.42 (b)
Four coordinate, P_2O_7 chain with new $R_2^0(4)$ ring	15.97	2	✓	×	Figure 4.43
Four coordinate, P_4O_{13} chain with separate P_2O_7 unit	15.23	1	✓	×	Figure 4.44
Four coordinate, P_3O_{11} chain with O interstitial	9.40	1	✓	×	Figure 4.45
2 P interstitials in different $R_2^2(8)$ rings, P_3O_{10} chain	7.88	2	✓	×	Figure 4.46 (a)
2 P interstitials and 1 O interstitial in same $R_2^2(8)$ ring, P_2O_7 chain	9.10	2	✓	×	Figure 4.46 (b)

Split interstitial about a Y lattice site	9.25	1	✓	✓	Figure 4.47
Orthogonal split about a P lattice site, P_4O_{12} chain, 1 $R_2^0(4)$ ring,	23.17	2	✓	✓	Figure 4.48 (a)
Orthogonal split about a P lattice site, P_4O_{12} chain, 2 $R_2^0(4)$ ring,	29.3	2	✓	✓	Figure 4.48 (b)
2 Y interstitials and 1 P interstitial	10.65	1	✓	×	Figure 4.49
Five coordinate, P_5O_{17} chain, Y anti-site.	11.21	1	✓	×	Figure 4.50 (a)
Four coordinate, P_5O_{16} chain, Y anti-site.	11.31	1	✓	×	Figure 4.50 (b)
Four coordinate, P_5O_{16} chain, Y anti-site.	11.90	1	✓	×	Figure 4.50 (c)
Four coordinate, P_5O_{16} chain, Y anti-site with O interstitial	11.37	1	✓	×	Figure 4.51
Four coordinate in $R_1^1(4)$ ring , P_5O_{16} chain, Y anti-site	13.46	N/A	✓	×	Figure 4.52

4.2.3.2.1 Infinite Dilution

Two defect configurations for a four coordinate phosphorus interstitial associated with the ideal site 1 position have been identified. In the configuration illustrated in Figure 4.26 (a), the phosphorus interstitial is corner sharing with four neighbouring phosphate tetrahedra forming a P_5O_{16} unit. The bridging oxygen atoms are located at a distance of 1.53 Å from the phosphorus interstitial, with the O-P-O angles range from 103.27 to 119.51°. There is also a slight repulsion of the neighbouring yttrium atoms at a P-Y distance of 2.75 Å. In the configuration illustrated in Figure 4.26 (b), the phosphorus interstitial is corner sharing with two neighbouring phosphate tetrahedra and edge sharing with one, forming a P_4O_{12} unit. The edge sharing oxygen atoms are located at a distance of 1.55 Å from the phosphorus interstitial, whilst the other bridging oxygen atoms are located at a distance of 1.52 Å. The O-P-O angles range from 70.43 to 128.18°, with the smallest angle between the phosphorus atom and the edge sharing oxygen atoms. The defect energies for these configurations have been calculated to be -26.81 and -19.20 eV respectively.

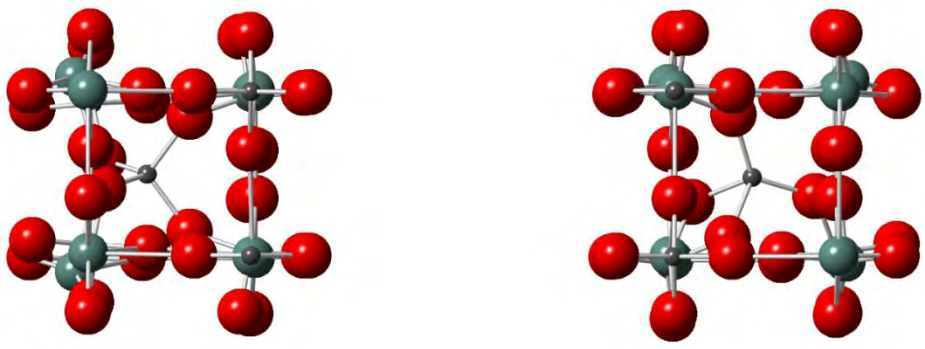

(a) (b)

Figure 4.26: P self-interstitials in the site 1 defect position

Similar configurations associated with the ideal site 1 position have also been identified with varying coordination. The defect configuration illustrated in Figure 4.27 (a) consists of a three coordinate phosphorus interstitial which is corner sharing with three neighbouring phosphate tetrahedra, forming a P_4O_{12} unit. The bridging oxygen atoms are located at a distances ranging from 1.51 to 1.52 Å with O-P-O angles ranging from 103.01 to 133.97°. The defect configuration illustrated in Figure 4.27 (b) consists of a five coordinate phosphorus interstitial which is corner sharing with three and edge sharing with one neighbouring phosphate tetrahedra, forming a P_5O_{16} unit. The P-O distances range from 1.54 to 1.61 Å with the longest distances relating to the edge sharing oxygen atoms. The O-P-O angles range from 66.29 to 126.40°, with the smallest angle between the phosphorus interstitial and the two edge sharing oxygen atoms. The defect energies for these defect configurations are calculated to be -22.34 and -18.47 eV, respectively.

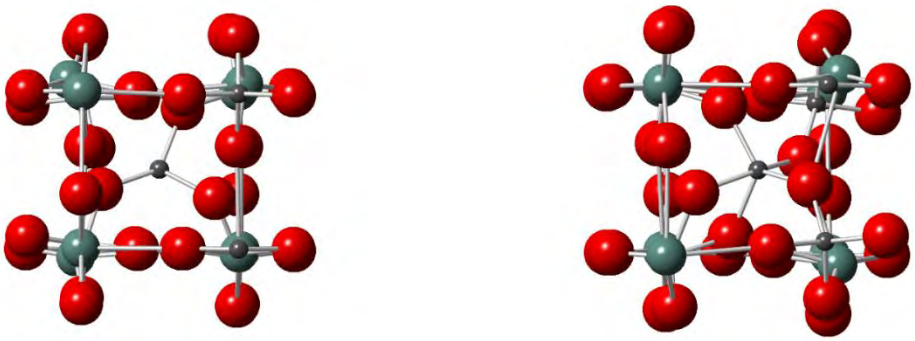

(a) (b)

Figure 4.27: P self-interstitials in the site 1 defect position (a) three coordinate and (b) five coordinate

One defect configuration has been identified at the ideal site 2 position, illustrated in Figure 4.28. This interstitial atom is four coordinate, face sharing with one and corner

sharing with another neighbouring phosphate tetrahedron, forming a P_3O_8 unit. This interstitial disrupts the $R_2^2(8)$ ring, generating new $R_3^2(10)$, $R_2^2(8)$ and $R_2^0(4)$ rings. The P-O distances for the interstitial atom range from 1.49 to 1.56 Å with the larger separations between the interstitial atom and the face sharing oxygen atoms. The O-P-O angles range from 72.06 to 140.54° with the smallest angles between the interstitial atom and the face sharing oxygen atoms. The defect energy for this configuration is calculated to be 3.94 eV.

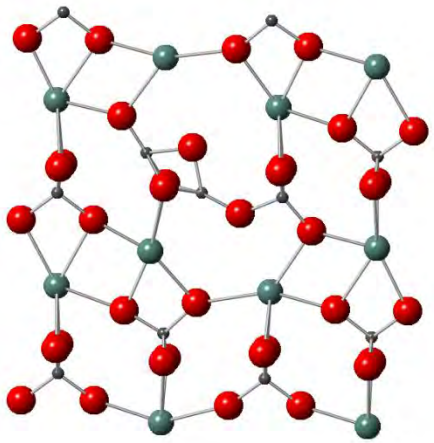

Figure 4.28: P self-interstitials in the site 2 defect position

No phosphorus self-interstitials were found to geometry optimise in the ideal site 3 position. However an interstitial was identified within the small $R_1^1(4)$ ring, illustrated in Figure 4.29 (a). A yttrium lattice atom is repelled by the interstitial atom, shifting it within the plane where it adopts a six coordinate octahedral geometry. The schematic illustrated in Figure 4.29 (b) and (c) highlight the oxygen atoms which adopt the axial and equatorial positions in blue and green respectively. The phosphorus interstitial adopts a tetrahedral geometry coordinating to two of the aforementioned equatorial oxygen atoms and two oxygen atoms from the adjacent phosphate tetrahedron. The adjacent lattice phosphorus atom is shifted out of the plane and becomes polymerised with a phosphate tetrahedron

from the subsequent plane, forming a P_5O_{16} unit. The defect energy for this configuration is calculated to be -24.05 eV.

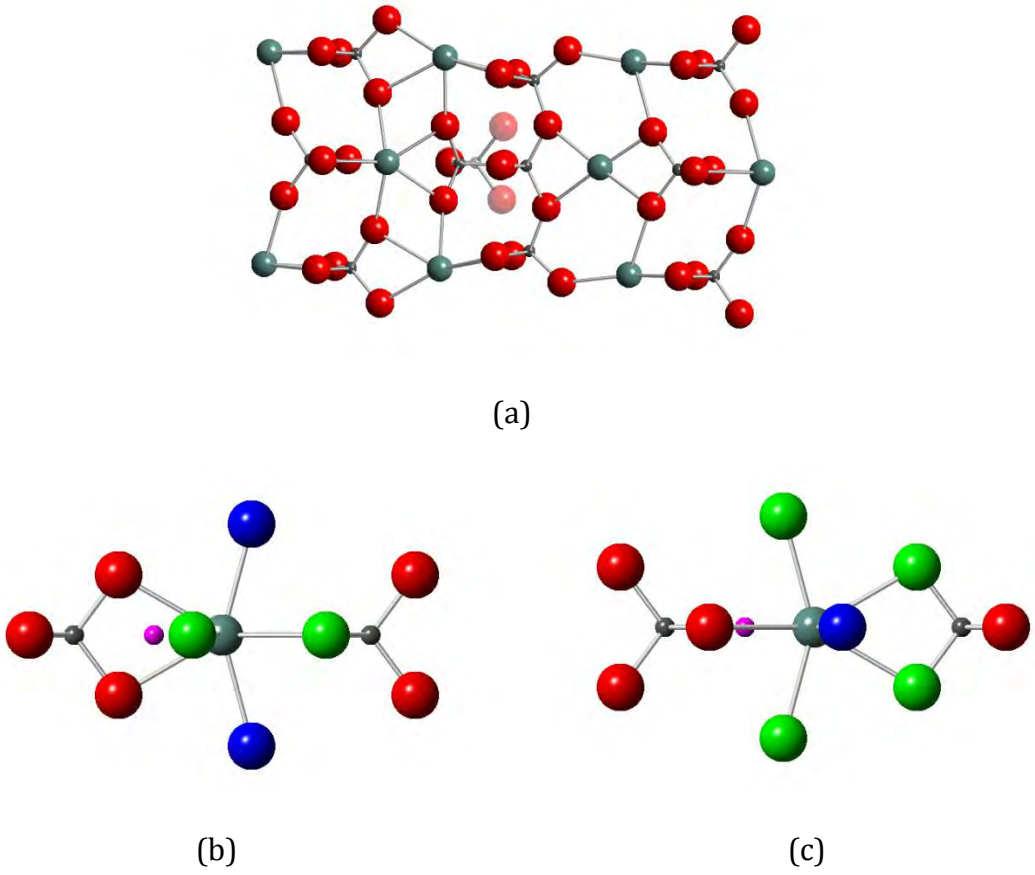

(a)

(b) (c)

Figure 4.29: P self-interstitials in the $R_1^1(4)$ ring, (b) and (c) show the six coordinate yttrium atom before relaxation. The phosphorus interstitial, pseudo-equatorial oxygen atoms and pseudo-axial oxygen atoms are highlighted in purple, green and blue respectively

A similar defect configuration was identified where the interstitial atom is located in a five coordinate position within the small $R_1^1(4)$ ring, illustrated in Figure 4.30. Here the interstitial is edge sharing with one and corner sharing with three neighbouring phosphate tetrahedra, forming a P_5O_{16} unit. The defect energy calculated for this configuration is -11.41 eV.

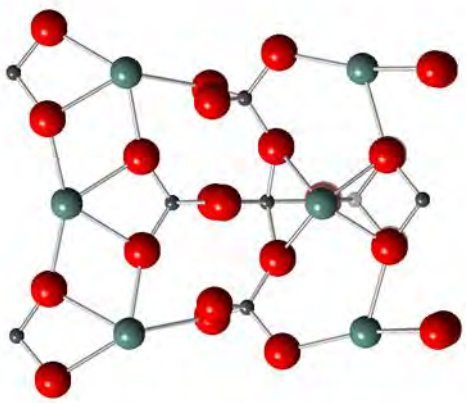

Figure 4.30: P self-interstitials in the $R_1^1(4)$ ring, five coordinate

The most energetically favourable phosphorus self-interstitial was found to be associated with the ideal site 1 position, located near the edge of the channel running parallel to the *c* axis as illustrated in Figure 4.31 (a). The phosphorus interstitial is corner sharing with three phosphate tetrahedra forming a branched P_4O_{13} unit. A local phosphorus lattice atom is shifted in the *ac* plane where it becomes polymerised with a neighbouring phosphate tetrahedron, forming a P_2O_7 unit. The residual oxygen atom from the shifted phosphorus atom remains coordinated to the phosphorus interstitial and is highlighted in blue. The defect energy for this configuration is calculated to be -27.41 eV. This configuration is closely related to the defect configuration illustrated in Figure 4.31 (b). Here the phosphorus interstitial adopts a tetrahedral geometry near to the corner of the channel running parallel to the *c* axis. There is also a shift of a phosphorus lattice atom in the *bc* plane which becomes polymerised to a neighbouring phosphate tetrahedron. In contrast to the defect configuration discussed previously, the shifted phosphorus atom remains polymerised to the interstitial. This produces a branched P_5O_{16} unit with the residual oxygen atom coordinating to the interstitial atom. The defect energy for this

configuration is calculated to be -27.41 eV. A third closely related configuration has been identified, illustrated in Figure 4.31 (c), where the phosphorus interstitial is in a four coordinate site related to the ideal site 1 position. This configuration is very similar to that shown in Figure 4.31 (b), however in this case the residual oxygen atom remains coordinated to both the interstitial atom and the shifted phosphorus atom. This causes the phosphorus interstitial atom to be edge sharing with a five coordinate phosphorus lattice atom, producing a P_5O_{16} unit. The defect energy for this configuration is calculated to be -18.64 eV.

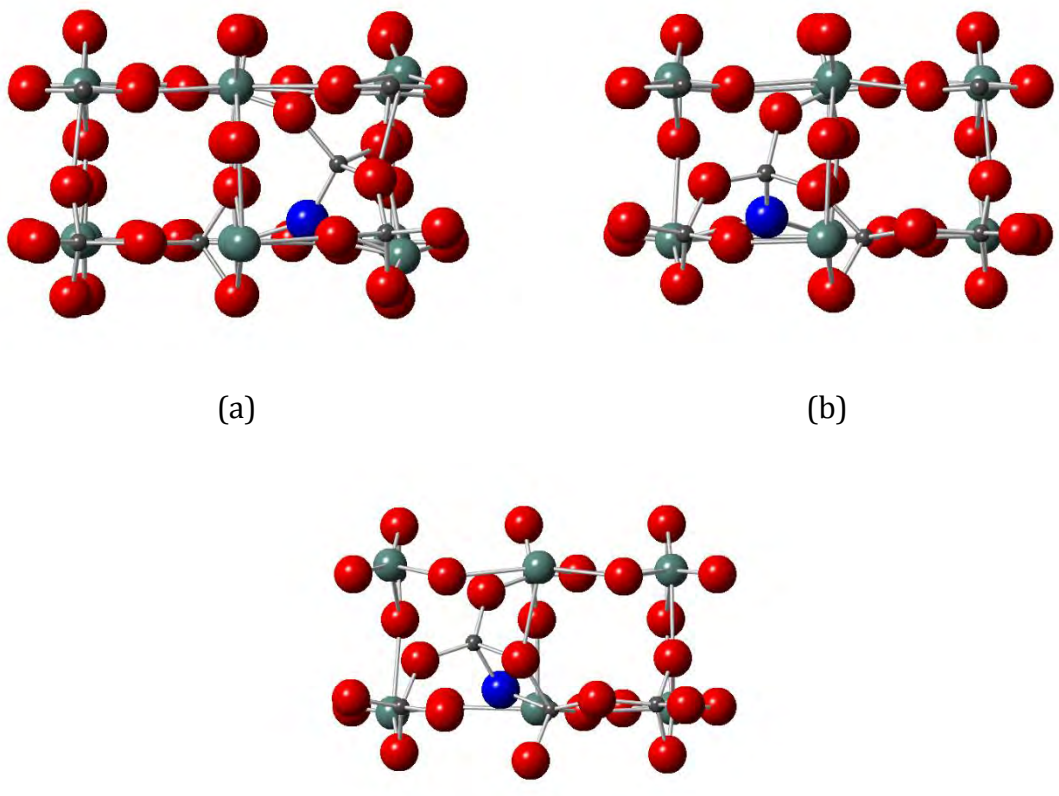

(a) (b)

(c)

Figure 4.31: P self-interstitials associated with the ideal site 1 position which include a polymerised phosphate unit. The residual oxygen atom is highlighted in blue.

A five coordinate phosphorus interstitial was also identified, illustrated in Figure 4.32, following a similar distortion to the lattice as discussed previously. Here the interstitial atom is five coordinate, edge sharing with one and corner sharing with two neighbouring phosphate tetrahedra. The residual oxygen from the shifted neighbouring phosphorus atom remains coordinated to the interstitial and shifts into the channel. This allows another lattice oxygen atom to displace towards the interstitial. This form a P_5O_{16} polymerised unit. The defect energy for this configuration is calculated to be -15.63 eV.

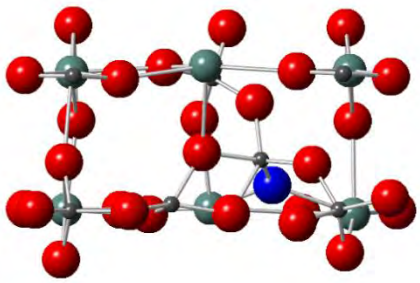

Figure 4.32: Five coordinate P self-interstitial associated with the ideal site 1 position, including a polymerised phosphate unit. The residual oxygen atom is highlighted in blue.

Some split interstitial defect configurations were also identified centred around a phosphorus lattice site. The configuration illustrated in Figure 4.33 shows a split interstitial within the *bc* plane. The vacancy site is highlighted in orange, about which the phosphorus atoms are split into the adjacent $R_2^2(8)$ rings. This disrupts four neighbouring $R_0^2(4)$ rings and the two aforementioned $R_2^2(8)$ rings. This creates two new $R_2^2(8)$ rings and an $R_2^3(10)$ ring. The interstitial atoms are edge sharing with each other and corner sharing with neighbouring phosphate groups, causing them to rotate slightly and forming a P_4O_{12} unit. The rotation of the phosphate groups remove two oxygen atoms from the coordination sphere of two adjacent yttrium atoms, reducing their coordination to six. The defect energy for this configuration is calculated to be -16.63 eV.

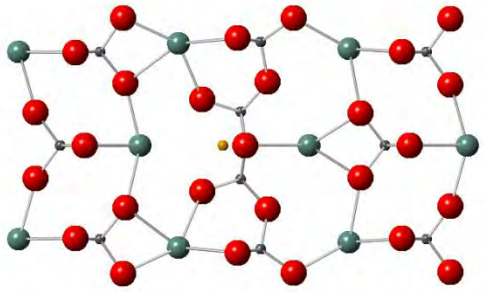

Figure 4.33: P split interstitial in the bc plane, vacancy site is highlighted in orange

The defect configuration illustrated in Figure 4.34 (a) is another split interstitial, however in this configuration the interstitials are split orthogonally from the lattice site. The interstitial atoms are edge sharing with each other and corner sharing with a neighbouring phosphate group, forming a P_4O_{12} unit with the $R_2^0(4)$ ring in the middle of the chain. The defect configuration in Figure 4.34 (b) is very similar to the aforementioned defect configuration with the interstitials split orthogonally from the lattice site. In contrast to the previous configuration only one of the interstitials is edge sharing with a neighbouring phosphate tetrahedron, forming a P_4O_{12} unit with the $R_2^0(4)$ ring at the end of the chain. The defect energies for these defect configurations were calculated to be -17.43 and -15.42 eV. respectively.

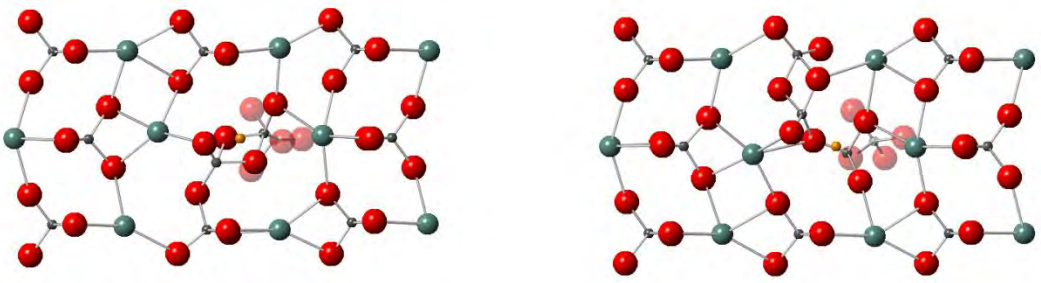

Figure 4.34: P split interstitial in orthogonal planes, vacancy site is highlighted in orange

A related split interstitial was also identified, illustrated in Figure 4.35, which is closely related to the defect illustrated in Figure 4.34 (a). In this case one of the interstitial atoms is only three coordinate whilst the other is four coordinate. This forms a P_4O_{12} unit with no $R_2^0(4)$ ring. The defect energy for this configuration is calculated to be -20.88 eV.

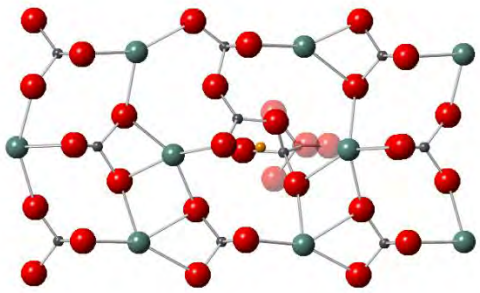

Figure 4.35: P split interstitial in orthogonal planes with no $R_2^0(4)$ ring, vacancy site is highlighted in orange

The following defect configurations are split about a yttrium lattice site. The configuration illustrated in Figure 4.36 (a) shows a diagonal split interstitial. Here the phosphorus atom adopts a four coordinate position near the edge of the channel running parallel to the *c* axis at a distance of 2.18 Å from the vacancy site. The yttrium interstitial adopts a six coordinate site at a distance of 1.95 Å from the vacancy site.. The phosphorus interstitial is corner sharing with four neighbouring phosphate tetrahedra, forming a P_5O_{16} unit. The defect energy for this configuration is calculated to be -27.11 eV. The defect configurations illustrated in Figure 4.36 (b) and (c) are also split interstitials however the interstitial are located in adjacent channels. The phosphorus interstitial is corner sharing with four neighbouring phosphate tetrahedra in both configurations, forming P_5O_{16} units. In the defect configuration shown in Figure 4.36 (b), the phosphorus interstitial is located at a distance of 2.29 Å from the vacancy whilst the yttrium interstitial is located at a distance

of 2.00 Å. In the defect configuration shown in Figure 4.36 (c), the phosphorus interstitial is located at a distance of 2.17 Å from the vacancy whilst the yttrium interstitial is located at a distance of 2.22 Å. The P-O distances between the interstitial and the bridging oxygen atoms range from 1.53 to 1.54 Å whilst the Y-O distances between the interstitial and the coordinating oxygen atoms range from 2.16 to 2.43 Å. The defect energies for these configurations are calculated to be -26.00 and -25.05 eV, respectively.

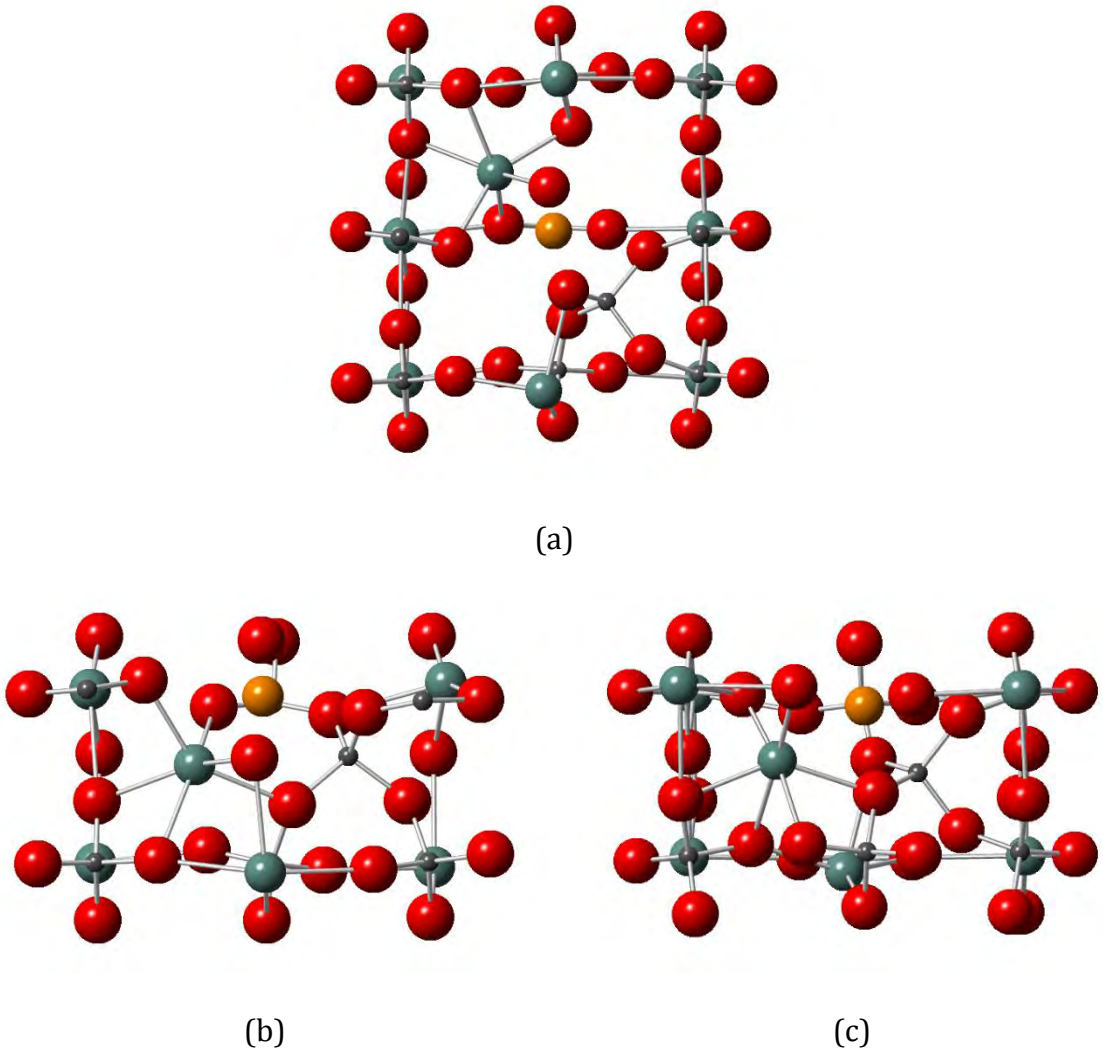

Figure 4.36: P split interstitial around a yttrium lattice site, vacancy site is highlighted in orange

4.2.3.2.2 Cluster Calculations

Four Frenkel defect cluster have been identified which are associated with the site 1 ideal position, with both the interstitial and vacancy within the same channel. The main differences between these configurations are the orientation of the interstitial tetrahedron with respect to the vacancy site and the distance between the interstitial and vacancy positions. In the defect configuration illustrated in Figure 4.37 (a), two of the oxygen atoms coordinating to the phosphorus interstitial are the nearest neighbours to the phosphorus vacancy site. The other two are bridging oxygen atoms with neighbouring phosphate tetrahedra, forming a P_3O_{10} unit. The interstitial atom is located at a distance of 2.00 Å from the vacancy site, with a defect energy of 6.021 eV. The defect configuration illustrated in Figure 4.37 (b) consists of a phosphorus interstitial which is coordinated to three bridging oxygen atoms and one non-bridging oxygen atom, which is one of the nearest neighbours to the vacancy site. This forms a branched P_4O_{13} unit. The interstitial atom is located at a distance of 3.30 Å from the vacancy site with a defect energy of 9.87 eV. The defect configuration illustrated in Figure 4.37 (c) consists of a phosphorus interstitial coordinated to four bridging oxygen atoms, forming a P_5O_{16} unit. The phosphorus interstitial is located at a distance of 5.93 Å from the vacancy site, with a defect energy of 15.77 eV. Figure 4.37 (d) illustrates a defect configuration with a phosphorus interstitial which is coordinated to one non-bridging and three bridging oxygen atoms. The interstitial tetrahedron is edge sharing with one and corner sharing with a second neighbouring phosphate group, forming a P_3O_9 unit with an $R_2^0(4)$ ring. Once again the non-bridging oxygen atom is one of the nearest neighbours to the vacancy site. The phosphorus interstitial is located at a distance of 2.92 Å from the vacancy site, with a defect energy of 17.47 eV.

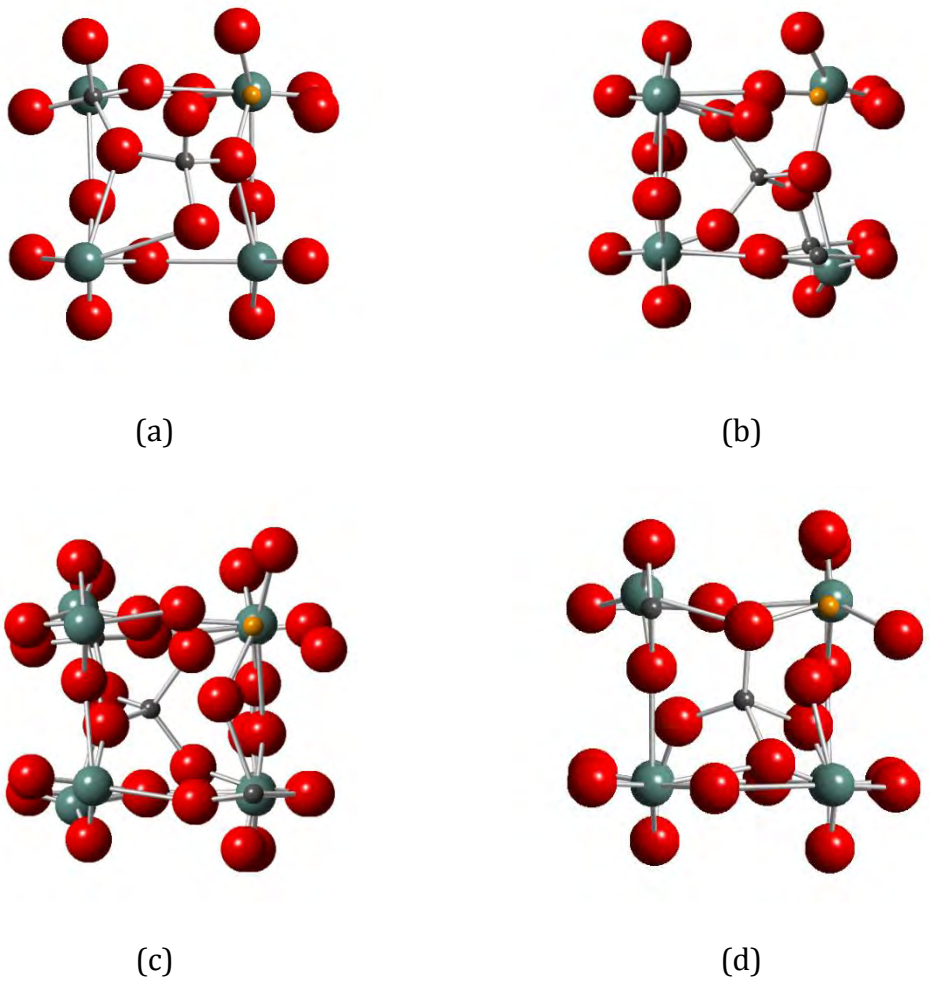

Figure 4.37: Phosphorus Frenkel pair clusters associated with the ideal site 1 position. The vacancy site is highlighted in orange.

Similarly a cluster defect configuration associated with the site 1 position has been identified with the vacancy and interstitial atom in the adjacent channel. In the defect configuration illustrated in Figure 4.38, the phosphorus interstitial is corner sharing with four adjacent phosphate tetrahedra, forming a P_5O_{16} unit. The interstitial atom is located at a distance of 7.27 Å from the vacancy site, with a defect energy of 16.11 eV

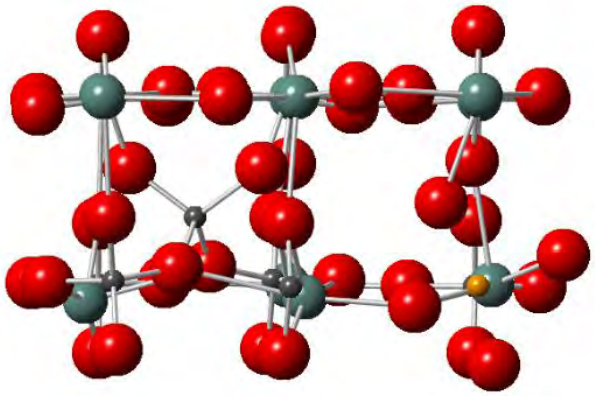

Figure 4.38: Phosphorus Frenkel pair cluster associated with the ideal site 1 position with vacancy site in the adjacent channel. The vacancy site is highlighted in orange.

One defect configuration has been identified consisting of a four coordinate phosphorus interstitial at the site 1 position with an oxygen interstitial in the adjacent channel, illustrated in Figure 4.39. Here the phosphorus interstitial is corner sharing with one neighbouring phosphate tetrahedron and a three coordinate phosphorus lattice atom, forming a P_3O_9 unit. The phosphorus interstitial is located at a distance of 3.02 Å from the phosphorus vacancy and 3.48 Å from the oxygen vacancy sites. The oxygen interstitial is again at the site 1 position at a distance of 1.27 Å from the oxygen vacancy site and 2.28 Å from the phosphorus vacancy. The defect energy calculated for this configuration was 13.44 eV.

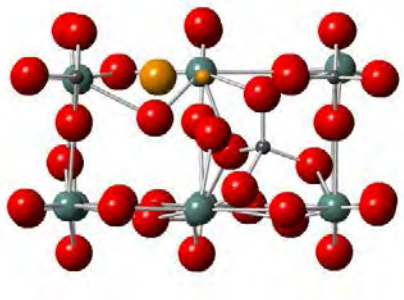

Figure 4.39: Phosphorus Frenkel pair clusters associated with the ideal site 1 position with an oxygen Frenkel pair in the adjacent channel. The vacancy sites are highlighted in orange.

Two defect clusters have been identified with the phosphorus interstitial in the site 1 position with an adjacent oxygen interstitial. In the defect configuration illustrated in Figure 4.40 (a) the phosphorus interstitial is corner sharing with two adjacent phosphate tetrahedra, forming a P_3O_{10} unit. The oxygen vacancy reduces the coordination of the associated yttrium lattice atom from eight to seven whilst the interstitial increases the coordination of the adjacent yttrium atom from eight to nine. A similar configuration has been identified, illustrated in Figure 4.40 (b). Here the phosphorus interstitial is corner sharing with two neighbouring phosphate tetrahedra, forming a P_3O_{10} unit. The oxygen vacancy reduces the coordination of three surrounding yttrium lattice atoms from eight to seven. The defect energies for these configuration are calculated to be 7.98 and 9.07 eV respectively.

(a) (b)

Figure 4.40: Phosphorus Frenkel pair clusters associated with the ideal site 1 position with an oxygen Frenkel pair. The vacancy sites are highlighted in orange.

A five coordinate phosphorus interstitial at the site 1 position has also been identified with a local oxygen interstitial, illustrated in Figure 4.41. The phosphorus interstitial is corner sharing with three neighbouring phosphate tetrahedra, forming a P_4O_{14} unit. The defect energy for this defect cluster is calculated to be 9.90 eV.

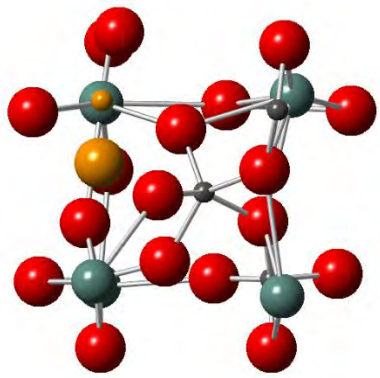

Figure 4.41: Five coordinate phosphorus Frenkel pair clusters associated with the ideal site 1 position with an oxygen Frenkel pair. The vacancy sites are highlighted in orange.

Two Frenkel pair clusters have been identified with a phosphorus interstitial in the site 2 position. In both cases the phosphorus interstitial is corner sharing with the neighbouring phosphate tetrahedron from the same $R_2^2(8)$ ring, forming a P_2O_7 unit. In the defect configuration illustrated in Figure 4.42 (a) the phosphorus interstitial is located at a distance of 1.09 Å from the vacancy site. A second similar defect configuration is illustrated in Figure 4.42 (b). The phosphorus interstitial is located at a distance of 1.10 Å from the vacancy site. These defect configurations were found to be the most stable, with defect energies of 3.02 and 4.60 eV respectively.

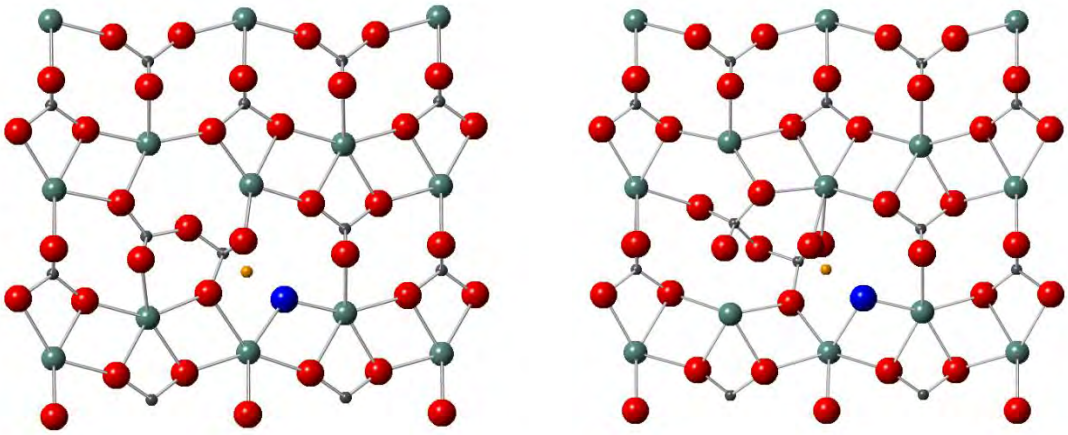

(a) (b)

Figure 4.42: phosphorus Frenkel pair clusters with phosphorus interstitials in the site 2 position. Residual oxygen atoms are highlighted in blue

A similar defect configuration is illustrated in Figure 4.43. Here the phosphorus interstitial is edge sharing with a neighbouring phosphate tetrahedron from the same $R_2^2(8)$ ring, forming a P_2O_7 ring containing an $R_2^0(4)$ ring. The P-O distance between the phosphorus interstitial and the bridging oxygen atoms are 1.62 Å, whilst the distances to the non-bridging oxygen atoms range from 1.52-1.55 Å. The phosphorus interstitial is located at a distance of 1.22 Å from the vacancy site. The polymerisation of the phosphate units disrupts the associated $R_2^2(8)$ rings to form new $R_2^1(6)$, $R_3^2(10)$ and $R_2^3(10)$ rings. Similarly the interstitial atom causes a rotation of the polymerising phosphate tetrahedron, expanding the neighbouring $R_0^2(4)$ and $R_1^1(4)$ rings into an $R_1^2(6)$ ring. The defect energy for this configuration is calculated to be 15.97 eV.

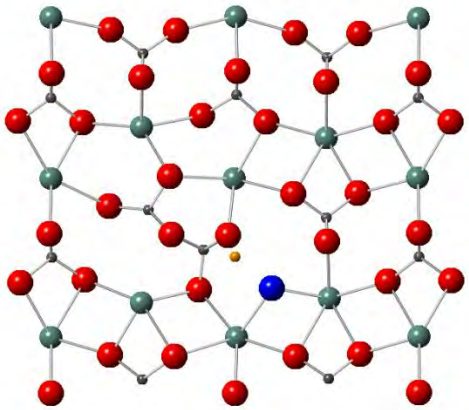

Figure 4.43: phosphorus Frenkel pair cluster with phosphorus interstitial in the site 2 position, edge sharing. Residual oxygen atom is highlighted in blue

One defect configuration has been identified with a phosphorus interstitial in a site 1 position with a separate neighbouring P_2O_7 unit, illustrated in Figure 4.44. The phosphorus interstitial is corner sharing with three neighbouring phosphate tetrahedra, forming a P_4O_{13} unit. A neighbouring phosphorus lattice atom is shifted away from the phosphorus interstitial, forming a P_2O_7 unit. The residual oxygen atom remains coordinated to the phosphorus interstitial. The phosphorus interstitial is located at a distance of 7.98 Å from the vacancy site and 4.34 Å from the neighbouring shifted phosphorus lattice atom. The defect energy for this defect configuration is calculated to be 15.23 eV.

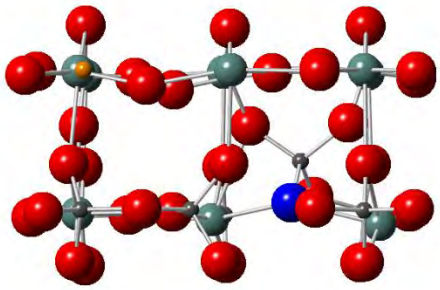

Figure 4.44: Phosphorus Frenkel pair cluster associated with the site 1 position with a polymerised phosphate unit in the adjacent channel. The residual oxygen atom is highlighted in blue and the vacancy site is highlighted in orange.

A similar defect configuration has been identified with a four coordinate phosphorus interstitial in the site 1 position, Figure 4.45. This interstitial is corner sharing with a neighbouring phosphate group which itself becomes shifted and polymerises with a subsequent phosphate tetrahedron. Additionally an oxygen interstitial is coordinated to the shifted phosphorus lattice atom, increasing its coordination to five. This results in the formation of a P_3O_{11} unit. The P-O distances between the phosphorus interstitial and the coordinating oxygen atoms range from 1.51-1.52 Å, whilst the P-O distances between the five coordinate phosphorus atom and the coordinating oxygen atoms range from 1.53-1.58 Å. The phosphorus interstitial is located at a distance of 2.00 Å from the phosphorus vacancy site and 2.69 Å from the oxygen vacancy site. The oxygen interstitial is located at a distance of 3.13 Å from the phosphorus vacancy site and 2.03 Å from the oxygen vacancy site. The defect energy for this configuration is calculated to be 9.40 eV.

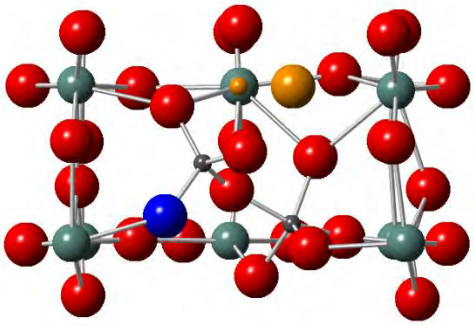

Figure 4.45: Phosphorus Frenkel pair cluster associated with the site 1 position with an oxygen Frenkel pair in the adjacent channel. The residual oxygen atom is highlighted in blue and the vacancy sites are highlighted in orange.

Two defect configurations have been identified with phosphorus interstitials in the site 2 position with vacancies on both phosphorus sites within the same $R_2^2(8)$ ring. The defect configuration illustrated in Figure 4.46 (a) consists of three corner sharing phosphate tetrahedra, forming a P_3O_{10} unit. The phosphorus interstitial is located at a distance of 1.95 and 2.02 Å from the phosphorus vacancies, with the P-O distances between the phosphorus interstitial and the coordinating oxygen atoms ranging from 1.52-1.54 Å. A similar defect configuration is illustrated in Figure 4.46 (b). Here both phosphorus atoms shift into the $R_2^2(8)$ ring and become polymerised through a bridging oxygen interstitial, forming a P_2O_7 unit. The P-O distances from the interstitials to the bridging oxygen atom are 1.50 Å whilst the distances to the non-bridging oxygen atoms range from 1.51-1.52 Å. The distances between the phosphorus interstitials and the nearest respective phosphorus vacancy sites are 1.81 and 1.83 Å, whilst the distances to the alternative phosphorus vacancy sites are 2.74 and 2.84 Å. The oxygen interstitial is located at a distance of 3.60 Å from the oxygen vacancy site. This results in the formation of new $R_1^1(4)$ and $R_3^3(12)$ rings. The defect energies calculated for these configurations are 7.88 and 9.10 eV, respectively.

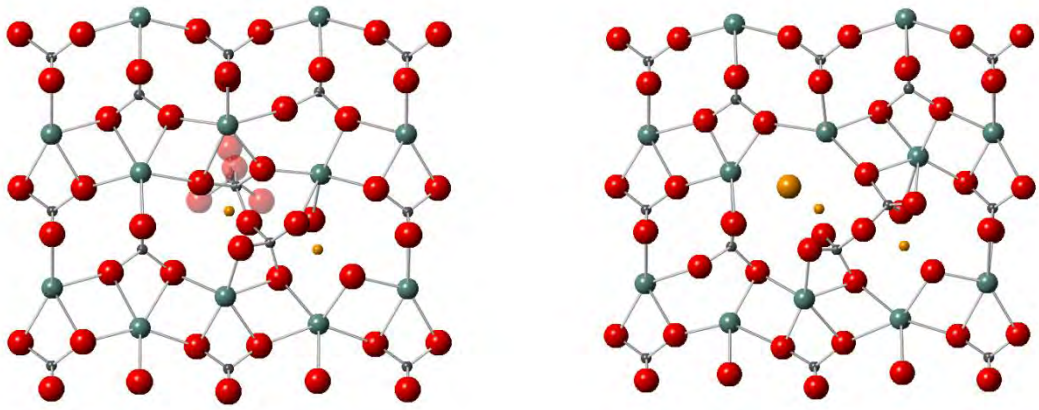

(a) (b)

Figure 4.46: Two neighbouring phosphorus Frenkel pairs associated with the site 2 position. Vacancy sites are highlighted in orange

A split interstitial centred on a yttrium lattice site has been identified, illustrated in Figure 4.47. Here the yttrium lattice atom is displaced into a six coordinate site 1 position whilst the phosphorus interstitial adopts a four coordinate site in the corner of the channel. The yttrium vacancy site is adjacent to the phosphorus vacancy site at a distance of 3.02 Å down the *c* axis. The phosphorus interstitial is corner sharing with two neighbouring phosphate tetrahedra, forming a P_3O_{10} unit. The P-O distances from the interstitial atom to the bridging oxygen atoms are 1.54 and 1.56 Å, whilst the distances to the non-bridging oxygen atoms are 1.51 and 1.52 Å. The distances from the yttrium and phosphorus interstitials to the yttrium vacancy are 2.08 and 1.32 Å respectively, whilst the distances to the phosphorus vacancy are 3.98 and 2.62 respectively. The defect energy for this defect configuration is calculated to be 9.25 eV.

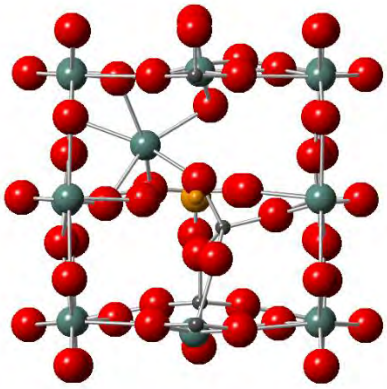

Figure 4.47: Phosphorus split interstitial centred on a yttrium lattice site. Vacancy sites are highlighted in orange

Similarly two defect configurations have been identified with a split interstitial about a phosphorus lattice site, where the phosphorus interstitial lies in orthogonal plane to the yttrium interstitial. In the defect configuration illustrated in Figure 4.48 (a), the phosphorus interstitial are edge sharing with each other and corner sharing with adjacent phosphate tetrahedra, forming a P_4O_{12} unit, consisting of one $R_2^0(4)$ ring. The phosphorus interstitials are located at distances of 1.36 and 1.43 Å from the central vacancy site. The alternative vacancy site is located on the subsequent plane at distances of 4.91 and 5.86 Å from phosphorus interstitials. A similar defect configuration is illustrated in Figure 4.48 (b). Here one phosphorus interstitial is four coordinate whilst the other is five coordinate. Both interstitials are edge sharing with each other, however the four coordinate phosphorus interstitial is corner sharing with a neighbouring phosphate tetrahedron whilst the five coordinate phosphorus interstitial is edge sharing. This forms a P_4O_{12} unit consisting of two $R_2^0(4)$ rings. The phosphorus interstitials are located at distances of 1.27 and 1.67 Å from the central vacancy site and distances of 4.89 and 5.72 Å from the other phosphorus vacancy, which is located on the subsequent plane. The defect energies calculated for these defect configurations are 23.17 and 29.27 eV, respectively.

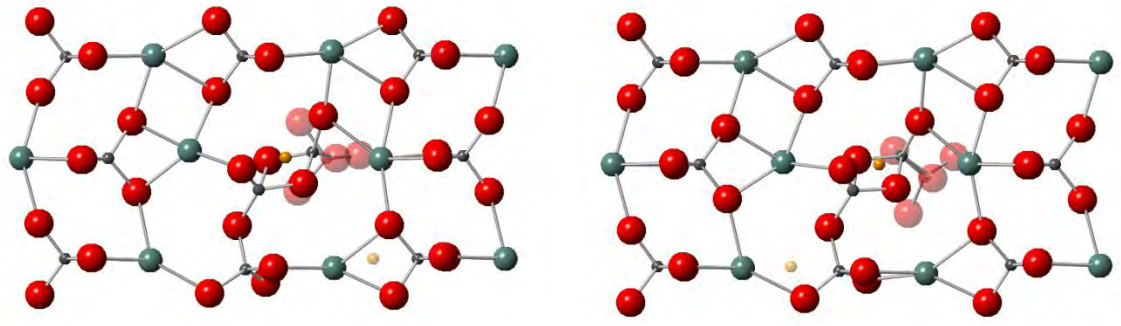

(a) (b)

Figure 4.48: Phosphorus split interstitial centred on a phosphorus lattice site with interstitials in orthogonal planes. Vacancy sites are highlighted in orange

An unusual defect cluster was identified consisting of two six coordinate yttrium interstitials located in adjacent channels and a local phosphorus interstitial, Figure 4.49. The phosphorus interstitial is corner sharing with four neighbouring phosphate tetrahedra, forming a P_5O_{16} unit. The yttrium vacancy sites are adjacent to the phosphorus interstitial, at distances of 2.28 and 3.31 Å, whilst the phosphorus vacancy site is located at a distance of 5.14 Å. The P-Y distance from the phosphorus interstitial to the yttrium interstitial in the adjacent channel (Y1) is 3.41 Å and 4.54 Å to the second yttrium interstitial (Y2). The yttrium vacancy sites are closest to the Y1 interstitial, at distances of 2.51 and 3.34 Å, in contrast to the Y2 interstitial at distances of 2.53 and 5.30 Å. Both yttrium interstitials are localised to the phosphorus vacancy, at distances of 2.56 and 2.12 Å for Y1 and Y2 respectively. The defect energy calculated for this defect configuration is 10.65 eV.

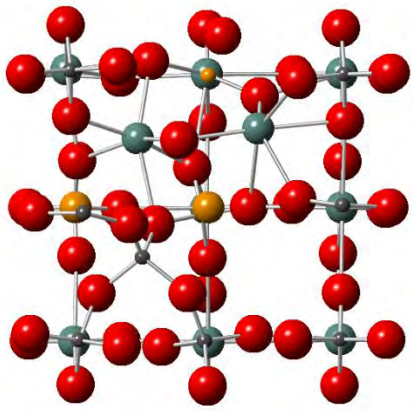

Figure 4.49: Phosphorus Frenkel pair cluster with two local yttrium Frenkel pairs. Vacancy sites are highlighted in orange

A series of defect clusters have been identified consisting of a phosphorus interstitial and a five coordinate yttrium anti-site on the phosphorus vacancy position. The defect configuration illustrated in Figure 4.50 (a) has the smallest separation between the phosphorus interstitial and the associated vacancy site of the three defect clusters. Here the phosphorus interstitial adopts a five coordinate geometry in the site 1 position, corner sharing with four neighbouring phosphate tetrahedra and forming a P_5O_{17} unit. In the remaining two defect clusters the phosphorus interstitial is in a four coordinate position, corner sharing with four neighbouring phosphate tetrahedra, forming a P_5O_{16} unit. In the defect configuration illustrated in Figure 4.50 (b), the phosphorus interstitial is located at distances of 5.63 and 2.09 Å from the phosphorus and yttrium vacancy sites respectively. The yttrium anti-site defect lies at slightly greater distances from the yttrium vacancy and phosphorus lattice site than in the previous configuration, at distances of 3.00 and 1.05 Å respectively. Finally in the third defect configuration illustrated in Figure 4.50 (c), the phosphorus interstitial is located at distances of 5.65 and 2.12 Å from the phosphorus and yttrium vacancy sites respectively. The yttrium anti-site defect lies at distances of 0.79 and 4.19 Å from the phosphorus lattice site and yttrium vacancy site respectively. The

defect energies calculated for these defect configurations are 11.21, 11.31 and 11.80 eV, respectively.

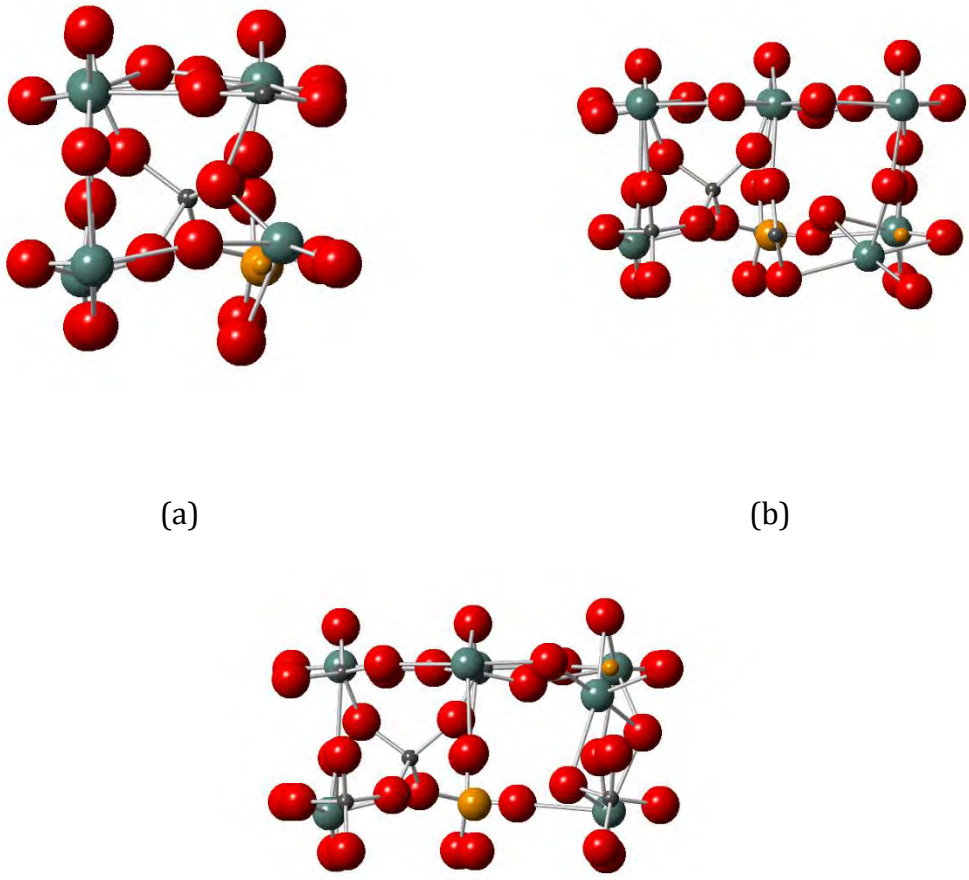

(a) (b)

(c)

Figure 4.50: Phosphorus Frenkel pair cluster with local yttrium anti-site. Vacancy sites are highlighted in orange

A similar configuration to that in Figure 4.50 (a) is illustrated in Figure 4.51. Here the phosphorus interstitial is in a four coordinate position, corner sharing with four neighbouring phosphate tetrahedra, forming a P_5O_{16} unit. The yttrium vacancy and phosphorus lattice site on which the yttrium anti-site is found are localised to phosphorus interstitial, at distances of 2.17 and 4.22 Å respectively. Similarly the yttrium anti-site is located at distances of 2.48 and 0.80 Å respectively. Additionally there is an oxygen

interstitial in the adjacent channel at a distance of 1.23 Å from the oxygen vacancy site. The defect energy for this configuration is calculated to be 11.37 eV.

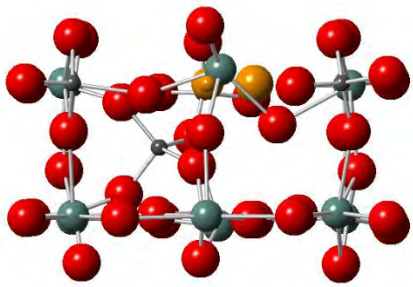

Figure 4.51: Phosphorus Frenkel pair cluster with an oxygen Frenkel pair in the adjacent channel. Vacancy sites are highlighted in orange

A final defect cluster involving a phosphorus interstitial and a yttrium anti-site has been identified, illustrated in Figure 4.52. Here the phosphorus interstitial lies within the small $R_1^1(4)$ ring, coordinating to three neighbouring phosphate tetrahedra. The interstitial also displaces one of the phosphorus lattice atoms, causing it to move out of the plane and polymerise with another neighbouring phosphate unit. The residual oxygen atom remains coordinated to the original phosphorus interstitial, resulting in the formation of a branched P_5O_{16} unit. The phosphorus interstitial also displaces the constituent yttrium atom from the $R_1^1(4)$ ring, generating a five coordinate yttrium anti-site on the phosphorus vacancy site. The phosphorus interstitial is located at distances of 4.59 and 1.57 Å from the phosphorus lattice site associated with yttrium anti-site and the yttrium vacancy site respectively. Similarly the yttrium anti-site is located at distances of 0.74 and 2.53 Å respectively. The defect energy for this configuration is calculated to be 13.46 eV.

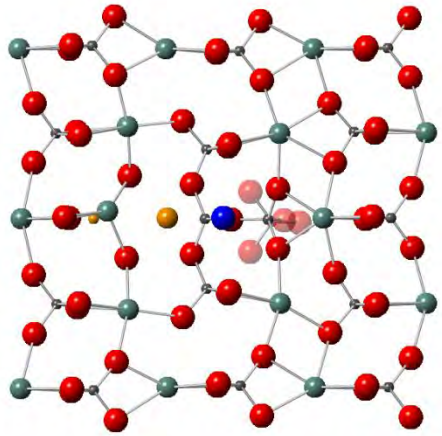

Figure 4.52: Phosphorus Frenkel pair cluster in the $R_1^1(4)$ ring with a local yttrium anti-site. The residual oxygen atom and vacancy sites are highlighted in blue and orange respectively

4.2.3.2.3 Formation Energies

The Frenkel defect formation energies and associated binding energies have been calculated following equation (4.6) and are summarised in Table 4.12. In the case where there are multiple similar configurations, the lowest energy configuration was used. There is a considerable negative binding energy calculated for all Frenkel pair configurations which indicates that the localised vacancy and interstitial stabilises the defect. The lowest energy configuration was found to be the site 2 phosphorus Frenkel pair cluster, forming a P_2O_7 unit.

Table 4.12: Summary of phosphorus Frenkel defect formation and binding energies

Frenkel Defect	Formation Energy at infinite dilution / eV	Formation Energy of cluster / eV	Binding Energy / eV
Site 1	21.44	6.02	-15.42
Inside $R_1^1(4)$ ring	24.20	13.46	-10.75
Site 1 with separate polymerised phosphate.	20.84	15.23	-5.61
Split interstitial centred on yttrium lattice site	21.14	9.25	-11.90
Orthogonal split on phosphorus site	30.82	23.17	-7.650
Site 2	-	3.02	-
Site 1 with yttrium anti-site	-	11.2	-
Two local site 2 interstitials	-	7.88	-
Split in *bc* plane	31.63	-	-

The formation energy for the phosphorus Frenkel pair at infinite dilution in the site 1 position was found to be considerably higher than the energy calculated by Gao *et. al.* Conversely the equivalent energy calculated by Urusov et al. is much greater (40.25 eV) than the formation energy calculated here. Therefore it can be seen that the results from this study lie well within the range of values reported in the literature.

Table 4.13: Comparison of phosphorus Frenkel defect formation energies.

Frenkel Defect	Formation Energy (Gao et al.) / eV	Formation Energy ∞ (this study) / eV	Δ / eV	Δ %	Formation Energy Cluster (this study) / eV	Δ / eV	Δ %
Site 1	16.86	21.44	4.58	23.9	6.02	-10.84	-94.7

4.2.3.3 Oxygen Frenkel Defects

A summary of the phosphorus defect configurations at infinite dilution can be found in Table 4.14. The lowest energy interstitial was found to be in the site 1 position. A summary of the defect energies for the oxygen Frenkel pair clusters can be found in Table 4.15. The lowest energy Frenkel pair cluster was associated with the site 2 position resulting in the rotation of a phosphate unit.

Table 4.14: Summary of defect energies for oxygen interstitial positions at infinite dilution

Description	Defect Energy / eV	Associated ideal site	Polymerised phosphate?	Split interstitial?	Figure
Three coordinate	1.69	1	×	×	Figure 4.53 (a)
Two coordinate	1.69	1	×	×	Figure 4.53 (b)
Zero coordinate	2.48	1	×	×	Figure 4.53 (c)
One coordinate, P coordinate phosphorus	3.06	1	×	×	Figure 4.53 (d)
Five coordinate P with $R_1^1(4)$ ring	3.40	2	×	×	Figure 4.54 (a)
Five coordinate P with no $R_1^1(4)$ ring	4.36	2	×	×	Figure 4.54 (b)
Two coordinate, no $R_1^2(6)$ ring	3.32	3	×	×	Figure 4.55 (a)
Two coordinate, with $R_1^2(6)$ ring	4.83	3	×	×	Figure 4.55 (b)
$R_1^1(4)$ site, five coordinate P	5.12	n/a	×	×	Figure 4.56 (a)
$R_1^1(4)$ site, Nine coordinate Y	12.21	n/a	×	×	Figure 4.56 (b)
One coordinate with separate P_2O_7 unit	3.19	1	✓	×	Figure 4.57 (a)
Three coordinate with separate P_2O_7 unit	4.22	1	✓	×	Figure 4.57 (b)
Bridging O, P_2O_8 unit	3.93	2	✓	×	Figure 4.58 (a)
Bridging O, P_2O_9 unit	5.27	2	✓	×	Figure 4.58 (b)
O split, four coordinate P	1.82	1	×	✓	Figure 4.59 (a)
O split, five coordinate P	2.95	1	×	✓	Figure 4.59 (b)
O split with P interstitial	5.08	1	✓	✓	Figure 4.60

Table 4.15: Summary of defect energies for oxygen Frenkel pair clusters.

Description	Defect Energy / eV	Associated ideal site	Polymerised phosphate?	Split interstitial?	Figure
Rotation of phosphate unit	6.97	1	×	×	Figure 4.61
Rotation of phosphate unit	3.85	2	×	×	Figure 4.62
Rotation of phosphate unit around P-O bond	4.01	n/a	×	×	Figure 4.63
Site 1 with separate P_2O_7 unit	6.33	1	✓	×	Figure 4.64
O coordinated to 1 Y atom	7.40	1	✓	×	Figure 4.65
Five coordinate P with separate P_2O_7 unit	7.89	1	✓	×	Figure 4.66 (a)
Five coordinate P with separate P_2O_7 unit	8.19	1	✓	×	Figure 4.66 (b)
Site 2, P_2O_8 unit	5.12	2	✓	×	Figure 4.67 (a)
Site 2, P_2O_7 unit	9.15	2	✓	×	Figure 4.67 (b)
Site 2, P_2O_8 and P_2O_7 unit	9.09	2	✓	×	Figure 4.67 (c)
Split interstitial with P_2O_7 unit	6.19	1	✓	✓	Figure 4.68
Split interstitial with P_2O_7 unit	4.93	2	✓	✓	Figure 4.69

4.2.3.3.1 Infinite Dilution

Four oxygen interstitials have been identified at the site 1 position. The lowest energy of these is illustrated in Figure 4.53 (a). Here the oxygen interstitial is bridging between three yttrium lattice atoms, increasing their coordination from eight to nine. There is some relaxation of the surrounding oxygen atoms causing them to be displaced slightly into the adjacent channels. A closely related configuration is illustrated in Figure 4.53 (b). Here the oxygen interstitial is bridging between two constituent yttrium atoms of an $R_0^2(4)$ ring. The third defect configuration, illustrated in Figure 4.53 (c), consists of an oxygen interstitial which is not coordinated to any of the neighbouring cations. The nearest cation is a phosphorus atom at 2.00 Å from the interstitial whilst the nearest yttrium atoms are at distances ranging from 2.61-2.73 Å. Finally a fourth defect configuration is illustrated in Figure 4.53 (d), where the oxygen interstitial is coordinated to a phosphorus atom, increasing its coordination from four to five. The coordinating phosphorus atom is located at a distance of 1.58 Å. The defect energies for these configurations are calculated to be 1.69, 1.69, 2.48 and 3.06 eV respectively.

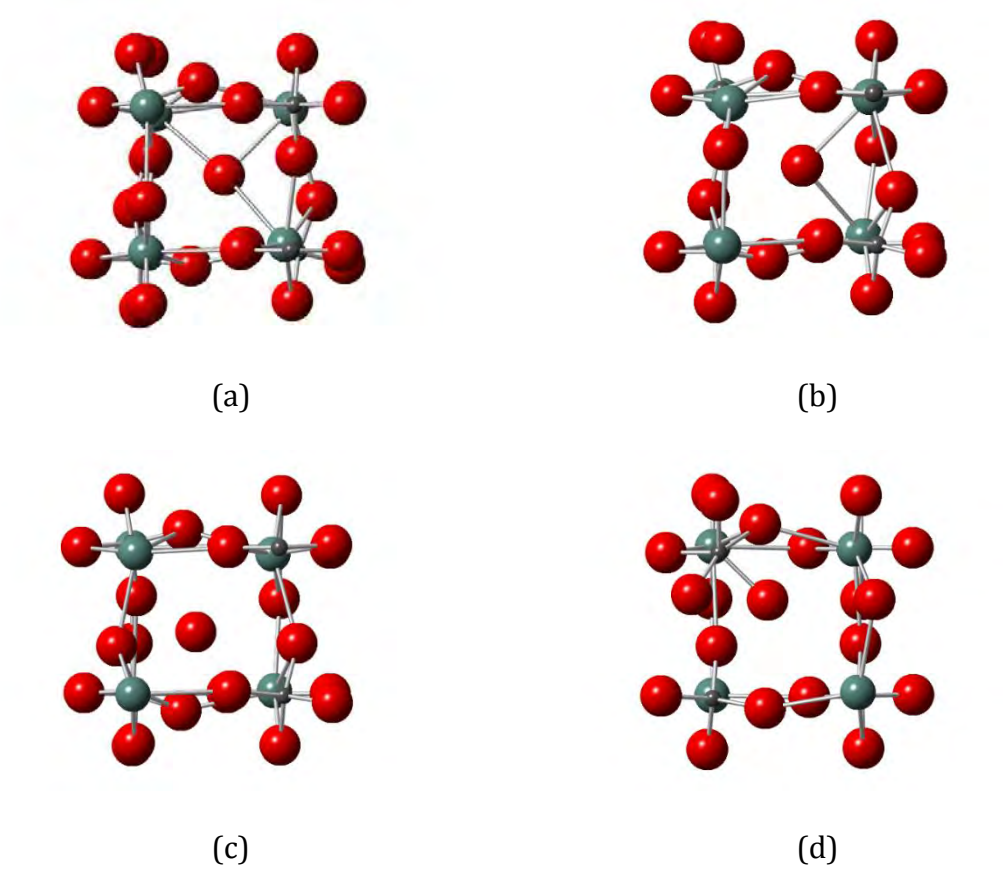

Figure 4.53: Oxygen self-interstitials in the site 1 defect position

Two oxygen interstitials have been identified at the site 2 position. The first of these is illustrated in Figure 4.54 (a). Here the oxygen interstitial is coordinated to a phosphorus and a yttrium atom which increases the coordination of the phosphorus atom to five and creates a new $R_1^1(4)$ ring. The P-O and Y-O distances to the oxygen interstitial are 1.58 and 2.52 Å respectively. The second configuration is illustrated in Figure 4.54 (b). Here the oxygen interstitial is coordinated to a phosphorus atom increasing its coordination to five. It is also coordinated to a yttrium atom, however two previously coordinated oxygen atoms are displaced and so the coordination of the yttrium is reduced to seven and the $R_1^1(4)$ ring is disrupted. The Y-O and P-O distances to the oxygen interstitial are 2.16 and 1.55 Å respectively. The defect energies for these configurations are calculated to be 3.40 and 4.36 eV, respectively.

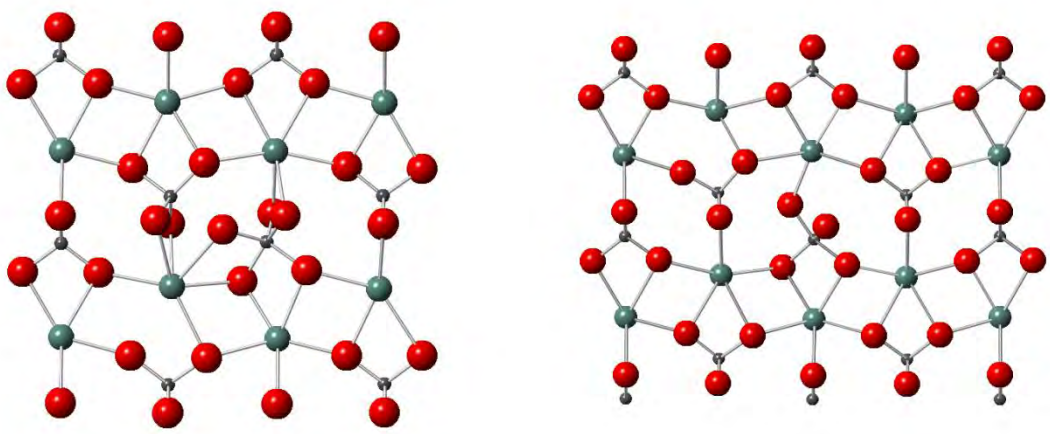

(a) (b)

Figure 4.54: Oxygen self-interstitials in the site 2 defect position

Two defect configuration have been identified with the oxygen interstitial in the site 3 position. The lowest energy of these is illustrated in Figure 4.55 (a). Here the oxygen interstitial is coordinated to the constituent yttrium atoms of the $R_0^2(4)$ ring. This disrupts the $R_0^2(4)$ ring and reduces the coordination of the yttrium atoms to seven. The two constituent oxygen atoms of the original $R_0^2(4)$ are left dangling, only coordinated to a single phosphorus atom. The second configuration is illustrated in Figure 4.55 (b). Here the oxygen interstitial is coordinated to the two yttrium atoms however only one yttrium atom has its coordination reduced to seven. The defect energy for these configurations are calculated to be 3.32 and 4.83 eV, respectively.

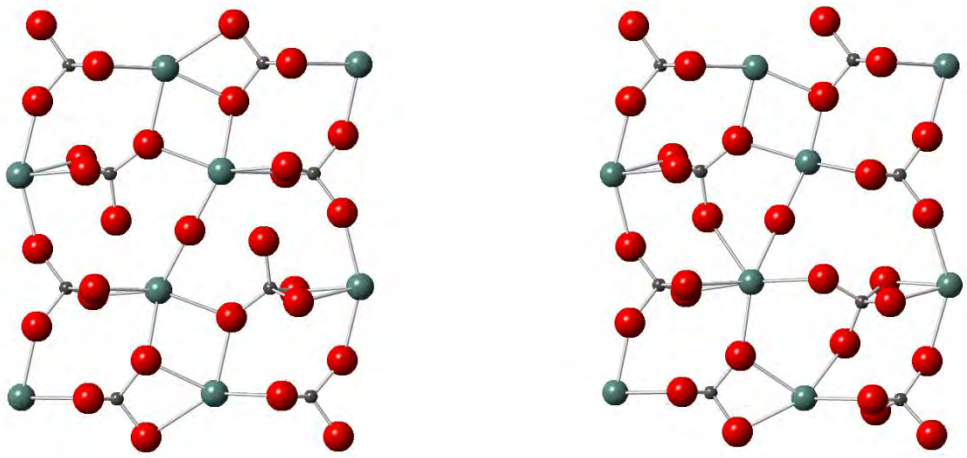

(a) (b)

Figure 4.55: Oxygen self-interstitials in the site 3 defect position

Two defect configurations with the oxygen interstitial in the small $R_1^1(4)$ ring have been identified. The lowest energy of these is illustrated in Figure 4.56 (a). Here the oxygen interstitial is coordinated to the constituent phosphorus and yttrium atoms of the $R_1^1(4)$ ring. This increases the coordination of the phosphorus atom to five but reduces the yttrium coordination to seven. There is some distortion to the lattice further from the interstitial, with the expansion of neighbouring $R_1^1(4)$ and $R_0^2(4)$ rings into $R_1^2(6)$ rings along with the reduction in coordination of the associated yttrium atoms to seven. The second configuration is illustrated in Figure 4.56 (b). Here the oxygen interstitial is in a similar position, however in this configuration the constituent oxygen atoms of the $R_1^1(4)$ ring remain coordinated to the associated yttrium atom. This increases the coordination of the yttrium atom to nine but decreases the coordination of the phosphorus atom to three. There is a considerable amount of distortion to the lattice with the neighbouring $R_2^2(8)$ rings expanding to $R_2^3(10)$ rings. This is also seen further from the interstitial,

reducing the coordination of four yttrium atoms to seven. The defect energies calculated for these configurations are 5.12 and 12.21 eV, respectively.

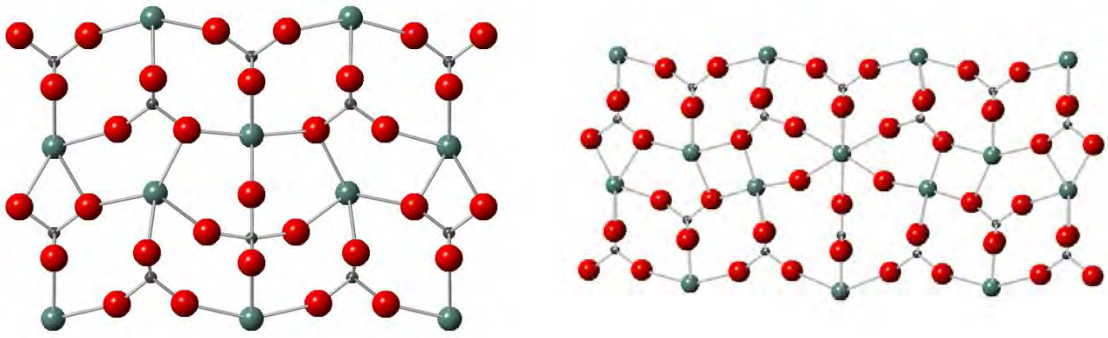

(a) (b)

Figure 4.56: Oxygen self-interstitials in the $R_1^1(4)$ ring

Two defect configurations have been identified with the oxygen interstitial in the site 1 position, with a local polymerised phosphate unit. The lowest energy of these is illustrated in Figure 4.57 (a). Here the oxygen interstitial is coordinated to a yttrium lattice atom at a distance of 2.23 Å, increasing its coordination to nine. The subsequent phosphorus to the coordinating yttrium atom in the *c* direction become displaced from its lattice site and polymerises with a neighbouring phosphate group, forming a P_2O_7 unit. The displaced phosphorus is at a distance of 3.15 Å from the interstitial. The second defect configuration is illustrated in Figure 4.57 (b). Here the oxygen interstitial is coordinated to three yttrium atoms. The displaced phosphorus atom is shifted into the adjacent channel, at a distance of 4.97 Å from the oxygen interstitial. The defect energies for these configurations are calculated to be 3.19 and 4.22 eV, respectively.

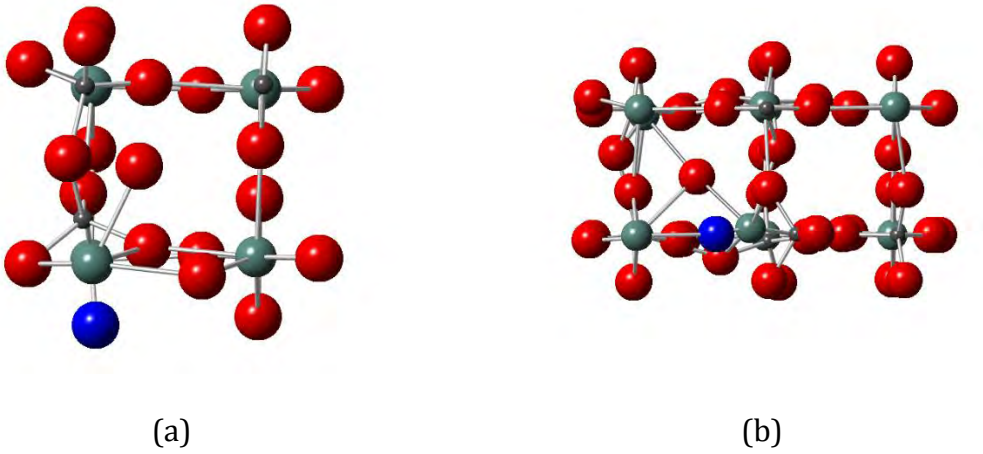

(a) (b)

Figure 4.57: Oxygen interstitial associated with the site 1 position with a local polymerised phosphate unit. The residual oxygen atom is highlighted in blue

Two defect configurations with the oxygen interstitial in the site 2 position and polymerised phosphate units have been identified. The lowest energy of these is illustrated in Figure 4.58 (a). Here the oxygen atom is bridging between the constituent phosphorus atoms of the $R_2^2(8)$ ring, creating new $R_2^1(6)$ rings and a P_2O_8 unit. This increases the coordination of one of the phosphorus atoms to five. The second defect configuration is illustrated in Figure 4.58 (b). Here the oxygen interstitial is in a similar position to the previous configuration but in this case both phosphorus atoms are now five coordinate, forming a P_2O_9 unit. The defect energies calculated for these configurations are 3.93 and 5.27 eV, respectively.

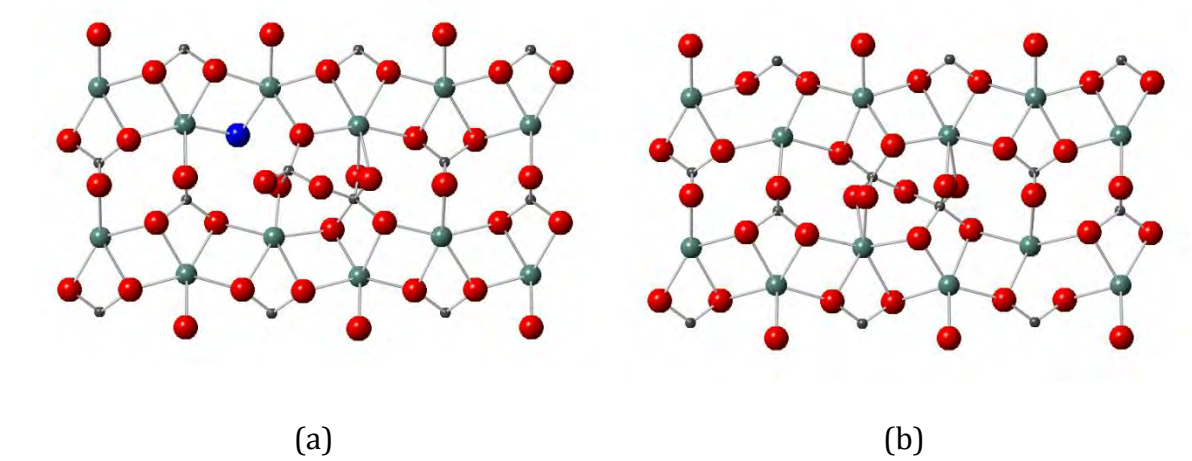

(a) (b)

Figure 4.58: Oxygen interstitial associated with the site 2 position with a local polymerised phosphate unit. The residual oxygen atom is highlighted in blue

Two split interstitial defect configurations have been identified. The lowest energy of these configuration is illustrated in Figure 4.59 (a). Here the oxygen interstitials are located at distances of 1.10 and 1.21 Å from the oxygen lattice site. One of the interstitials is coordinated to two yttrium atom, preserving the $R_0^2(4)$ ring. The second interstitial is coordinated to a phosphorus and a yttrium atom. The second configuration is illustrated in Figure 4.59 (b). Here the oxygen interstitials are located at distances of 1.02 and 1.04 Å from the oxygen lattice site. Both interstitials are coordinated to a phosphorus atom and a yttrium atom. This increases the coordination of the phosphorus and yttrium to five and nine respectively. The defect energies for these configurations are calculated to be 1.82 and 2.95 eV, respectively.

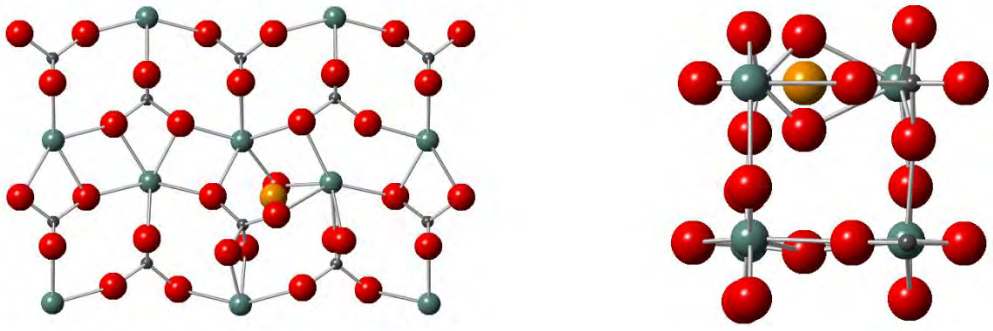

(a) (b)

Figure 4.59: Oxygen split interstitial. Vacancy site is highlighted in orange

A similar split interstitial has been identified which also includes a phosphorus Frenkel pair, Figure 4.60. The oxygen interstitials are located at distances of 0.91 and 1.46 Å from the oxygen lattice site. The phosphorus interstitial is corner sharing with a neighbouring phosphate tetrahedron, forming a P_2O_7 unit. The phosphorus interstitial is located at a distance of 2.39 Å from the oxygen lattice site about which the oxygen interstitials are centralised. The defect energy for this configuration is calculated to be 5.08 eV.

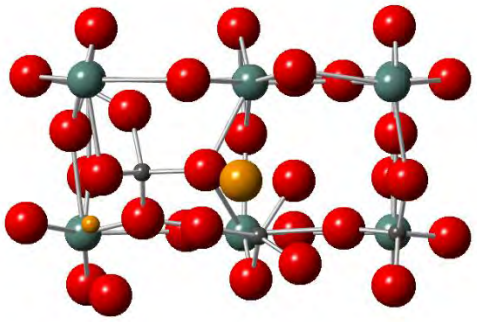

Figure 4.60: Oxygen split interstitial with local phosphorus Frenkel pair. Vacancy sites are highlighted in orange

4.2.3.3.2 Cluster Calculations

An oxygen Frenkel defect cluster has been identified with the interstitial in the site 1 position, illustrated in Figure 4.61. Here the interstitial atom is located at a distance of 3.43 Å from the vacancy site. The interstitial atom remains coordinated to the neighbouring phosphorus atom, at a distance of 1.51 Å, causing a rotation of the phosphate unit. The defect energy for this configuration is calculated to be 3.96 eV.

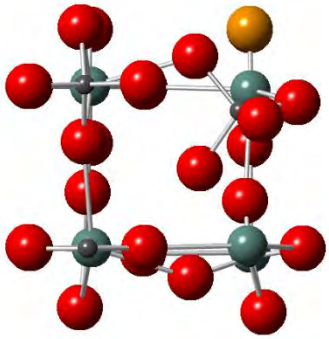

Figure 4.61: Oxygen Frenkel pair cluster in the site 1 position. Vacancy site is highlighted in orange.

A similar defect configuration has been identified with the oxygen interstitial in the site 2 position, illustrated in Figure 4.62. Here the oxygen interstitial is located at a distance of 1.55 Å from the vacancy site. The oxygen interstitial remains coordinated to the neighbouring phosphorus atom at a distance of 1.52 Å, causing a rotation of the phosphate unit. The defect energy for this configuration is calculated to be 3.85 eV.

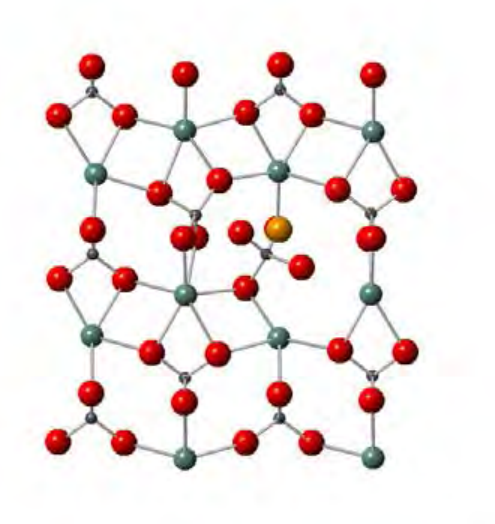

Figure 4.62: Oxygen Frenkel pair cluster in the site 2 position. Vacancy site is highlighted in orange.

An interesting defect configuration has been identified with essentially three Frenkel pairs, illustrated in Figure 4.63, which can be simply thought of as a rotation of the phosphate group by 90° about one of the P-O bonds. In doing so the coordination of the four constituent yttrium atoms is reduced to seven. The defect energy for this configuration is calculated to be 4.01 eV.

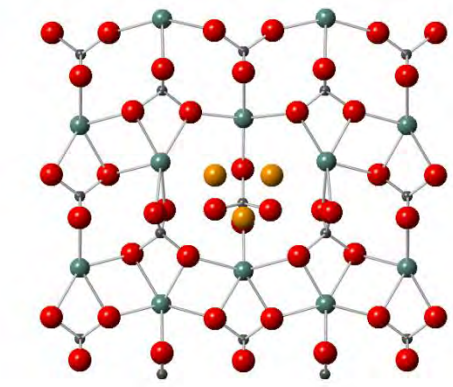

Figure 4.63: Three neighbouring oxygen Frenkel pairs. Vacancy sites are highlighted in orange.

Four defect clusters have been identified with the oxygen interstitial in the site 1 position, with a separate polymerised phosphate unit. In all four cases the oxygen vacancy is located on the site of the residual oxygen atom from the polymerisation of the phosphate units and the interstitial atom is bridging between two nine coordinate yttrium atoms. The lowest energy of these configurations is illustrated in Figure 4.64. Here the oxygen interstitial is located at a distance of 3.63 Å from the vacancy site and the shifted phosphorus atom is at a distance of 3.52 Å.

Figure 4.64: Oxygen Frenkel pair clusters associated with the site 1 position which include a polymerised phosphate unit. The vacancy site is highlighted in orange.

A similar configuration has been identified, illustrated in Figure 4.65, with the oxygen interstitial in the site 1 position, with a separate polymerised phosphate unit. In this configuration the oxygen interstitial is only coordinated to one yttrium atom at a distance of 2.44 Å. The oxygen interstitial is located at a distance of 5.61 and 5.31 Å from the oxygen vacancy and shifted phosphorus atom respectively. The defect energy calculated for this configuration is 7.40 eV.

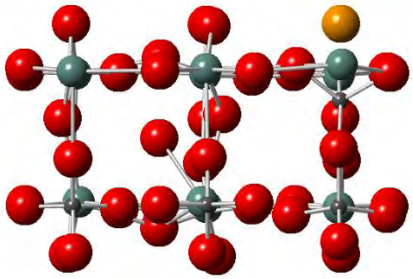

Figure 4.65: Oxygen Frenkel pair cluster associated with the site 1 position which includes a polymerised phosphate unit. The vacancy site is highlighted in orange.

Two defect configurations were identified with the oxygen interstitial in the site 1 position, with a separate polymerised phosphate group. Again the vacancy is located on the site of the residual oxygen atom from the polymerisation of the phosphate unit, however in these configurations the oxygen interstitial is coordinated to a five coordinate phosphorus atom. The lowest energy of these configurations is illustrated in Figure 4.66 (a). Here the oxygen interstitial is located at distances of 4.03 and 6.13 Å from the oxygen vacancy and the shifted phosphorus atom respectively. The second configuration is illustrated in Figure 4.66 (b). Here the oxygen interstitial is located at distances of 5.23 and 6.65 Å from the oxygen vacancy and the shifted phosphorus atom respectively. The defect energies calculated for these configurations are 7.89 and 8.19 eV, respectively.

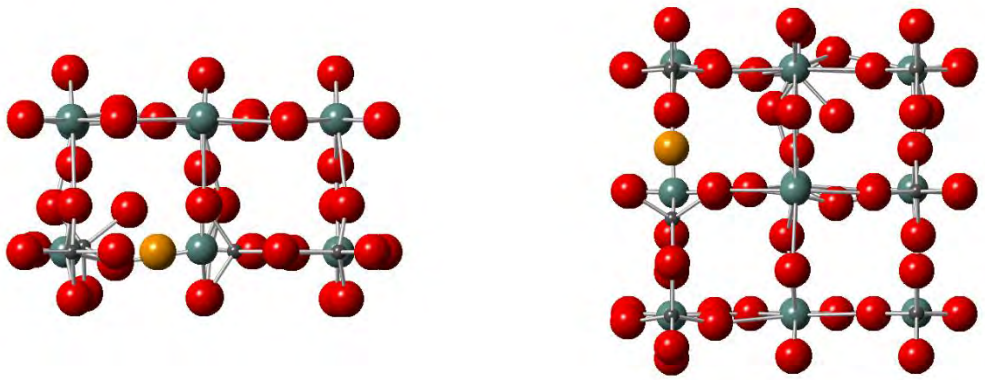

(a) (b)

Figure 4.66: Oxygen Frenkel pair cluster associated with the site 1 position which includes a five coordinate phosphorus atom and a polymerised phosphate unit. The vacancy site is highlighted in orange.

Three defect configurations have been identified with the oxygen interstitial in the site 2 position, with a polymerised phosphate unit. The lowest energy of these is illustrated in Figure 4.67 (a). Here the oxygen interstitial is displaced into its parent $R_2^2(8)$ ring where it is bridging between the two constituent phosphorus atoms, forming a P_2O_8 unit. This causes the coordination of one of the phosphorus atoms to increase to five and the other to rotate. The oxygen interstitial is located at a distance of 1.35 Å from the vacancy site. The second defect configuration is illustrated in Figure 4.67 (b). Here the oxygen interstitial is located in the adjacent $R_2^2(8)$ ring, coordinating to a seven coordinate yttrium atom and a five coordinate phosphorus atom. The vacancy is located on the site of the residual oxygen from the polymerisation of neighbouring phosphate units, forming a P_2O_7 unit. The oxygen interstitial is located at distances of 4.37 and 4.43 Å from the shifted phosphorus atom and oxygen vacancy site respectively. The third configuration is illustrated in Figure 4.67 (c). Here the oxygen interstitial is located in the subsequent plane to the vacancy site, bridging between the two constituent phosphorus atoms of an

$R_2^2(8)$ ring, forming a P_2O_8 unit. This increases the coordination of one of the phosphorus atoms to five. The oxygen vacancy is located on the site of a residual oxygen atom from the polymerisation of neighbouring phosphate units. The oxygen interstitial is located at a distance of 5.13 Å from the vacancy site. The defect energies calculated for these configurations are 5.12, 9.15 and 9.09 eV, respectively.

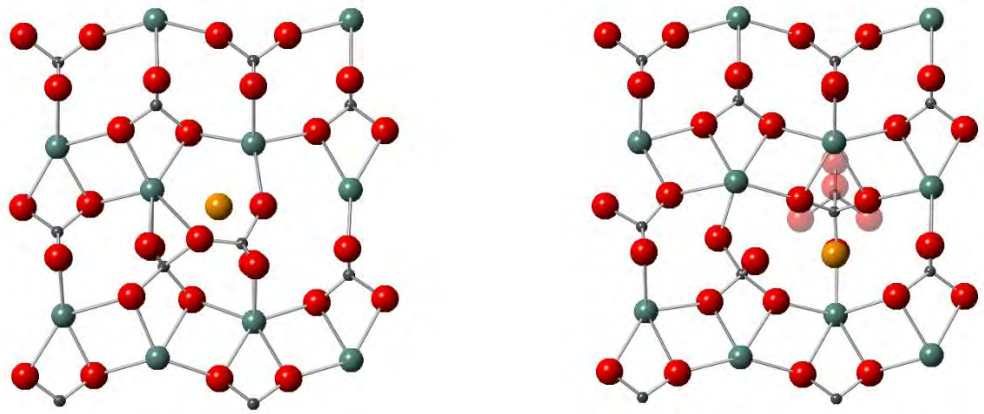

(a) (b)

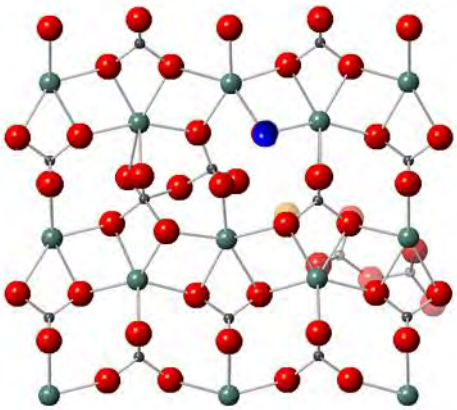

(c)

Figure 4.67: Oxygen Frenkel pair cluster associated with the site 2 position which includes a polymerised phosphate unit. The residual oxygen atom and vacancy sites are highlighted in blue and orange respectively

A split interstitial configurations have been identified with the oxygen interstitials in the site 1 position. The vacancy site is located on the lattice site of the residual oxygen atom

resulting from the polymerisation of two neighbouring phosphate groups, forming a P_2O_7 unit, Figure 4.68. Here the oxygen interstitials are located at distances of 0.98 and 1.28 Å from the central vacancy site. One interstitial is coordinated to two yttrium atoms, preserving the $R_0^2(4)$ ring whilst the second is coordinated to a yttrium and a phosphorus atom, creating a new $R_1^2(6)$ ring. The oxygen interstitials are located at distances of 3.41 and 4.63 Å from the shifted phosphorus atom and 5.14 and 5.63 Å from the other vacancy site. The defect energy was calculated to be 6.19 eV.

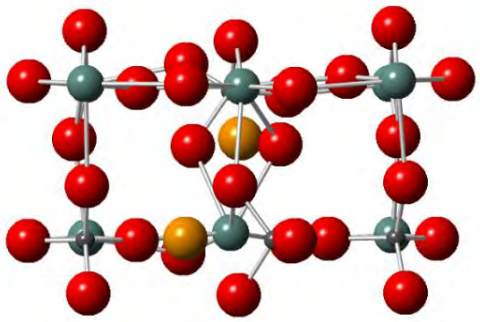

Figure 4.68: Oxygen split interstitial cluster associated with the site 1 position which includes a polymerised phosphate unit. The vacancy sites are highlighted in orange

Finally a split interstitial defect configurations has been identified with the split interstitial in the site 2 position, Figure 4.69. Here the oxygen interstitial is in the adjacent $R_2^2(8)$ ring to the vacancy site where it is bridging between the two constituent phosphorus atoms, forming a P_2O_7 unit. The interstitials are located at distances of 1.15 and 1.32 Å from the central vacancy site. The defect energy for this configuration is calculated to be 4.93 eV.

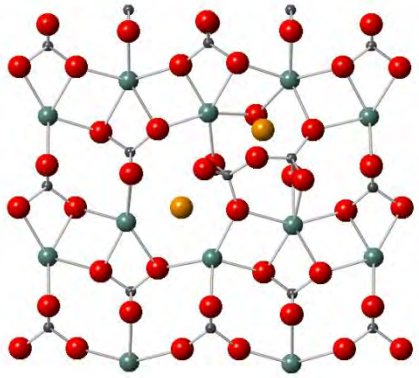

Figure 4.69: Oxygen split interstitial cluster associated with the site 2 position which includes a polymerised phosphate unit. The vacancy sites are highlighted in orange

4.2.3.3.3 Formation Energies

The Frenkel defect formation energies and associated binding energies have been calculated following equation (4.7) and are summarised in Table 4.16. In the case where there are multiple equivalent configurations, the lowest energy configuration was used. There is a considerable negative binding energy calculated for all Frenkel pair configurations which indicates that the localised vacancy and interstitial stabilises the defect. The lowest energy configuration was found to be the site 2 phosphorus Frenkel pair cluster, forming a P_2O_7 unit.

Table 4.16: Summary of oxygen Frenkel defect formation and binding energies

Frenkel Defect	Formation Energy at infinite dilution / eV	Formation Energy of cluster / eV	Binding Energy / eV
site 1	7.67	3.96	-3.71
site 2	9.39	3.85	-5.54
Site 1 with poly	9.17	6.33	-2.85
Site 2 with poly	9.92	5.12	-4.79
Split interstitial site 1	7.80	8.01	0.20
Site 3	9.30	-	-
$\boldsymbol{R_1^1(4)}$ **ring**	11.10	-	-
Rotation of phosphate unit	-	4.01	-
Split interstitial site 2	-	4.93	-

The formation energies calculated in this study vary quite considerably from the values reported by Gao *et. al.*, with the values at infinite dilution reported here being larger. However the equivalent energy calculated by Urusov *et al*[2]. was 10.79 eV which is greater than the results of this study and so the formation energies calculated in this study lie within the range of values reported in the literature. The trend in formation energies at infinite dilution is comparable between this study and that of Gao *et al.* with the interstitial in site 1 having the lower formation energy.

Table 4.17: Comparison of oxygen Frenkel defect formation energies.

Frenkel Defect	Formation Energy (Gao et al.) / eV	Formation Energy ∞ (this study) / eV	Δ / eV	Δ %	Formation Energy Cluster (this study) / eV	Δ / eV	Δ %
Site 1	4.43	7.67	3.24	53.5	3.96	-0.58	-11.2
Site 2	4.51	9.39	4.88	70.2	3.85	-0.66	-15.8

4.2.4 Anti-site Defects

4.2.4.1 Infinite Dilution

The two components of the anti-site defect at infinite dilution are illustrated in Figure 4.70. Here the yttrium anti-site on the phosphorus lattice site is shown in Figure 4.70 (a), where it is found to adopt a four coordinate site. The Y-O distance to the coordinating oxygen atoms is 2.09 Å. This slightly compresses the Y-O distances to the adjacent yttrium atoms down the *c* axis to 2.31 Å, whilst the Y-O distances to the adjacent yttrium atoms in the *a* and *b* directions are reduced to 2.15 Å. There is considerably more distortion to the lattice around the phosphorus anti-site on the yttrium lattice site, illustrated in Figure 4.70 (b). Here the phosphorus atom is not shown to be coordinated to the surrounding oxygen atoms as they are located at distances of 1.95-1.98 Å. The P-O distances for the surrounding phosphate units remain relatively unchanged whilst the O-P-O angles become compressed to ca. 91°. The defect energies for these configurations are calculated to be 32.97 and -11.04 eV, respectively.

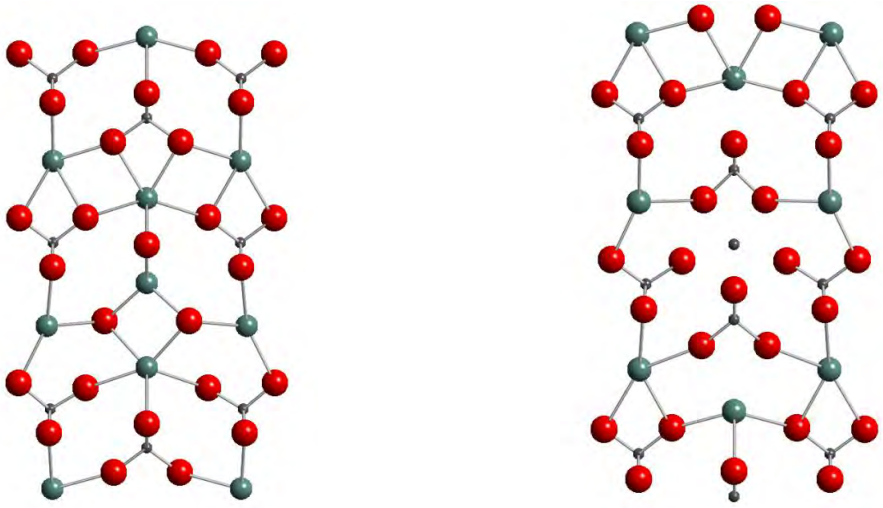

(a) (b)

Figure 4.70: Anti-site defects at infinite dilution

4.2.4.2 Clusters

Two anti-site defect clusters have been highlighted in Figure 4.71. The first of these is illustrated in Figure 4.71 (a), where the yttrium and phosphorus anti-sites lie within the same chain down the *c* axis. Here the yttrium atom adopts a four coordinate geometry with Y-O distances ranging from 2.10-2.12 Å, whilst the phosphorus atom is located at distances ranging from 1.86-2.00 Å from its nearest neighbour atoms. The local ring structure is disrupted and generates a new $R_6^7(26)$ ring. The second configuration is illustrated in Figure 4.71 (b). Here the two anti-sites are in separate planes, with the relaxation closely resembling that of the defects at infinite dilution. The defect energies for these configurations are calculated to be 18.50 and 21.07 eV, respectively.

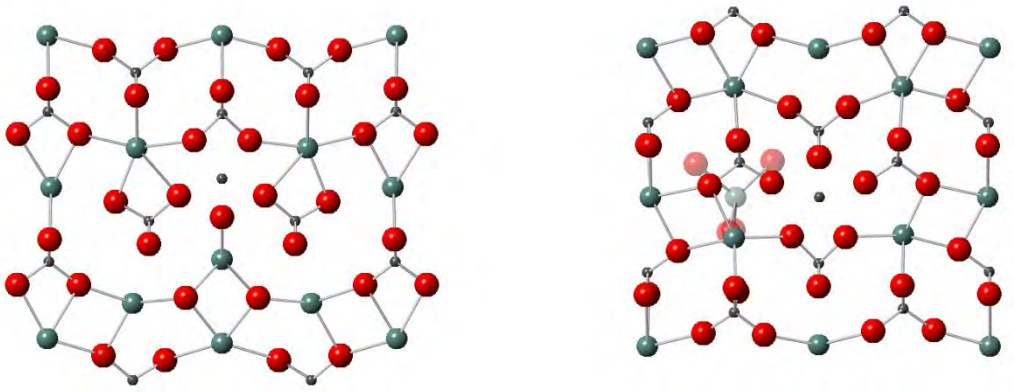

(a) (b)

Figure 4.71: Anti-site defect clusters

An anti-site cluster was observed during the phosphorus Frenkel pair grid search, illustrated in Figure 4.72. Here the yttrium and phosphorus atoms sit slightly offset from the corresponding lattice sites and distances of 1.15 and 1.05 Å respectively. The phosphorus anti-site is four coordinate, corner sharing with two neighbouring phosphate units, forming a P_3O_{10} unit. The yttrium anti-site is six coordinate, with Y-O distances

ranging from 2.14-2.48 Å. There is a substantial amount of distortion to the surrounding lattice with the creation of new $R_4^3(14)$, $R_2^2(8)$, $R_1^2(6)$ and $R_0^2(4)$ rings. The defect energy for this configuration is calculated to be 7.60 eV.

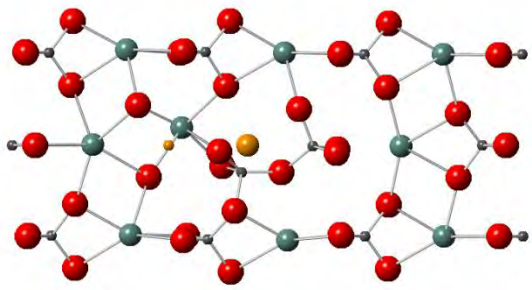

Figure 4.72: Anti-site defect cluster found from the grid search methodology

Table 4.18: Summary of anti-site defect formation and binding energies

Schottky Defect	Formation Energy / eV	Binding Energy / eV
$Y_P^{''} + P_Y^{\cdot\cdot}$	21.93	-
$\{Y_P^{''} + P_Y^{\cdot\cdot}\}$	7.60	-14.33

The formation energies for the anti-site defects are summarised in Table 4.18. The anti-site cluster with both anti-sites in the same chain in the *c* axis, forming a P_3O_{10} unit, was found to be the lowest energy configuration with a formation energy of 7.60 eV. The binding energy for this cluster was calculated to be -14.33 eV, indicating that it is much more energetically favourable for the defects to be clustered in this way as opposed to the defects at infinite dilution.

4.3 Extrinsic Defects

The interatomic potentials derived in chapter 3 have been used to calculate the solution energy for a selection of lanthanide elements onto the isovalent yttrium site. The solution

energy gives an insight into the relative stability of the substituted element in the host phase and can be calculated following equations (4.9) and (4.10).

$$Y_Y^{\times} + LnPO_4 \rightleftharpoons Ln_Y^{\times} + YPO_4 \quad \textbf{(4.9)}$$

$$Y_Y^{\times} + \frac{1}{2}Ln_2O_3 \rightleftharpoons Ln_Y^{\times} + \frac{1}{2}Y_2O_3 \quad \textbf{(4.10)}$$

The results following equation (4.9) are summarised in Table 4.19 and Figure 4.73. Here it can be seen that the general trend in solution energy is parabolic in nature and is not symmetrical about the origin. The minimum in solution energy is associated with the substitution of gadolinium on the yttrium site, with a solution energy of -0.02 eV. The solution energy decreases with increasing ionic radius from lutetium to gadolinium, which indicates that the smaller lanthanides compared to yttrium introduce strain into the host phase, making it less energetically favourable for them to be dissolved. This becomes less pronounced for the larger lanthanides up to gadolinium which is the largest lanthanide to adopt the xenotime structure. The solution energy begins to increase for lanthanides with larger ionic radii than gadolinium. This indicates that strain is being introduced into the host phase and as such it is less energetically favourable for these lanthanides to be dissolved. Furthermore the larger lanthanide orthophosphates from europium to lanthanum adopt the monazite structure in which the lanthanides are nine coordinate and as such they are under-coordinated when dissolved in the xenotime host phase. Although the solution energies have been found to be favourable for the lanthanides from erbium to neodymium, the magnitude of the solution energies is minimal indicating that lanthanides are only sparingly soluble in the xenotime host phase.

Table 4.19: Solution energies for lanthanide substitution onto the yttrium site in the xenotime host phase from the $LnPO_4$ parent phase

Ln	r / Å	Δr / Å	E_{sol} / eV
La	1.16	0.14	0.126
Nd	1.11	0.09	-0.009
Sm	1.08	0.06	-0.014
Gd	1.05	0.03	-0.017
Er	1.00	-0.02	-0.009
Lu	0.98	-0.04	0.046

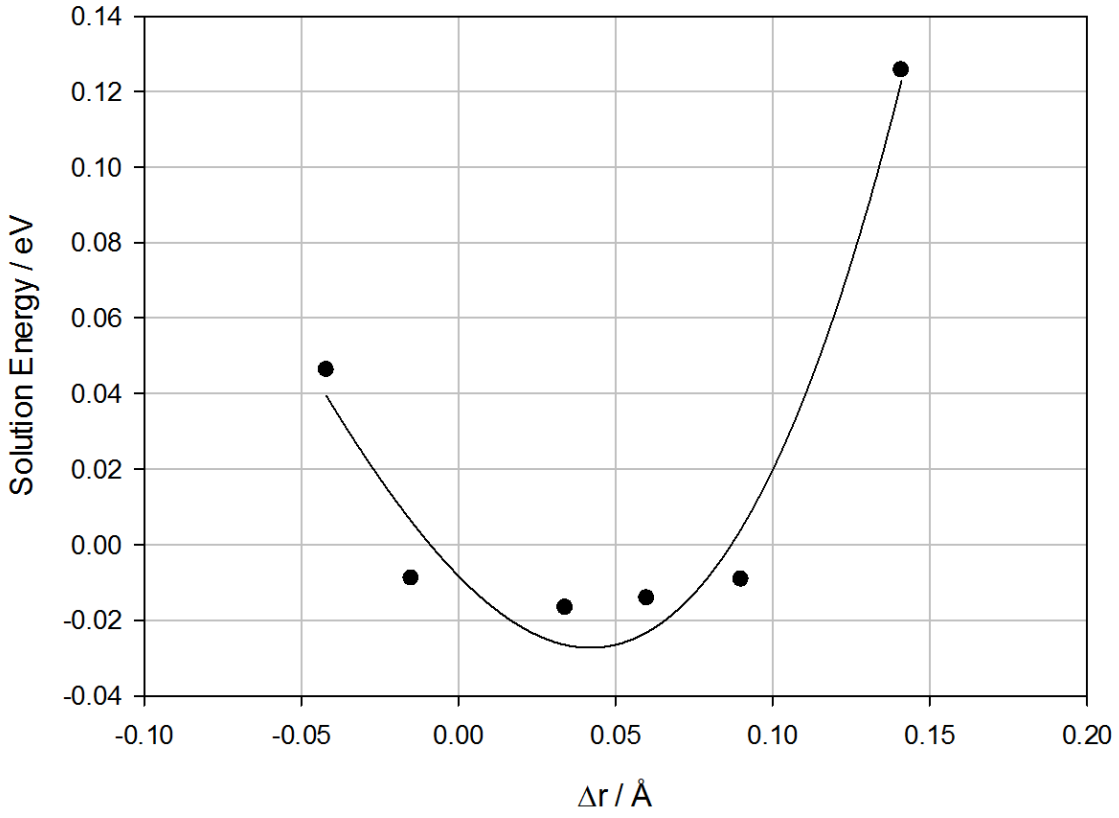

Figure 4.73: Solution energy for Ln substitution onto the Y lattice site in the xenotime host phase from the $LnPO_4$ parent phase. The curve fit to the data is a guide for the eye only

Similarly the solution energy from the lanthanide sesquioxide phases into the xenotime host phase have been calculated and are summarised in Table 4.20 and Figure 4.74. Here

it can be seen that a similar trend is observed which is parabolic in nature. The solution energies are found to decrease with increasing ionic radius from lutetium to gadolinium where a minimum of -1.02 eV is reached. Conversely the solution energy increases with increasing ionic radius for the lanthanides from gadolinium to lanthanum. The solution energy for samarium is slightly anomalous but can be rationalised by considering the crystallography of the lanthanide sesquioxide phases. The smaller lanthanides (Lu, Er and Gd) adopt the cubic Ln_2O_3 structure whereas the larger lanthanides (Nd and La) adopt the hexagonal Ln_2O_3 structure. Samarium is the only lanthanide investigated here to preferentially adopt the monoclinic Ln_2O_3 structure which may highlight a limitation of the interatomic potentials used. All solution energies were found to be negative indicating that it is energetically favourable for the lanthanide elements to dissolve in the xenotime host phase from the lanthanide sesquioxide parent phase.

Table 4.20: Solution energies for lanthanide substitution onto the yttrium site in the xenotime host phase from the Ln_2O_3 parent phase

Ln	r / Å	Δr / Å	E_{sol} / eV
La	1.16	0.14	-0.55
Nd	1.11	0.09	-0.97
Sm	1.08	0.06	-0.86
Sm*	1.08	0.06	-0.72
Gd	1.05	0.03	-1.02
Er	1.00	-0.02	-0.41
Lu	0.98	-0.04	-0.17

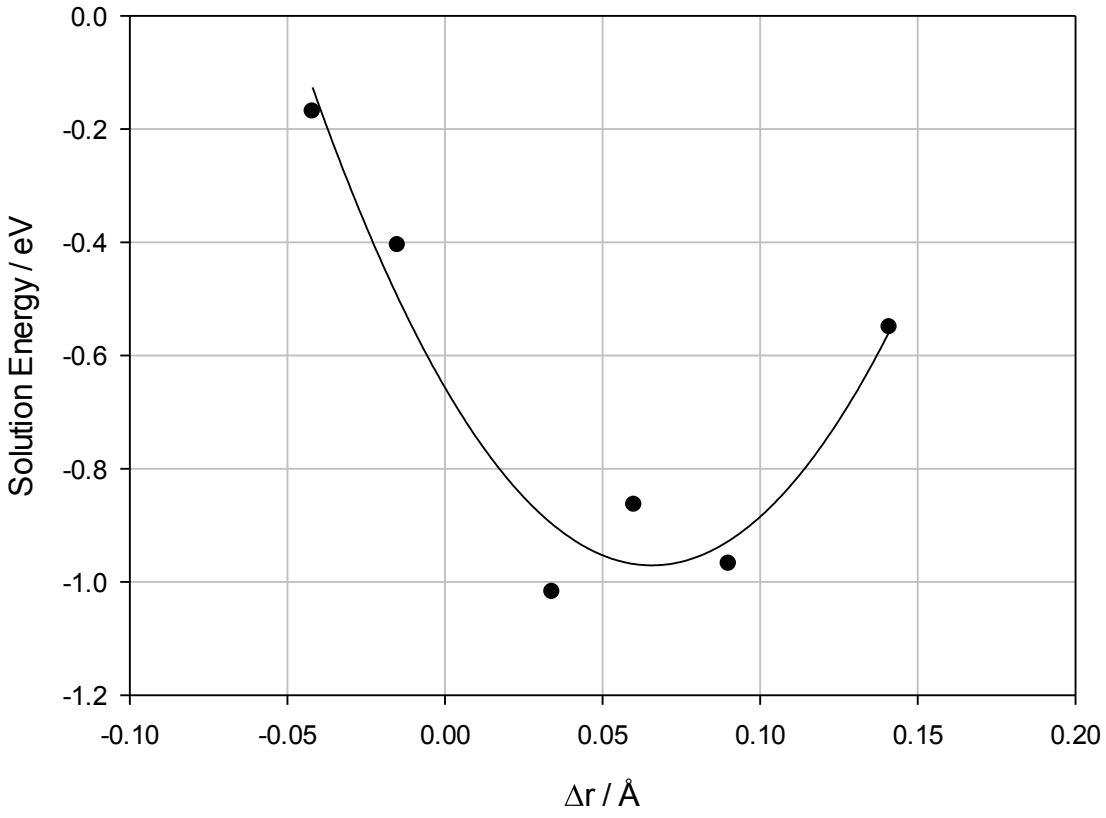

Figure 4.74: Solution energy for Ln substitution onto the Y lattice site in the xenotime host phase from the Ln_2O_3 parent phase. The curve fit to the data is a guide for the eye only

4.4 Conclusion

In this chapter the intrinsic and extrinsic defects within the xenotime system have been investigated. Schottky defects were simulated at infinite dilution and as a selection of defect clusters. The lowest energy configuration was found to be the cluster with the phosphate and yttrium vacancies adjacent to each other down the *c* axis, with a formation energy of 6.03 eV. This configuration is illustrated in Figure 4.75. This was found to be more energetically favourable than the Y_2O_3 and P_2O_5 Schottky-like defects investigated with formation energies of 11.48 and 10.14 eV, respectively.

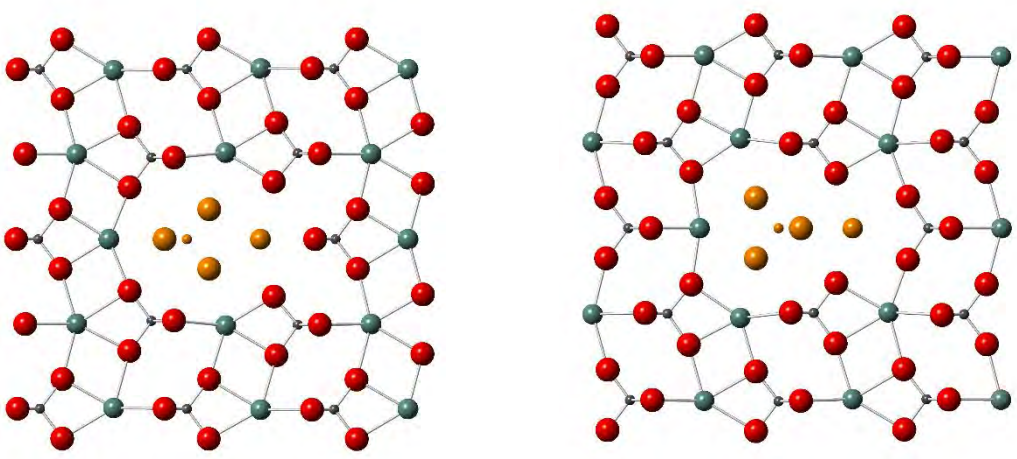

Figure 4.75: Lowest energy Schottky defect cluster. The vacancy sites are highlighted in orange

A grid searching methodology has been employed to investigate Frenkel pair defects in the xenotime system. In the context of radiation damage simulations it is important to consider a wide range of defects which may appear to a lesser or greater extent in the damaged configurations from cascade or fission track simulations. As such the unique defects have been discussed individually. The defect energies for the yttrium Frenkel pair clusters ranged from 4.50 to 10.16 eV, with the lowest energy isolated yttrium Frenkel pair found to be in the six coordinate site 1 position, with defect energy of 6.53 eV, Figure 4.76 (a). The lowest energy defect cluster actually consisted of two neighbouring six coordinate yttrium Frenkel pairs in the site 1 position, Figure 4.76 (b). This defect configuration could be considered as a rotation of the $R_0^2(4)$ ring, with a formation energy of 4.50 eV (2.25 eV per Frenkel pair). The formation energy for this cluster with the Frenkel pairs at infinite dilution to each other can be calculated following equation (4.11) to be 13.06 eV, giving a binding energy of -8.56 eV. This extremely large binding energy shows that it is energetically favourable for these defects to cluster together. These findings are concurrent with those of Crocombette[3] for the zirconium interstitial in zircon.

$$Y_Y^{\times} + Y_Y^{\times} \rightleftharpoons \{V_Y^{'''} + Y_i^{\cdots}\} + \{V_Y^{'''} + Y_i^{\cdots}\} \quad \textbf{(4.11)}$$

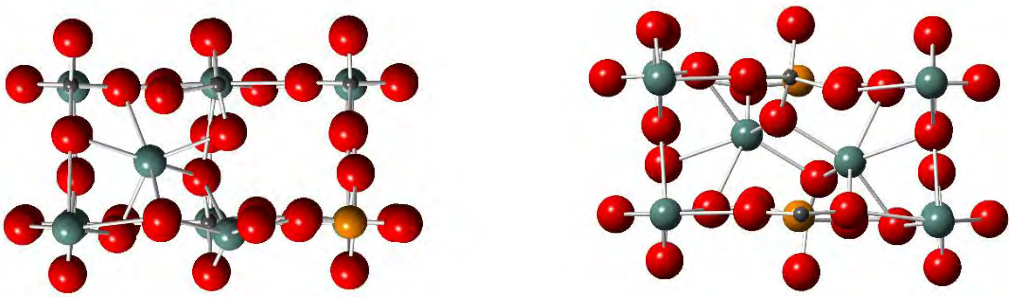

(a) (b)

Figure 4.76: Defect configuration for yttrium Frenkel pair clusters (a) for the lowest energy isolated Frenkel pair and (b) the lowest energy cluster. Vacancy sites are highlighted in orange

The phosphorus Frenkel pair clusters ranged in energy from 3.02 to 29.27 eV. The lowest energy isolated Frenkel defect was found to be in the site 2 position, bridging with the other constituent phosphorus atom of the $R_2^2(8)$ ring, forming a P_2O_7 unit, Figure 4.77 (a). This defect cluster was also the lowest energy defect of all the clusters identified, with a defect energy of 3.02 eV. A wide range of polymerised phosphate units were observed across the range of Frenkel pairs identified, indeed all phosphorus Frenkel pairs identified contained a polymerised unit, indicating that this polymerisation may be an import damage mechanism. The second lowest Frenkel defect consisted of an interstitial in the site 1 position, forming a P_3O_{10} unit, with a formation energy of 6.02 eV, Figure 4.77 (b). This shows a clear preference for the interstitial at the site 2 position. There was generally a large binding energy across the defect clusters investigated here, indicating that there is an energetic driving force for the interstitials to occupy positions near to phosphorus

vacancies. These can be compared to the lowest energy silicon point defect identified by Crocombette[3] where the silicon interstitial adopts the site 1 position. This could mark a key difference in the defect properties between these systems with the phosphorus interstitials in xenotime preferentially forming P_2O_7 units whilst the silicon atoms would form Si_3O_{10} or Si_5O_{16} units.

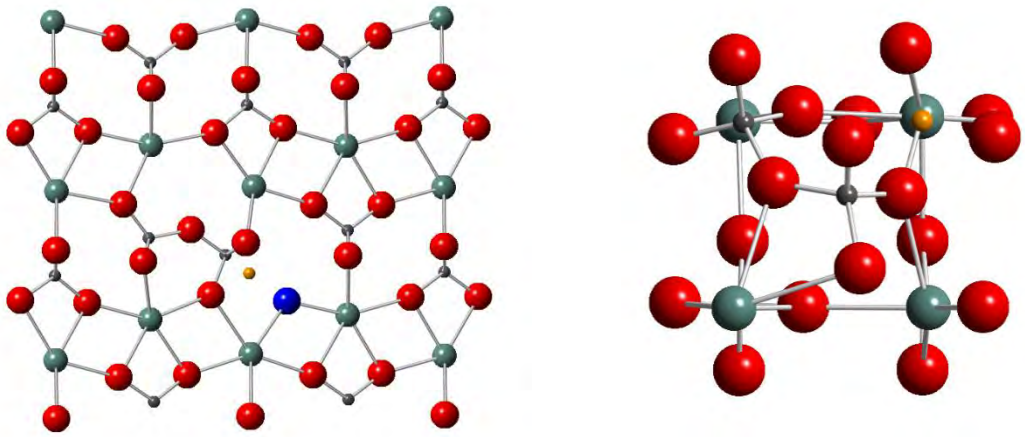

(a) (b)

Figure 4.77: Defect configuration for phosphorus Frenkel pair clusters (a) for the lowest energy Frenkel pair and (b) the second lowest energy cluster. The residual oxygen atom and vacancy sites are highlighted in blue and orange respectively

The oxygen Frenkel pair cluster defects ranged in energy from 3.85 to 9.15 eV. The lowest energy of these is with the oxygen interstitial in the site 2 position, causing a rotation of the phosphate tetrahedron, Figure 4.78 (a). This is closely followed by the interstitial in the site 1 position, with a formation energy of 3.96 eV, Figure 4.78 (b). This indicates that there is little preference for the oxygen interstitial over the two sites. A cluster defect was also identified with three oxygen Frenkel pair surrounding a single phosphorus lattice

atom, resulting in the rotation of the phosphate unit around a P-O bond, Figure 4.78 (c). The formation energy for this cluster was 4.01 eV. A split interstitial in the site 1 position was identified with a local phosphorus Frenkel pair, Figure 4.78 (d). This cluster has a formation energy of 6.19 eV. The lowest energy oxygen interstitial in zircon identified by Crocombette[3] was a split interstitial which resulted in 5 coordinate silicon atoms. In general, the lowest energy oxygen interstitials identified in this study result in rotation of phosphate polyhedra, which does not increase the coordination of the neighbouring phosphorus atoms.

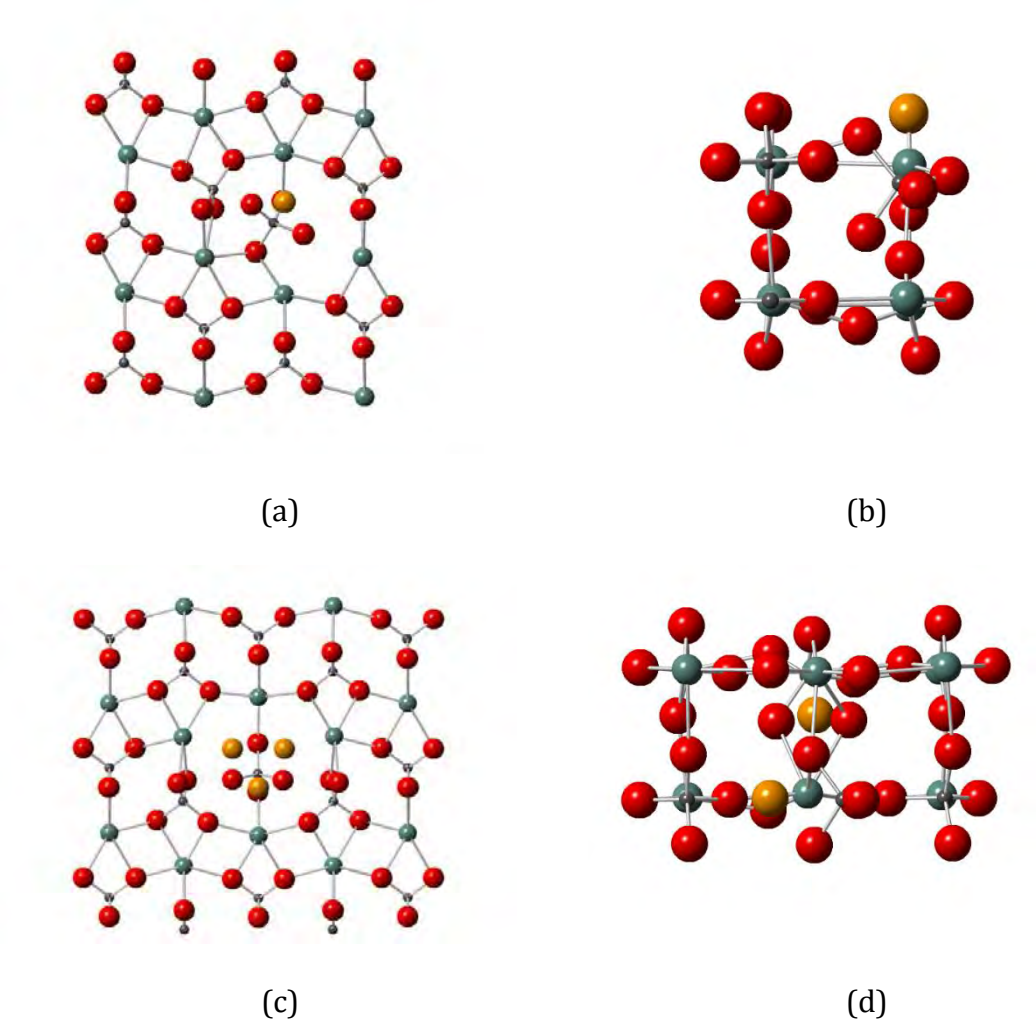

Figure 4.78: Defect configuration for oxygen Frenkel pair clusters (a) for the lowest energy isolated Frenkel pair and (b) in the site 1 position, (c) resulting in rotation of a phosphate tetrahedron and (d) a split interstitial. Vacancy sites are highlighted in orange

The lowest energy anti-site defect was found to accommodate both the yttrium and phosphorus anti-sites in neighbouring positions within the same chain down the *c* axis, illustrated in Figure 4.79. This defect configuration was found to have a formation energy of 7.60 eV and results in the formation of a P_3O_{10} unit. This anti-site was actually found using the Frenkel pair grid search methodology, highlighting one of the strengths of this methodology.

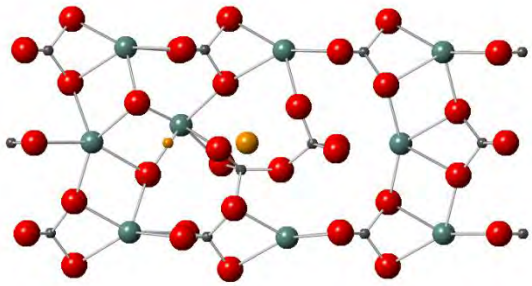

Figure 4.79: Lowest energy anti-site defect

Finally extrinsic defect were investigated using pair potentials derived in chapter 3 for a selection of lanthanide elements. The solution energies following the substitution process for each Lanthanide element onto the yttrium lattice site were calculated. It was found that in both cases the lowest solution energies followed a parabolic trend with ionic radius, with the minimum in solution energy for the dissolution of gadolinium into the xenotime phase. The solution process was found to be favourable for all lanthanide elements from the Ln_2O_3 parent phase whereas the lanthanides were only found to be sparingly soluble from the $LnPO_4$ phase.

4.5 Future Work

- Once a transferable and consistent set of potentials has been fit for actinide elements (including U and Pu), defect calculations can be performed in the xenotime and monazite systems. This would require a charge compensation mechanism and as such this could also be investigated.
- Apply ring statistics to analyse the defect structures and identify motifs which could then be searched for within radiation damage simulations.

4.6 References

1. F. Gao, H. Y. Xiao, Y. G. Zhou, R. Devanathan, S. Y. Hu, Y. L. Li, X. Sun and M. A. Khaleel, *Computational Materials Science*, 2012, **54**, 170-175.
2. V. S. Urusov, A. E. Grechanovsky and N. N. Eremin, *Glass Physics and Chemistry*, 2012, **38**, 55-62.
3. J. P. Crocombette, *Physics and Chemistry of Minerals*, 1999, **27**, 138-143.

CHAPTER 5

Atomistic Simulation of Xenotime Surfaces

Table of Contents

Table of Figures

5.1 Introduction

In this chapter we investigate the validity of the potentials derived previously by calculating surface and attachment energies for the low index surfaces of xenotime and use these to predict crystal morphologies. Xenotime is often found as an accessory mineral, occurring alongside other minerals such as zircon and monazite. It is especially difficult to separate zircon and xenotime based on habit alone as they adopt very similar morphologies[1]. The difficulty in comparing the calculations that follow with experimental data arise from three main assumption:

- The model assumes pure xenotime with no impurity species within the bulk or at the surface.
- The calculations here are carried out in a vacuum and assume no interaction with any sort of medium or with other neighbouring minerals.
- These are static calculations and performed at a temperature of 0 K.

The first assumption is important as most natural samples of xenotime will contain varying levels of Ln^{3+} and Ac^{4+} amongst other impurities[2]. These impurity species can have an impact on the properties of the material, including the surface morphology. It has been shown in similar studies that the defects at the surface can alter the relative surface energies of the surfaces and ultimately alter the morphology[3, 4]. The other two assumptions can be considered as the conditions in which the natural crystals are formed. It is well documented that crystals of the same mineral can adopt very different morphologies based on the crystallisation conditions[5]. Not only that but these conditions may also be variable with time. This can also be seen computationally with surface hydration altering the surface energies and having a considerable impact on the simulated morphology[6]. Despite these assumptions it has been shown that these type of

simulations can produce results that are in considerable agreement with experimental data. Figure 5.1 (a) shows an assortment of xenotime crystals from Brazil[7]. This demonstrates the variation in morphology which can be observed from samples within the same geological site. Figure 5.1 (b) shows a scanning electron micrograph of an unusual xenotime morphology identified from a sample from Mozambique[8]. This morphology features the {101} and {301} surfaces.

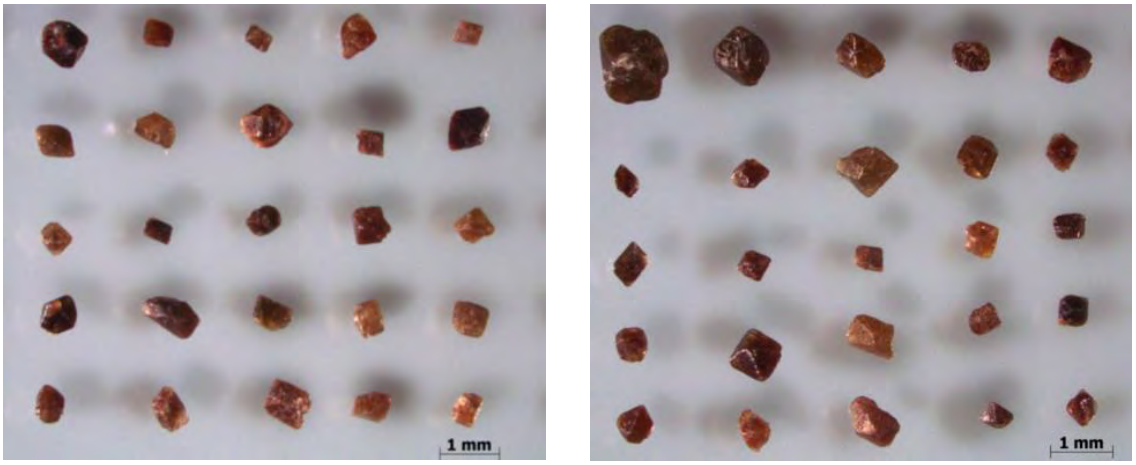

(a)

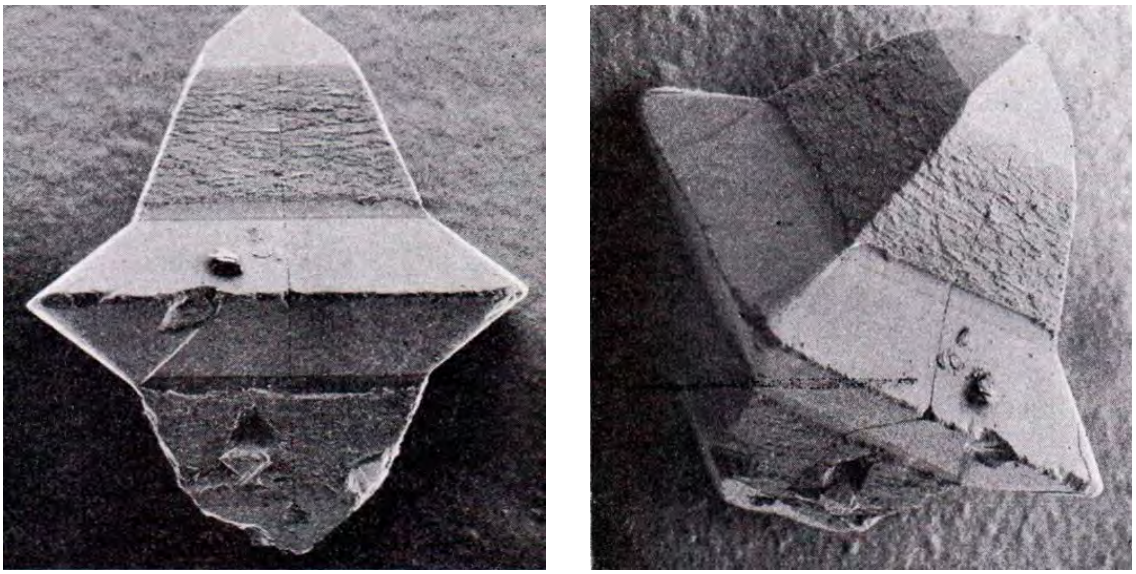

(b)

Figure 5.1: Experimentally observed xenotime morphologies from (a) Brazil[7] and (b) Mozambique[8]

5.2 Surface Energy Calculations

The surface energies for a selection of the bulk terminated and geometry optimised surfaces in Xenotime have been calculated. The lowest energy bulk terminated surface is found to be the {100} surface with a calculated surface energy of 1.078 J m^{-2} whilst the lowest energy surface after geometry optimisation is found to be the {211} surface, with a surface energy of 0.776 J m^{-2}. As discussed previously it has been shown in similar studies that micro-faceting a surface by introducing systematic vacancies can reduce the surface energy considerably. As such the ten low Miller index surfaces investigated in this study are discussed in more detail hereafter.

Table 5.1: Surface and attachment energies for the bulk terminated and geometry optimised surfaces. Only the lowest energy cut is shown with no consideration for micro-faceting of the surfaces.

Surface	Bulk Terminated Surface Energy / J m^{-2}	Geometry Optimised Surface Energy / J m^{-2}	Attachment Energy / eV per unit cell
{100}	1.078	1.022	-0.116
{110}	1.334	1.244	-0.201
{101}	1.508	1.337	-0.246
{112}	1.991	1.773	-0.624
{021}	2.333	2.044	-0.584
{301}	2.579	2.263	-0.894
{111}	2.727	2.467	-0.531
{211}	2.744	0.776	-0.733
{012}	3.488	1.503	-0.966
{001}	5.324	5.036	-0.660

5.2.1 {100} surface

Only one surface cut was identified for the {100} surface. Here the surface is terminated by phosphate units and seven coordinate yttrium atoms. This is a type II surface consisting of neutral repeating units, composed of positive and negative charged layers.

It can be seen in Figure 5.2 that there is very little relaxation of the surface ions. There is a small reduction in the distance between the first repeating unit at the surface and the second repeating unit upon relaxation, as demonstrated by the Y-Y distance shortening from 3.769 to 3.700 Å. In contrast there is an elongation of the distance between the second and third repeating layer with the Y-Y distance lengthening from 3.769 to 3.786 Å. This small relaxation is manifested in the surface relative surface energies or 1.078 and 1.022 J m^{-2} for the bulk terminated and geometry optimised surfaces, respectively.

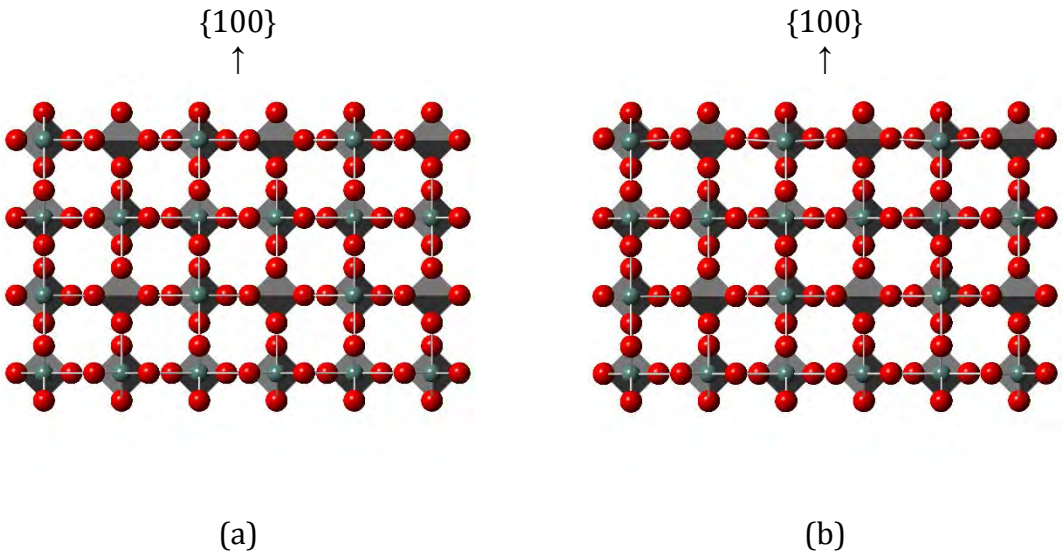

Figure 5.2: Simulated {100} surface, (a) bulk terminated and, (b) geometry optimised.

5.2.2 {110} surface

Two surface cuts have been identified for the {110} surface. The most stable surface is illustrate in Figure 5.3. This is a type II surface consisting of neutral repeating units, composed of positive and negative charged layers, arranged in an ABCD packing sequence. The surface is terminated by phosphate tetrahedra and six coordinate yttrium atoms. Here the main relaxation effects are seen in the top layer with the yttrium atoms descending slightly down towards the bulk and the phosphorus atoms shifting towards the surface. This is evident from the Y-P distances between the A and C layers which are equivalent for the bulk terminated configuration at a distance of 4.889 Å. In contrast the

Y_A-P_C distance in the optimised configuration is reduced to 4.813 Å whilst the P_A-Y_C distance is elongated to 5.020 Å. This has the effect of shortening the Y-O bonds between the yttrium in the surface layer and the oxygen atoms in the subsequent repeating layer from 2.315 to 2.277 Å. The oxygen atoms at the surface are also pulled down along with the yttrium, shortening the Y-O distance from 2.425 to 2.340 Å. This distorts the phosphate tetrahedra by increasing the O-P-O angle between these oxygen atoms and the associated phosphorus atom from 110.85 to 113.68°. These small relaxations reduce the surface energy from 1.334 to 1.244 J m^{-2}.

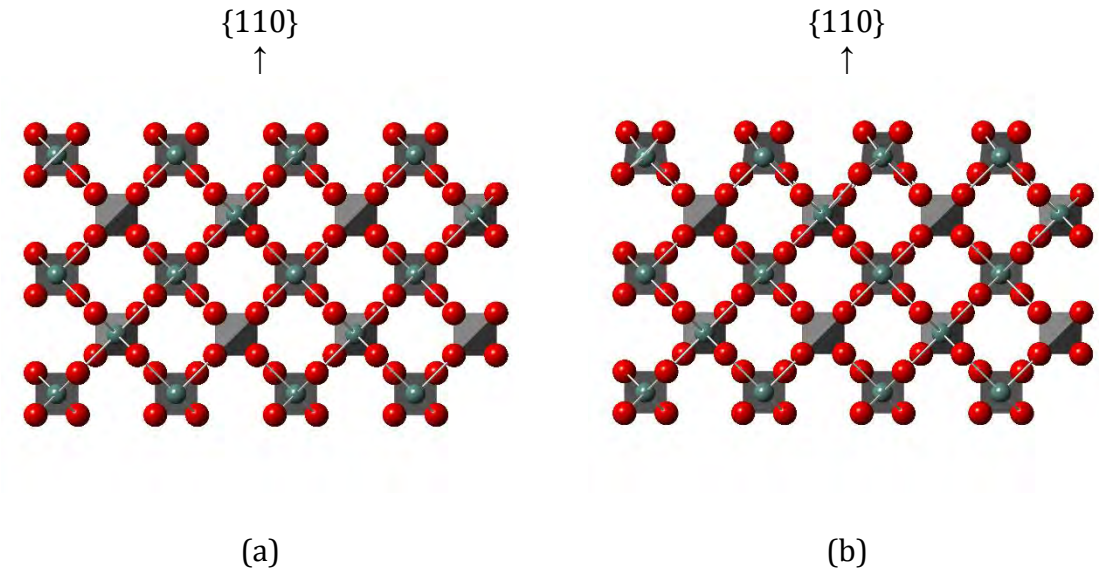

Figure 5.3: First surface cut for the simulated {110} surface, (a) bulk terminated and, (b) geometry optimised.

A second less stable cut was also identified which is illustrated in Figure 5.4. This cut is a type II surface made of neutral repeating units which have a dipole perpendicular to the surface. This surface is terminated by two coordinate phosphorus atoms and four and eight coordinate yttrium atoms. The eight coordinate yttrium atoms are coordinated to dangling oxygen atoms. Upon geometry optimisation there is a great deal of relaxation, with the aforementioned dangling oxygen atoms coordinating with the two coordinate

phosphorus atoms to form phosphate tetrahedra at the surface. As such the previously eight coordinate yttrium atoms are reduced to seven coordinate. This relaxation reduces the surface energy from 6.984 to 1.304 J m^{-2}.

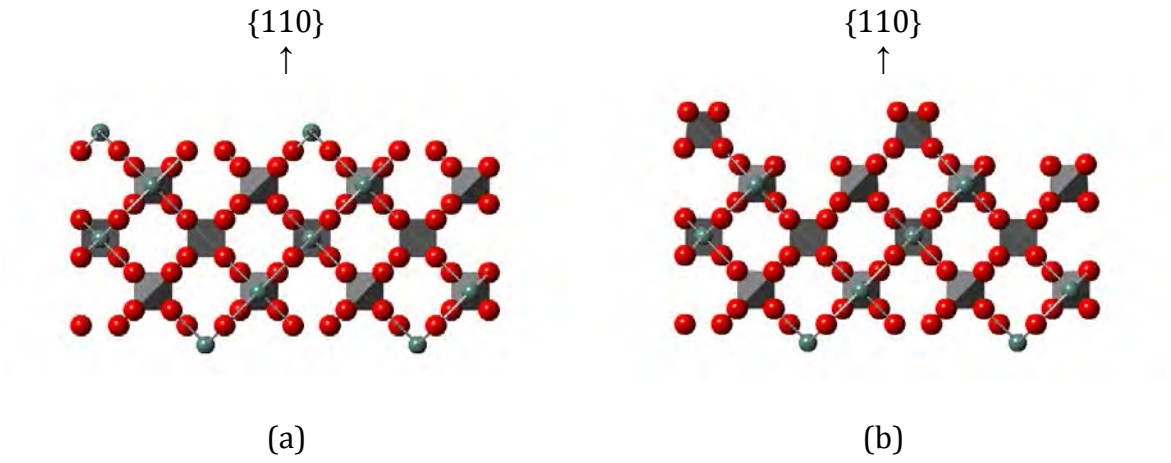

Figure 5.4: Second surface cut for the simulated {110} surface (a) bulk terminated and, (b) geometry optimised.

The micro-faceted surface is illustrated in Figure 5.5. This was achieved by translating oxygen atoms from the bottom of region 1 to the surface to satisfy the coordination of the phosphorus atoms, whilst maintaining charge neutrality by translating an equivalent number of oxygen atoms from the surface to the bottom of region 1. This forms a type II surface with no dipole perpendicular to the surface, where the neutral layers have been labelled A-D ranging from the surface towards the bulk. The surface is terminated by phosphate units and yttrium atoms with coordination ranging from eight to six. The lowest coordination yttrium atoms are found at the peaks of the faceted surface whilst the eight coordinate yttrium atoms are located in the troughs. Again it can be seen that the O-P-O angle between the outermost oxygen atoms and the associated phosphorus atom at the peaks is distorted from 110.85 to 113.43°. This distortion is correlated to the position of the phosphate groups on the surface, with the phosphate units in the subsequent layers having a smaller distortion to 112.71 and 111.82° for the phosphate

groups in layers B and C respectively. The yttrium atoms at the surface move towards the bulk upon geometry optimisation whilst the phosphorus atoms move away from the bulk, as seen previously for the lowest energy cut. Here the Y_A-P_C distance is reduced from 4.889 to 4.788 Å whilst the P_A-Y_C distance is increased to 4.956 Å. This magnitude of this effect is less for the surface atoms in subsequent layers, with Y_B-P_D, Y_C-P_E, P_B-Y_D and P_C-Y_E distances of 4.865, 4.861, 4.940 and 4.849 Å. The surface energy for the micro-faceted surface was calculated to be 1.414 and 1.327 J m^{-2} before and after geometry optimisation respectively

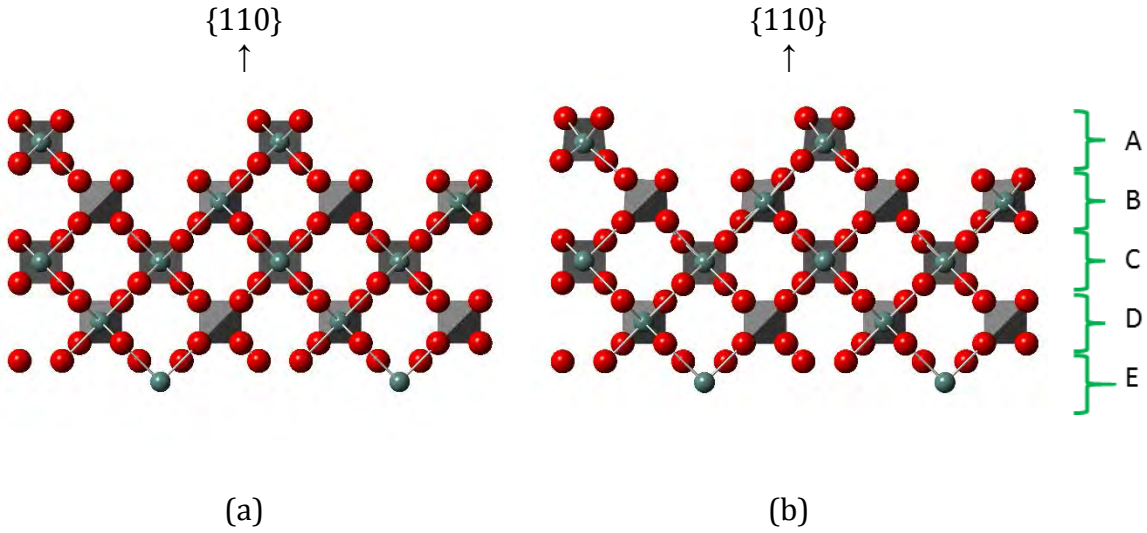

Figure 5.5: Second surface cut for the simulated {110} surface after micro-faceting, (a) bulk terminated and, (b) geometry optimised.

5.2.3 {101} surface

Four surface cuts have been identified for the {101} surface. The lowest energy cut is illustrated in Figure 5.6. This is a type II surface consisting of neutral layers with no dipole perpendicular to the surface. The surface is terminated by phosphate groups and five coordinate yttrium atoms. Once again there is little relaxation upon geometry optimisation, with the surface yttrium atoms shifting toward the bulk. This can be seen from the Y-Y distances between the two constituent yttrium atoms in the $R_0^2(4)$ rings within the surface layer reducing from 3.769 to 3.582 Å. In contrast the surface

phosphorus atoms shift slightly away from the bulk with P-P distance elongating from 3.769 to 3.837 Å. The surface energy calculated before and after geometry optimisation was 1.508 and 1.337 J m^{-2} respectively.

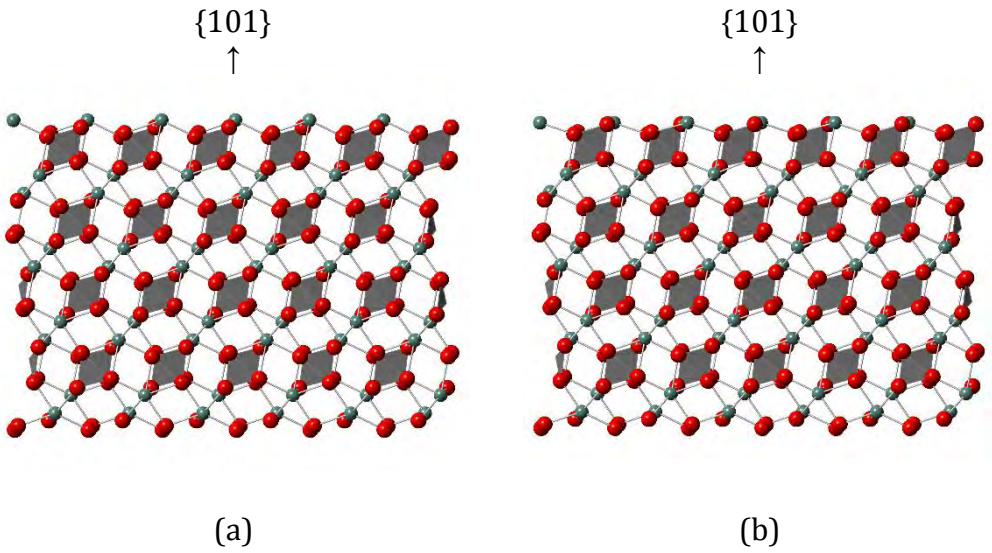

Figure 5.6: First surface cut for the simulated {101} surface (a) bulk terminated and, (b) geometry optimised.

The second cut is another type II surface terminated by seven coordinate yttrium atoms and three coordinate phosphorus atoms illustrated in Figure 5.7. There is minimal distortion to the yttrium atoms at the surface with the Y-Y distance elongating from 3.769 to 3.784 Å. The phosphorus atoms on the surface shift toward the bulk after geometry optimisation with the P-P distance shortening from 3.769 to 3.534 Å. The surface energy was calculated to be 3.602 and 3.290 J m^{-2} for the bulk terminated and geometry optimised surfaces respectively.

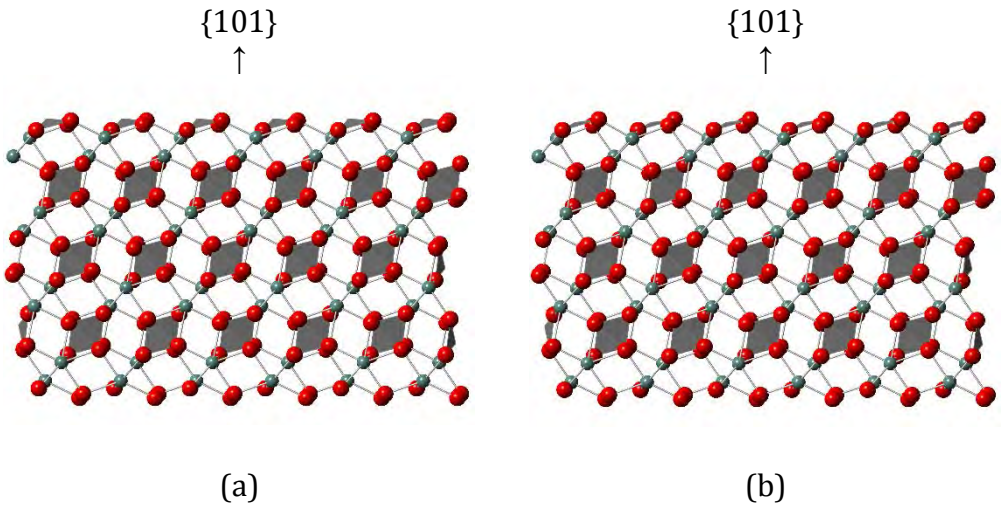

Figure 5.7: Second surface cut for the simulated {101} surface (a) bulk terminated and, (b) geometry optimised.

It is possible to micro-facet the surface by translating the surface oxygen atoms which are part of the $R_0^2(4)$ rings to the bottom of region 1 and translating the oxygen atoms from the bottom of region 1 to the surface to satisfy the coordination of the phosphorus atoms at the surface and maintain charge neutrality, shown in Figure 5.8. This surface is terminated by phosphate groups and both seven and six coordinate yttrium atoms. There is very little relaxation upon geometry optimisation with a small stabilisation of the surface from 1.652 to 1.556 J m^{-2}.

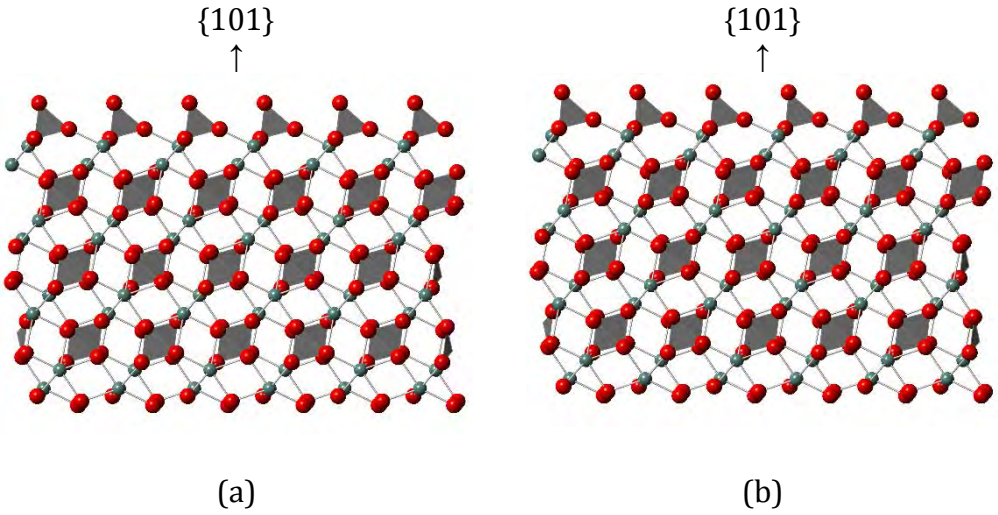

Figure 5.8: Second surface cut for the simulated {101} surface after micro-faceting, (a) bulk terminated and, (b) geometry optimised.

The third surface cut is illustrated in Figure 5.9. This surface is terminated by two, three and four coordinate phosphorus atoms. This surface undergoes a great deal of relaxation upon geometry optimisation with the two coordinate phosphorus atoms polymerising with the adjacent four coordinate phosphate groups. This polymerisation increases the coordination of the phosphorus atom from two to three, however the rotation and translation of the two coordinate phosphorus atom removes the two oxygen atoms from the coordination sphere of the adjacent yttrium atom, reducing its coordination from eight to six. This large relaxation is manifested in the relative surface energies for the bulk terminated and geometry optimised surfaces of 3.885 and 2.268 J m^{-2} respectively.

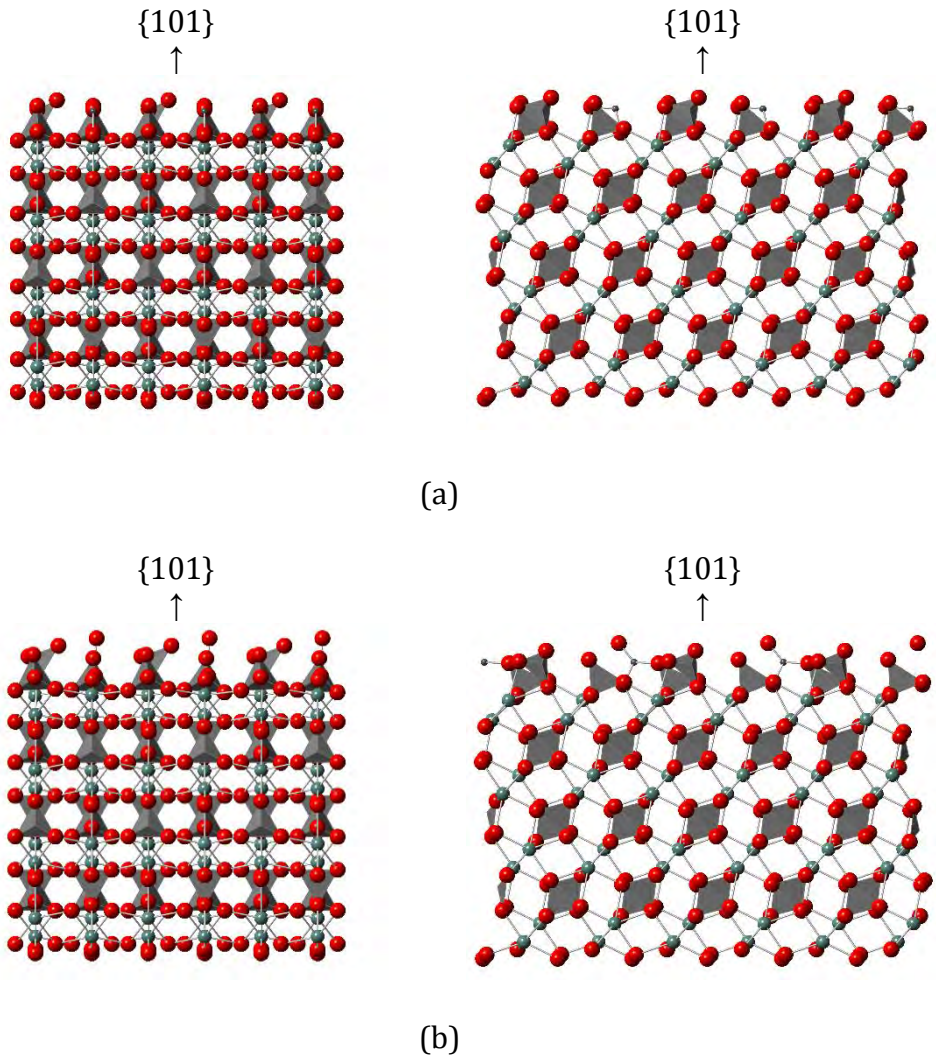

Figure 5.9: Third surface cut for the simulated {101} surface (a) bulk terminated and, (b) geometry optimised.

The fourth surface cut is illustrated in Figure 5.10. This surface is terminated by yttrium atoms with coordination ranging from four to seven. Once again, there is a considerable relaxation with a distortion of the $R_0^2(4)$ ring between the five and seven coordinate yttrium atoms. This also causes a rotation of the phosphate group which is edge sharing with the five coordinate yttrium atoms. This large relaxation is manifested in the relative surface energies for the bulk terminated and geometry optimised surfaces of 3.885 and 3.492 J m^{-2}, respectively.

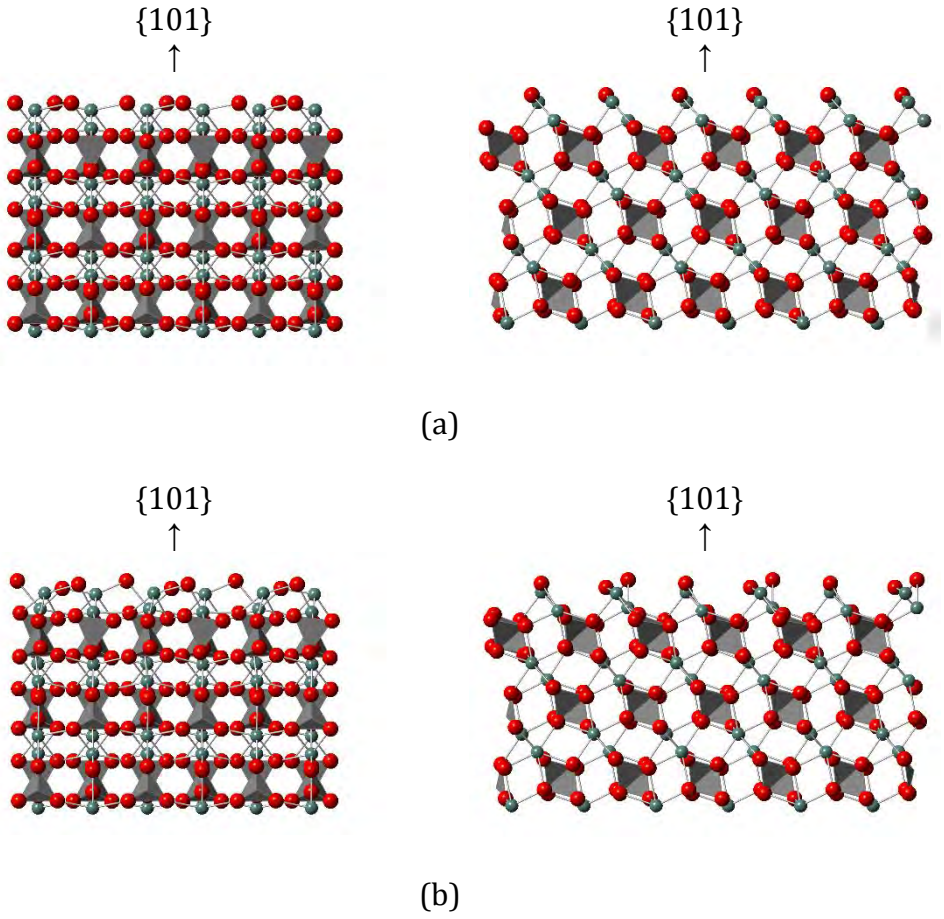

Figure 5.10: Fourth surface cut for the simulated {101} surface (a) bulk terminated and, (b) geometry optimised.

5.2.4 {112} surface

One surface cut has been identified for the {112} surface, illustrated in Figure 5.11. The surface is a type II surface, terminated by phosphate groups and five coordinate yttrium atoms. There is very little distortion to the phosphate tetrahedra upon geometry optimisation, with the main differences in the Y-Y and P-P distances within the surface layer. These are elongated from 3.769 Å to 3.921 and 3.854 Å respectively. These small relaxations reduce the surface energy from 1.991 to 1.773 J m^{-2}.

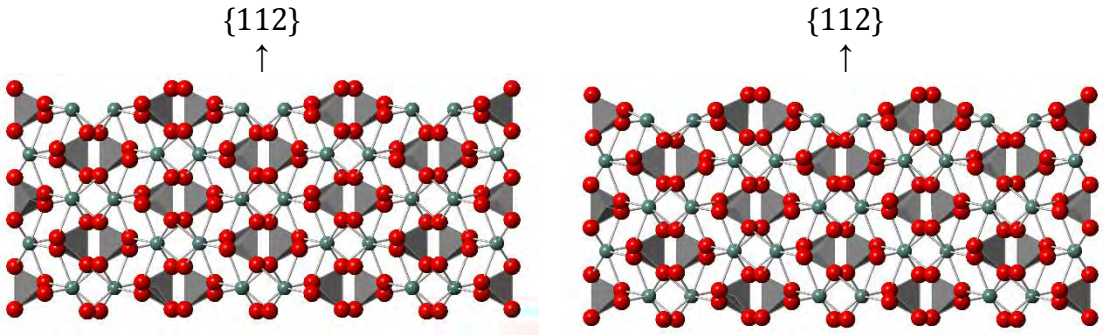

Figure 5.11: Simulated {112} surface (a) bulk terminated and, (b) geometry optimised.

5.2.5 {021} surface

Two surface cuts have been identified for the {021} surface. The lowest energy cut is illustrated in Figure 5.12. Once again this is a type II surface, terminated by yttrium atoms with coordination ranging from five to seven, phosphate groups and three coordinate phosphorus atoms. The five coordinate yttrium atoms shift towards the bulk upon geometry optimisation with the distance between the constituent yttrium atoms of the $R_0^2(4)$ rings reducing from 3.769 to 3.615 Å. In contrast, two of the oxygen atoms, which are coordinated to the three coordinate phosphorus atom and are edge sharing with the seven coordinate yttrium atom, move away from the bulk. This elongates the Y-O bonds from 2.425 to 2.506 Å whilst the Y-O distance to the adjacent six coordinate yttrium atom elongates from 2.315 to 2.345 Å. These small relaxations are manifested in the calculated surface energies of 2.333 and 2.044 J m^{-2} for the bulk terminated and geometry optimised surfaces respectively.

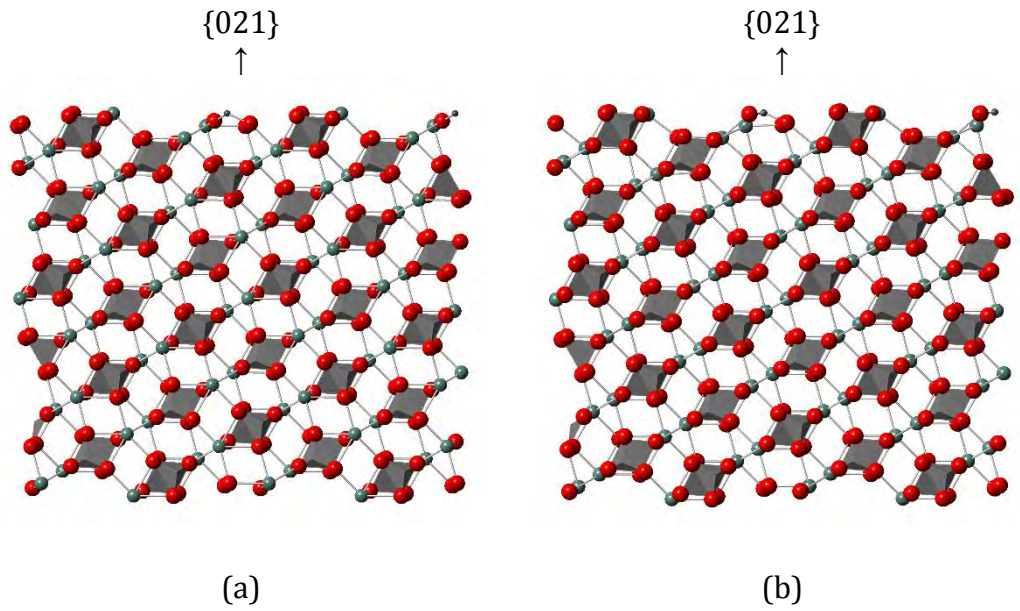

Figure 5.12: First surface cut for the simulated {021} surface (a) bulk terminated and, (b) geometry optimised.

It is also possible to micro-facet this surface by translating a YPO_4 cluster from the surface to the bottom of region 1. This surface is illustrated in Figure 5.13. This surface is terminated by five and seven coordinate yttrium atoms and phosphate units. The main relaxation upon geometry optimisation occurs with the five coordinate yttrium atoms which move toward the bulk. This is evident from the Y-Y distance between the constituent yttrium atoms of the $R_0^2(4)$ rings, which reduces upon optimisation. The magnitude of this effect is greater for the five coordinate yttrium atoms at the peaks which see a contraction of the Y-Y distance from 3.769 to 3.582 Å compared with the other five coordinate yttrium atom where the equivalent distance is reduced to 3.616 Å. The surface energy was calculated to be 1.457 and 1.318 J m^{-2} before and after optimisation respectively. This gives a stabilisation of 0.726 J m^{-2} between the geometry optimised surfaces with and without micro-faceting.

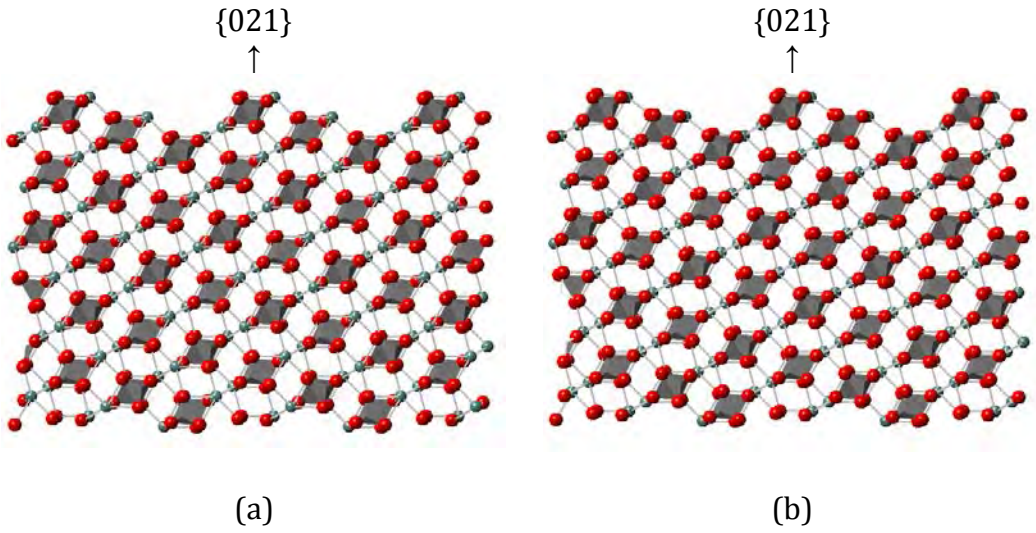

Figure 5.13: First surface cut for the simulated {021} surface after micro-faceting, (a) bulk terminated and, (b) geometry optimised.

The second cut is illustrated in Figure 5.14. This surface is terminated by yttrium atoms with coordination ranging from six to eight along with phosphorus atoms with a coordination of one, three and four. The seven coordinate yttrium atom which is closest to the one coordinate phosphorus atom is coordinated to a dangling oxygen atom. Unsurprisingly this surface undergoes a large relaxation upon geometry optimisation. Most notably the one coordinate phosphorus atom is shifted and polymerises with the phosphate group on the surface, highlighted in blue. The dangling oxygen is removed from the coordination sphere of the aforementioned seven coordinate yttrium atom and coordinated to the previously one coordinate phosphorus atom. As the phosphorus atom shifts it also removes the oxygen atom, which it was originally coordinated to, out of the coordination sphere of the adjacent seven coordinate yttrium atom and an eight coordinate yttrium atom further into the bulk, disrupting an $R_0^2(4)$ ring. The phosphate group that becomes polymerised is also rotated slightly, removing an oxygen atom from the coordination sphere of an adjacent seven coordinate yttrium atom, reducing its

coordination to six. The six coordinate yttrium atoms move towards the bulk, distorting the $R_0^2(4)$ ring with the adjacent yttrium atom. The geometry optimised surface is terminated by five, six and eight coordinate yttrium atoms, along with polymerised P_2O_6 units and three coordinate phosphorus atoms. This large relaxation is evident in the relative surface energies before and after geometry optimisation of 6.919 and 3.268 J m^{-2}, respectively.

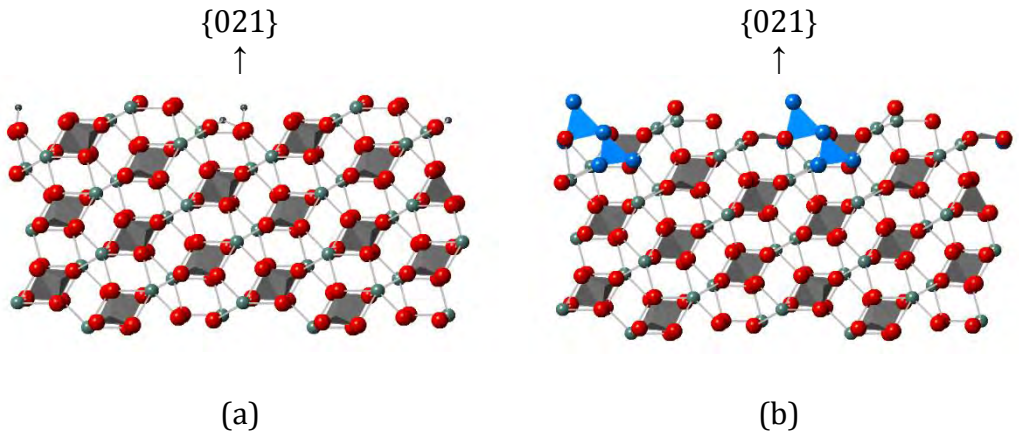

Figure 5.14: Second surface cut for the simulated {021} surface (a) bulk terminated and, (b) geometry optimised.

It is also possible to modify the surface so that it becomes terminated by four, five, seven and eight coordinate yttrium atoms along with three and four coordinate phosphorus atoms, as illustrated in Figure 5.15. Upon optimisation two three coordinate and one four coordinate phosphorus atoms polymerise to form P_3O_{10} chains at the surface, highlighted in blue. The surface energy was calculated to be 3.685 and 1.940 J m^{-2} before and after geometry optimisation, respectively.

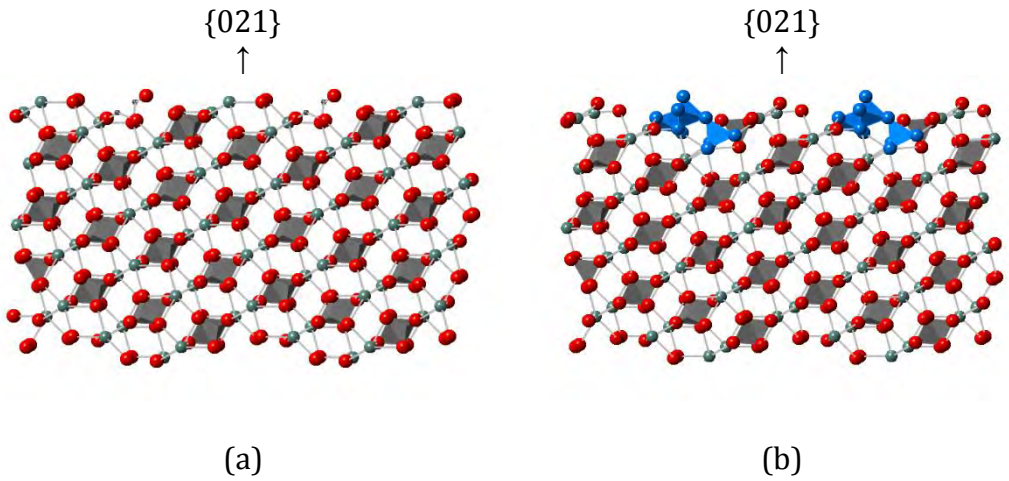

Figure 5.15: Second surface cut for the simulated {021} surface after micro-faceting, (a) bulk terminated and, (b) geometry optimised.

5.2.6 {301} surface

Two surface cuts have been identified for the {301} surface. The lowest energy cut is illustrated in Figure 5.16. This surface is terminated by six, seven and eight coordinate yttrium atoms along with three and four coordinate phosphorus atoms. As with the previous surfaces the under-coordinated yttrium atoms move towards the bulk upon geometry optimisation with the $R_0^2(4)$ Y-Y distance reducing from 3.769 to 3.612 and 3.725 Å for the six coordinate and seven coordinate yttrium atoms respectively. The surface energy was calculated to be 2.579 and 2.263 J m^{-2} before and after geometry optimisation, respectively.

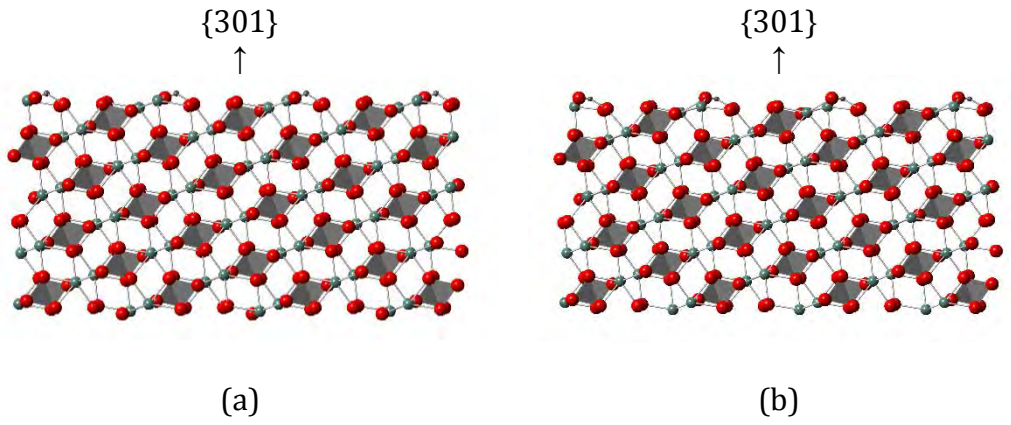

Figure 5.16: First surface cut for the simulated {301} surface (a) bulk terminated and, (b) geometry optimised.

This surface can also be micro-faceted by disrupting the $R_0^2(4)$ rings on the surface and translating one of the oxygen atoms to the bottom of region 1. An oxygen atom can then be translated from the bottom of region 1 to fulfil the coordination of the phosphorus atoms at the surface and maintain charge neutrality. The surface is terminated by five, seven and eight coordinate yttrium atoms along with phosphate tetrahedra and is illustrated in Figure 5.17. There is very little relaxation upon geometry optimisation, with a calculated surface energy of 1.500 and 1.405 J m^{-2} before and after optimisation, respectively.

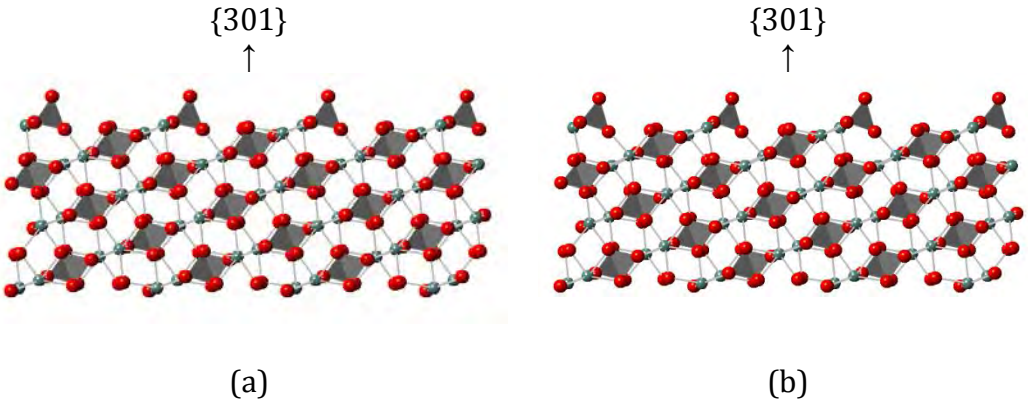

Figure 5.17: First surface cut for the simulated {301} surface after micro-faceting, (a) bulk terminated and, (b) geometry optimised.

The second surface cut is illustrated in Figure 5.18. This surface is terminated by four, seven and eight coordinate yttrium atoms along with three and four coordinate phosphorus atoms. There is substantial relaxation upon geometry optimisation with the polymerisation of both a three and four coordinate phosphorus atoms to form P_2O_7 units, highlighted in blue. There is also a large shift of the dangling oxygen atom coordinated to the seven coordinate yttrium atom. Unsurprisingly, this is a high energy surface which is stabilised greatly upon geometry optimisation, with surface energies of 4.855 and 3.149 J m^{-2} before and after geometry optimisation respectively.

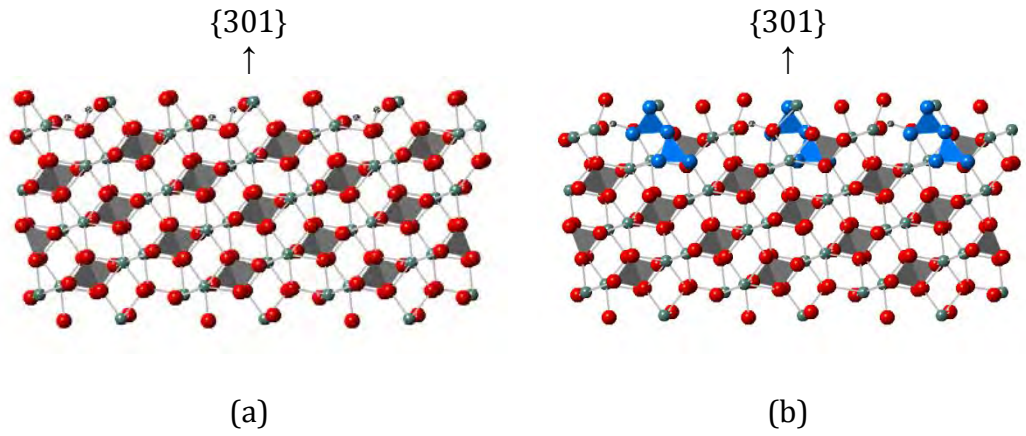

Figure 5.18: Second surface cut for the simulated {301} surface (a) bulk terminated and, (b) geometry optimised.

It is also possible to micro-facet this surface by translating the dangling oxygen atoms to the bottom of region 1 and translating oxygen atoms to the surface to complete the coordination of the phosphorus atom and maintain charge neutrality, illustrated in Figure 5.19. The surface is terminated by five and seven coordinate yttrium atoms along with phosphate tetrahedra. There is little relaxation upon geometry optimisation with the five coordinate yttrium atoms shifting slightly toward the bulk, reducing the $R_0^2(4)$ Y-Y distance from 3.769 to 3.603 Å. The surface energy before and after optimisation is

calculated to be 1.383 and 1.260 J m^{-2} respectively, making this cut the lowest energy cut for the {301} surface after geometry optimisation.

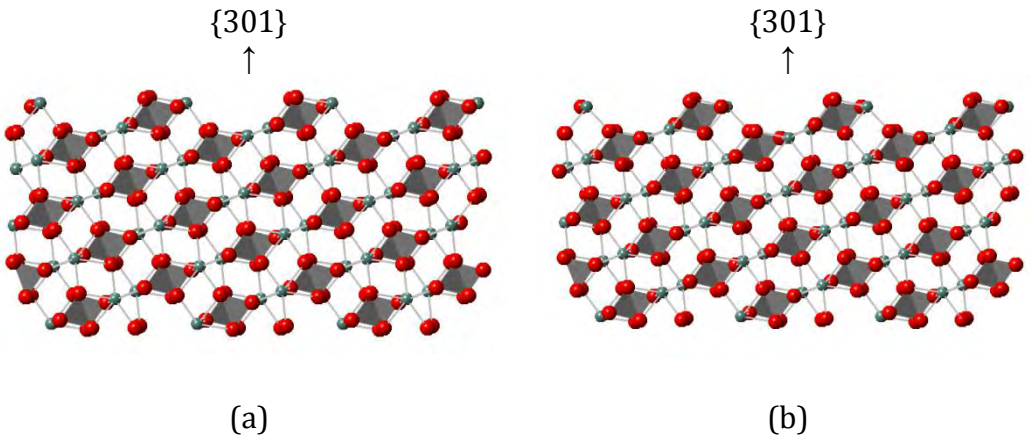

Figure 5.19: Second surface cut for the simulated {301} surface after micro-faceting, (a) bulk terminated and, (b) geometry optimised.

5.2.7 {111} surface

A single surface cut has been identified for the {111} surface, illustrated in Figure 5.20. This surface is terminated by four, six and eight coordinate yttrium atoms, along with three and four coordinate phosphorus atom. There is little relaxation upon geometry optimisation with the under-coordinated yttrium atoms shifting slightly towards the bulk. The Y-Y distance within the $R_0^2(4)$ ring is shortened from 3.769 to 3.684 and 3.670 Å for the six and eight coordinate yttrium atoms, respectively. The surface energy for the bulk terminated and geometry optimised surface were calculated to be 2.727 and 2.467 J m^{-2}, respectively.

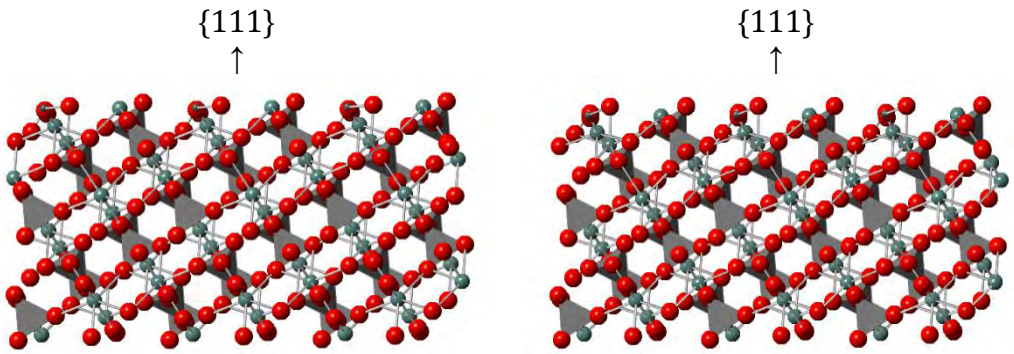

Figure 5.20: Simulated {111} surface (a) bulk terminated and, (b) geometry optimised.

It is also possible to micro-facet the surface by disrupting the $R_0^2(4)$ associated with the six coordinate yttrium atom by translating one of the oxygen atoms to the bottom of region 1. Charge neutrality is maintained by translating an oxygen atom from the bottom or region 1 to satisfying the coordination of the phosphorus atoms at the surface. The surface is terminated by four, five and seven coordinate yttrium atoms along with phosphate tetrahedra and is illustrated in Figure 5.21. There is a large amount of relaxation upon optimisation with the dangling phosphate group rotating, which brings the dangling oxygen into the coordination sphere of the previously four coordinate yttrium, increasing its coordination to five. There is also a considerable shift in the position of the five coordinate yttrium atom, which moves toward the previously four coordinate yttrium. This shift increases the coordination to five and reduces the associated $R_0^2(4)$ Y-Y distance from 3.769 to 3.285 Å. This large relaxation is manifested in the relative surface energies of 1.991 and 1.477 J m^{-2} before and after optimisation, respectively.

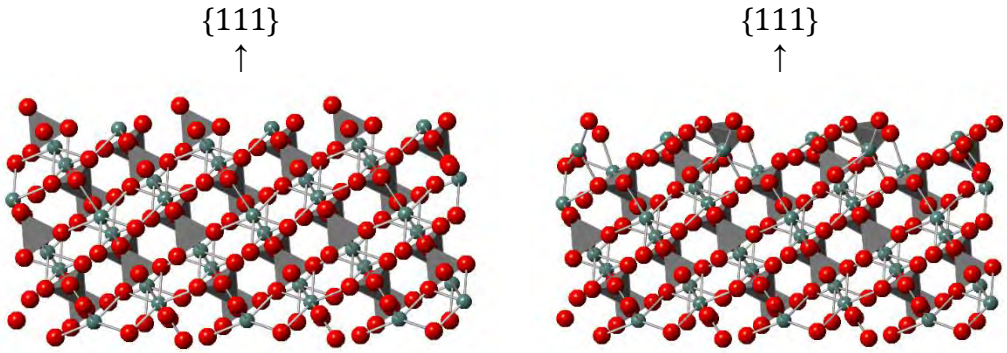

Figure 5.21: Simulated {111} surface after micro-faceting (a) bulk terminated and, (b) geometry optimised.

5.2.8 {211} surface

There are four cuts identified for the {211} surface. The lowest energy surface is illustrated in Figure 5.22. The surface is terminated by seven and eight coordinate yttrium atoms along with three and four coordinate phosphorus atoms. There is a considerable amount of relaxation upon geometry optimisation, mainly effecting the under-coordinated phosphorus atoms. Here the three coordinate phosphorus atoms which are adjacent to each other polymerise with a phosphate group from a lower layer to form P_3O_{10} chains at the surface. This reduces the coordination of the seven coordinate yttrium to five. Similarly the remaining three coordinate phosphorus atoms polymerise with an adjacent phosphate tetrahedron to form a P_2O_7 chain. This relaxation is evident from in the relative surface energies of 2.744 and 0.776 J m^{-2} for the bulk terminated and geometry optimised surfaces, respectively.

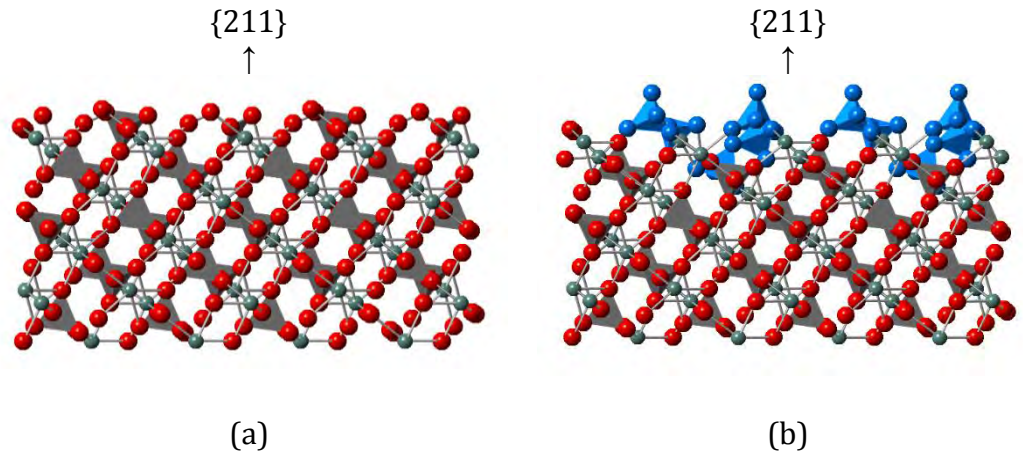

Figure 5.22: First surface cut for the simulated {211} surface (a) bulk terminated and, (b) geometry optimised.

The second lowest energy cut is illustrated in Figure 5.23. This surface is terminated by five and six coordinate yttrium atoms along with phosphate tetrahedra. There is a small amount of relaxation upon geometry optimisation with the oxygen atom which is a member of the $R_0^2(4)$ ring and not coordinated to a phosphorus atom is shifted away from the bulk, distorting the $R_0^2(4)$ ring. The five coordinate yttrium atom is also shifted slightly towards the bulk with a reduction of the $R_0^2(4)$ Y-Y distance from 3.769 to 3.684 Å. The surface energy calculated for the bulk terminated and geometry optimised surfaces are 2.744 and 2.523 J m^{-2}, respectively.

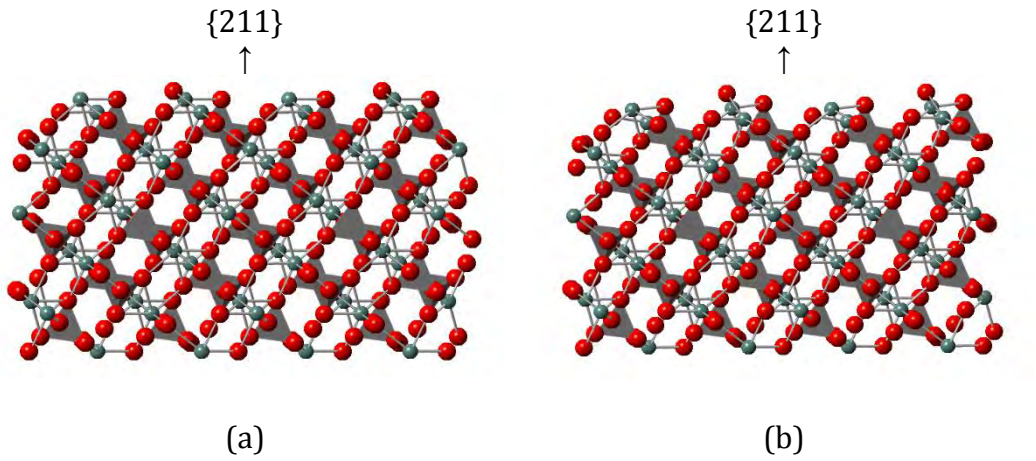

Figure 5.23: Second surface cut for the simulated {211} surface (a) bulk terminated and, (b) geometry optimised.

It is also possible to micro-facet this surface as shown in in Figure 5.24. This surface is terminated by five and seven coordinate yttrium atoms along with two and four coordinate phosphorus atoms. Upon geometry optimisation the two coordinate phosphorus atom shifts towards the seven coordinate yttrium atom, coordinating to the dangling oxygen, and removing it from the coordination sphere of the yttrium atom. It also becomes coordinated to another oxygen atom, increasing the coordination of the phosphorus atom to four. The coordination of the yttrium atom is maintained by the rotation of the phosphate units at the surface, bringing another oxygen into its coordination sphere. The rotation of the phosphate tetrahedra also causes a shift in the position of the five coordinate yttrium atom, increasing its coordination to seven and elongating the $R_0^2(4)$ Y-Y distance from 3.769 to 3.894 Å. This considerable amount of relaxation is manifested in the calculated surface energies before and after relaxation of 3.965 and 1.405 J m^{-2}, respectively.

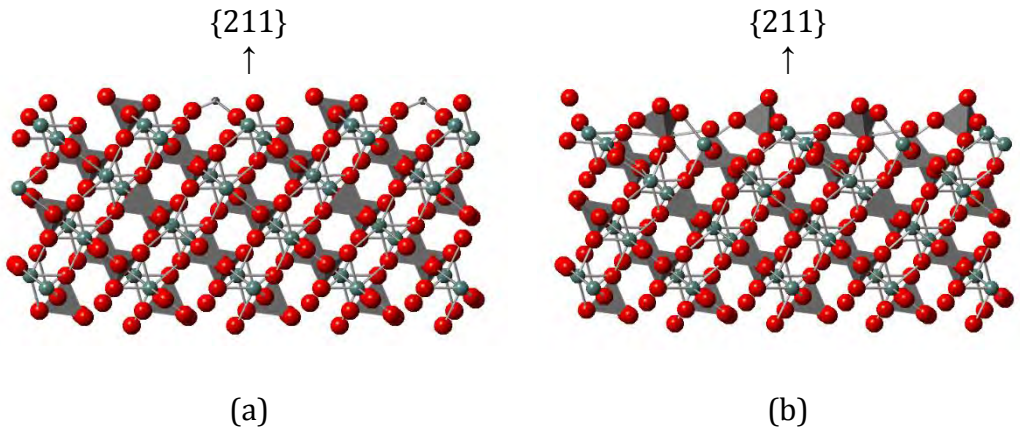

Figure 5.24: Second surface cut for the simulated {211} surface after micro-faceting (a) bulk terminated and, (b) geometry optimised.

The third cut is illustrated in Figure 5.25. The surface is terminated by five coordinate yttrium atoms and three coordinate phosphorus atoms. There is a small amount of relaxation upon optimisation with the five coordinate yttrium atom shifting slightly toward the bulk, shortening the $R_0^2(4)$ Y-Y distance from 3.769 to 3.560 Å. This small relaxation reduces the surface energy from 2.940 to2.691 J m^{-2} after geometry optimisation.

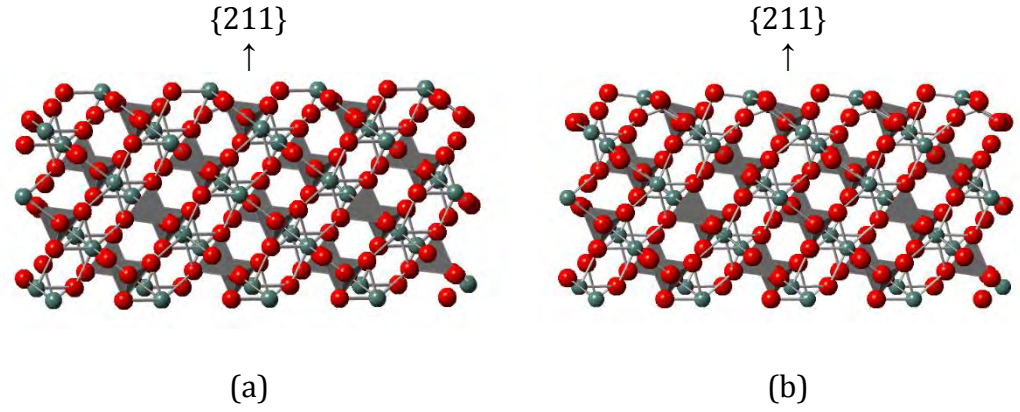

Figure 5.25: Third surface cut for the simulated {211} surface (a) bulk terminated and, (b) geometry optimised.

The final surface cut is illustrated in Figure 5.26. This surface is terminated by six and seven coordinate yttrium atoms along with two coordinate phosphorus atoms. The seven coordinate yttrium atom is coordinated to a dangling oxygen atom. There is considerable relaxation upon geometry optimisation with the two coordinate phosphorus atom shifting and polymerising with a phosphate group further into the bulk. In doing so the dangling oxygen also becomes coordinated to the phosphorus atom, creating P_2O_7 units at the surface. The polymerised phosphate unit is rotated which removes an oxygen atom from the coordination sphere of the six coordinate yttrium atom, reducing its coordination to five. Similarly the dangling oxygen is removed from the coordination sphere of the seven coordinate yttrium atom, reducing its coordination to six. This relaxation in manifested in the relative surface energies before and after optimisation of 5.333 and 1.750 J m^{-2} respectively.

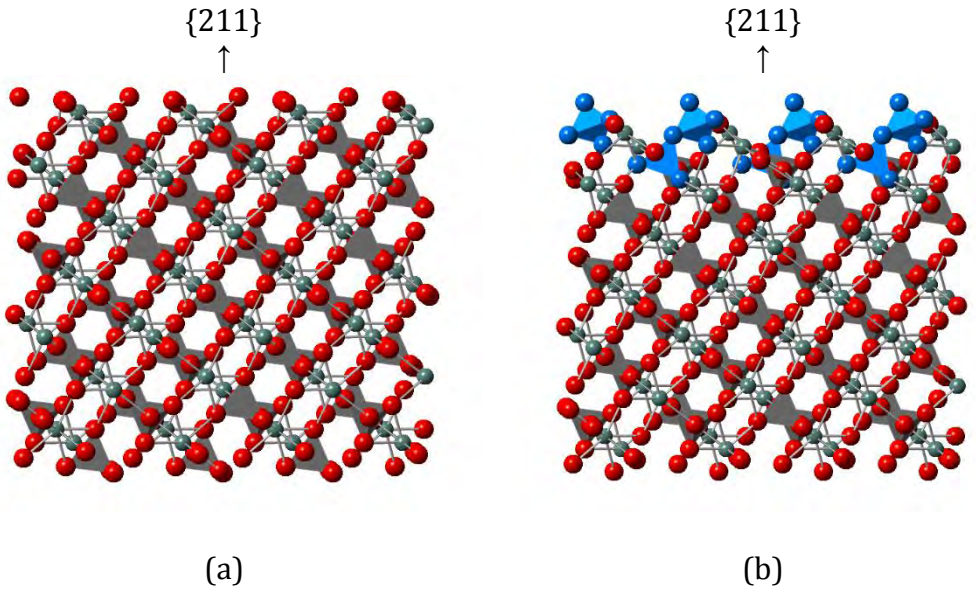

Figure 5.26: Fourth surface cut for the simulated {211} surface (a) bulk terminated and, (b) geometry optimised.

It is also possible to micro-facet the surface as illustrated in Figure 5.27. The surface is terminated by five and six coordinate yttrium atoms along with phosphate tetrahedra.

There is very little relaxation upon geometry optimisation with a slight rotation of the surface phosphate tetrahedra. The surface energy of the surface before and after optimisation was calculated to be 1.890 and 1.628 J m^{-2}, respectively.

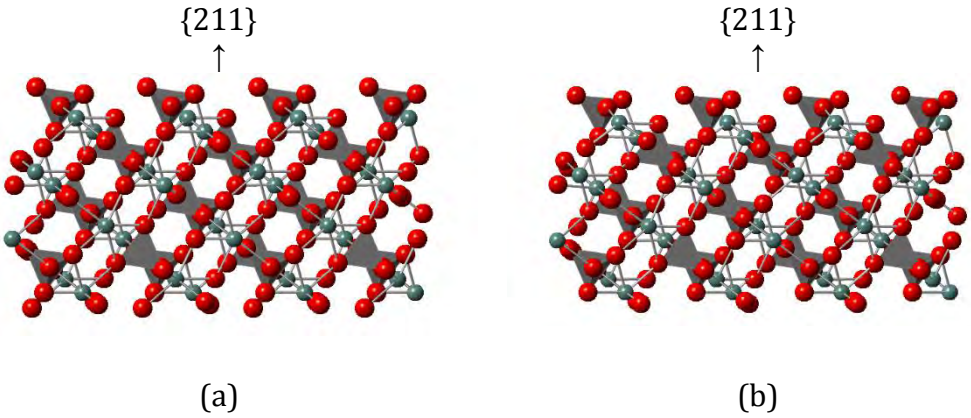

Figure 5.27: Fourth surface cut for the simulated {211} surface after micro-faceting (a) bulk terminated and, (b) geometry optimised.

5.2.9 {012} surface

Three cuts have been identified for the {012} surface. The lowest energy cut is illustrated in Figure 5.28. This surface is terminated by five and six coordinate yttrium atoms along with two and four coordinate phosphorus atoms. There is a large amount of relaxation upon geometry optimisation with a rotation of the two coordinate phosphorus atom to coordinate with two oxygen atoms from two adjacent $R_0^2(4)$ rings. This rotation removes an oxygen atom from the coordination sphere of the previously five coordinate yttrium atom, reducing its coordination to four. This relaxation is manifest in the relative surface energies of the bulk terminated and geometry optimised surfaces of 3.488 and 1.503 J m^{-2} respectively.

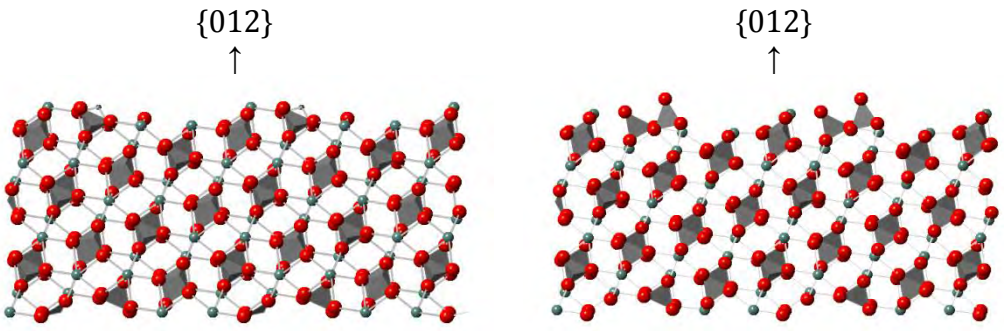

Figure 5.28: First surface cut for the simulated {012} surface (a) bulk terminated and, (b) geometry optimised.

The second lowest energy cut is illustrated in Figure 5.29. This surface is terminated by five, six and seven coordinate yttrium atoms along with two, three and four coordinate phosphorus atoms. There is a large amount of relaxation upon geometry optimisation with the three coordinate phosphorus atom shifting and polymerising with a phosphate group from a deeper layer, forming P_2O_7 units highlighted in blue. This polymerisation causes a rotation of the polymerising phosphate group. These deformations cause an eight coordinate yttrium atom to shift away from the bulk, toward the six coordinate yttrium atom at the surface, reducing the $R_0^2(4)$ Y-Y distance from 32.769 to 3.524 Å. There is also a small rotation of the two coordinated phosphorus atom which disrupts an $R_0^2(4)$ and an $R_1^1(4)$ ring to form an $R_1^2(6)$ ring. This considerable relaxation is manifest in the relative surface energies of 4.576 and 3.512 J m^{-2} for the bulk terminated and geometry optimised surfaces, respectively.

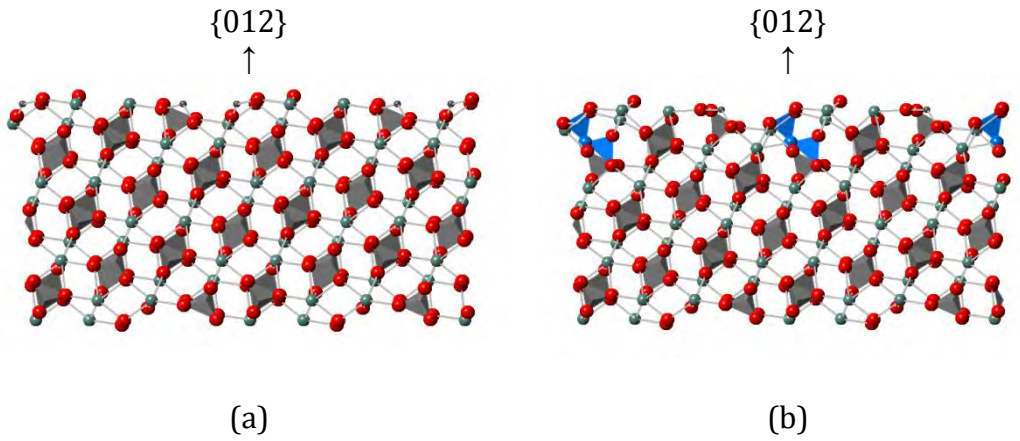

Figure 5.29: Second surface cut for the simulated {012} surface (a) bulk terminated and, (b) geometry optimised.

The final cut is illustrated in Figure 5.30. The surface is terminated by three, five, six and eight coordinate yttrium atoms, along with two and four coordinate phosphorus atoms. This surface undergoes a considerable amount of relaxation upon geometry optimisation. Here the eight coordinate yttrium is coordinated to a dangling oxygen atom which becomes coordinated to the two coordinate phosphorus atom, ultimately removing it from the coordination sphere of the yttrium atom and reducing its coordination to seven. This causes a rotation of the formerly two coordinate phosphorus atom, bringing it into coordination with another oxygen atom, forming a phosphate tetrahedron at the surface. There is also a large lateral shift in the position of the three coordinate yttrium to a site which is edge sharing with one and corner sharing with two phosphate tetrahedra, increasing its coordination to four. This large amount of relaxation is clear in the relative surface energies of 5.500 and 1.504 J m^{-2} for the bulk terminated and geometry optimised surfaces respectively.

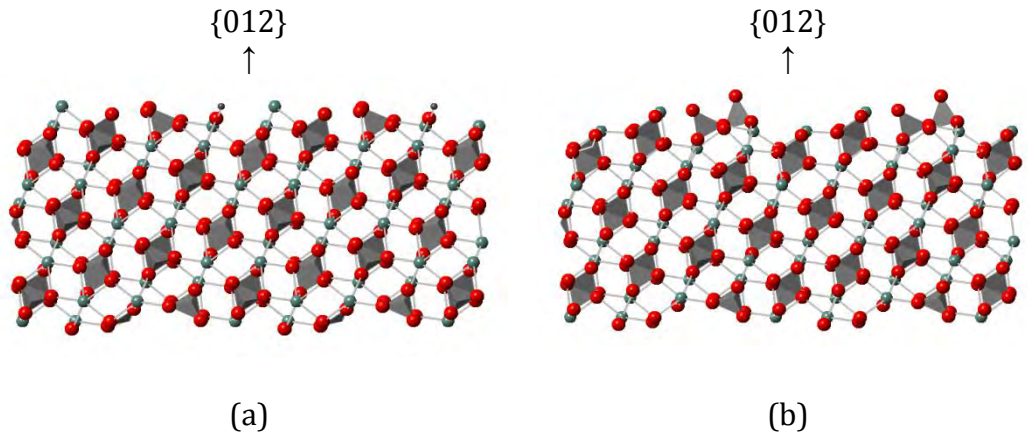

Figure 5.30: Third surface cut for the simulated {012} surface (a) bulk terminated and, (b) geometry optimised.

5.2.10 {001} surface

One surface cut has been identified for the {001} surface. This surface is terminated by six and eight coordinate yttrium atoms along with two and four coordinate phosphorus atoms and is illustrated in Figure 5.31. There is minimal relaxation upon geometry optimisation with the $R_1^1(4)$ Y-P distance reducing from 3.002 to 2.873 Å after geometry optimisation. This small amount of relaxation reduces the surface energy from 5.324 to 5.036 J m^{-2}.

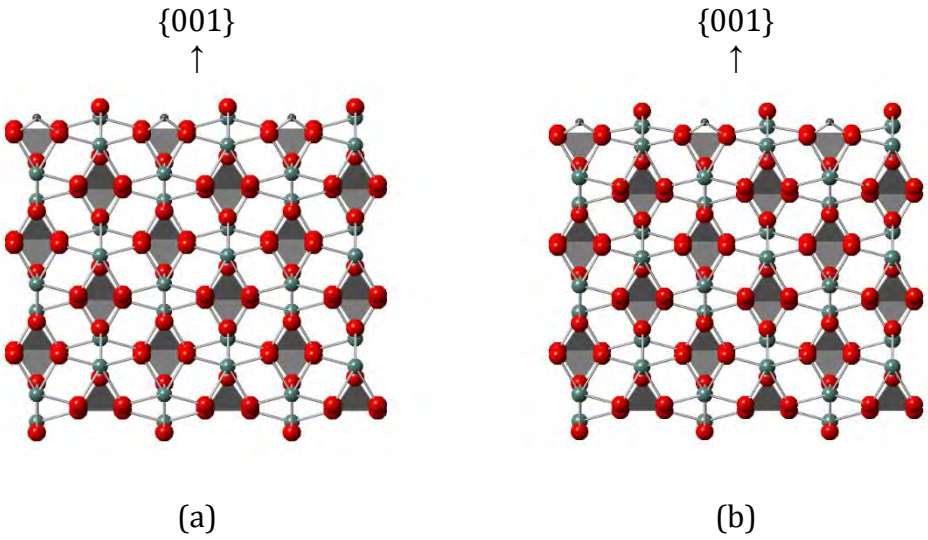

Figure 5.31: Simulated {001} surface, (a) bulk terminated and, (b) geometry optimised.

It is possible to micro-facet this surface by translating the oxygen atoms coordinated to the yttrium atom from the surface to the bottom of region 1 and maintaining charge neutrality by translating oxygen atoms to the surface to satisfy the coordination of the phosphorus atoms. This surface is terminated by four and six coordinate yttrium atoms along with phosphate groups and is illustrated in Figure 5.32. There is minimal relaxation upon geometry optimisation with the four coordinate yttrium atom moving toward the bulk, reducing the $R_1^1(4)$ Y-P distance from 3.002 to 2.906 Å. This small relaxation reduces the surface energy from 2.016 to 1.907 J m^{-2}.

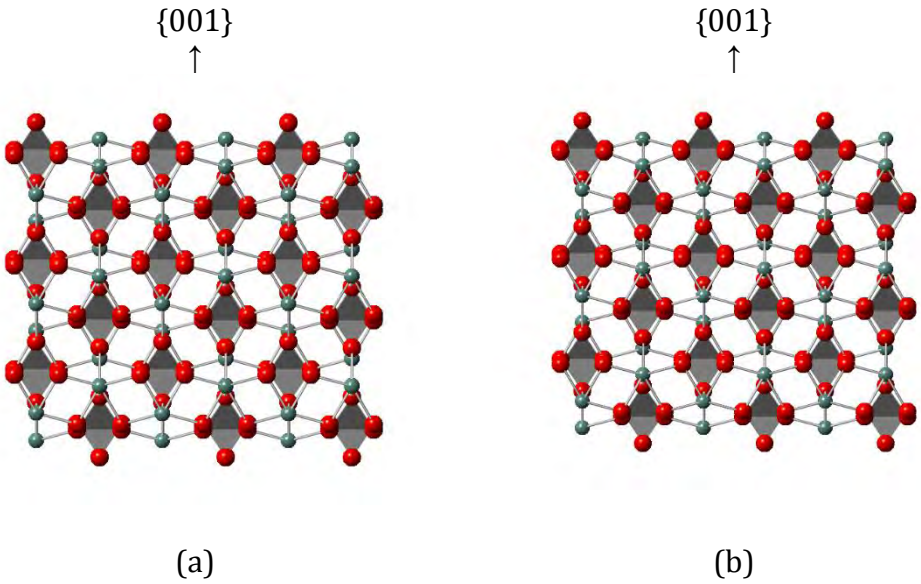

Figure 5.32: Simulated {001} surface after micro-faceting, (a) bulk terminated and, (b) geometry optimised.

5.3 Xenotime Morphology

As discussed previously in chapter 2, it is possible to predict the equilibrium and kinetic morphologies from calculated surface and attachment energies respectively using Wulff's theorem. This can be used to test the validity of the set of interatomic potentials being used.

5.3.1 Equilibrium Morphology

The first morphology, illustrated in Figure 5.33, has been produced using the lowest surface energies for each set of surface planes before geometry optimisation. It can be seen that the morphology is dominated by the {100} and {101} surfaces with percentage surface coverage of 43.59 and 40.72 % respectively. The {110} surface is also expressed to a lesser degree with a surface coverage of 15.69 %.

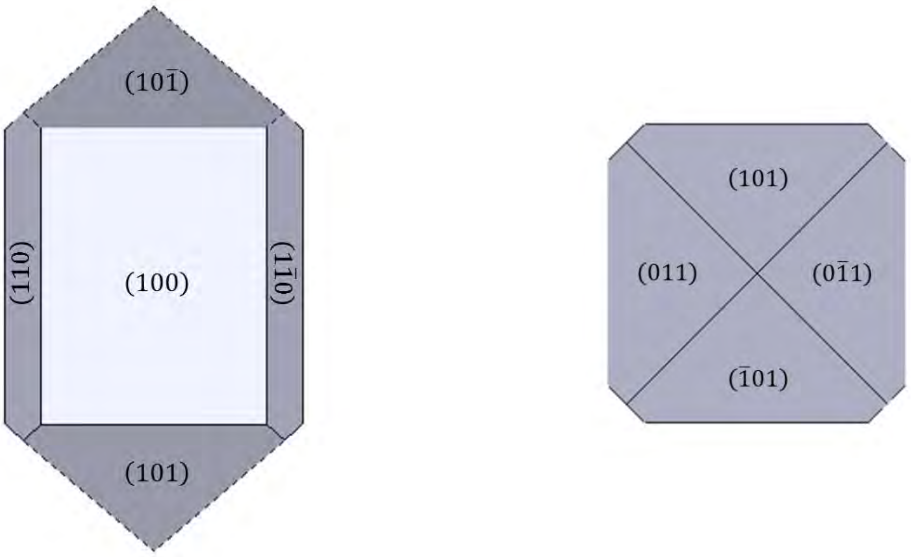

Figure 5.33: Equilibrium morphology generated from the lowest energy bulk terminated surfaces.

Table 5.2: Summary of surface energies used to generate the bulk terminated equilibrium morphology, and the relative surface coverage for each surface.

Surface	Unrelaxed Surface Energy / J m^{-2}	Surface Area / %
{100}	1.078	43.59
{110}	1.334	15.69
{101}	1.508	40.72
{112}	1.991	0.00
{021}	2.333	0.00
{301}	2.579	0.00
{111}	2.727	0.00
{211}	2.744	0.00
{012}	3.488	0.00
{532}	3.669	0.00
{321}	4.487	0.00
{001}	5.324	0.00

The morphology generated from the geometry optimised surface energies is illustrated in Figure 5.34. Here it can be seen that there is a large difference between the morphology generated from the geometry optimised surface energies compared with the bulk terminated surface energies. This morphology is almost entirely dominated by the {211} surfaces with a percentage coverage of 97.53 %. In contrast to the bulk terminated morphology, the {100}, {110} and {101} surfaces are not expressed at all. The {012} surfaces are expressed to a very small degree with a surface coverage of 2.47 %. This discrepancy between the two morphologies highlights the importance of geometry optimising the surfaces and the impact of the considerable relaxation described in the previous section.

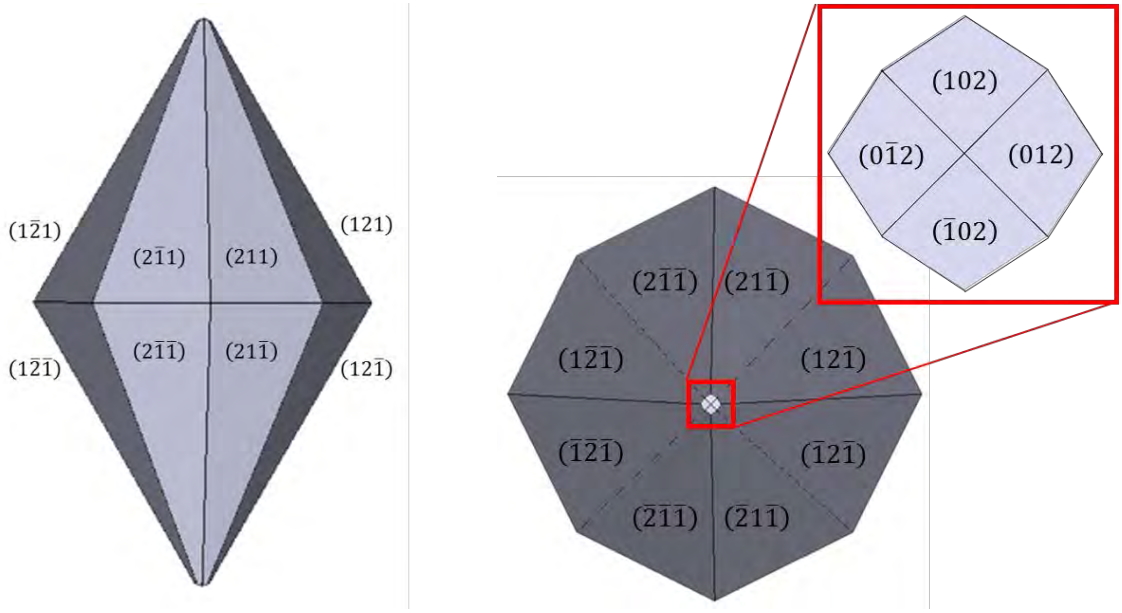

Figure 5.34: Equilibrium morphology generated from the lowest energy geometry optimised surfaces.

Table 5.3: Summary of surface energies used to generate the geometry optimised equilibrium morphology, and the relative surface coverage for each surface.

Surface	Relaxed Surface Energy / J m^{-2}	Surface Area / %
{211}	0.776	97.53
{100}	1.022	0.00
{110}	1.244	0.00
{101}	1.337	0.00
{012}	1.503	2.47
{321}	1.637	0.00
{112}	1.773	0.00
{021}	2.044	0.00
{532}	2.086	0.00
{301}	2.263	0.00
{111}	2.467	0.00
{001}	5.036	0.00

The surface morphology generated from the geometry optimised surface energies, including the micro-faceted surfaces is essentially identical to the morphology when

micro-faceting is not included. This is due to the considerable relaxation of the {211} surface which lowers the surface energy of the {211} surface to a much lower energy relative to any other surface. This may be attributed to the degree of polymerisation which occurs upon relaxation. To investigate the importance of the polymerisation behaviour at the surface, the morphology has been generated using the lowest energy relaxed surfaces which do not contain polymerised phosphate units. These morphologies are illustrated in Figure 5.35 for the relaxed surfaces both with and without micro-faceted surfaces.

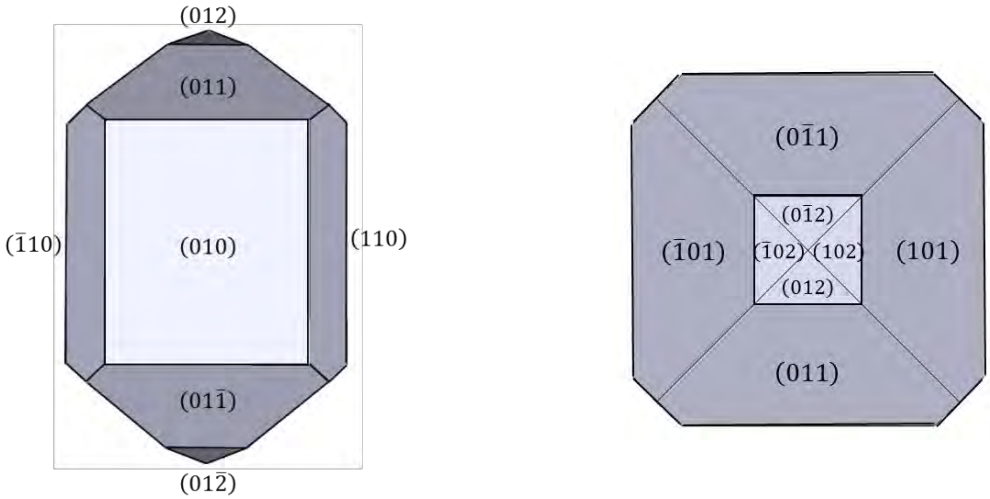

(a)

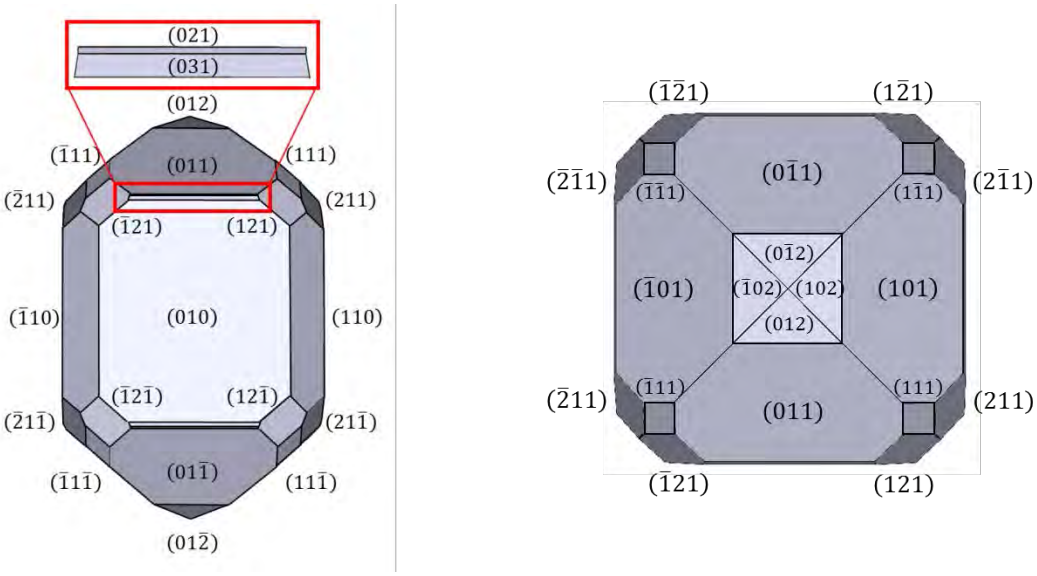

(b)

Figure 5.35: Equilibrium morphology generated from the lowest energy geometry optimised surface cuts without polymerisation, (a) without micro-faceting, (b) with micro-faceting.

Table 5.4: Summary of surface energies used to generate the geometry optimised equilibrium morphologies without polymerisation, and the relative surface coverage for each surface.

	No micro-faceting		Micro-faceting	
Surface	Relaxed Surface Energy / J m^{-2}	Surface Area / %	Relaxed Surface Energy / J m^{-2}	Surface Area / %
{100}	1.022	26.49	1.022	22.63
{110}	1.244	11.10	1.244	3.94
{101}	1.337	46.45	1.337	32.14
{012}	1.503	15.95	1.503	8.24
{112}	1.773	0.00	1.773	0.00
{021}	2.044	0.00	1.318	8.52
{301}	2.263	0.00	1.260	14.17
{111}	2.467	0.00	1.477	0.98
{211}	2.523	0.00	1.405	9.39
{001}	5.036	0.00	1.907	0.00

Here it can be seen that the removal of the polymerised surfaces has completely changed the morphology to more closely resemble the un-optimised morphology discussed previously. This highlights the important role that the polymerisation of phosphate units may play in determining the morphology of xenotime crystallites. It is also clear that surface micro-faceting is also an important factor to address when simulating the morphology of a material. This is demonstrated by the expression of the {301}, {211}, {021} and {111} surfaces which are only seen in the morphology when micro-faceting is found to lower the energy of the surfaces relative to those without modification.

5.3.2 Kinetic morphology

Similarly, the kinetic morphology has been predicted using the calculated attachment energies for each surface and is illustrated in Figure 5.36. Here it can be seen that the morphology produced is most similar to that generated using the bulk terminated

surface energies. This morphology is dominated by the {100} surface, covering 73.04 % of the total surface area. The {101} surfaces are also expressed to a minor degree, covering 26.96 % of the surface.

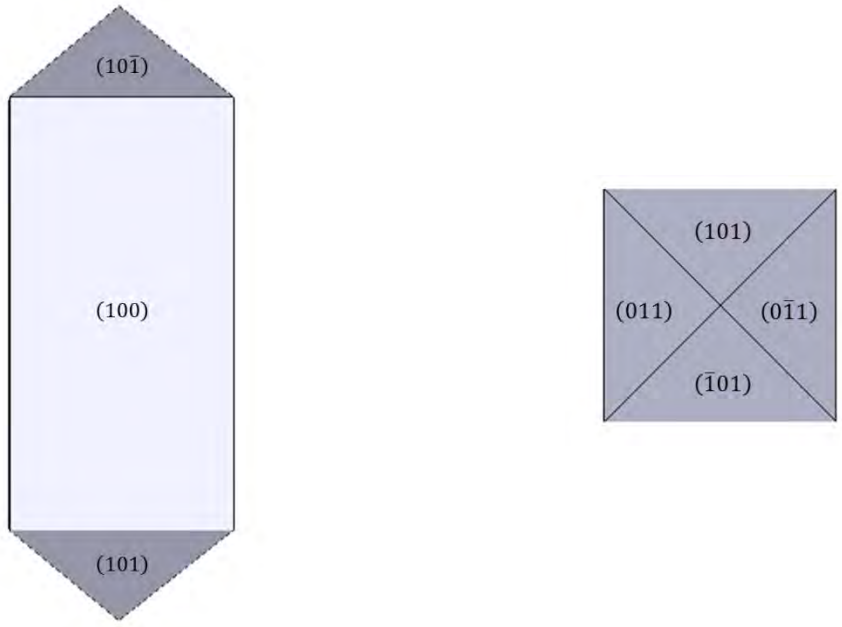

Figure 5.36: Kinetic morphology generated from the attachment energies for the bulk terminated surfaces.

Table 5.5: Summary of attachment energies used to generate the kinetic morphology, and the relative surface coverage for each surface.

Surface	Attachment Energy / eV per unit cell	Surface Area / %
{100}	0.1162	73.04
{110}	0.2012	0.00
{101}	0.2461	26.96
{111}	0.5307	0.00
{021}	0.5844	0.00
{112}	0.6241	0.00
{001}	0.6601	0.00
{211}	0.7333	0.00
{301}	0.8943	0.00
{012}	0.9656	0.00
{321}	1.8806	0.00
{532}	2.3902	0.00

5.4 Discussion and Conclusion

A summary of the lowest energy geometry optimised surfaces is listed in Table 5.6. Here it can be seen that the lowest energy surface is the {211} surface which is the only one to exhibit polymerisation of phosphate units. It has been demonstrated that micro-faceting of surfaces can reduce the energy of a surface and has done so here for the {021}, {301}, {111} and {001} surfaces. The equilibrium and kinetic morphology of xenotime crystallites have been simulated to validate the set of potential parameters derived in chapter 3. These morphologies were found to be completely different with the equilibrium morphology expressing the {211} and {012} surfaces, in contrast to the kinetic morphology which expresses the {100} and {101} surfaces. It is important to note that the effect of surface relaxation is extremely important in determining the equilibrium morphology, without which the morphology would more closely resemble

the kinetic morphology. This relaxation is not included when using the attachment energy of the surface to predict the kinetic morphology, which is a known limitation of the model.

Table 5.6: Summary of the lowest energy geometry optimised surfaces for xenotime.

Surface	Geometry Optimised Surface Energy / J m^{-2}	Polymerised?	Micro-faceted?
{100}	1.022	×	×
{110}	1.244	×	×
{101}	1.337	×	×
{112}	1.773	×	×
{021}	1.318	×	✓
{301}	1.260	×	✓
{111}	1.477	×	✓
{211}	0.776	✓	×
{012}	1.503	×	×
{001}	1.907	×	✓

As previously discussed it has been noted that it is difficult to distinguish natural samples of xenotime and zircon based on morphology as they are extremely similar. As such it is assumed that it is valid to compare the simulated results with experimental data collected for both xenotime and zircon. In reality the morphology and growth of a crystal is driven by a complex combination of factors, giving rise to a variety of different observed morphologies depending on the history of the natural sample. As such it has been suggested by Pupin *et al.*[5] that the morphology of zircon crystals can be used as a geothermometer and a way of inferring the composition of the magma from which the sample was formed. These empirical observations are summarised in Figure 5.37 where it is suggested that the crystallites formed from magmas with high concentrations of aluminium and low concentrations of alkali metals express a {211} pyramid

morphology. Conversely, those formed from magmas with high alkali metal concentrations develop a morphology consisting of {101} pyramids. The temperature of the medium also has an effect, determining the relative growth rates of the other surfaces. These observations align very well with the equilibrium morphology (*i.e.* the most thermodynamically favourable morphology) being observed as the lowest temperature morphology produced from magmas with relatively low alkali metal concentrations, expressing almost uniquely the {211} surface. This can be approximated to the morphology labelled B in the table. Similarly the kinetic morphology is observed as the highest temperature morphology from magmas with relatively high alkali metal concentrations, perhaps described as a metastable morphology, expressing the {100} and {101} surfaces. This can be approximated to the morphology labelled D in the table. It may be possible to suggest the impact that the alkali metal concentration has on the surface morphology by considering the polymerisation at the surface. As shown previously the removal of the polymerised surfaces from the morphological model inhibits the growth of the {211} surface, producing a morphology consisting of {101} pyramids which can be approximated to the morphology labelled S19 in the table. This morphology is observed from magmas containing relatively high alkali metal concentrations. It is possible that the alkali metals are interacting with the dangling oxygen atoms at the surface, which often become the bridging oxygen atom of the polymerised units, therefore inhibiting the polymerisation process.

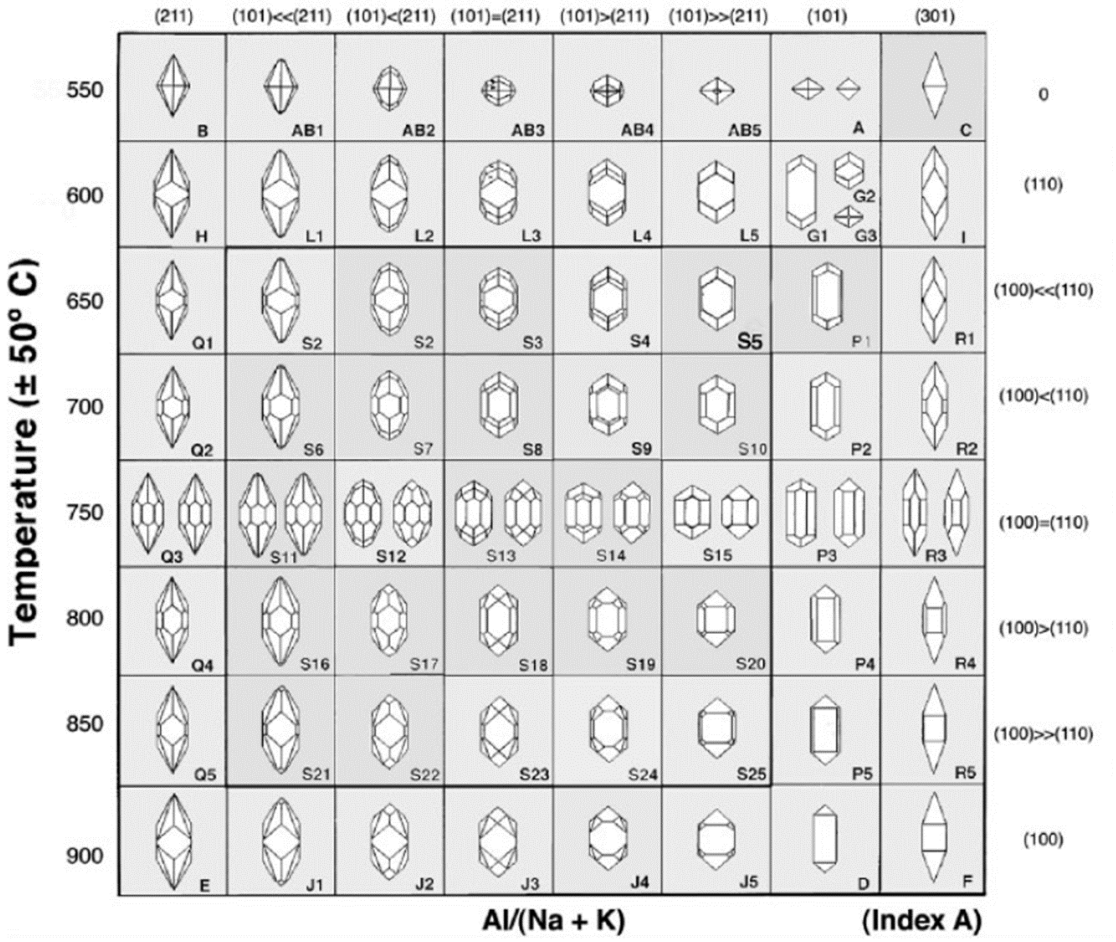

Figure 5.37: Range of zircon morphologies outlined by Pupin depending on temperature and magma composition[5].

The equilibrium morphologies produced without polymerisation shown in Figure 5.35 in the previous section can also be compared with experimental samples of zircon originating from Turkey[9]. The electron micrographs and schematics for each morphology are illustrated in Figure 5.38. Here it can be seen that there is a great deal of agreement with the predicted morphology when micro-faceting is included. A key feature to note is the presence of the {211} surfaces, featured in many of the morphologies. This surface is only present in the predicted morphology when micro-faceting is accounted for. Similarly the {301} surfaces are expressed to a lesser degree in the zircon samples, which again are only observed in the predicted morphology as a

result of the stabilisation of these surfaces through micro-faceting. This strongly emphasises the need to investigate micro-faceting of surfaces in surface simulations to accurately predict morphologies. The similarities between the predicted morphologies and those determined experimentally provide strong evidence that the set of atomistic potentials used here are robust and valid.

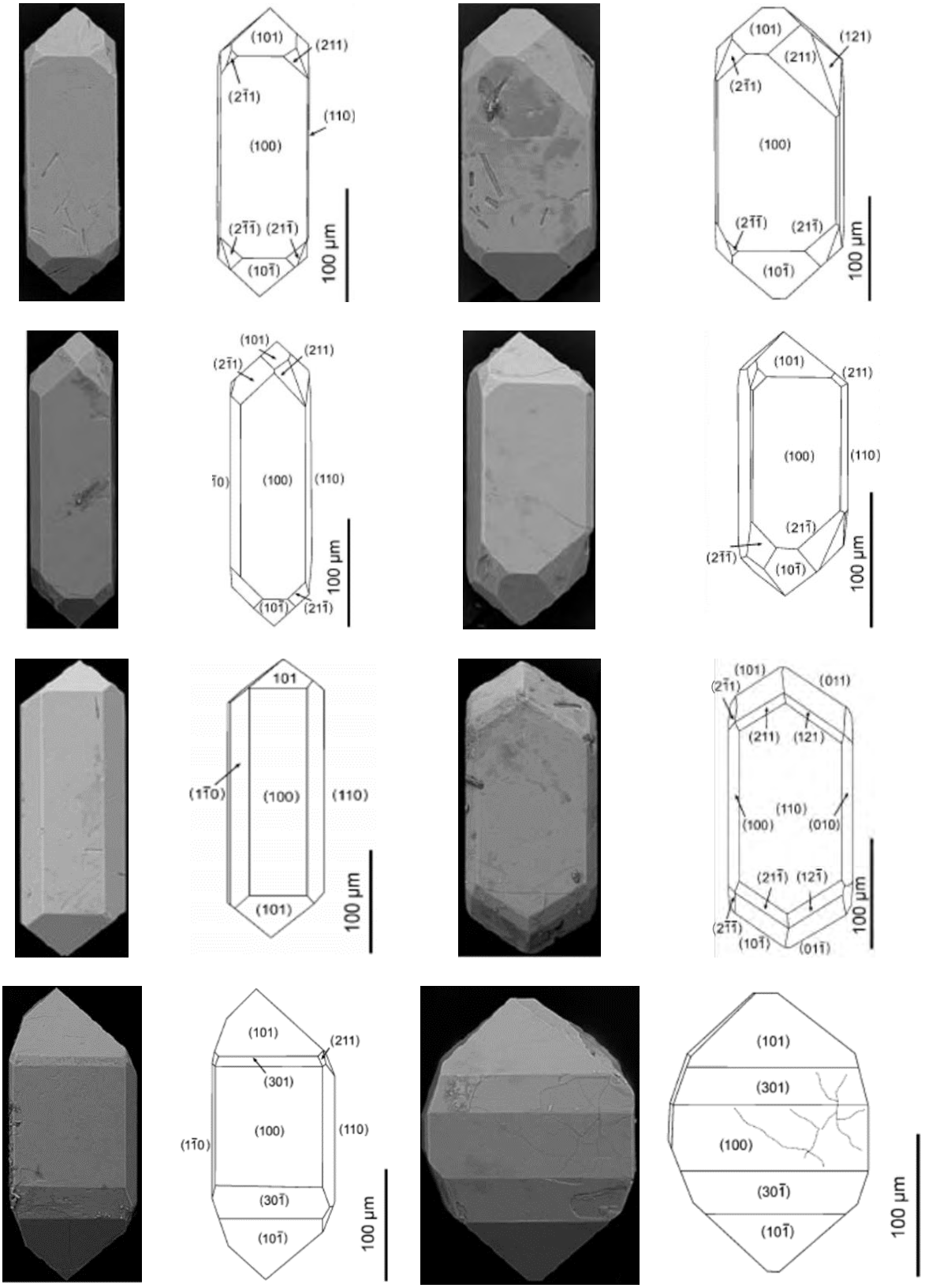

Figure 5.38: A range of zircon morphologies which are concordant with the predicted equilibrium morphology without polymerisation.

5.5 Further Work

- One factor which can drastically impact on the morphology of a crystal is the intrinsic impurity content. Unfortunately it has not been possible to investigate the effect of impurity species on the relative surface energies in this study as the current version of METADISE does not support surface defect calculations using three-body potentials.
- With calculated values for the defect formation energy of impurity species at the surface, it is then possible to predict the surface and bulk segregation of impurities.
- Continuing on the impurity theme, it may also be of value to model extended defects such as grain boundaries within xenotime and the relative energies of impurity species at these boundaries with which to compare with the bulk and surfaces. Moreover, grain boundaries (being lower density regions of the crystal) will exhibit different behaviour when irradiated thus extending the radiation damage simulations present in chapter 6.
- It is possible to calculate the surface energy for hydrated surfaces which may alter the relative surface energies and therefore modify the predicted morphology. This could also be expanded to investigate the impact of the alkali metals in solution on the surface energies to further rationalise the effect of the magma composition on the crystal morphology.

5.6 References

1. C. O. Hutton, *American Mineralogist*, 1947, **32**, 141-145.
2. H. J. Forster, *American Mineralogist*, 1998, **83**, 1302-1315.
3. T. E. Littleford, R. A. Jackson and M. S. D. Read, *Physica Status Solidi C: Current Topics in Solid State Physics, Vol 10, No 2*, 2013, **10**, 156-159.
4. T. E. Littleford, R. A. Jackson and M. S. D. Read, *Surface Science*, 2012, **606**, 1550-1555.
5. J. P. Pupin, *Contributions to Mineralogy and Petrology*, 1980, **73**, 207-220.
6. D. Mkhonto and N. H. de Leeuw, *Journal of Materials Chemistry*, 2002, **12**, 2633-2642.
7. I. V. Santana, F. Wall and N. F. Botelho, *Journal of Geochemical Exploration*, 2015, **155**, 1-13.
8. T. G. SAHAMA, *Bull. Geol. Soc. Finland*, 1973, **45**, 67-71.
9. S. Koksal, M. C. Goncuoglu, F. Toksoy-Koksal, A. Moller and H. Kemnitz, *Mineralogy and Petrology*, 2008, **93**, 185-211.

CHAPTER 6

Simulation of Radiation Damage Cascades

Table of Contents

Table of Figures

6.1 Introduction

Experimental studies of radiation damage in solids often use the SRIM (the Stopping and Range of Ions in Matter) code to predict the stopping power and range of ions in a target material and to convert radiation dose to displacements per atom. This code predicts radiation damage based on a Monte Carlo algorithm, using the binary collision approximation. One of the key parameter inputs into this code is the value of the threshold displacement energy (E_d) for each atom type. However the exact definition for this parameter is open to interpretation[1-7] with both the minimum and average values having their merits. In general the threshold displacement energy can be defined as the minimum kinetic energy required to produce a stable defect. Previously the threshold displacement energy surface has been investigated using MD simulations in zircon by Moreira et al[8]. Here threshold displacement energies were calculated along thirteen different crystallographic directions and repeated for two different lattice atoms. A permanent defect was defined based on the occupancy of Voronoi polyhedra centred on lattice sites after simulation for approximately 4 ps. There was found to be a great deal of anisotropy between the values of E_d in the different directions with average displacement energies ($E_{d(av)}$) of ca. 120 and 75 eV for cations and 60 and 64 eV for oxygen for the equal charge potentials and unequally charged potentials respectively. Similar work has been carried out in xenotime by Urusov et al.[9] where the threshold displacement energy of an oxygen atom was calculated over ten different crystallographic directions, however it is not clear by what criteria they define a stable defect and the calculations were not repeated for multiple atoms. The average energy was taken over the five lowest energy directions to give a value for $E_{d(av)}$ of 42 eV.

Radiation damage cascades were also performed by Urusov et al. which were performed in the NVE ensemble using a 20 keV thorium PKA. They identified that the number of phosphorus Frenkel pairs was proportional to a quarter of the number of oxygen Frenkel pairs, indicating the displacement of a large number of phosphate tetrahedra. Peak damage was achieved by ca. 0.82 ps after the PKA atom was initiated. Molecular dynamics simulations of radiation damage cascades have been performed previously in zircon which have identified polymerisation of silicate tetrahedra as an important damage process. Trachenko et al.[10] observed polymerised silicate chains containing four, five and six coordinate silicon atoms. Some of these chains also contained edge sharing polyhedra or formed small ring structures. This polymerisation was also observed by Devanathan et al.[11], who's potentials have been adapted for use in this study. Radiation damage cascades performed in fluorapatite by Jay et al.[12] identified similar behaviour of the phosphate tetrahedra forming phosphate chains. They observed that the most frequently observed chains contained two phosphorus atoms with varying degrees of coordination. Longer chains were also observed to a lesser degree. The number of defects at peak damage was ca 10000 for a 5 keV PKA initiated in the (0001) direction. The percentage of these defects which were annealed was calculated to be ca. 70 %.

6.2 Threshold displacement energy

In this study a supercell containing 3000 atoms (5 x 5 x 5 supercell) was equilibrated for 20 ps in the NPT anisotropic ensemble at 300 K and zero external pressure using the Berendsen thermostat and barostat. The resulting configuration was then equilibrated in the NVE ensemble for a further 20 ps before initiating the primary knock-on atom (PKA) in a given direction. Periodic boundary conditions were employed throughout the simulations and a variable time step algorithm was used to dynamically reduce the time step to below 1 fs to obey the condition that an atom can only travel a distance of r Å per time step, where $0.03 \text{ Å} \leq r \leq 0.10 \text{ Å}$. A flow diagram describing the process followed to determine the threshold displacement energy is outlined in Figure 6.1. Here a permanent defect was defined by two conditions. Firstly, the presence of at least one interstitial and vacancy pair at the end of the simulation as determined by the defect detection algorithm within DL_POLY, outlined in chapter 2, using a cut off of 0.70 Å. Subsequently the presence of both Frenkel and antisite defects were analysed over the final ca. 2 ps of the simulations using the Voronoi defect algorithm described in chapter 2. A permanent defect (stable for $\geq$ 2 ps) was deemed to have been produced when both of these conditions were true. The final value of E_d is recorded when the new energy step size is less than 1, in which case the value of E is rounded to the nearest integer. The average threshold displacement energy of each species was investigated by initiating the PKA in eighty nine different directions.

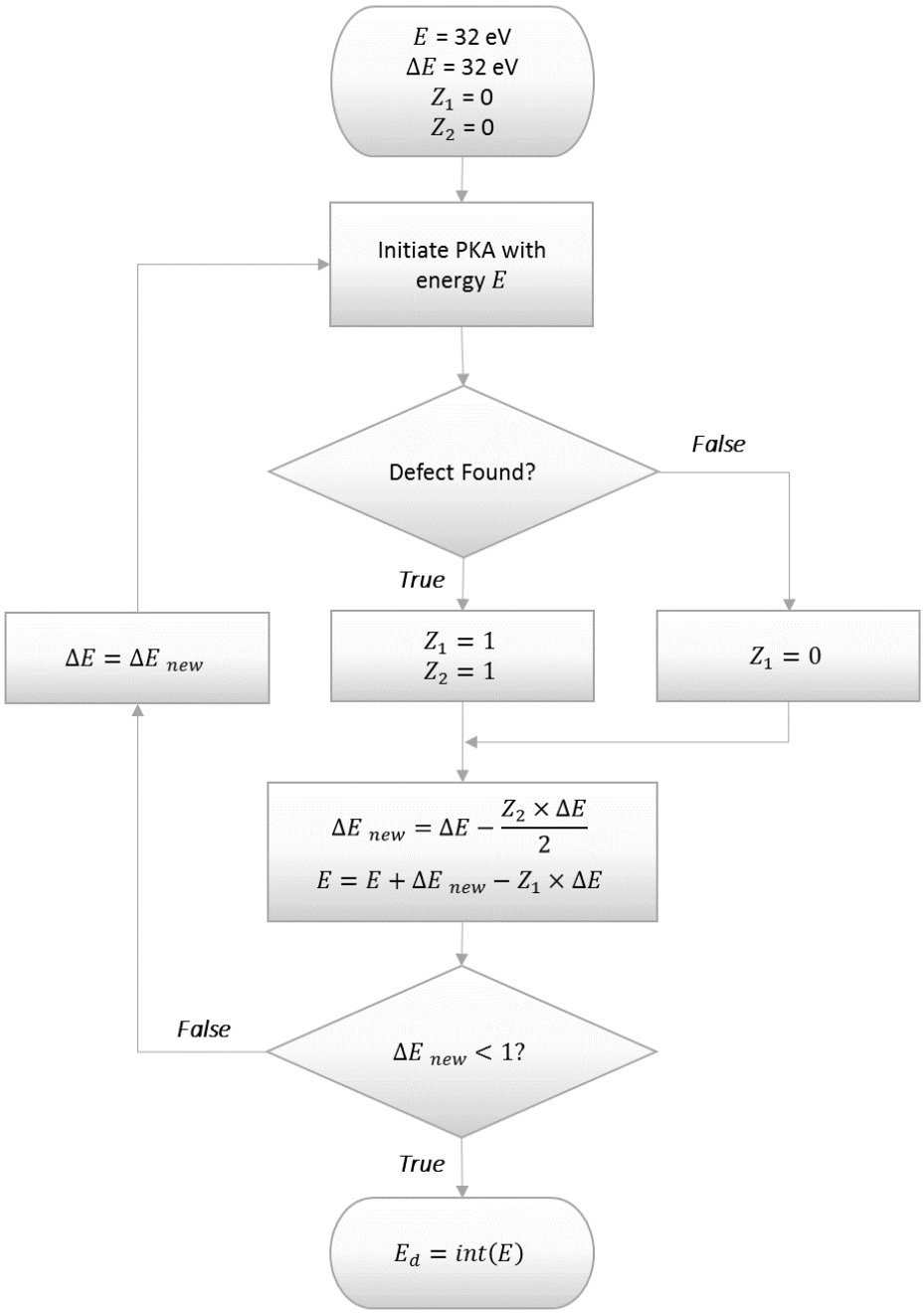

Figure 6.1: Flow chart illustrating the process used to determine E_d

6.2.1 Lattice Construction

To obtain an accurate value for $E_{d(av)}$ it is important that a variety of different PKA directions are sampled rather than just a select few select crystallographic directions. Indeed there is no ideal solution as to the regular distribution of an arbitrary number of points ($|P|$) on the surface of a sphere except in special cases where $|P| = 4, 6, 8, 12$ and 20 which correspond to the Platonic solids. In this study the Fibonacci lattice was employed (Figure 6.2 (a)) to give a good approximation to the ideal distribution of points[13]. One of the main advantages to using this lattice construction is that the area occupied by each lattice point is very similar, as opposed to the latitude-longitude lattice in which the rotation angle between each point is equal which results in increased sampling near the poles. This is clearly visible in Figure 6.2 (b).

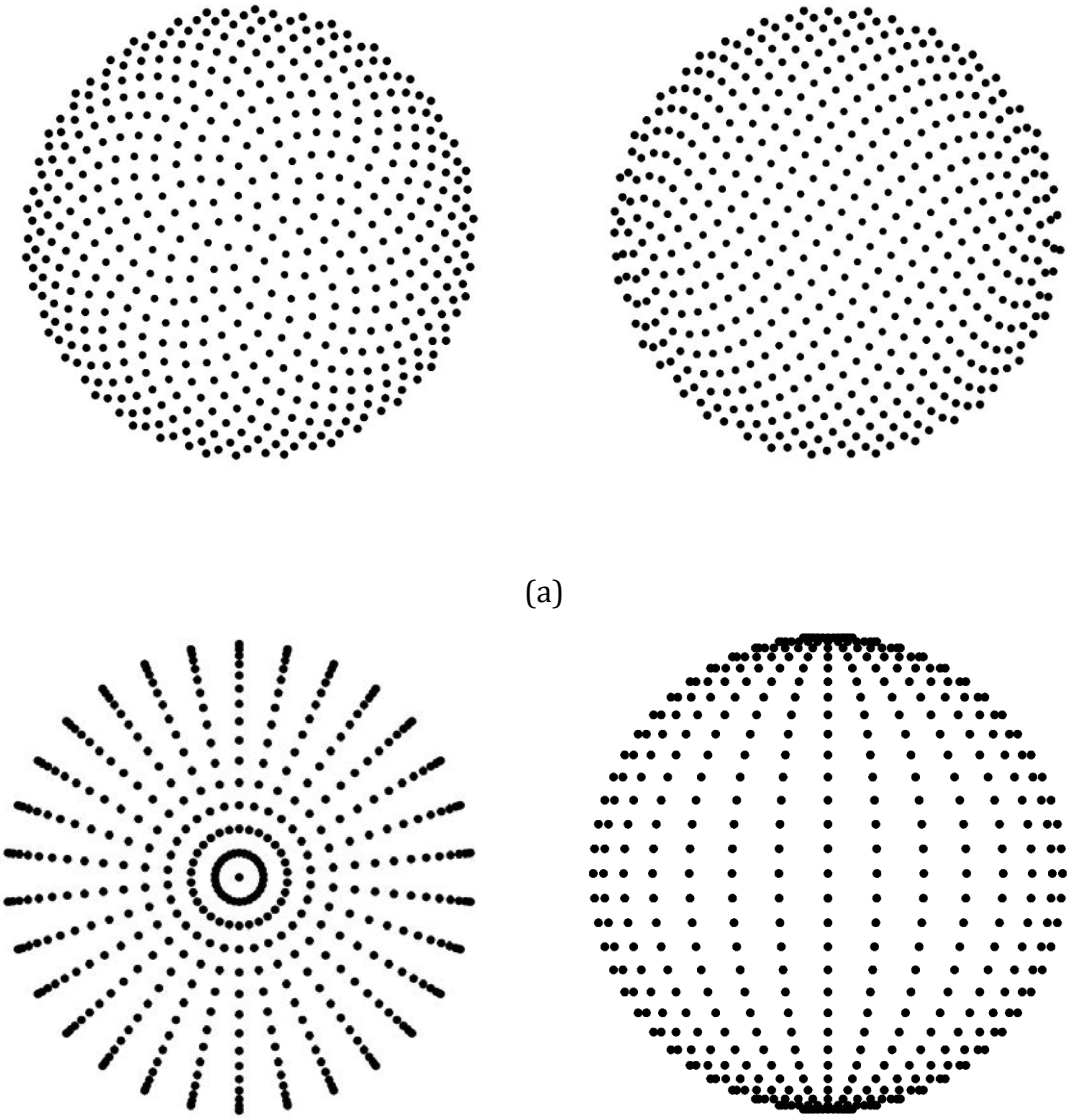

Figure 6.2: 1000 points distributed on the surface of a sphere using, (a) the Fibonacci lattice and (b) the latitude-longitude lattice.

This lattice is based around the golden ratio, Φ, which is defined in equation (6.1). This ratio is derived from the Fibonacci sequence, F (where $= 0, 1, 1, 2, 3, 5, 8, \dots$) in which the ratio between consecutive terms tends toward the golden ratio as i tends to infinity as shown in equation (6.2).

$$\Phi = 1 + \Phi^{-1} = \frac{1+\sqrt{5}}{2} \tag{6.1}$$

$$\lim_{i\to\infty}\left(\frac{F_i}{F_{i+1}}\right) = \Phi \tag{6.2}$$

$$P = \{x \in \mathbb{Z} | -N \leq x \leq N\} \tag{6.3}$$

The spherical and Cartesian coordinates for the i^{th} point on the surface of a sphere are defined in equations (6.4) - (6.8); where P_i is the value at index i in set P.

$$\varphi = \sin^{-1}\left(\frac{2P_i}{|P|}\right) \tag{6.4}$$

$$\theta = 2\pi P_i \Phi^{-1} \tag{6.5}$$

$$x = \cos(\varphi)\cos(\theta) \tag{6.6}$$

$$y = \cos(\varphi)\sin(\theta) \tag{6.7}$$

$$z = \sin(\varphi) \tag{6.8}$$

It has also been shown previously that there can be a great deal of variation in the value of E_d between different atoms of the same species due to lattice vibrations and variations in the kinetic energy of the atoms within the simulation[1]. As a result the simulations here are repeated for three different atoms for each species. In total ca. 8000 trajectories have been analysed.

6.2.2 Yttrium

The threshold displacement energy surfaces for the three yttrium atoms analysed are shown in Figure 6.3. The general shape of the surface is similar for all three atoms however there are also some clear differences. This highlights the degree of variation that is possible between atoms of the same species, due to the thermal motion of the atoms within the simulation. As such the average energy surface will be considered for further analysis.

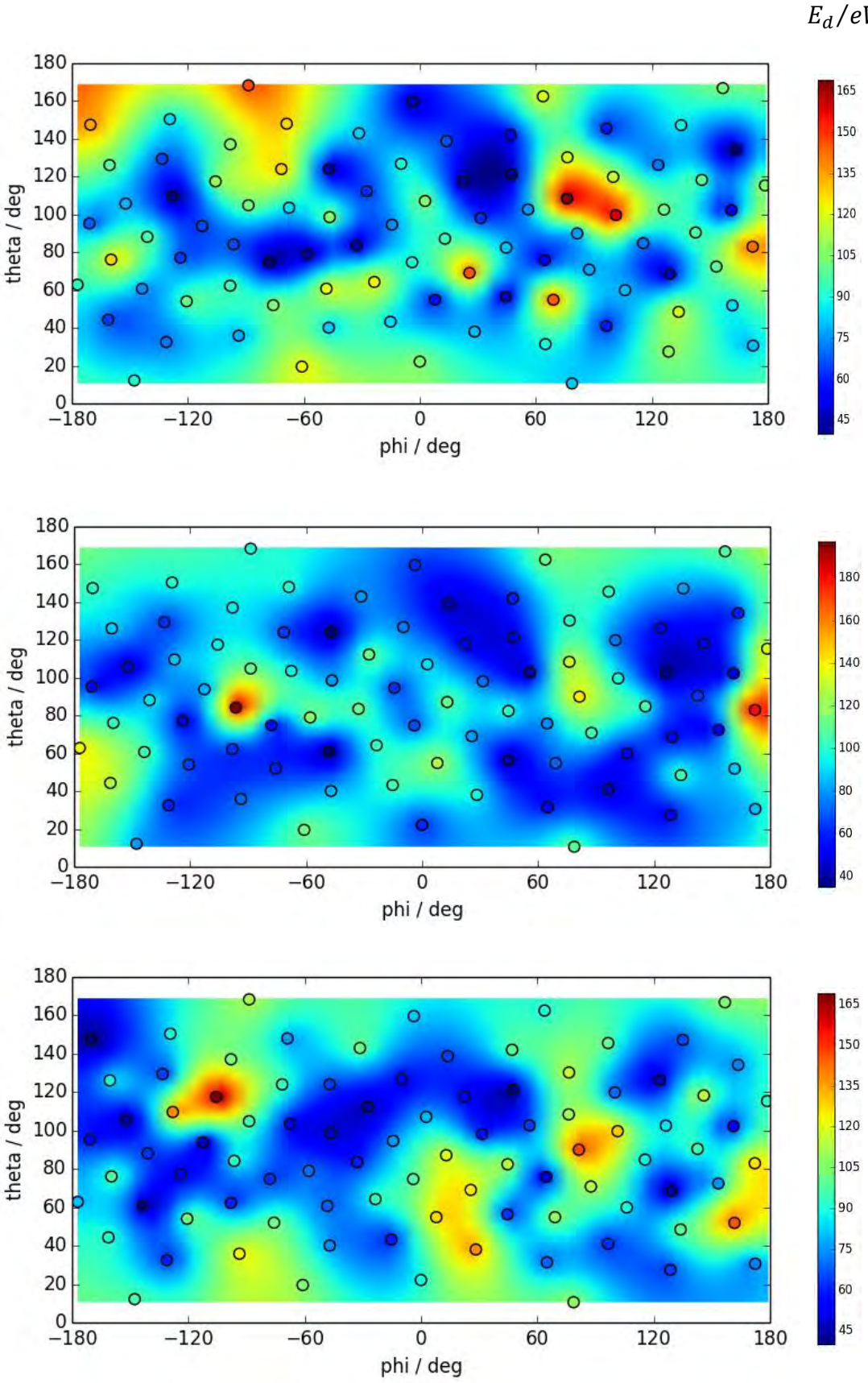

Figure 6.3: Threshold displacement energy surfaces for the three yttrium atoms analysed in this study.

The value of $E_{d(av)}$ for the yttrium atom was calculated to be 84 ± 28 eV. The large standard deviation reflects the degree of variation across the different directions and atoms averaged. The average threshold displacement energy surface for the yttrium PKA is shown in Figure 6.4. A grid has been overlaid to indicate different crystallographic planes to aid with orientation. The *a* axis is defined by the coordinates (0°, 90°) and (180°, 90°) corresponding to the positive and negative direction respectively. Similarly the *b* axis passes through the surface at (90°, 90°) and (-90°, 90°) corresponding to the positive and negative direction respectively, whilst the c axis passes through the points (0°, 0°) and (0°, 180°) corresponding to the positive and negative direction respectively. In general the PKA vectors resulting in higher E_d values seem to be those with a large component in the *ac* and *bc* planes, whilst the opposite is true for the lowest energy PKA vectors.

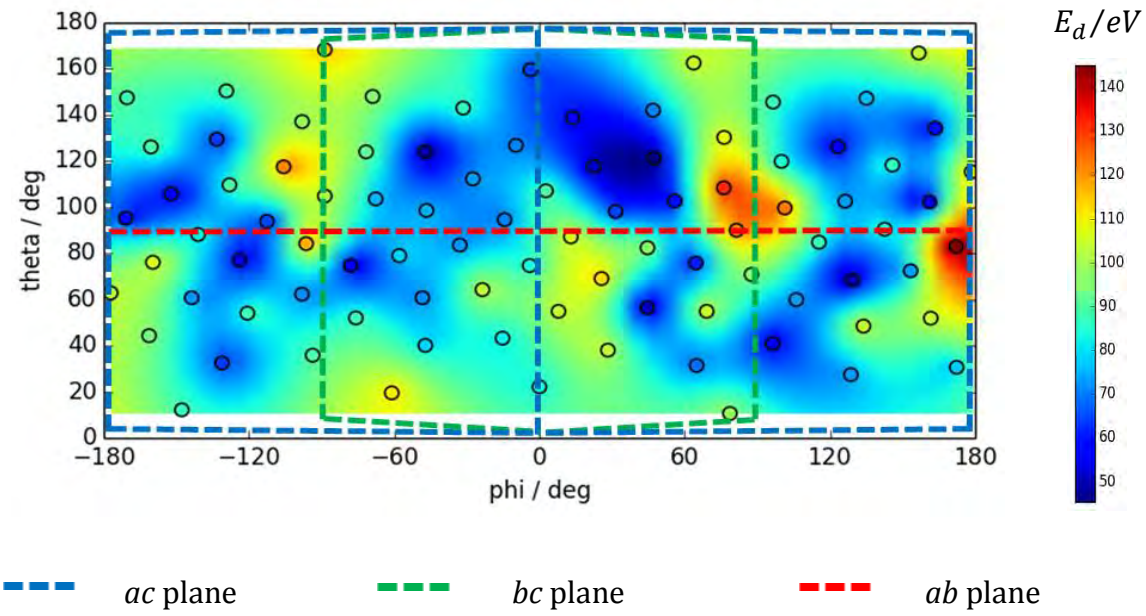

Figure 6.4: Average threshold displacement energy surfaces for the three yttrium atoms analysed in this study. The red, blue and green reference lines indicate the ab, ac and bc planes respectively

The four lowest energy PKA vectors are summarised in Table 6.1 and are illustrated in Figure 6.5, where they are represented by green arrows and initial PKA atom is

highlighted in blue. It is clear that these directions correlate to the yttrium PKA atom being initiated into the channels running parallel to the c axis. This is as would be expected as it allows the yttrium PKA to move away from its lattice site whilst avoiding the other neighbouring atoms. This may also assist in channelling the PKA atom, allowing it to use its momentum travel further within the lattice and form a Frenkel defect with a larger separation between the vacancy site and the interstitial atom, lowering the probability of defect recombination and annihilation. The average threshold displacement energy taken over the lowest ten PKA trajectories was calculated to be $52 \pm 9\ eV$.

Table 6.1: Lowest energy PKA vectors for the yttrium PKA

φ / degrees	θ / degrees	E_d/eV
47.42	121.29	45
-47.12	124.10	49
129.37	68.45	49
44.57	56.36	51

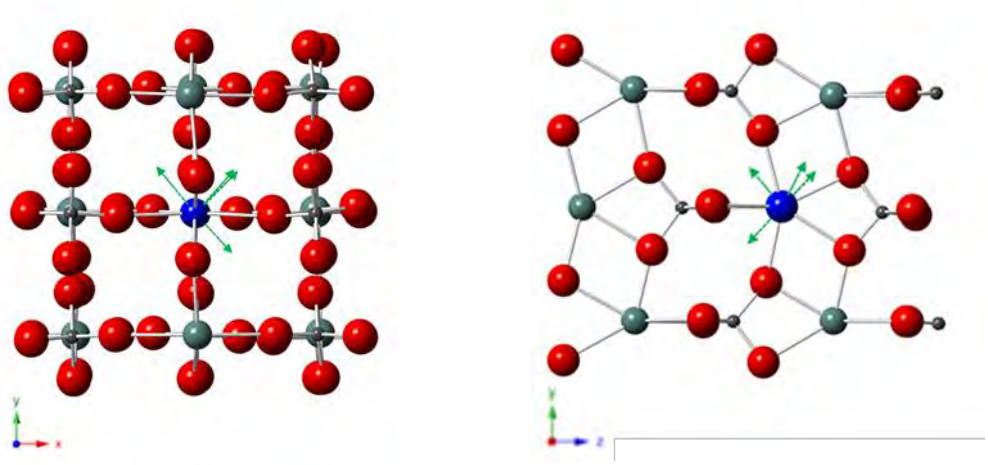

(a) (b)

Figure 6.5: Lowest energy PKA vectors for the yttrium PKA. The PKA atom is highlighted in blue

As stated before, the vectors with large components in the *ac* and *bc* planes tend to have higher values of E_d. There are however some localised areas of high E_d which are summarised in Table 6.2 and illustrated in Figure 6.6

Table 6.2: Highest energy PKA vectors for the yttrium PKA

φ / degrees	θ / degrees	E_d/eV
172.19	82.96	145
76.18	108.41	131
-105.69	117.50	121
-88.65	168.33	115

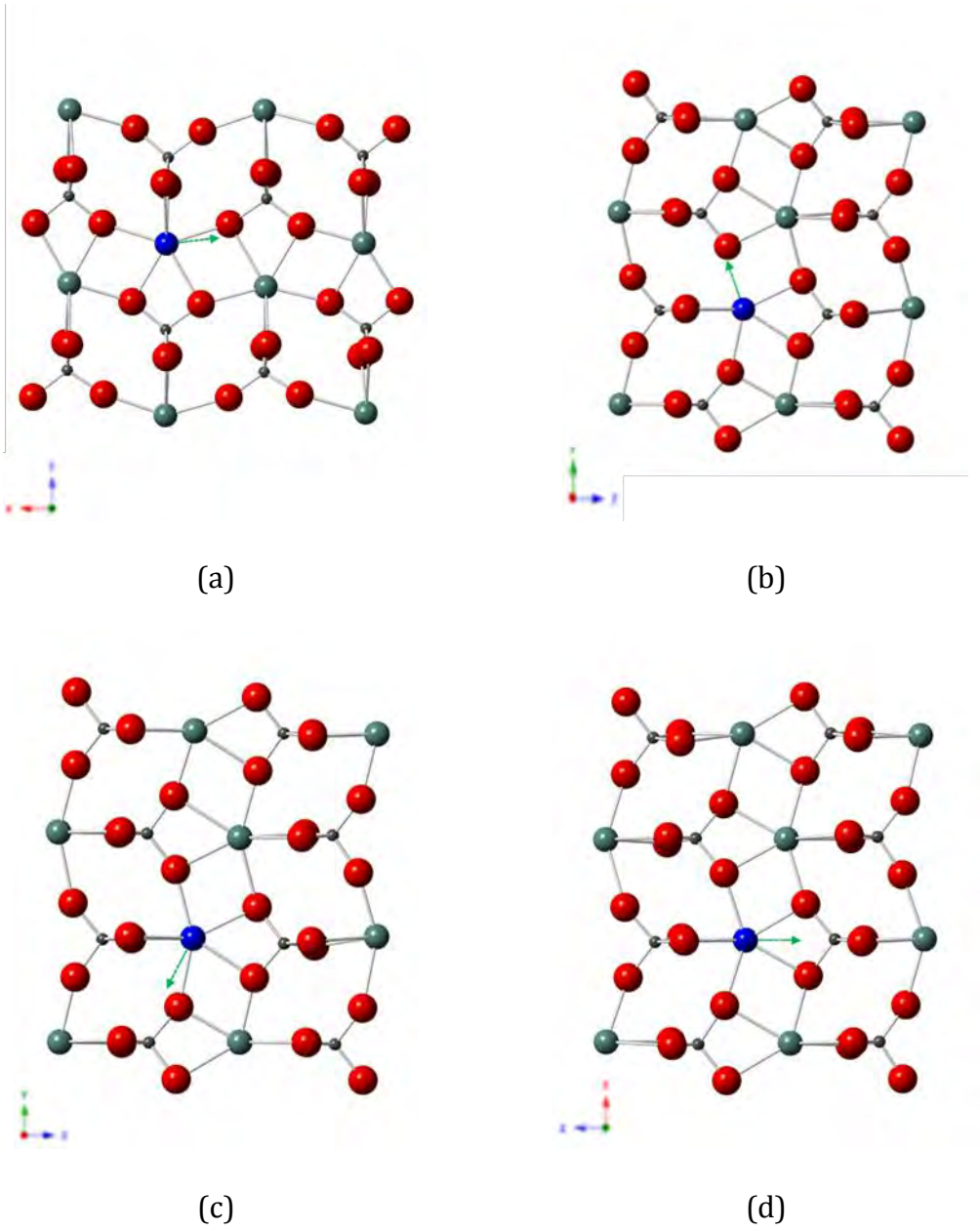

Figure 6.6: Highest energy PKA vectors for the yttrium PKA. The PKA atom is highlighted in blue

In contrast to the low energy PKA vectors, the high energy PKA vectors are directed towards other local atoms. This is understandable as the yttrium PKA is likely to collide with these atoms and transfer momentum, making it more likely to recombine with the vacancy at the PKA lattice site and annihilate the Frenkel defect. The average threshold displacement energy taken over the ten PKA trajectories with the highest values of E_d was calculated to be $121 \pm 29\ eV$.

6.2.3 Phosphorus

The threshold displacement energy surfaces for the three phosphorus atoms analysed are shown in Figure 6.7. Again the general shape of the surface is similar for all three atoms however there are also some clear differences.

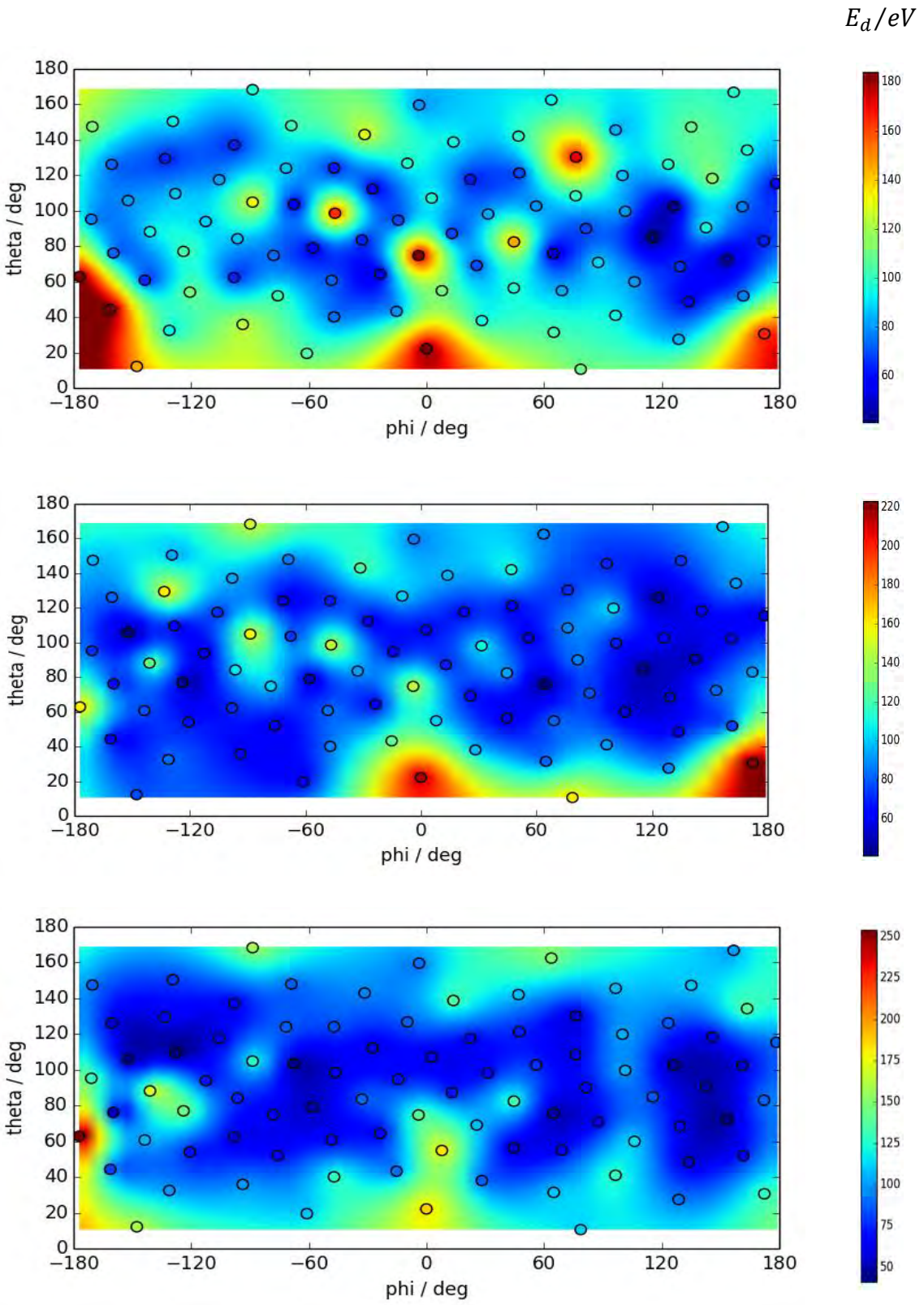

Figure 6.7: Threshold displacement energy surfaces for the three phosphorus atoms analysed in this study

The value of $E_{d(av)}$ for the phosphorus atom was calculated to be 90 ± 35 eV. The large standard deviation reflects the degree of variation across the different directions and atoms averaged. The average threshold displacement energy surface for the phosphorus PKA is shown in Figure 6.8 with the grid indicating the low index lattice planes overlaid to aid orientation. The lowest energy vectors seem to be located around the *ab* plane whereas the highest energy vectors seem more localised to the *c* axis.

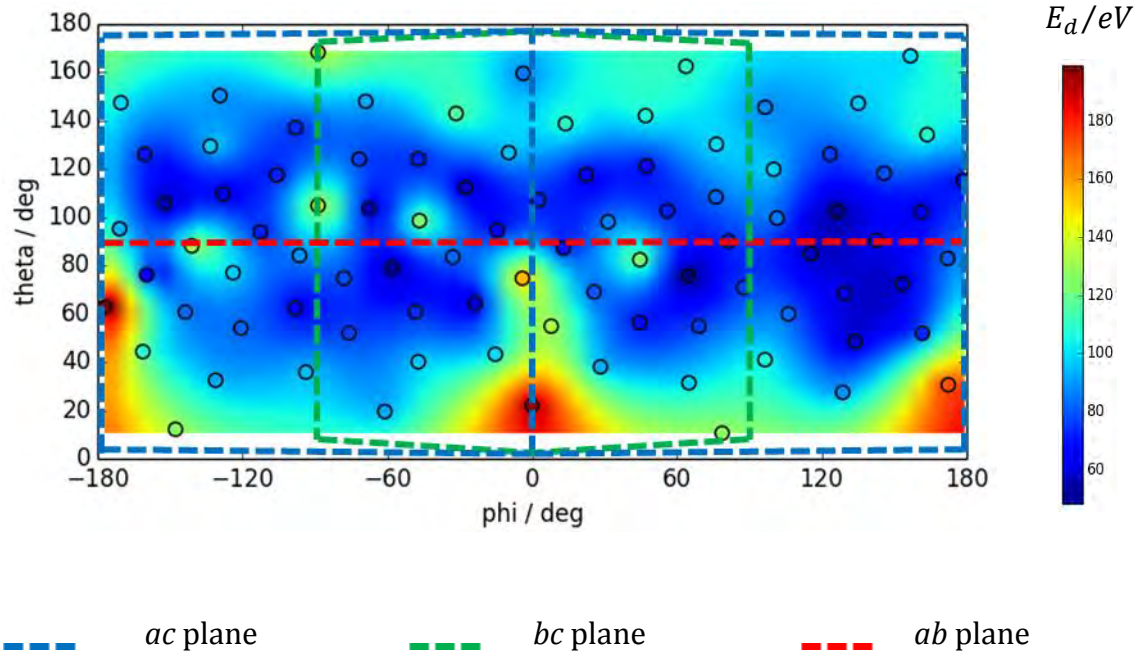

Figure 6.8: Average threshold displacement energy surfaces for the three phosphorus atoms analysed in this study. The red, blue and green reference lines indicate the ab, ac and bc planes respectively

The four lowest energy PKA vectors are summarised in Table 6.3 and illustrated in Figure 6.9. Here it can be seen that these vectors relate to the phosphorus PKA being initiated into the channels in between two adjacent oxygen atoms within the phosphate group. The average E_d taken over the ten lowest energy vectors was calculated to be 56 ± 12 eV.

Table 6.3: Lowest energy PKA vectors for the phosphorus PKA

φ / degrees	θ / degrees	E_d/eV
64.70	75.79	48
126.31	102.56	52
-57.89	79.01	54
-152.16	105.75	56

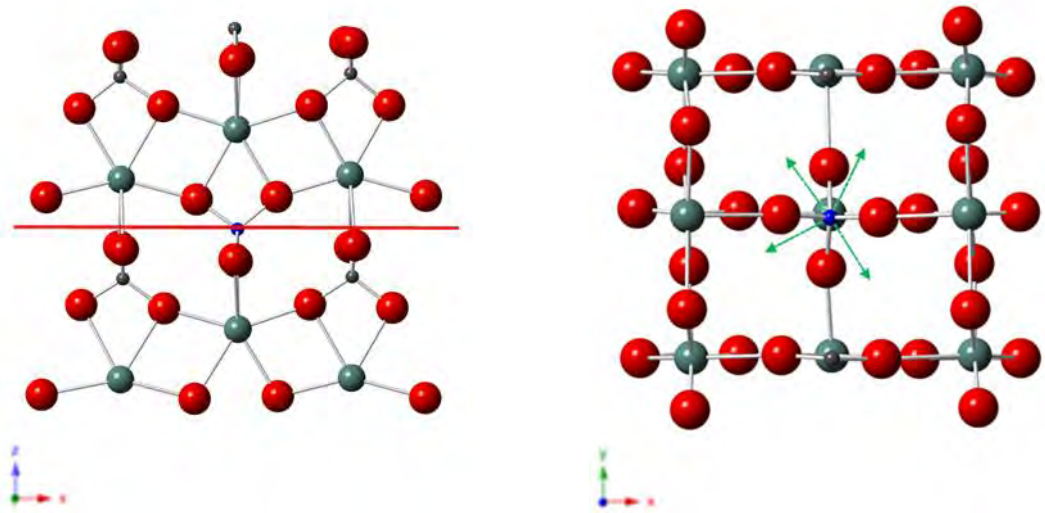

(a) (b)

Figure 6.9: Lowest energy PKA vectors for the phosphorus PKA. The PKA atom is highlighted in blue and the red reference line indicates the ab plane

The seven highest energy PKA vectors are summarised in Table 6.4 and illustrated in Figure 6.10. In contrast the highest energy PKA vectors are associated with the PKA being initiated towards a neighbouring atom. The average threshold displacement energy taken over the ten PKA trajectories with the highest values of E_d was calculated to be $151 \pm 40\ eV$.

Table 6.4: Highest energy PKA vectors for the phosphorus PKA

φ / degrees	θ / degrees	E_d/eV
-177.11	62.86	199
0.00	22.15	196
172.39	30.59	172
-4.01	74.71	156
-88.67	104.86	138
-88.65	168.33	134
7.90	54.87	132

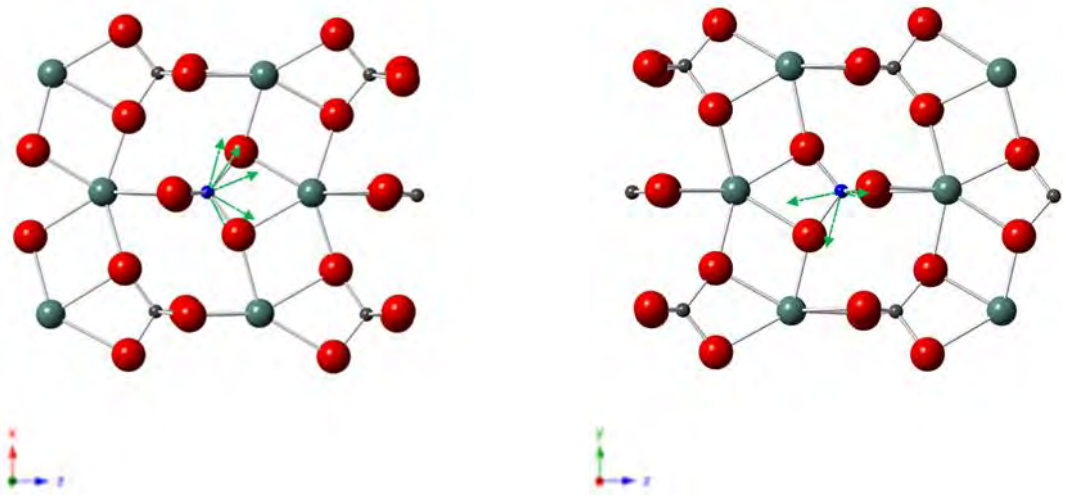

Figure 6.10: Highest energy PKA vectors for the phosphorus PKA. The PKA atom is highlighted in blue

6.2.4 Oxygen

The threshold displacement energy surfaces for the three oxygen atoms analysed are shown in Figure 6.11. Again the general shape of the surface is similar.

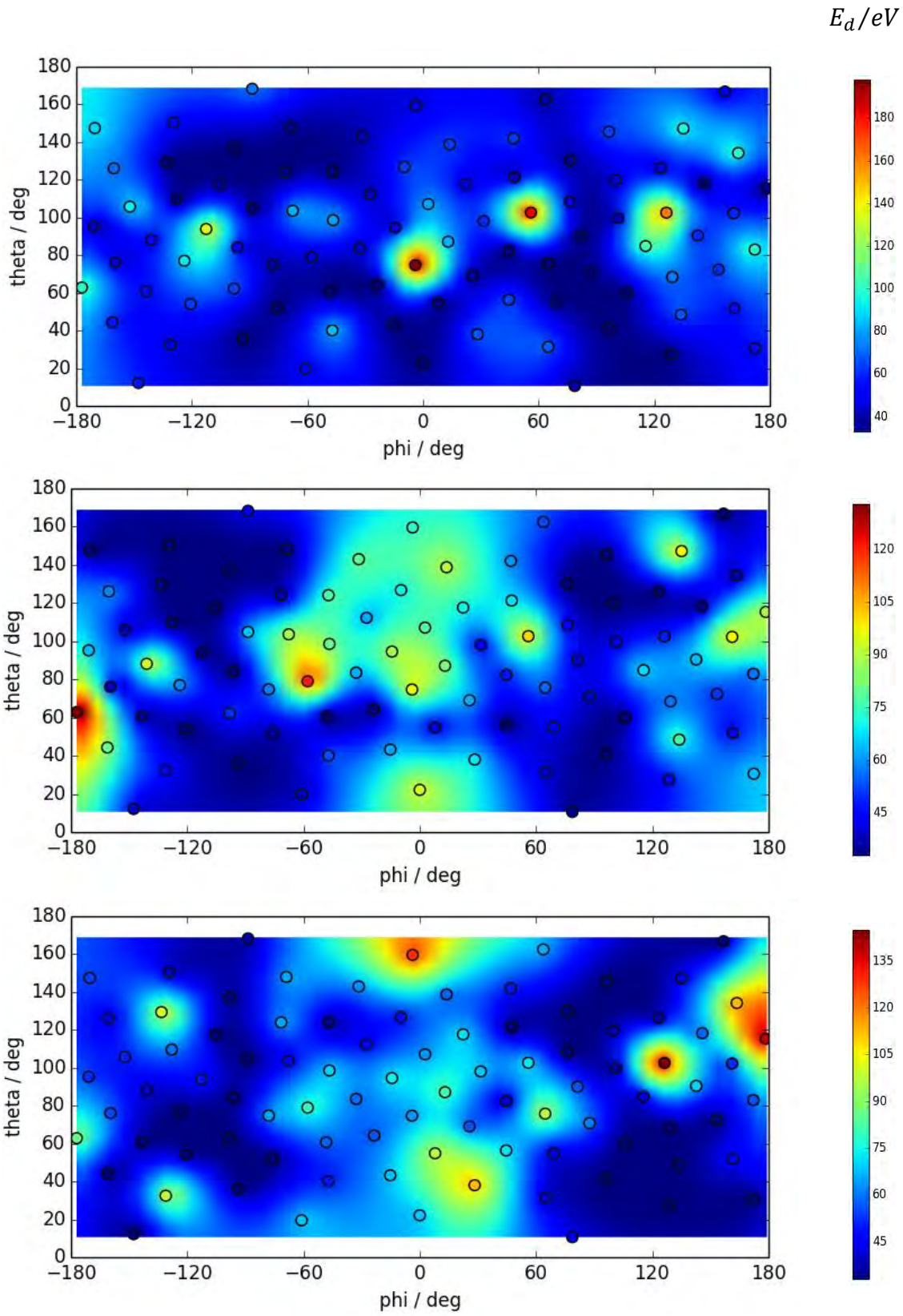

Figure 6.11: Threshold displacement energy surfaces for the three oxygen atoms analysed in this study.

The value of $E_{d(av)}$ for the oxygen atom was calculated to be 57 ± 27 eV. The large standard deviation shows the degree of variation across the different directions and atoms averaged. The average E_d values for each direction can be seen in Figure 6.12.

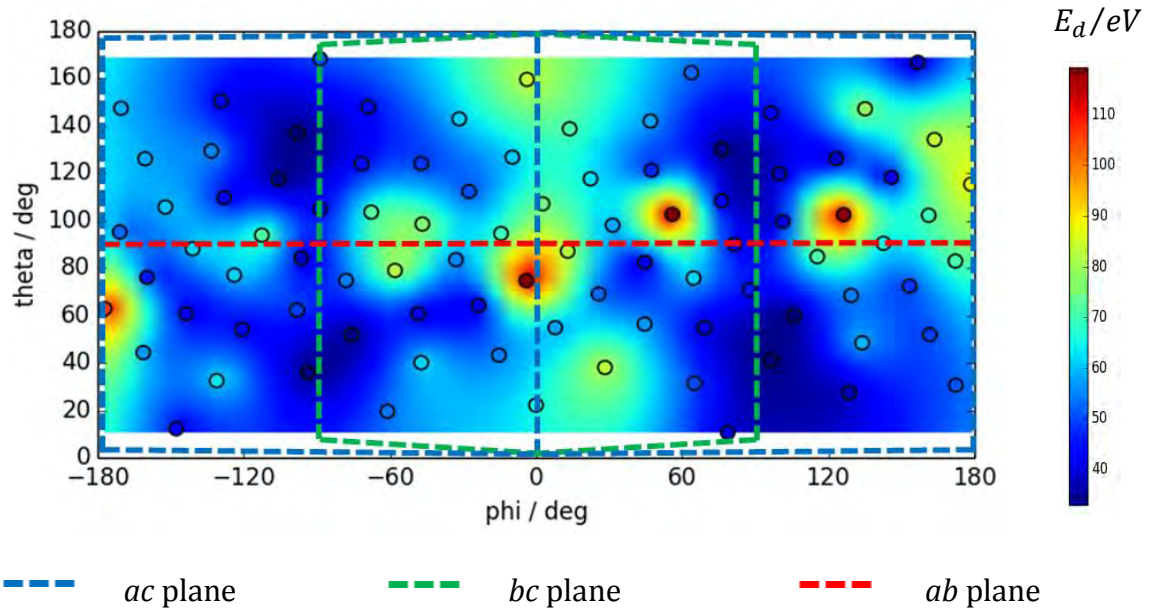

Figure 6.12: Average threshold displacement energy surfaces for the three oxygen atoms analysed in this study. The red, blue and green reference lines indicate the ab, ac and bc planes respectively

It is evident from the average contour plot that the directions with lower threshold displacement energies lie in the *bc* plane. This is understandable as the trajectory of the PKA is in the direction of the large channels running parallel to the *c* axis, as shown in Figure 6.13 (a) and (b). Here the *bc* plane is indicated by the solid green line. It is also clear that there are four minima in the contour plot at $\varphi \approx \pm 90°$ and $\theta \approx 90 \pm 40°$. The four trajectories that have been investigated which are closest to these minima have been summarised in Table 6.5 and illustrated in Figure 6.13 (c). These equate to an elevation from the $\pm c$ axis, in the *bc* plane of ca. $\pm 40°$, which allows the PKA to enter the channel. This may be evidence of channelling as the PKA can essentially enter these channels and

travel a greater distance from its lattice site, generating a stable Frenkel pair which in turn gives a lower value of E_d. The average threshold displacement energy for the ten PKA trajectories with the lowest E_d was calculated to be 35 ± 5 eV.

Table 6.5: Lowest energy PKA vectors for the oxygen PKA

φ / degrees	θ / degrees	E_d/eV
-93.67	35.84	33
96.45	40.98	33
-98.01	137.09	33
76.32	130.25	35

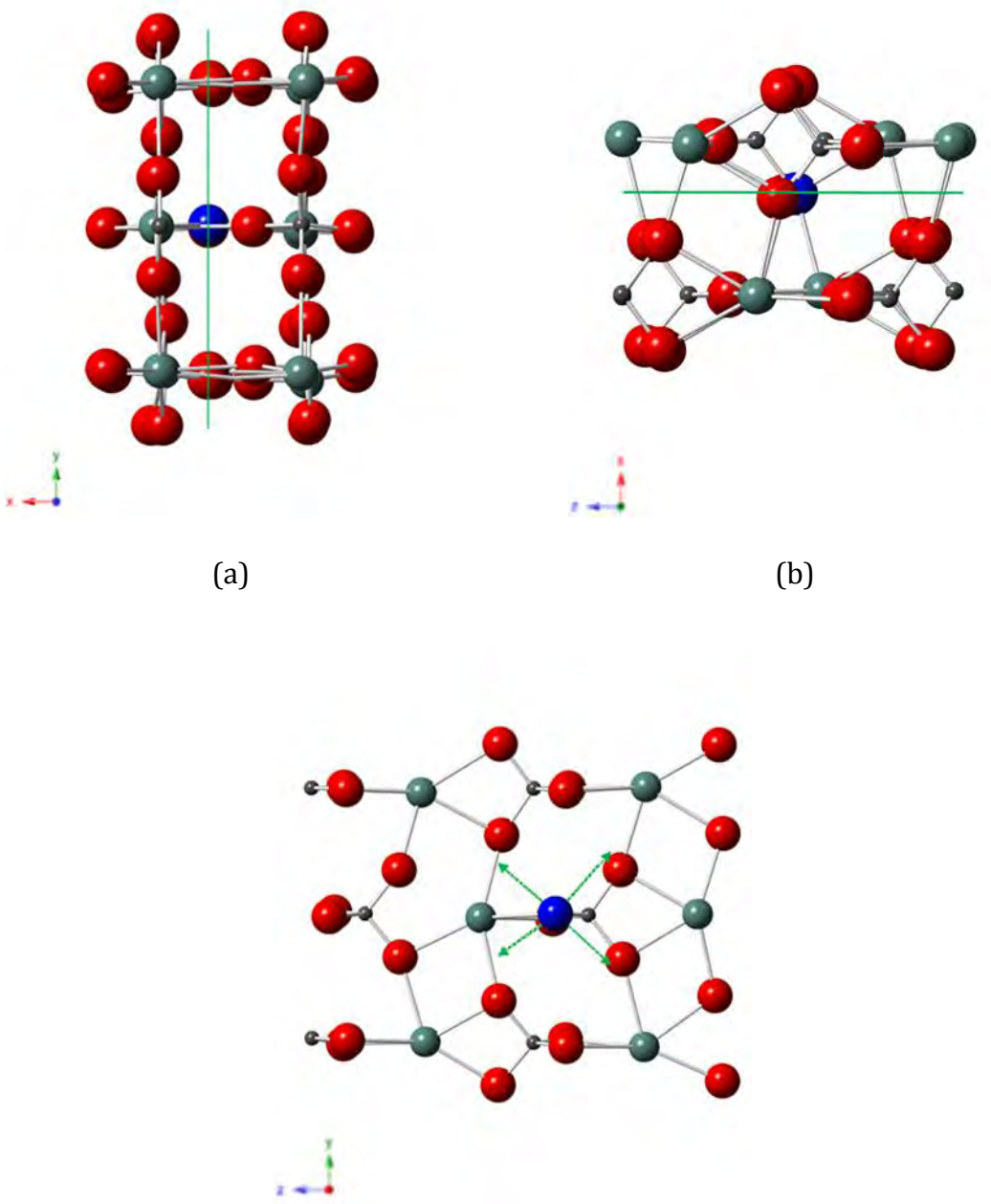

(a) (b)

(c)

Figure 6.13: Lowest energy PKA vectors for the oxygen PKA. The PKA atom is highlighted in blue and the green reference line indicates the bc plane

Similarly the contour plot also shows distinct areas corresponding to higher energy directions. The six highest energy PKA vectors that are closest to these local maxima are summarised in Table 6.6 and illustrated in Figure 6.14. Here it can be seen that these PKA

vectors are associated with the PKA atom being initiated towards other neighbouring atoms. The average threshold displacement energy taken over the ten PKA trajectories with the highest values of E_d was calculated to be $96 \pm 41\ eV$.

Table 6.6: Highest energy PKA vectors for the oxygen PKA

φ / degrees	θ / degrees	E_d/eV
-4.01	74.71	119
56.01	102.65	119
126.31	102.56	118
-177.11	62.86	107
178.58	115.35	87
-3.70	159.62	83

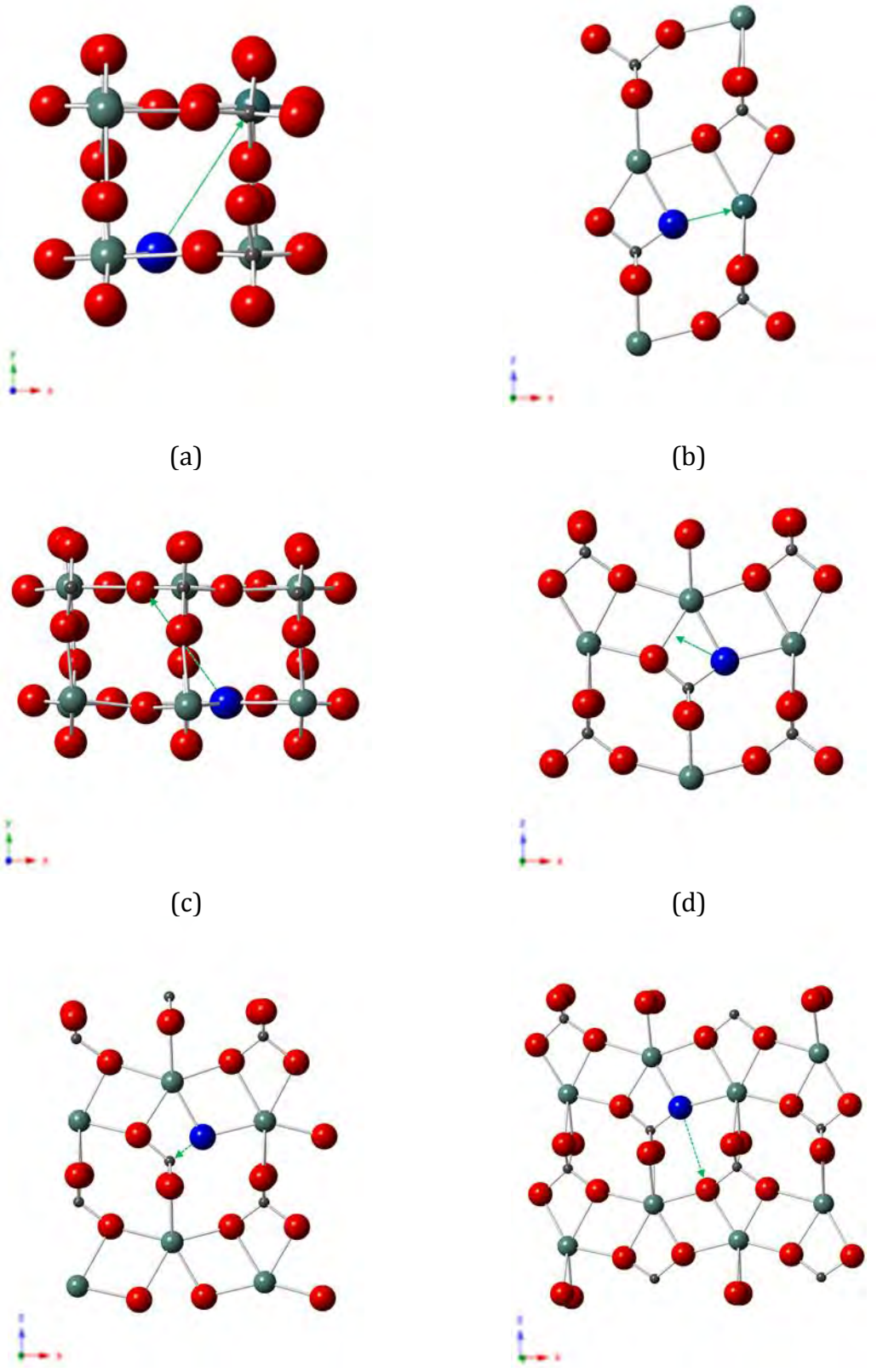

(a) (b)

(c) (d)

(e) (f)

Figure 6.14: : Highest energy PKA vectors for the oxygen PKA

6.3 Collision Cascades

In this study a supercell containing 405000 atoms (25 x 25 x 27 supercell) was equilibrated for 20 ps in the NPT anisotropic ensemble at 300 K and zero external pressure using the Berendsen thermostat and barostat. The resulting configuration was then equilibrated in the NVE ensemble for a further 20 ps before initiating the yttrium PKA in a given direction with an energy, E. Periodic boundary conditions were employed throughout the simulations and a variable time step algorithm was used to dynamically reduce the time step to below 1 fs to obey the condition that an atom can only travel a distance of r Å per time step, where 0.03 Å $\leq r \leq$ 0.10 Å. The PKA atoms were initiated with an energy of either 1, 3, 5 7 or 10 keV within the NVE ensemble for approximately 24 ps. The cascade simulations were repeated for five different PKA atoms that were randomly selected from a spherical volume with radius 10 Å centred on a point 20 Å from the cell boundary along the negative PKA vector. This was to ensure the PKA was initiated towards the centre of the simulation cell and so as the damaged region did not extend over the periodic boundary. The Frenkel pair defect evolution as a function of time has been analysed using the radius method for Frenkel pair detection outlined in chapter 2. An example of the defects present for a 10 keV PKA atom initiated in the (100) direction at peak damage and at the end of the simulation are illustrated in Figure 6.15. The final damage structure was then analysed using the Voronoi defect detection methodology described in chapter 2 to investigate the number of Frenkel pairs and anti-site defects. In chapter 4 the intrinsic defects were analysed which indicated that the degree of polymerisation is an important metric when considering defects in xenotime and so this is also analysed through the detection of bridging oxygen atoms.

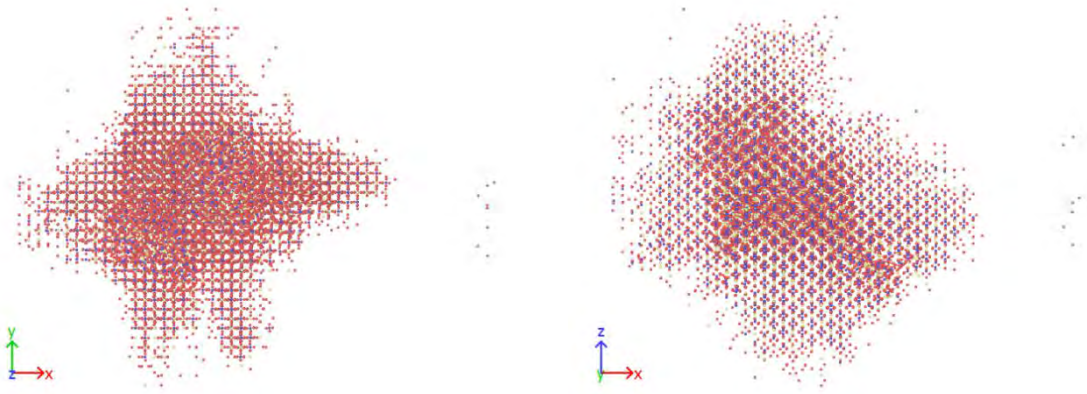

(a)

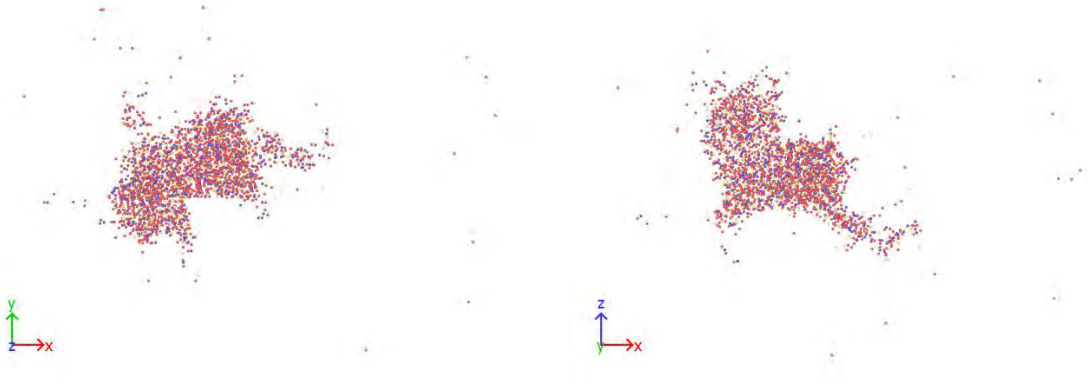

(b)

Figure 6.15: Defect configurations illustrating the interstitial atoms at (a) 0.81 ps and (b) 11.97 ps after a yttrium PKA was in initiated with a PKA energy of 10 keV in the (100) direction. The yttrium, phosphorus and oxygen atoms are shown in yellow, blue and red respectively

6.3.1 Xenotime (100) Cascades

The defect evolution as a function of time for Frenkel pairs identified by the radius method is illustrated in Figure 6.16. Here it can be seen that there is a reasonable amount of variation across the five different PKA atoms for all five energies, highlighting the importance of repeating cascade simulations. For all PKA energies the number of Frenkel pairs rises to a maximum within 1 ps, this is known as the ballistic phase. After this time the system undergoes rapid epitaxial recrystallization where the majority of the Frenkel pairs recombine leaving far fewer Frenkel pairs in the final damaged configuration.

Pressure waves can also be observed, especially for higher PKA energies, resulting in small peaks which become progressively less intense with simulation time. It can be seen that the time taken to reach peak damage increases with PKA energy, along with the total number of Frenkel pairs, both at peak damage and in the final damaged configuration. A summary of this information can be found in Table 6.7. The cation defects within the final damage configuration were analysed using the Voronoi method, Figure 6.17. Here it can be seen that there is again a great deal of variation over the five different PKAs used for all PKA energies. The general trend indicates that the yttrium Frenkel pairs dominate for PKAs with lower energy, whilst anti-site defect play a much greater role for higher energy PKAs. The number of cation Frenkel pairs identified by the Voronoi method was ca. 19 % of the number identified by the radius method for all PKA energies, Table 6.8.

Table 6.7: Summary of the time evolved defect properties for the ⟨100⟩ cascade in xenotime

PKA Energy / keV	Peak Time / ps	Maximum Frenkel Pairs	Final Frenkel Pairs	Percentage Annealed / %
1	0.36	768	146	81
3	0.50	3187	523	84
5	0.61	6564	978	85
7	0.67	9532	1333	86
10	0.80	19686	2356	88

Table 6.8: Comparison of the cation Frenkel defects defined by the radius and Voronoi method for the ⟨100⟩ cascade in xenotime

PKA Energy / keV	Cation Frenkel pairs (Radius Method)	Cation Frenkel pairs (Voronoi Method)	Percentage / %
1	52	10	19
3	185	36	19
5	343	68	20
7	458	90	20
10	786	150	19

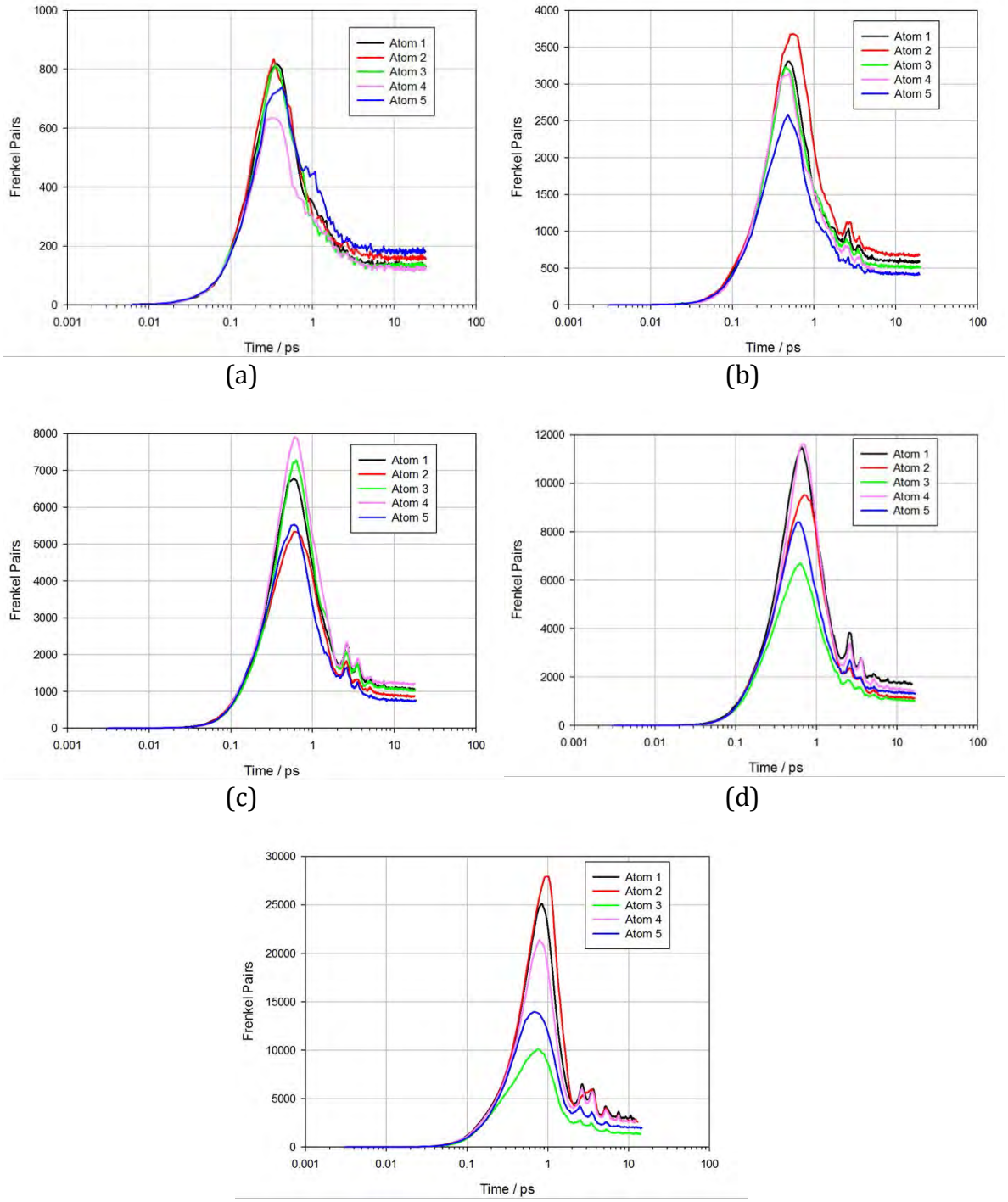

Figure 6.16: Frenkel pair evolution with time for the five different PKA atoms in the ⟨100⟩ direction with PKA energies of (a) 1 keV, (b) 3 keV, (c) 5 keV, (d) 7 keV and (e) 10 keV, as defined by the radius method fo defect detection.

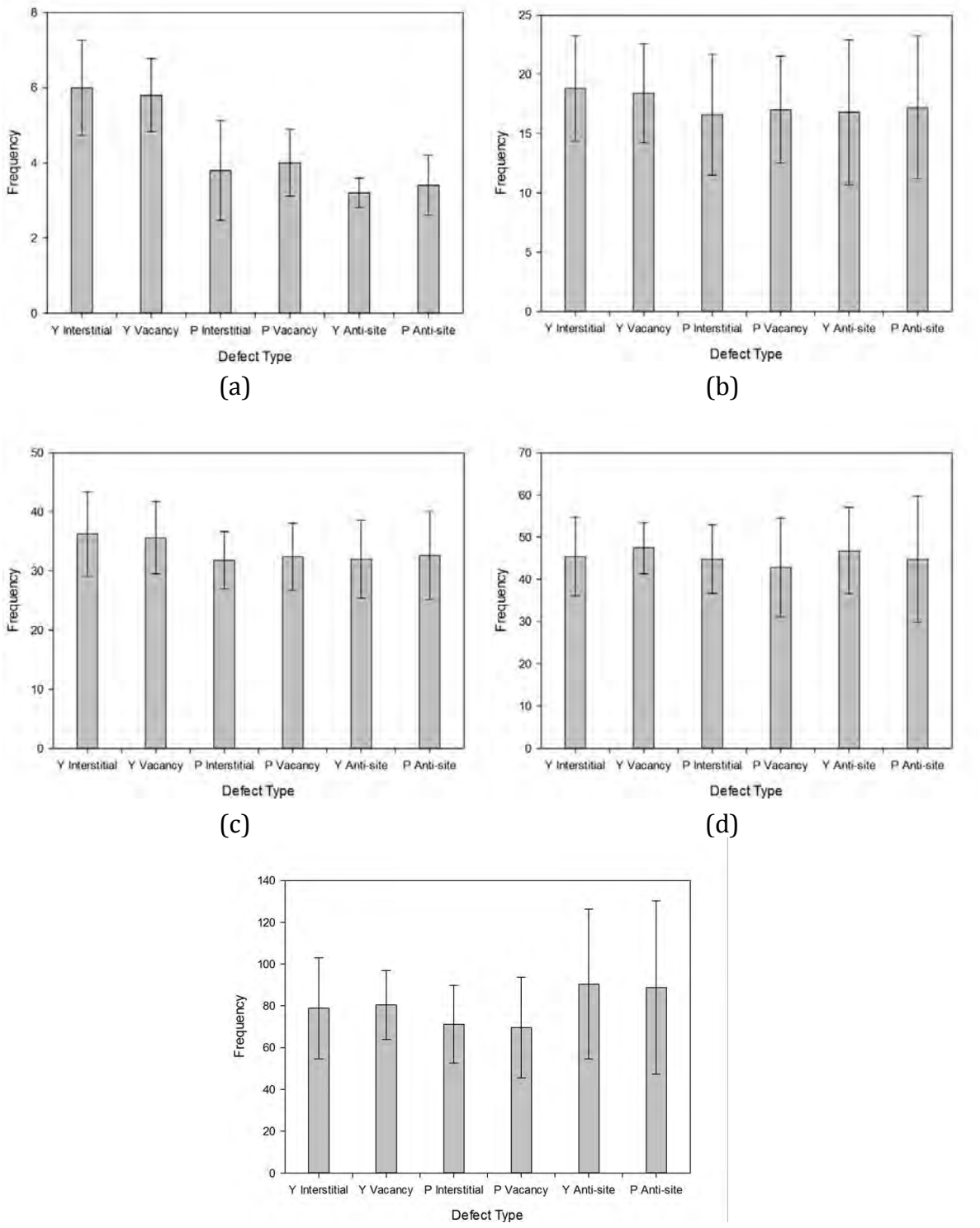

Figure 6.17: Average defect distribution, as identified by the Voronoi method, for the cascades in the ⟨100⟩ direction in xenotime, with PKA energies of (a) 1 keV, (b) 3 keV, (c) 5 keV, (d) 7 keV and (e) 10 keV

The degree of polymerisation of the phosphate tetrahedra within the final damaged configuration has also been analysed. Here the chain length is defined as the total number of atoms within a polymerised chain, including both phosphorus and oxygen atoms. The total number of polymerised chains within the final damaged configuration can be seen to increase with increasing PKA energy, whilst the distribution of chain lengths tends to become broader, Table 6.9. The average distributions of the polymerised units within the final damaged configuration with differing chain lengths for the five PKA energies are illustrated in Figure 6.18. Here it can be seen that there are clear peaks in the distribution for chains with length of ca. 9, 14 and 18. For the 1 keV PKA cascades the most common polymerised unit has a chain length of 10 atoms, whilst the most common chains have a length of 9 atoms for all other PKA energies investigated. Similarly the phosphorus content of the chains has been investigated, summarised in Table 6.10 and illustrated in Figure 6.19. A similar trend can be seen across all PKA energies with the most common chains containing 2 phosphorus atoms, with the relative frequency decreasing rapidly with increasing phosphorus content. Finally the P:O ratio of the chains has been analysed to investigate the relative net coordination of these chains compared to the archetypal polymerised phosphate chain consisting of corner sharing tetrahedra. The number of oxygen atoms within these standard chains relative to the number of phosphorus atoms can be evaluated following equation (6.9).

$$N_O = 3N_P + 1 \tag{6.9}$$

As such the P:O ratio for the polymerised chains identified in the final damaged configuration can be seen in Figure 6.20 as a function of the number of phosphorus atoms within the chains. Here the size of the data point indicates the relative frequency with

which the chains were observed. The dotted trend lines indicate chains with the ideal P:O ratio (black) and subsequently chains with increasing net oxygen over-coordination which are shifted to lower P:O ratios. Those data points that lie above the ideal curve correspond to chains that have a net oxygen under-coordination. Whilst the relative coordination of the phosphorus atoms within the chains inherently increases or decreases the P:O ratio of the polymerised units, factors such as edge sharing of the polyhedra within the chain also serves to decrease the P:O ratio. As such the chains are described by the net coordination, as any one chain may contain a combination of these features.

The most common polymerised unit found within the final damaged configuration for the 1 keV PKA cascades was the P_2O_8 unit. The ideally coordinated P_2O_7 unit was found to be the most common unit for all other PKA energies. It can be seen that there are a wide range of polymerised units found in all of the cascade simulations, with the degree of under-coordination of these chains generally increasing with PKA energy. Similarly chains with higher net over-coordination are generally seen more frequently for the higher PKA energies. This information is summarised in Table 6.11.

Table 6.9: Summary of the total number of polymerised chains and the range of chain lengths observed for the (100) cascades in xenotime

PKA Energy / keV	Average Number of Polymerised Chains	Smallest Chain	Largest Chain
1	13.8 ± 1.9	9	31
3	42.2 ± 4.0	9	45
5	71.0 ± 4.9	8	88
7	101.2 ± 5.3	8	44
10	151.8 ± 4.0	8	67

Table 6.10: Summary of the distribution of polymerised chains as a function of phosphorus content for the (100) cascades in xenotime

PKA Energy / keV	Containing 2 Phosphorus Atoms / %	Containing 3 Phosphorus Atoms / %	No. of Phosphorus Atoms In Longest Chain
1	56.7 ± 9.8	19.3 ± 5.1	7
3	59.0 ± 4.6	16.8 ± 5.8	10
5	57.2 ± 2.2	21.4 ± 4.9	20
7	57.9 ± 3.5	20.4 ± 1.9	10
10	58.1 ± 2.5	21.4 ± 2.4	16

Table 6.11: Summary of the net coordination of the polymerised chains and the most common polymerised unit for the (100) cascades in xenotime

PKA Energy / keV	Most Common Polymerised Unit	Net Oxygen Coordination Of Polymerised Chains	
		Lowest	Highest
1	P_2O_8	0	3
3	P_2O_7	-1	5
5	P_2O_7	-1	7
7	P_2O_7	-1	7
10	P_2O_7	-1	5

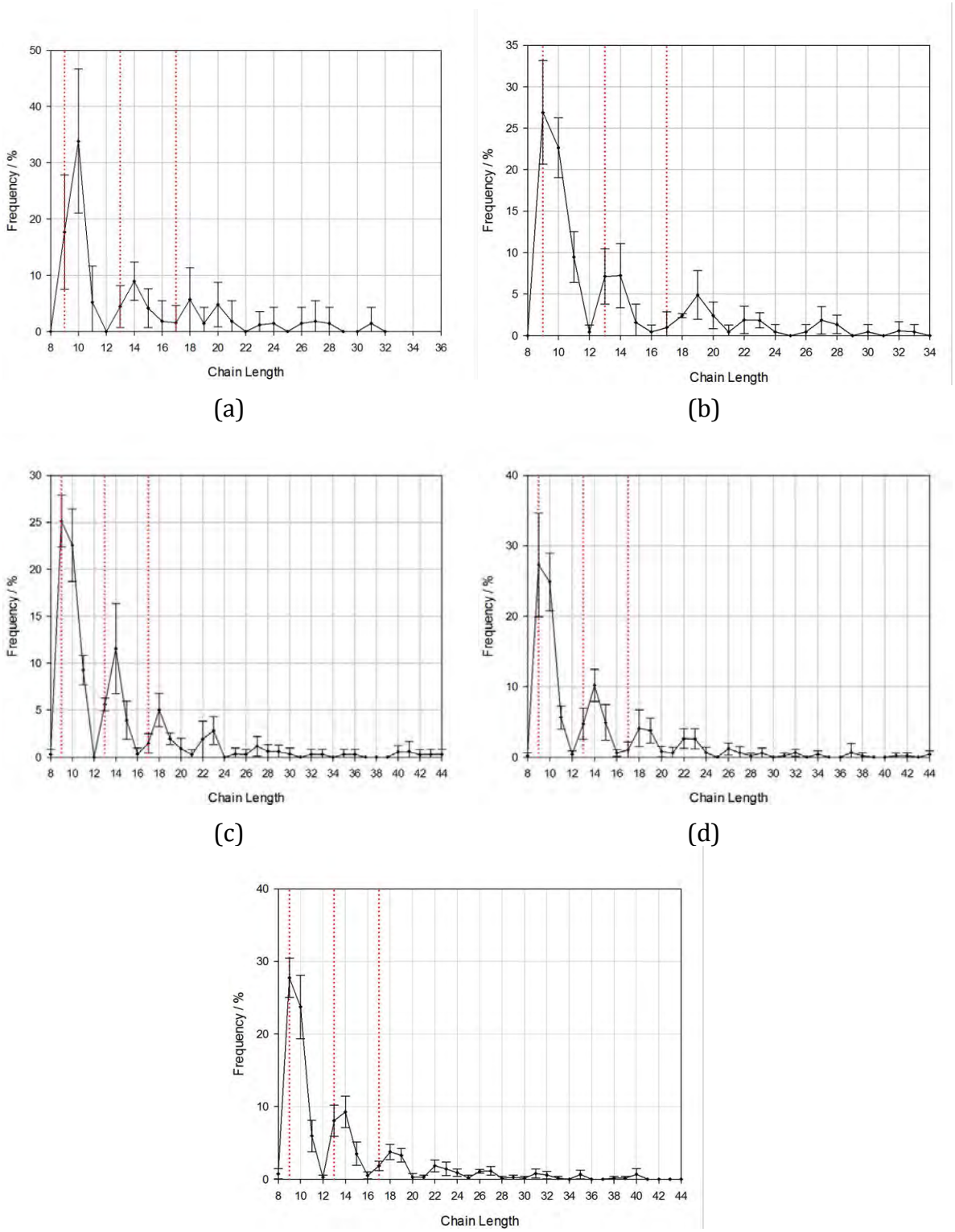

Figure 6.18: Average distribution of polymerised phosphate chains as a function of chain length for cascades in the ⟨100⟩ direction in xenotime for PKA energies of (a) 1 keV, (b) 3 keV, (c) 5 keV, (d) 7 keV and (e) 10 keV

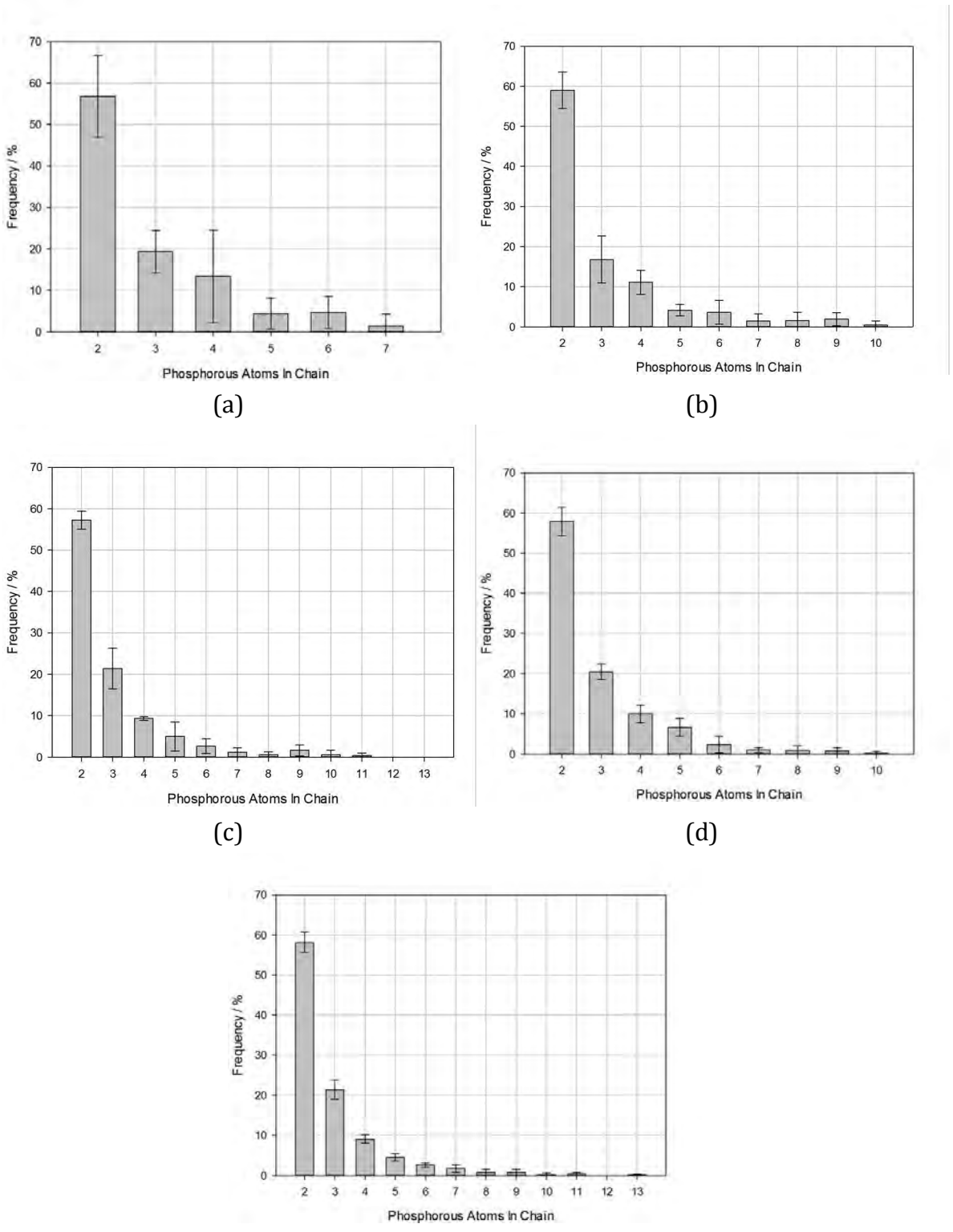

Figure 6.19: Average distribution of polymerised phosphate chains as a function of the phosphorus content for cascades in the ⟨100⟩ direction in xenotime for PKA energies of (a) 1 keV, (b) 3 keV, (c) 5 keV, (d) 7 keV and (e) 10 keV

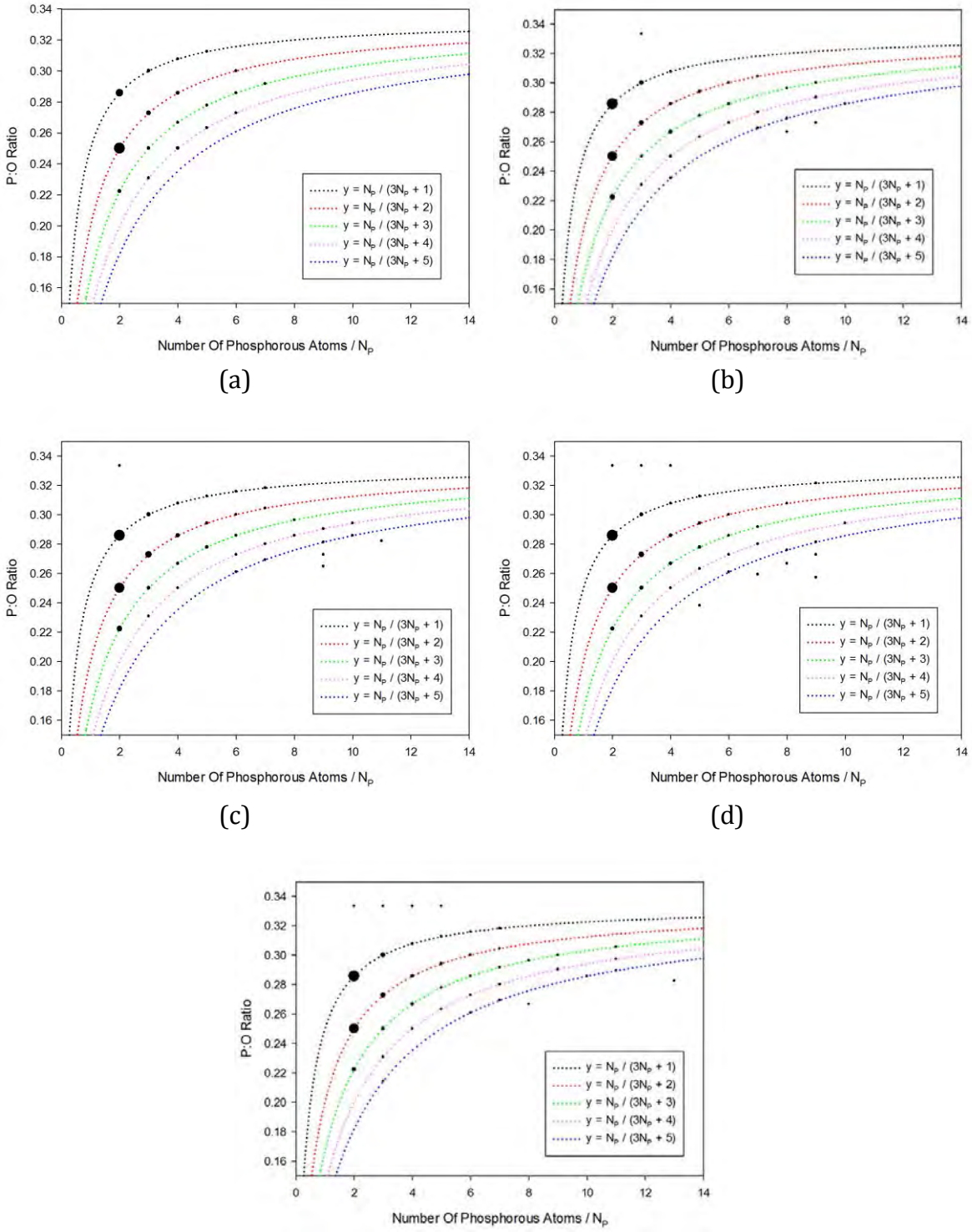

Figure 6.20: Average P:O ratio of the polymerised chains as a function of the phosphorus content for cascades in the ⟨100⟩ direction in xenotime for PKA energies of (a) 1 keV, (b) 3 keV, (c) 5 keV, (d) 7 keV and (e) 10 keV. The size of the data point corresponds to the relative frequency with which the chains were observed. The black dotted reference line indicates the ideal P:O ratio for an archetypal corner sharing phosphate chain.

6.3.2 Xenotime (001) Cascades

The defect evolution as a function of time for Frenkel pairs identified by the radius method is illustrated in Figure 6.21. Again it can be seen that there is a reasonable amount of variation across the five different PKA atom, especially for higher PKA energies. Pressure waves can also be observed, especially for higher PKA energies, resulting in small peaks which become progressively less intense with simulation time. It can be seen that the time taken to reach peak damage (the end of the ballistic phase) increases with PKA energy, along with the total number of Frenkel pair, both at peak damage and in the final damaged configuration. A summary of this information can be found in Table 6.12. The cation defects within the final damage configuration were analysed using the Voronoi method, Figure 6.22. Here once again it can be seen that there is again a great deal of variation over the five different PKAs used for all PKA energies. The general trend indicates that the yttrium Frenkel pairs are the most common defects for PKAs with lower energy, whilst anti-site defect play become more common at higher PKA energies. The number of cation Frenkel pairs identified by the Voronoi method was ca. 20 % of the number identified by the radius method for all PKA energies, Table 6.13.

Table 6.12: Summary of the time evolved defect properties for the (001) cascade in xenotime

PKA Energy / keV	Peak Time / ps	Maximum Frenkel Pairs	Final Frenkel Pairs	Percentage Annealed / %
1	0.33	735	132	82
3	0.54	3687	553	85
5	0.64	6398	900	86
7	0.71	10916	1468	87
10	0.86	20302	2532	88

Table 6.13: Comparison of the cation Frenkel defects defined by the radius and Voronoi method for the (001) cascade in xenotime

PKA Energy / keV	Cation Frenkel pairs (Radius Method)	Cation Frenkel pairs (Voronoi Method)	Percentage / %
1	45	10	22
3	191	37	19
5	316	66	21
7	502	96	19
10	841	161	19

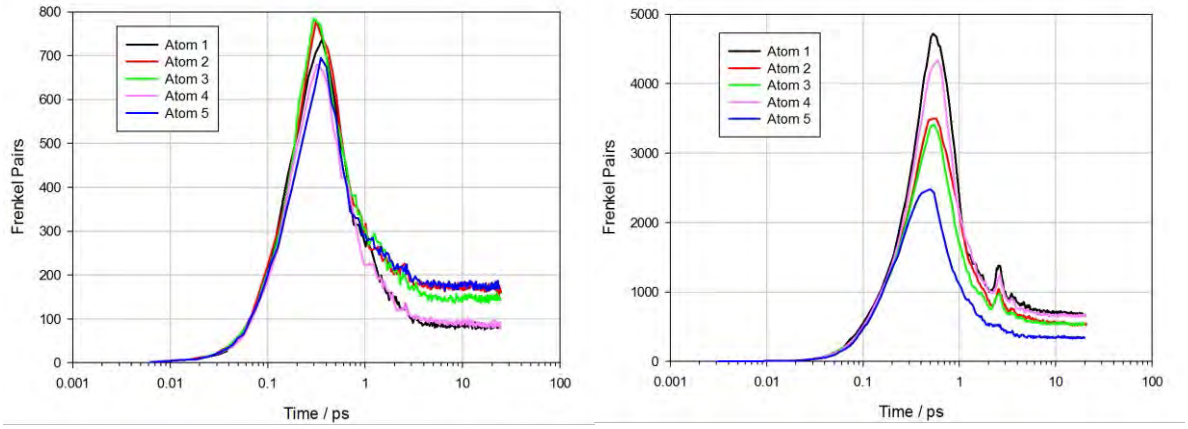

(a) (b)

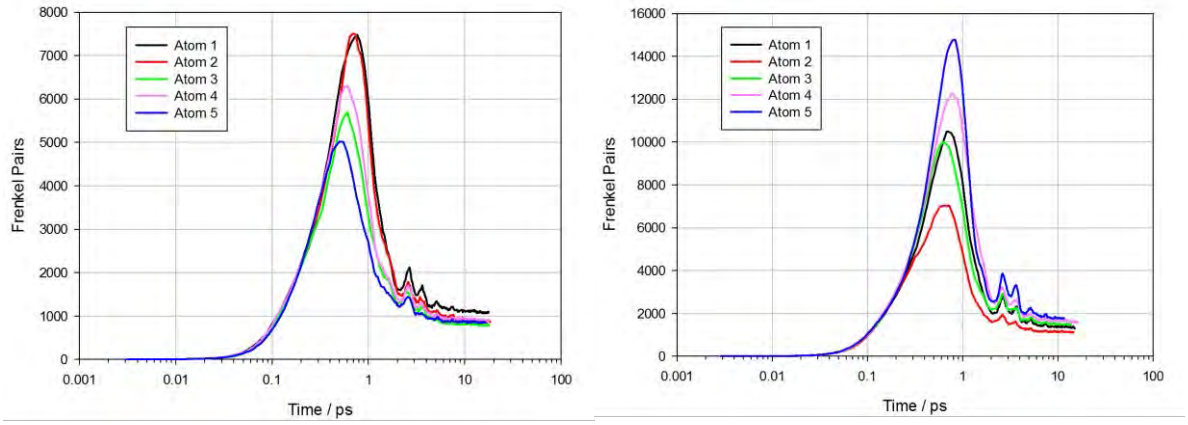

(c) (d)

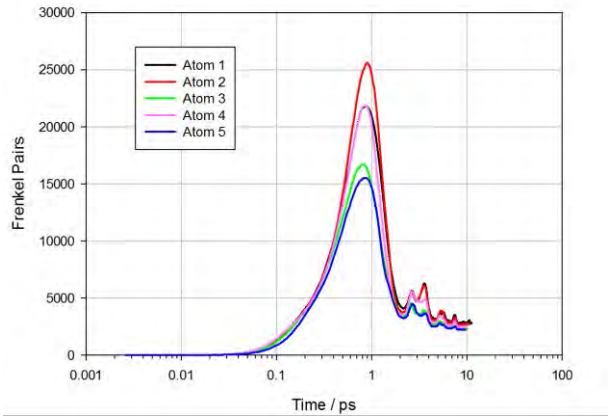

(e)

Figure 6.21: Frenkel pair evolution with time for the five different PKA atoms in the ⟨001⟩ direction in xenotime with PKA energies of (a) 1 keV, (b) 3 keV, (c) 5 keV, (d) 7 keV and (e) 10 keV, as defined by the radius method of defect detection.

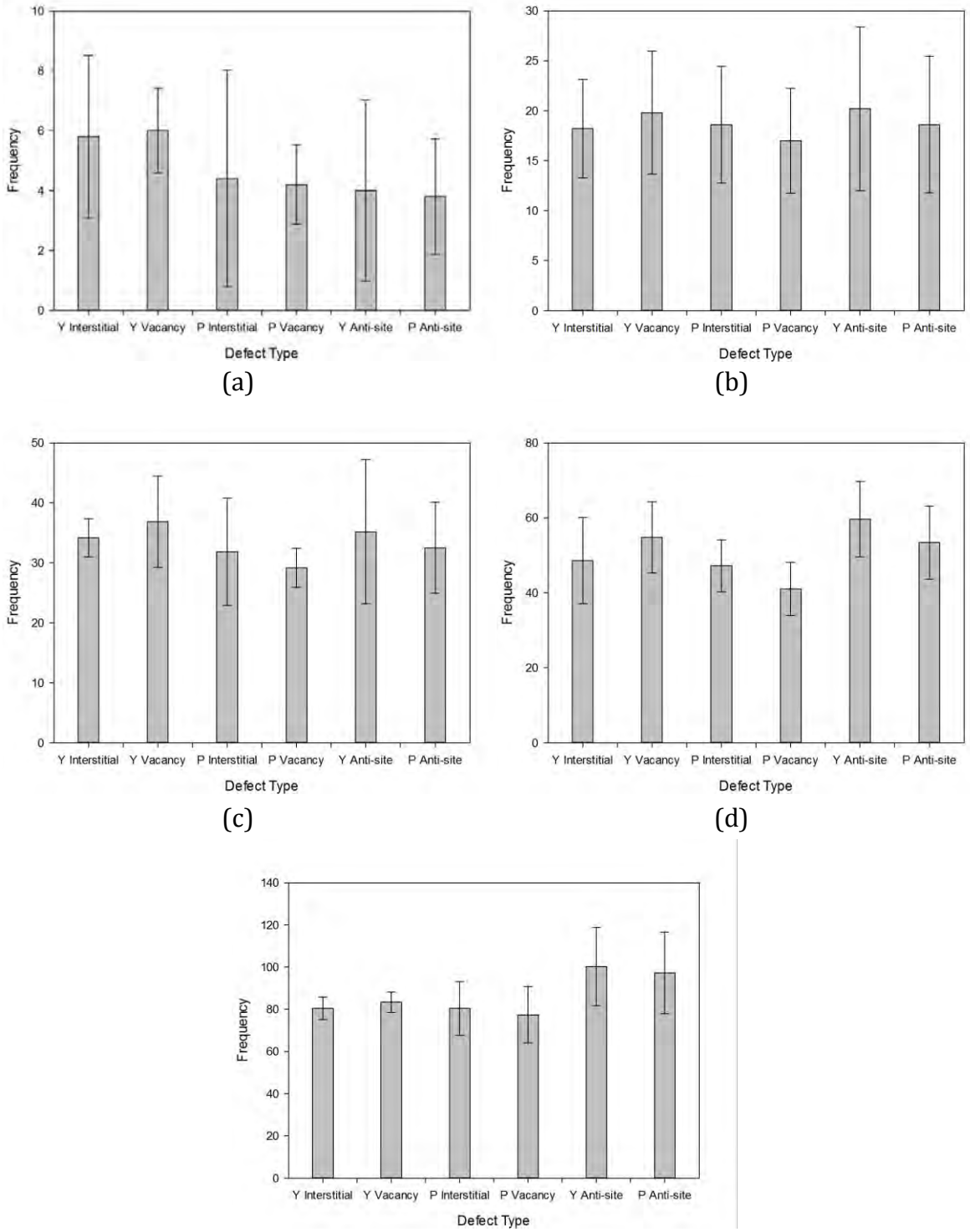

Figure 6.22: Average defect distribution, as identified by the Voronoi method, for the cascades in the ⟨001⟩ direction in xenotime, with PKA energies of (a) 1 keV, (b) 3 keV, (c) 5 keV, (d) 7 keV and (e) 10 keV

The degree of polymerisation of the phosphate tetrahedra within the final damaged configuration have also been analysed. The total number of polymerised chains within the final damaged configuration can be seen to increase with increasing PKA energy, whilst the distribution of chain lengths initially broadens before remaining relatively constant for higher PKA energies, Table 6.14. The average distributions of the polymerised units within the final damaged configuration with differing chain lengths for the five PKA energies are illustrated in Figure 6.23. It can be seen that there are clear peaks in the distribution for chains with length of ca. 9, 14 and 18 as for the previously discussed PKA trajectory. At lower PKA energies the most common polymerised unit has a chain length of 10 atoms, with this peak shifting to 9 atoms for higher PKA energies. Similarly the phosphorus content of the chains has been investigated, summarised in Table 6.15 and illustrated in Figure 6.24. A similar trend can be seen across all PKA energies with the most common chains containing 2 phosphorus atoms, with the relative frequency decreasing rapidly with increasing phosphorus content. Finally the P:O ratio of the chains has been analysed to investigate the relative net coordination of these chains compared to the archetypal polymerised phosphate chain consisting of corner sharing tetrahedra, Figure 6.25. The most common polymerised unit found within the final damaged configuration for the 1 and 3 keV PKA cascades is the P_2O_8 unit, whilst the ideally coordinated P_2O_7 unit is the most common unit for all other PKA energies. It can be seen that there are a wide range of polymerised units found in all of the cascade simulations, with the degree of under-coordination of these chains generally increasing with PKA energy. Similarly chains with higher net over-coordination are generally seen more frequently for the higher PKA energies. This information is summarised in Table 6.16.

Table 6.14: Summary of the total number of polymerised chains and the range of chain lengths observed for the (001) cascades in xenotime

PKA Energy / keV	Average Number of Polymerised Chains	Smallest Chain	Largest Chain
1	11.4 ± 1.9	9	40
3	41.2 ± 4.0	8	67
5	64.6 ± 4.6	8	69
7	96.8 ± 7.5	8	69
10	151.8 ± 4.0	8	67

Table 6.15: Summary of the distribution of polymerised chains as a function of phosphorus content for the (001) cascades in xenotime

PKA Energy / keV	Containing 2 Phosphorus Atoms / %	Containing 3 Phosphorus Atoms / %	No. of Phosphorus Atoms In Longest Chain
1	51.0 ± 7.9	21.9 ± 10.3	9
3	55.5 ± 8.4	21.1 ± 6.9	15
5	56.7 ± 3.7	16.6 ± 3.9	16
7	60.1 ± 2.8	18.0 ± 3.2	15
10	61.2 ± 3.4	19.7 ± 2.6	15

Table 6.16: Summary of the net coordination of the polymerised chains and the most common polymerised unit for the (001) cascades in xenotime

PKA Energy / keV	Most Common Polymerised Unit	Net Oxygen Coordination Of Polymerised Chains	
		Lowest	Highest
1	P_2O_8	0	4
3	P_2O_8	-1	6
5	P_2O_7	-1	5
7	P_2O_7	-2	6
10	P_2O_7	-2	6

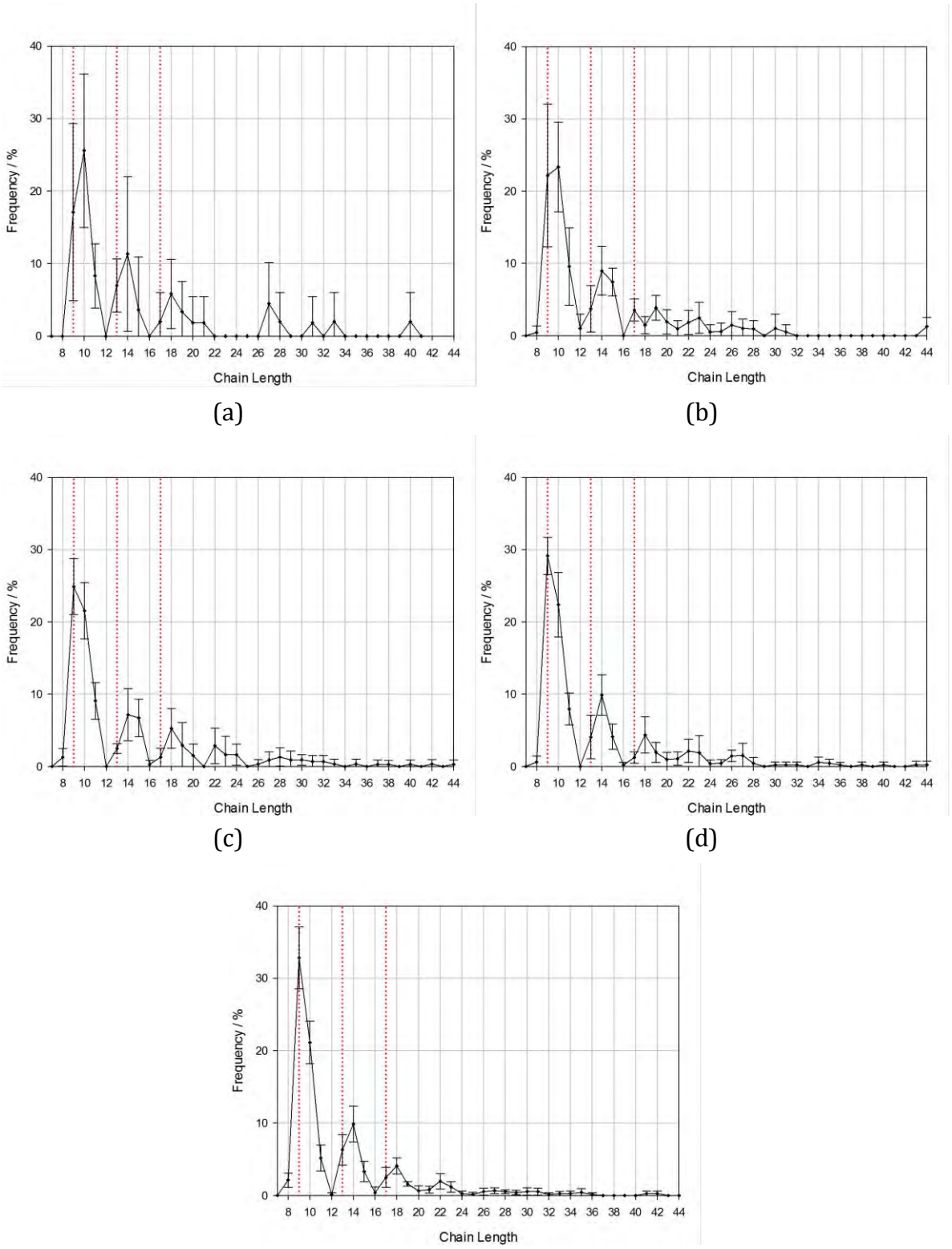

Figure 6.23: Average distribution of polymerised phosphate chains as a function of chain length for cascades in the (001) direction in xenotime for PKA energies of (a) 1 keV, (b) 3 keV, (c) 5 keV, (d) 7 keV and (e) 10 keV

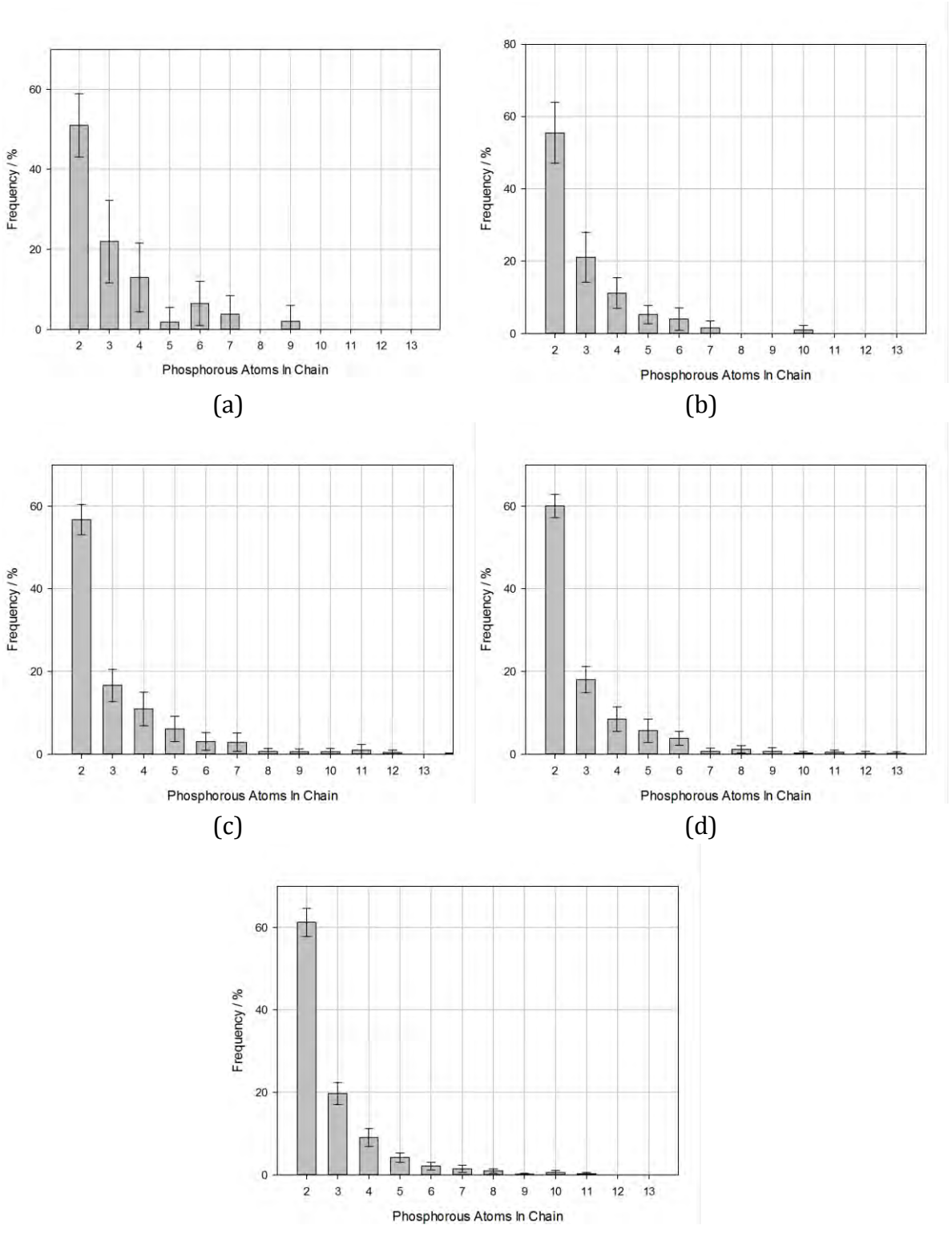

Figure 6.24: Average distribution of polymerised phosphate chains as a function of the phosphorus content for cascades in the (001) direction in xenotime for PKA energies of (a) 1 keV, (b) 3 keV, (c) 5 keV, (d) 7 keV and (e) 10 keV

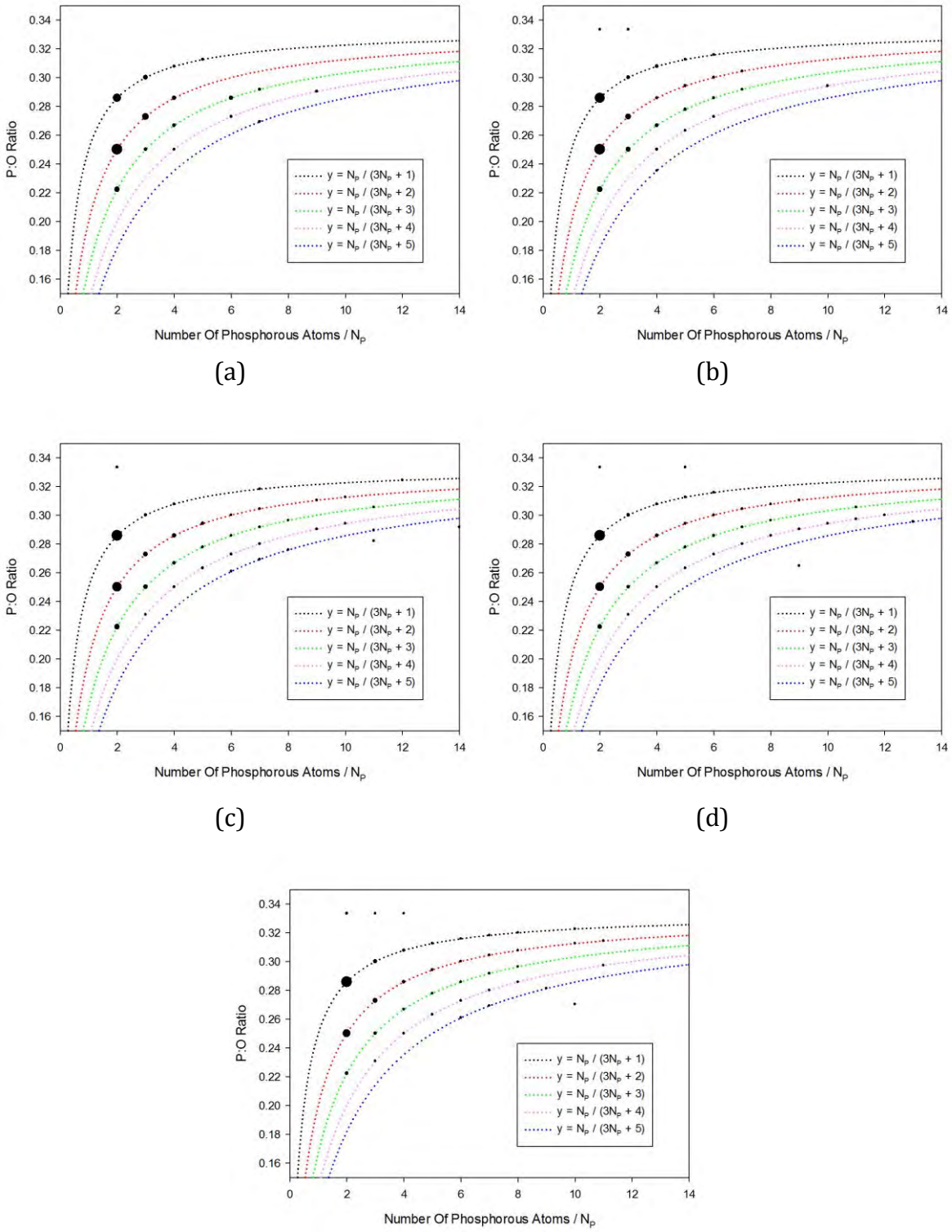

Figure 6.25: Average P:O ratio of the polymerised chains as a function of the phosphorus content for cascades in the (001) direction in xenotime for PKA energies of (a) 1 keV, (b) 3 keV, (c) 5 keV, (d) 7 keV and (e) 10 keV. The size of the data point corresponds to the relative frequency with which the chains were observed. The black dotted reference line indicates the ideal P:O ratio for an archetypal corner sharing phosphate chain.

6.3.3 Xenotime $(1\bar{1}9)$ Cascades

The defect evolution as a function of time for Frenkel pairs identified by the radius method is illustrated in Figure 6.26. Once again it can be seen that there is a reasonable amount of variation across the five different PKA atoms for all PKA energies. Pressure waves can also be observed, especially for higher PKA energies. It can be seen that the time taken to reach the end of the ballistic phase increases with PKA energy, along with the total number of Frenkel pair, both at peak damage and in the final damaged configuration. A summary of this information can be found in Table 6.17. The cation defects within the final damage configuration were analysed using the Voronoi method, Figure 6.27. Here once again it can be seen that there is again a great deal of variation over the five different PKAs used for all PKA energies. The general trend indicates that the yttrium vacancy and phosphorus interstitial are the most common defects for PKAs with lower energy, whilst for higher PKA energies there is little preference. The number of cation Frenkel pairs identified by the Voronoi method was ca. 20 % of the number identified by the radius method for all PKA energies, Table 6.18.

Table 6.17: Summary of the time evolved defect properties for the $(1\bar{1}9)$ cascade in xenotime

PKA Energy / keV	Peak Time / ps	Maximum Frenkel Pairs	Final Frenkel Pairs	Percentage Annealed / %
1	0.32	685	130	81
3	0.53	3532	513	85
5	0.63	7149	1023	86
7	0.75	12274	1700	86
10	0.87	18763	2336	88

Table 6.18: Comparison of the cation Frenkel defects defined by the radius and Voronoi method for the $(1\bar{1}9)$ cascade in xenotime

PKA Energy / keV	Cation Frenkel pairs (Radius Method)	Cation Frenkel pairs (Voronoi Method)	Percentage / %
1	45	9	20
3	185	36	19
5	352	69	20
7	586	116	20
10	788	160	20

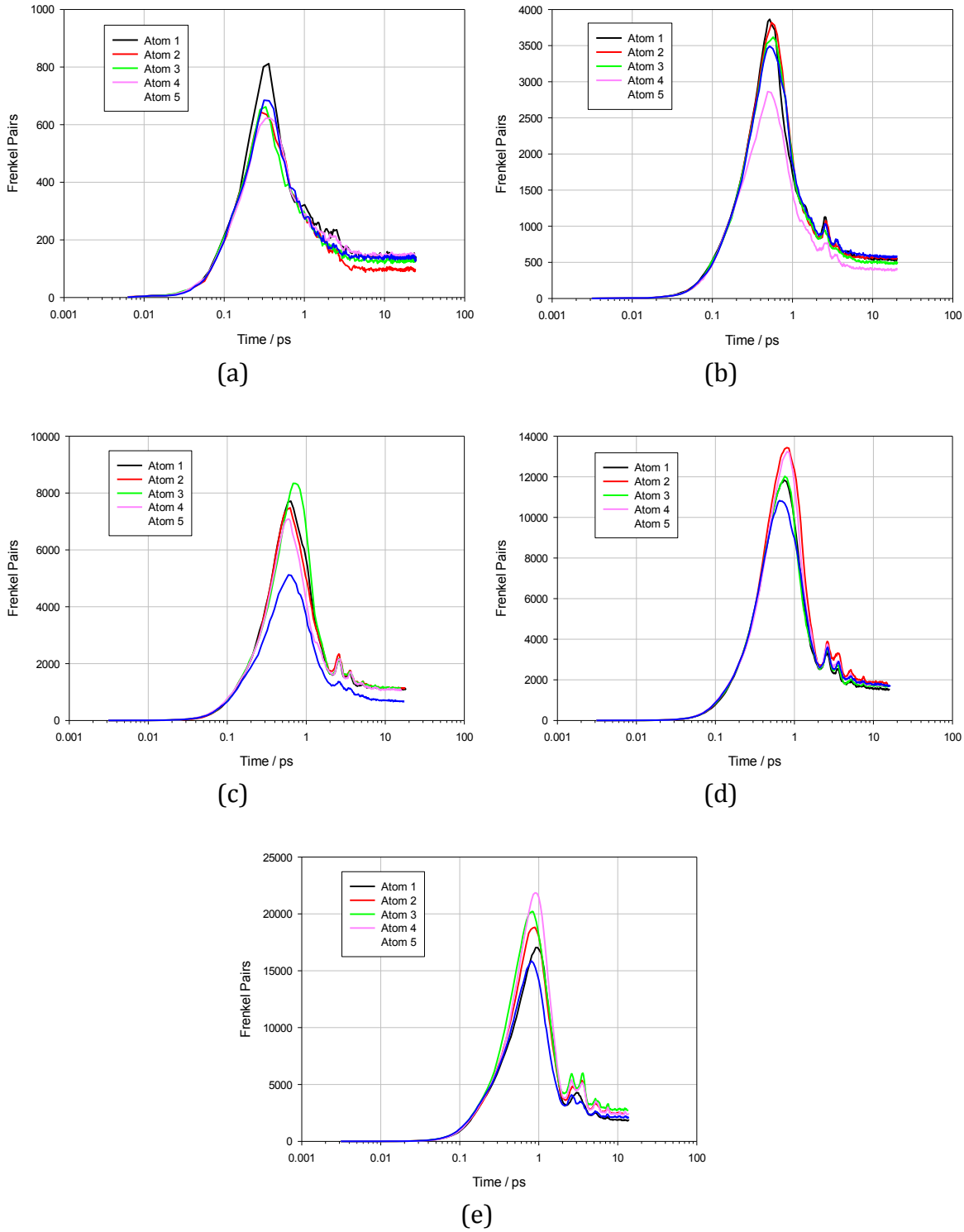

Figure 6.26: Frenkel pair evolution with time for the five different PKA atoms in the $(1\bar{1}9)$ direction in xenotime with PKA energies of (a) 1 keV, (b) 3 keV, (c) 5 keV, (d) 7 keV and (e) 10 keV, as defined by the radius method of defect detection.

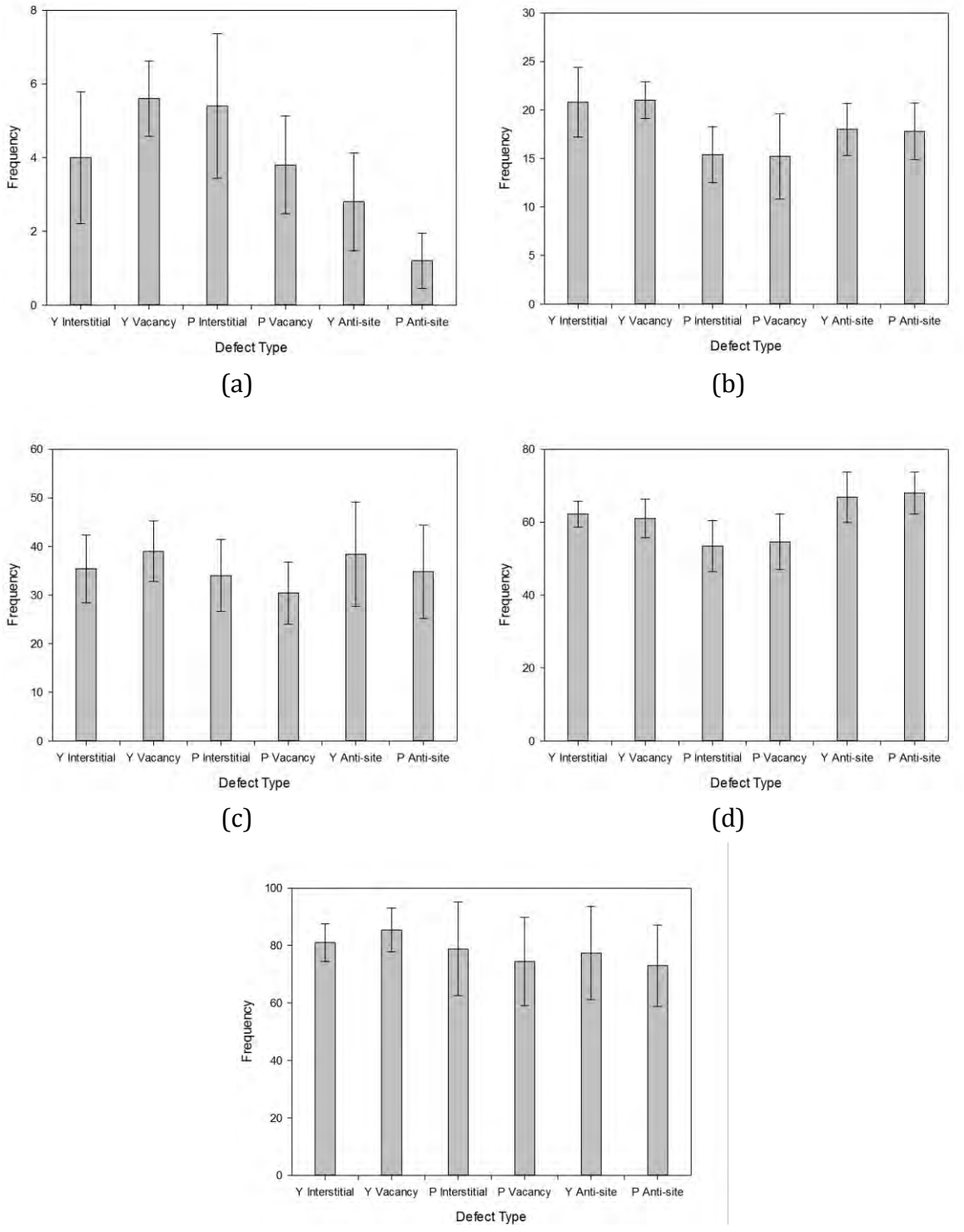

Figure 6.27: Average defect distribution, as identified by the Voronoi method, for the cascades in the $(1\bar{1}9)$ direction in xenotime, with PKA energies of (a) 1 keV, (b) 3 keV, (c) 5 keV, (d) 7 keV and (e) 10 keV

The degree of polymerisation of the phosphate tetrahedra within the final damaged configuration have also been analysed. The total number of polymerised chains within the final damaged configuration can be seen to increase with increasing PKA energy, whilst the distribution of chain lengths initially broadens before remaining relatively constant for higher PKA energies, Table 6.19. The average distributions of the polymerised units within the final damaged configuration with differing chain lengths for the five PKA energies are illustrated in Figure 6.28. It can be seen that there are clear peaks in the distribution for chains with length of ca. 9, 14 and 18 as for the previously discussed PKA trajectory. At lower PKA energies the most common polymerised unit has a chain length of 10 atoms, with this peak shifting to 9 atoms for higher PKA energies. Similarly the phosphorus content of the chains has been investigated, summarised in Table 6.20 and illustrated in Figure 6.29. A similar trend can be seen across all PKA energies with the most common chains containing 2 phosphorus atoms, with the relative frequency decreasing rapidly with increasing phosphorus content. Finally the P:O ratio of the chains has been analysed to investigate the relative net coordination of these chains compared to the archetypal polymerised phosphate chain consisting of corner sharing tetrahedra, Figure 6.30. The most common polymerised unit found within the final damaged configuration for the 1 and 3 keV PKA cascades is the P_2O_8 unit, whilst the ideally coordinated P_2O_7 unit is the most common unit for all other PKA energies. It can be seen that there are a wide range of polymerised units found in all of the cascade simulations, with the degree of under-coordination of these chains generally increasing with PKA energy. Similarly chains with higher net over-coordination are generally seen more frequently for the higher PKA energies. This information is summarised in Table 6.21.

Table 6.19: Summary of the total number of polymerised chains and the range of chain lengths observed for the $(1\bar{1}9)$ cascades in xenotime

PKA Energy / keV	Average Number of Polymerised Chains	Smallest Chain	Largest Chain
1	13.6 ± 1.4	9	35
3	42.0 ± 1.7	9	42
5	72.4 ± 6.3	9	45
7	100.8 ± 3.9	9	107
10	150.8 ± 6.4	9	64

Table 6.20: Summary of the distribution of polymerised chains as a function of phosphorus content for the $(1\bar{1}9)$ cascades in xenotime

PKA Energy / keV	Containing 2 Phosphorus Atoms / %	Containing 3 Phosphorus Atoms / %	No. of Phosphorus Atoms In Longest Chain
1	68.8 ± 6.8	12.9 ± 7.9	8
3	59.5 ± 6.1	18.1 ± 4.2	10
5	56.5 ± 6.1	23.7 ± 4.2	13
7	58.9 ± 3.5	17.8 ± 2.7	24
10	59.2 ± 5.2	19.1 ± 4.0	15

Table 6.21: Summary of the net coordination of the polymerised chains and the most common polymerised unit for the $(1\bar{1}9)$ cascades in xenotime

PKA Energy / keV	Most Common Polymerised Unit	Net Oxygen Coordination Of Polymerised Chains	
		Lowest	Highest
1	P_2O_8	0	5
3	P_2O_7	0	4
5	P_2O_7	-1	1
7	P_2O_8	-1	10
10	P_2O_7	-1	5

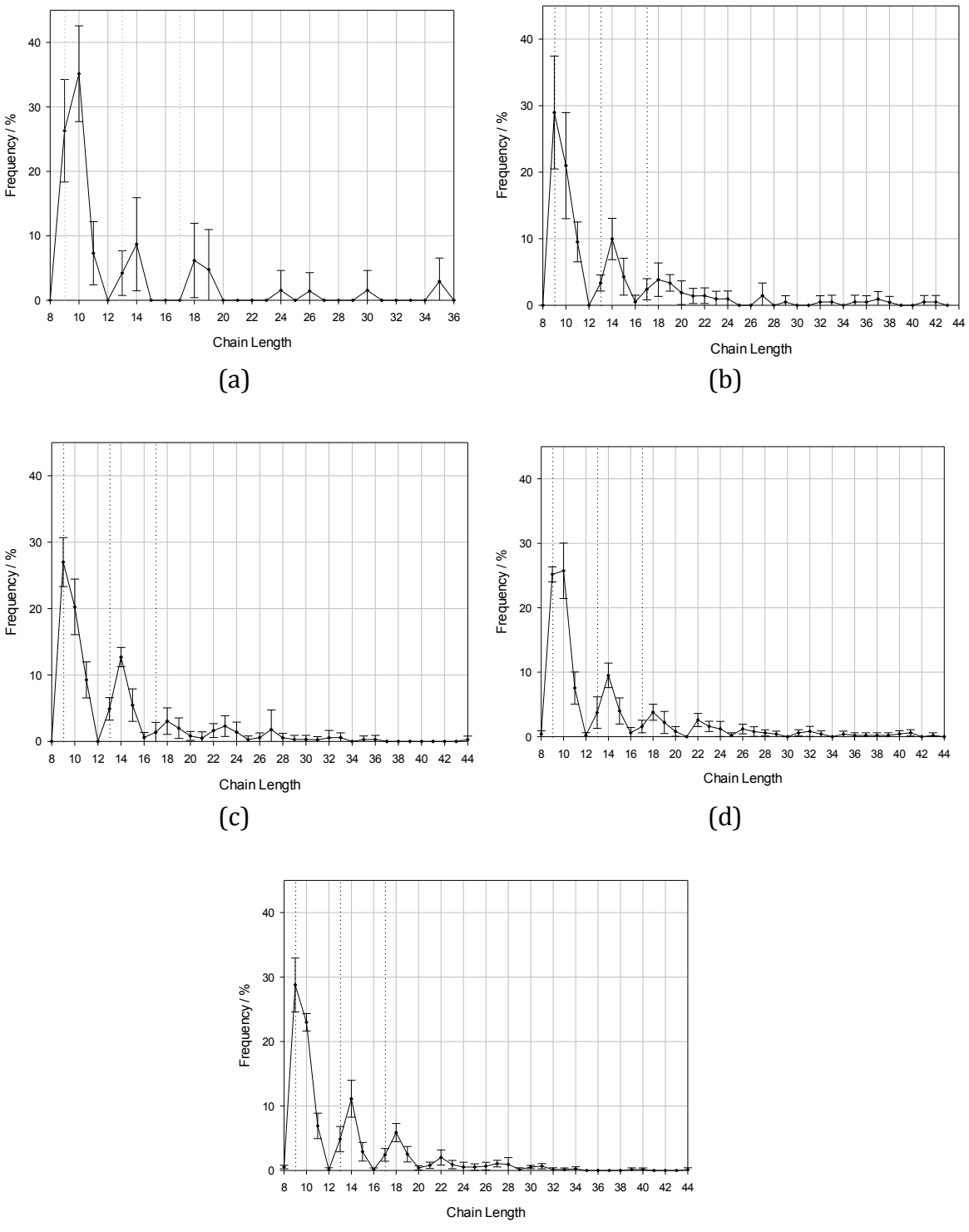

Figure 6.28: Average distribution of polymerised phosphate chains as a function of chain length for cascades in the $(1\bar{1}9)$ direction in xenotime for PKA energies of (a) 1 keV, (b) 3 keV, (c) 5 keV, (d) 7 keV and (e) 10 keV

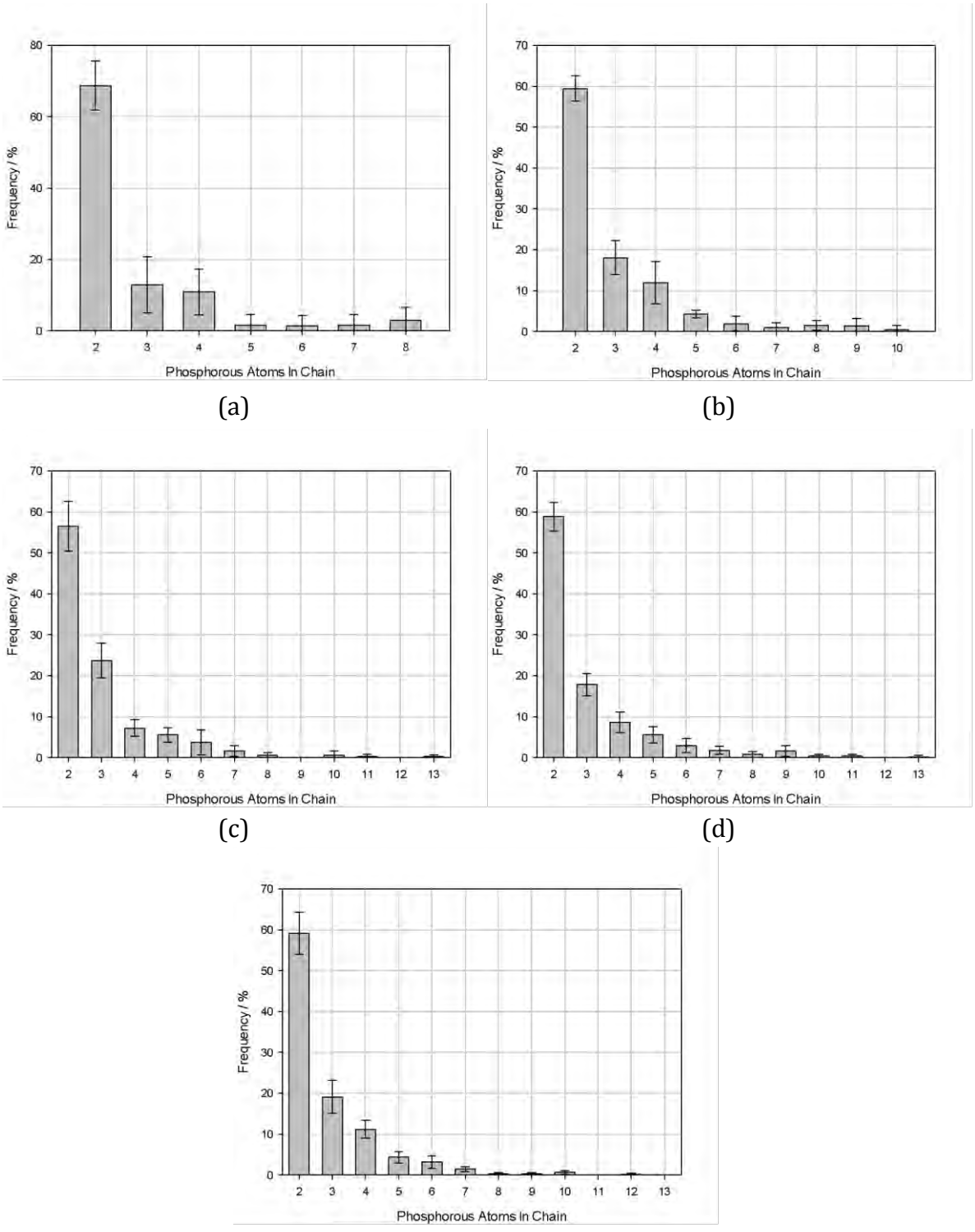

Figure 6.29: Average distribution of polymerised phosphate chains as a function of the phosphorus content for cascades in the $(1\bar{1}9)$ direction in xenotime for PKA energies of (a) 1 keV, (b) 3 keV, (c) 5 keV, (d) 7 keV and (e) 10 keV

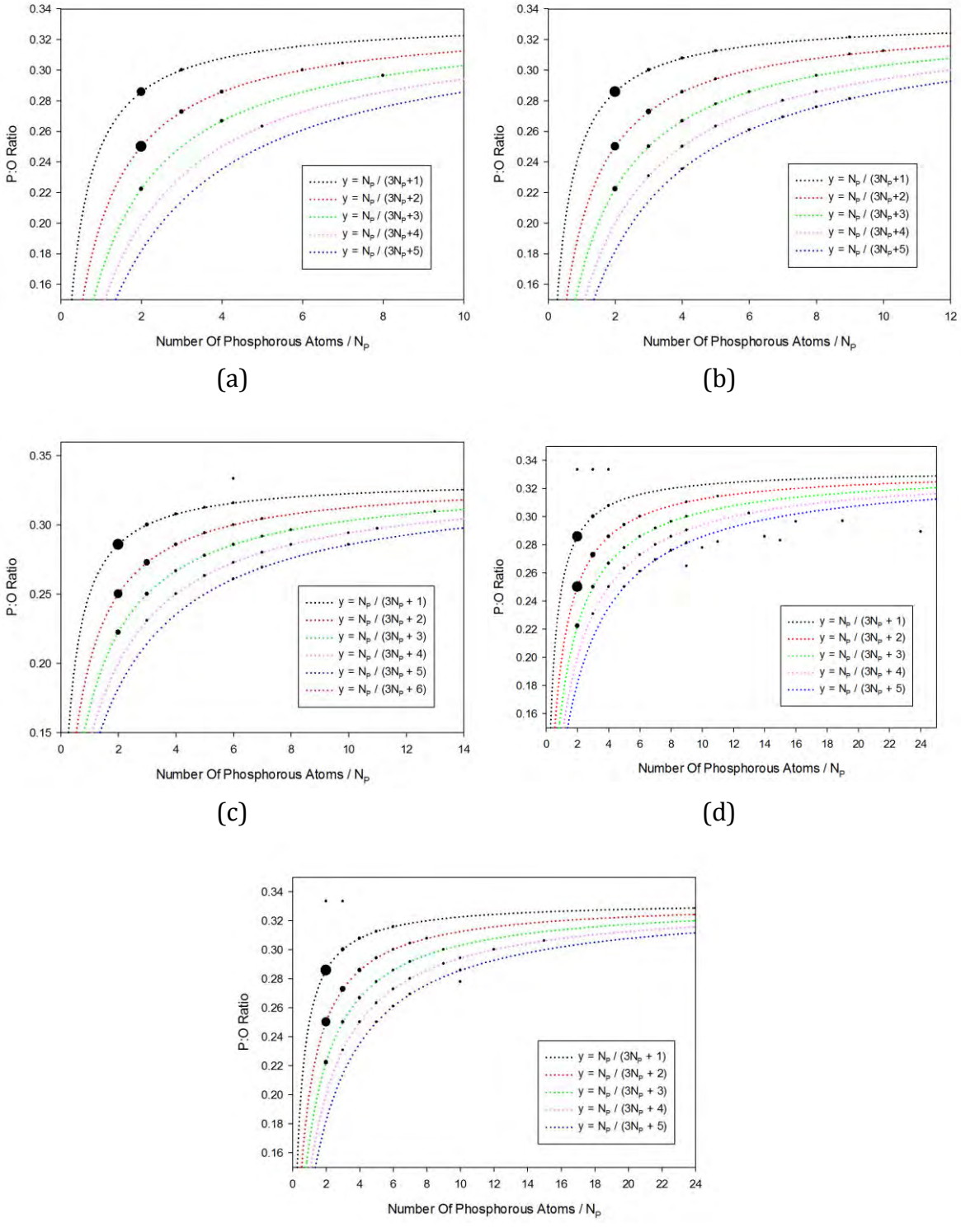

Figure 6.30: Average P:O ratio of the polymerised chains as a function of the phosphorus content for cascades in the $(1\bar{1}9)$ direction in xenotime for PKA energies of (a) 1 keV, (b) 3 keV, (c) 5 keV, (d) 7 keV and (e) 10 keV. The size of the data point corresponds to the relative frequency with which the chains were observed. The black dotted reference line indicates the ideal P:O ratio for an archetypal corner sharing phosphate chain.

6.3.4 Zircon $(1\bar{1}9)$ Cascades

The defect evolution as a function of time for Frenkel pairs identified by the radius method is illustrated in Figure 6.31. Much smaller pressure waves can be observed for higher PKA energies than were observed in the xenotime system. It can be seen that the time taken to reach the end of the ballistic phase increases with PKA energy, along with the total number of Frenkel pair, both at peak damage and in the final damaged configuration. Far fewer Frenkel pairs were identified than for the xenotime system. Evidence of a sub-cascade can be seen for the 10 keV PKA, with a shoulder peak evident in the first peak for several PKA atoms. A summary of this information can be found in Table 6.22. The cation defects within the final damage configuration were analysed using the Voronoi method, Figure 6.32. The zirconium interstitial was found to be the least common defect for all PKA energies. The silicon interstitial is the most common defect at low PKA energies with the anti-site defects becoming more prominent with increasing PKA energy. The number of cation Frenkel pairs identified by the Voronoi method was ca. 22 % of the number identified by the radius method for all PKA energies, Table 6.23.

Table 6.22: Summary of the time evolved defect properties for the $(1\bar{1}9)$ cascade in zircon

PKA Energy / keV	Peak Time / ps	Maximum Frenkel Pairs	Final Frenkel Pairs	Percentage Annealed / %
1	0.19	240	32	87
3	0.25	777	82	89
5	0.29	1564	189	88
7	0.28	2283	268	88
10	0.31	2931	352	88

Table 6.23: Comparison of the cation Frenkel defects defined by the radius and Voronoi method for the $(1\bar{1}9)$ cascade in zircon

PKA Energy / keV	Cation Frenkel pairs (Radius Method)	Cation Frenkel pairs (Voronoi Method)	Percentage / %
1	15	4	27
3	37	8	22
5	84	17	20
7	123	25	20
10	155	31	20

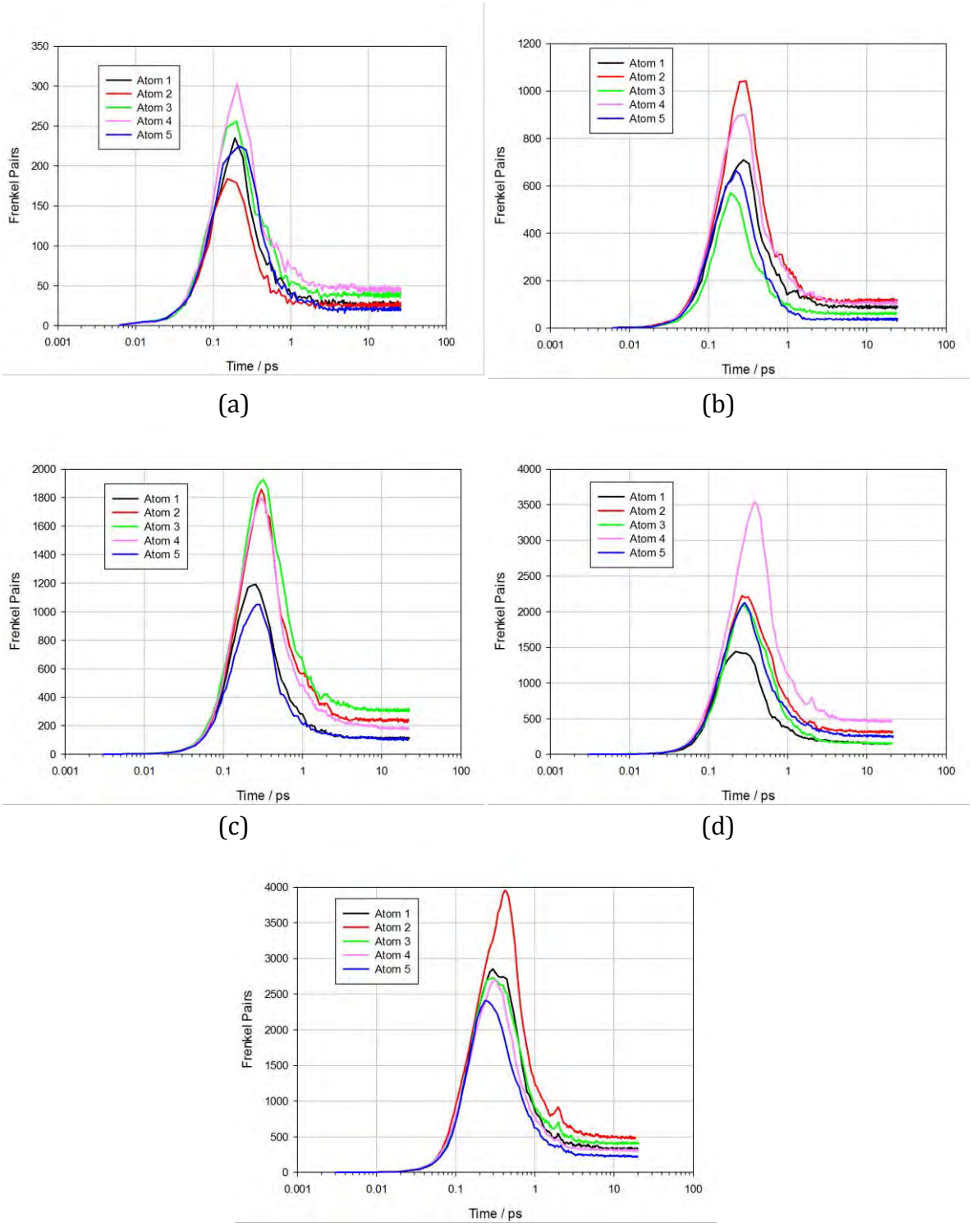

Figure 6.31: Frenkel pair evolution with time for the five different PKA atoms in the $(1\bar{1}9)$ direction in zircon with PKA energies of (a) 1 keV, (b) 3 keV, (c) 5 keV, (d) 7 keV and (e) 10 keV, as defined by the radius method of defect detection.

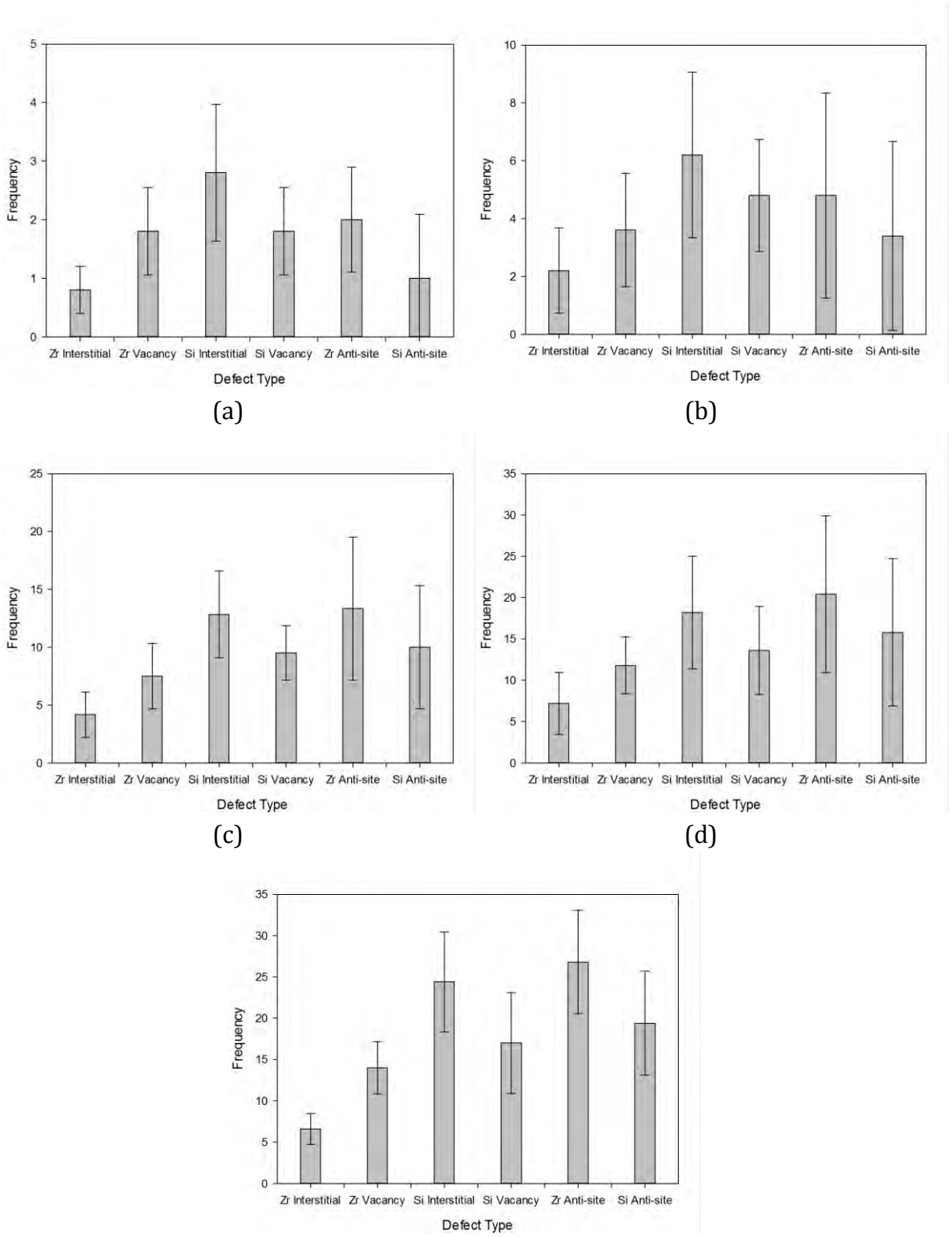

Figure 6.32: Average defect distribution, as identified by the Voronoi method, for the cascades in the $(1\bar{1}9)$ direction in zircon, with PKA energies of (a) 1 keV, (b) 3 keV, (c) 5 keV, (d) 7 keV and (e) 10 keV

The degree of polymerisation of the silicate tetrahedra within the final damaged configuration have also been analysed, Table 6.24. The total number of polymerised chains within the final damaged configuration can be seen to increase with increasing PKA energy, though fewer chains were observed than in the xenotime system. There is a considerable amount of variation in the size of the longest chains, with no clear trend across the PKA energies, though some of the chains were much larger than any seen for the xenotime system. The average distributions of the polymerised units within the final damaged configuration with differing chain lengths for the five PKA energies are illustrated in Figure 6.33. It can be seen that there are peaks in the distribution for chains with lengths of ca. 9, 13 and 17 atoms which indicate ideally coordinated chains of corner sharing polyhedra. There is also a peak at a chain length of 11 for higher PKA energies. Similarly the silicon content of the chains has been investigated, summarised in Table 6.25 and illustrated in Figure 6.34. The most common chains containing 2 silicon atoms, with the relative frequency decreasing rapidly with increasing silicon content. Finally the Si:O ratio of the chains has been analysed to investigate the relative net coordination of these chains, Figure 6.35. The most common polymerised chain for the majority of the PKA energies is the ideally coordinated Si_2O_7 unit. However, this is not the case for the 3 keV cascade where the most common unit is the over-coordinated Si_2O_9 unit. The unit is also a common feature for the higher energy PKAs. It can be seen that there are a wide range of polymerised units found in all of the cascade simulations, with the degree of under-coordination of these chains generally increasing with PKA energy. There is a great deal of variation in the degree of over-coordination across all PKA energies. This information is summarised in Table 6.26.

Table 6.24: Summary of the total number of polymerised chains and the range of chain lengths observed for the $(1\bar{1}9)$ cascades in zircon

PKA Energy / keV	Average Number of Polymerised Chains	Smallest Chain	Largest Chain
1	7.0 ± 1.1	9	31
3	19.6 ± 4.1	9	74
5	30.4 ± 3.8	9	39
7	47.8 ± 5.2	8	265
10	64.8 ± 3.9	8	128

Table 6.25: Summary of the distribution of polymerised chains as a function of phosphorus content for the $(1\bar{1}9)$ cascades in zircon

PKA Energy / keV	Containing 2 Silicon Atoms / %	Containing 3 Silicon Atoms / %	No. of Silicon Atoms In Longest Chain
1	43.0 ± 10.8	20.1 ± 6.1	7
3	56.7 ± 15.6	13.0 ± 6.7	17
5	49.2 ± 5.8	14.2 ± 4.5	23
7	53.0 ± 7.5	16.9 ± 7.3	61
10	53.9 ± 8.9	12.3 ± 0.6	30

Table 6.26: Summary of the net coordination of the polymerised chains and the most common polymerised unit for the $(1\bar{1}9)$ cascades in zircon

PKA Energy / keV	Most Common Polymerised Unit	Net Oxygen Coordination Of Polymerised Chains	
		Lowest	Highest
1	Si_2O_7	0	4
3	Si_2O_9	0	22
5	Si_2O_7	-1	6
7	Si_2O_7	-1	21
10	Si_2O_7	-1	7

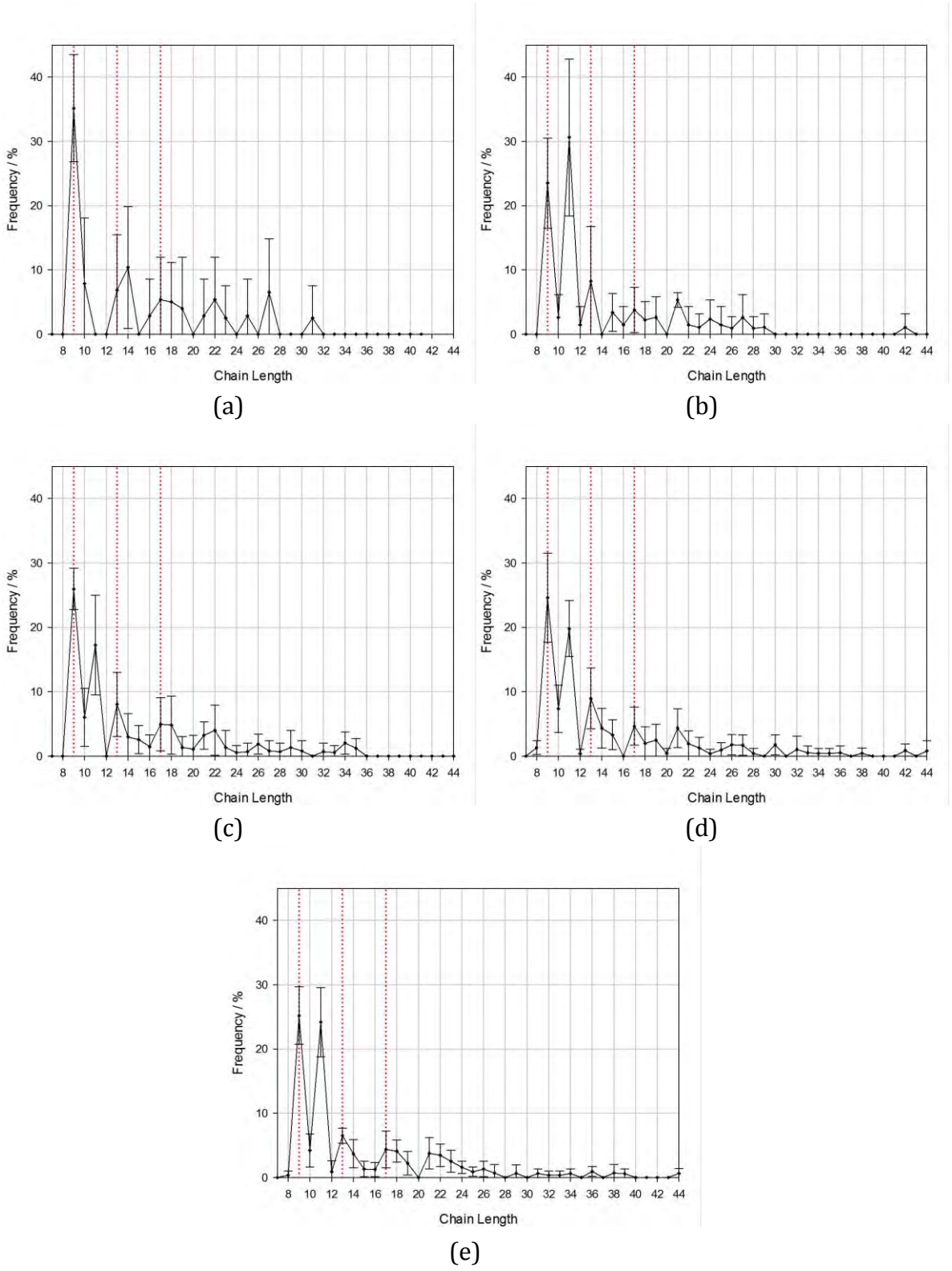

Figure 6.33: Average distribution of polymerised silicate chains as a function of chain length for cascades in the $(1\bar{1}9)$ direction in zircon for PKA energies of (a) 1 keV, (b) 3 keV, (c) 5 keV, (d) 7 keV and (e) 10 keV

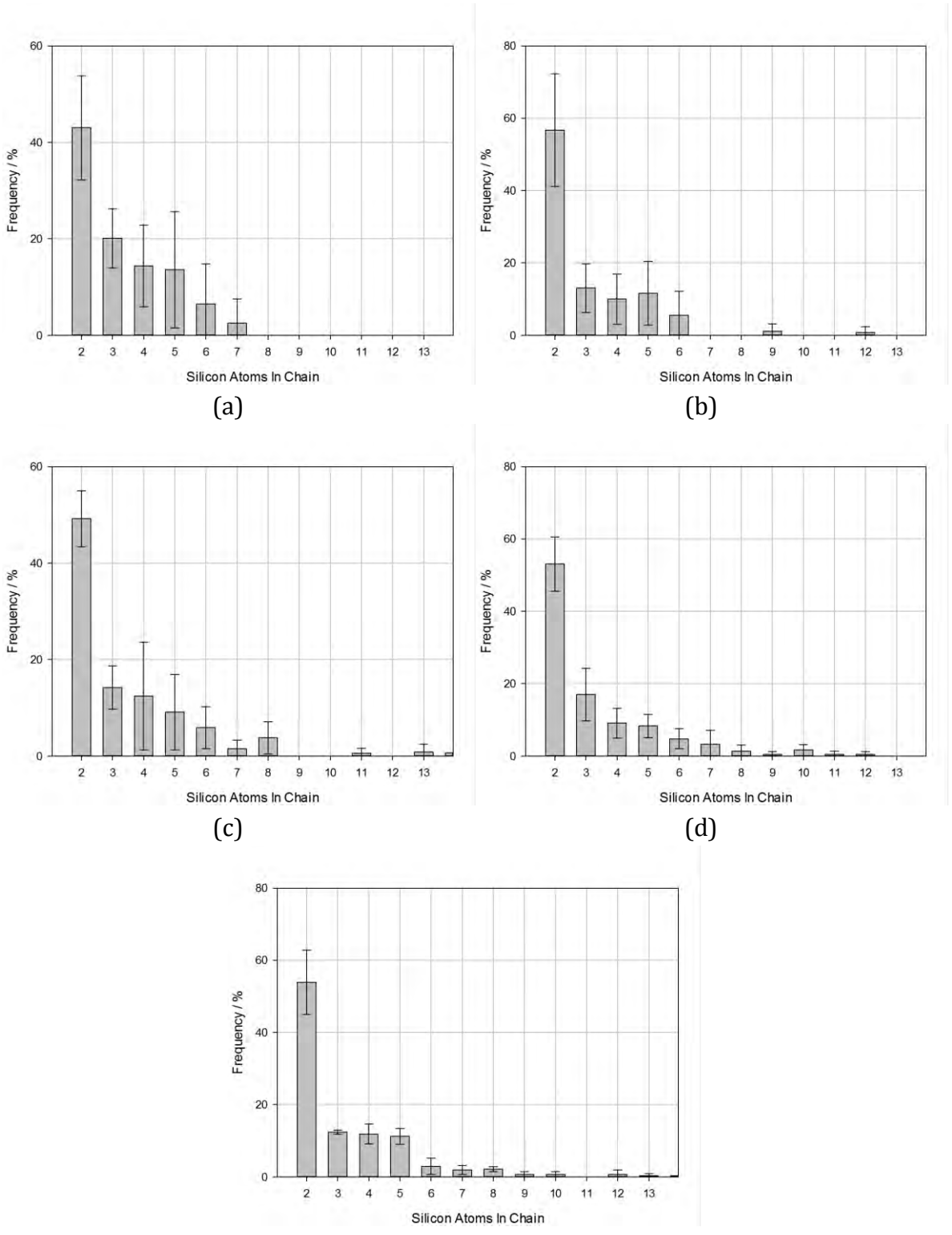

Figure 6.34: Average distribution of polymerised silicate chains as a function of silicon content for cascades in the $(1\bar{1}9)$ direction in zircon for PKA energies of (a) 1 keV, (b) 3 keV, (c) 5 keV, (d) 7 keV and (e) 10 keV

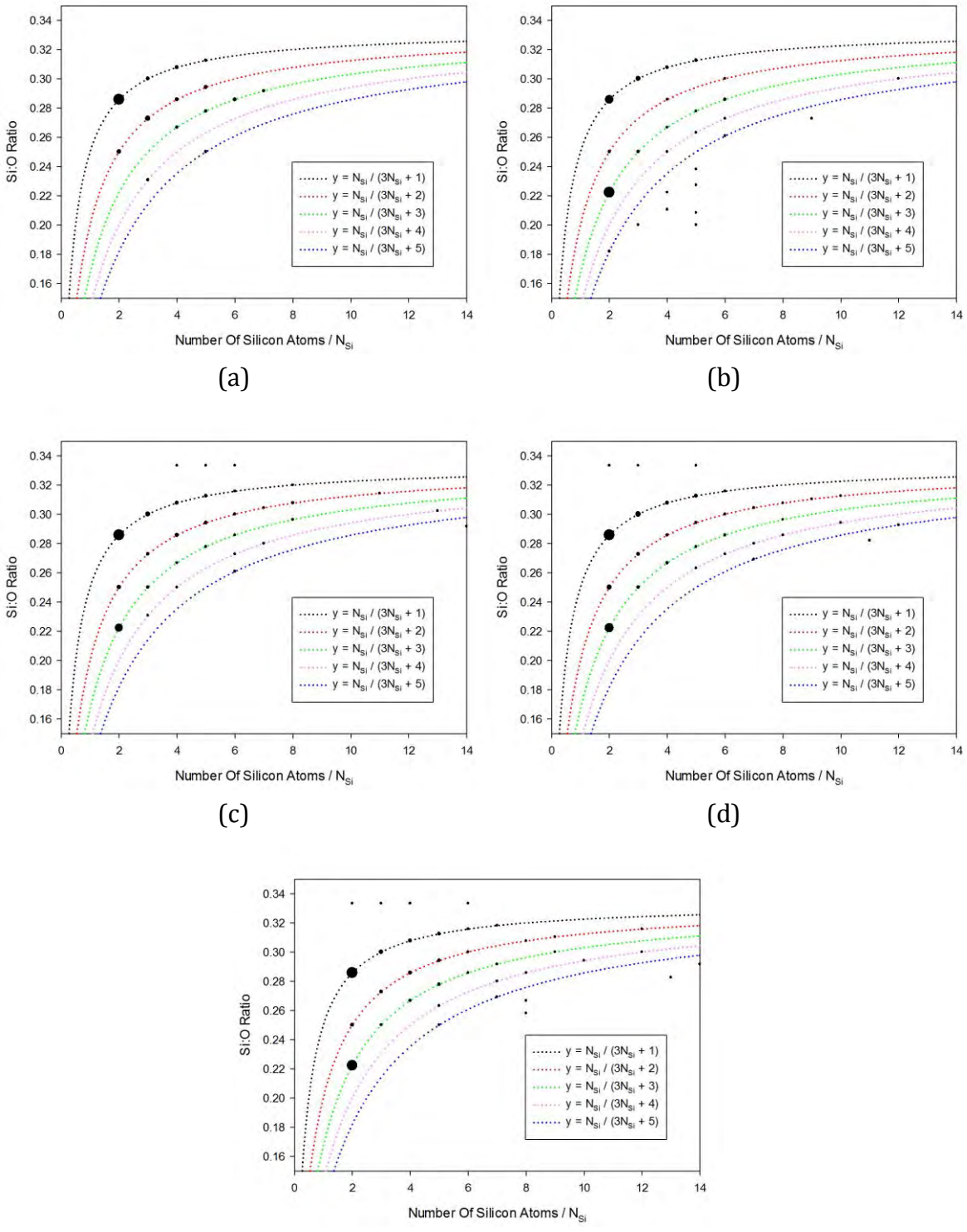

Figure 6.35: Average Si:O ratio of the polymerised chains as a function of the silicon content for cascades in the $(1\bar{1}9)$ direction in zircon for PKA energies of (a) 1 keV, (b) 3 keV, (c) 5 keV, (d) 7 keV and (e) 10 keV. The size of the data point corresponds to the relative frequency with which the chains were observed. The black dotted reference line indicates the ideal Si:O ratio for an archetypal corner sharing phosphate chain.

6.4 Discussion and Conclusion

The Fibonacci lattice has been employed as a way to sample PKA trajectories to produce accurate averages for determining the threshold displacement energy within xenotime. Values of $E_{d(min)}$ and $E_{d(max)}$ have been calculated by taking averages over the ten PKA directions with the lowest and highest E_d values respectively, whilst $E_{d(av)}$ is the average of all 267 PKA trajectories analysed for each species. The results are summarised in Table 6.27. It can be seen that the E_d values for the yttrium and phosphorus atoms are fairly similar with the E_d values for oxygen being lower. The standard deviation for $E_{d(av)}$ and $E_{d(max)}$ are much larger than for $E_{d(min)}$, indicating that there is a great deal of variation in E_d over the different directions. This variation was evident from the contour plots which showed that the PKA trajectories with the lowest E_d values were calculated when the PKA atom were initiated towards the channels running parallel to the *c* axis, conversely the highest energy PKA trajectories were found to be in the direction of neighbouring lattice atoms. The threshold displacement energy calculated by Urusov et. al.[9] for oxygen within xenotime compares quite favourable to the value of $E_{d(min)}$ calculated in this study (42 and 35 ± 5 eV respectively) though the prior value was only averaged over five of the ten direction analysed for one PKA atom. It has been shown that there is a reasonable amount of variation in the values of E_d between different PKA atoms even when initiated in the same direction which has not been taken into account in the aforementioned study.

Table 6.27: Summary of the threshold displacement energies for yttrium, phosphorus and oxygen in the xenotime system.

Species	$E_{d(min)}$ / eV	$E_{d(av)}$ / eV	$E_{d(max)}$ / eV
Y	52 ± 9	84 ± 28	121 ± 29
P	56 ± 12	90 ± 35	151 ± 40
O	35 ± 5	57 ± 27	96 ± 41

It may be useful to compare the average threshold displacement energies calculated here to those determined for zircon by Moreira et al[8] as both xenotime and zircon share the same ABO_4 structure. These results are summarised in Table 6.28. Here it can be seen that the values calculated here are comparable with the unequal charge model of zircon though the general trend is the same for all potentials with the B cation having the largest value of $E_{d(av)}$, which is very similar to that of the A cation, whilst oxygen has the lowest value of $E_{d(av)}$. The equal charge model for zircon predicts higher values of $E_{d(av)}$ for the cation species than the potentials used in this study for the equivalent cations in xenotime. This may indicate a factor that could contribute to the observed differences in radiation resistance between the two minerals. Equally the similarities to the unequal charge model may suggest that the structure is more important in determining the threshold displacement energy than the nature of the species in the mineral themselves. In either case the values of $E_{d(av)}$ calculated in this study provide a more reliable reference to be used to guide experimental studies of radiation damage in xenotime and in other damage prediction codes such as SRIM[14].

Table 6.28: Comparison of threshold displacement energies calculated previously for zircon and those calculated for xenotime in this study

Species	Moreira et al		This study
	Equal charge model, $E_{d(av)}$ / eV	Unequal charge model, $E_{d(av)}$ / eV	$E_{d(av)}$ / eV
Y / Zr	121 ± 32	81 ± 37	84 ± 28
P / Si	132 ± 54	82 ± 36	90 ± 35
O	62 ± 34	63 ± 26	57 ± 27

The defect evolution in xenotime during an α-decay event has been analysed for PKAs initiated in the (100), (001) and $(1\bar{1}9)$ directions with PKA energies of 1, 3, 5, 7 and 10 keV. It has been shown previously in the chapter that the number of Frenkel pairs produced in a damage cascade rises to a maximum within 1 ps after the PKA is initiated, followed by rapid epitaxial recrystallization of the majority of the Frenkel pairs formed during the ballistic phase. The time taken to reach peak damage is illustrated in Figure 6.36. Here it can be seen that time taken to reach peak damage increases with increasing PKA energy and this trend is fairly consistent across the PKA trajectories investigated. As shown previously[15] a power law can be fit to the data with the exponent estimated to be 0.426.

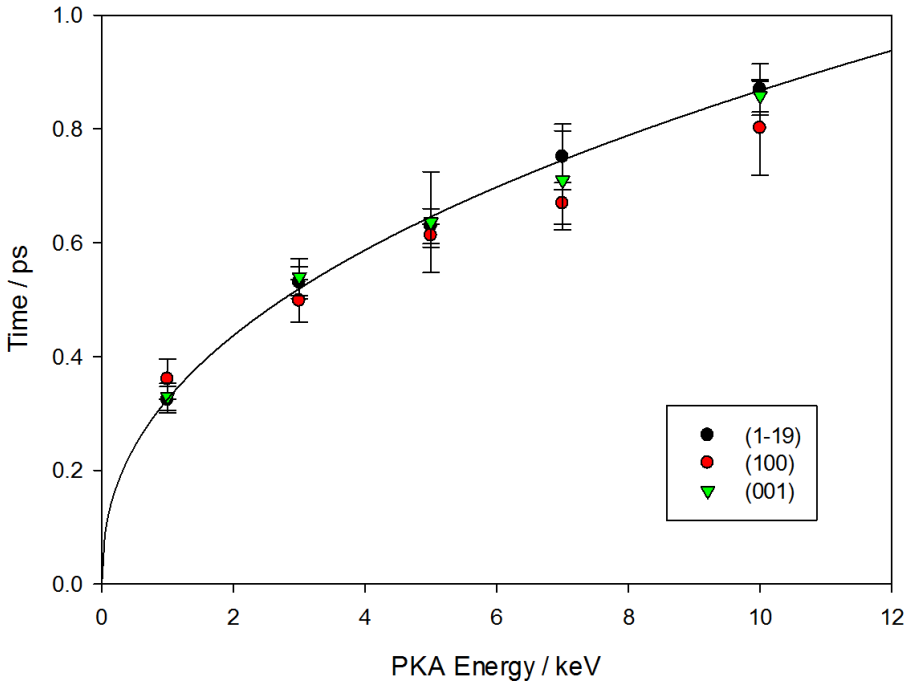

Figure 6.36: Average time taken to reach peak damage for the three different PKA vectors in xenotime

The average number of Frenkel pairs as determined by the DL_POLY methodology at peak damage and over the final 2 ps of the cascade simulation are summarised in Figure 6.37(a) and (b) respectively. In general all PKA directions follow the same trend with the total number of Frenkel pair defects at peak damage and in the final damage configurations increasing with increasing PKA energy. It can be seen that there is much more variation in the peak number of Frenkel pairs, especially for higher PKA energies, compared to the number of Frenkel pairs in the final damaged configurations. This may be as a result of the cut off distance used in the defect detection algorithm which causes more of the atoms displaced temporarily by the pressure waves to be included in the count. The number of Frenkel pairs observed for these calculations is consistent with those determined by Jay et al.[12] for fluorapatite.

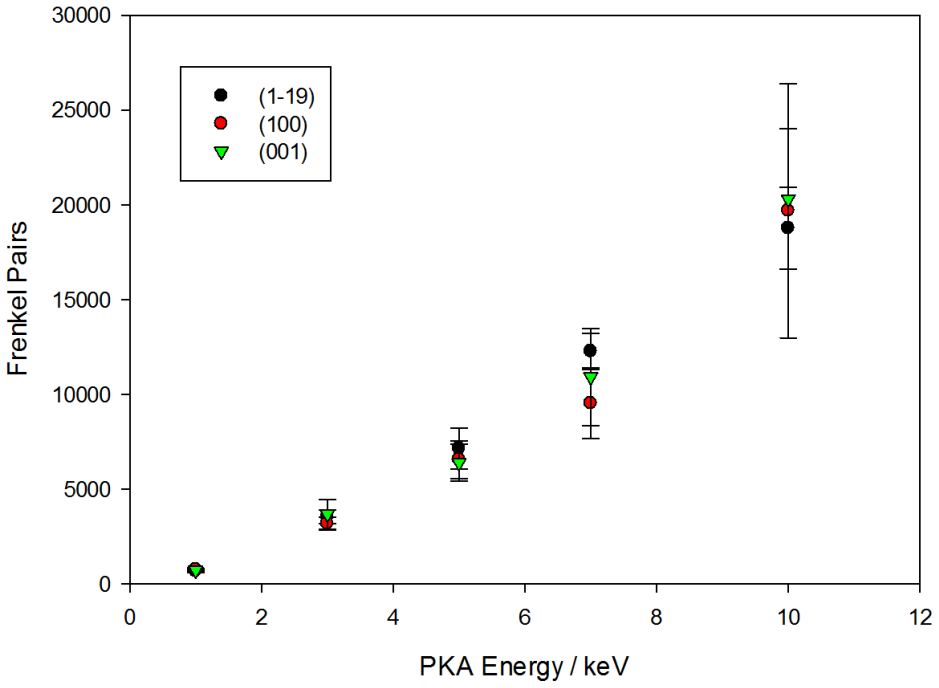

(a)

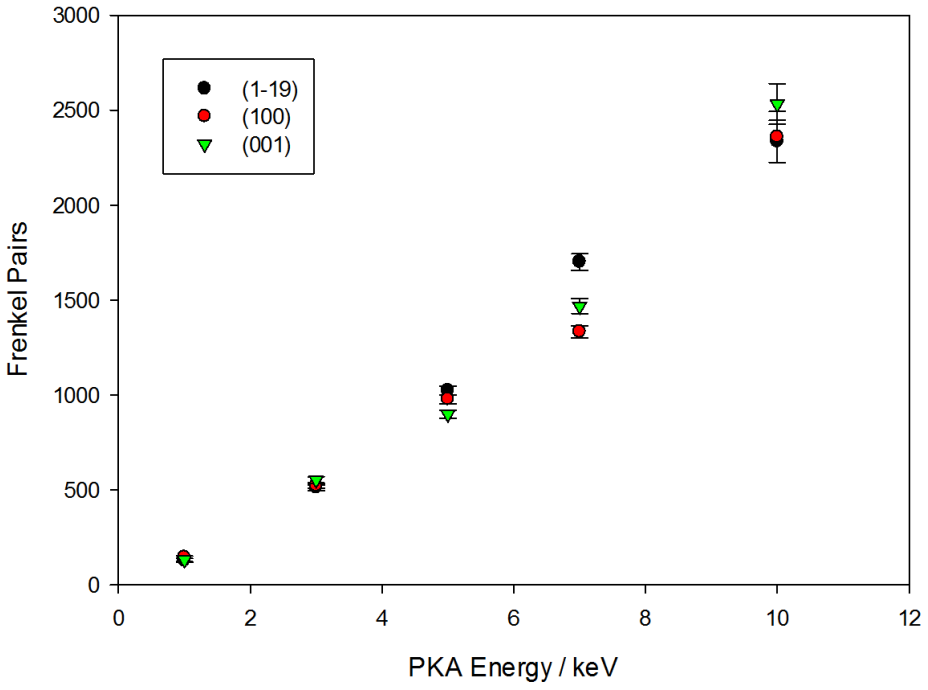

(b)

Figure 6.37: Average number of Frenkel pairs at (a) peak damage and (b) in the final damaged configurations for the three different PKA vectors in xenotime

The rapid recrystallization of the Frenkel pairs formed in the ballistic phase reduces the number of Frenkel pairs in the final damaged configurations considerably. The percentage of Frenkel pairs which are annealed as a function of PKA energy is illustrated in Figure 6.38 (a). It can be seen that the percentage of defects which become annealed is consistent for all three PKA directions investigated in this study, with the percentage of annealed defect generally increasing with increasing PKA energy. The percentage of annealed defects ranged from 81 – 88 %. The increase in the annealing with increased PKA energy may be rationalised by the increase in temperature of the simulation cell with increasing PKA energy, illustrated in Figure 6.38 (b). All cascades were initiated from a starting configuration which had been equilibrated to 300 K and it can be seen that there is a much larger increase in the temperature of the cell for the high energy PKAs. For the 10 keV PKA the simulation cell reaches a maximum temperature of ca. 495 K which decreases over the course of the simulation to a final temperature of ca 387 K, compared to the 1 keV PKA which reached temperatures of 323 and 309 K respectively. This increased temperature may facilitate the recombination of the Frenkel pairs and therefore increase the percentage of Frenkel pairs which are annealed for higher PKA energies. This effect could be reduced in future simulations by employing a boundary thermostat to act as a heat sink and moderate the temperature of the simulation cell. The percentage of Frenkel pairs which are annealed calculated here is higher than that reported by Jay et al.[12] for fluorapatite. This may indicate a difference between the two minerals and contribute to the radiation damage 'resistance' of these phases.

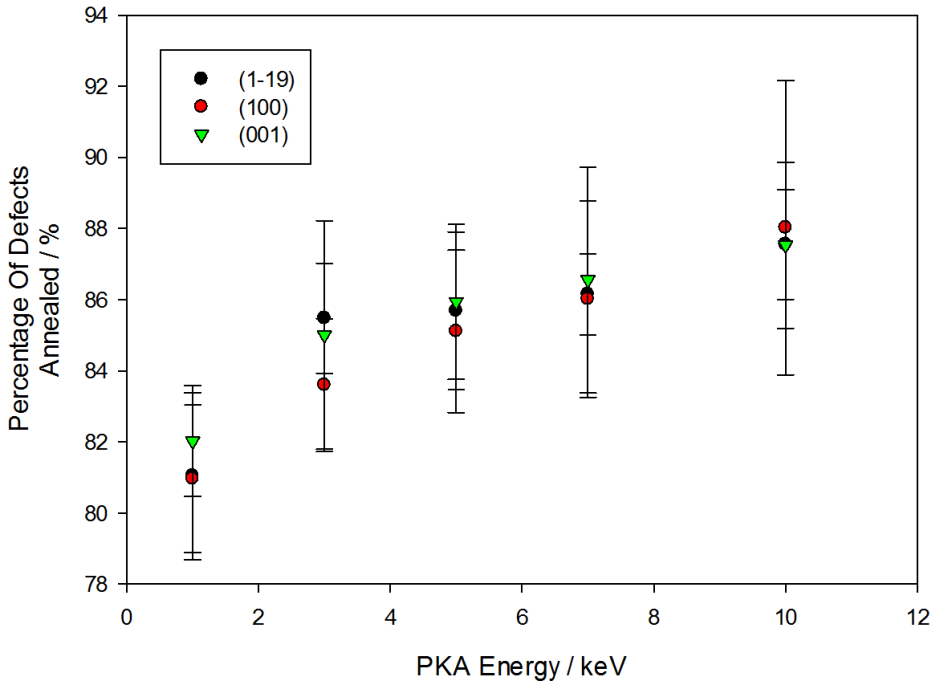

(a)

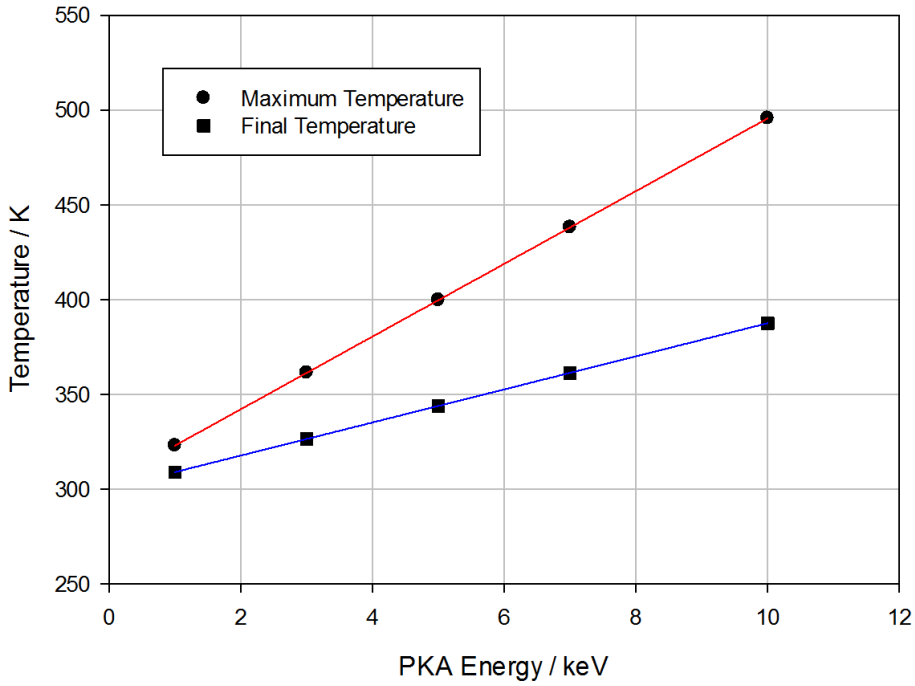

(b)

Figure 6.38: (a) Average percentage of annealed Frenkel pairs and (b) peak and final temperatures of the simulation cell

The other method of defect detection employed here considers the population of Voronoi polyhedra defined by the cations in an undamaged reference configuration. The proportion of each defect type which involve a yttrium cation can be seen as a function of PKA energy for the (100) cascades in Figure 6.39. Here the yttrium vacancy and phosphorus anti-site can be considered as sources of yttrium atoms whilst the yttrium interstitials and anti-sites can be considered as sinks. It is clear that at lower PKA energies the main source of yttrium atoms is the yttrium vacancy defect, composing ca 22 % compared to the phosphorus anti-site which composes ca 13 %. This gap is reduced as the PKA energy increases, with the yttrium vacancy and phosphorus anti-sites composing ca 18 and 16 % of the defects at a PKA energy of 5 keV. At a PKA energy of 10 keV the phosphorus anti-site becomes the greatest source of yttrium atoms with a percentage of ca. 19 % compared to ca 16 % for the yttrium vacancy defects. A similar trend is observed for the sinks with the yttrium interstitial dominating at low PKA energy and the yttrium anti-site dominating at higher PKA energy. At lower PKA energy the composition of yttrium defects follows the trend Y interstitial > Y vacancy >phosphorus anti-site > yttrium anti-site. The trend becomes inverted at a PKA energy of 10 keV as the anti-site defects begin to dominate over the Frenkel pairs.

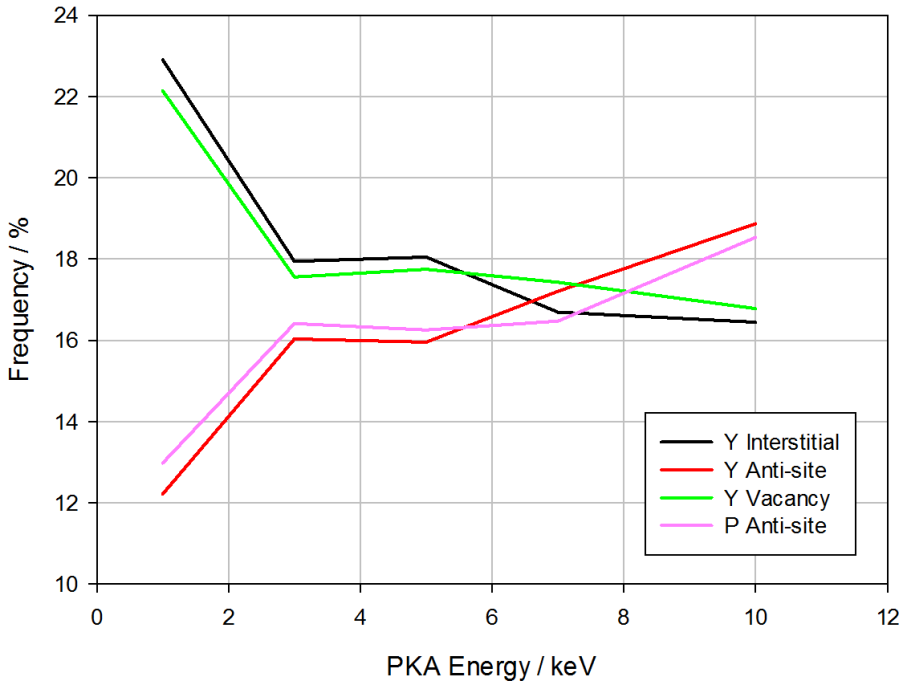

Figure 6.39: Proportion of different defect types involving a yttrium atom as determined by the Voronoi method for the (100) cascades in xenotime

A similar trend can be observed for the (001) cascades, illustrated in Figure 6.40. Again the Frenkel defects dominate at low PKA energy, although in this case the vacancy defect is slightly more common than the interstitial, whilst the anti-site defects are the least common. This trend is inverted for higher PKA energies as seen for the previous direction with the yttrium and phosphorus anti-site defects dominating for the 10 keV PKA, followed by the vacancy and interstitial defects respectively. The transition between these two regimes is not as clear as for the previous direction.

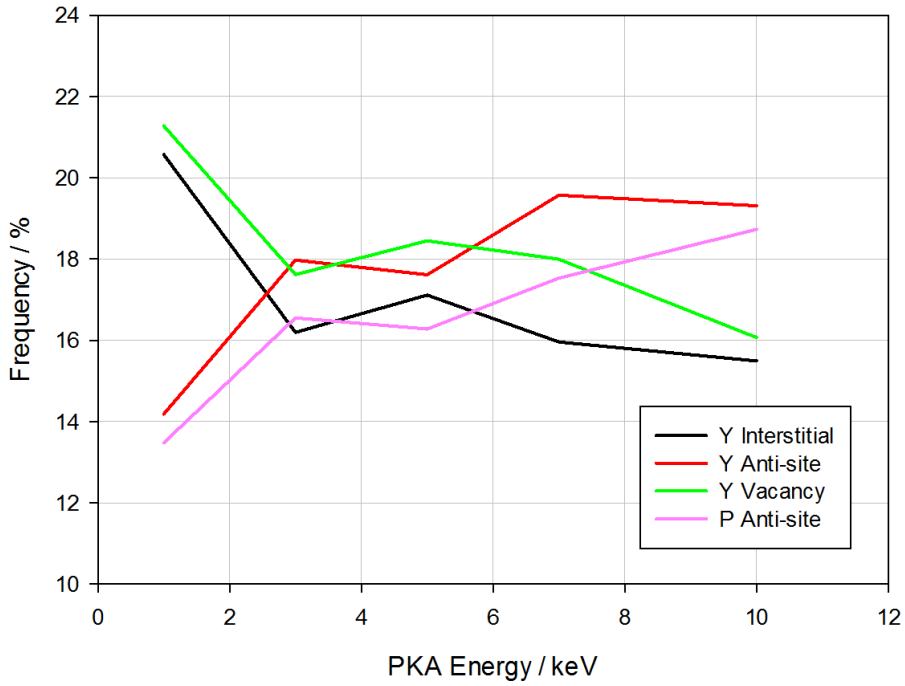

Figure 6.40: Proportion of different defect types involving a yttrium atom as determined by the Voronoi method for the (001) cascades in xenotime

A similar trend can be observed for the $(1\bar{1}9)$ cascades, illustrated in Figure 6.41. Again the Frenkel defects dominate at low PKA energy whilst the anti-site defects are the less common. As the PKA energy increases the different defect types converge to ca. 17 %.

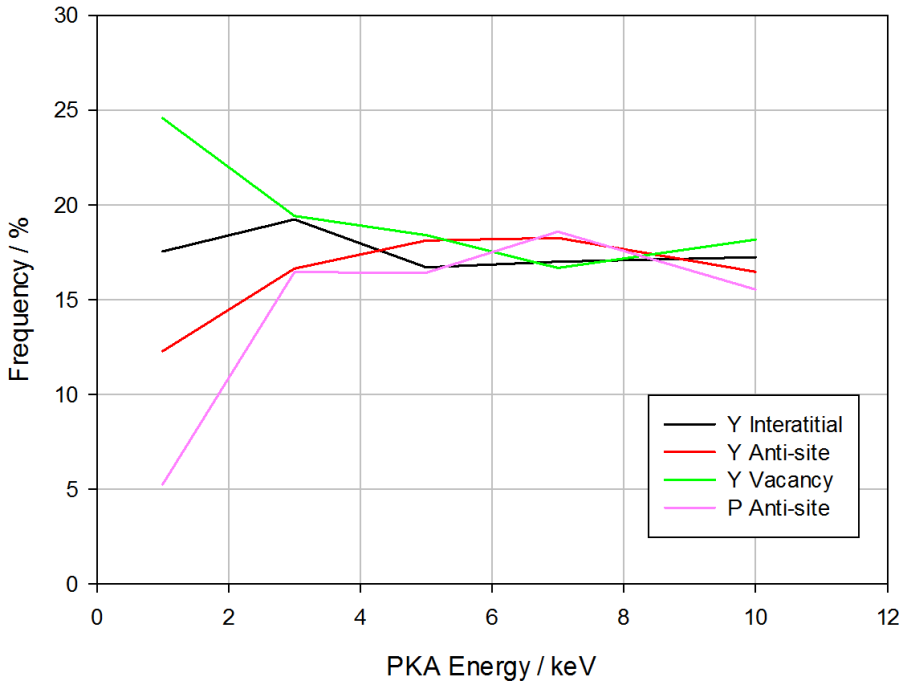

Figure 6.41: Proportion of different defect types involving a yttrium atom as determined by the Voronoi method for the $(1\bar{1}9)$ cascades in xenotime

Similarly the proportion of each defect type which involve a phosphorus cation can be seen as a function of PKA energy for the (100) cascade in Figure 6.42. Here the phosphorus vacancy and yttrium anti-site can be considered as sources of phosphorus atoms whilst the phosphorus interstitials and anti-sites can be considered as sinks. At lower PKA energies the main source of phosphorus atoms is the phosphorus vacancy defect, composing ca. 15 % compared to the yttrium anti-site which comprises ca 12 %. This difference is much smaller than seen previously for the yttrium defects and is reduced further as the PKA energy increases, with both the phosphorus vacancy and yttrium anti-sites composing ca 16 % of the defects at a PKA energy of 5 keV. At a PKA energy of 10 keV the yttrium anti-site becomes the greatest source of phosphorus atoms with a percentage of ca. 19 % compared to ca 15 % for the phosphorus vacancy defects. A

similar trend is observed for the sinks with the phosphorus interstitial dominating at very low PKA energy and the phosphorus anti-site dominating at PKA energies as low as 3 keV. At very low PKA energy the composition of phosphorus defects follows the trend phosphorus vacancy > phosphorus interstitial > phosphorus anti-site > yttrium anti-site, this trend becomes phosphorus anti-site >phosphorus vacancy > yttrium anti-site > P interstitial by a PKA energy of 3 keV. The trend becomes fully inverted at a PKA energy of 10 keV compared to that at 1 keV as the anti-site defects dominate over the Frenkel pairs.

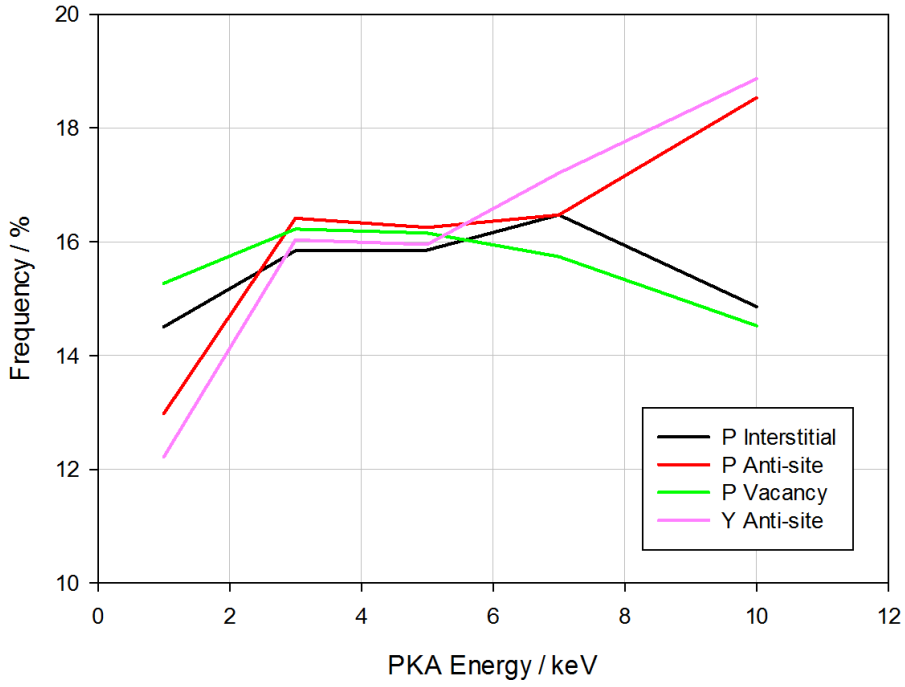

Figure 6.42: Proportion of different defect types involving a phosphorus atom as determined by the Voronoi method for the (100) cascades in xenotime

A similar trend is observed for the (001) cascades, illustrated in Figure 6.43. Again the Frenkel defects dominate at lower PKA energies but to a lesser degree than for the yttrium defects, with the anti-site defects dominating for higher PKA energies. The phosphorus anti-site and interstitial defects behave in a very similar manner to the equivalent defects

for the previous direction though the phosphorus vacancies and yttrium anti-site defects diverge to a greater extent for the intermediate PKA energies.

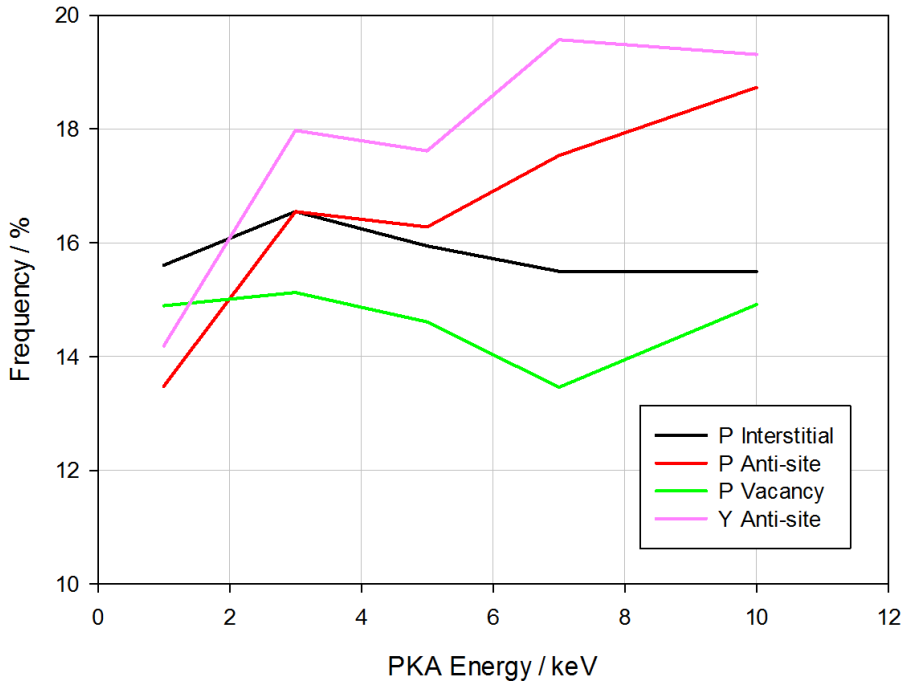

Figure 6.43: Proportion of different defect types involving a phosphorus atom as determined by the Voronoi method for the (100) cascades in xenotime

A different trend can be observed for the $(1\bar{1}9)$ cascades, illustrated in Figure 6.44. Again the Frenkel defects dominate at low PKA energy whilst the anti-site defects are the less common. As the PKA energy increases the different defect types converge to ca. 16 %.

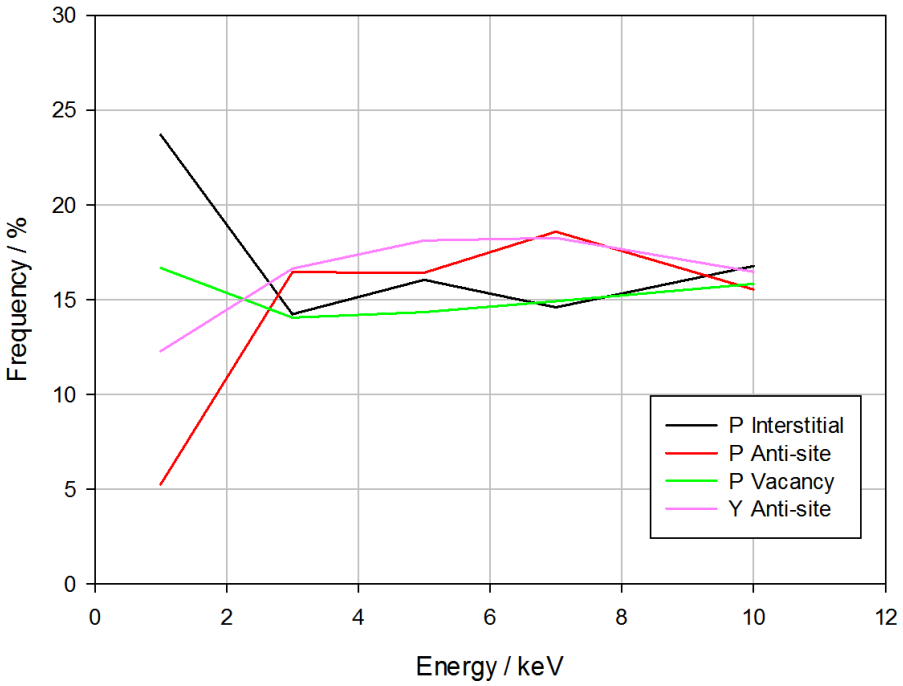

Figure 6.44: Proportion of different defect types involving a phosphorus atom as determined by the Voronoi method for the $(1\bar{1}9)$ cascades in xenotime

The polymerisation of phosphate units was identified as an important defect mechanism in chapter 4 with the phosphate tetrahedra polymerising to form a wide range of phosphate units. The number of phosphate chains present at the end of the cascade simulations as a function of PKA energy is illustrated in Figure 6.45. It appears that the number of phosphate chains increases fairly linearly with PKA energy at a rate of ca. 0.015 chains eV^{-1} for all three cascade directions.

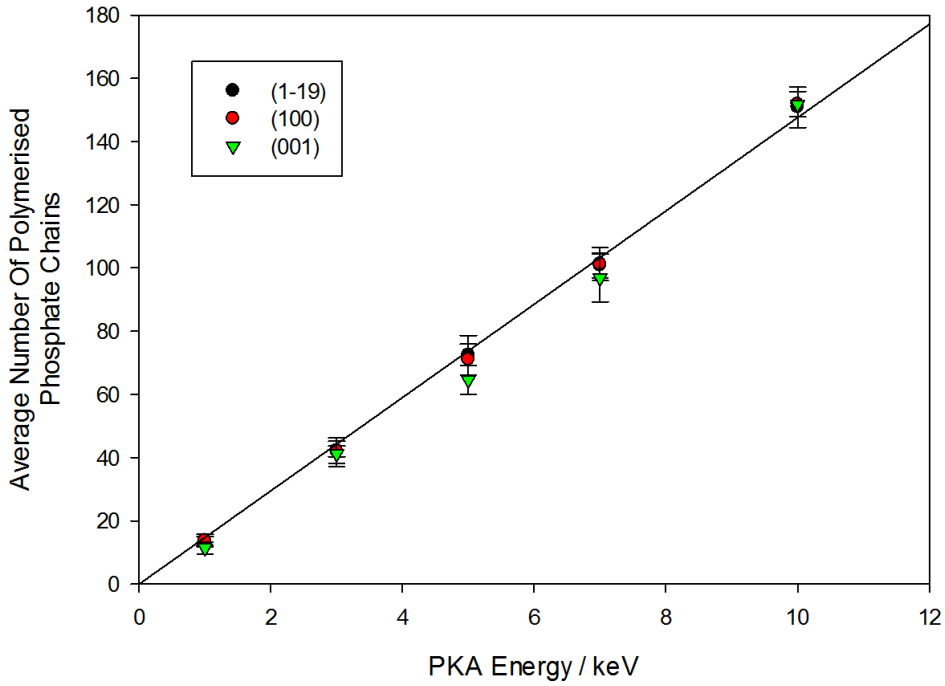

Figure 6.45: Average number of polymerised phosphate chains for the three different PKA vectors in xenotime

The distribution of the number of atoms in each chain was fairly consistent across all PKA directions and energies and as such the average distribution is illustrated in Figure 6.46. Here it can be seen that there are clear peaks in the distribution which reduce in intensity with increasing chain length. The most common chains contain nine or ten atoms and correspond to P_2O_7 and P_2O_8 units respectively. Although the distributions were very similar for all PKA atoms it has been observed that for all directions the 1 keV PKAs produced more of the ten atom chains whilst all other PKAs produced more of the nine atom chains, contributing to the broadness of the first peak. The peaks at chain lengths of fourteen and eighteen are also fairly well resolved which indicate a preference for over-coordination of the longer phosphate chains. The longest polymerised chain observed in these simulations contained one hundred and seven atoms.

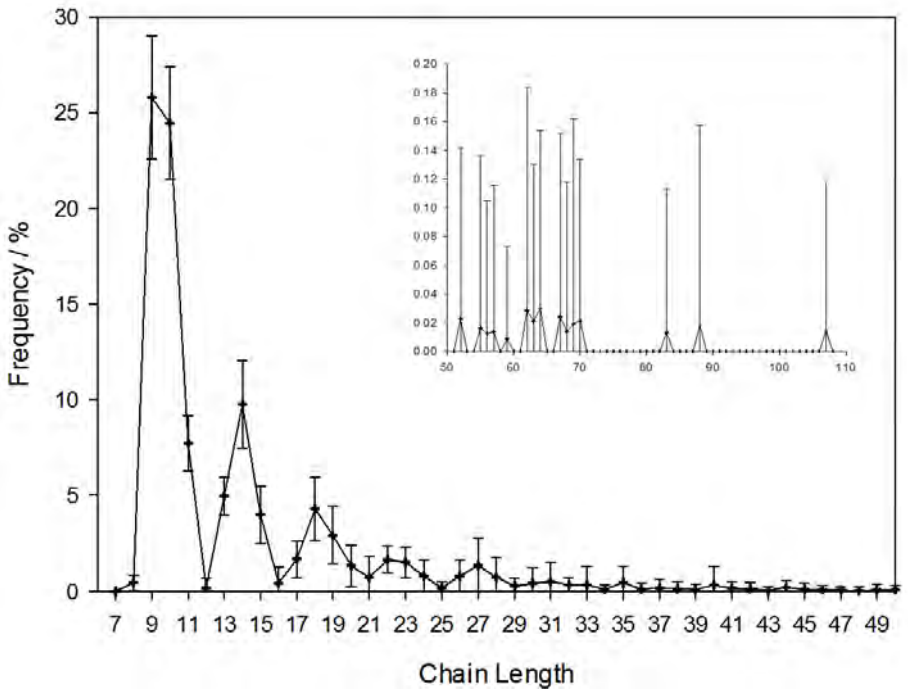

Figure 6.46: Average distribution of the polymerised phosphate chain lengths taken over all PKA vectors in xenotime

Similarly the average number of phosphorus atoms in each chain has been analysed across all PKA directions and energies and is illustrated in Figure 6.47. This distribution was found to be very similar across all of the simulations and the trend can be described very well using the reciprocal cubic function described in equation (6.10), where y_0, a, b and c are 0.22, -12.15, 124.60 and 265.90 respectively. The longest chain observed in the damaged configurations contained twenty-four phosphorus atoms.

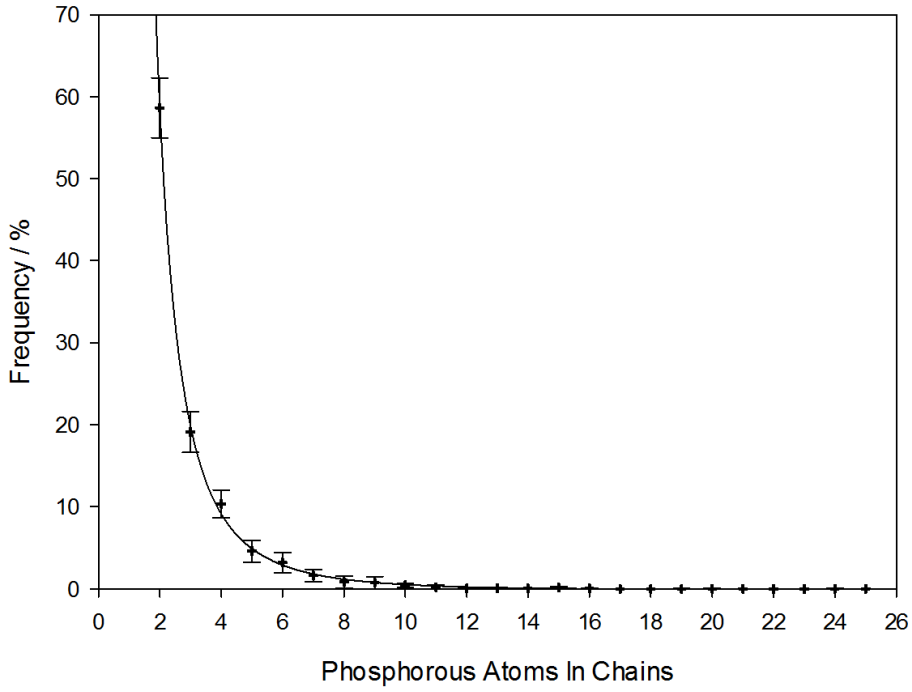

Figure 6.47: Average distribution of the number of phosphorus atoms in the polymerised chains taken over all PKA vectors in xenotime

$$y = y_0 + ax^{-1} + bx^{-2} + cx^{-3} \quad \textbf{(6.10)}$$

It has been shown previously in the chapter that the most common polymerised units are the P_2O_7 and P_2O_8 units, although a wide range of chain lengths with varying degrees of coordination were also observed. The degree of coordination of the chains has been analysed for the cascades. A net coordination of zero indicates a chain which has the ideal P:O ratio for a chain containing only corner sharing phosphate tetrahedra. The net coordination of the chains can be increased by over-coordination of the phosphorus atoms in the chain whilst the net coordination can be decreased by under-coordination of the phosphorus atoms or edge or face sharing of polyhedra within the chains. It is important to note that it is possible for a chain to contain multiple features that both

increase and decrease the coordination of the chain and therefore the net coordination is the sum of these features. The distribution of these chains are summarised for the PKAs initiated in the (100) direction in Figure 6.48. It can be seen that there is a peak in the distribution corresponding to chains which are net over-coordinated by one oxygen atom for all PKA energies. The general trend would indicate that there is a small shift in the distribution towards ideally coordinated chains and under-coordinated chains with increasing PKA energy. The most over-coordinated chain identified for this PKA direction was over-coordinated by seven oxygen atoms whilst the most under-coordinated chains were under-coordinated by one oxygen atom.

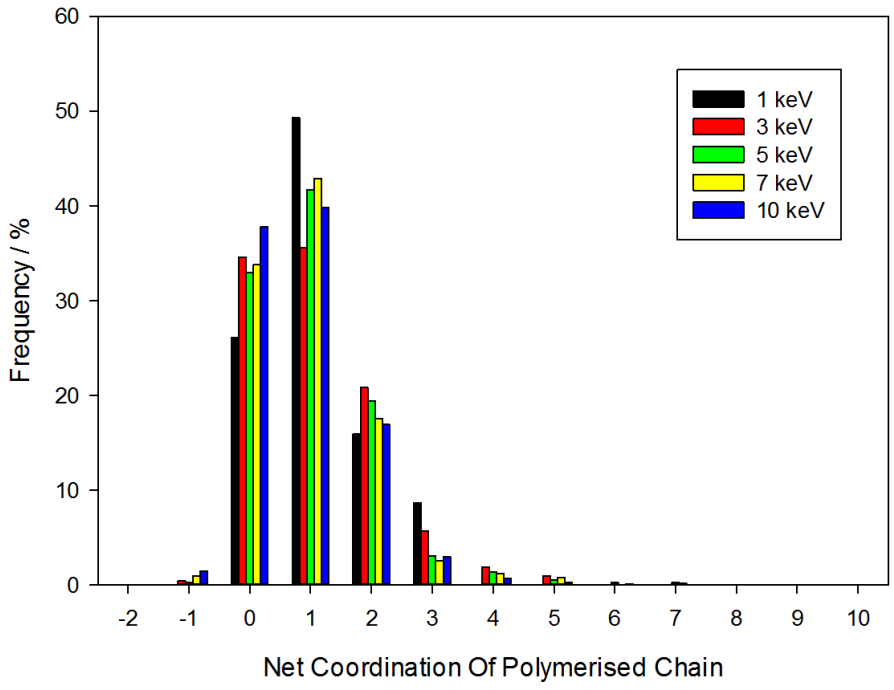

Figure 6.48: Distribution of the net coordination of the polymerised chains in xenotime for the (100) cascades

Similarly the distribution for the PKAs initiated in the (001) direction are summarised in Figure 6.49. A similar trend is observed with a peak at a net coordination of one for PKAs

with energy ranging from 1-7 keV whilst the 10 keV PKA reaches a maximum at a net coordination of zero. Again the distribution shifts towards negative net coordination with increasing PKA energy. The most over-coordinated chain identified for this PKA direction was over-coordinated by six oxygen atoms whilst the most under-coordinated chain was under-coordinated by two oxygen atoms.

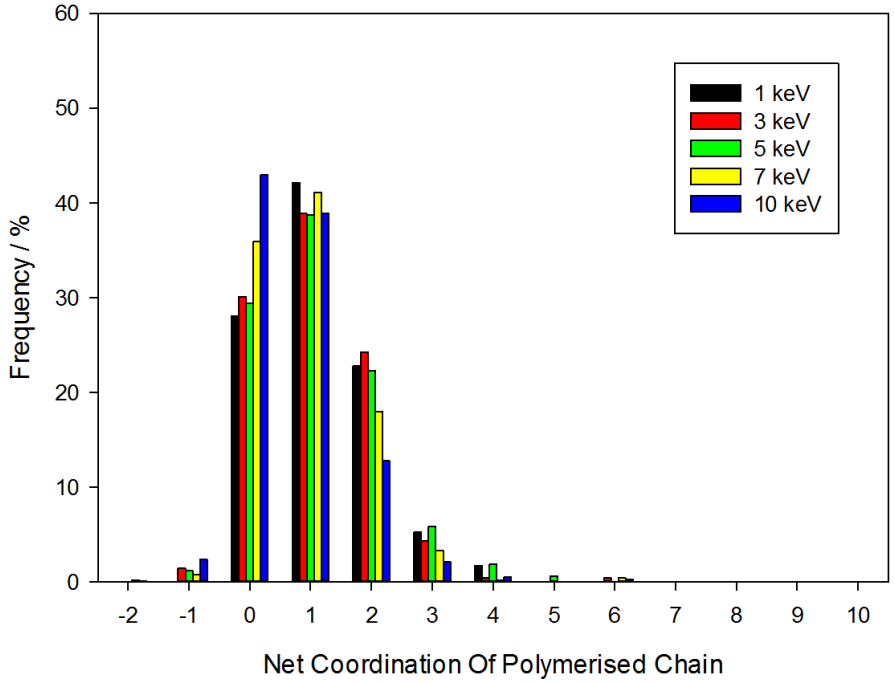

Figure 6.49: Distribution of the net coordination of the polymerised chains in xenotime for the (001) cascades

Finally the distribution for the PKAs initiated in the $(1\bar{1}9)$ direction are summarised in Figure 6.50. Again a similar trend is observed with a peak at a net coordination of one for all PKA energies however the shift in the distribution with increasing PKA energy is not as clear as for the other PKA directions. The most over-coordinated chain identified for this PKA direction was over-coordinated by ten oxygen atoms whilst the most under-

coordinated chains were under-coordinated by one oxygen atom. The polymerisation of the phosphate tetrahedra is consistent with that observed by Jay et al.[12] in fluorapatite.

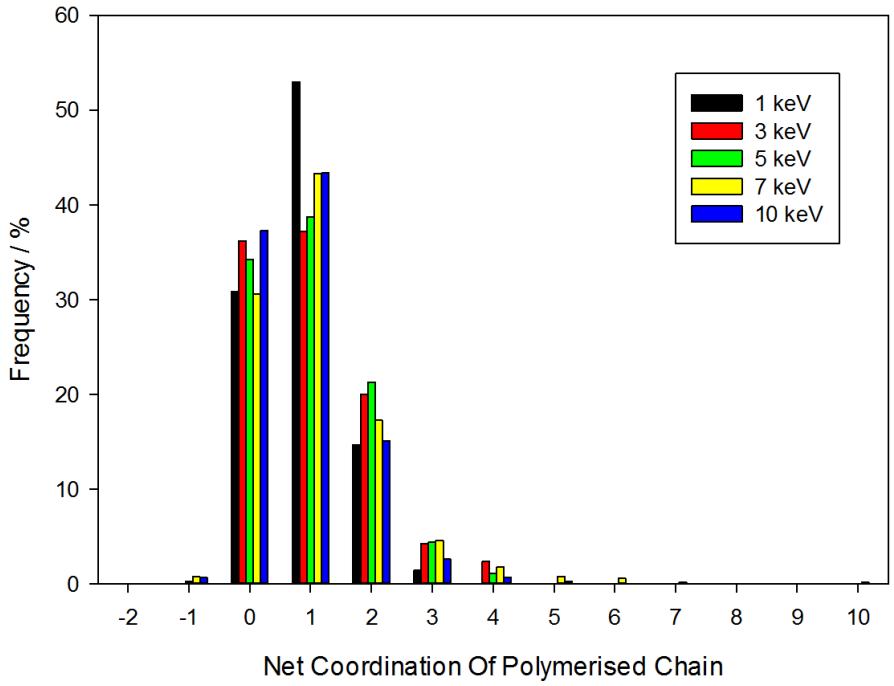

Figure 6.50: Distribution of the net coordination of the polymerised chains in xenotime for the $(1\bar{1}9)$ cascades

Cascade simulations were also performed in the zircon system using the pair potentials discussed in chapter 3, with the PKA initiated in the $(1\bar{1}9)$ direction, which may be compared to the equivalent cascades in the xenotime system. The time taken to reach maximum damage as a function of PKA energy is illustrated in Figure 6.51. Here it can be seen that the time taken to reach peak damage in zircon is much shorter than for xenotime though a power function can still be fit with an exponent estimated to be 0.198 compared to 0.426 for xenotime.

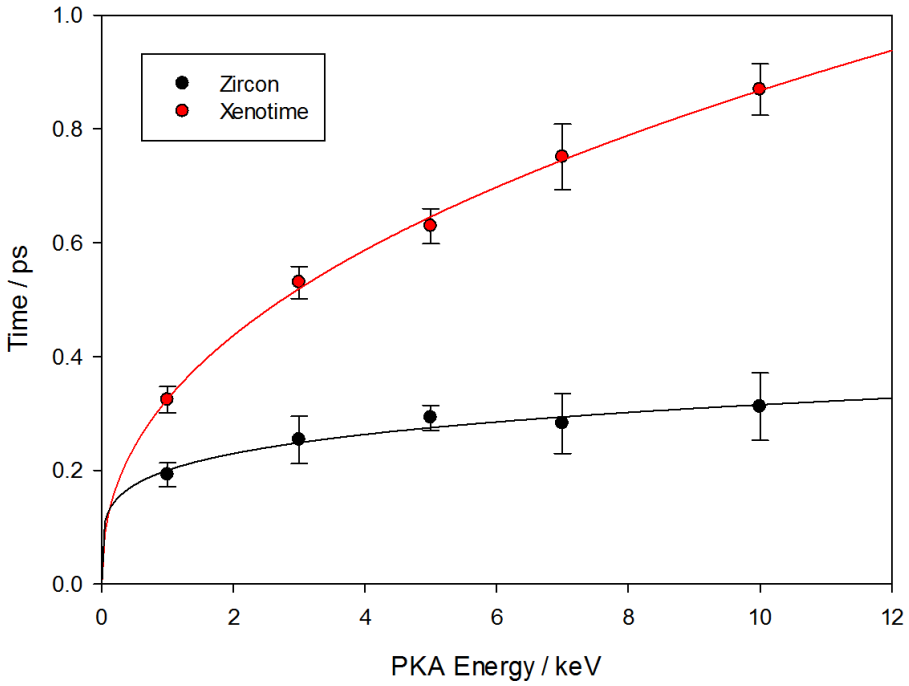

Figure 6.51: Comparison of the time taken to reach peak damage in zircon and xenotime for the $(1\bar{1}9)$ cascades

The average number of Frenkel pairs as determined by the DL_POLY methodology at peak damage and over the final 2 ps of the cascade simulation are summarised in Figure 6.52 a and b respectively for both the zircon and xenotime $(1\bar{1}9)$ cascades. It can be seen that the number of Frenkel pairs detected in xenotime was much greater than for zircon at both peak damage and in the final damaged configurations.

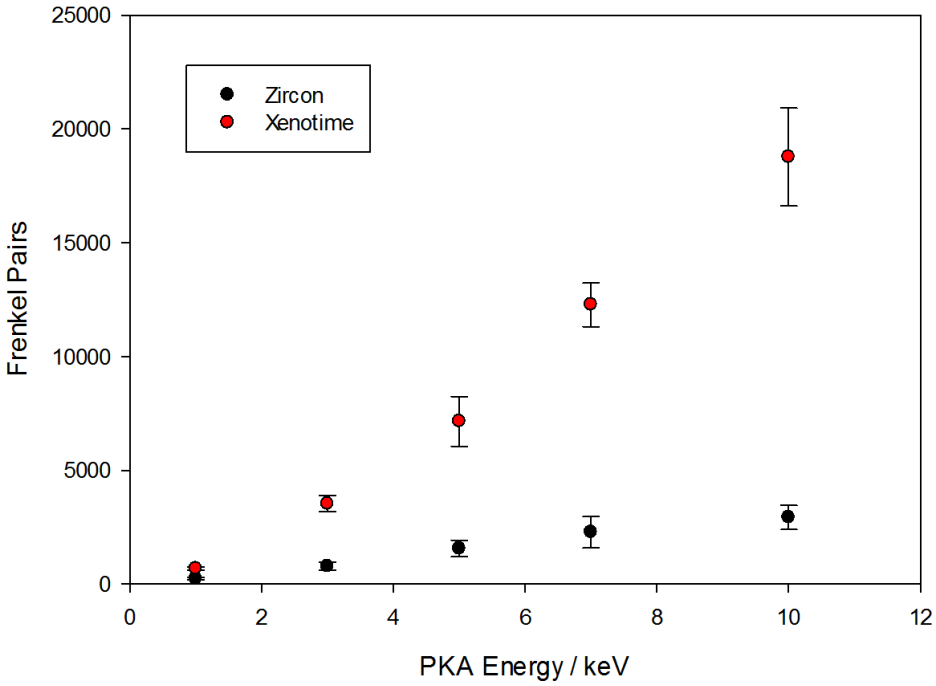

(a)

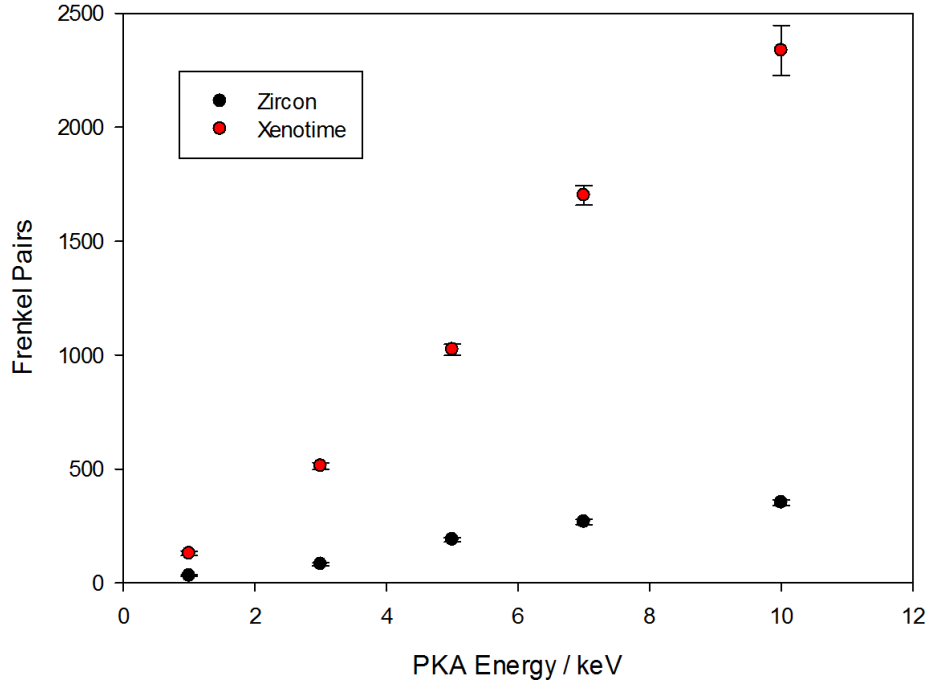

(b)

Figure 6.52: Comparison of the number of Frenkel pairs at (a) peak damage and (b) in the final damaged configurations in zircon and xenotime for the $(1\bar{1}9)$ cascades

The percentage of the Frenkel pairs produced in the ballistic phase which were annealed in the final damaged configuration are summarised in Figure 6.53. It can be seen that at lower PKA energies the percentage of annealed Frenkel pairs is greater for zircon than in xenotime, however this becomes much more similar with increasing PKA energy. It can also be seen that the percentage of annealed Frenkel pairs remains much more consistent in zircon than for xenotime.

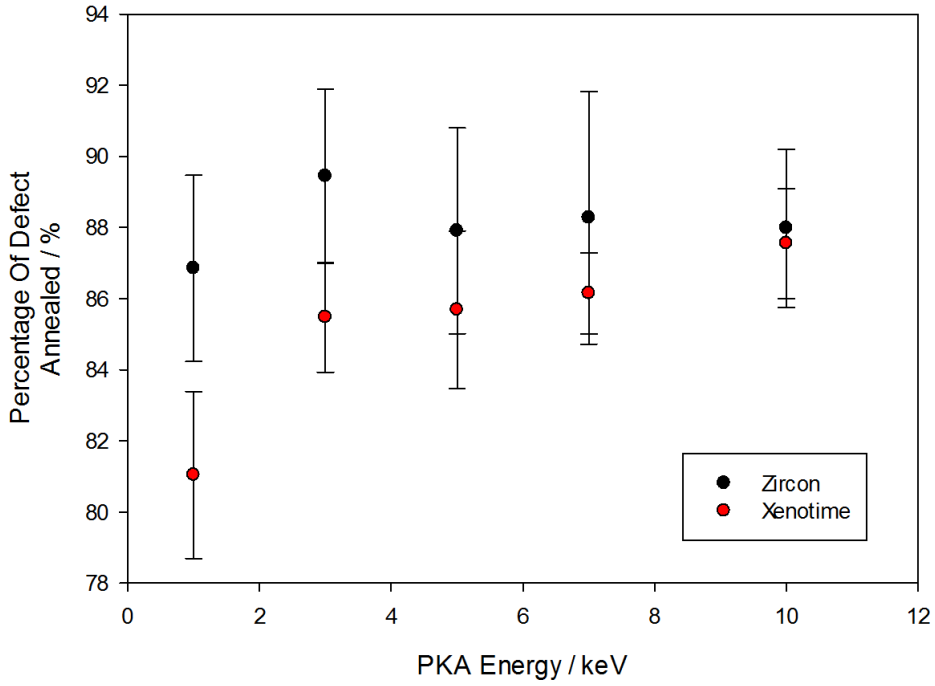

Figure 6.53: Comparison of the percentage of annealed Frenkel pairs in zircon and xenotime for the $(1\bar{1}9)$ cascades

The relative frequency with which the vacancy, interstitial and anti-site defects are observed in the final defect configurations of zircon and xenotime can be compared to investigate how these defect interact within the two systems. The relative proportions of the defects which act as sinks for the A cations are summarised in Figure 6.54. Here it can be seen that whereas the yttrium interstitial and anti-site defects converge with

increasing PKA energy, the zirconium equivalents diverge. Additionally there are fewer zirconium interstitials compared to the yttrium interstitials, a trend which is inverted for the anti-sites.

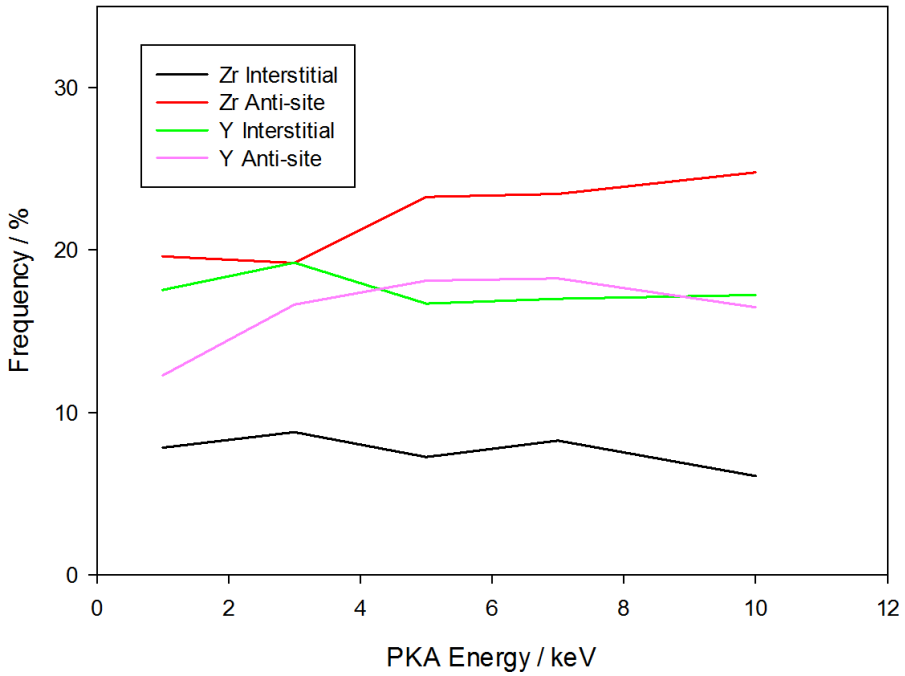

Figure 6.54: Proportion of A cation defects considered as sinks as identified by the Voronoi method for the $(1\bar{1}9)$ cascades in zircon and xenotime

A similar comparison can be seen for the sources of the respective A cations in Figure 6.55. Here it can be seen that the silicon anti-site defects are observed to a similar extent to the phosphorus anti-site equivalents whereas the yttrium vacancies are more common than the zirconium vacancies

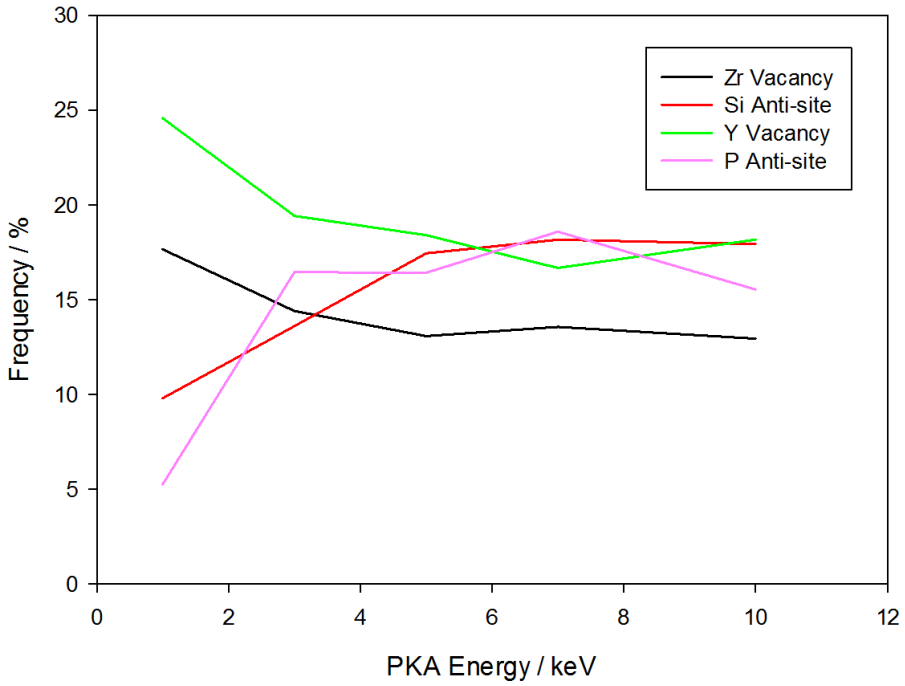

Figure 6.55: Proportion of A cation defects considered as sources as identified by the Voronoi method for the $(1\bar{1}9)$ cascades in zircon and xenotime

The same analysis has been performed for the B cation sinks, illustrated in Figure 6.56. Here it can be seen that the silicon interstitials are observed to greater extent and do not converge with the anti-site defects to the same extent as the phosphorus interstitials in xenotime.

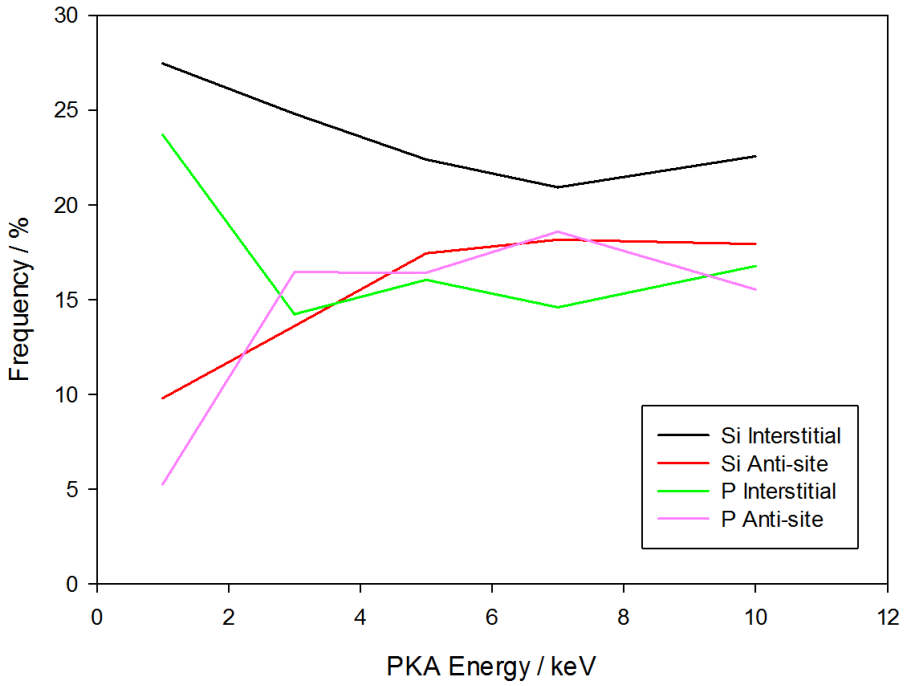

Figure 6.56: Proportion of B cation defects considered as sinks as identified by the Voronoi method for the $(1\bar{1}9)$ cascades in zircon and xenotime

Finally the sources of B cations have been analysed and are shown in Figure 6.57. Here it can be seen that the silicon and phosphorus vacancies converge with increasing PKA energy and follow a generally similar trend, with the yttrium anti-sites converging to a similar percentage. Through considering the sources and sinks of the relative A and B cations in both systems it can be seen that there are more zirconium anti-site defects and silicon interstitials than the yttrium and phosphorus counterparts whilst relatively fewer zirconium interstitials are observed than the yttrium counterpart. This may suggest that the zirconium interstitials created during the ballistic phase are recombining with the silicon vacancies upon annealing to form anti-site defects, leaving the displaced silicon atoms as interstitials. This is not observed to as great an extent in xenotime and may contribute to the radiation 'resistance' of xenotime relative to zircon as the zirconium

anti-sites in zircon may be less mobile than the yttrium interstitials in xenotime and so require higher temperatures to allow for diffusion and recombination with a zirconium vacancy site compared to the equivalent process for the yttrium interstitials in xenotime. As seen previously the errors associated with these averages are large and as such more repeat simulations for different PKA atoms are required to draw more meaningful conclusions.

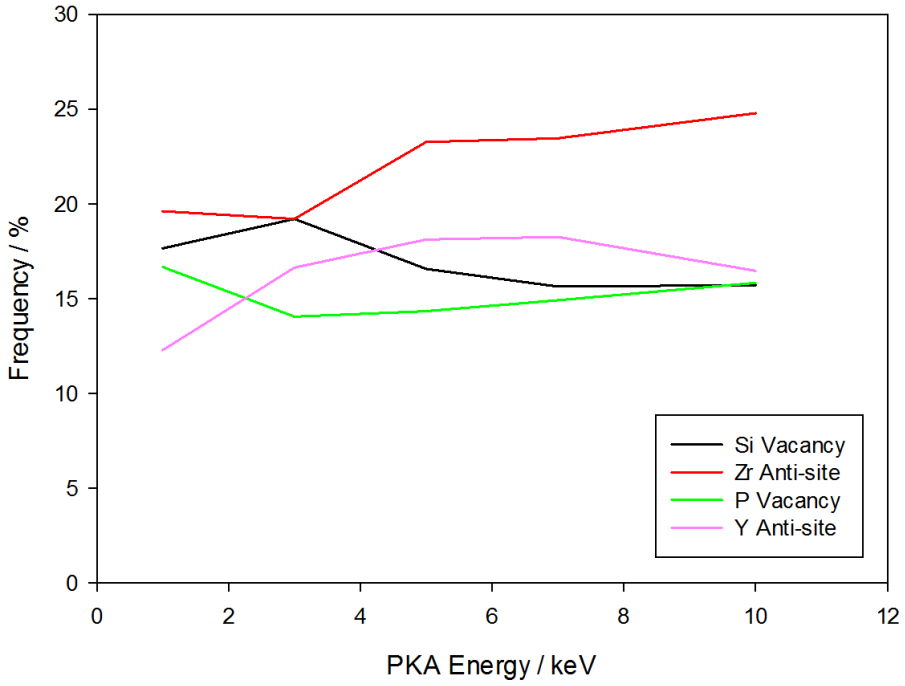

Figure 6.57: Proportion of B cation defects considers as sources as identified by the Voronoi method for the $(1\bar{1}9)$ cascades in zircon and xenotime

The polymerisation of phosphate and silicate units in xenotime and zircon respectively have been analysed and compared in Figure 6.58. Here it can be seen that the total number of polymerised chains increases linearly for both systems with the rate of formation of the polymerised chains estimated to be ca. 0.007 chains eV^{-1} compared to 0.015 chains eV^{-1} in xenotime.

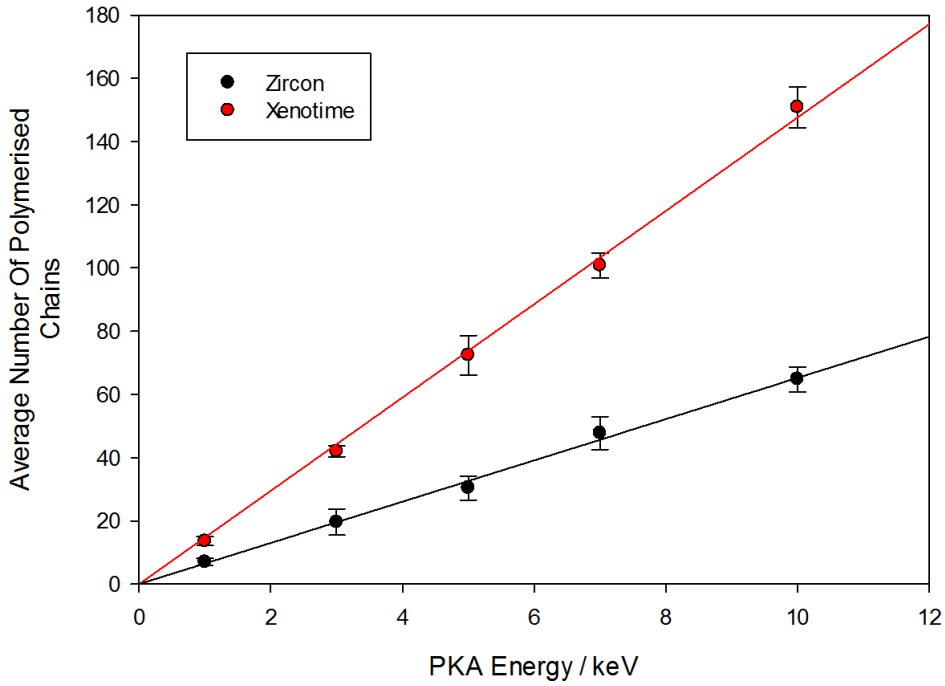

Figure 6.58: Comparison of the number of polymerised chains in zircon and xenotime for the $(1\bar{1}9)$ cascades

The distribution of the number of atoms in each chain was very similar across all PKA energies and as such the average distribution is illustrated in Figure 6.59 of the $(1\bar{1}9)$ cascades in zircon and xenotime. There is a clear difference in the frequency with which the shorter chains were observed. The peak at a chain length of ten in xenotime is not present in zircon whereas the peak at a chain length of eleven in zircon is not present in xenotime. This indicates that there is a propensity for the chains containing two phosphorus atoms to form P_2O_8 units, with the equivalent silicate units being observed much less frequently. Conversely there is a propensity for the formation of Si_2O_9 units which are observed with a much higher frequency than the phosphate equivalents in xenotime. As the chain lengths increase it is clear that the peaks in the distribution for zircon occur at lengths corresponding to chains made of corner sharing tetrahedra

whereas the equivalent phosphate chains have a propensity to be over-coordinated by one oxygen atom. Finally there were much longer chains observed in the zircon system, with the longest chain containing 265 atoms, compared to 107 in xenotime.

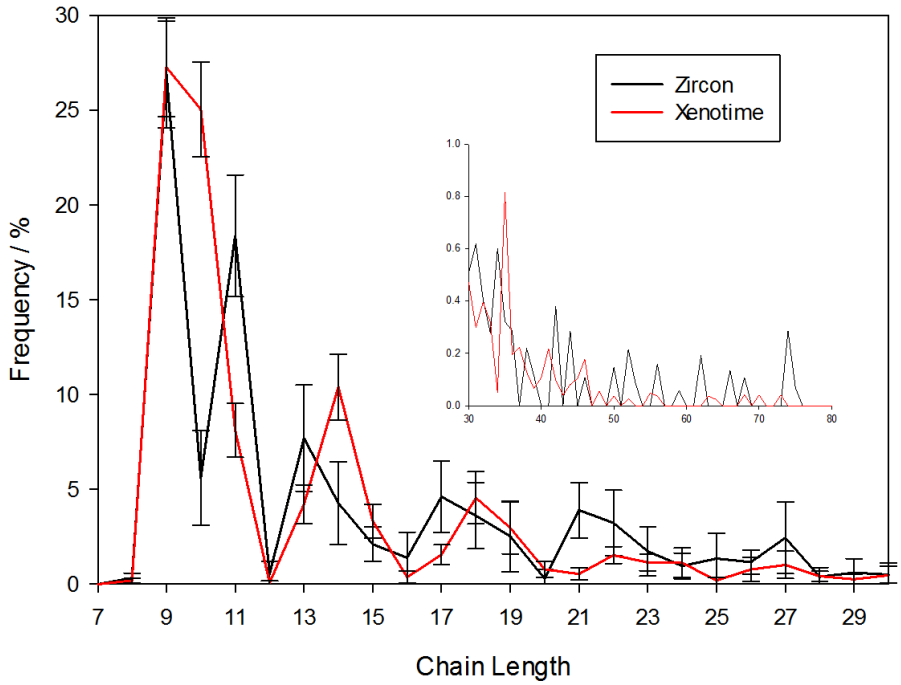

Figure 6.59: Comparison of the distribution of the polymerised chains with varying lengths in zircon and xenotime for the $(1\bar{1}9)$ cascades

The average number of B cations in the polymerised chains are illustrated in Figure 6.60 for the zircon and xenotime $(1\bar{1}9)$ cascades. It can be seen that they follow a similar trend whereby the frequency decreases quickly with increasing cation content, however chains which contain five silicon atoms are observed with a higher frequency that the equivalent phosphate chains in xenotime. This supports the differences observed in chapter 4 with the silicon atom adopting the site 1 position which would result in more Si_5O_{16} units. There is also evidence of much longer silicate chains in zircon, with the longest chain

containing sixty-one silicon atoms compared to the phosphate equivalents in xenotime containing twenty-four phosphorus atoms.

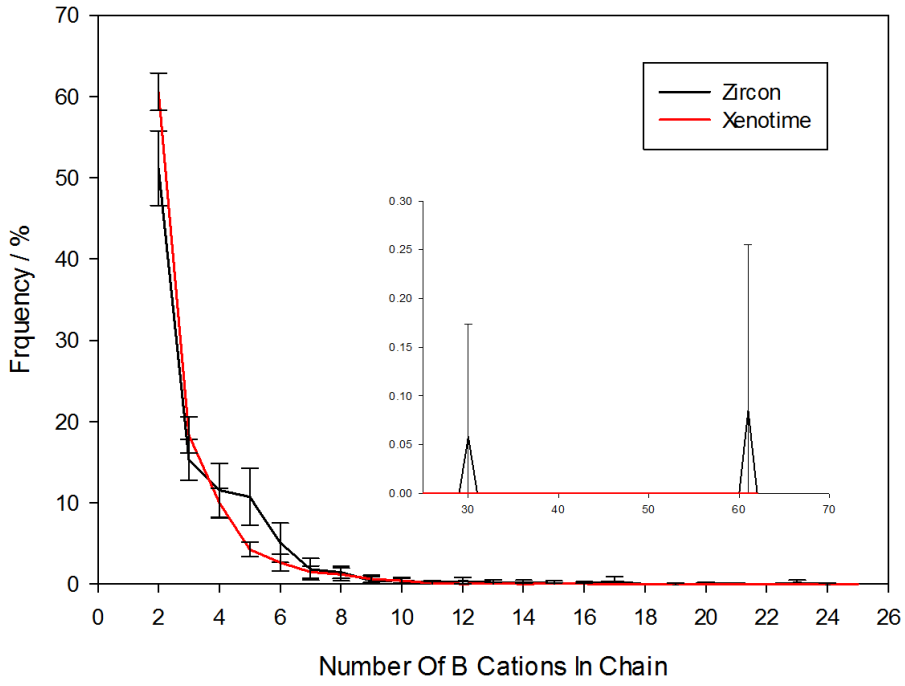

Figure 6.60: Comparison of the distribution of the number of B cations in the polymerised chains in zircon and xenotime for the $(1\bar{1}9)$ cascades

The distribution for the PKAs initiated in the $(1\bar{1}9)$ direction in zircon are summarised in Figure 6.61. Here it can be seen that there are some key differences compared to the equivalent cascades in xenotime. Whereas the distribution in xenotime had a peak at a net over-coordination of one, the silicate chains are most likely to have the ideal Si:O ratio for corner sharing silicate tetrahedra. Additionally there is a propensity for the silicate chains to have a net over-coordination of two which was not observed in xenotime. These chains generally become more frequently observed with increasing PKA energy. The most under-coordinated chains were under-coordinated by one oxygen atom, similar to the

xenotime system, however the most over-coordinated chain was over-coordinated by twenty-two oxygen atoms, compared to ten for the $(1\bar{1}9)$ cascades in xenotime.

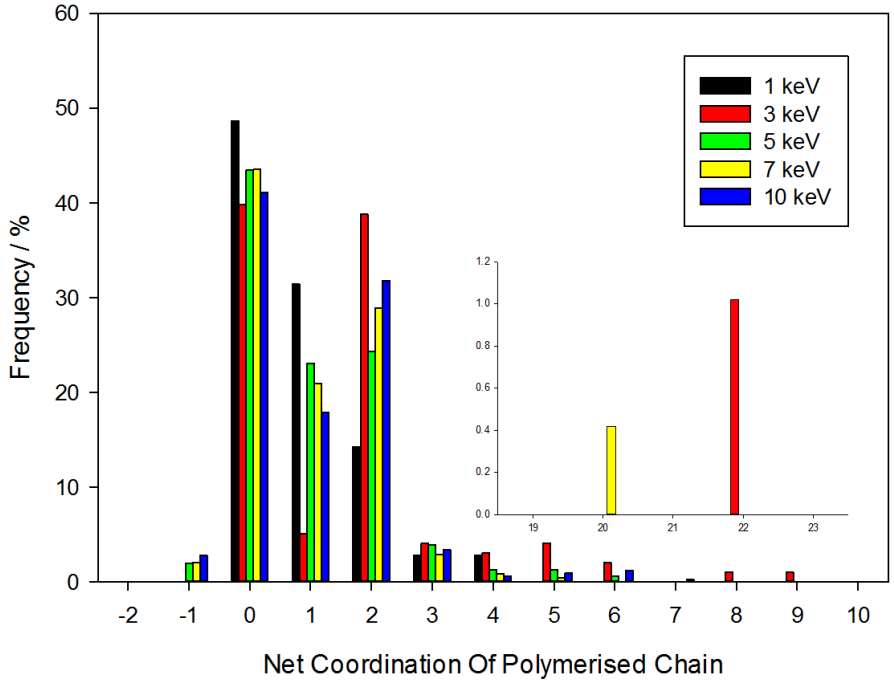

Figure 6.61: Distribution of the net coordination of the polymerised chains in zircon for the $(1\bar{1}9)$ cascades

A comparison of the coordination number of the B cations in the phosphate and silicate polymerised units can be seen in Figure 6.62. The distributions have been averaged across all cascades in the $(1\bar{1}9)$ direction as the distribution was found to be similar for all PKA energies. Here it can be seen that both the phosphate and silicate chains follow a similar trend with the majority of the cations being four coordinate. Three and six coordinate cations were observed in both materials but to a much lesser extent. The chains do however contain an appreciable percentage of five coordinate cations, which are observed to a greater extent in xenotime. This difference may contribute to the relative stability of the polymerised networks with the static calculations in chapter 4

demonstrating that the over-coordination of the phosphorus atoms increases the energy of the defects, making them less stable.

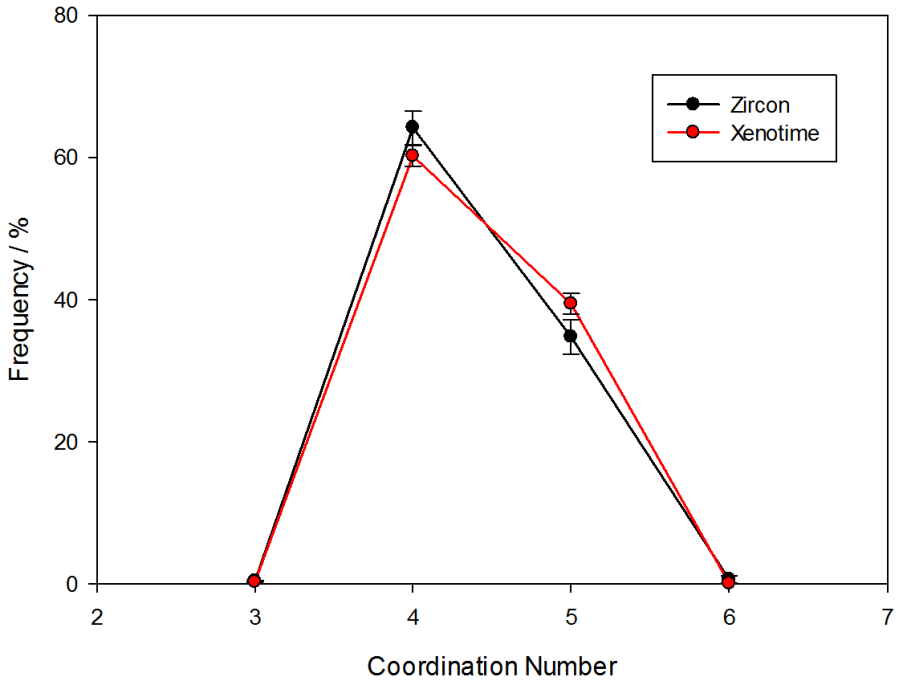

Figure 6.62: Comparison of the distribution of coordination number of the B cations in the polymerised chains in zircon and xenotime for the $(1\bar{1}9)$ cascades

As stated previously, edge sharing polyhedra can serve to reduce the P:O ratio and help reduce the net over-coordination of chains which may contain over-coordinated cations. As such the distribution of cations which are edge sharing with neighbouring polyhedra has been analysed and summarised in Figure 6.63. Here it can be seen that both phases follow a very similar trend with the majority of polyhedra in the chains corner sharing with the neighbouring polyhedra. There are a small percentage of cations which are edge sharing with one neighbouring polyhedron, ca. 10 % which is consistent for both systems. There was a very small percentage of cations observed which were edge sharing with two

neighbouring polyhedra, < 1 %, whilst cations which were edge sharing with three neighbouring polyhedra were only observed in the zircon system.

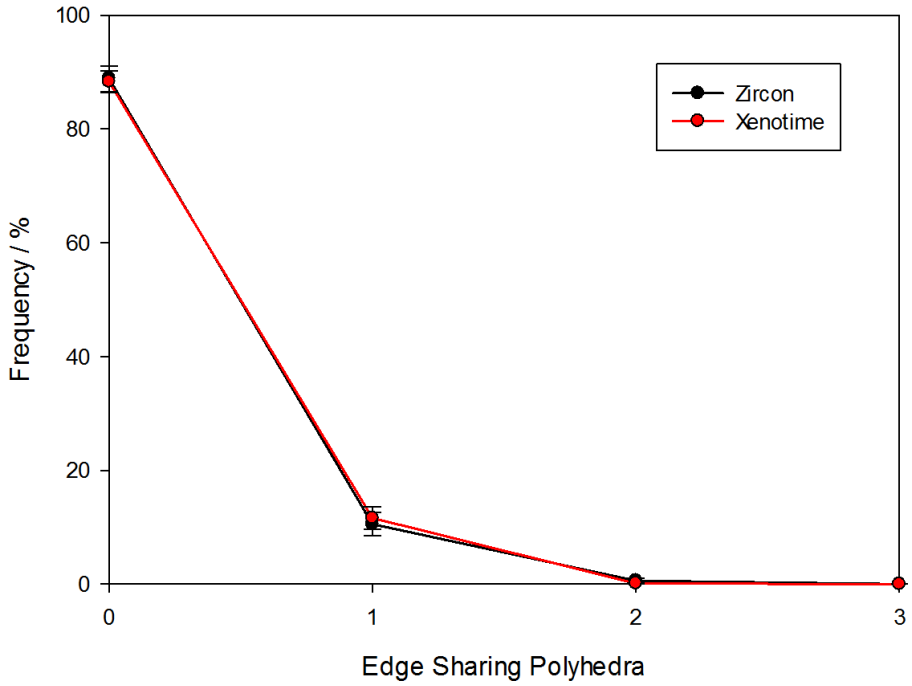

Figure 6.63: Comparison of the distribution of the number and degree of edge sharing cation polyhedra in the polymerised chains in zircon and xenotime for the $(1\bar{1}9)$ cascades

It is possible to describe the polymerised network in terms of how many bridging oxygen atoms are coordinated to the cations in the chains, illustrated in Figure 6.64. The Q^n value can be used to describe the degree of polymerisation of the cations with the value of n relating to the number of bridging oxygen atoms which are coordinated to the cation, such that Q^0 corresponds to an isolated polyhedron. It can be seen that both systems follow a similar trend with the cations with a higher Q^n being observed less frequently than those which are less polymerised. This is in accordance with the previous observation that the most common chains contained two polymerised polyhedra. The percentage of Q^4 cations can be seen to be greater in zircon than in xenotime, with frequencies of ca. 3 and 1 %

respectively. This increased degree of cross-linking of the polymerised chains may contribute to the increased stability of the silicate network and may be a contributing factor to the radiation 'resistance' of these minerals.

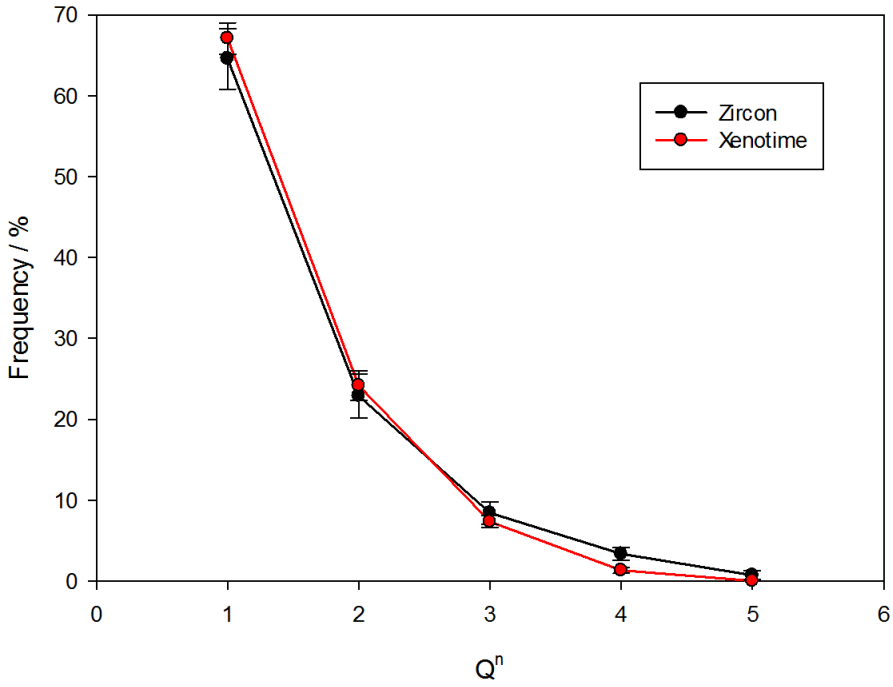

Figure 6.64: Comparison of the distribution of the degree of polymerisation of the cations in the polymerised chains in zircon and xenotime for the $(1\bar{1}9)$ cascades

It is difficult to compare directly across simulations which use different sets of pair potentials which are not transferable and so it is more appropriate to consider the trends which are observed. These cascade simulations have highlighted some of the differences which may occur when using different defect detection methods to analyse the configurations, which can make it difficult when comparing results between studies. The degree of polymerisation has been identified as an important difference in the type of damage which is accumulated in xenotime and zircon which may contribute to the differences in the resistance to radiation damage observed between the two minerals.

6.5 Further Work

- Apply the methodology utilised here to determine the threshold displacement energy in other systems, including monazite, and compare the results to other literature sources.
- Repeat the cascade simulations for more PKA atoms and in different directions to gain better statistics.
- Perform cascade simulations in different ensembles (ie. NPT) to observe how this impacts the defect evolution in both xenotime and zircon and additionally measure volume changes which may occur.
- Employ a boundary thermostat to allow for moderation of the temperature of the simulation cell to compare with the simulations in this study and identify any differences.
- Perform multiple overlapping cascades within the same simulation cell to compare to other models of radiation damage
- Combine the cascade simulations with the surface simulations from chapter 5 to produce grain boundaries and to investigate the effect of damage cascades at these boundaries.
- Apply the cluster detection code developed throughout this work, which was unfortunately not used due to time constraints, to identify defect clustering within the damaged configurations.
- Apply ring statistics to better understand motifs in the damaged configurations.
- Use the consistent set of potentials derived across a range of $LnPO_4$ phases to compare radiation damage in monazite to xenotime.

- Perform radiation damage simulations over longer timescales to investigate the annealing behaviours of the damaged structures.

6.6 References

1. K. Nordlund, J. Wallenius and L. Malerba, *Nuclear Instruments & Methods in Physics Research Section B-Beam Interactions with Materials and Atoms*, 2006, **246**, 322-332.
2. L. Kittiratanawasin, R. Smith, B. P. Uberuaga and K. Sickafus, *Nuclear Instruments & Methods in Physics Research Section B-Beam Interactions with Materials and Atoms*, 2010, **268**, 2901-2906.
3. E. Gonzalez, Y. Abreu, C. M. Cruz, I. Pinera and A. Leyva, *Nuclear Instruments & Methods in Physics Research Section B-Beam Interactions with Materials and Atoms*, 2015, **358**, 142-145.
4. B. Park, W. J. Weber and L. R. Corrales, *Nuclear Instruments & Methods in Physics Research Section B-Beam Interactions with Materials and Atoms*, 2000, **166**, 357-363.
5. H. Tsuchihira, T. Oda and S. Tanaka, *Nuclear Instruments & Methods in Physics Research Section B-Beam Interactions with Materials and Atoms*, 2011, **269**, 1707-1711.
6. G. Lucas and L. Pizzagalli, *Nuclear Instruments & Methods in Physics Research Section B-Beam Interactions with Materials and Atoms*, 2005, **229**, 359-366.
7. S. J. Zinkle and C. Kinoshita, *Journal of Nuclear Materials*, 1997, **251**, 200-217.

8. P. Moreira, R. Devanathan, J. G. Yu and W. J. Weber, *Nuclear Instruments & Methods in Physics Research Section B-Beam Interactions with Materials and Atoms*, 2009, **267**, 3431-3436.

9. V. S. Urusov, A. E. Grechanovsky and N. N. Eremin, *Glass Physics and Chemistry*, 2012, **38**, 55-62.

10. K. Trachenko, E. Zarkadoula, I. T. Todorov, M. T. Dove, D. J. Dunstan and K. Nordlund, *Nuclear Instruments & Methods in Physics Research Section B-Beam Interactions with Materials and Atoms*, 2012, **277**.

11. J. G. Yu, R. Devanathan and W. J. Weber, *Journal of Materials Chemistry*, 2009, **19**, 3923-3930.

12. E. E. Jay, P. C. M. Fossati, M. J. D. Rushton and R. W. Grimes, *Journal of Materials Chemistry A*, 2015, **3**, 1164-1173.

13. A. Gonzalez, *Mathematical Geosciences*, 2010, **42**, 49-64.

14. J. F. Ziegler, M. D. Ziegler and J. P. Biersack, *Nuclear Instruments & Methods in Physics Research Section B-Beam Interactions with Materials and Atoms*, 2010, **268**, 1818-1823.

15. J. T. Buchan, M. Robinson, H. J. Christie, D. L. Roach, D. K. Ross and N. A. Marks, *Journal of Applied Physics*, 2015, **117**.

Chapter 7

Structural Analysis of Xenotime and Fluorapatite Samples Using X-Ray PDF

Table of Contents

Table of Figures

7.1 Introduction

The cascade simulations reported in chapter 6 are more appropriate for modelling PKAs with relatively low energy, where the majority of the interactions with the surrounding ions are through elastic collisions. As the energy of the PKA increases, the contribution from inelastic interactions increases and elastic collisions become less frequent. As a result the damage induced in samples by swift heavy ion radiation may be better modelled through the simulation of fission tracks. A variety of different simulation procedures have been suggested to achieve this[1-3].

As discussed in chapter 1, apatite minerals ($A_{10}(BO_4)_6X_2$) represent a group of materials which are found in nature as common accessary minerals near natural reactors. Natural apatite minerals are known for their ability to incorporate a wide range of substituents, of which Sr is one of the most common. As a result they are strong candidate phases for the immobilisation of nuclear waste (in particular U, ^{90}Sr and ^{90}Y) to prevent these species from reaching the biosphere where they pose a great risk to humans. The immobilisation of ^{90}Sr is a major issue as it is readily incorporated and accumulates in hard tissues such

as bone and teeth which are comprised of the hydroxyapatite phase themselves, again demonstrating the high affinity of the apatite structure for Sr.

Though there is known to be a solid solution between Ca-fluorapatite and Sr-fluorapatite, the distribution and indeed ordering of Sr over the two possible sites is still a topic of ongoing debate for intermediate compositions. In 1964, Klevtsova et al.[4] demonstrated through structural refinement of single crystal X-ray photographs that Sr has a strong preference for the M(2) site. However it was also concluded that the symmetry of the natural sample of fluorapatite with ca. 60% Sr incorporated for Ca, degenerates from $P6_3/m$ to $P6_3$ due to ordering of the Sr and Ca on the M(1) site, with a 50% site occupancy of Ca and Sr, giving the formula $Ca_2(Sr,Ba)_2(Ca_{0.56}Sr_{4.14}X)P_6O_{24}(F,OH)_2$. These two space groups are illustrated in Figure 7.1. The sample was however a natural sample containing other impurities (X= Ba, Mg, REE, Fe and Na) which may have competed with the Sr for the occupancy of site 2 and therefore makes the interpretation of this result much more difficult. Later, a powder X-ray diffraction study by Khudoloz et al.[5] concluded similar results in a sample containing ca. 10% Sr, whereby the Sr preferentially occupies the M(2) site with no degeneration of symmetry from the space group $P6_3/m$. They did however conclude that the degree of affinity of Sr for the M(2) site decreases with increasing Sr content. Hughes et al. subsequently used high precision refinements of single crystal X-ray diffraction data to determine the distribution of Ca/Sr in two natural samples containing 6.3 and 2.9% Sr. They concluded that the Sr occupancy of the Ca(2) site was 0.5639 (90 %) and 0.2889 (97 %) for the two samples respectively. This demonstrates a very high affinity of Sr for the M(2) site at these low substitution levels with a decrease in preference for the M(2) site with increasing Sr content and no loss of symmetry, in

agreement with Khudoloz et al. However, Bigi et al.[6] analysed 3 synthetic apatite phases containing 5, 20 and 60 % Sr using Rietveld refinement of diffraction data and determined that although there was a preference for the Sr to occupy the M(2) site, this preference increases with increasing Sr content which is in contrast to Khudoloz et al. They do not report any loss of symmetry for the 60% Sr sample which is again contradictory to the findings of Klevtsova et al. Seven synthetic samples of hydroxyapatite with varying Sr contents (x = 1, 2, 4, 5, 6, 8 and 9) where analysed using X-ray diffraction (Heijligers et al.[7]) and IR spectroscopy (Andrés-Vergés et al.[8]) and it was concluded, based on the intensity/area ratios of 7 pairs of reflections and the presence of only one ν_S(OH) band respectively, that there is an 'isotropic distribution' of Ca and Sr over the two sites, the ratio of which varies as a function of composition. Furthermore they suggested that an equilibrium is reached between the two species over the two sites and that the distribution was not static but there was in fact a continuous migration mechanism of the species over the two sites. This is in contrast to the earlier observations made for fluorapatite samples. Contradictory yet again is a study by Kikuchi et al.[9] who grew synthetic crystals of hydroxyapatite using a hydrothermal method (x = 0.19) and concluded that the Sr preferentially occupies the M(1) site and that the synthesis conditions may have an impact. This short, and by no means comprehensive, review of the literature clearly demonstrates the need for a more in depth study. X-ray PDF may provide an alternative approach to analyse the distribution and site preference of Sr atoms within fluorapatite.

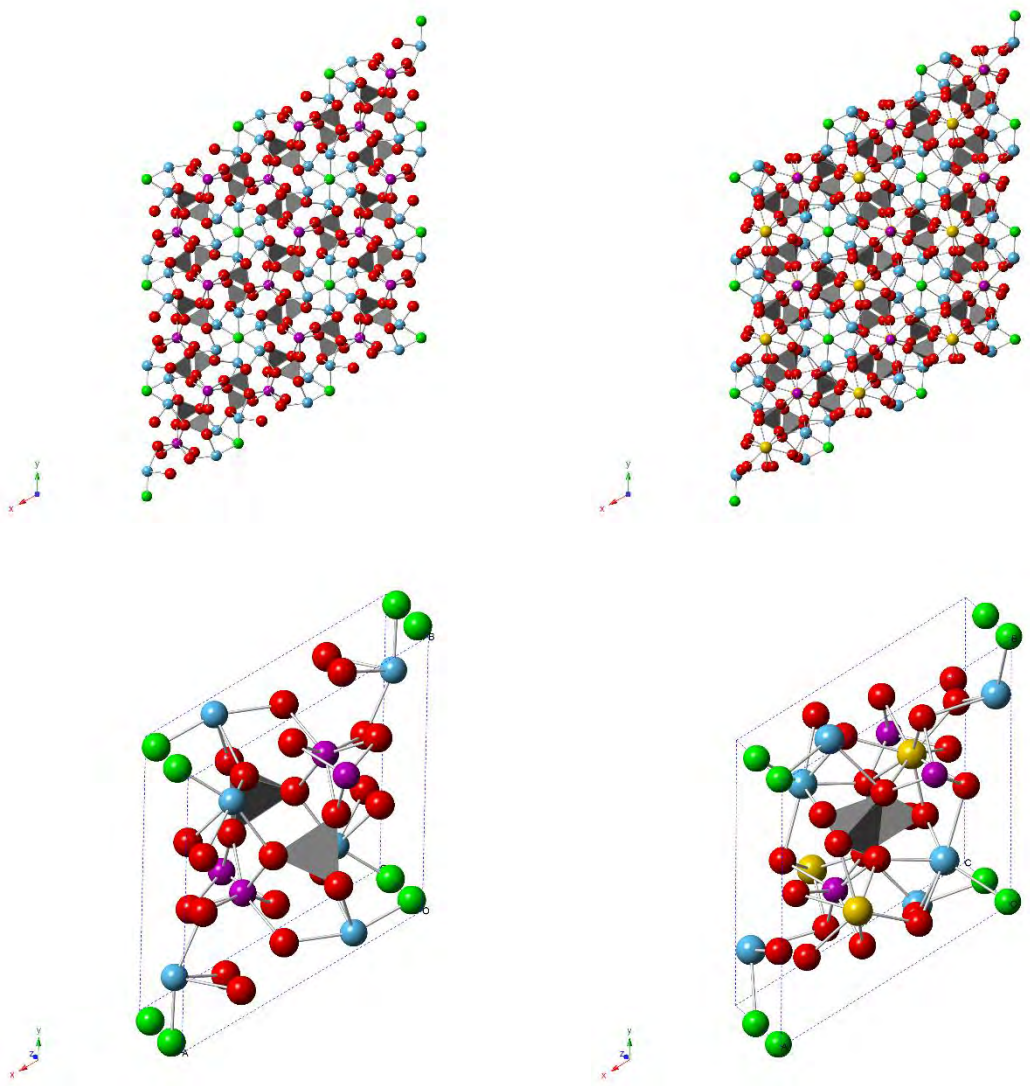

(a) (b)

Figure 7.1: The two suggested space groups for the mixed Ca/Sr fluorapatite system (a) $P6_3/m$ and (b) $P6_3$. The M(1) position is highlighted in purple whilst the M(2) position is highlighted in blue. In the $P6_3$ space group the M(1) site is split and the M(3) position is highlighted in yellow. Oxygen and fluorine atoms are shown in red and green respectively, while phosphorus atoms are depicted as grey tetrahedra.

7.2 Radiation Damaged Xenotime

7.2.1 Pair Distribution Function (PDF) Analysis

Samples of xenotime which had been exposed to swift heavy ion radiation at the Grand Accélérateur National d'Ions Lourds (GANIL) facility in France were donated by the Farnan group within the department of earth sciences at the University of Cambridge. The samples were prepared as thin wafers, < ca. 71 μm thick, taken from a sample which had been hot isostatic pressed (HIPed) at 1350 °C and 100 MPa for 2 hours for complete densification. The samples were then irradiated with Pb ions with an energy of 11 MeV nucleon^{-1} at a range of fluences. PDF analysis was performed at the Diamond Light Source in Oxfordshire on beamline I15. The samples were pressed into holes drilled into a rhenium gasket and secured on both sides with Kapton tape. The gasket was secured to a Diamond Anvil Cell holder at a distance of ca. 255 mm from the detector plate. The samples as ground powders were irradiated with X-rays of wavelength 0.172 Å and data was collected using a Perkin Elmer flat panel 1621 EN detector. The sample-detector distance, the beam centre on the detector and the tilt angles of the detector were calibrated against a CeO_2 standard held in a separate hole in the same gasket. The PDFs for the un-irradiated and irradiated samples of xenotime are illustrated in Figure 7.2. Here it can be seen that even after being irradiated at a fluence of 10 x 10^{12} ions cm^{-2} the local structure remains relatively unchanged. The discrepancies between the two curves may be rationalised by artefacts within the PDFs as a result of the data processing.

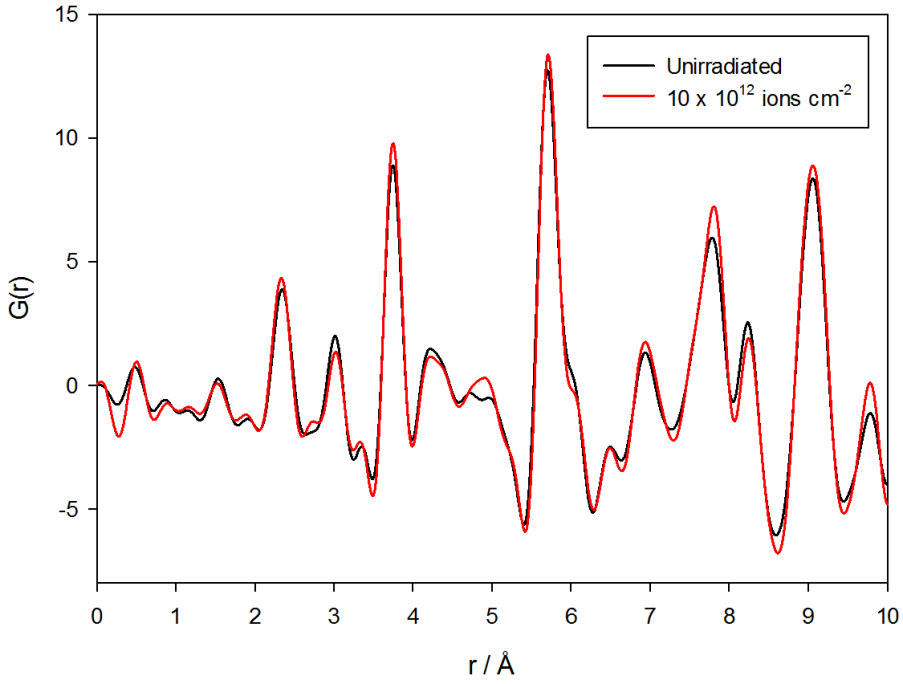

Figure 7.2: The PDFs for the unirradiated (black) and irradiated (red) samples of xenotime

The PDF can be decomposed into the partial PDFs to help identify the interatomic separations that contribute to each peak, Figure 7.3. The peak at ca. 1.54 Å corresponds to the P-O distances whilst the peak at ca. 2.33 Å corresponds to the Y-O distances. The peak at ca. 3.01 Å has a primary contribution from the Y-P distances whilst the peak at ca. 3.75 Å has major contributions from the Y-Y, Y-P, P-P and P-O distances.

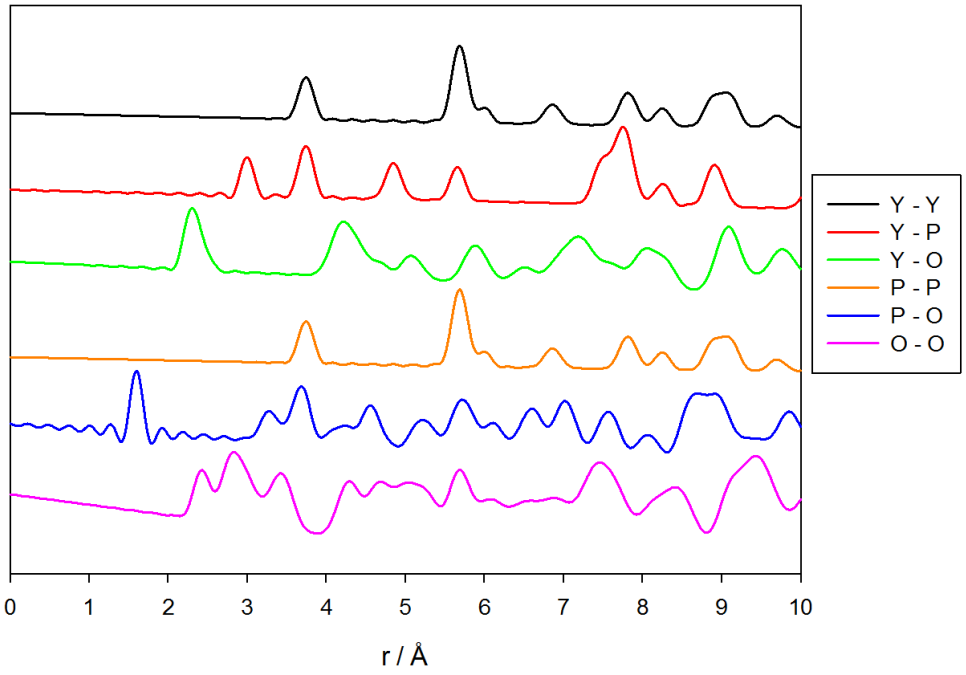

Figure 7.3: Partial PDFs between the different pairs of ions for the unirradiated sample of xenotime

The experimental PDFs can be converted to the radial distribution functions (RDF) following equation (7.1), and are illustrated in Figure 7.4. The peaks of interest can be fit using a Gaussian function and the peak position and full width at half maximum (FWHM) can be approximated (appendix 3). From this analysis it was found that the position of the P-O peak remains relatively unchanged at 1.54 and 1.53 Å for the un-irradiated and irradiated sample respectively. The peak becomes slightly broader for the irradiated sample with a ΔFWHM of 0.02 Å. A similar observation was made for the Y-O peak at 2.34 and 2.33 Å for the un-irradiated and irradiated samples respectively; here the peak becomes less broad with a ΔFWHM of -0.01 Å. Similarly the Y-P peak is shifted by 0.01 Å from 3.01 Å for the un-irradiated sample to 3.02 Å in the irradiated sample, with a FWHM of 0.25 Å for both samples. Finally the Y-Y peak remains unchanged at 3.75 Å with a

FWHM of 0.24 Å for both samples. This indicates that the xenotime sample is not damaged to a sufficiently high degree to be detected using X-ray PDF analysis.

$$g(r) = \left(\frac{G(r)}{4\pi r \rho_0}\right) + 1 \tag{7.1}$$

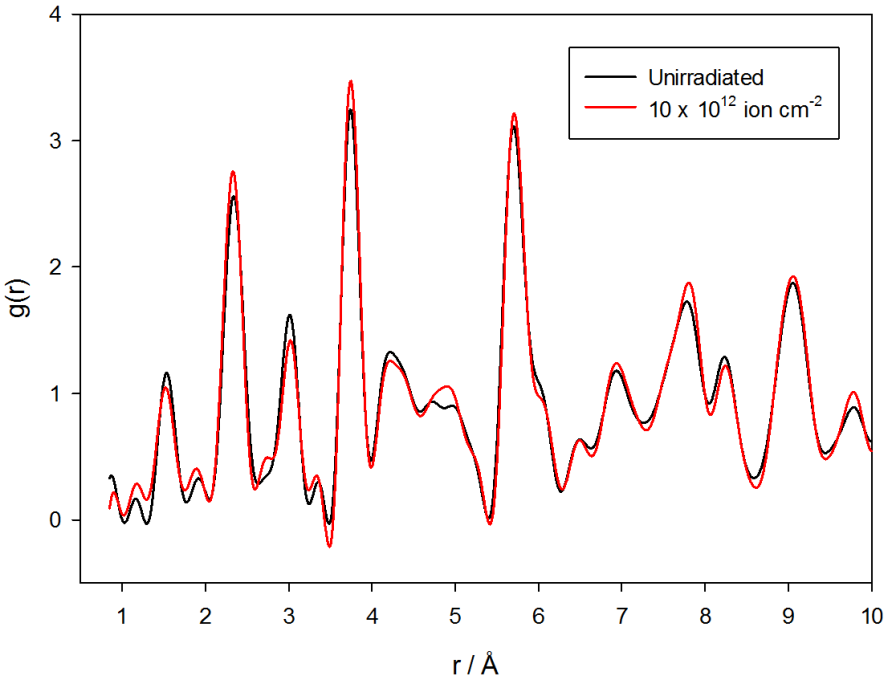

Figure 7.4: The RDFs for the unirradiated (black) and irradiated (red) samples of xenotime

7.2.2 Fission Track Model

Fission track simulations were performed in a 50 x 50 x 20 supercell which was first equilibrated in the NPT ensemble before the fission track simulations were performed in the NVE ensemble. The simulation cell was equilibrated within the NVE ensemble before the energy of the atoms contained within a cylindrical volume of radius 3 nm was increased by 1 eV atom^{-1} and the ions were initiated with a random trajectory. In total

28482 eV was deposited into the system over a track length of ca. 121 Å. This equated to a dE/dx value of 2.35 keV nm^{-1}. Caution is advised when comparing this value with experimental data as this model assumes no reduction in energy deposition along the length of the track and perfect electron-phonon coupling. The simulation was allowed to run for ca. 111 ps using a variable time step algorithm as described in chapter 2. The defects which were identified *via* the radius method are illustrated in Figure 7.5 at various time steps. It can be seen that large pressure waves extend along the *a* and *b* axis at peak damage which reflect minor displacements of the atoms from the lattice sites. The final damaged region can be seen to have a much smaller diameter than the initial track which could indicate annealing of the defects at the periphery of the track or a concentration of damage at the track core, in accordance with the thermal spike model[10, 11].

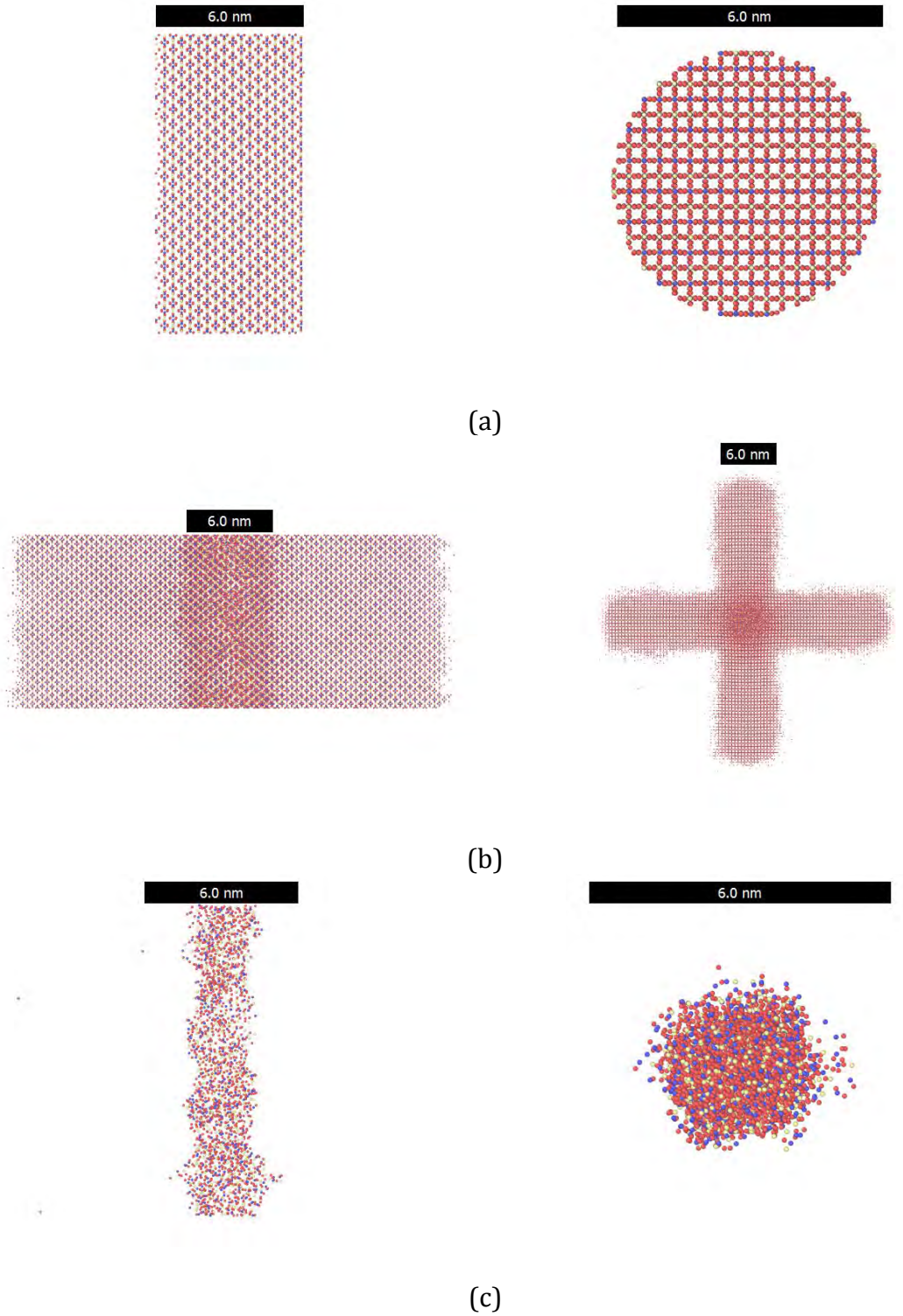

Figure 7.5: Defects as determined by the radius method at (a) 0.00 ps, (b) 2.10 ps and (c) 111.48 ps after the fission track was initiated. Yttrium, phosphorus and oxygen interstitials are shown in yellow, blue and red respectively

An RDF can be calculated for the configuration to describe the distribution of atoms as a function of perpendicular distance from the axis of the fission track following equation (7.2; where $N(r)$ is the number of atoms in a cylindrical shell, L is the length of the fission track and ρ_0 is the average number density of the simulation cell.

$$g(r) = \frac{N(r)}{2\,\pi\,r\,dr\,L\,\rho_0} \tag{7.2}$$

A reference RDF for the un-damaged xenotime configuration is illustrated in Figure 7.6. Here it can be seen that there are sharp intense peaks corresponding to the ordered distribution of the atoms on the lattice sites. As with the archetypal RDF, the cylindrical RDF tends towards 1 with increasing distance.

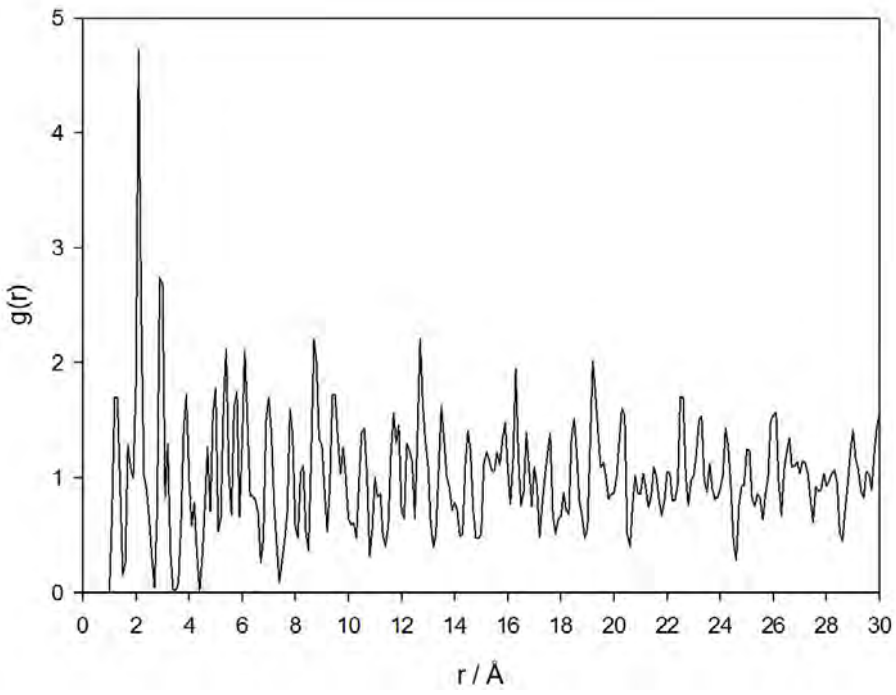

Figure 7.6: Total cylindrical RDF for the un-damaged configuration

The normalised partial RDFs are illustrated in Figure 7.7. Here it can be seen that the yttrium and phosphorus partial RDFs are extremely similar as the two crystallographic sites are related by symmetry. There are two strong peaks at ca. 2.1 and 2.9 Å, with no yttrium or phosphorus atoms found at distances less than 1.9 Å from the axis of the fission track. The oxygen partial RDF is much broader than for the cations, with no oxygen atoms found at distances less than 1.1 Å from the axis of the fission track.

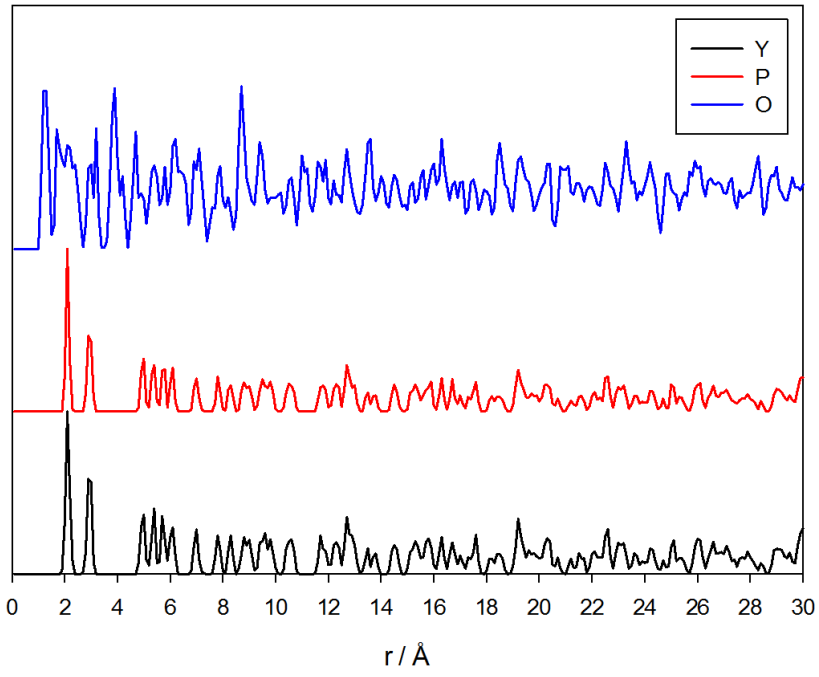

Figure 7.7: Partial cylindrical RDFs for the un-damaged configuration

The strong correlation between the yttrium and phosphorus partial RDFs can be utilised to determine the diameter of the fission track in the final damaged configuration. The correlation coefficient can be calculated following equation (7.3), using moving boxcar samples spanning 2 Å segments of the RDFs. The average correlation coefficient taken

over the two partial RDFs to a distance of 80 Å was calculated to be 0.978 with a standard deviation of 0.010, with ~ 99.7 % of the values greater than 0.947.

$$Correl(X,Y) = \frac{\sum(x-\bar{x})(y-\bar{y})}{\sqrt{\sum(x-\bar{x})^2 \sum(y-\bar{y})^2}} \quad \textbf{(7.3)}$$

The cylindrical RDFs were averaged over the final five frames to generate the RDF for the damaged structure. The partial RDFs for the yttrium atoms in the un-damaged and damaged configurations are illustrated in Figure 7.8. Here it can be seen that the sharp peaks from the crystalline structure are no longer present at short distances from the centre of the fission track, with the RDF now oscillating about 1, indicating a much more random distribution of atoms and therefore an amorphised region. This continues to a distance of ca. 11.5 Å. Between ca. 11.5 and 17.5 Å the partial RDFs become much more similar, though there are still some differences. Finally after ca. 17.5 Å the RDFs are very similar, indicating a return to a crystalline structure. Yttrium atoms are found much closer to the centre of the fission track, at distances greater than 0.6 Å, compared to 1.8 Å in the un-damaged structure.

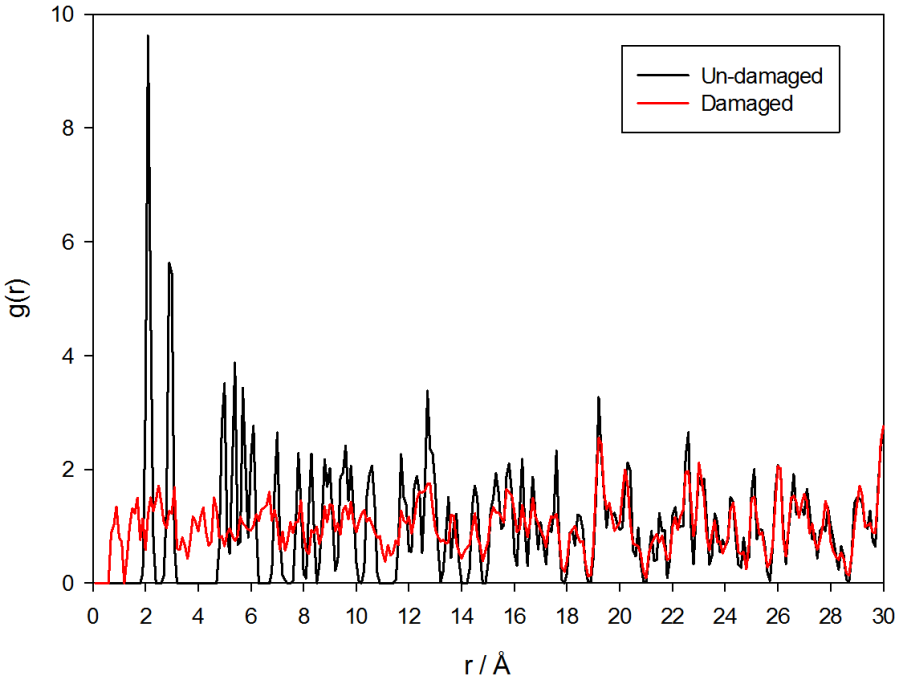

Figure 7.8: Comparison of the Y partial cylindrical RDFs between the un-damaged (black) and damaged (red) configurations

Similar analysis can be performed on the phosphorus RDFs, Figure 7.9. Again similar regions can be identified with the region up to ca. 9.0 Å identified as amorphised. The region between 9.0 and 17.5 Å corresponds to the damaged region, showing some resemblance to the pristine RDF, and the crystalline region at distances greater than 17.5 Å, where the RDFs are extremely similar. In the damaged configuration phosphorus atoms are found to be present at distances greater than 0.3 Å from the centre of the fission track, compared to 1.9 Å for the un-damaged configuration.

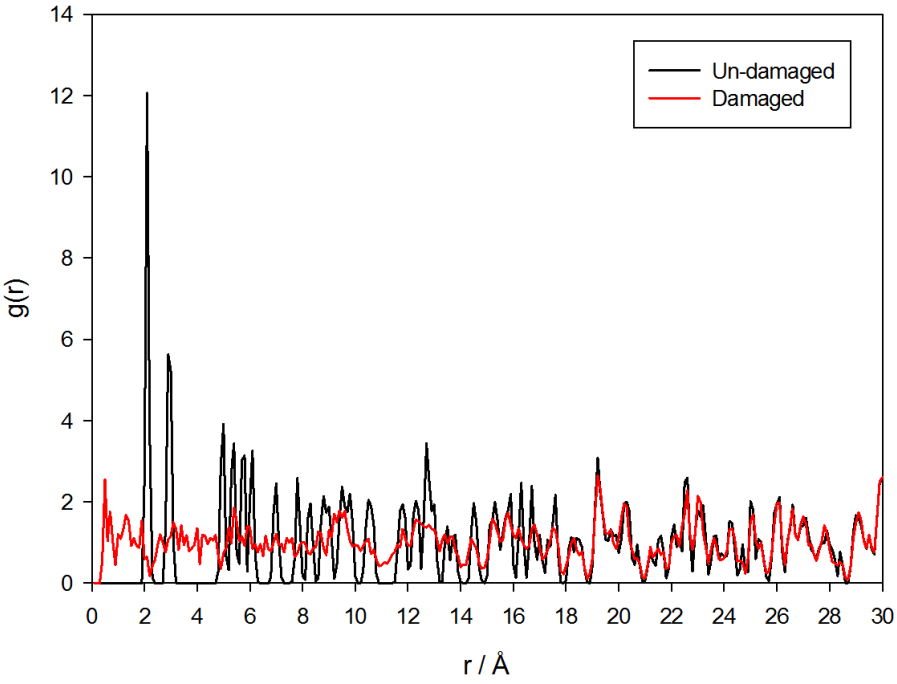

Figure 7.9: Comparison of the P partial cylindrical RDFs between the un-damaged (black) and damaged (red) configurations

Finally the oxygen partial RDF was analysed, Figure 7.10. The amorphous region can be seen to extend to ca. 9.0 Å, with the damaged region extending to ca 17.0 Å. At distances greater than ca. 17.0 Å the RDFs become very similar, indicating the crystalline region. It can be seen that there is a much higher probability of finding an oxygen atom closer to the track centre than for the cations, with oxygen atoms found at distances less than 0.1 Å.

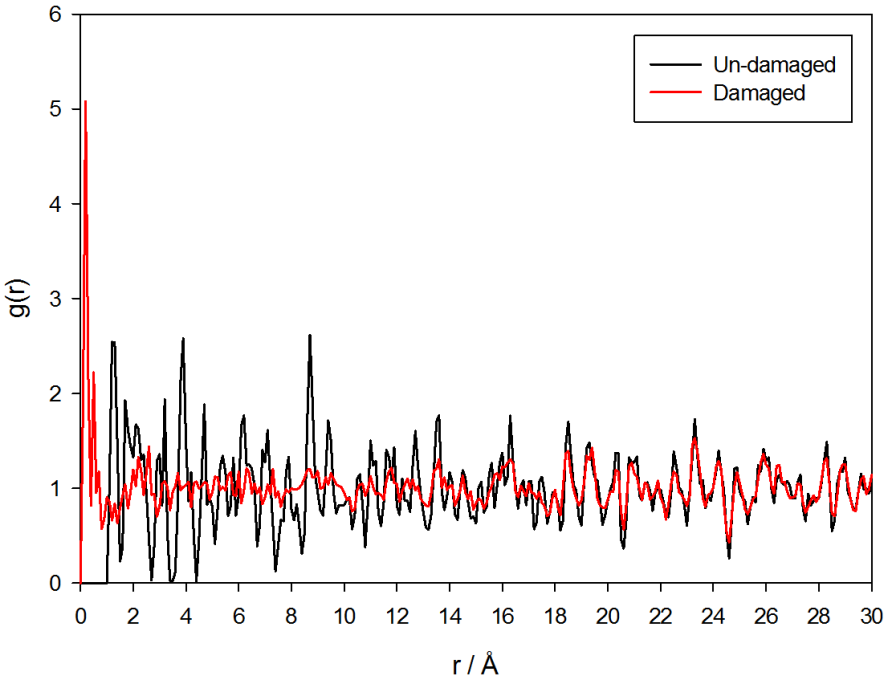

Figure 7.10: Comparison of the O partial cylindrical RDFs between the un-damaged (black) and damaged (red) configurations

In the amorphised region both the yttrium and phosphorus atoms are essential randomly distributed, disrupting the correlation between the two partial RDFs. As such the correlation coefficient was calculated in the same way as for the un-damaged system earlier in this chapter, the results are illustrated in Figure 7.11. Here it can be seen that there is indeed a large decrease in the correlation between the two datasets as the correlation coefficient is reduced to ca. 0.0 within the first 10 Å, indicating that there is no correlation and that the atoms are essentially randomised. There are some negative peaks within this region which indicate distances which are partially negatively correlated (ie. partial overlap of a peak and a trough in the partial RDFs). These can be seen at ca. 0.6, 1.4 and 5.4 Å where there are small peaks in the phosphorus partial RDF which are not

observed for yttrium. Similarly the peaks at ca. 0.9 and 2.4 Å in the yttrium RDF are not present for phosphorus. At distances between ca. 10.0 and 17.0 Å there is a more positive correlation between the data sets, however it is still less than for distances greater than ca 17.0 Å which show a strong positive correlation in line with that seen for the un-damaged configuration. A lower limit was defined previously for the correlation coefficient within the un-damaged structure of 0.947 which can be used to estimate the track radius by considering the last consecutive distance with a correlation coefficient less than this value. As such the track radius in the final damaged configuration was estimated to be 16.8 Å, giving a track diameter of 33.6 Å which is a reduction of 44 % from the initial diameter of 60 Å.

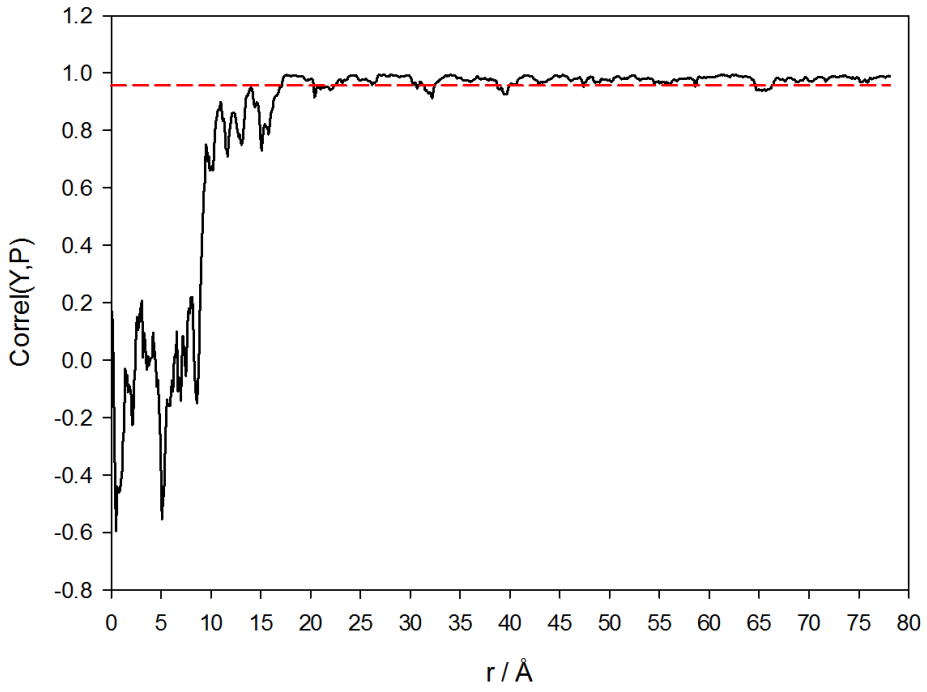

Figure 7.11: Correlation coefficient between the Y and P partial RDFs as a function of distance from the fission track axis in the final damaged configuration. The red reference line represents the lower limit for the correlation coefficient in the un-damaged configuration

This method is very useful in systems with different elements on highly correlated lattice sites, however it can be applied more generally by comparing the total RDFs and calculating the correlations coefficient over the same length scales, Figure 7.12. Here the lower limit for the correlation coefficient in the un-damaged region was estimated by calculating the average and standard deviation of the correlation coefficients for distances greater than 40.0 Å, well within the crystalline region. This gave a lower threshold of 0.794 and a track radius of 9.3 Å. This somewhat underestimates the total track radius but does well describe the amorphised region of the fission track.

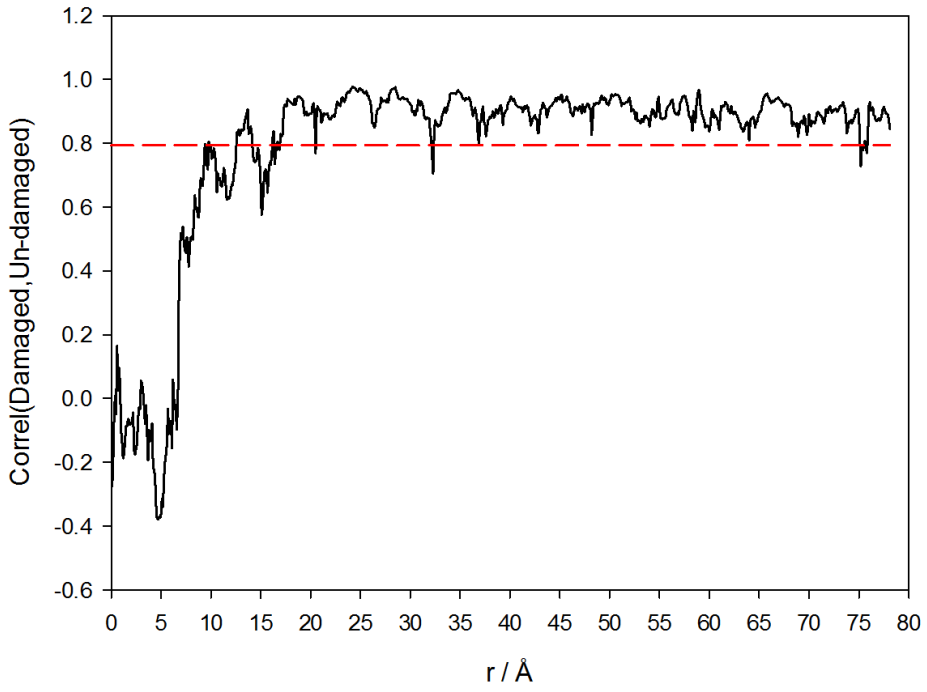

Figure 7.12: Correlation coefficient between the total RDFs for the un-damaged and damaged configurations. The red reference line represents the lower limit for the correlation coefficient in the un-damaged region.

The evolution of the damaged region as a function of time was investigated using the radius method of defect identification within DL_POLY, Figure 7.13. The configuration

reaches a maximum number of Frenkel pairs of 246544 at a time of 2.2 ps. Approximately 98 % of these are annealed after ca. 80 ps, equilibrating to ca. 4224 Frenkel pairs in the final configuration. There are clear peaks which reduce in intensity with time which correspond to pressure waves within the simulation cell.

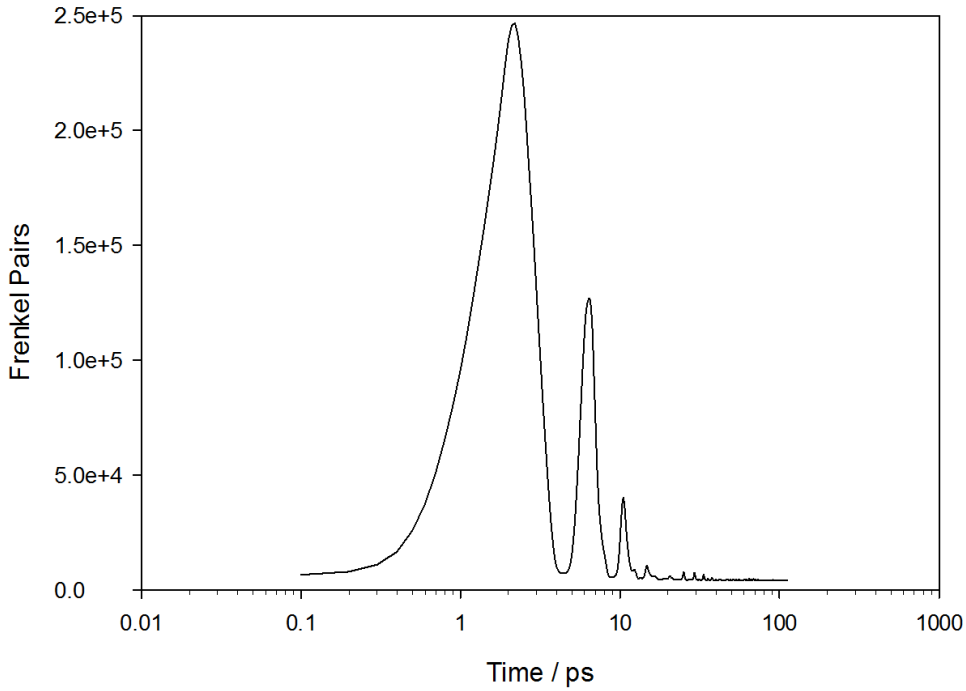

Figure 7.13: Defect evolution as a function of simulation time. Frenkel pairs were identified using the radius method

The configuration was also analysed using the Voronoi method of defect identification, Figure 7.14. The yttrium Frenkel pairs were found to be the least common defect, with 146 interstitials and vacancies identified. Similarly there were found to be 151 phosphorus Frenkel pairs, whilst the most common defects were the yttrium and phosphorus anti-site defects with 176 identified respectively. This damage profile is

similar to the high energy cascades in the (001) direction performed in chapter 6, although in this case the yttrium Frenkel pairs are slightly more common than their phosphorus counterparts.

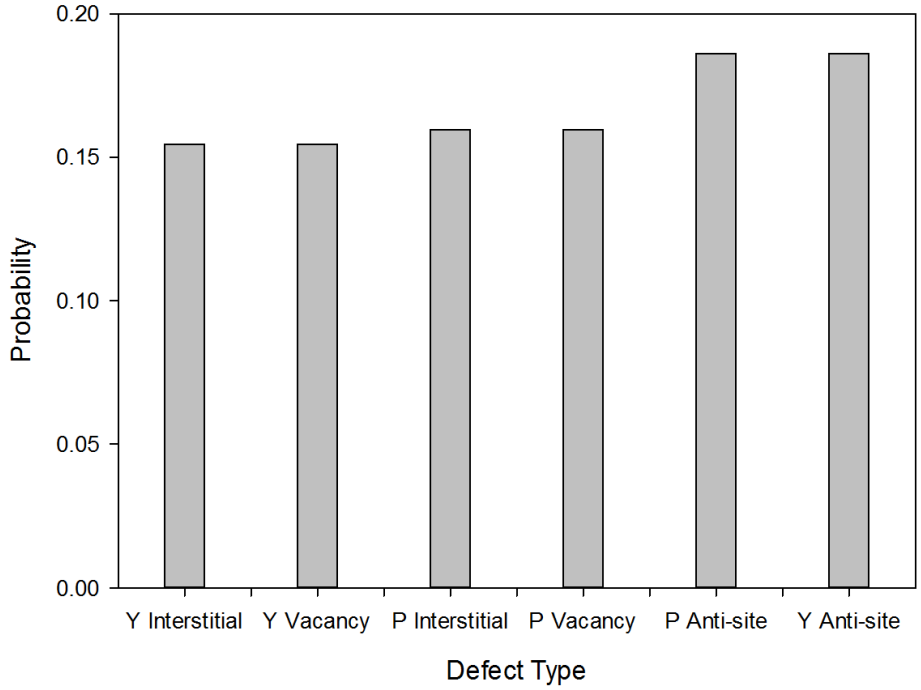

Figure 7.14: Distribution of defect types as identified by the Voronoi method

The degree of polymerisation of the phosphate tetrahedra has also been investigated with 229 polymerised chains identified in the final damaged configuration. The length of these chains ranged from seven to forty-two atoms, with the most common chains containing ten atoms. The distribution of chain lengths is illustrated in Figure 7.15. There are clear peaks in the distribution at ten, fifteen, nineteen and twenty-four atoms which indicates some over-coordination of the polymerised chains. The shortest chains contained seven atoms which indicates a chain which is net under-coordinated by two oxygen atoms.

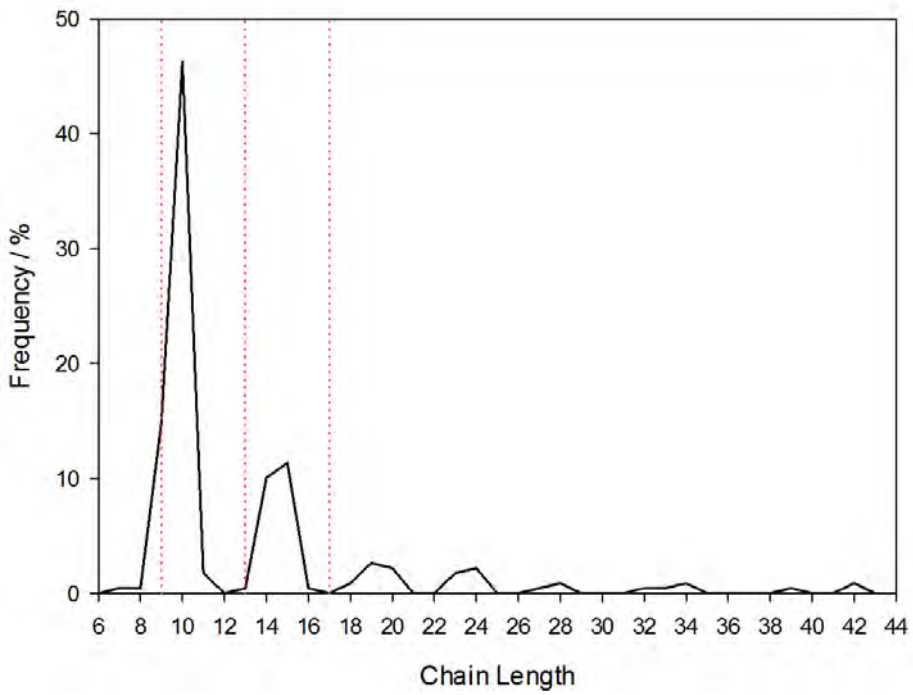

Figure 7.15: Distribution of polymerised chain lengths

The distribution of the number of phosphorus atoms in each chain is illustrated in Figure 7.16. By far the most common chains contain two phosphorus atoms, with 63.8 % of the chains meeting this criteria. The frequency with which the chains are observed drop rapidly with increasing phosphorus content with the second most frequently observed chains containing three phosphorus atoms with a frequency of 22.3 %. The longest chain contained ten phosphorus atoms. The trend line represents the inverse cubic function that was fit for the cascades in chapter 6, with parameters y_0, a, b and c of 0.22, -12.15, 124.60 and 265.90 respectively. It can be seen to describe the distribution in the fission track simulation fairly well.

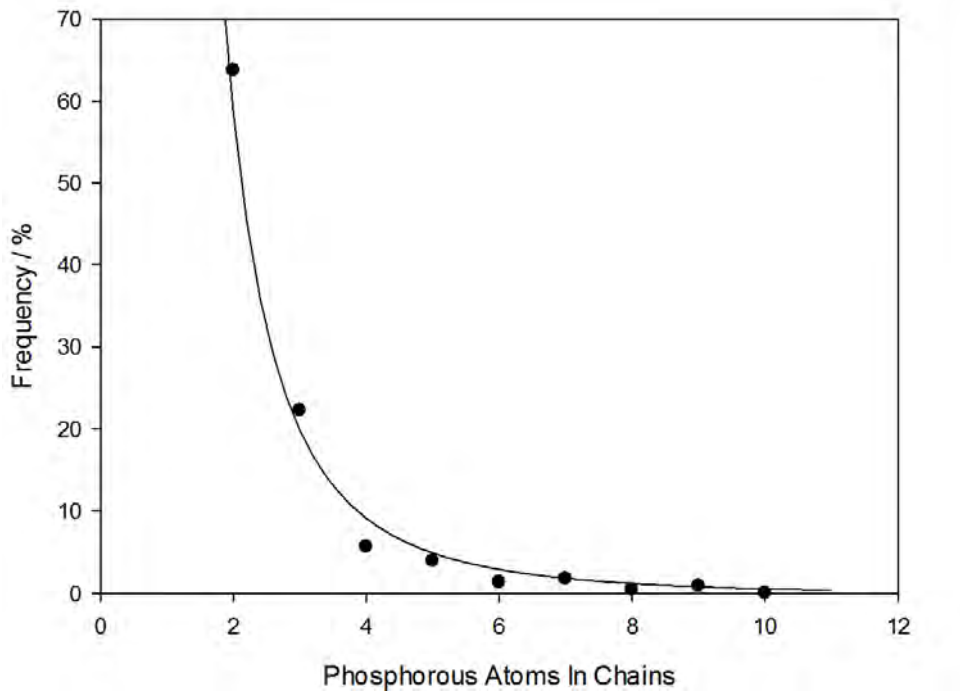

Figure 7.16: Distribution of the number of phosphorus atoms in the polymerised chains. The inverse cubic function is a guide for the eye

The P:O ratio for chains containing varying numbers of phosphorus atoms are shown in Figure 7.17. Here the trend lines are a guide for the eye, highlighting the contours for chains with net over-coordination ranging from zero to four. It is clear that there is a large amount of over-coordination of the chains in the damaged configuration. By far the most common chains contain two phosphorus atoms and are over-coordinated by one oxygen atom, forming P_2O_8 units. The ideally coordinated P_2O_7 units are the second most common chains but are far less common than the aforementioned P_2O_8 units. The chain with the highest net over-coordination contained eight phosphorus atoms and correspond to chains which are over-coordinated by six oxygen atoms. There is also evidence of some

under-coordination, with chains containing two phosphorus atoms. These chains are under-coordinated by one or two oxygen atoms, forming P_2O_6 and P_2O_5 units respectively.

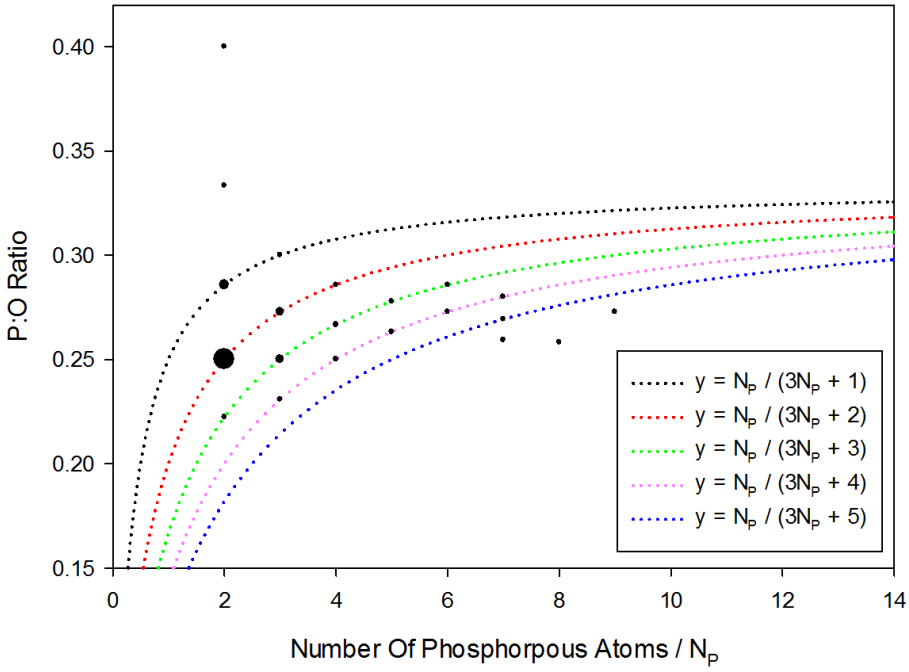

Figure 7.17: Average P:O ratio for polymerised chains containing varying numbers of phosphorus atoms. The size of the points gives an indication of the relative frequency with which the chains were observed and the black dotted reference line indicates the ideal P:O ratio for the respective number of phosphorus atoms per polymerised chain.

The net coordination of the polymerised chains are summarised in Figure 7.18. Here it can be seen that ca. 57 % of the chains are over-coordinated by one oxygen atom, whilst ca. 18 % of the chains are over-coordinated by two oxygen atoms and the ideally coordinated chains account for just 15 % of the chains observed. This highlights the propensity for the chains to be net over-coordinated. This distribution is different to that seen for the cascade simulations in chapter 6, with a much sharper peak at a net over-coordination of one.

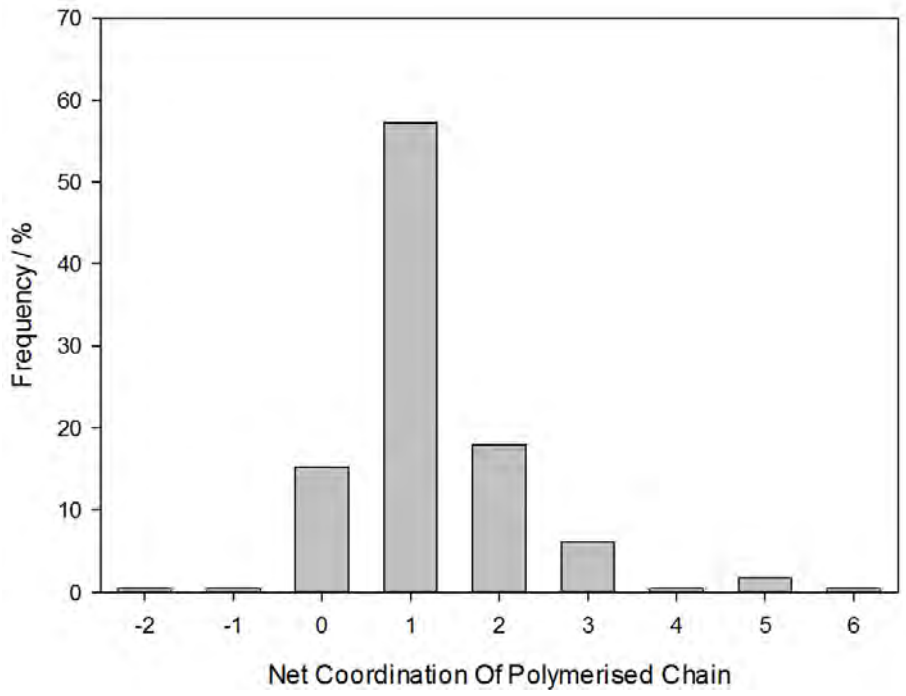

Figure 7.18: Distribution of the relative degree of coordination of the polymerised chains

The coordination number of the phosphorus atoms in the polymerised chains are summarised in Figure 7.19. Here it can be seen that the distribution is shifted towards higher coordination number compared to the cascade simulations in chapter 6. Approximately 56 % of the phosphorus atoms within the polymerised chains are five coordinate with only 43 % of the atoms in a four coordinate geometry. Phosphorus atoms with a coordination number of two, three and six were also identified, though these are much less common with frequencies of one, three and four atoms respectively.

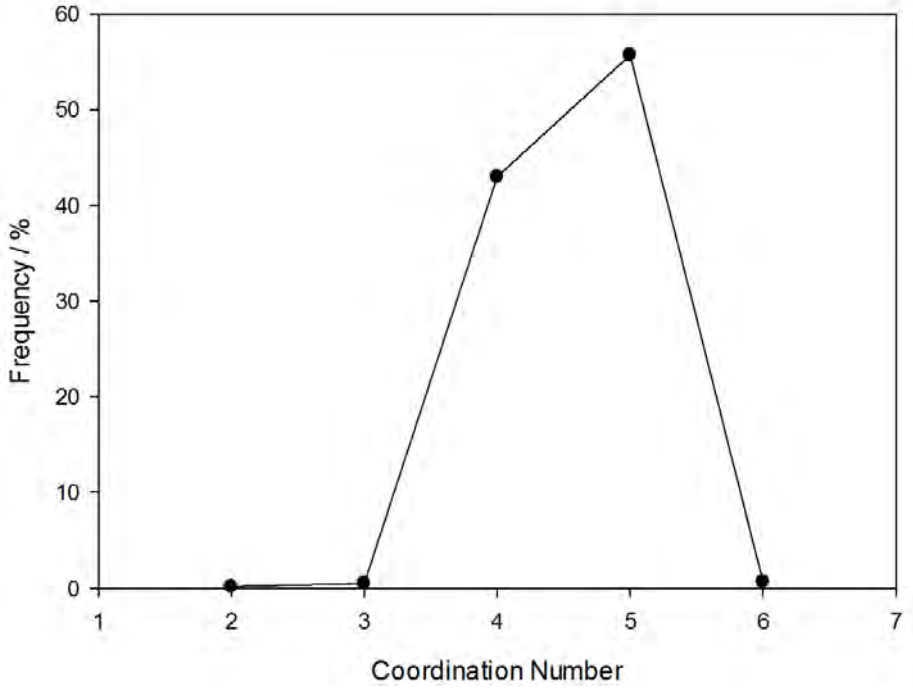

Figure 7.19: Distribution of the number of phosphorus atoms as a function of coordination number

Edge sharing polyhedra can serve to reduce the P:O ratio and help reduce the net over-coordination of chains which may contain over-coordinated cations. As such the distribution of cations which are edge sharing with neighbouring polyhedra has been analysed and summarised in Figure 7.20. Here it can be seen that the majority of atoms are corner sharing with the neighbouring polyhedra, with ca. 80 % of the phosphate polyhedra containing no edge sharing units. Only 20 % of the phosphate polyhedra contain one edge sharing unit, with only one phosphate polyhedron containing two edge sharing units. This distribution if shifted slightly compared to the cascade simulations in chapter 6, with fewer corner sharing polyhedra and more which contain one edge sharing unit.

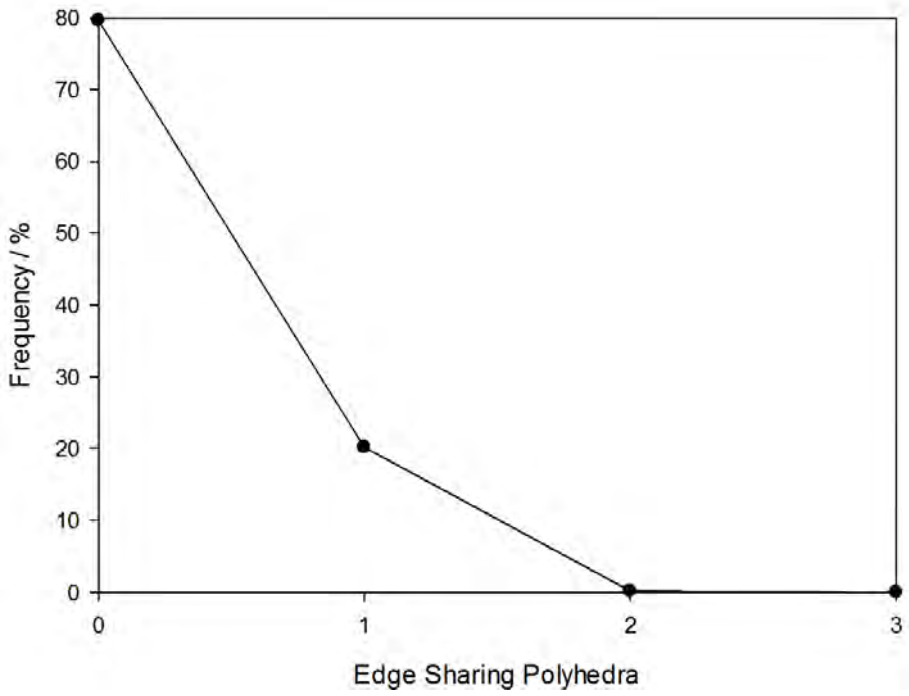

Figure 7.20: Distribution of the number and degree of edge sharing polyhedra within the polymerised chains

It is possible to describe the polymerised network in terms of how many bridging oxygen atoms are coordinated to the cations in the chains, illustrated in Figure 7.21. Here the majority of phosphorus atoms are coordinated to one bridging oxygen atom, with a frequency of ca. 64 %. The frequency reduces with increasing number of bridging oxygens in a similar trend as was observed in the cascade simulations in chapter 6.

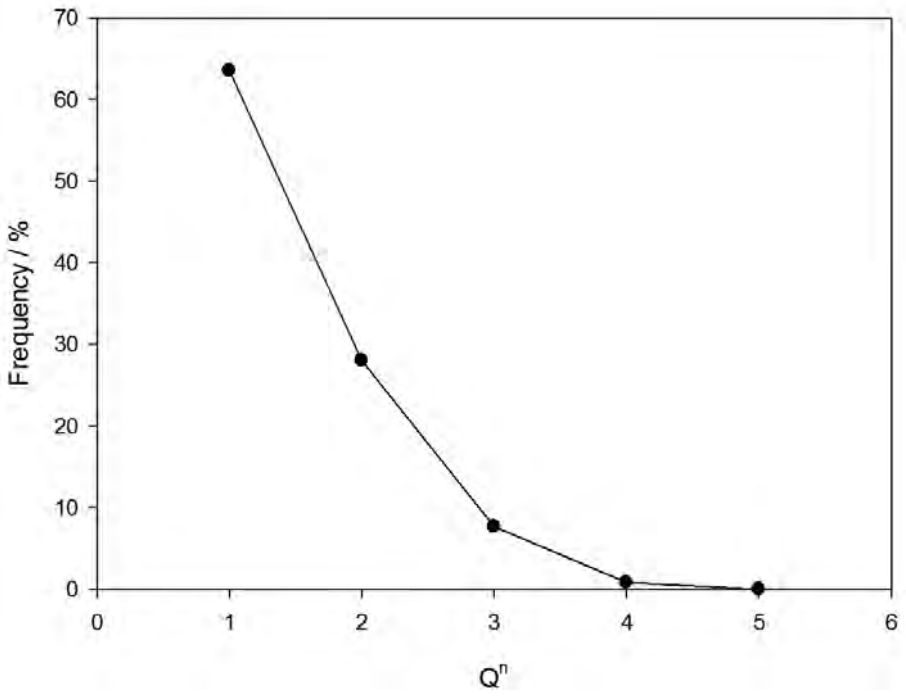

Figure 7.21: Q^n distribution for the phosphate polyhedra within the polymerised chains

The distribution of the atoms in the polymerised chains has been analysed as a function of perpendicular distance from the fission track core, illustrated in Figure 7.22. Here it can be seen that there is a fairly uniform probability of finding the polymerised chains within a radius of ca. 10 Å from the track core, which is in good agreement with the calculated radius of the amorphised core. The probability then decreases steadily over the damaged region, with no atoms which are involved in polymerised chains present at distances greater than 23.5 Å from the track core.

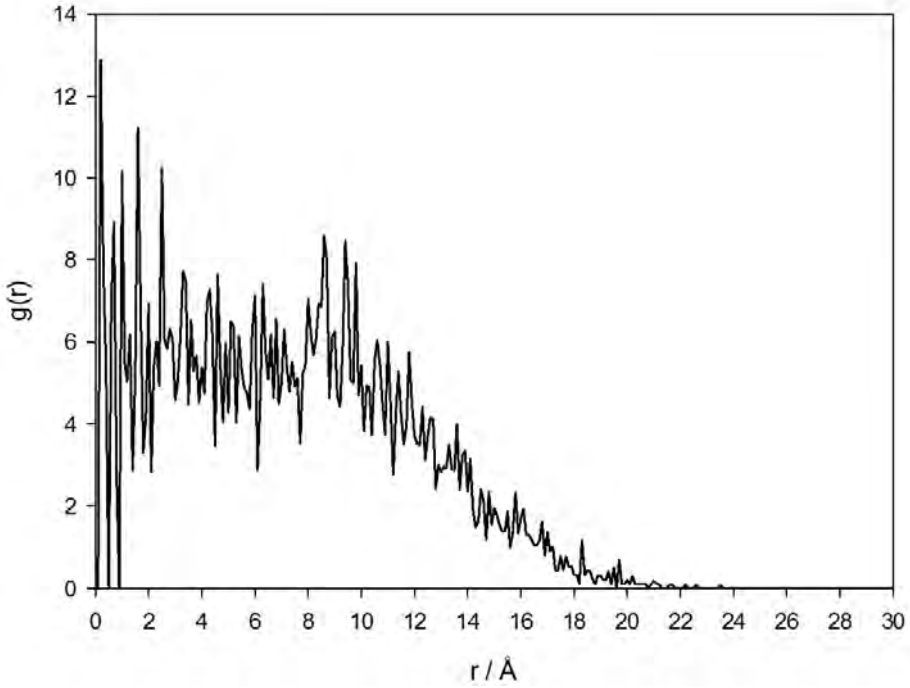

Figure 7.22: Cylindrical RDF for the P and O atoms with polymerised chains.

7.3 Site Ordering In Mixed Ca/Sr Fluorapatite

Samples of fluorapatite containing varying concentrations of strontium were synthesised using two different synthesis methods, solution and microwave synthesis (described in chapter 2). The Sr content of the samples were determined using WD-XRF and are summarised in Table 7.1. The samples were prepared for WD-XRF analysis following the procedure outlined in chapter 2.

Table 7.1: Concentration of Sr within the fluorapatite samples, determined by WD-XRF

Sample	Sr Concentration / mol %
Solution 1	4.76
Solution 2	12.06
Solution 3	20.82
Solution 4	38.16
Solution 5	70.04
Microwave 1	5.86
Microwave 2	19.84
Microwave 3	50.69
Microwave 4	74.33

X-ray diffraction data were collected using the in-house Bruker D8 diffractometer described in chapter 2, over a 2θ range from 10-90° for 3 hours. These were then analysed using GSAS to extract unit-cell volumes for data normalisation and to check for sample purity. The refinements are illustrated in appendix 2. All samples were deemed appropriate for further PDF analysis.PDF data were collected for the samples of the mixed Ca/Sr Fluorapatite in a similar way to that outlined previously in this chapter for the irradiated xenotime samples. The samples were loaded into 1 mm Kapton capillaries and positioned on the ample auto-changer at a distance of ca. 236 mm from the detector plate.

7.3.1 PDF Analysis of Solution Synthesis Samples

The PDFs for the mixed Ca/Sr Fluorapatite samples synthesised by the solution method are illustrated in Figure 7.23. Here it can be seen that the PDFs are very similar with small shifts in peak positions to increased interatomic separation with increasing strontium content. There are also changes to peak intensity.

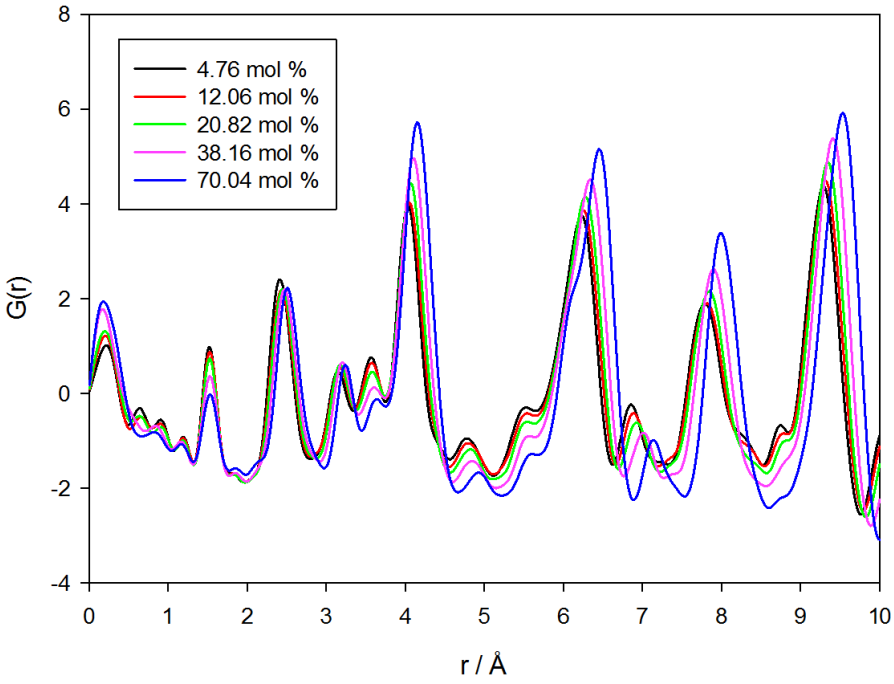

Figure 7.23: PDFs for the fluorapatite samples with increasing strontium content, synthesised using the solution method

The peaks in the PDF can be decomposed into partial PDFs which are summarised in Figure 7.24, where they have been normalised for ease of comparison. These can be used to help identify individual peaks and the interatomic separations that they represent. It can be seen that there is great deal of overlap of the partial PDFs making it difficult to isolate individual peaks of interest. The peak at ca. 1.54 Å corresponds to P-O distances whilst the peak at ca. 2.50 Å has a primary contribution from the M-O distances. The following subsequent peaks at ca. 3.20 and 3.62 Å correspond primarily to the M-M and M-P distances whilst the peak at 4.10 Å is primarily from the M-M distances.

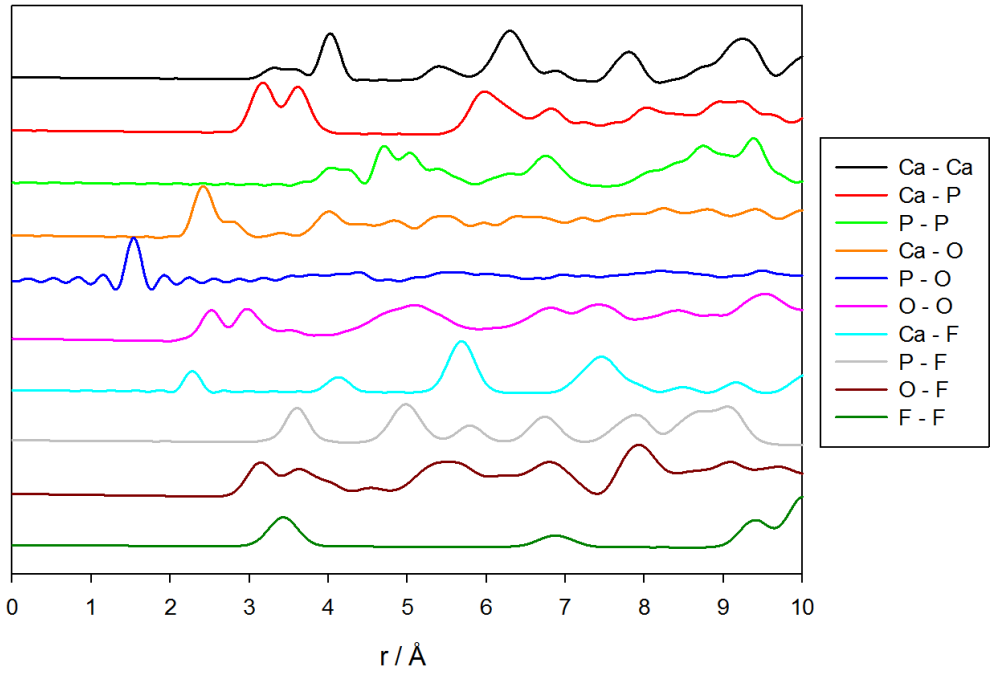

Figure 7.24: Partial PDFs between the different pairs of ions for the fluorapatite samples synthesised using the solution method, with a Sr concentration of 4.76 mol %

The experimental PDFs were converted to RDFs and are illustrated in Figure 7.25. The peaks of interest can be fit using a Gaussian function and the peak position and full width at half maximum (FWHM) can be approximated (appendix 3). The P-O peak position increases minimally, ranging from 1.52-1.54 Å with increasing strontium content, whereas the M-O peak shifts from 2.41-2.51 Å. The FWHM of the P-O and M-O peaks remain fairly constant with a ΔFWHM of 0.024 and -0.005 Å respectively. The M-M and P-P peaks at ca. 3.20 and 3.62 Å are shifted by a similar amount, with peak positions ranging from 3.15-3.24 and 3.57-3.65 Å respectively. Finally the M-M peak is shifted by ca. 0.12 Å, ranging from 4.03 to 4.15 Å.

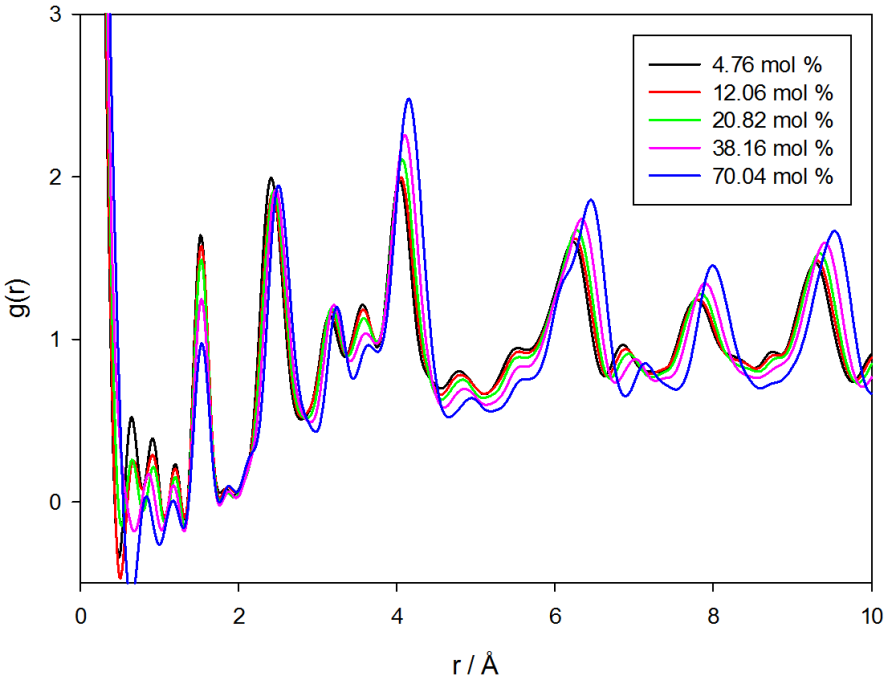

Figure 7.25: RDFs for the fluorapatite samples with increasing strontium content, synthesised using the solution method

The peaks shift in a fairly linear trend as shown in Figure 7.26. The P-O peak increases negligibly with increasing strontium content, at a rate of 0.0002 Å per mol %. The other four peaks ranging from ca. 2.50 to 4.10 Å shift at fairly similar rates of 0.0013, 0.0012, 0.0014 and 0.0017 Å per mol %. This linear shift is as would be expected for a continuous solid solution.

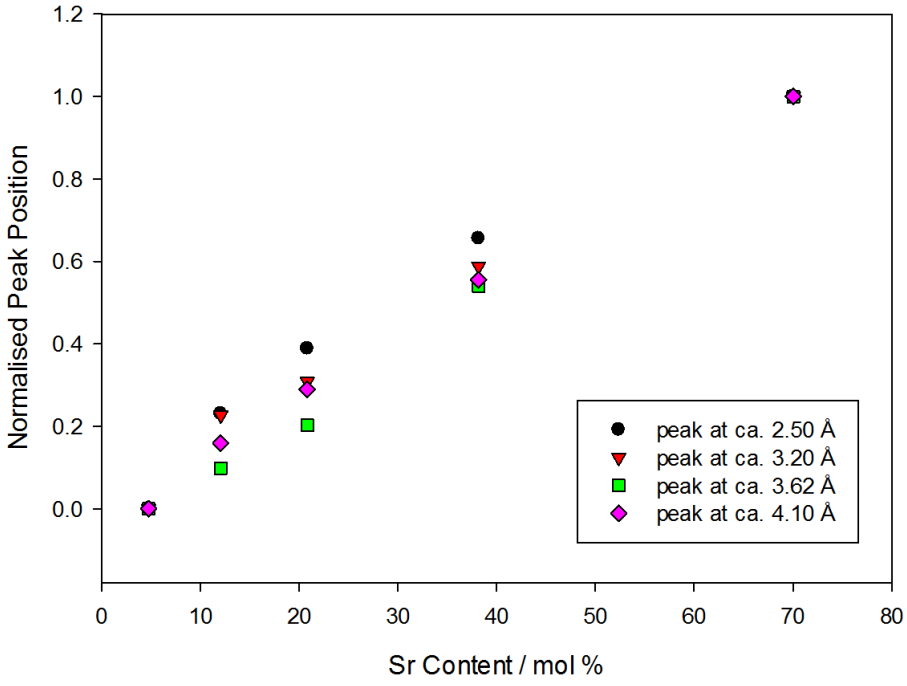

Figure 7.26: Relative position for the four peaks at distances < ca. 4.1 Å which involve the A cation as a function of Sr concentration for the samples synthesised using the solution method

Radial distribution functions were simulated for configurations with similar strontium content to the synthesised samples, illustrated in Figure 7.27. The strontium atoms were distributed over the two sites randomly within a 3 x 3 x 3 super cell for which the atomic position and cell parameters were fixed. As a result the peak positions are fixed in the simulated pattern. Similarly there are no displacements from the ideal lattice sites and so the peaks would have zero width, to compensate a broadening function was used to produce peaks with similar widths to those in the experimental data. As a result any observed differences in the simulated patters can be attributed to the strontium content and distribution. By comparing the two plots it can be seen that in general there is good agreement with the experimental data. However, the peak at ca. 3.62 Å changes intensity

more in the experimental RDFs than the simulated data would predict and therefore this peak was investigated further. The contribution to this peak from the M-M partial PDF can be decomposed further into the different contributions from the two crystallographic sites. The site 1 cations are found to be separated by a distance of ca. 3.62 Å whilst the M1-M2 and M2-M2 distances are at ca. 4.15 Å. This indicates that the peak at ca. 3.62 Å may be a useful peak for investigating cation ordering on the site 1 position, but unfortunately the peak at ca. 3.62 Å also has contributions from both the M1-P and M2-P distances, making analysis less straightforward.

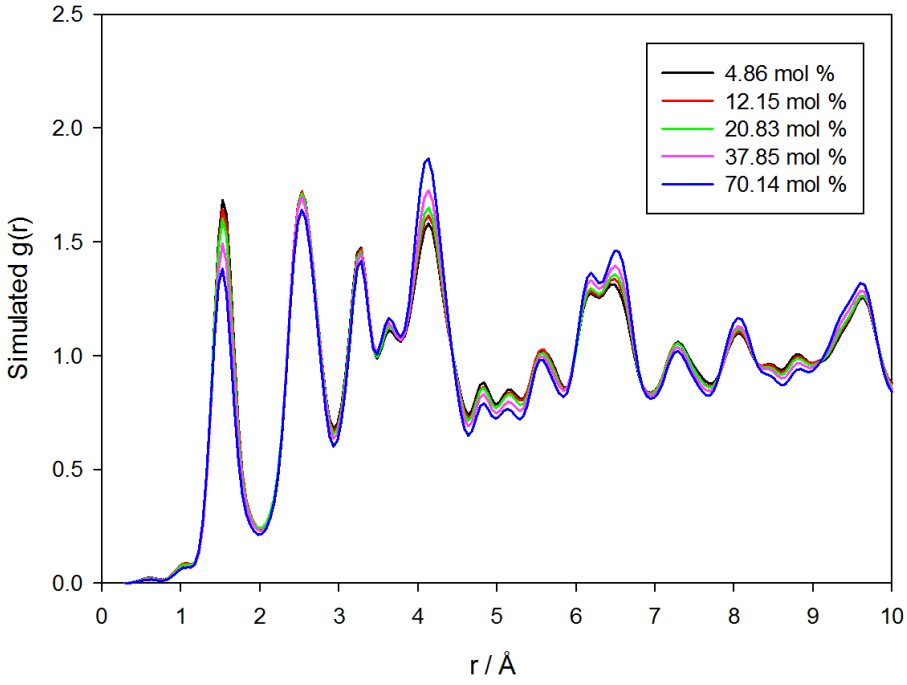

Figure 7.27: Simulated radial distribution functions for mixed Ca/Sr Fluorapatite configurations, where Sr atoms were randomly distributed over site 1 and site 2 for configurations with a Sr content ranging from 4.86 – 70.14 mol %.

As discussed previously, it has been suggested that the calcium and strontium atoms may order on the site 1 positions, alternating between the two species down the *c* axis. To see

if this could account for the discrepancy between the models and the experimental data, supercells were constructed in a similar way to earlier in the chapter with the unit cell and atomic positions held constant so as any changes in the RDFs would be as a result of the Ca/Sr distribution. The configuration with the lowest strontium content was constructed with all site 2 positions occupied by calcium atoms, whereas these sites were occupied by strontium atoms in the configuration with the highest strontium content. In both cases the site 1 positions had a 50 % Ca/Sr occupancy as described previously. This produced the two ordered configurations with strontium concentration of 21.875 and 78.125 mol % respectively. The randomly distributed configurations contained the same concentrations of strontium but these atoms were distributed over both site 1 and site 2 randomly. The RDFs are illustrated in Figure 7.28. It can be seen that the peak at ca. 3.62 Å does change in intensity more than the surrounding peaks, with the intensity of the peak for the ordered configuration at higher concentrations of strontium being reduced compared to the solid solution configuration. This difference is quite subtle and as such it may be difficult to identify this feature in the experimental samples.

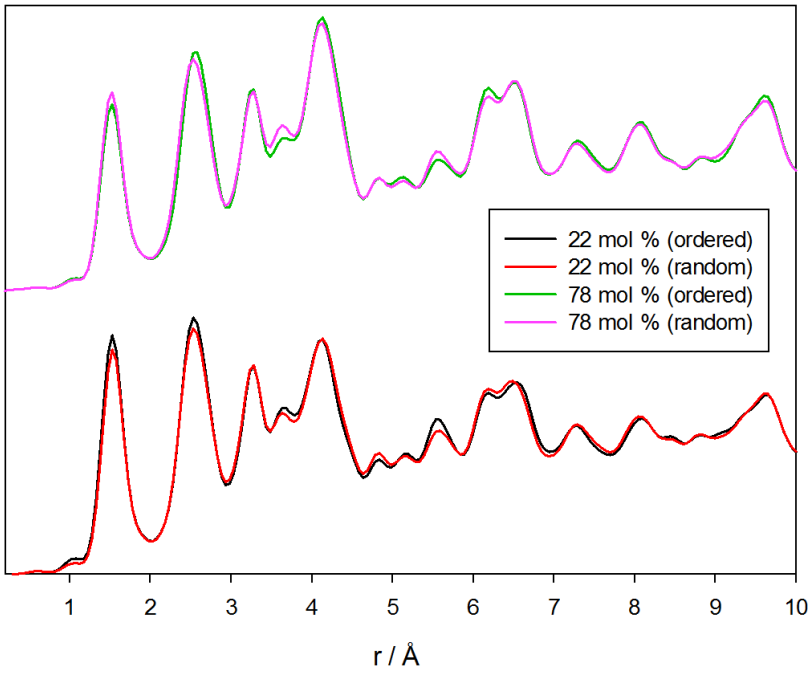

Figure 7.28: Comparison of simulated radial distribution functions for mixed Ca/Sr Fluorapatite configuration with Sr atoms occupying alternating site 1 positions, compared to a random distribution

Two models have been generated with a Sr concentration of 40 mol %. In these models the Sr atoms were randomly distributed to occupy either site 1 or site 2 positions. The simulated g(r) is illustrated in Figure 7.29. Here it can be seen that the model where 100 % of the Sr atoms are distributed onto the site 2 positions appears very similar to the simulated RDFs where the Sr atoms are randomly distributed over both sites, with the peak at ca. 3.62 Å less intense than the neighbouring peak at ca. 3.20 Å. There is a clear difference in the intensity of the peak at ca. 3.62 Å when the Sr atoms occupy the site 1 positions. Here the peak is much more intense, comparable to the peak at ca. 3.20 Å. This ratio of peak intensities bares more of a resemblance to that of the samples which contained lower concentrations of Sr. The peak intensity decreases with increasing Sr content which may

indicate a change in the way the atoms are distributed, with a preference for the site 1 positions at low doping levels which becomes less distinct with increasing Sr concentration.

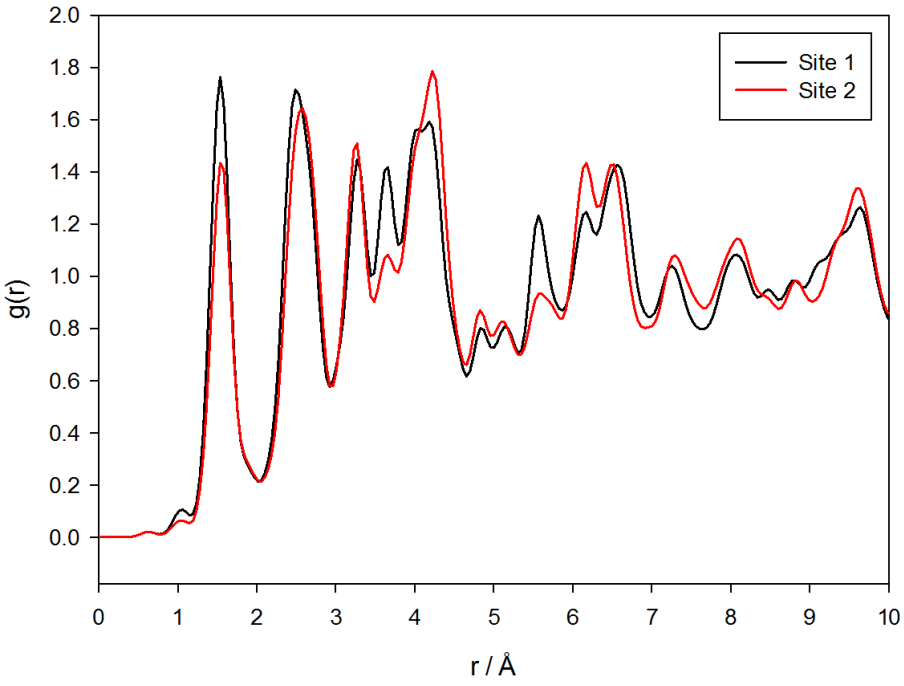

Figure 7.29: Comparison of the simulated RDFs for fluorapatite configurations containing a Sr concentration of 40 mol %. The Sr atoms were segregated between the two sites, distributed over the site 1 (black) and the site 2 (red) positions.

7.3.2 PDF Analysis of Microwave Synthesis Samples

The PDFs for the mixed Ca/Sr Fluorapatite samples produced by the microwave synthesis method are illustrated in Figure 7.30. Here it can be seen that the peak positions shift to higher values of interatomic separation with increasing strontium content, along with some intensity changes. The PDFs are almost identical to those for samples with equivalent concentrations of strontium, synthesised by the solution method. This indicates that there is no detectable difference between the samples of fluorapatite as a result of the different synthesis methods.

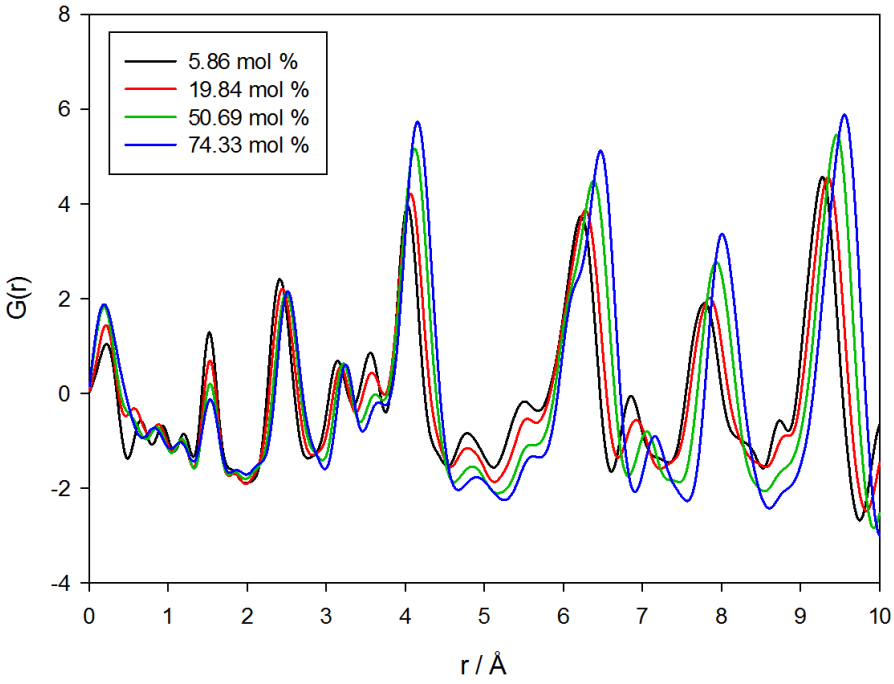

Figure 7.30: PDFs for the fluorapatite samples synthesised using the microwave method

As with the previous section, the PDFs are converted to RDFs and Gaussian functions can be fitted to the peaks to estimate the peak position and FWHM (appendix 3). The RDFs for the microwave samples are illustrated in Figure 7.31. The P-O peak position increases minimally, ranging from 1.52-1.54 Å with increasing strontium content, whereas the M-O peak shifts from 2.41-2.51 Å. The FWHM of the P-O and M-O peaks remain fairly constant with a ΔFWHM of 0.051 and 0.052 Å respectively. The M-M and P-P peaks ranged from 3.15-3.25 and 3.56-3.66 Å respectively with ΔFWHM of 0.072 and 0.177 Å respectively. Finally the M-M peak is shifted by ca. 0.12 Å, ranging from 4.03 to 4.15 Å, with a ΔFWHM of 0.072 Å.

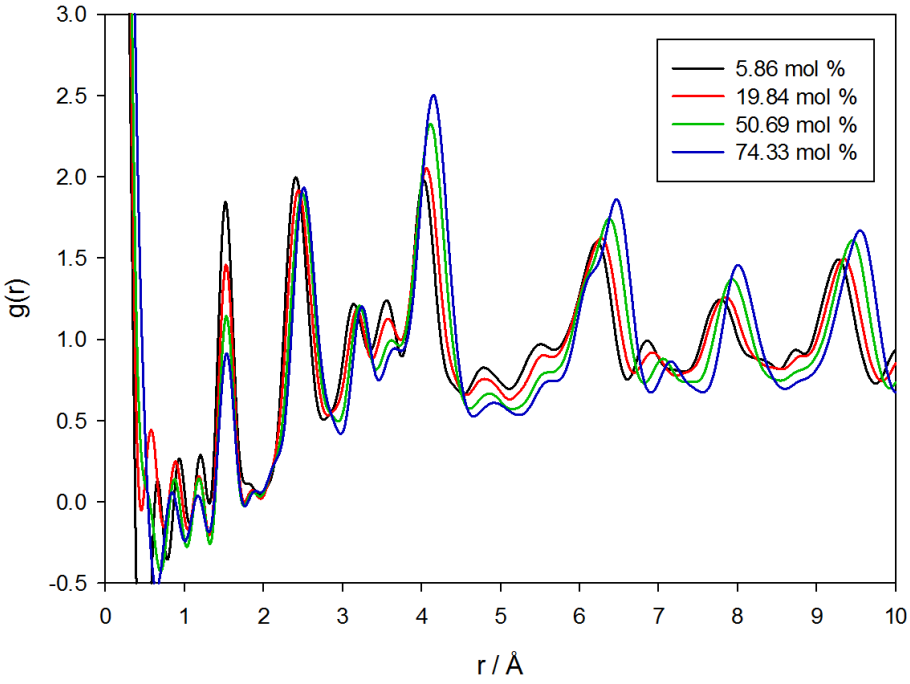

Figure 7.31: RDFs for the fluorapatite samples synthesised using the microwave method

The peaks shift in a fairly linear trend as shown in Figure 7.32. The P-O peak increases negligibly with increasing Strontium content, at a rate of 0.0002 Å per mol %. The other four peaks ranging from ca. 2.50 to 4.10 Å shift at fairly similar rates of 0.0014, 0.0013, 0.0015 and 0.0017 Å per mol %. This linear shift is as would be expected for a continuous solid solution.

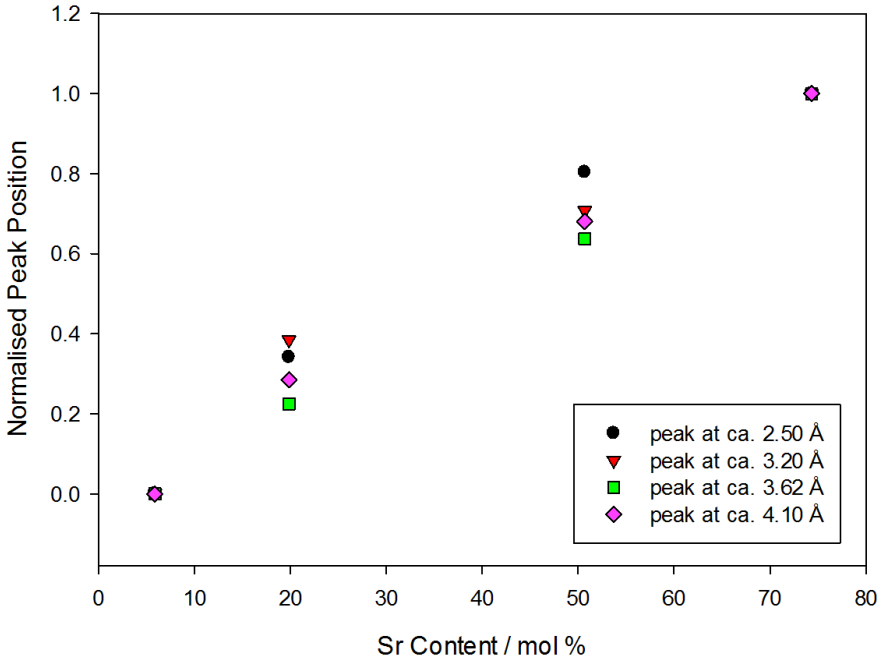

Figure 7.32: Relative position for the four peaks at distances < ca. 4.1 Å which involve the A cation as a function of Sr concentration for the samples synthesised using the microwave method

As with the solution samples, the intensity of the peak at ca. 3.62 Å decreases more than the model would suggest with increasing strontium content alone. This may be indicative of a preference for the Sr atoms to occupy the site 1 position at lower concentrations.

7.4 Conclusion

X-ray PDF analysis was carried out on samples of both irradiated and un-irradiated xenotime. The PDFs were found to be extremely similar indicating that the damage accumulated within the sample is not of a sufficiently high level to be detectable by X-ray PDF or the sample contains too much undamaged material. A fission track simulation has been used to try and predict the type of damage that would be present in samples after irradiation with swift heavy ions. The simulations showed that fission track was formed

of an amorphised core with a similar density to that of the xenotime phase, surrounded by a damaged region. The defect distribution of defects as detected by the Voronoi method share similarities with the high energy PKA cascades in chapter 6, with the anti-site defects being slightly more common than the Frenkel pairs. There was also a considerable number of polymerised phosphate chains which reside predominantly within the amorphous region. The distribution of the number of phosphorus atoms within the chains follows a similar trend to that described previously for the cascade simulations, fit to an inverse cubic function. The P_2O_8 unit was by far the most common polymerised chain identified. This gave a slightly different distribution for the net coordination of the polymerised chains than for the cascade simulations, with a much sharper peak at a net over-coordination of oxygen atom. The number of edge sharing polyhedra and the Q^n distribution were similar to that determined for the cascade simulations with a slight increase in the relative number of edge sharing units.

Samples of fluorapatite containing increasing concentrations of Sr were synthesised using solution based and microwave synthesis methods. These samples were then investigated using X-ray PDF analysis. The PDFs for comparable samples were very similar across both synthesis methods with the peaks from interatomic separations < ca. 4.1 Å which involve the A cations shifting to increased interatomic separation with increasing Sr content. These shifts follow a fairly linear trend as would be expected for a solid solution. The crude models generated in this study suggest that the X-ray PDF is not very sensitive to the ordering of the cations on the site 1 positions, however differences can be seen when considering the distribution of the cations over the two sites. The drop in intensity of this peak at ca. 3.62 Å in the experimental data has been identified as a feature of interest

which may be indicative of a preference for the Sr atoms to occupy the site 1 position at low Sr concentrations, which becomes less distinct with increasing Sr concentration. However, due to the ambiguity of the various contributions to this peak and the crude nature of the models used, it has not been possible to quantify the degree of ordering of the cations. As such alternative methods such as RMCProfile[12] may be more appropriate for analysing this data, using a combination of high quality X-ray diffraction data and the X-ray PDF data to iteratively modify the position and distribution of atoms within a large super cell to minimise the difference between the model and the experimental data.

7.5 Further Work

- Undertake radiation damage experiments on samples of xenotime and monazite, attempting to damage a larger volume of the sample so as to be detectable by X-ray PDF analysis.
- Evaluate different fission track models and apply these within the xenotime system.
- Combine the fission track models with the work presented in chapter 5 on xenotime surfaces to construct fission track simulations at surfaces or grain boundaries.
- Compare damage in the fission track core to that of a melt quench simulation to establish if the core of the fission track shares similar characteristics and therefore represents localised melting of the material.
- Collect high quality X-ray diffraction data on the mixed Ca/Sr fluorapatite samples for analysis of the cation distribution using RMCProfile.

7.6 References

1. P. Moreira, S. Guedes, C. T. Saenz and J. C. Hadler, *Radiation Measurements*, 2013, **48**, 68-72.
2. P. Moreira, R. Devanathan and W. J. Weber, *Journal of Physics-Condensed Matter*, 2010, **22**, 9.
3. J. Rabone, A. Carter, A. Hurford and N. H. de Leeuw, *Physics and Chemistry of Minerals*, 2008, **35**, 583-596.
4. R. F. Klevtsova, *Journal of Structural Chemistry*, 1965, **5**, 292-294.
5. Khudoloz.Vo, V. S. Urusov and K. I. Tobelko, *Geokhimiya*, 1972, 1236.
6. A. Bigi, G. Falini, M. Gazzano, N. Roveri and E. Tedesco, *Epdic 5, Pts 1 and 2*, 1998, **278-2**, 814-819.
7. H. J. M. Heijligers, R. M. H. Verbeeck and F. C. M. Driessens, *Journal of Inorganic & Nuclear Chemistry*, 1979, **41**, 763-764.
8. M. Andresverges, F. J. Higes and P. F. Gonzalezdiaz, *Journal of Solid State Chemistry*, 1980, **33**, 125-126.
9. M. Kikuchi, A. Yamazaki, R. Otsuka, M. Akao and H. Aoki, *Journal of Solid State Chemistry*, 1994, **113**, 373-378.
10. G. H. Vineyard, *Radiation Effects and Defects in Solids*, 1976, **29**, 245-248.
11. L. T. Chadderton, *Nuclear Tracks and Radiation Measurements*, 1988, **15**, 11-29.
12. M. G. Tucker, D. A. Keen, M. T. Dove, A. L. Goodwin and Q. Hui, *Journal of Physics-Condensed Matter*, 2007, **19**, 16.

Appendices

Table of Contents

1 Appendix 1

1.1 Potential Fitting Lutetium

Lu_2O_3 (cubic)	Experiment	Δ%
Lattice Parameters (Å)		
a	10.391	-0.99
Interatomic Separation (Å)		
Lu-O	2.25	-1.37
Lu-O	2.18	1.07
Lu-O	2.24	-0.83
Lu-O	2.28	-1.95
Bulk Modulus (Gpa)		
Voigt	158	-4.34

$LuPO_4$ (tetragonal)	Experiment	Δ%
Lattice Parameters (Å)		
a	6.7827	0.69
c	5.9467	-0.87
Interatomic Separation (Å)		
Lu-O	2.26	0.53
Lu-O	2.34	1.30
P-O	1.53	-0.94
Bulk Modulus (Gpa)		
Reuss	175	1.18
Voigt		1.30
Hill		1.24

1.2 Potential Fitting Erbium

Er_2O_3 (cubic)	Experiment	Δ%
Lattice Parameters (Å)		
a	10.536	-0.71
Interatomic Separation (Å)		
Er-O	2.27	-0.76
Er-O	2.24	0.05
Er-O	2.24	0.58
Er-O	2.31	-1.46
Bulk Modulus (Gpa)		
Voigt	136	-0.33

$ErPO_4$ (tetragonal)	Experiment	Δ%
Lattice Parameters (Å)		
a	6.783	0.69
c	5.9467	-0.87
Interatomic Separation (Å)		
Er-O	2.26	0.53
Er-O	2.34	1.30
P-O	1.53	-0.94
Bulk Modulus (Gpa)		
Reuss	175	1.18
Voigt		1.30
Hill		1.24

1.3 Potential Fitting Gadolinium

Gd_2O_3 (cubic)	Experiment	Δ%
Lattice Parameters (Å)		
a	10.536	-0.71
Interatomic Separation (Å)		
Gd-O	2.27	-0.76
Gd-O	2.24	0.05
Gd-O	2.24	0.58
Gd-O	2.31	-1.46
Bulk Modulus (Gpa)		
Voigt	136	-0.33

$GdPO_4$ (monoclinic)	Experiment	Δ%
Lattice Parameters		
a / Å	6.644	-2.83
***b* / Å**	6.841	-1.05
c / Å	6.328	-1.24
β / °	103.98	-0.98
Interatomic Separation (Å)		
Gd-O	2.47	-3.80
Gd-O	2.57	-4.88
Gd-O	2.78	1.62
Gd-O	2.38	-0.11
Gd-O	2.45	-1.87
Gd-O	2.36	-0.36
Gd-O	2.44	-1.03
Gd-O	2.37	1.39
Gd-O	2.47	2.84
P-O	1.54	-1.57
P-O	1.53	-0.99
P-O	1.55	-2.35
P-O	1.53	-1.04
Bulk Modulus (Gpa)		
Reuss	137	2.22
Voigt		3.52
Hill		2.87

1.4 Potential Fitting Samarium

Sm_2O_3 (cubic)	Experiment	Δ%
Lattice Parameters (Å)		
a	10.920	0.22
Interatomic Separation (Å)		
Sm-O	2.31	1.79
Sm-O	2.29	-0.27
Sm-O	2.36	-0.63
Sm-O	2.45	0.00
Bulk Modulus (Gpa)		
Voigt	121	-1.71

Sm_2O_3 (monoclinic)	Experiment	Δ%
Lattice Parameters		
a / Å	14.177	-1.30
b/ Å	3.633	1.05
c/ Å	8.847	1.37
β / °	99.96	-0.06
Interatomic Separation (Å)		
Sm-O	2.55	1.34
Sm-O	2.25	3.32
Sm-O	2.48	-2.90
Sm-O	2.29	0.91
Sm-O	2.70	0.65
Sm-O	2.29	1.53
Sm-O	2.32	1.42
Sm-O	2.49	0.81
Sm-O	2.38	-1.91
Sm-O	2.75	-0.78
Sm-O	2.26	-1.17
Sm-O	2.31	2.14
Sm-O	2.28	0.50
Sm-O	2.56	0.56

$SmPO_4$ (monoclinic)	Experiment	Δ%
Lattice Parameters		
a / Å	6.682	-2.05
***b* / Å**	6.888	-0.42
c / Å	6.365	-0.56
β / °	103.86	-0.97
Interatomic Separation (Å)		
Sm-O	2.49	-2.78
Sm-O	2.59	-4.10
Sm-O	2.77	2.75
Sm-O	2.40	1.03
Sm-O	2.48	-1.29
Sm-O	2.39	0.13
Sm-O	2.47	-0.44
Sm-O	2.39	2.27
Sm-O	2.51	2.52
P-O	1.54	-1.67
P-O	1.54	-1.09
P-O	1.53	-1.14
P-O	1.54	-1.41
Bulk Modulus (Gpa)		
Reuss	127	-0.30
Voigt		1.09
Hill		0.40

1.5 Potential Fitting Neodymium

Nd_2O_3 (hexagonal)	Experiment	Δ%
Lattice Parameters (Å)		
a	3.831	0.49
c	5.999	-0.90
Interatomic Separation (Å)		
Nd-O	2.66	-0.27
Nd-O	2.30	-0.20
Nd-O	2.40	2.56
Nd-O	3.60	-3.28
Bulk Modulus (Gpa)		
Reuss	136	-2.82
Voigt		-1.51
Hill		-2.16

$NdPO_4$ (monoclinic)	Experiment	Δ%
Lattice Parameters		
a / Å	6.554	-2.73
***b* / Å**	6.875	-1.09
c / Å	6.332	-1.15
β / °	102.71	-0.94
Interatomic Separation (Å)		
Nd-O	2.53	-3.90
Nd-O	2.62	-4.86
Nd-O	2.77	2.83
Nd-O	2.43	-0.08
Nd-O	2.50	-1.88
Nd-O	2.42	-0.88
Nd-O	2.48	-0.97
Nd-O	2.43	1.23
Nd-O	2.55	1.29
P-O	1.55	-2.02
P-O	1.53	-0.56
P-O	1.54	-1.32
P-O	1.54	-1.44
Bulk Modulus (Gpa)		
Reuss	127	0.02
Voigt		1.52
Hill		0.77

1.6 Potential Fitting Lanthanum

La_2O_3 (hexagonal)	Experiment	Δ%
Lattice Parameters (Å)		
a	3.934	1.06
c	6.136	-1.32
Interatomic Separation (Å)		
La-O	2.73	-0.14
La-O	2.37	0.26
La-O	2.46	2.91
La-O	3.68	-4.25
Bulk Modulus (Gpa)		
Reuss	113	-8.73
Voigt		-7.28
Hill		-8.00

$LaPO_4$ (monoclinic)	Experiment	Δ%
Lattice Parameters		
a / Å	6.8313	-1.92
***b* / Å**	7.0705	-0.60
c / Å	6.5034	-0.16
β / °	103.27	-0.91
Interatomic Separation (Å)		
La-O	2.61	-4.03
La-O	2.67	-3.59
La-O	2.77	4.56
La-O	2.45	1.84
La-O	2.57	-1.40
La-O	2.46	0.70
La-O	2.54	0.24
La-O	2.52	0.80
La-O	2.62	1.58
P-O	1.55	-2.27
P-O	1.52	-0.21
P-O	1.54	-1.28
P-O	1.54	-1.50
Bulk Modulus (Gpa)		
Reuss	99	2.10
Voigt		3.85
Hill		2.98

2 Appendix 2

2.7 Mixed Ca/Sr Fluorapatite Samples

2.7.1 Solution Method Samples (GSAS)

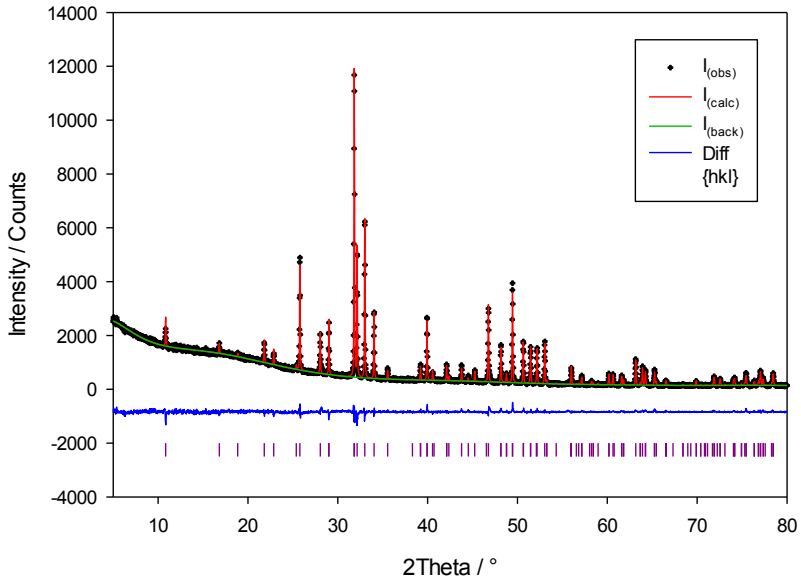

(a)

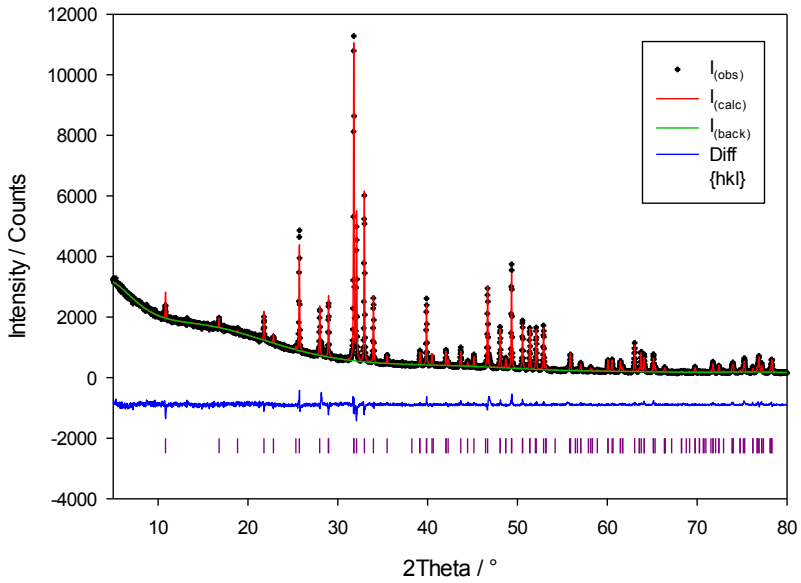

(b)

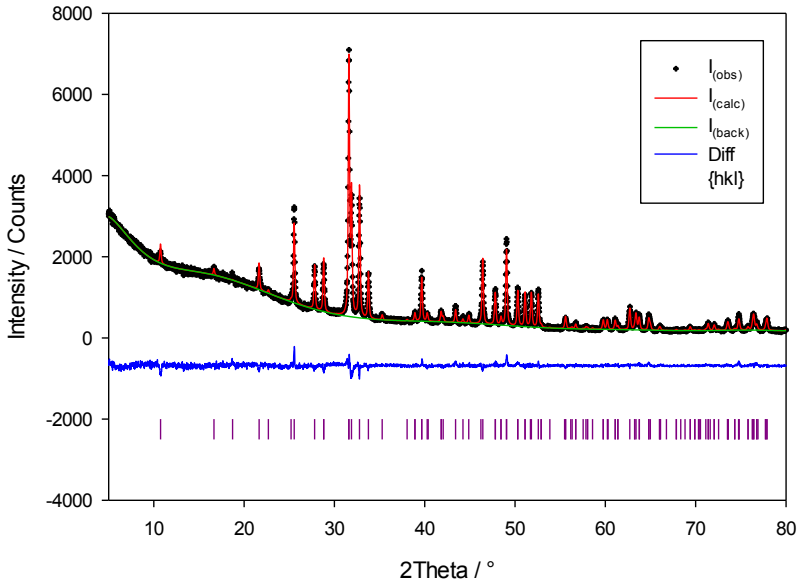
8000
6000
4000
2000
0
-2000
-4000
Intensity / Counts
10
20
30
40
50
60
70
80
2Theta / °
I(obs)
I(calc)
I(back)
Diff
{hkl}

(c)

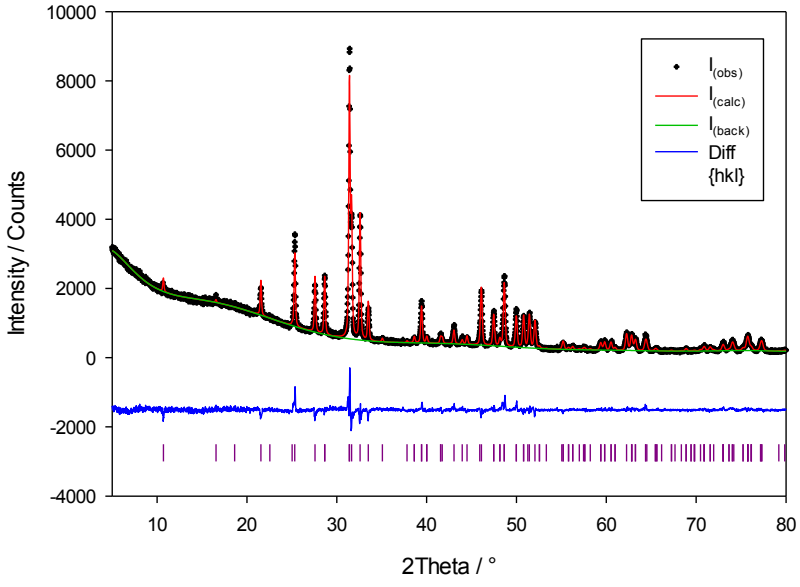
10000
8000
6000
4000
2000
0
-2000
-4000
Intensity / Counts
10
20
30
40
50
60
70
80
2Theta / °
I(obs)
I(calc)
I(back)
Diff
{hkl}

(d)

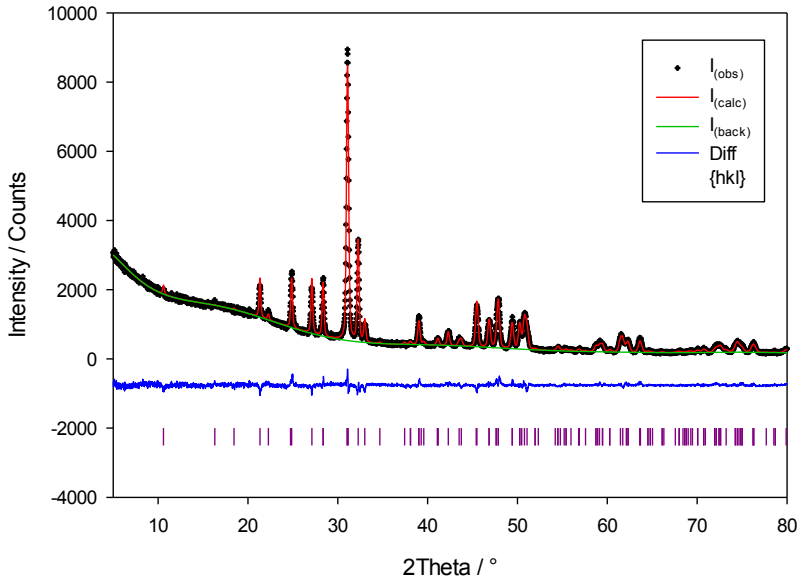

(e)

Figure 2.1: GSAS refinements for the samples synthesised using the solution method with strontium concentrations of (a) 4.76, (b) 12.06, (c) 20.82, (d) 38.16 and (e) 70.04 mol %

2.7.2 Microwave Method Samples (GSAS)

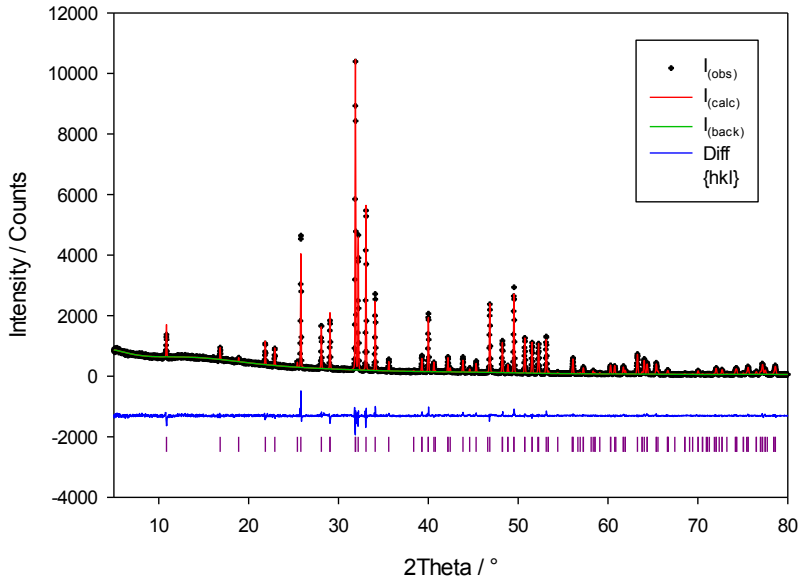

(a)

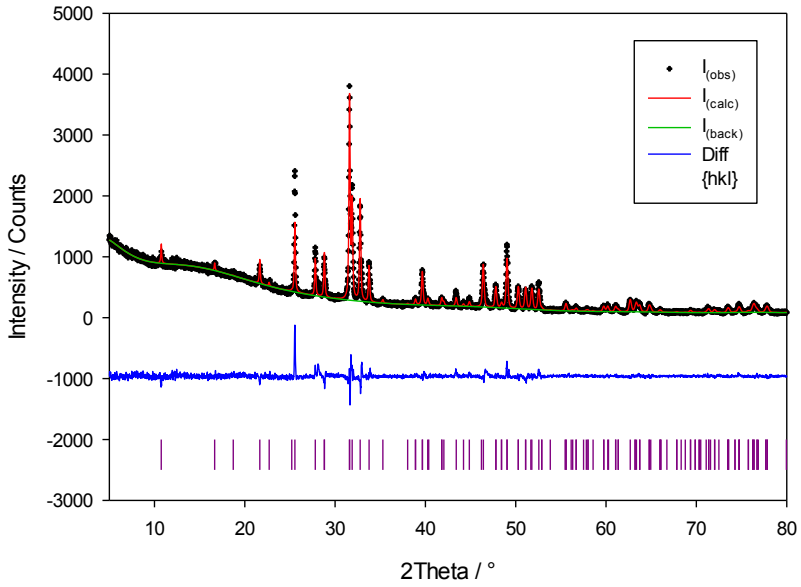
5000
4000
3000
2000
1000
0
-1000
-2000
-3000
Intensity / Counts
10
20
30
40
50
60
70
80
2Theta / °
I(obs)
I(calc)
I(back)
Diff
{hkl}

(b)

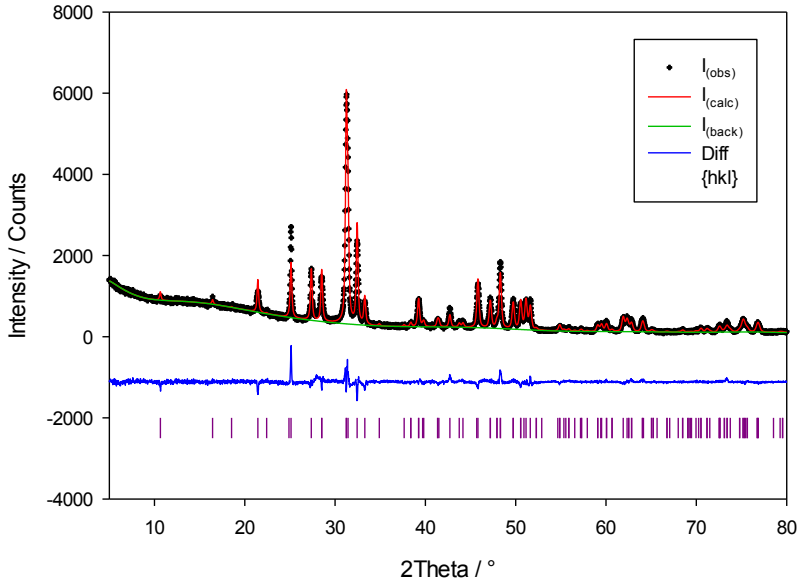
8000
6000
4000
2000
0
-2000
-4000
Intensity / Counts
10
20
30
40
50
60
70
80
2Theta / °
I(obs)
I(calc)
I(back)
Diff
{hkl}

(c)

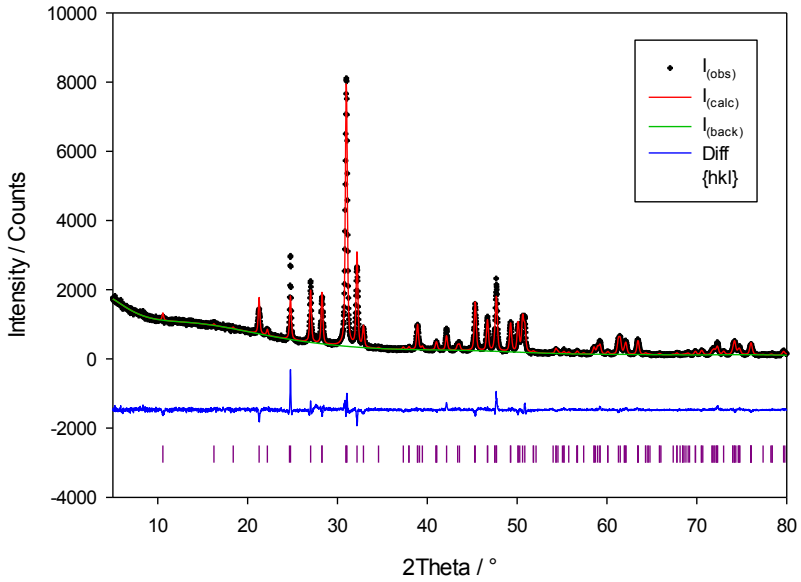

(d)

Figure 2.2: GSAS refinements for the samples synthesised using the microwave method with strontium concentrations of (a) 5.86, (b) 19.84, (c) 50.69 and (d) 74.33 mol %

3 Appendix 3

3.1 Peak Fitting Xenotime

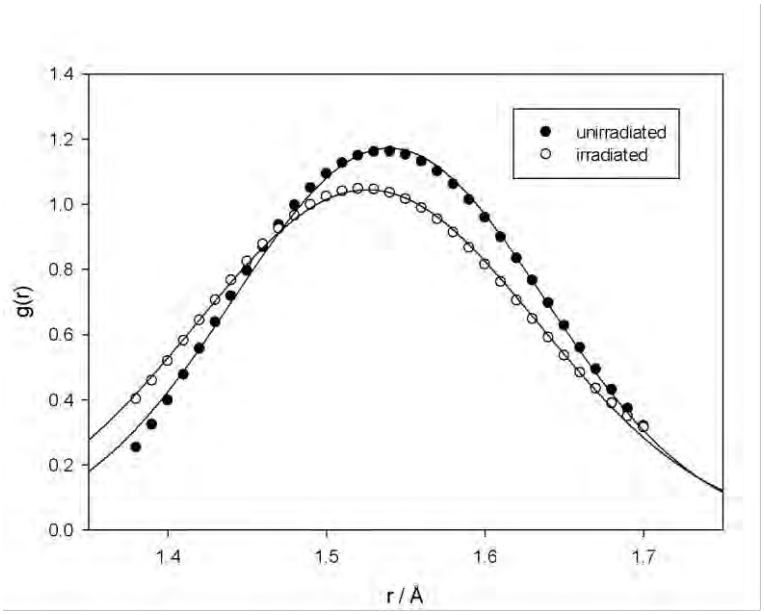

Figure 3.1: Least-squares fit of a Gaussian function to the peak in the RDF at ca. 1.54 Å

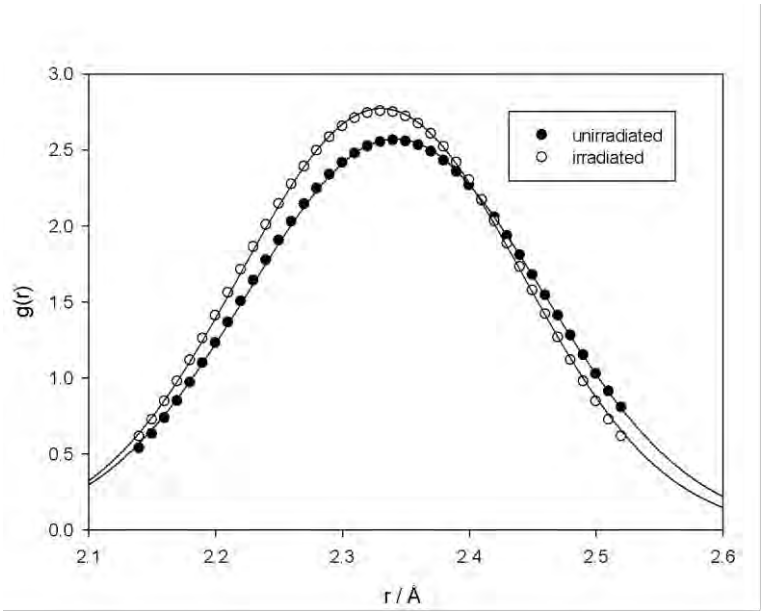

Figure 3.2: Least-squares fit of a Gaussian function to the peak in the RDF at ca. 2.33 Å

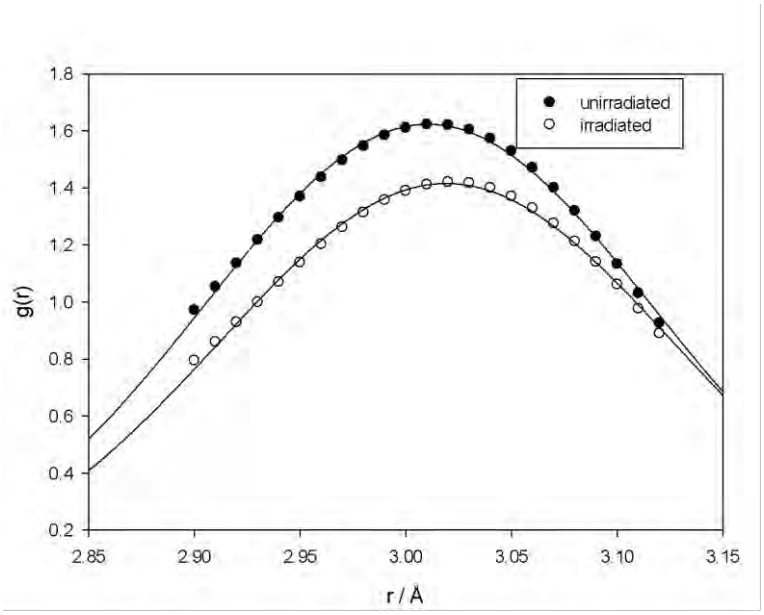

Figure 3.3: Least-squares fit of a Gaussian function to the peak in the RDF at ca. 3.01 Å

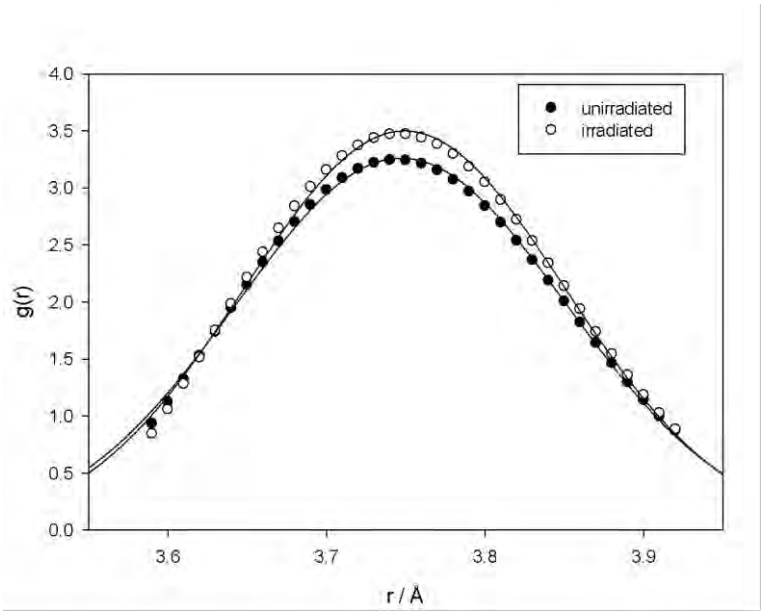

Figure 3.4: Least-squares fit of a Gaussian function to the peak in the RDF at ca. 3.75 Å

3.2 Peak Fitting Ca/Sr Fluorapatite (Solution)

3.2.1 4.76 mol % Sr

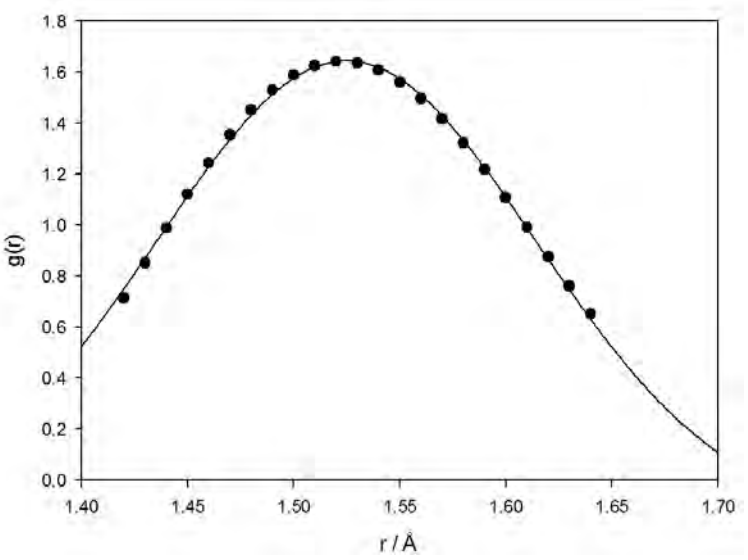

Figure 3.5: : Least-squares fit of a Gaussian function to the peak in the RDF at ca. 1.54 Å

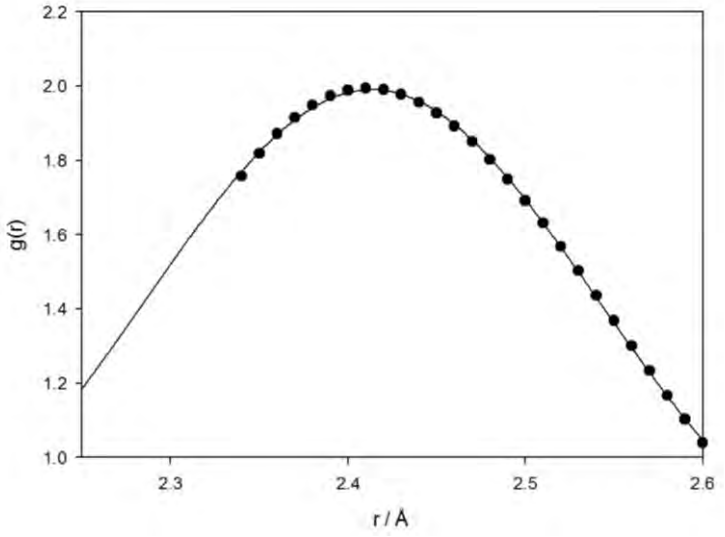

Figure 3.6: Least-squares fit of a Gaussian function to the peak in the RDF at ca. 2.50 Å

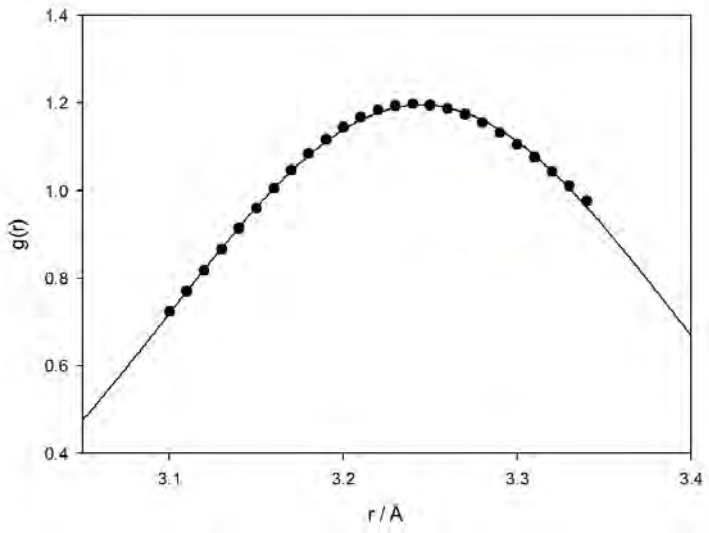

Figure 3.7: Least-squares fit of a Gaussian function to the peak in the RDF at ca. 3.20 Å

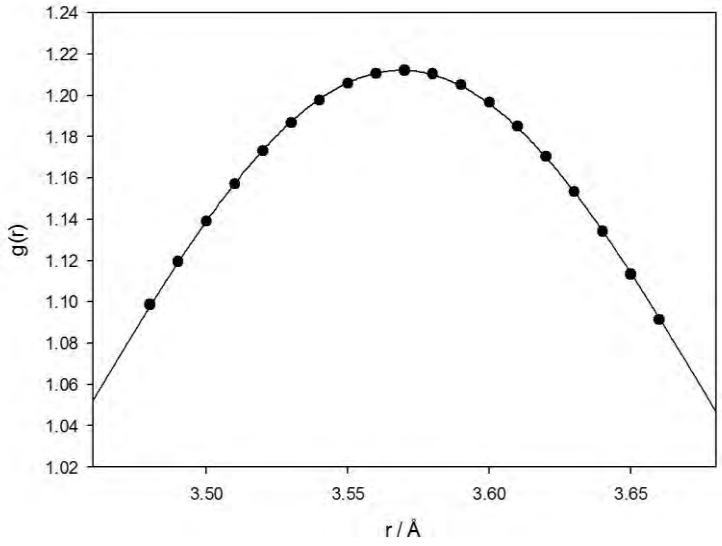

Figure 3.8: Least-squares fit of a Gaussian function to the peak in the RDF at ca. 3.62 Å

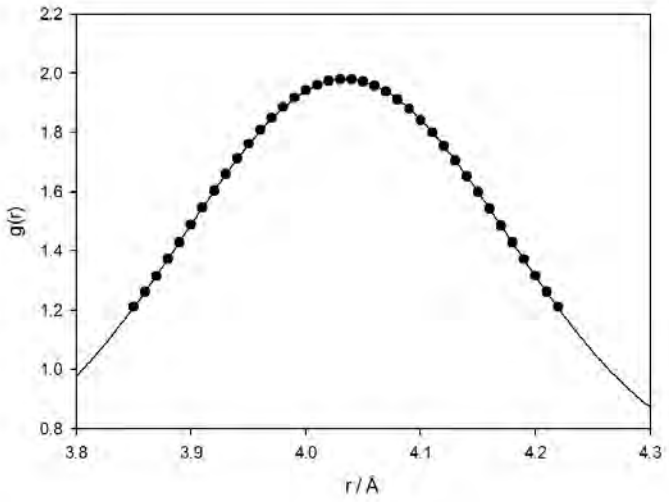

Figure 3.9: Least-squares fit of a Gaussian function to the peak in the RDF at ca. 4.10 Å

3.2.2 12.06 mol % Sr

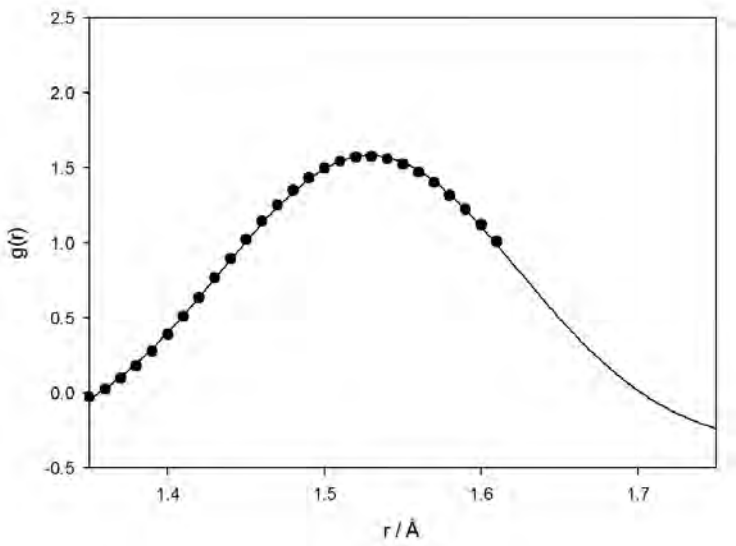

Figure 3.10: Least-squares fit of a Gaussian function to the peak in the RDF at ca. 1.54 Å

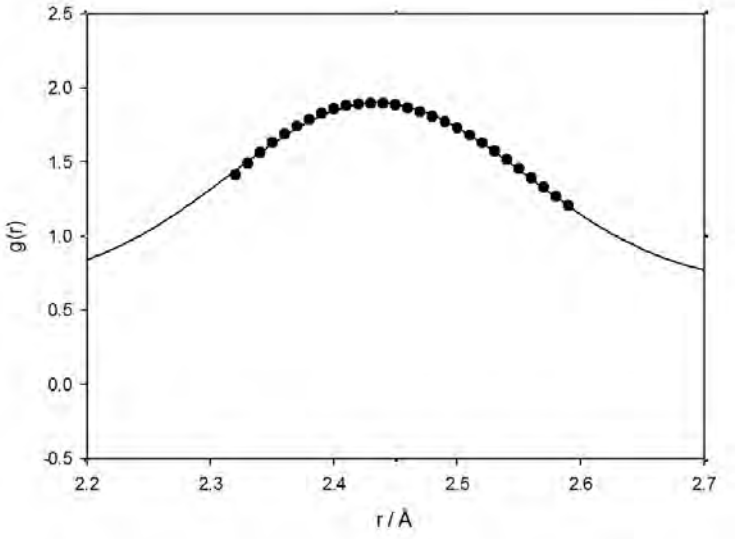

Figure 3.11: Least-squares fit of a Gaussian function to the peak in the RDF at ca. 2.50 Å

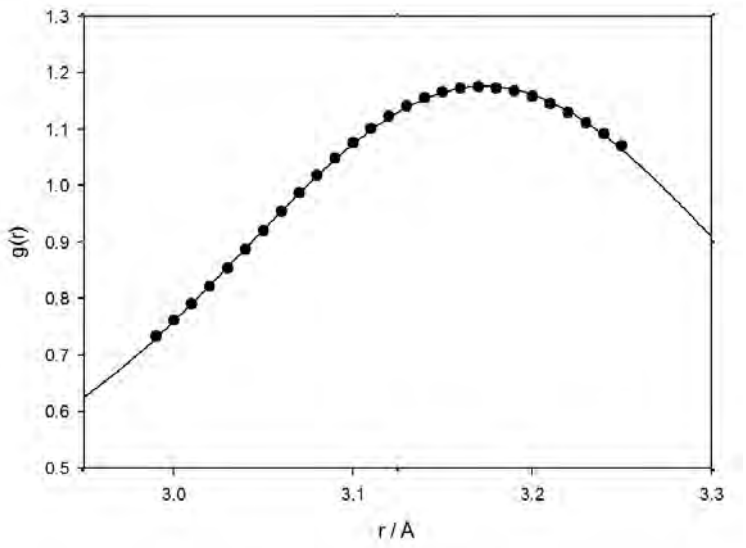

Figure 3.12: Least-squares fit of a Gaussian function to the peak in the RDF at ca. 3.20 Å

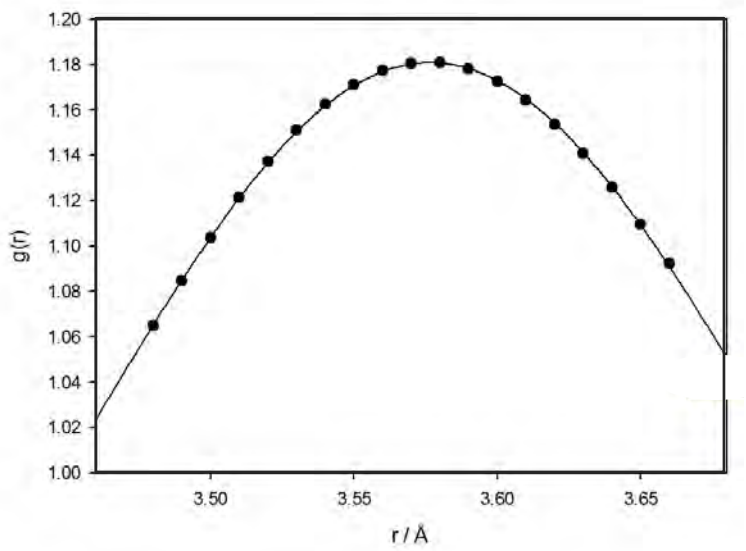

Figure 3.13: Least-squares fit of a Gaussian function to the peak in the RDF at ca. 3.62 Å

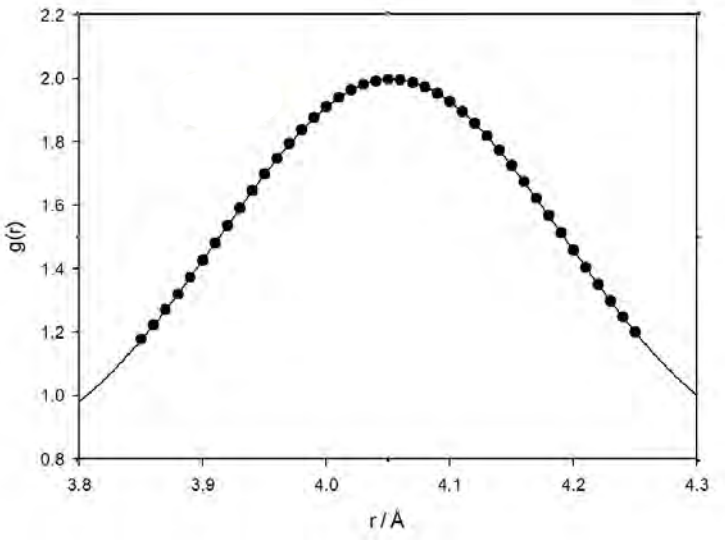

Figure 3.14: Least-squares fit of a Gaussian function to the peak in the RDF at ca. 4.10 Å

3.2.3 20.82 mol % Sr

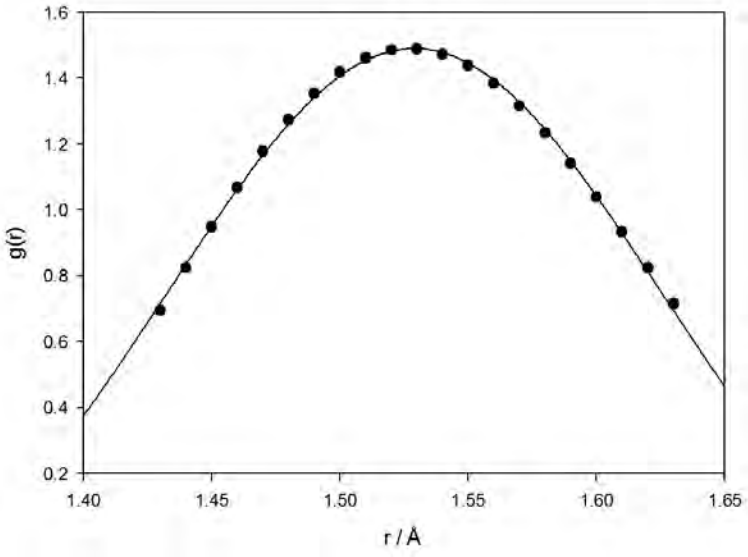

Figure 3.15: Least-squares fit of a Gaussian function to the peak in the RDF at ca. 1.54 Å

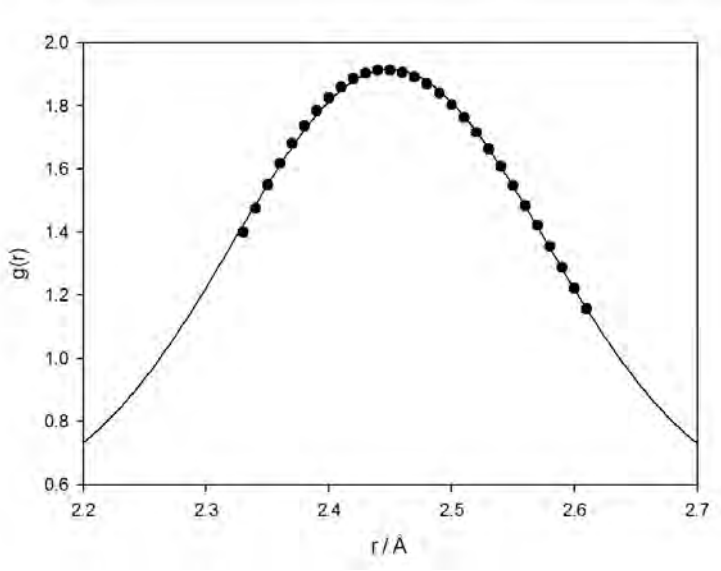

Figure 3.16: Least-squares fit of a Gaussian function to the peak in the RDF at ca. 2.50 Å

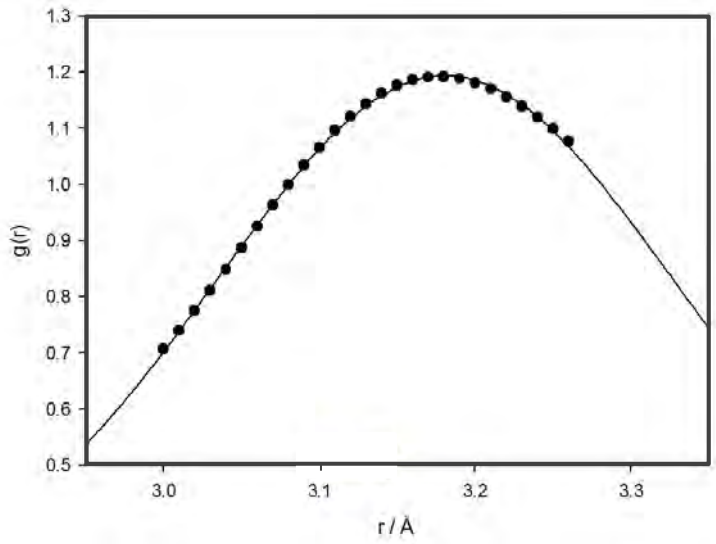

Figure 3.17: Least-squares fit of a Gaussian function to the peak in the RDF at ca. 3.20 Å

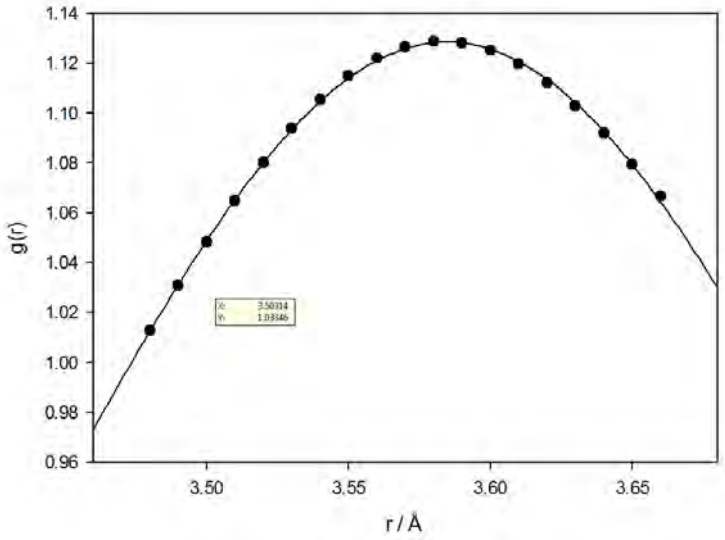

Figure 3.18: Least-squares fit of a Gaussian function to the peak in the RDF at ca. 3.62 Å

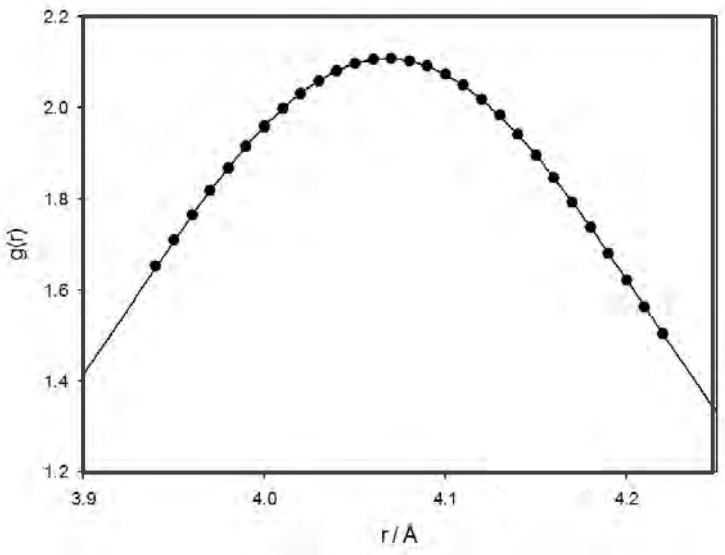

Figure 3.19: Least-squares fit of a Gaussian function to the peak in the RDF at ca. 4.10 Å

3.2.4 38.16 mol % Sr

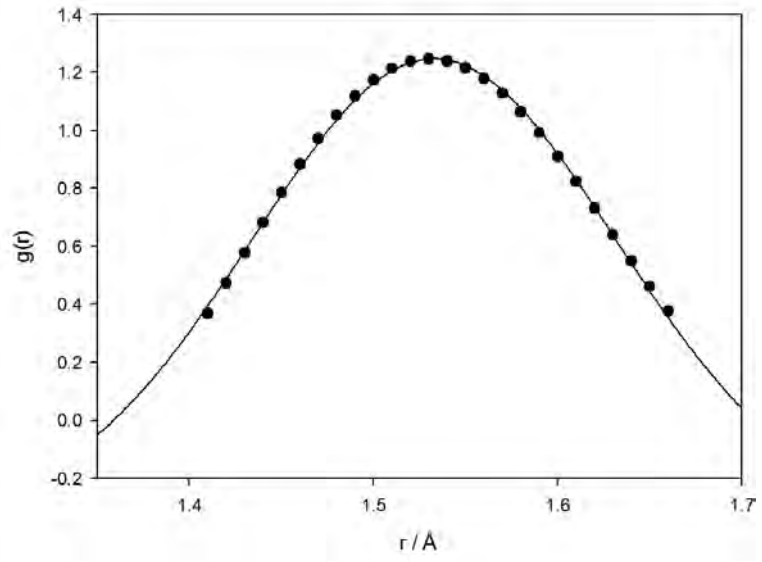

Figure 3.20: Least-squares fit of a Gaussian function to the peak in the RDF at ca. 1.54 Å

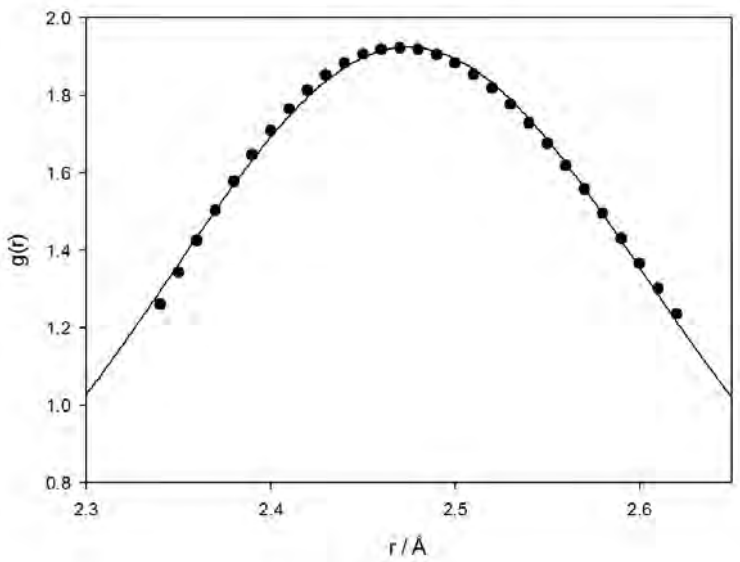

Figure 3.21: Least-squares fit of a Gaussian function to the peak in the RDF at ca. 2.50 Å

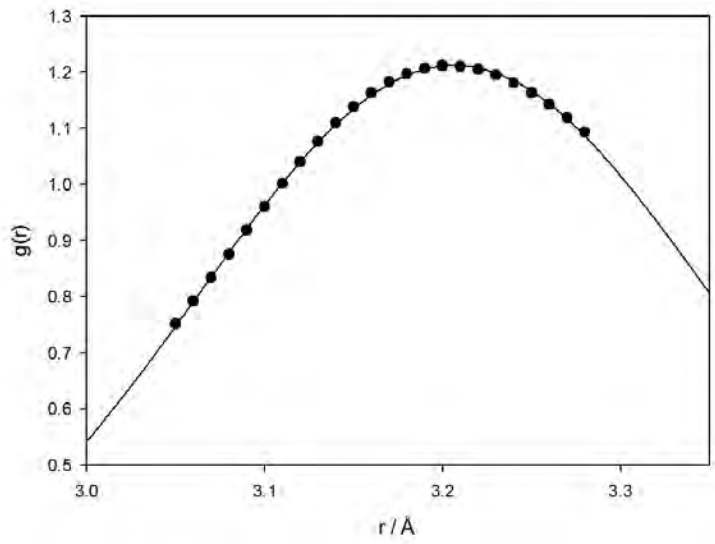

Figure 3.22: Least-squares fit of a Gaussian function to the peak in the RDF at ca. 3.20 Å

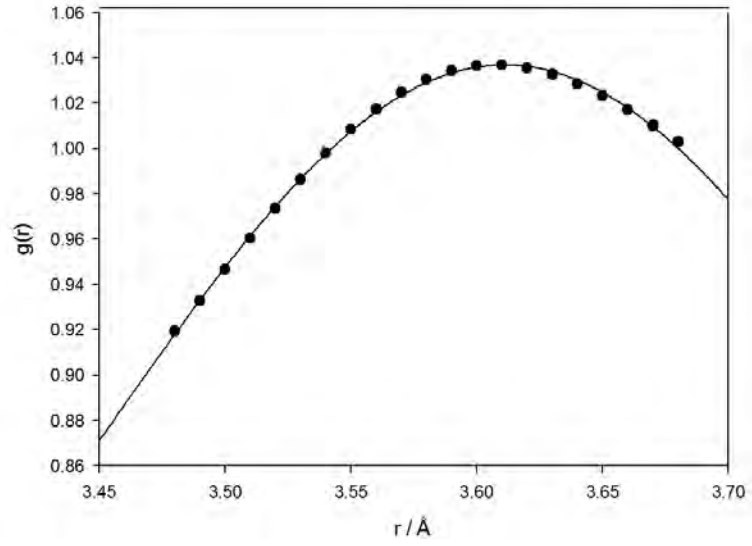

Figure 3.23: Least-squares fit of a Gaussian function to the peak in the RDF at ca. 3.62 Å

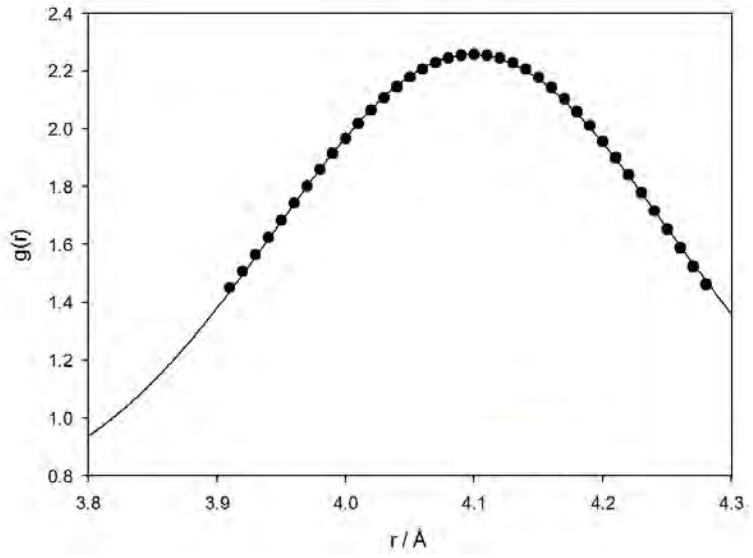

Figure 3.24: Least-squares fit of a Gaussian function to the peak in the RDF at ca. 4.10 Å

3.2.5 70.04 mol % Sr

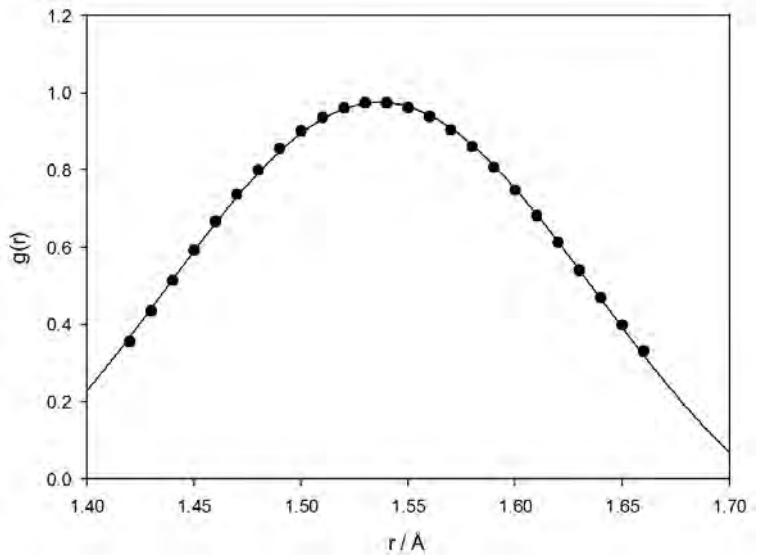

Figure 3.25: Least-squares fit of a Gaussian function to the peak in the RDF at ca. 1.54 Å

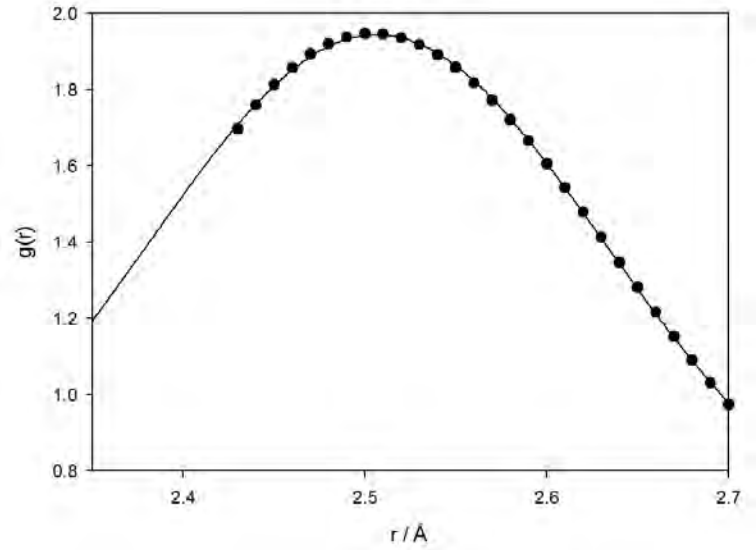

Figure 3.26: Least-squares fit of a Gaussian function to the peak in the RDF at ca. 2.50 Å

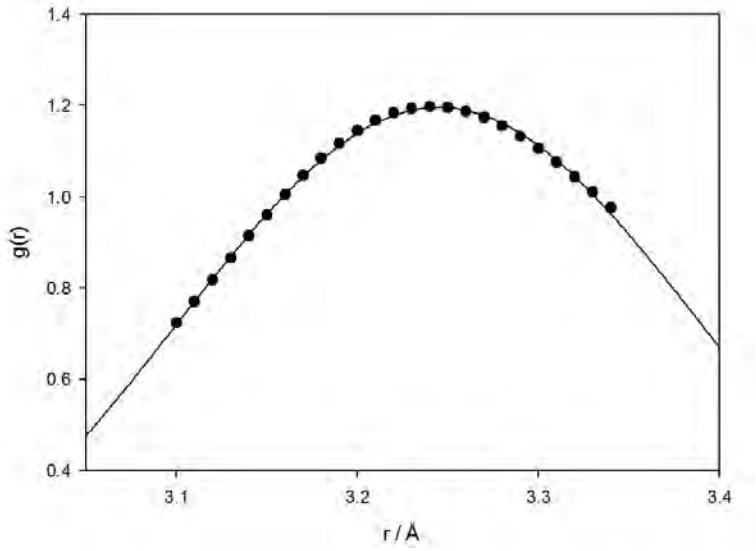

Figure 3.27: Least-squares fit of a Gaussian function to the peak in the RDF at ca. 3.20 Å

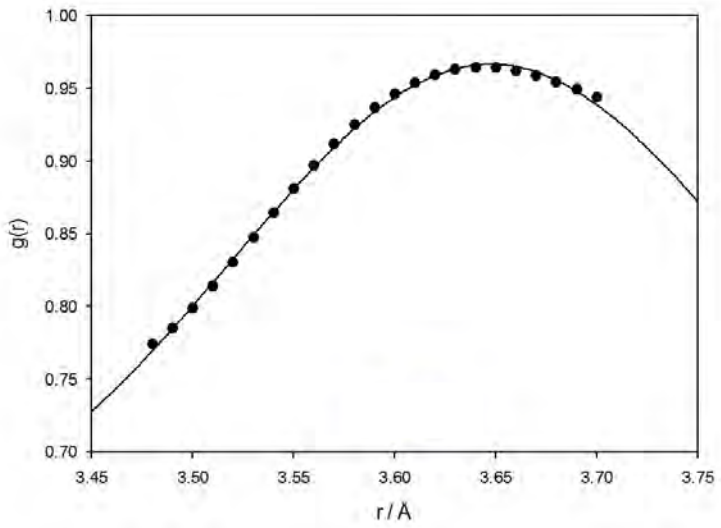

Figure 3.28: Least-squares fit of a Gaussian function to the peak in the RDF at ca. 3.62 Å

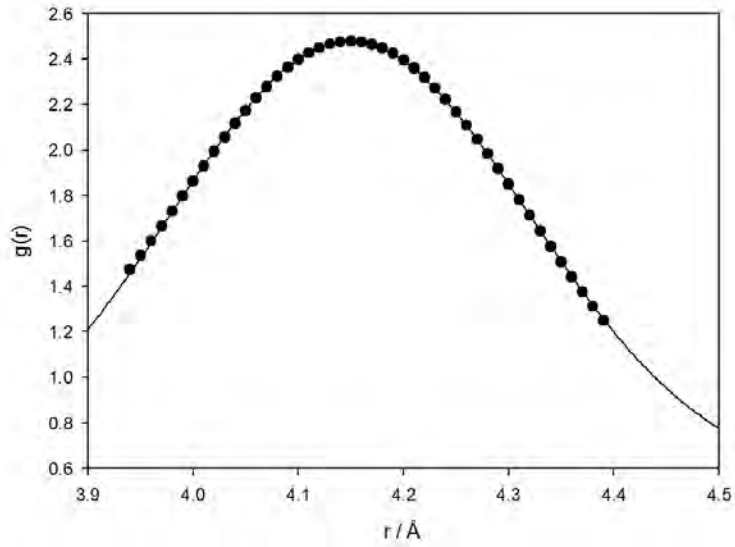

Figure 3.29: Least-squares fit of a Gaussian function to the peak in the RDF at ca. 4.10 Å

3.3 Peak Fitting Ca/Sr Fluorapatite (Microwave)

3.3.1 5.86 mol % Sr

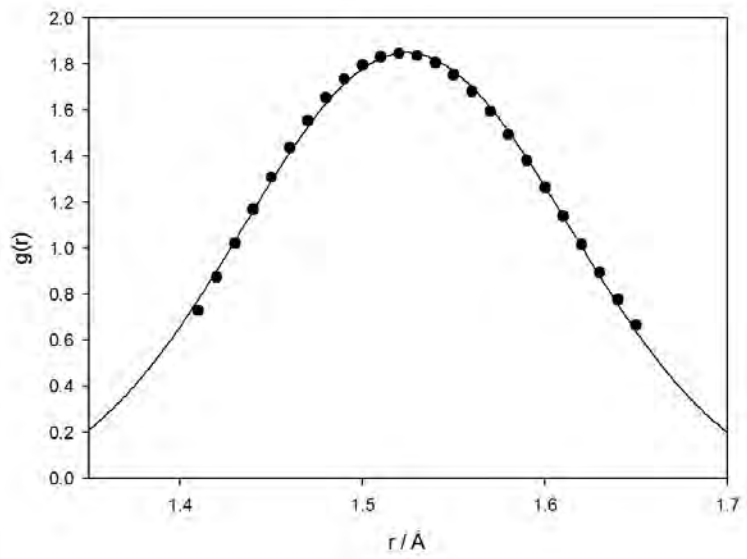

Figure 3.30: Least-squares fit of a Gaussian function to the peak in the RDF at ca. 1.54 Å

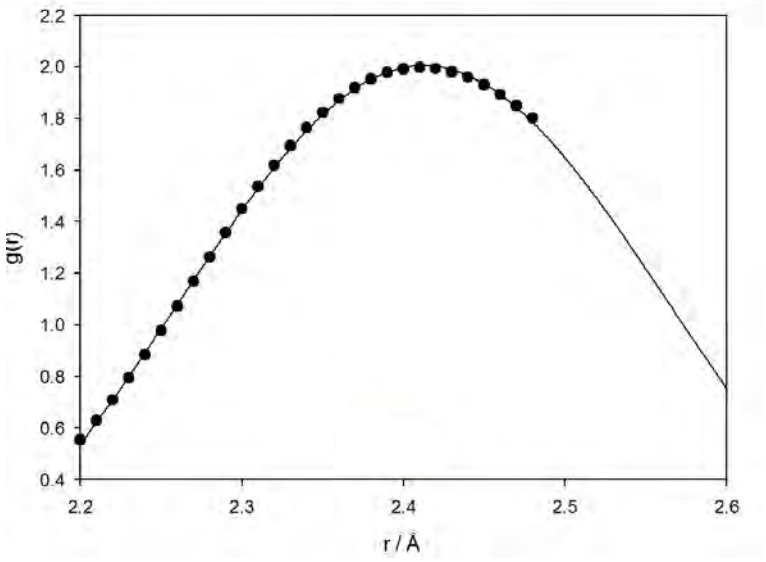

Figure 3.31: Least-squares fit of a Gaussian function to the peak in the RDF at ca. 2.50 Å

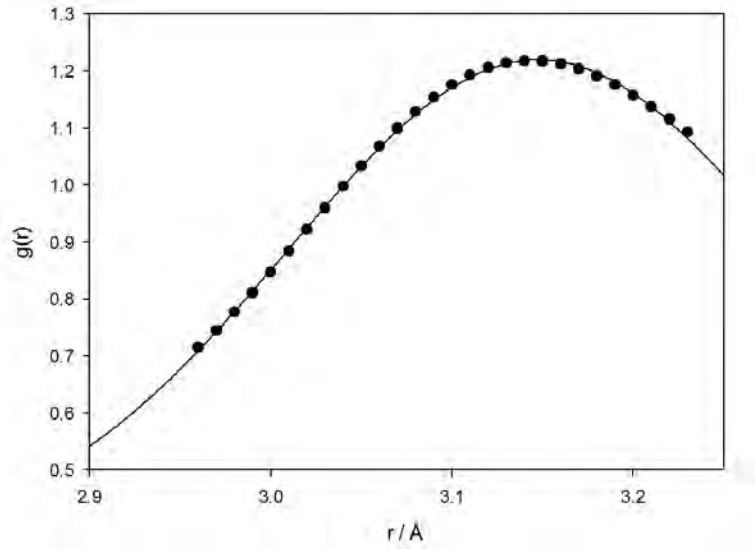

Figure 3.32: Least-squares fit of a Gaussian function to the peak in the RDF at ca. 3.20 Å

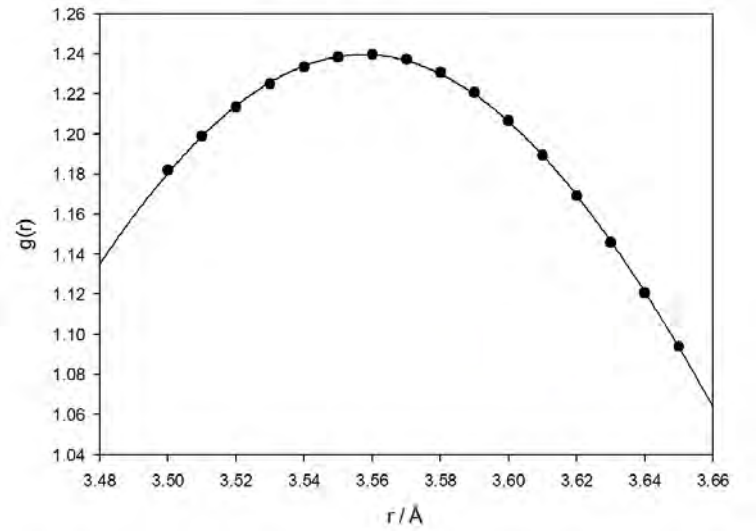

Figure 3.33: Least-squares fit of a Gaussian function to the peak in the RDF at ca. 3.62 Å

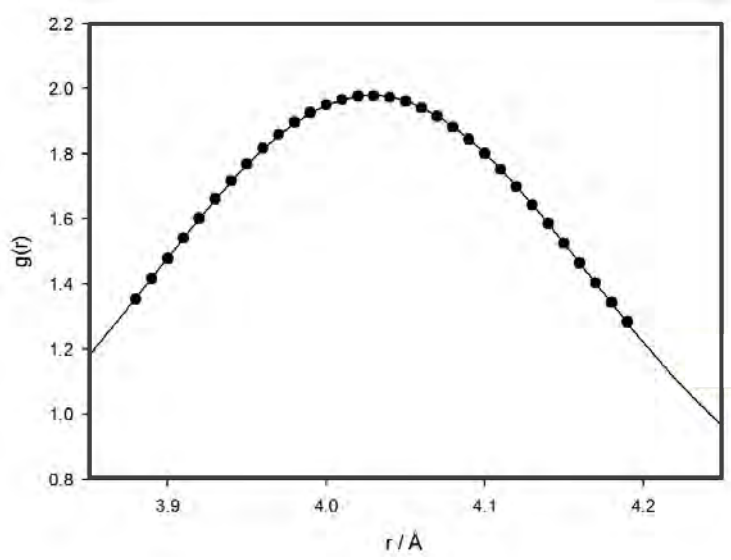

Figure 3.34: Least-squares fit of a Gaussian function to the peak in the RDF at ca. 4.10 Å

3.3.2 19.84 mol % Sr

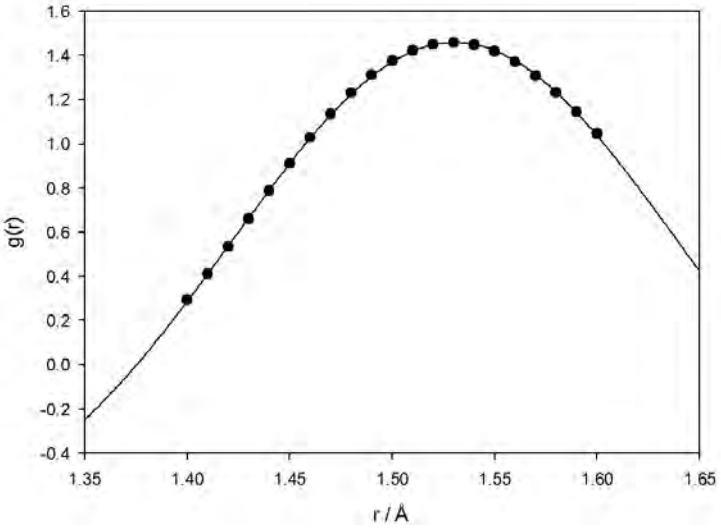

Figure 3.35: Least-squares fit of a Gaussian function to the peak in the RDF at ca. 1.54 Å

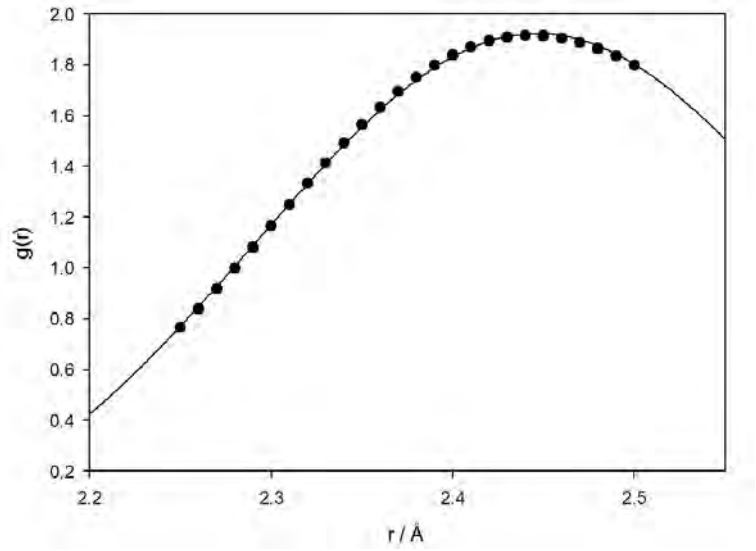

Figure 3.36: Least-squares fit of a Gaussian function to the peak in the RDF at ca. 2.50 Å

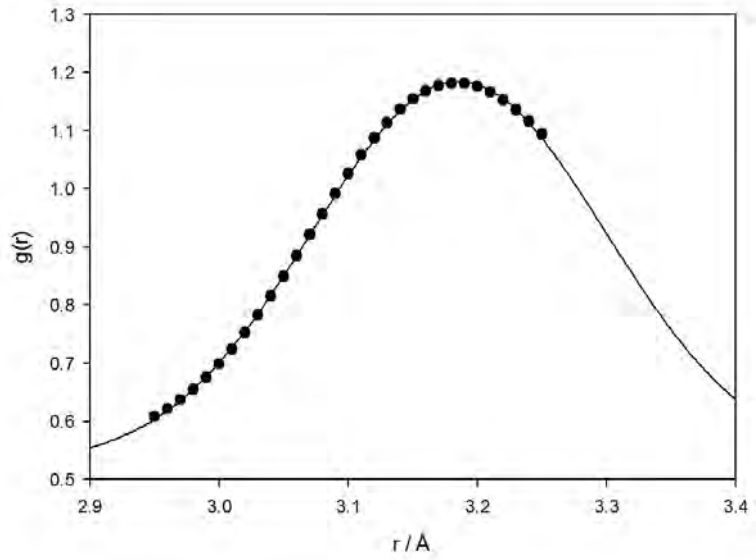

Figure 3.37: Least-squares fit of a Gaussian function to the peak in the RDF at ca. 3.10 Å

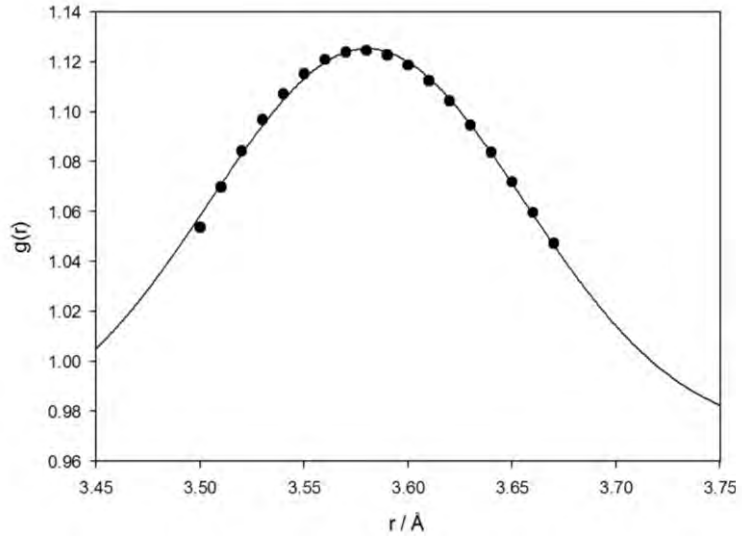

Figure 3.38 Least-squares fit of a Gaussian function to the peak in the RDF at ca. 3.62 Å

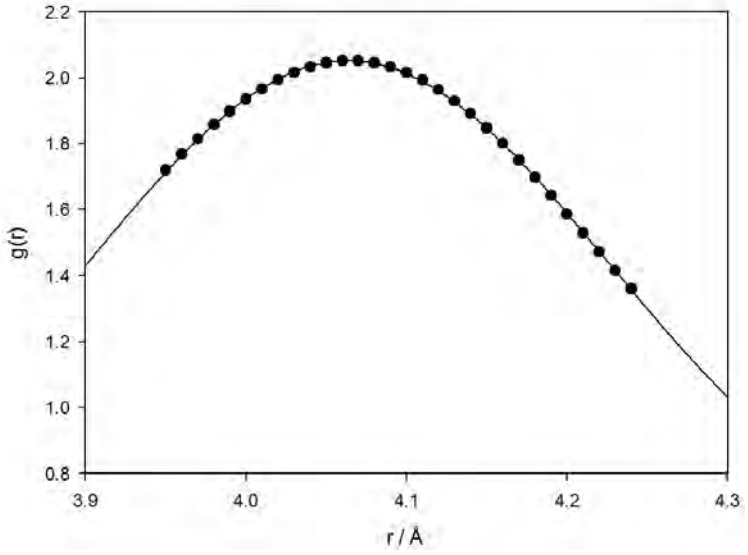

Figure 3.39: Least-squares fit of a Gaussian function to the peak in the RDF at ca. 4.10 Å

3.3.3 50.69 mol % Sr

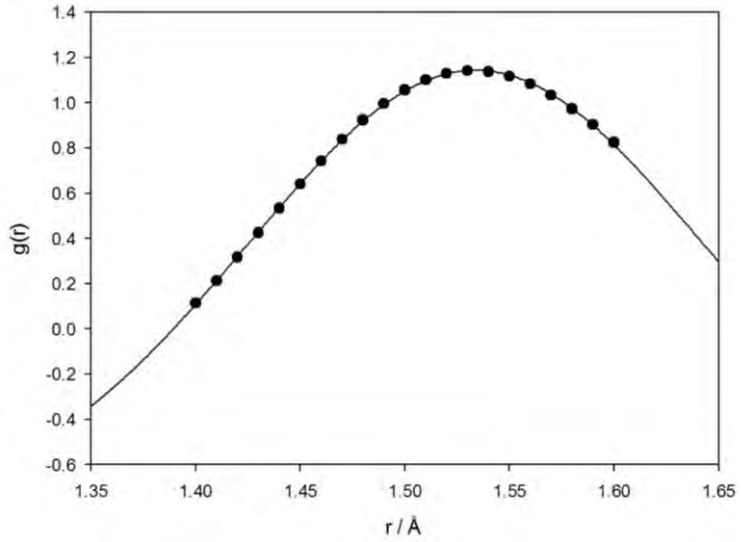

Figure 3.40: Least-squares fit of a Gaussian function to the peak in the RDF at ca. 1.54 Å

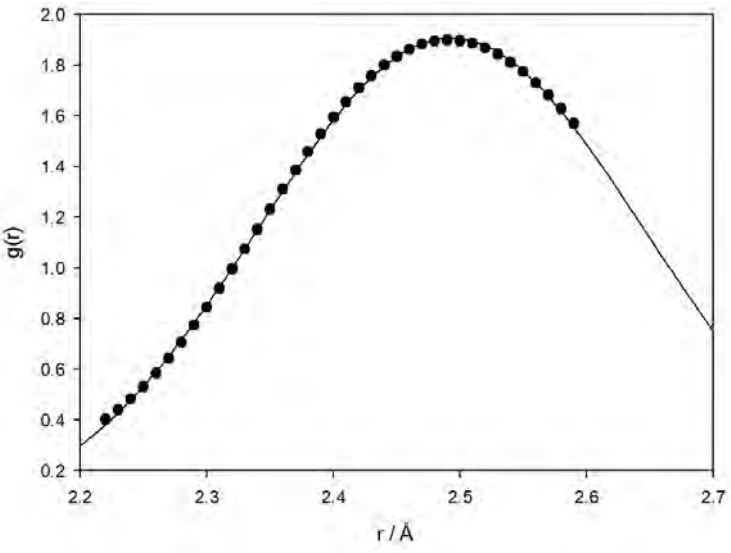

Figure 3.41: Least-squares fit of a Gaussian function to the peak in the RDF at ca. 2.50 Å

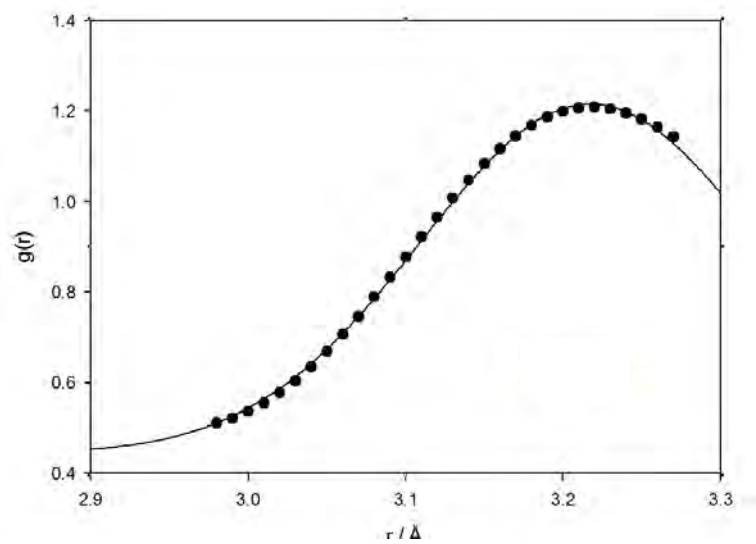

Figure 3.42: Least-squares fit of a Gaussian function to the peak in the RDF at ca. 3.20 Å

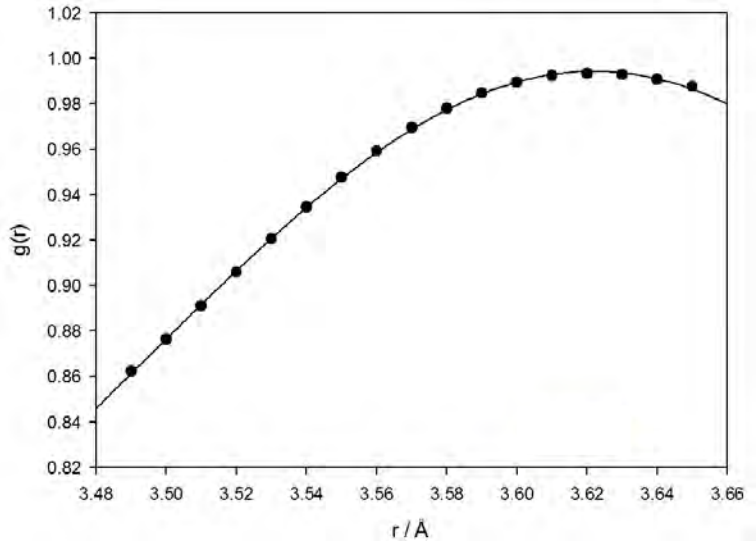

Figure 3.43: Least-squares fit of a Gaussian function to the peak in the RDF at ca. 3.62 Å

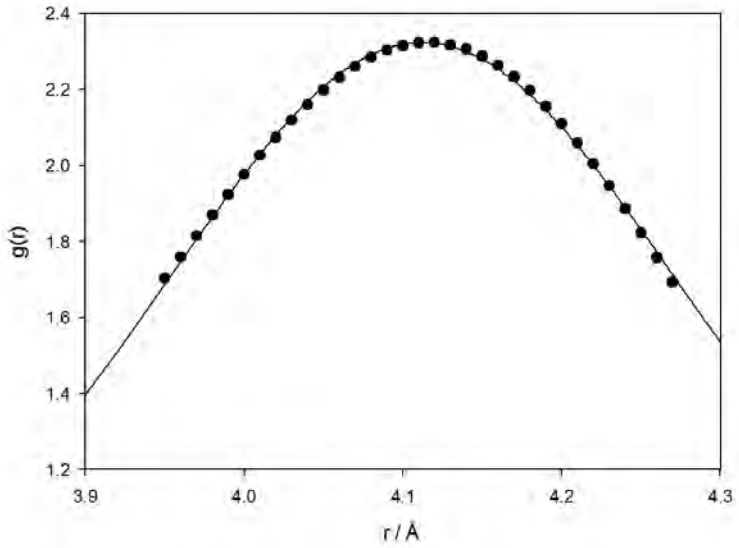

Figure 3.44: Least-squares fit of a Gaussian function to the peak in the RDF at ca. 4.10 Å

3.3.4 74.33 mol % Sr

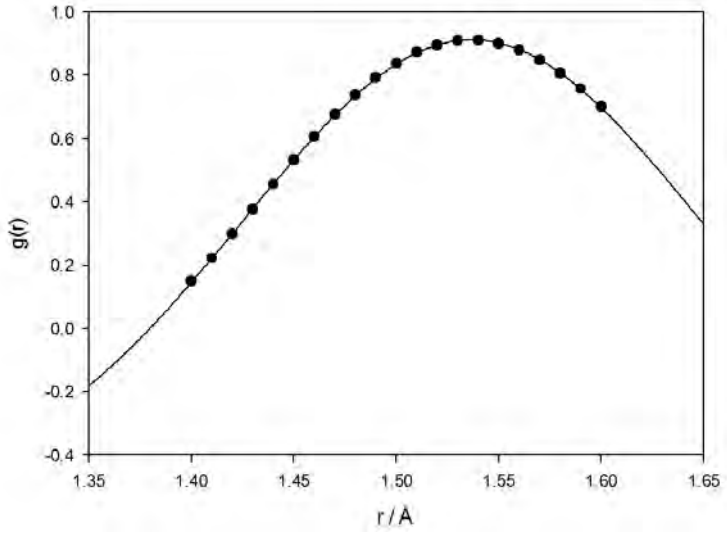

Figure 3.45: Least-squares fit of a Gaussian function to the peak in the RDF at ca. 1.54 Å

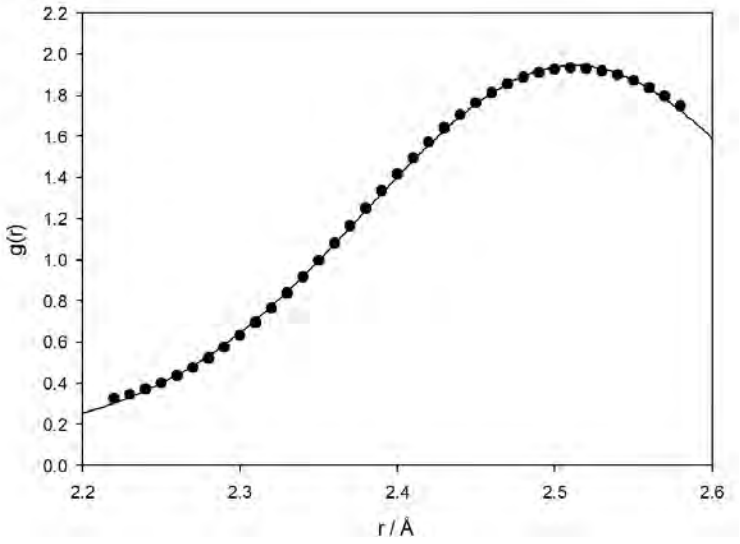

Figure 3.46: Least-squares fit of a Gaussian function to the peak in the RDF at ca. 2.50 Å

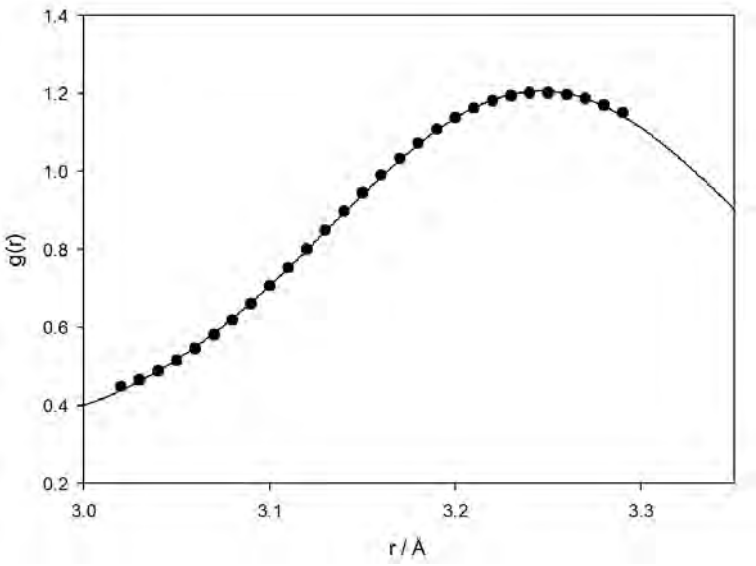

Figure 3.47: Least-squares fit of a Gaussian function to the peak in the RDF at ca. 3.20 Å

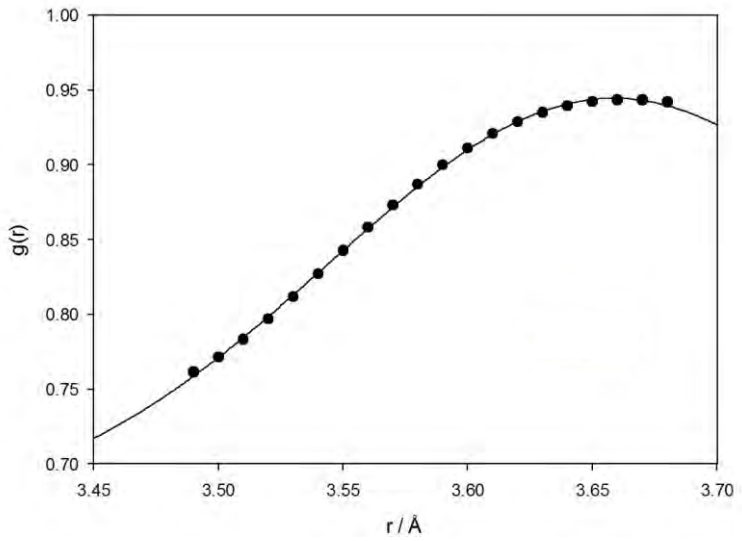

Figure 3.48: Least-squares fit of a Gaussian function to the peak in the RDF at ca. 3.62 Å

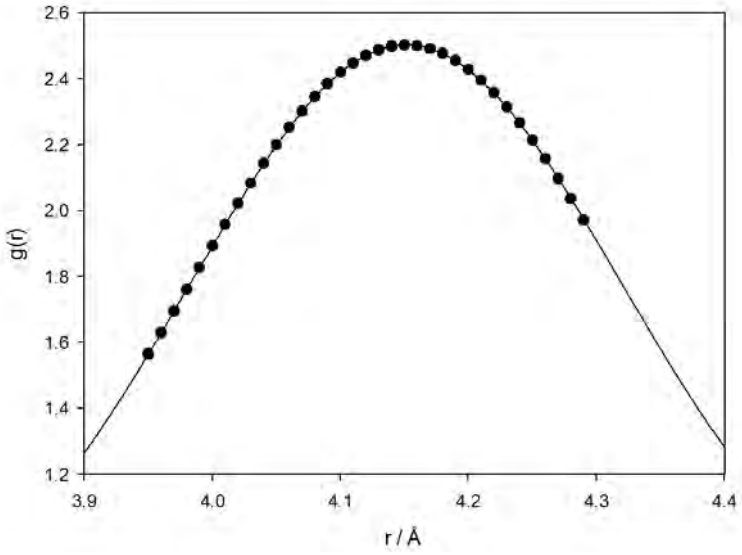

Figure 3.49: Least-squares fit of a Gaussian function to the peak in the RDF at ca. 4.10 Å